CENTRO INTERNACIONAL DE ESTUDOS
DE DOUTORAMENTO E AVANZADOS
DA USC (CIEDUS)

TESIS DE DOCTORADO

HYDRODYNAMIC INSTABILITIES COUPLED WITH COMPLEX CHEMICAL REACTIONS: CONTROL, CHARACTERIZATION, AND THEIR MODELING

DARÍO MARTÍN ESCALA VODOPIVEC

ESCUELA DE DOCTORADO INTERNACIONAL

PROGRAMA DE DOCTORADO EN CIENCIA DE MATERIALES

SANTIAGO DE COMPOSTELA

AÑO 2020

USC
UNIVERSIDADE
DE SANTIAGO
DE COMPOSTELA

DECLARACIÓN DEL AUTOR DE LA TESIS

HYDRODYNAMIC INSTABILITIES COUPLED WITH COMPLEX CHEMICAL REACTIONS: CONTROL, CHARACTERIZATION, AND THEIR MODELING

D. Darío Martín Escala Vodopivec

Presento mi tesis, siguiendo el procedimiento adecuado al Reglamento, y declaro que:

1) *La tesis abarca los resultados de la elaboración de mi trabajo.*
2) *En su caso, en la tesis se hace referencia a las colaboraciones que tuvo este trabajo.*
3) *La tesis es la versión definitiva presentada para su defensa y coincide con la versión enviada en formato electrónico.*
4) *Confirmo que la tesis no incurre en ningún tipo de plagio de otros autores ni de trabajos presentados por mí para la obtención de otros títulos.*

En Santiago de Compostela, 29 de diciembre de 2020

Fdo. Darío Martín Escala Vodopivec

USC
UNIVERSIDADE
DE SANTIAGO
DE COMPOSTELA

AUTORIZACIÓN DEL DIRECTOR / TUTOR DE LA TESIS

HYDRODYNAMIC INSTABILITIES COUPLED WITH COMPLEX CHEMICAL REACTIONS: CONTROL, CHARACTERIZATION, AND THEIR MODELING

D. Alberto Pérez Muñuzuri
D. Jorge Carballido-Landeira

INFORMAN:

Que la presente tesis, corresponde con el trabajo realizado por D. ***Darío Martín Escala Vodopivec****, bajo mi dirección, y autorizo su presentación, considerando que reúne los requisitos exigidos en el Reglamento de Estudios de Doctorado de la USC, y que como director de ésta no incurre en las causas de abstención establecidas en Ley 40/2015.*

En Santiago de Compostela, 29 de diciembre de 2020

Fdo. Alberto Pérez Muñuzuri

Fdo. Jorge Carballido-Landeira

USC
UNIVERSIDADE
DE SANTIAGO
DE COMPOSTELA

Así quedaron terminados los cielos y la tierra, y todo lo que hay en ellos. Al llegar el séptimo día, Dios descansó porque había terminado la obra que había emprendido.

Génesis 2:1-2

...Y en el octavo día dio comienzo una tesis... que hoy, afortunadamente, ha llegado a su fin...

Thus the heavens and the earth were finished, and all the host of them. And on the seventh day God finished his work that he had done, and he rested on the seventh day from all his work that he had done.

Genesis 2:1-2

...And on the eighth day a thesis began... which fortunately today has come to an end...

Quedaron así rematados o ceo e a terra e todos os elementos. Deus concluíu no día sexto a obra que emprendera, e o sétimo día repousou de todo o seu traballo.

Xénese 2:1-2

...E no oitavo día deu comezo unha tese... que hoxe, afortunadamente, chegou ao seu fin...

USC
UNIVERSIDADE
DE SANTIAGO
DE COMPOSTELA

Dedicado a
Mi Familia, Amigos,
Recuerdos y Creencias.

USC
UNIVERSIDADE
DE SANTIAGO
DE COMPOSTELA

Agradecimientos

Después de muchos años, de muchos experimentos, muchas horas invertidas, varias pandemias, tres planes de doctorado, incontable burocracia, permisos de residencia, muchas mudanzas, trámites, motivación, desmotivación, motivación de nuevo, algunas tristezas, muchas alegrías y un año 2020 para el olvido, me gustaría aprovechar esta sección para plasmar un poco más que simples frases formales. Después de todo, ya hace más de una década que llegué a este país y eso implica vivir cantidad incontable de experiencias y conocer muchísimas personas. Lamentablemente, esto es solo una pequeña sección de un trabajo más grande y por lo tanto, no puedo ir con los detalles que quisiera (que porque si no los agradecimientos serían aún mayores que la tesis en sí).

En primer lugar, quiero agradecer a mi familia, que sin su apoyo esto hubiese sido imposible. Y cuando digo familia no me refiero a toda la gente que comparte sangre con uno, sino a la verdadera familia. A mi mamá Cristina, que me ha dado la posibilidad de que pudiera estudiar, inclusive ante situaciones extremadamente difíciles que nos tocó vivir. Me ha acompañado en todo este tiempo a pesar de la distancia y fue la que primero plantó esa pequeña semilla para que le "*tomara el gustito a la investigación*". A mi hermano Julio, que si bien el fue el pionero en eso de buscar un mejor destino para su vida, siempre hemos estado unidos. Tal vez no hablamos todos los días, pero tampoco hace falta porque siempre estamos. A mi abuela Norma con la que he compartido momentos y charlas hermosas acompañadas de un buen vino durante toda mi carrera. A mis tías por siempre estar y acompañarme a la distancia y sobre todo a mi mamá presencialmente. A mi primo Daniel por siempre estar y compartir tantos buenos momentos juntos entre *cocodrilos mutantes y garras asesinas* y a mi prima Ángela (la Peke) por ser la única que puso el pecho en los momentos más complicados y por siempre sacarme una sonrisa. A mi madrina, Liliana, y toda su familia, por el constante apoyo. Por estar presente y ayudarme a mí como a mi mamá en los cambios de estos últimos años.

También quiero aprovechar a recordar a los que ya no están más físicamente, pero que viven eternamente, por lo que representaron para mi vida. A la memoria de mi padre, que era un enamorado de la ciencia (y de la ficción también). A la memoria de mi abuela Kristina, que también tuvo que dejar su casa muy joven para buscar una vida mejor y ha sido un ejemplo de vida e integridad.

A mis amigos Argentinos, con los cuales he podido demostrar que la distancia no importa: Marcos, Leandro, Maxi y Pablo, Mariana, la Galle y Cintia. A Lucas y su familia que me han dado el privilegio de ser padrino de Benjamín. A Roberto y Raúl, los discípulos del Sensei Machado, por todas las risas durante este tiempo.

A mis amigos de la Universidad Nacional de Quilmes (UNQUI), mi primer *Alma Máter*: Lucas, Belén, Cecilia, Aldana, Luz, Betina (mi hermana postiza), Ástor, Gonzalo, Dieguito, Pelu, Vanina, Cintia, Dani Albanese, Gabi. Gracias por acompañarme en todo este camino.

También quiero agradecer a toda el área de matemática de la UNQUI, lugar que fue el gérmen del gusto por las matemáticas y donde aprendí la pasión por enseñar y a disfrutar de ello. A Claudia Pellet, María Inés Baragatti, Cristina Cossutti, Patricia Blondheim, Matías Cerrudo, Mariana Suárez. Quiero agradecer muy especialmente a Ernesto Aljinovic, ya que él fue el primer ejemplo que tuve de biotecnólogo-matemático, y que si no hubiese sido por la monografía de geometría fractal, definitivamente, hoy este trabajo no existiría. A Pedro Pascual, porque fue con él con quien hice el *click* que me hizo ver que la matemática no es algo imposible de entender, y a Nicolás Coleff, que si bien al principio no le gustaba la idea de que los "*biólogos*" hiciéramos cursos extra de matemática, se dio cuenta de que todos tenemos algo que aportar. También me gustaría agradecer especialmente a Diana Roncaglia, por su confianza y por ser ser el nexo que ha hecho posible que hoy esté aquí y a Juliana Palma, por haberme dicho a quién tenía que consultar sobre las reacciones oscilantes. Gracias de corazón.

Como tampoco hubiese existido si no hubiese sido por mis directores de tesis Alberto Pérez Muñuzuri y Jorge Carballido-Landeira. Gracias por su constante apoyo en este trabajo y por la confianza depositada desde el primer momento, aunque haya costado un poco arrancar. Soy consciente de que las cosas a veces se me van de las manos y más de alguna vez les habré puesto los pelos de punta, pero también estoy seguro de que todos hemos aprendido un poco con este trabajo. Gracias por darme esta oportunidad.

Esta tesis tampoco hubiese existido sin la financiación recibida durante todo el trabajo, tanto de la Xunta de Galicia mediante las "Axudas de apoio á etapa predoutoral do Plan Galego de Investigación, Innovación e Crecemento 2011-2015", como al instituto CRETUS, sobre todo en este último tiempo. Quiero agradecer también la financiación aportada por el grupo de Física No Lineal de la USC.

Gracias también por supuesto al GFNL, ya que después de tantos años es normal que haya tenido muchos compañeros en el laboratorio. Yo lo denomino temporadas, como las series, porque encuentro tres especialmente muy marcadas: De la primera temporada a Dani Cuiñas, Jorge (¡sí!, mi codirector, pero que en esa época era doctorando), Alberto el cordobés, Alexandra, Florian, Alexandre, Carlos y Xaco. Mención especial para estos últimos dos con los cuales más me ha tocado compartir tiempo: con Carlos, churrascos y sistemas operativos, y con Xaco, aburrimiento cuando éramos los dos únicos en el laboratorio. En la segunda temporada a Dani Garaboa, el Teniente General Jorge Eiras, Sabela, Breo, Miguel, y en la tercera temporada a Mariamo, Sara, Martín, Damián, Ana, Ismael y a la última incorporación, Néstor (¡ánimo con el Viscous Fingering!). Especialmente de esta última temporada quiero agradecer a Irma, que es mi compañía, apoyo moral y sentimental en este último tiempo y con la que hemos aprendido y crecido juntos. También agradecer a los otros profesores del grupo, Vicente Pérez (Padre e Hijo) y Gonzalo Míguez.

I want to thank Professor Anne De Wit for giving me the opportunity to learn and enjoy

during my short stay in Belgium. I also want to thank all the amazing people that I met from the Nonlinear Physical Chemistry Unit of the Université libre de Bruxelles, that shared time with me and made me feel extremely comfortable: Lorena, Marcello, Doménico, Igal, Yannick, Carelle, Florence, and Laurence. I also want to thank my eastern friends: Itana, Ivelina, and my British friends Aoife, Lucy y Katy for the good moments.

También agradezco a la gente de la facultad de física: A Félix (aunque sé que le da grima aparecer en agrecimientos...), por todos estos años de proyectores, dietas, press banca, *Trini's everywhere*, y sobre todo las Fiestas Hortera. Gracias al Dr. Aaron por toda la buena onda construida y por todas las charlas de café del McDonald's a las tantas de la noche. A María Villanueva y todo su grupo por aguantarme tanto tiempo en el reómetro y ayudarme para que pudiera hacer todas las medidas que necesitaba. A Conchi, por las eternas charlas, los incontables cafés y las súper "*conchicenas*". A Pablo Taboada por su buena disposición durante todos estos años de trámites y adaptaciones.

A mis amigos del máster, Alex y Quela, con los cuales hemos compartido hermosos momentos en todo este tiempo y siempre han estado presente. A mi tutora, Elena Vázquez Cendón, por la paciencia durante en el proceso de hacer el TFM, y por preocuparse por el estatus de este trabajo cada vez que nos cruzamos por la calle.

Un agradecimiento especial para los dos argentinos que llegaron antes que yo: uno es Diego Ferrero, el compatriota que vino a estas tierras un poco antes que yo y con el cual fuimos mutuos soportes morales. Gracias por todos esos momentos y aguantarme durante todo este proceso. Desde que nos pasábamos un fin de semana en la UNQUI haciendo docking de proteínas, hasta los llantos por amores frustrados. Sos una persona invaluable en mi vida y espero que en un futuro podamos colaborar en algo, así recordamos esos buenos momentos científicos. El otro es Mariano Ribas, amigo desde el primario (en el Perpetuo Socorro de Quilmes) desde tercer grado y un compañero inestimable que por esas cuestiones de la vida había llegado a Santiago unos años antes que yo. No me voy a olvidar nunca el sabor del primer "*Pulpo a Feira*" que probé en el 42 al segundo día de haber llegado. Te admiro enormemente como profesional y como persona, y te agradezco todas las charlas y cañas que compartimos juntos. Espero que algún día podamos hacernos una escapada a algún lado. Aprovecho este espacio para promocionar (gratuitamente) sus locales: La parrillada (en Ames) y tapería Milongas® (en Santiago) y O Mesón 42 (en Rua do Franco). ¡Si alguien está leyendo esto, vaya a tomar algo ahí y pregunte por Mariano de mi parte!

A mi hermano del alma, Sebastián, a Rocío, Belinda e Inti, por ser mi familia en en esta tierra. Realmente si no me he sentido solo aquí, fue por haberlos conocido a ustedes. Gracias por hacer un pequeño hueco en su hogar. Además, estaré infinitamente agradecido por permitirme ser el pardino de Belinda.

A las personas que me hay ayudado a forjar la mente y el cuerpo, y por lo tanto a madurar como persona: a Manchy, que con sus enseñanzas he aprendido a poder controlar mis emociones y me dio las herramientas para poder buscar muchas respuestas. A Jacobo y Pilar, por ser los que me ayudaron a afrontar la realidad una vez pasada la novedad y que me hicieron poner los pies en la tierra en más de una ocasión, y a Jose y su equipo que fueron los

que arreglaron más de una vez la natural respuesta de mi cuerpo al estrés de hacer este trabajo.

Quiero agradecer también a los Doguillos, simplemente por ser criaturas maravillosas que más de una vez me han sacado una sonrisa, y con sus locuras me han dado ánimos para no bajar los brazos. El lector de esta tesis podrá encontrar alguno que otro escondido a lo largo del texto.

Hablando de Doguillos, no puedo no agradecer a Isa (o Isus, alternativamente). Gracias por estar todos estos años acompañándome y aguantándome durante todo este largo proceso. Hemos pasado juntos momentos muy alegres y algunos otros difíciles también, pero siempre hemos estado al pie del cañón y espero que así sea por muuuuuuuchos (léase con tono de vaquilla) años más. ¡Ah!, y si algún día tienes algún problema, no temas, porque... "Lord Doguillo, el Cerdicornio, y todos los demás seres cornios... te... defenderán".

También quiero agradecer a todos los amigos de Doguillo, en especial a Furancho, Toca, Manolo, Ricky, Tiza, Canela y Lola, y por supuesto a sus humanos: María, Natalia, Juan y Luis, porque en estos últimos años han sido una inestimable compañía, sobre todo en esas noches frías en los soportales de Fonseca.

Al sitio que fue mi hogar durante la mayoría del tiempo que he estado aquí, el Colegio Mayor Fonseca, el cual tuve que dejar por las regulaciones derivadas de la COVID-19. Aquella habitación 421 que me deja innumerable buenos recuerdos, amigos y anécdotas. No me puedo olvidar de los buenos momentos que pasé junto a la troop que conocí en las novatadas: Pablo (me debes un gorrito), Míriam, Mario, Bea, Alaine (la próxima... *puenting*), Antía, Eli, Raquel, Leti, Javi Yépez, Gemma. También a la gente que fui conociendo en la cocina y con la cual forjamos una linda amistad: mi hermano italiano Claudio, Ana y Eustolia y Aziza, Erika, Mayra, Sonia. Imposible olvidarme de Chus, siempre dispuesta a ayudarme en lo que necesitaba. A Juanjo, por todas las charlas nocturnas. A Juan y a Jose por el excelente trato y todos los cafés "*bendecidos*" de los viernes a la noche, y a Anxo, por estar siempre a disposición por lo que hiciera falta.

Finalmente quiero agradecer a España y a su gente, por acogerme y permitirme ser un ciudadano más de este hermoso país. Independientemente de toda su burocracia, le estoy eternamente agradecido a esta tierra por todo lo que me dio en todo este tiempo. A Galicia, por dejarme ver estos hermosos paisajes (más allá de la lluvia), y por dejarme crecer tanto profesionalmente como personalmente (que fue lo más importante). Yo nací en el Centro Gallego de la Ciudad de Buenos Aires, así que se podría decir que estoy predestinado a ser un poco gallego desde siempre.

¡GRACIAS!

Santiago de Compostela, Diciembre de 2020

Darío

USC
UNIVERSIDADE
DE SANTIAGO
DE COMPOSTELA

USC
UNIVERSIDADE
DE SANTIAGO
DE COMPOSTELA

Contents

USC
UNIVERSIDADE
DE SANTIAGO
DE COMPOSTELA

Summary

This thesis presents the work realized in the Non-Linear Physics Group of the University of Santiago de Compostela. This work introduces an interdisciplinary study of systems created from coupling hydrodynamic instabilities in Hele-Shaw cells and complex chemical reactions.

Objective and State of the Art

The main objective of this thesis is to find a nexus between two different fields: On the one hand, the hydrodynamic instabilities, and on the other hand, the extensive world of complex chemical reactions. Inside the field of hydrodynamics, this work will study a more specific type of instabilities known as fingering instabilities. These instabilities occur when a fluid with low mobility is displaced by a fluid with high mobility [45, 44, 93, 168]. The mobility can be affected by the viscosity, density, surface tension, or temperature of the fluid. The main characteristic of these instabilities is that they exhibit well-defined patterns similar to fingers, that occur during the fluid displacement [45].

The fingering phenomenon was observed in many fields of science and industry. Some examples are:

- Enhanced Oil Recovery (EOR). In this case, fingering occurs during the oil extraction process, when water is used to displace the more viscous oil. This phenomenon directly affects the efficiency of the displacement and it is detrimental to the recovery process [132, 206, 41, 21, 207, 210].

- Hydrogeological phenomena. Many studies predict the occurrence of saline fingers within the transport of subsurface aquifers. These types of fingers are observed when the colder and more saline seawater makes contact with fresh water. The differences in salinity and temperature produce a characteristic fingering known as salt fingers. This process favors nutrient oxidation in freshwater transport [111, 200, 171, 76].

- In chromatographic processes. In this separation technique, the components of a mixture are separated when the solution passes through a porous matrix. It has been demonstrated the occurrence of viscous fingering when a viscous sample is eluted using a less viscous solvent. Similar to the EOR case, this process is detrimental for the extraction [173, 32, 42, 198, 166].

However, this work will be more focused on those instabilities produced in experimental devices known as Hele-Shaw cells [89]. These cells are made of two parallel plates separated by a very small gap. This device allows studying the fingering phenomenon in a controlled and

relatively easy manner. The flow inside a Hele-Shaw cell is identical to the flow in a porous medium. Therefore, studies performed on such devices can be representative of more complex systems.

Fingering instabilities in Hele-Shaw cells were and are extensively studied and characterized for decades. The first studies were focused on the destabilization produced by non-reactive and immiscible displacements. These studies demonstrated the major role played by factors like surface tension and diffusivity [45, 25, 44, 9].

More recently were studied systems driven by chemical reactions, in which formerly stable systems were destabilized by physical-chemical processes coupled to the fluid displacement [45, 25, 44, 9].

The intrinsic complexity of the study of chemo-hydrodynamic instabilities has been increased over the years. More elementary processes like neutralization reactions and chemical precipitation were extensively studied and characterized showing a broad variety of behaviors. In such systems, the instability is related to the change in the mobility ratio produced by changes in the viscosity or density of the fluids involved, or the permeability of the medium [141, 138, 137, 139, 73, 65, 9, 176].

The complexity of chemo-hydrodynamic instabilities can be substantially incremented by the inclusion of the so-called complex chemical reactions. These types of reactions are chemical processes that occur in several elementary steps with at least one reaction intermediary [116]. There are a few examples of chemically driven instabilities coupled with complex chemical reactions, such as autocatalytic processes [101, 49, 96].

In the thesis context, even more complex reactions will be considered to find couplings with hydrodynamic instabilities: The Belousov-Zhabotinsky (BZ) [18] reaction and pH-shifting reactions [106, 108, 107, 159, 160, 145].

The BZ reaction is one of the most well-known chemical oscillators. It is a redox process in which the reaction intermediaries oscillates in time due to inhibitor/activator dynamics [82]. The oscillations can be followed by the changes in the redox indicator (if the system is homogeneously stirred), or by spatio-temporal pattern formation in spatially extended non-homogeneous systems. However, there are several variations of this reaction. In this particular work, the BZ-CHD was considered as the main alternative for the classical BZ reaction. In this reaction, the organic substrate of the original formulation is replaced by CHD (1,4-Cyclohexanedione) [113, 112, 187, 188, 190, 114]. This modification in the original recipe presents several advantages, however, the most significant one is that no carbon dioxide is generated as a secondary product.

On the other hand, the pH-shifting reactions are chemical processes in which the pH of the system changes from a basic (or acid) state into an acid (or basic) state. This change is produced by the reaction intermediaries [107, 108, 159, 153, 145]. There exist inorganic pH-shiting reactions, which are also redox processes and can exhibit oscillations in some experimental conditions. However, due to their redox nature, these systems can not be coupled with organic elements such as polymers of drug delivery carriers.

More recently, organic pH-shifting reactions were developed. Contrary to the inorganic ones, these are not redox processes, and therefore, there are less aggressive with organic molecules [106, 108, 107]. These reactions also show oscillations and they were well characterized and studied.

In this work, two different organic pH-shifting reactions will be used, the Formaldehyde-Sulfite (FS) [212, 106, 213] and the Formaldehyde-Sulfite-Gluconolactone

(FSG) [108, 107] reactions.

Therefore, the objective of this thesis is to find experimental couplings between hydrodynamic instabilities in Hele-Shaw cells with the aforementioned complex chemical reactions. More specifically, the following systems will be addressed:

- **System 1**: Coupling between the BZ-CHD reaction and a buoyancy-driven hydrodynamic instability in a vertically oriented Hele-Shaw cell.
- **System 2**: Coupling between the FS reaction and viscous fingering instability in a horizontally oriented Hele-Shaw cell.
- **System 3**: Coupling between the FSG reaction and viscous fingering instability in a horizontally oriented Hele-Shaw cell.

In this sense, the main objective is to find synergies between the hydrodynamic and chemical processes, in which both phenomena occur with similar timescales. All systems will be experimentally studied, completely characterized, and numerically modeled.

Thesis Structure

The present work is divided into three parts. Each part includes its introduction, a methods chapter, an experimental results chapter, a numerical results chapter, and a general discussion.

Thus, **Chapters 2**, **6**, and **10**, are the methods chapters of **Parts I**, **II**, and **III** respectively. The experimental methods chapters include all the information regarding chemical formulations, protocols, and explanations concerning the experimental setups. In the numerical sections are included general descriptions such as numerical domains, software and solver configurations, simulation parameters, etc. However, and to facilitate the lecture, the specific model developments are included in their corresponding numerical results chapter, as they depend on experimental results.

All basic concepts are given in the introductory **Chapter 1**. This is a general chapter in which are explained all the fundamentals needed to properly understand the thesis subjects.

Part I begins after the introductory chapter. This part presents the coupling between the BZ-CHD reaction with a buoyancy-driven hydrodynamic instability in a vertically oriented Hele-Shaw cell.

Chapter 3 shows the experimental results obtained from System 1. The results are studied qualitatively and quantitatively, analyzing the effects produced by changes in the density ($\Delta\rho$) and the excitability (ε). The effects produced by these two parameters were studied coupled and uncoupled and were characterized by the use of measuring observables such as the chemical period (T_C), the hydrodynamic wavelength λ_H, the chemical t_{ind-C}, and hydrodynamic t_{ind-H} induction times.

Chapter 4 presents a detailed chemical analysis realized to unveil the mechanism of the instability observed in Chapter 3. This study was performed by an extensive series of control experiment and chemical characterization that made possible to discover the main actor in the chemo-hydrodynamic coupling.

Chapter 5 presents the numerical model and results obtained by utilizing the discoveries of **Chapter 4**. The numerical model was created by using the existing kinetic models. Simulations

were done for both, the homogeneous and the spatially extended systems. The results were analyzed identically to the experimental results.

Part II begins after **Chapter 5**. In this case, the study is about the coupling between the FS pH-shifting reaction and viscous fingering hydrodynamic instability in a horizontally oriented Hele-Shaw cell.

Before the study of the instability, **Chapter 7** presents the development of a chemical system in which the pH reaction dynamically affects the viscosity of a solution. This is achieved by coupling the aforementioned pH-shifting (FS and FSG) reactions with a pH-sensitive polymer Poly(Acrylic Acid). Both couplings were characterized by rheological and analytical techniques, measuring observables such as the viscosity and pH jumps ($\Delta\mu$ and Δ pH respectively), the induction time, and the temporal dynamics. Finally, this chapter introduces some alternatives to the pH-viscosity coupling and demonstrates the dynamic mechanism.

In Chapter 8, all the previous developments are spatially extended into a radial Hele-Shaw cell to create a chemo-hydrodynamic viscous fingering instability. The system is studied qualitatively and quantitatively by analyzing the effects produced by the most important parameters like the flow rate (Q) and the concentrations of the chemical species. The pattern morphology is studied by calculating the circularity (C), and the Schlieren technique is used as a supplementary technique to understand the instability mechanism.

Chapter 9 shows the numerical results of the systems presented in **Chapters 7** and **8**. In the first sections, the existing kinetic models of the FS and the FSG reactions are adapted to the experimental context by adapting the parameters obtained from the experiments. The results are analyzed analogously to the results presented in **Chapter 7**. The next sections introduced the reaction-diffusion-convection model of the system presented in **Chapter 8**. The results are analyzed measuring the numerical circularity similar to the experimental case, showing a more than an acceptable agreement between simulations and experiments.

Finally, **Part III** begins after **Chapter 9**. This part will study the coupling between the FSG reaction and viscous fingering instability. This study presents to experimental situations derived from the same system. Both cases are obtained by only exchanging positions between the displacing and displaced solutions. In the so-called Case I, it will be studied complex pattern generation in hydrodynamic stable conditions. In Case II, it will be studied viscous fingering stabilization through physical-chemical processes.

Thus, **Chapter 11** studies the dynamics of both experimental cases. Both situations were studied descriptively and quantitatively for reactive and non-reactive conditions. The quantitative analysis was performed by measuring the circularity, demonstrating the major influence of the flow rate and the chemistry. In both cases, the injection flow rate was chosen as the main analysis parameter.

Chapter 12 focuses on understanding the mechanisms of the observed phenomena. This is achieved by means of several control experiments in which the chemical formulations were carefully modified to understand the effect of each species in the system behavior.

Finally, **Chapter 13** presents the numerical reaction-diffusion-convection model and results of the systems cases presented in Chapter 11. The numerical results are analyzed similarly to the experiments, showing a very good agreement between them.

After **Part III**, a series of Appendices are shown:

Appendix A presents all the recipes of stock solutions used in this work. Also, the specific mixtures used in each part are detailed.

Appendix B presents the experimental and numerical results of the reaction-diffusion

system derived from Part I. These results were important for the development and the understanding of the mechanism proposed in such part. However, they are included as supplementary information. This appendix studies the occurrence of spatio-temporal patterns in 1D capillary and 2D agarose systems.

Appendix C presents the methods and protocols used for image processing experimental and numerical results. These methods are fundamental to obtain quantitative information. The appendix is divided into the methods used for each part.

Appendix D includes information and supplementary calculations that were used in the development of the main chapters. These results were not included in the main text because their contribution to the work is not significant.

Finally, **Appendix E** shows the uses-permission for all those results taken, modified or derived from publications protected by copyrights. These permissions are included in order to avoid any legal issue related to plagiarism or self-plagiarism.

USC
UNIVERSIDADE
DE SANTIAGO
DE COMPOSTELA

Resumen

La presente memoria resume el trabajo realizado en el Grupo de Física No Lineal de la USC. En la misma se expone el estudio tanto experimental como numérico de sistemas generados mediante el acoplamiento entre las inestabilidades hidrodinámicas en celdas de Hele-Shaw y reacciones químicas complejas.

Objetivo y Estado del Arte

El objetivo de esta tesis es el de encontrar un nexo común entre dos mundos aparentemente muy diferentes. Por un lado, el campo de las inestabilidades hidrodinámicas y por otro, el campo de lo que en este contexto denominamos reacciones químicas *complejas*. Como todo trabajo de especialización, es fundamental definir concretamente los límites del estudio. Esto es aun más necesario, teniendo en cuenta que ambos mundos son extremadamente extensos.

Dentro del campo de las inestabilidades hidrodinámicas, en este trabajo se estudiarán un tipo particular de inestabilidades conocidas como digitaciones (o *fingering* en inglés). Estas inestabilidades aparecen cuando un fluido con ciertas propiedades termodinámicas (como la temperatura, viscosidad, densidad o la tensión superficial), entra en contacto con otro y lo desplaza [45, 44, 93, 168]. Si las condiciones de desplazamiento son desfavorables, el arrastre se produce de manera inhomogénea generando patrones similares a dedos (de ahí el nombre de digitación) [45]. Estos sistemas son considerados *inestables* desde el punto de vista de la fluidodinámica.

El fenómeno de digitación se ha observado ampliamente en muchos campos de la ciencia y la industria, así por nombrar algunos pueden citarse:

- La extracción mejorada de petróleo (o más conocido como EOR - *Enhanced Oil Recovery* por sus siglas en inglés). En este caso, el fenómeno de digitación viscosa ocurre al querer desplazar crudo (un fluido con una mayor viscosidad) mediante la inyección de agua a presión (un fluido con una viscosidad menor). El desplazamiento inestable afecta directamente al proceso de extracción haciendo que este sea ineficiente, y por lo tanto produciendo unos rendimientos reducidos [132, 206, 41, 21, 207, 210].

- En fenómenos hidrogeológicos. Varios estudios predicen la aparición de digitaciones salinas en el transporte de acuíferos subterráneos. Este tipo de digitaciones suceden cuando el agua del mar, que posee una concentración salina y temperatura característica, entra en contacto con agua dulce. Las diferencias de salinidad y temperatura producen digitaciones conocidas como dedos de sal (o *salt fingers* en inglés) que interfieren negativamente en las descargas de agua dulce, favoreciendo la oxidación de nutrientes [111, 200, 171, 76].

- En los procesos cromatográficos. La cromatografía de exclusión molecular es una técnica de separación ampliamente utilizada en la química, biología molecular, biotecnología, entre otros. Es un proceso mediante el cual los solutos de una mezcla son separados por diferencias de tamaño, al pasar la misma por un medio poroso. Se ha demostrado, que al querer eluir una muestra viscosa con un solvente menos viscoso se produce digitación viscosa que afecta negativamente tanto a la extracción como a los rendimientos [173, 32, 42, 198, 166].

Sin embargo, este trabajo se enfoca en el estudio de las inestabilidades producidas en dispositivos experimentales conocidos como celdas de Hele-Shaw [89]. Estos dispositivos están conformadas por dos placas separadas estrechamente una de la otra, permitiendo el estudio del proceso de digitación de una manera relativamente sencilla y controlada. Poseen además la particularidad de que el flujo dentro de ellas es idéntico al de un fluido a través de un medio poroso, por lo que los estudios llevados a cabo en ellas pueden ser representativos de sistemas muchos más complejos y de particular interés en la industria.

El fenómeno de digitación en celdas de Hele-Shaw fue y sigue siendo extensamente estudiado y caracterizado desde hace décadas . Los primeros estudios abordaron la problemática de desplazamientos no reactivos tanto miscibles como inmiscibles, demostrando la importancia de factores como la tensión superficial o la difusividad en la desestabilización de sistemas [93, 48, 127, 197, 8, 45].

Más recientemente, se estudiaron los procesos mediados por reacciones químicas, en donde sistemas con movilidades iniciales favorables (y por lo tanto, estables), son desestabilizados por procesos fisicoquímicos acoplados al desplazamiento [45, 25, 44, 9].

El estudio de reacciones químicas acopladas al fenómeno de digitación fue incrementando su complejidad con el tiempo. Así, reacciones elementales como procesos de neutralización o de precipitación química, fueron y son hoy en día extensamente caracterizados mostrando un rico abanico de comportamientos. El efecto de estas reacciones en las inestabilidades está mediado principalmente por el cambio en las razones de movilidad debido al incremento de factores como la densidad o la viscosidad de los fluidos involucrados o la permeabilidad del medio [141, 138, 137, 139, 73, 65, 9, 176].

La complejidad de los procesos químicos acoplados al desarrollo de inestabilidades puede incrementarse considerando lo que denominamos reacciones químicas complejas. En un contexto general, estas reacciones son definidas como procesos químicos que se producen en varias etapas (al menos dos) y cuentan con al menos un intermediario de reacción [116]. Dentro de esta definición, se engloba un campo muy extenso de reacciones. Algunas de estas, ya han sido acopladas a inestabilidades con anterioridad, como por ejemplo los procesos autocatalíticos [101, 49, 96].

En el contexto de este trabajo, utilizaremos reacciones químicas cuyos mecanismos aportan un paso más de complejidad respecto a las reacciones autocatalíticas y donde los intermediarios de reacción desempeñan un papel fundamental para el desarrollo de la dinámica de las mismas. Así pues, en este trabajo, se analizará el acople de las inestabilidades hidrodinámicas con dos tipos de reacciones complejas: La reacción oscilante de Belousov-Zhabotinsky (BZ) [18] y las reacciones de cambio de pH [106, 108, 107, 159, 160, 145].

La reacción BZ, es uno de los osciladores químicos más extensamente conocidos. Es un proceso redox en donde los intermediarios de reacción oscilan en el tiempo mediante la dinámica de activador/inhibidor [82]. Estas oscilaciones se aprecian con cambios de color periódicos en el caso de un sistema perfectamente agitado o con la formación de patrones

espaciotemporales en sistemas espacialmente extendidos. Existen variaciones de esta reacción. En este trabajo en particular se optó por usar una reacción conocida como reacción BZ-CHD, en donde el sustrato orgánico de la receta original se reemplaza por el componente CHD (1,4-Ciclohexanodiona) [113, 112, 187, 188, 190, 114]. Esta formulación presenta varias ventajas respecto a la receta original, pero la más significativa es que no produce dióxido de carbono como producto secundario, lo cual es fundamental si se pretende acoplar esta reacción a fenómenos hidrodinámicos en medios confinados.

Por otra parte, las reacciones de cambio de pH son reacciones en donde el pH del sistema cambia de un estado básico (o ácido) a un estado ácido (o básico) debido a la interacción de los intermediarios de reacción [107, 108, 159, 153, 145]. Existen reacciones de cambio de pH inorgánicas, las cuales son también procesos redox y pueden mostrar oscilaciones tanto en sistemas abiertos como en sistemas semi abiertos. Estos sistemas han sido extensamente caracterizados habiendo una gran lista de formulaciones disponibles [145]. Sin embargo, debido a su naturaleza redox, estos sistemas no pueden acoplarse a elementos orgánicos, como son los polímeros o sistemas de liberación de fármacos (o *drug delivery* por su nombre de inglés).

Recientemente, se desarrollaron reacciones de cambio de pH orgánicas que a diferencia de las anteriores no son procesos redox, y por lo tanto son menos agresivas con elementos orgánicos como los antes indicados [106, 108, 107]. Estas reacciones también muestran comportamientos oscilatorios en sistemas abiertos y han sido relativamente bien caracterizadas. Sin embargo, debido a no ser reacciones del tipo redox, hay pocas formulaciones disponibles.

En este trabajo se utilizarán dos reacciones de cambio de pH orgánicas, la reacción de Formaldehido-Sulfito (FS) [212, 106, 213] y la reacción de Formaldeido-Sulfito-Gluconolactona (FSG) [108, 107]. La primera es también conocida como reacción *Clock*, porque el pH de la solución cambia en un momento determinado de ácido a básico. El tiempo de cambio depende de las concentraciones de las especies involucradas. La segunda reacción, es una derivación de la primera en donde se acopla la hidrólisis de la gluconolactona al cambio de pH de la reacción de Sulfito-Formaldehido.

Así pues, el objetivo de estudio de esta tesis es acoplar entre si todos los fenómenos descritos anteriormente. De manera específica se estudiarán los siguientes sistemas:

- **Sistema 1**: Acople entre la reacción BZ-CHD y una inestabilidad de digitación inducida por efecto de la flotabilidad en una celda orientada verticalmente.
- **Sistema 2**: Acople entre la reacción FS y una inestabilidad de digitación viscosa en una celda orientada horizontalmente.
- **Sistema 3**: Acople entre la reacción FSG y una inestabilidad de digitación viscosa en una celda orientada horizontalmente.

De esta manera se pretende construir estos sistemas experimentalmente y trabajar con ellos en un rango de parámetros en donde los tiempos característicos sean comparables y ocurran sinergia entre ambos fenómenos. Se realizará la completa caracterización, se plantearán hipótesis respecto a los mecanismos de interacción involucrados y se establecerán modelos matemáticos que permitan simular la dinámica de los mismos.

Estructura de la tesis

Esta trabajo está dividido en tres partes. Cada parte cuenta con una introducción, un capítulo de métodos experimentales y numéricos, un capítulo de resultados experimentales, un capítulo de resultados numéricos y una discusión general. Independientemente del hilo conductor común que poseen las partes, se eligió organizar el trabajo de esta forma no solo para facilitar su lectura, sino además porque cada parte en sí posee suficiente contenido independiente que justifica el uso del formato.

De esta manera, los **Capítulos 2**, **6** y **10**, son capítulos que desarrollan los métodos tanto experimentales como numéricos de las **Partes I**, **II** y **III** respectivamente. En la sección experimental de estos capítulos se encuentran todas las recetas, formulaciones químicas y protocolos utilizados en los experimentos, así como la descripción de los arreglos experimentales y estudios previos necesarios para el desarrollo del trabajo. En la sección numérica, se incluyen consideraciones generales, como la descripción de los dominios computacionales, configuración de los programas empleados en las simulaciones, parámetros utilizados, entre otros aspectos. Sin embargo y para facilitar la lectura de la tesis, el desarrollo de las ecuaciones fundamentales de los modelos se reserva para los correspondientes capítulos de resultados numéricos, ya que en la mayoría de los casos, éstos dependen de los resultados experimentales.

Los conceptos básicos son introducidos en el **Capítulo 1**. En este capítulo se explican una serie de cuestiones fundamentales para el entendimiento del trabajo. Así, se describen las reacciones oscilantes clásicas, como la reacción de Belousov-Zhabotinsky y los osciladores de pH tanto inorgánicos como los orgánicos. También se introducen las inestabilidades hidrodinámicas en celda Hele-Shaw y los fenómenos de digitación por diferencia de viscosidad y de densidad. Complementariamente, se incluye una sección para describir las propiedades más importantes del ácido poliacrílico, que es un componente ampliamente utilizado en el desarrollo de este trabajo, más precisamente en las **Partes II** y **III**. Finalmente, se describe la técnica óptica de Schlieren. Esta es una técnica de visualización de fluidos ampliamente utilizada durante todo el desarrollo de la tesis y que fue fundamental para el entendimiento de los mecanismos físicos y químicos de los fenómenos observados experimentalmente.

La **Parte I** comienza inmediatamente después del capítulo introductorio. En esta parte se estudia el acople entre la reacción BZ-CHD (una variación de la reacción Belousov-Zhabotinsky), y la inestabilidad hidrodinámica de digitación inducida por flotabilidad en una celda Hele-Shaw orientada verticalmente.

En el **Capítulo 3** se presentan los resultados experimentales obtenidos para este sistema. Los mismos son analizados de forma tanto descriptiva como cuantitativa, estudiando los efectos producidos por los cambios en la densidad ($\Delta\rho$) y la excitabilidad (ε). Estos parámetros fueron modificados tanto de manera desacoplada como acoplada, y su efecto fue caracterizado mediante el estudio de observables específicos como los tiempos de inducción químicos (t_{ind-C}) e hidrodinámicos (t_{ind-H}), la longitud de onda (λ_H) y el período (T_C). De esta forma, se presenta un estudio de caracterización completo de los fenómenos observados, pudiéndose establecer las principales influencias de la hidrodinámica y la química en la dinámica del sistema.

En el **Capítulo 4** se presenta un estudio químico detallado realizado con la finalidad de descubrir el mecanismo detrás de los resultados experimentales en el Capítulo 3. Dicho estudio se llevó a cabo mediante una extensiva serie de experimentos de control y caracterización química, en donde se utilizaron diversas herramientas de análisis tales como espectrofotometría

y resonancia magnética nuclear. Mediante estos estudios, es identificado el factor principal en el acople entre la reacción BZ-CHD y la inestabilidad hidrodinámica.

En el **Capítulo 5**, se aplican los resultados obtenidos en el **Capítulo 4** en combinación con los modelos cinéticos ya existentes, para reproducir de forma natural los resultados experimentales mediante simulaciones. Así, en este capítulo se comparan primeramente los resultados experimentales y los modelos cinéticos con la finalidad de obtener un rango de parámetros de trabajo equivalente. Luego, se propone un modelo numérico extensivo de reacción-difusión-convección incluyendo los mecanismos descubiertos y desarrollando paso a paso todas las ecuaciones fundamentales. Finalmente, los resultados numéricos son analizados análogamente a los experimentales demostrando las equivalencias entre ambos sistemas.

La **Parte II** comienza inmediatamente luego del **Capítulo 5**. En este caso se estudia el acople entre una inestabilidad hidrodinámica de digitación viscosa y una reacción de cambio de pH en una celda de Hele-Shaw orientada horizontalmente.

Previamente al estudio del sistema hidrodinámico, es necesario desarrollar un sistema químico en donde la viscosidad sea afectada por cambios en el pH. De esta manera, en el **Capítulo 7** se desarrolla un sistema en donde se observan experimentalmente variaciones de temporales sinérgicas entre el pH y la viscosidad. Esto se logra acoplando un polímero sensible al pH, (el ácido poliacrílico), con dos reacciones de cambio de pH: la reacción de Formaldehido-Sulfito y la reacción de Formaldehido-Sulfito-Gluconolactona. Ambos sistemas son extensamente caracterizados mediante técnicas reológicas y analíticas, midiendo observables como los saltos de viscosidad y pH ($\Delta\mu$ y ΔpH respectivamente), los cambios en la dinámica temporal respecto a la formulación original y los tiempos de inducción del sistema. Los observables fueron estudiados para cada especie química involucrada en las formulaciones utilizadas. Finalmente, la última parte de este capítulo demuestra el mecanismo de acople mediante experimentos de control y rutas alternativas considerando formulaciones diversas.

En el **Capítulo 8**, los desarrollos obtenidos en el capítulo anterior son adaptados a una celda de Hele-Shaw para generar, con éxito, una inestabilidad de digitación viscosa. Este sistema se estudia de manera descriptiva analizando los efectos producidos por los parámetros más importantes como son el caudal volumétrico (Q) y la composición de las formulaciones utilizadas. Seguidamente el sistema se caracteriza cuantitativamente, estudiando la morfología de los patrones observados mediante el cálculo de la circularidad (C). También se utiliza la técnica de Schlieren como complemento para dilucidar el mecanismo de la inestabilidad.

El **Capítulo 9** presenta los resultados numéricos de los sistemas presentados en los **Capítulos 7** y **8**. En la primera parte, se adaptan los modelos cinéticos existentes de las reacciones de pH a los experimentos. Esto se realiza encontrando el conjunto de parámetros que mejor ajusta los modelos a los resultados experimentales. Los modelos ajustados son analizados de manera análoga a como se hace en el **Capítulo 7**. Seguidamente, se presentan las ecuaciones fundamentales de un modelo numérico de convección-difusión para simular el sistema introducido en el **Capítulo 8**. Los resultados son analizados midiendo la circularidad numérica de la misma forma que se hizo en los experimentos. Se demuestra que tanto los resultados experimentales como los numéricos concuerdan más que aceptablemente.

Seguidamente comienza la **Parte III** en donde se estudia el acople entre la reacción de Sulfito-Formaldehido-Gluconolactona y el fenómeno de digitación viscosa en celda de Hele-Shaw orientada horizontalmente. En esta parte se estudian dos situaciones provenientes de un mismo sistema experimental. Estos casos se obtienen intercambiando solamente la solución desplazante por la desplazada. En el llamado Caso I, se analiza la generación de patrones

complejos en condiciones de aparente estabilidad hidrodinámica. En el Caso II se analiza la estabilización de digitación viscosa mediante procesos fisicoquímicos. Si bien el sistema experimental estudiado en esta parte es derivado de la **Parte II**, la riqueza, versatilidad y complejidad de los resultados obtenidos han hecho necesario dedicar un espacio aparte para ellos.

Así, el **Capítulo 11** estudia la dinámica de los dos casos considerados. En ambas situaciones, se realizaron estudios descriptivos seguidos de estudios cuantitativos para casos reactivos y no reactivos. Los estudios cuantitativos se realizaron mayormente midiendo la circularidad, siendo posible demostrar una fuerte dependencia de los resultados con la velocidad de desplazamiento y la composición química de los sistemas. En ambos casos, el caudal volumétrico fue elegido como el parámetro de análisis fundamental, siendo este variado en un amplio rango de valores y permitiendo la caracterización completa del sistema.

El **Capítulo 12** se centra en encontrar un mecanismo que dé explicación a los fenómenos observados. Esto se lleva a cabo mediante un extensivo análisis con experimentos de control, en donde las formulaciones químicas fueron modificadas minuciosamente para poder entender el efecto producido por cada uno de las especies en el sistema. Basándose en estos resultados, se propone un modelo químico y se realizan cálculos complementarios para fundamentarlo.

Finalmente, en el **Capítulo 13** se presenta un modelo numérico de reacción-difusión-convección que simula los fenómenos descritos en el **Capítulo 11**, en donde se detallan paso por paso el desarrollo de las ecuaciones fundamentales del mismo. Los resultados numéricos se analizan una vez más imitando el análisis realizado a los resultados experimentales, demostrando una gran concordancia entre los mismos. El modelo también se utiliza como herramienta para explicar el efecto de la difusión en la dinámica de los casos de estudio.

Una vez finalizada la tercera parte, se presenta una serie de apéndices con información complementaria.

En el **Apéndice A** se muestran todas las recetas de las soluciones madres utilizadas para llevar a cabo este trabajo. En las mismas, se detallan referencias, protocolos y cantidades de los químicos utilizados. También se detallan las recetas de las soluciones reactivas usadas en cada parte.

En el **Apéndice B**, se presentan los resultados, tanto numéricos como experimentales, de los sistemas de reacción-difusión derivados de la **Parte I**. Estos resultados fueron importantes para el desarrollo y el entendimiento previo del mecanismo propuesto en dicha parte. Sin embargo, se ha decidido incluirlo en un apéndice como resultados complementarios. En este apéndice se estudian sistemas capilares en 1D y con matriz de agarosa en 2D.

En el **Apéndice C** se presentan los métodos y protocolos utilizados para el tratamiento de imágenes experimentales y numéricas. Estos métodos son fundamentales para la obtención de los valores cuantitativos presentados a lo largo del trabajo. El apéndice está dividido en los métodos utilizados en cada parte.

En el **Apéndice D** se incluye información y cálculos complementarios que fueron utilizados para el desarrollo de los capítulos principales, pero que no son incluidos directamente en el cuerpo de la tesis debido a que su aporte no es especialmente significativo.

Finalmente, el **Apéndice E** muestra los permisos para el uso, reproducción, modificación y publicación del material perteneciente a aquellas publicaciones en donde los derechos de autor fueron cedidos. Estos permisos se incluyen para evitar cualquier problema legal referente al plagio o autoplagio de información.

Resumo

A presente memoria resume o traballo realizado no Grupo de Física Non Lineal da USC. Na mesma exponse o estudo tanto experimental como numérico de sistemas xerados mediante a combinación entre as inestabilidades hidrodinámicas en células de Hele-Shaw e reaccións químicas complexas

Obxectivo e Estado do Arte

O obxectivo desta tese é o de atopar un nexo común entre dous mundos aparentemente moi diferentes. Por unha banda, o campo das inestabilidades hidrodinámicas e por outra, o campo do que neste contexto denominamos reaccións químicas *complexas*. Como todo traballo de especialización, é fundamental definir concretamente os límites do estudo. Isto é aínda máis necesario, tendo en conta que ámbolos dous mundos son extremadamente extensos

Dentro do campo das inestabilidades hidrodinámicas, neste traballo estudásense un tipo particular de inestabilidades coñecidas como dixitacións (ou *fingering* en inglés). Estas inestabilidades obsérvanse cando un fluído con certas propiedades termodinámicas (como a temperatura, viscosidade, densidade ou a tensión superficial), entra en contacto con outro, e desprázao [45, 44, 93, 168]. Se as condicións de desprazamento son desfavorables, o arrastre prodúcese de maneira non homoxénea, xerando patróns similares a dedos (de aí o nome de dixitación) [45]. Estes sistemas son considerados *inestables* desde o punto de vista da fluidodinámica.

O fenómeno de dixitación observouse amplamente en moitos campos da ciencia e a industria, así por nomear algúns poden citarse:

- A extracción mellorada de petróleo ou Enhanced Oil Recovery-EOR polas súas siglas en inglés. Neste caso, o fenómeno de dixitación viscosa ocorre ao querer desprazar o petróleo (un fluído cunha maior viscosidade) mediante a inxección de auga a presión (un fluído cunha viscosidade menor). O desprazamento inestable afecta directamente o proceso de extracción, facendo que este sexa ineficiente, e por tanto producindo uns rendementos reducidos [132, 206, 41, 21, 207, 210].

- En fenómenos hidroxeolóxicos: Varios estudos predín a aparición de dixitacións salinas no transporte de acuíferos subterráneos. Este tipo de dixitacións sucede cando a auga do mar, que posúe unha concentración salina e temperatura característica, entra en contacto con auga doce. As diferenzas de salinidade e temperatura producen dixitacións coñecidas como dedos de sal (ou *salt fingers* en inglés) que interfiren negativamente nas descargas de auga doce, favorecendo a oxidación de nutrientes [111, 200, 171, 76].

- Nos procesos cromatográficos. A cromatografía de exclusión molecular é unha técnica de separación amplamente utilizada na química, bioloxía molecular, biotecnoloxía, entre outros. É un proceso mediante o cal una os solutos dunha mestura son separados por diferenzas de tamaño, ao pasar a mesma por un medio poroso. Demostrouse, que ao querer eluir unha mostra viscosa cun solvente menos viscoso prodúcese un fenómeno de dixitación viscosa que afecta negativamente tanto á extracción como aos rendementos [173, 32, 42, 198, 166].

Con todo, este traballo enfócase no estudo das inestabilidades producidas en dispositivos experimentais coñecidos como células de Hele- Shaw [89]. Estes dispositivos están conformadas por dúas placas separadas estreitamente una da outra, permitindo o estudo do proceso de dixitación dunha maneira relativamente sinxela e controlada. Posúen ademais a particularidade de que o fluxo dentro delas é idéntico ao dun fluído a través dun medio poroso, polo que os estudos levados a cabo nelas poden ser representativos de sistemas moitos máis complexos e de particular interese na industria.

O fenómeno de dixitación en células de Hele-Shaw foi e segue sendo cumpridamente estudado e caracterizado desde hai décadas. Os primeiros estudos abordaron a problemática de desprazamentos non reactivos tanto miscibles como inmiscibles, demostrando a importancia de factores como a tensión superficial ou a difusión na desestabilización dos sistemas [93, 48, 127, 197, 8, 45].

Mais recentemente, estudáronse os procesos mediados por reaccións químicas, onde sistemas con mobilidades iniciais favorables (e por tanto, estables), son deestabilizados por procesos fisicoquímicos axustados ao desprazamento [45, 25, 44, 9].

O estudo de reaccións químicas axustadas ao fenómeno de dixitación foi incrementando a súa complexidade co tempo. Así, reaccións elementais como procesos de neutralización ou de precipitación química, foron e son hoxe en día cumpridamente caracterizados mostrando un rico abanico de comportamentos. O efecto destas reaccións nas inestabilidades está mediado principalmente polo cambio nas razóns de mobilidade debido ao incremento de factores como a densidade ou a viscosidade dos fluídos involucrados ou á permeabilidade do medio [141, 138, 137, 139, 73, 65, 9, 176].

A complexidade dos procesos químicos axustados ao desenvolvemento de inestabilidades pode incrementarse considerando o que denominamos reaccións químicas complexas. Nun contexto xeral, estas reaccións son definidas como procesos químicos que se producen en varias etapas (polo menos dúas) e contan con polo menos un intermediario de reacción [116]. Dentro desta definición, englóbase un campo moi extenso de reaccións. Algunhas destas, xa foron axustadas a inestabilidades con anterioridade, por exemplo os procesos autocatalíticos [101, 49, 96].

No contexto deste traballo, utilizaremos reaccións químicas cuxos mecanismos achegan un paso máis de complexidade respecto a as reaccións autocatalíticas e onde os intermediarios de reacción desempeñan un papel fundamental para o desenvolvemento da dinámica das mesmas. Así pois, neste traballo, analizarase o acoplamento das inestabilidades hidrodinámicas con dous tipos de reaccións complexas: A reacción oscilante de Belousov- Zhabotinsky (BZ) [18] e as reaccións de cambio de pH [106, 108, 107, 159, 160, 145].

A reacción BZ, é un dos osciladores químicos máis cumpridamente coñecidos. É un proceso redox onde os intermediarios de reacción oscilan no tempo mediante a dinámica de activador/inhibidor [82]. Estas oscilacións aprécianse con cambios de cor periódicos no caso dun sistema perfectamente axitado ou coa formación de patróns espaciotemporales en sistemas

espacialmente estendidos. Existen variacións desta reacción. Neste traballo en particular optouse por usar unha reacción coñecida como reacción BZ- CHD, onde o substrato orgánico da receita orixinal substitúese polo compoñente CHD (1,4-Ciclohexanodiona) [113, 112, 187, 188, 190, 114]. Esta formulación presenta varias vantaxes respecto a a receita orixinal, pero a máis significativa é que non produce dióxido de carbono como produto secundario, o cal é fundamental se se pretende axustar esta reacción a fenómenos hidrodinámicos.

Por outra banda, as reaccións de cambio de pH son reaccións onde o pH do sistema cambia dun estado alcalino (ou aceda) a un estado acedo (ou alcalino) debido á interacción dos intermediarios de reacción [107, 108, 159, 153, 145]. Existen reaccións de cambio de pH inorgánicas, as cales son tamén procesos redox e poden mostrar oscilacións tanto en sistemas abertos como en sistemas semi abertos. Estes sistemas foron cumpridamente caracterizados habendo unha gran lista de formulacións dispoñibles [145]. Con todo, debido á súa natureza redox, estes sistemas non poden axustarse a elementos orgánicos, como os polímeros ou elementos de transporte de fármacos (ou *drug delivery* polo seu nome de inglés).

Mais recentemente, desenvolvéronse reaccións de cambio de pH orgánicas que a diferenza das anteriores non son procesos redox, e por tanto son menos agresivas con elementos orgánicos como os antes indicados [106, 108, 107]. Estas reaccións tamén mostran comportamentos oscilatorios en sistemas abertos e foron relativamente caracterizadas. Con todo, debido a non ser reaccións do tipo redox, hai poucas formulacións dispoñibles.

Neste traballo utilizaranse dúas reaccións de cambio de pH orgánicas, a reacción de Formaldehido-Sulfito (FS) [212, 106, 213], e a reacción de Formaldeido-Sulfito-Gluconolactona (FSG) [108, 107]. A primeira é tamén coñecida como reacción *Clock*, porque o pH da solución cambia nun momento determinado de acedo a alcalino. O tempo de cambio depende das concentracións das especies involucradas. A segunda reacción, é unha derivación da primeira onde se axusta a hidrólise da gluconolactona ao cambio de pH da reacción de Formaldehido-Sulfito. A hidrólise converte a gluconolactona en ácido glucónico producindo un incremento puntual do pH.

Así pois, o obxectivo de estudo desta tese é axustar entre se todos os fenómenos descritos anteriormente. De maneira específica estudaranse tres sistemas axustados:

- **Sistema 1**: Acoplamento entre a reacción BZ-CHD e unha inestabilidade de dixitación inducida por flotabilidade en nunha célula orientada verticalmente.
- **Sistema 2**: Acoplamento entre a reacción FS e unha inestabilidade de dixitación viscosa nunha célula orientada horizontalmente.
- **Sistema 3**: Acoplamento entre a reacción FSG e unha inestabilidade de dixitación viscosa nunha célula orientada horizontalmente.

Desta maneira preténdese construír estes sistemas experimentalmente, e traballar con eles nun rango de parámetros onde os tempos característicos sexan comparables e ocorran sinerxias entre ambos fenómenos. Realizarase a completa caracterización, exporanse hipótese respecto a os mecanismos de interacción involucrados e estableceranse modelos matemáticos que permitan simular a dinámica dos mesmos.

Estrutura da Tese

Esta traballo está dividido en tres partes. Cada parte conta cunha introdución, un capítulo de métodos experimentais e numéricos, un capítulo de resultados experimentais, un capítulo de resultados numéricos e unha discusión xeral. Independentemente do fío condutor común que posúen as partes, elixiuse organizar o traballo desta forma non só para facilitar a súa lectura, senón ademais porque cada parte en si posúe suficiente contido independente que xustifica o uso do formato.

Así, os **Capítulos 2**, **6** e **10** son capítulos que desenvolven tanto o método experimental como o numérico das **Partes I**, **II** e **III** respectivamente. Na sección experimental destes capítulos atoparás todas as receitas, formulacións químicas e protocolos empregados nos experimentos, así como a descrición dos arranxos experimentais e estudos previos necesarios para o desenvolvemento do traballo. Na sección numérica inclúense consideracións xerais, como a descrición dos dominios computacionais, a configuración dos programas empregados nas simulacións, parámetros empregados, entre outros. Non obstante, e para facilitar a lectura da tese, o desenvolvemento das ecuacións fundamentais dos modelos resérvase para os correspondentes capítulos de resultados numéricos, xa que na maioría dos casos, estes dependen dos resultados experimentais.

Os conceptos básicos son introducidos no **Capítulo 1**. Neste capítulo explícanse unha serie de cuestións fundamentais para o entendemento do traballo. Así, descríbense as reaccións oscilantes clásicas, como a reacción de Belousov- Zhabotinsky e os osciladores de pH tanto inorgánicos como os orgánicos. Tamén se introducen as inestabilidades hidrodinámicas en célula Hele-Shaw e os fenómenos de dixitación por diferenza de viscosidade e de densidade. Complementariamente, inclúese unha sección para describir as propiedades máis importantes do ácido poliacrílico, que é un compoñente amplamente utilizado no desenvolvemento deste traballo, máis precisamente nas **Partes II** e **III**. Finalmente, descríbese a técnica óptica de Schlieren. Esta é unha técnica de visualización de fluídos amplamente utilizada durante todo a tese e que foi fundamental para o entendemento dos mecanismos físicos e químicos observados experimentalmente.

A **Parte I** comeza inmediatamente despois do capítulo introdutorio. Nesta parte estúdase o axuste entre a reacción BZ-CHD, e a inestabilidade hidrodinámica de dixitación por inducida pola flotabilidade nunha célula Hele-Shaw orientada verticalmente.

No **Capítulo 3** preséntanse os resultados experimentais obtidos para este sistema. Os mesmos son analizados de forma tanto descritiva como cuantitativa, estudando os efectos producidos polos cambios na densidade ($\Delta\rho$) e da excitabilidade (ε). Estas parámetros foron modificados tanto de maneira independente como axustada, e o seu efecto foi caracterizado mediante o estudo de observables específicos como os tempos de indución químicos (t_{ind-C}) e hidrodinámicos (t_{ind-H}), a lonxitude de onda (λ_H) e o período (T_C). Desta forma, preséntase un estudo de caracterización completo dos fenómenos observados, podéndose establecer as principais influencias da hidrodinámica e a química na dinámica do sistema.

No **Capítulo 4** preséntase un estudo químico detallado realizado coa finalidade de descubrir o mecanismo detrás dos resultados experimentais no **Capítulo 3**. Devandito estudo levou a cabo mediante unha extensiva serie de experimentos de control e caracterización química, onde se utilizaron diversas ferramentas de análises tales como espectrofotometría e resonancia magnética nuclear. Mediante estes estudos, é identificado o factor principal no acoplamento entre a reacción BZ-CHD e a inestabilidade hidrodinámica.

No **Capítulo 5**, aplícanse os resultados obtidos no **Capítulo 4** en combinación coa os modelos cinético xa existentes, para reproducir de forma natural os resultados experimentais mediante simulacións. Así, neste capítulo compáranse primeiramente os resultados experimentais e os modelos cinéticos coa finalidade de obter un rango de parámetros de traballo equivalente. Logo, proponse un modelo numérico extensivo de reacción-difusión-convección incluíndo os mecanismos descubertos e desenvolvendo paso a paso todas as ecuacións fundamentais. Finalmente, os resultados numéricos son analizados analogamente aos experimentais demostrando as equivalencias entre ámbolos sistemas.

A **Parte II** comeza inmediatamente a finalizar o **Capítulo 5**. Neste caso estúdase o axuste entre unha inestabilidade hidrodinámica de dixitación viscosa e unha reacción de cambio de pH nunha célula de Hele-Shaw orientada horizontalmente.

Previamente ao estudo do sistema hidrodinámico, é necesario desenvolver un sistema químico onde a viscosidade sexa afectada por cambios no pH. Desta maneira, no **Capítulo 7** desenvólvese un sistema onde se observan experimentalmente variacións de temporais sinérgicas entre o pH e a viscosidade. Isto lógrase mediante o acoplamento entre un polímero sensible ao pH, (o ácido poliacrílico), con dúas reaccións de cambio de pH: a reacción de Formaldehido-Sulfito e a reacción de Formaldehido-Sulfito-Gluconolactona. Ámbolos sistemas son cumpridamente caracterizados mediante técnicas reolóxicas e analíticas, medindo observables como os saltos de viscosidade e pH (ΔpH e $\Delta\mu$ respectivamente), os cambios na dinámica temporal respecto a a formulación orixinal e os tempos de indución do sistema. Os observables foron estudados para cada especie química involucrada nas formulacións utilizadas. Finalmente, a última parte deste capítulo demostra o mecanismo de acoplamento mediante experimentos de control e roteiros alternativas considerando formulacións diversas.

No **Capítulo 8**, o os desenvolvementos obtidos no capítulo anterior son adaptados a unha célula de Hele-Shaw para xerar, con éxito, unha inestabilidade de dixitación viscosa. Este sistema estúdase de maneira descritiva analizando os efectos producidos polos parámetros máis importantes como son o caudal volumétrico (Q) e a composición das formulacións utilizadas. Seguidamente o sistema caracterízase cuantitativamente, estudando a morfoloxía dos patróns observados mediante o cálculo da circularidade (C). Tamén se utiliza a técnica de Schlieren como un complemento para dilucidar o mecanismo da inestabilidade.

O **Capítulo 9** presenta os resultados numéricos dos sistemas presentados nos **Capítulos 7** e **8**. Na primeira parte, adáptanse os modelos cinéticos existentes das reaccións de pH a experimentos. Isto realízase atopado en conxunto de parámetros que mellor axustan os modelos aos resultados experimentais. Os modelos axustados son analizados de maneira análoga a como se fai no **Capítulo 7**. Seguidamente, preséntanse as ecuacións fundamentais dun modelo numérico convección-difusión para simular o sistema introducido no **Capítulo 8**. Os resultados son analizados medindo a circularidade numérica da mesma forma que se fixo nos experimentos. Demóstrase que os resultados experimentais e numéricos concordan máis aceptablemente.

Seguidamente comeza a **Parte III** onde se estuda o acoplamento entre unha reacción de pH e o fenómeno de dixitación viscosa en célula de Hele-Shaw orientada horizontalmente. Aínda que parece repetido á parte anterior, aquí darase un paso máis no incremento de complexidade. Nesta parte estúdanse dúas situacións provenientes dun mesmo sistema experimental. Estes casos obtéñense intercambiado soamente a solución desplazante pola desprazada. No chamado Caso I, analízase a xeración de patróns complexos en condicións de aparente estabilidade hidrodinámica. No Caso II analízase a estabilización de dixitación viscosa mediante procesos

fisicoquímicos. Aínda que o sistema experimental estudado nesta parte é derivado da **Parte II**, a riqueza e versatilidade dos resultados obtidos fixeron que fose necesario dedicar un espazo aparte para eles.

Así, o **Capítulo 11** estuda a dinámica dos dous casos considerados. En ambas as situacións, realizáronse estudos descritivos seguidos de estudos cuantitativos para casos reactivos e non reactivos. Os estudos cuantitativos realizáronse maiormente medindo a circularidade, sendo posible demostrar unha forte dependencia dos resultados coa velocidade de desprazamento e a composición química dos sistemas. En ámbolos casos, o caudal volumétrico foi elixido como o parámetro de análise fundamental, sendo este variado nun amplo rango de valores e permitindo a caracterización completa do sistema.

No **Capítulo 12** céntrase en atopar un mecanismo que dea explicación aos fenómenos observados. Isto levase a cabo mediante unha extensiva análise con experimentos de control, onde as formulacións químicas foron modificadas minuciosamente para poder entender o efecto producido por cada un das especies no sistema. Baseándose neses resultados, proponse un modelo químico e realízanse cálculos complementarios para fundamentalo.

Finalmente, no **Capítulo 13** preséntase un modelo numérico de reacción-difusión-convección que simula os fenómenos descritos no **Capítulo 11**, e onde se detallan paso por paso o desenvolvemento das ecuacións fundamentais do mesmo. Os resultados numéricos analízanse unha vez máis imitando a análise realizada aos resultados experimentais, demostrando unha gran concordancia entre os mesmos. O modelo tamén se utiliza como ferramenta para explicar o efecto da difusión na dinámica dos casos de estudo.

Unha vez finalizada a terceira parte, preséntase unha serie de apéndices con información complementaria.

No **Apéndice A** móstranse todas as receitas das solucións **de accións** utilizadas para levar a cabo este traballo. Nas mesmas, detállanse referencias, protocolos e cantidades dos químicos utilizados. Tamén se detallan as receitas das solucións reactivas usadas en cada parte.

No **Apéndice B**, preséntanse os resultados, tanto numéricos como experimentais, dos sistemas de reacción-difusión derivados da Parte I. Estes resultados foron fundamentais para o desenvolvemento e o entendemento do mecanismo proposto na devandita parte. Con todo, decidiuse incluílo nun anexo por non considerarse resultados complementarios. Neste apéndice estúdanse sistemas capilares en 1D e con matriz de agarosa en 2D.

No **Apéndice C** preséntanse os métodos e protocolos utilizados para en tratamento de imaxes experimentais e numéricas. Estes métodos son fundamentais para a obtención dos valores cuantitativos presentados ao longo do traballo. O anexo esta dividido nos métodos utilizados en cada parte.

No **Apéndice D** inclúese información e cálculos complementarios que foron utilizados para o desenvolvemento dos capítulos principais, pero que non son incluídos directamente no corpo da tese debido que a súa achega non é especialmente significativo.

Finalmente, o **Apéndice E** mostra os permisos para o uso, reprodución, modificación e publicación do material pertencente a aquelas publicacións onde os dereitos de autor foron cedidos. Estes permisos inclúense para evitar calquera problema legal referente ao plaxio ou autoplaxio de información.

Nomenclature and Abbrevations

α_i	Solutal Expansion Coefficient of Species i
ΔpH	pH Variation
$\Delta\mu$	Viscosity Variation
$\Delta\rho$	Density Gradient
$\dot{\gamma}_f$	Shear Rate
ε	Excitability
κ	Porous Matrix Permeability
λ_H	Hydrodynamic Wavelength
μ	Viscosity
ϕ	Porosity
ρ	Density
ρ_{Si}	Density of species i
$\vec{r}$	Radial Coordinate
ξ_{max}	Ferroin Absorptive Molar Coefficient
a	Hele-Shaw Cell Gap
C	Circularity
c^*	Polymer Overlap Concentration
C_i	Molar Concentration of Species i
D_a	Damkhöler Number
d_A	Density Area
D_i	Diffusion Coefficient of Species i
k	Reaction Rate Constant

N_1	First Normal Stress Difference
p	Pressure
Q	Injection Flow Rate
R	Hele-Shaw Cell Radius
R_κ	Permeability Log-Mobility Ratio
R_b	Viscosity Log-Mobility Ratio
r_{Max}	Effective Hele-Shaw Cell Radius
t	time
T_C	Chemical Period
t_{ind-C}	Chemical Induction Time
t_{ind-H}	Hydrodynamic Induction Time
v_r	Chemical Front Velocity
C.I.	Color Indicator
DMSO-d_6	Deuterated Dimethyl Sulfoxide
FBS-PAA	Formaldehyde-BiSulfite-PAA Reaction
FS	Formaldehyde-Sulfite Reaction
FSG	Formaldehyde-Suflite-Gluconolactone Reaction
GA	Gluconic Acid
GLN	Gluconolactone
MetOH-d_4	Deuterated Methanol
NMR	Nuclear Magnetic Resonance
PAA	Poly(Acrylic Acid)
Pe	Péclect Number
PeDa	Péclet-Damkhöler Number
RDC	Reaction-Diffusion-Convection
SEM	Scanning Electron Microscopy
STP	Space-Time Plot

List of Figures

List of Tables

List of Publications

The following list indicates the publications derived from this research that were used to create the thesis. I declare that I am the main author of all these publications and no other non-doctor collaborator was part of them. I also declare that I am properly authorized to use this articles in this context, and they were not used in any other thesis work. The corresponding authorizations are detailed in Appendix E.

(I) D. M. Escala, M. A. Budroni, J. Carballido-Landeira, A. De Wit, and A. P. Muñuzuri. Self-organized traveling chemo-hydrodynamic fingers triggered by a chemical oscillator. *Journal of Physical Chemistry Letters*, 5(3):413–418, 2014.
Impact Factor (JCR): 7.458 (2014)
Quartile: Q1

(II) D. M. Escala, A. P. Muñuzuri, A. De Wit, and J. Carballido-Landeira. Temporal viscosity modulations driven by a pH sensitive polymer coupled to a pH-changing chemical reaction. *Physical Chemistry Chemical Physics*, 19(19):11914–11919, 2017.
Impact Factor (JCR): 3.906 (2017)
Quartile: Q1

(III) D. M. Escala, A. De Wit, J. Carballido-Landeira, and A. P. Munuzuri. Viscous Fingering Induced by a pH-Sensitive Clock Reaction. *Langmuir*, 35(11):4182–4188, 2019.
Impact Factor (JCR): 3.557 (2019)
Quartile: Q1

(IV) D. M. Escala and A. P. Muñuzuri. Interface Fingering Instability Triggered by a Density-Coupled Oscillatory Chemical Reaction via Precipitation. *Langmuir*, 35(42):13769–13781, 2019.
Impact Factor (JCR): 3.557 (2019)
Quartile: Q1

(V) D. M. Escala and A. Pérez-Muñuzuri. Constructing or Deconstructing a Fluid Instability: A Bottom-Up Approach. *Submitted*, 2021.
Status: Submitted

The next lists indicate the publications that are derived from the thesis research, but they were not included as part of the manuscript due to copyright or permission issues:

Articles

- D. M. Escala, J. Guiu-Souto, and A. P. Muñuzuri. Externally controlled anisotropy in pattern-forming reaction-diffusion systems. *Chaos*, 25(6), 2015.

- C. A. Middleton, C. Thomas, D. M. Escala, J. L. Tison, and A. De Wit. Imaging the Evolution of Brine Transport in Experimentally Grown Quasi-two-dimensional Sea Ice. In *Procedia IUTAM*, volume 15, pages 95–100, 2015.

- M. A. Budroni, L. Lemaigre, D. M. Escala, A. P. Muñuzuri, and A. De Wit. Spatially Localized Chemical Patterns around an A + B $\rightarrow$ Oscillator Front. *Journal of Physical Chemistry A*, 120(6):851–860, 2016.

Book Chapters

- D. M. Escala, J. Guiu-Souto, J. Carballido-Landeira, A. Pérez-Muñuzuri, and M. E. Vázquez-Cendón. Changes in buoyancy-driven instabilities using a reaction-diffusion system. *Numerical Methods for Hyperbolic Equations: Theory and Appl., An Int. Conf. to Honour Professor E.F. Toro - Proc. of the Int. Conf. on Numerical Methods for Hyperbolic Equations: Theory and Appl.*, pages 397–400, 2013.

- J. Guiu-Souto, D. M. Escala, J. Carballido-Landeira, A. Pérez-Muñuzuri, and E. Martín-Ortega. Viscous fingering instabilities in reactive miscible media. *Numerical Methods for Hyperbolic Equations: Theory and Appl., An Int. Conf. to Honour Professor E.F. Toro - Proc. of the Int. Conf. on Numerical Methods for Hyperbolic Equations: Theory and Appl.*, 409:409–412, 2013.

Chapter 1

Introduction

Abstract: *This chapter will present the most basics concepts related to all subjects addressed in this work. In this way, a general and descriptive review of the most important concepts on every single studied field will be addressed. The topics will be introduced from simplicity to complexity, emphasizing all that is necessary to understand the experimental and theoretical developments.*

1.1 Homogeneous Systems and Chemical Reactions

From the point of view of an active environment, a homogeneous system is defined as a material system in which all its intensive properties (such as density, elasticity, temperature, pressure, etc) are constant in the medium. In other words, its composition is uniform for every point of the system. Thus, a perfectly mixed dissolution of salt in water or a block of iron can be considered homogeneous systems. These types of systems can be classified is five different categories [116, 13]:

- **Dissolutions**: Systems composed of only one single phase. These types of systems are composed of at least, one solvent and one solute.
- **Pure substances**: Systems composed of only one substance.
- **Open systems**: Systems where mass and energy are exchanged from the medium to the environment.
- **Closed systems**: Systems where only energy is exchanged between the medium and the environment, but not mass.
- **Isolated systems**: Systems where neither mass nor energy are exchanged with the medium.

Due to its homogeneous character, these types of systems can be represented by a zero spatial dimension model. Regardless of the intrinsic complexity of every individual case, most active mediums can be studied in a deterministic manner by using differential equations. Thus, the state and dynamics of the system can be described by defining a set of time-dependent variables $C_i(t) = (C_1(t), C_2(t), \ldots, C_n(t))$, and a coupled system of differential equations as:

$$\frac{dC_i(t)}{dt} = f_i(C_i(t), p_i) \tag{1.1}$$

where f_i describes the dynamics of the system and depends on a set of parameters $p_i = (p_1, p_2, \ldots, p_m)$. The expressions of f and p depend on the system of study [116].

The set of Eqs. (1.1) are often used to describe the kinetics of chemical reactions. In this case, the dynamics are described by the rates of reaction of the species involved.

Considering the following homogeneous reaction:

$$aA + bB + \cdots \rightarrow eE + fF + \ldots \tag{1.2}$$

where $a, b, \ldots, e, f, \ldots$ are the stoichiometric coefficients, and $A, B, \ldots, E, F, \ldots$ are the chemical species. The rate of consumption or conversion rate (J) of each reactant is proportional to their correspondent stoichiometric coefficient (if the reaction occurs in a closed system), thus:

$$J \equiv -\frac{1}{a}\frac{dn_A}{dt} = -\frac{1}{b}\frac{dn_B}{dt} = \cdots = -\frac{1}{e}\frac{dn_E}{dt} = -\frac{1}{f}\frac{dn_F}{dt} = \ldots \tag{1.3}$$

where n_i are the moles of the species $i = A, B, \ldots$.

The conversion rate, J, is an extensive property that depends on the volume of the system. The conversion rate per volume unit J/V is defined as the reaction rate r [116, 13]:

$$r \equiv \frac{J}{V} = \frac{1}{V}\left(-\frac{1}{a}\frac{dn_A}{dt}\right) \tag{1.4}$$

r is an intensive magnitude and depends on the temperature (T), the pressure (p), and the concentration of the species [116].

If the volume of the system remains constant, then:

$$\frac{1}{V}\frac{dn_A}{dt} = \frac{dn_{A/V}}{dt} = \frac{d[A]}{dt} \rightarrow r = -\frac{1}{a}\frac{d[A]}{dt} = \ldots \frac{1}{e}\frac{d[E]}{dt} = \ldots \tag{1.5}$$

where $[i]$ indicates the molar concentration of the species $i = A, B, E \ldots$.

For most systems, it was experimentally demonstrated that the reaction rate at a given time is related to the concentration of the involved species:

$$r = k[A]^{\alpha}[B]^{\beta} \cdots [L]^{\lambda} \tag{1.6}$$

where k is known as the reaction rate (or kinetic) constant and, the exponents $\alpha, \beta, \ldots, \lambda$ are the partial orders of the reaction. $\alpha + \beta + \cdots + \lambda \equiv n$ is known as the overall order of the reaction. The expression of the reaction rate r shown in Eq. (1.6) is known as the law of mass action [116].

1.2 Types of Reactions

The present section will briefly introduce several types of reactions. All of them are important to the development of this thesis.

Elementary Reactions: An elementary chemical reaction consists of a single step, in which no intermediate compounds are observed. The chemical transformations occur in only one single step and pass through a single transition state [116, 13]. In these reactions, the molecularity and the reaction orders are well defined and can be derived from the stoichiometry. There are several types of elementary reactions, the most common ones are the unimolecular (first-order) and bimolecular (second-order) reactions. The dynamics of these reactions are modeled by the mass action law, that assumes that the rate of the elementary reaction is directly proportional to the product of the activities or concentrations of the reactants [116].

In a first-order elementary reaction, a molecule or a chemical species dissociates, polymerizes, or directly converts into one or more products (P). These reactions can be generally expressed as:

$$\mathrm{A} \xrightarrow{k} \mathrm{P} \tag{R1}$$

where the reaction rate is given by:

$$r = -\frac{d[A]}{dt} = k[A] \tag{1.7}$$

Some examples of unimolecular reactions are:

$$\mathrm{O_3} \rightleftharpoons \mathrm{O_2 + O} \tag{R2}$$

$$\mathrm{H_2O_2(l) \longrightarrow H_2O(l) + 0.5\,O_2\,(g)} \tag{R3}$$

On the other hand, in second-order elementary reaction, two species A and B react to produce one or more products (P). These reactions can be expressed generically as follow:

$$\mathrm{A + B} \xrightarrow{k} \mathrm{P} \tag{R4}$$

whose reaction rate is given by:

$$r = -\frac{d[A]}{dt} = -\frac{d[B]}{dt} = k[A][B] \tag{1.8}$$

A simple example of bimolecular reaction can be:

$$\mathrm{C_{12}H_{22}O_{11} + H_2O} \xrightarrow{k} \mathrm{C_6H_{12}O_6 + C_6H_{12}O_6} \tag{R5}$$

Complex chemical reactions: a complex chemical (or multistep) reaction is a chemical process that consists of several steps of elementary reactions and has one or more reaction intermediaries. These processes must be described by reaction mechanisms detailing all the involved elementary steps. The rate law of a complex chemical reaction is obtained by combining the rate laws of the multiple elementary steps, where every elementary step follows

the mass action law. This often derives into complex expressions for the reaction rate. The overall reaction rate is determined by the velocity of the slower elementary step [116, 13].

One common generic example of a complex reaction is the following consecutive reaction:

$$\mathrm{A} \xrightarrow{k_1} \mathrm{B} \tag{R6}$$

$$\mathrm{B} \xrightarrow{k_2} \mathrm{C} \tag{R7}$$

where the dynamics are described for every species by the following set of differential equations:

$$\frac{d[A]}{dt} = -k_1[A] \tag{1.9}$$

$$\frac{d[B]}{dt} = k_1[A] - k_2[B] \tag{1.10}$$

$$\frac{d[C]}{dt} = k_2[B] \tag{1.11}$$

The oxidation of ethylene is an example of a consecutive reaction:

$$2\,\mathrm{C_2H_4} + \mathrm{O_2} \xrightarrow{k_1} 2\,\mathrm{C_2H_4O} \tag{R8}$$

$$\mathrm{C_2H_4O} + \frac{5}{2}\,\mathrm{O_2} \xrightarrow{k_2} 2\,\mathrm{CO_2} + 2\,\mathrm{H_2O} \tag{R9}$$

As previously stated, in single steps reactions the partial orders $\alpha, \beta, \ldots, \lambda$ of Eq.(1.6) are equal to the stoichiometric coefficient for each reactant, and the overall order and n is equal to the molecularity (total number of molecules involved) of each elementary reaction. However, this is not the case for complex chemical reactions, where the partial orders must be determined experimentally [116].

All the previous chemical reactions are examples of irreversible reactions, which means that the reactants are only consumed to generate the products. However, there are situations in which products can react to form reactants. These are another broad group of chemical reactions known as reversible reactions.

Reversible reactions: A reversible chemical reaction is a chemical process in which the substrates form products that react together to produce the reactants back. The irreversible reactions are indicated with a straightforward arrow pointing from the reactants to the products, while the reversible reactions are indicated by a double arrow pointing both directions. Thus, a simple model of a reversible chemical reaction can be:

$$\mathrm{A} + \mathrm{B} \underset{k_r}{\overset{k_f}{\rightleftharpoons}} \mathrm{C} \tag{R10}$$

where k_f and k_r are the kinetic constants of the forward and the reverse steps respectively.

The kinetics equations have to include the reverse step as:

$$\frac{d[A]}{dt} = -k_f[A][B] + k_r[C] \tag{1.12}$$
$$\frac{d[B]}{dt} = -k_f[A][B] + k_r[C] \tag{1.13}$$
$$\frac{d[C]}{dt} = k_f[A][B] - k_r[C] \tag{1.14}$$

Reversible reactions lead to a chemical equilibrium condition even if they do not occur at the same rate in both directions. The chemical equilibrium is defined as the state in which both, reactants and products, are present in concentrations that remain invariant in time [13]. If dynamic equilibrium occurs, the product of one reaction is forming at the same rate as it is used up for the reverse reaction[90]. The equilibrium of a reversible reaction depends on the initial concentrations of the reactants, products, and the equilibrium constant, K_c. The equilibrium constant is defined as:

$$K_c = \frac{k_f}{k_r} = \frac{[PRODUCTS]}{[REACTANTS]} \tag{1.15}$$

A simple real example of a reversible chemical reaction is:

$$2\,NO_2(g) \underset{k_r}{\overset{k_f}{\rightleftharpoons}} 2\,NO(g) + O_2(g) \tag{R11}$$

Autocatalytic Reactions: Autocatalytic chemical reactions are a special type of complex chemical reactions in which at least one of the products is also a reactant. A simple model to exemplify an autocatalytic reversible reaction can be written as:

$$A + B \underset{k_r}{\overset{k_f}{\rightleftharpoons}} 2\,B \tag{R12}$$

where the rate equations are given by:

$$\frac{d[A]}{dt} = -k_f[A][B] + k_r[B]^2 \tag{1.16}$$
$$\frac{d[B]}{dt} = k_f[A][B] - k_r[B]^2 \tag{1.17}$$

where the final product consists on the original B molecule plus the B molecule created in the reaction [183].

Autocatalytic reactions are examples of nonlinear chemistry. Autocatalytic processes are vastly observed in Nature, like in the acid-catalyzed hydrolysis of some esters to carboxylic acids and alcohols [130], or in the dynamics of proteins and gene expression [6, 119].

Due to their characteristic and intrinsic nonlinearity, the autocatalytic reactions are essential to describe the complex dynamics of the chemical processes addressed here. Thus, these types

of reactions are responsible for many of the phenomena observed during the development of this work.

1.3 Types of Reactors

There are three main types of reactors to deal with homogeneous reactions: batch, semibatch, and continuous stirred-tank reactor (CSTR) reactors [56]. Schematics of these three types of reactors are presented in Figure 1.1.

- **Batch reactors**: In batch reactors, all the reagents are located and mixed without any addition or removal to/from the system. In a normal batch reactor, the system is filled with reactants in a single stirred tank at the beginning of the experiment and the reaction proceeds (Fig. 1.1(a)).
- **Semibatch reactors**: Similar to batch reactors but they allow the addition of fresh reactants as time progresses (Fig. 1.1(b)).
- **Continuous reactors**: These reactors are modified to allow reactant addition and product removal at the same flow rate in such a way that the total volume is kept constant during the experimental procedure (Fig. 1.1(c)).

In contrast to CSTR or batch, in a semibatch reactor the volume slightly increases which affects the concentration of the species inside. If the change in volume (ΔV) is relatively small compared to the total volume or the reactor, such changes can be ignored. In any case, stirring must be efficient to allow a uniform distribution of the concentrations and temperature [56].

Some complex reactions may change their dynamics depending on whether they occur in a batch, semibatch, or a CSTR reactor. Some examples are given in the forthcoming sections.

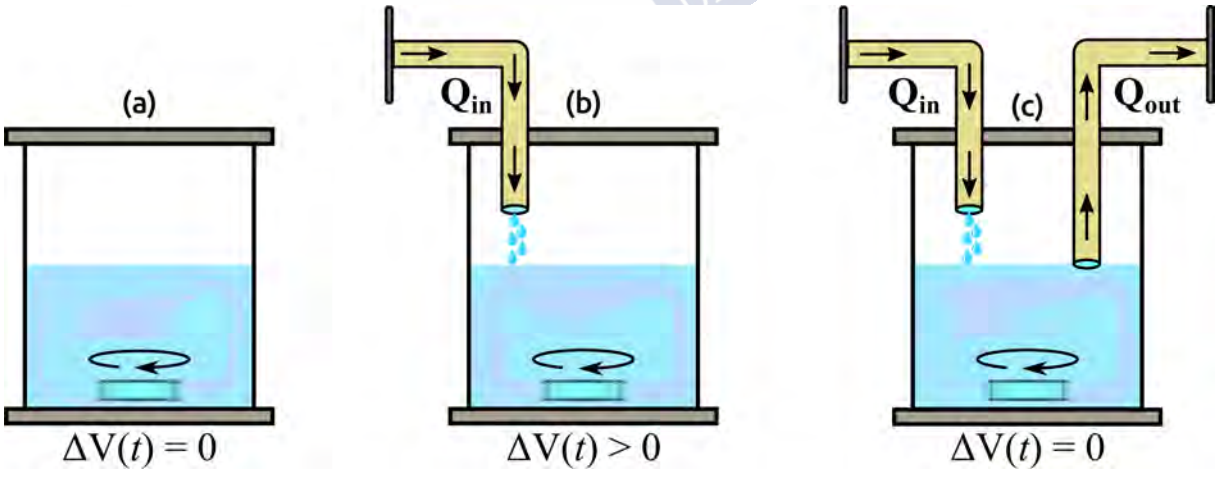

Figure 1.1: Most common types of reactors used for the chemical systems studied in this work: (a) Batch reactor, (b) Semibatch or feed batch reactor and, (c) CSTR reactor. Q_{in} and Q_{out} stand for the inlet and outlet flowrate respectively.

As indicated in the title of this theses, this work is in part about complex chemical reactions. As previously stated, there are literally infinite possibilities for reactive processes to be considered "*complex*". This work will be focused on two special types of complex chemical

reactions. On one hand, the redox oscillators based on the Belousov-Zhabotinsky reaction, and on the other hand, the pH-shifting reactions derived from the classical pH-oscillators. The forthcoming sections will briefly introduce both groups of reactions.

1.4 The Belousov-Zhabotinsky Reaction

The Belousov-Zhabotinsky (BZ) reaction was discovered in the late 50s by Boris Pavlovich Belousov (1893-1970) in the U.R.S.S. Belousov was a biophysicist who was trying to obtain an *in vitro* model of the Krebs cycle. He experimentally observed periodic oscillations between the oxidations states of the cerium (Ce^{4+} and Ce^{3+}) in a solution composed of bromate ($BrO_3{}^-$), sulfuric acid (H_2SO_4), and malonic acid (MA) as the organic substrate. The changes in the the oxidation states of the cerium produced a change in the coloration of the solution [18]. Sadly, even considering the major importance of such discoveries, the results of Belousov were rejected in the scientific community because it was thought that such a reaction violated the Second Law of Thermodynamics [216].

Ten years later, Anatol Markovich Zhabotinsky (1938-2008), recovered the original studies of Belousov and performed a much more detailed description of the system. Contrarily to Belousov, the studies of Zhabotinsky were well accepted and founded the basis of what is now known as the Belousov-Zhabotinsky reaction [220].

Figure 1.2: Example of the ferroin catalyzed Belousov-Zhabotinsky reaction in a in a batch reactor. For this particular experiment: $[MA]_0 = 0.15$ M, $[BrO_3{}^-]_0 = 0.15$ M, $[H_2SO_4]_0 = 0.3$ M and $[[Fe(phen)_3]^{3+}]_0 = 0.001$ M.

In 1972, Field, Körös, and Noyes from Oregon University (USA) developed the first extensive kinetic model of the BZ reaction including 18 elementary steps, 21 reaction intermediaries, 12 species, and 11 reactions [66]. This complex model, known as the FKN model, was the first detailed description of the mechanism of the BZ reaction.

The mechanism consists of the oxidation and bromination of the organic substrate (usually, malonic acid) through bromate ions. This process can be catalyzed through the reduction-oxidation (redox) of a couple of metallic ions, more commonly Ce^{3+}/Ce^{4+}, Fe^{2+}/Fe^{3+}, Ru^{2+}/Ru^{3+}. The overall equation is indicated in reaction R13.

$$2\,H^+ + 2\,BrO_3{}^- + 3\,CH_2(COOH)_2 \longrightarrow 2\,BrCH(COOH)_2 + 3\,CO_2 + 4\,H_2O \qquad \text{(R13)}$$

Even though the full mechanism is rather complex, it can be simplified considering the three elemental sub-processes schematized in Figure 1.3 and described as following [204, 53]:

- **P1**: Oxidation of the metal-ion catalyst coupled by conversion of BrO_2^* to $HBrO_2$. This results in the autocatalytic formation of $HBrO_2$.
- **P2**: Reduction of the metal-ion catalyst accompanied by the oxidation of BrMA.
- **P3**: Reaction between $HBrO_2$ and Br^- to produce HOBr. This step is inhibitory of the autocatalytic process.

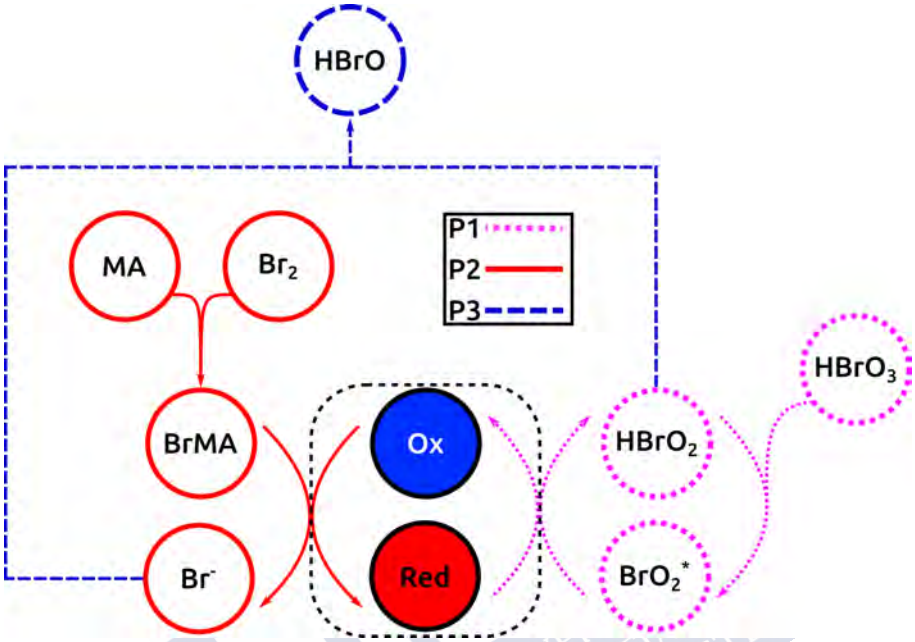

Figure 1.3: Schematic of the key processes involved in the BZ reaction. The bromous acid ($HBrO_2$) is produced through autocatalysis in process P1 (dotted dashed lines in magenta). The reduction of the catalyst by the brominated organic substrate (BrMA) in P2 (red solid lines) produces Br^-. The bromine inhibits process P1 via a delayed negative feedback mechanism in P3 (blue line dashed lines), generating HBrO as the waste product.

Processes P1 and P2 are responsible for the oscillations. In process P3, the bromine generated in P2 interacts with the $HBrO_2$ inhibiting the autocatalytic process P1 and generating the secondary product HBrO. The color changes depend on the metal ion catalyst. Thus, for cerium, the mixture oscillates between yellow (Ce^{4+}) and colorless (Ce^{3+}), and between red (Fe^{2+}) and blue Fe^{3+} when ferroin is used (Fig. 1.2).

The oscillatory character of the BZ reaction can be studied in several ways. One example is presented in Figure 1.4, where the oscillations of the experiment showed in Figure 1.2 were plotted by tracking the color changes by direct image processing algorithms. As can be seen, the oscillatory behavior exhibits a well defined period in the range of time studied. More detailed quantitative information can be also obtained by more advanced spectroscopic techniques.

The BZ reaction was the first example of a class of inorganic chemical reactions that shows out-of-equilibrium phenomena, such as oscillations, bistability, and synchronization [52, 182, 82, 201].

1.4.1 Reduced Kinetic Models of the BZ Reaction

Due to the large number of variables and equations of the model created by Field, Körös and Noyes, (the FKN model), made it very difficult to numerically simulate in the time

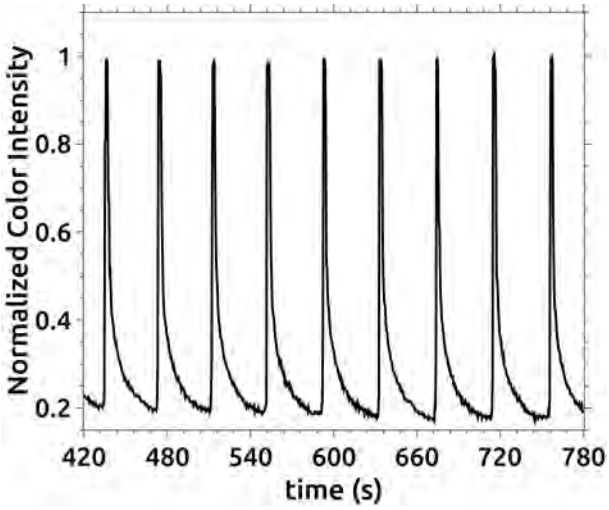

Figure 1.4: Oscillations of the BZ reaction presented in Figure 1.2. This plot was constructed by tracking the color changes in the aforementioned experiment by image processing techniques.

when it was created (1974). For such reason, reduced models were developed to numerically and theoretically study the dynamics of the BZ reaction. These models were developed to preserve the complex behavior of the oscillating reaction by using a reduced amount of variables/equations.

The first hypothetical model is known as the Brusselator [1], which was proposed by Ilya Prigogine at the Université Libre de Bruxelles [4]. This model reduces the variables of the system in two, considering an activator (X) and an inhibitor (Y). This simple description can reproduce the dynamics of an oscillating. The mechanism of the Brusselator is given by:

$$\mathrm{A} \xrightarrow{k_1} \mathrm{X} \tag{R14}$$

$$2\mathrm{X} + \mathrm{Y} \xrightarrow{k_2} 3\mathrm{X} \tag{R15}$$

$$\mathrm{X} + \mathrm{B} \xrightarrow{k_3} \mathrm{Y} + \mathrm{D} \tag{R16}$$

$$\mathrm{X} \xrightarrow{k_4} \mathrm{E} \tag{R17}$$

by considering that the reactants A and B are in large excess, and fixing the concentrations of the products D and E to zero, the kinetics rate equations of the Brusselator are given by:

$$\begin{aligned} \frac{d[X]}{dt} &= k_1[A] + k_2[X]^2[Y] - k_3[X][B] - k_4[X] \\ \frac{d[Y]}{dt} &= k_3[X][B] - k_2[X]^2[Y] \end{aligned} \tag{1.18}$$

where X and Y are reaction intermediaries. The net reaction of the Brusselator is A + B $\rightarrow$ C + D.

A more realistic model is the Oregonator [2]. This model, as can be suggested from its name,

[1] The name Brusselator is a combination of the words Brussels and oscillator.

[2] Analogously to the Brusselator, the word *Oregonator* is a combination of the words Oregon and Oscillator.

was developed at the University of Oregon by Field and Noyes in 1974 [67]. The model was obtained as a direct reduction of the FKN mechanism and it was achieved by the application of standard methods of chemical kinetics like the rate-determining-step approximations [201, 183, 130]. In contrast to the Brusselator, the Oregonator model includes three dynamic variables (the inhibitor, the activator, and the catalyst), and an adjustable kinetic modulator. This makes the model much richer in terms of the complexity and behaviors that can be reproduced by it, like for example, bistability and chaos in CSTR [81, 80, 164].

The Oregonator is described by the following set of chemical equations:

$$\mathrm{A} + \mathrm{Y} \xrightarrow{k_1} \mathrm{X} + \mathrm{P} \tag{R18}$$

$$\mathrm{X} + \mathrm{Y} \xrightarrow{k_2} 2\,\mathrm{P} \tag{R19}$$

$$\mathrm{A} + \mathrm{X} \xrightarrow{k_3} 2\,\mathrm{X} \tag{R20}$$

$$2\,\mathrm{X} \xrightarrow{k_4} \mathrm{A} + \mathrm{P} \tag{R21}$$

$$\mathrm{B} + \mathrm{Z} \xrightarrow{k_5} \frac{1}{2} f\,\mathrm{Y} \tag{R22}$$

where kinetic equations are given by:

$$\begin{aligned} \frac{d[X]}{dt} &= k_1[A][Y] + k_2[X][Y] - k_3[X][A] - 2k_4[X]^2 \\ \frac{d[Y]}{dt} &= k_1[A][Y] - k_2[X][Y] + \frac{1}{2}k_5 f[B][Z] \\ \frac{d[Z]}{dt} &= 2k_3[A][X] - k_5[B][Z] \end{aligned} \tag{1.19}$$

where X represents the activator, Y the inhibitor, and Z the catalyst which corresponds to $HBrO_2$, Br^- and Fe^{2+} from the original BZ reaction respectively. f is an adjustable stoichiometric factor that makes it possible to modulate the dynamics of the reactions.

Example simulations of both, the Brusselator and the Oregonator kinetic models are presented in Figure 1.5. These simulations were done by using the GNU software COPASI [95].

1.4.2 The 1,4-Cyclohexanedione-Bromate-Acid Oscillatory Reaction

As it was mentioned, one of the secondary products of the original BZ formulation is CO_2 (see reaction $R_1 13$). The formation of carbon dioxide can be appreciated as tiny bubbles that emerge from the BZ solution. In some cases, this can be detrimental for some studies, as the bubbles may, for example, interact with the measurement equipment or hinder the subsequent analysis of the experiments.

In order to overcome such an issue, in 1994, Kurin-Csörgei *et al* developed an alternative formulation of the classical BZ reaction by replacing the original organic substrate with 1,4-Cyclohexanedione (hereafter CHD - Fig. 1.6) [114, 187, 188, 190, 189]. This alternative formulation is usually called the BZ-CHD reaction of *Bubble-Free* BZ reaction.

The replacement of the malonic acid not only eliminates the formation of carbon dioxide

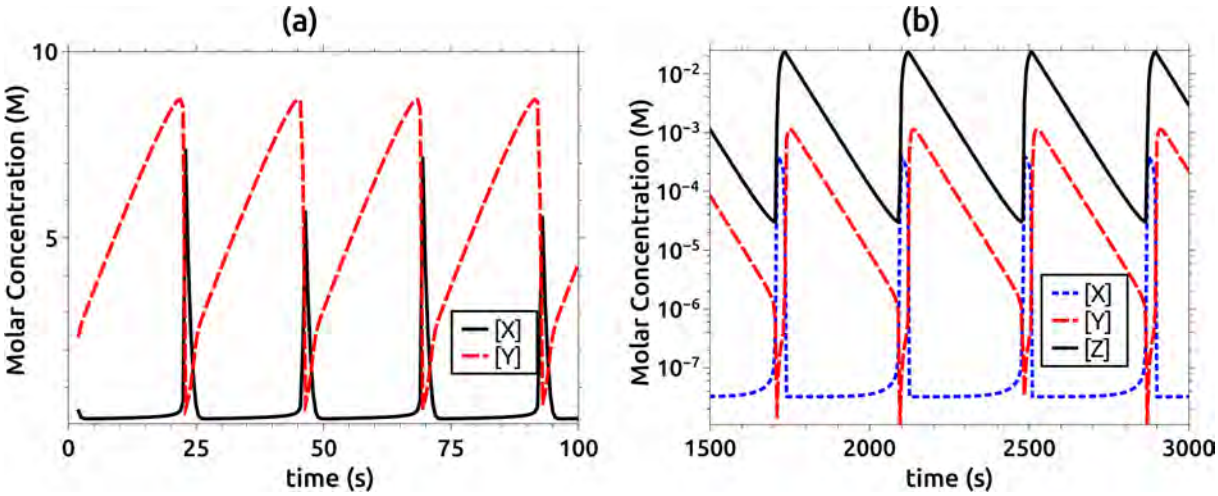

Figure 1.5: Simulations of the temporal dynamics of (a) the Brusselator and (b) the Oregonator kinetics models. In both cases [X] and [Y] represent the molar concentration of the activator and the inhibitor species respectively. In (b), [Z] represents the molar concentration of the catalyst species

but also produces dynamics significantly different compared to those observed in the original BZ system [123, 84, 122]. Thus, traveling shock structures, long-lived oscillations, light sensitivity, wave merging, stacked wavefronts, densely packed patterns, and segregated clusters are examples of the broad variety of behaviors observed in the bromate-CHD-ferroin system [190, 189]. All these characteristics made the BZ-CHD to be considered superior over the classical BZ reaction, and more suitable to study multitude of different phenomena [190, 188, 187, 189].

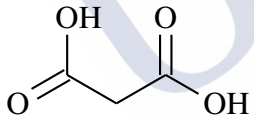

(a) Malonic Acid (MA)

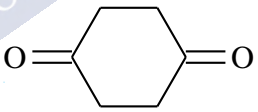

(b) 1,4-Cyclohexanedione (CHD)

Figure 1.6: Organic substrates for (a) the original BZ reaction, (b) the BZ-CHD reaction

Several studies were made to understand and fully characterize the mechanism of the BZ-CHD reaction [113, 112, 187, 188, 114, 190, 189]. An extensive kinetic model was also proposed by Szalai *et al*, where the dynamics and properties of the BZ-CHD reaction were studied for different catalysts and for the uncatalyzed reaction [189, 190]. Similar to the FKN model, reduced or skeleton models were also developed. In such models, the main characteristics of the systems are preserved even with a reduced number of variables. This makes possible its numerical implementation without requiring sophisticated computational resources [189, 190, 188]. The kinetic models of the BZ-CHD reactions are not indicated in this introductory section, as they will be extensively used and described in the forthcoming chapters.

For this thesis, the ferroin catalyzed BZ-CHD reaction will be preferred over the classical BZ formulation. This reaction will be extensively used in Part I to study its coupling with hydrodynamic systems.

1.5 pH-Shifting Reactions

A pH-shifting reaction is defined as a system in which the hydrogen ion plays the most important kinetic role in the overall dynamics. In these systems, the driving force of such changes is the variation in pH, which can be as large as 6 pH-units [145, 153]. pH-shifting reactions are a well-known group of reactions that exhibit relatively simple chemistry. The reaction mechanism in these systems is better understood compared to other types of complex reactions [145, 153]. This is possible since the stoichiometry and the kinetics of the global and intermediary reactions were thoroughly studied, making it possible to easily identify the positive and negative feedback processes.

As was mentioned in Section 1.3, some complex reactions change their dynamics depending on the experimental conditions. This is the case for most pH-shifting reactions[145]. Some formulations exhibit oscillations or complex dynamics when studied in CSTR or semibatch reactors, and only a single pH switch when the same reaction occurs in a batch reactor. When producing oscillations, the pH-shifting reactions are also known as pH-oscillators [145, 153, 129].

There are two main categories of pH-shifting reactions that will be addressed in this introduction. One are the so-called inorganic, in which the key components are inorganic, and the other are the so-called organic (or special) in which part of its formulations are composed of organic species.

1.5.1 Inorganic pH-Oscillators

Inorganic pH-oscillators were well known and vastly studied. In most cases, studies were focused on the oscillating dynamics observed in CSTR or semibatch reactors. These reactions are usually composed of an oxidant and a reductant species, thus they are redox processes. A broad description of all known pH-oscillators is presented in Orbán *et al* [145].

Additionally to the oxidant and the reductant, in some systems, a second substrate is necessary for the oscillations to occur [145]. The dynamics of a pH-oscillator will depend on whether a second substrate is needed or not [145, 153]. Both situations are schematized in Figure 1.7.

In the one-substrate systems, the reductant is oxidized by a partial oxidation mechanism producing a reaction intermediary. This step is proton-consuming (negative feedback), thus it produces an increment in the pH (Step 1, Fig. 1.7(a). In a second step, the intermediary will react with both, oxidant and reductant through a total oxidation mechanism. In this step apart from the end product, protons are generated by an autocatalytic mechanism decreasing the pH (Positive feedback, Step 2, Fig. 1.7(a)). Oscillations are produced by the repetition of steps 1-2. The cycle will continue until the substrates are consumed.

In a two-substrate system, oscillations occur as a consequence of two consecutive reactions. In the first step, protons are produced autocatalitically by an oxidation mechanism causing the pH to decrease (positive feedback, Step 1, Fig. 1.7(b)). The generated protons are consumed in a second step in which another substrate is oxidized to produce the end product (negative feedback, Step 2, Fig 1.7(b)). As this is a proton consuming reaction, the pH increases and the cycle starts again. Oscillations will continue until the first substrate is consumed. The second substrate can be a reductant or a H^+ consuming reagent.

An experimental example of the dynamics of a one-substrate oscillator is presented in

Figure 1.7(c)). These results were obtained from the BrO_3^-/SO_3^{-2} system [145]. In this particular case, a small amount of Mn^{+2} was added as a catalyst. The reaction was performed in a semibatch reaction at 45 °C [153]. The changes in the pH were followed by using a pH-meter.

Inorganic pH-oscillators can be modeled by considering a simple skeleton mechanism. This model was suggested by Rábai *et al* [158, 129] and it consists on three steps:

$$A^- + H^+ \rightleftharpoons HA \tag{R23}$$

$$B + HA \xrightarrow{H^+} H^+ + P \tag{R24}$$

$$C + H^+ \longrightarrow Q \tag{R25}$$

where A^- is the conjugate base of a weak acid (HA), the reductant. This species is oxidized by B to a conjugate base of a strong acid (P). The second substrate is indicated by C and the end product is Q.

The positive feedback is represented by the autocatalytic step in the second reaction. The third reaction is the negative feedback which is the proton consuming step. This simple model can reproduce the oscillatory dynamics of the pH oscillator both in homogeneous and spatially extended systems [129].

pH-Oscillators are attractive, not only for their simplicity but also for their potential applications. One of these applications is their use for drug delivery in living systems. The fundamentals of such techniques will be not addressed here, but the idea is to couple a pH-sensitive material to the dynamics of the pH-shifting reaction to create a chemo-mechanical device. In this way, a specific drug or compound could be specifically released due to changes in the conformation of the material produced by dynamics in the pH [36, 174, 14, 118, 203, 5, 196, 110].

Even though the idea is promising, there is a major problem: Most of the pH-sensitive materials are often organic, and these inorganic pH reactions result too aggressive for such types of molecules [107]. To overcome this issue, organic pH-shifting reactions were created

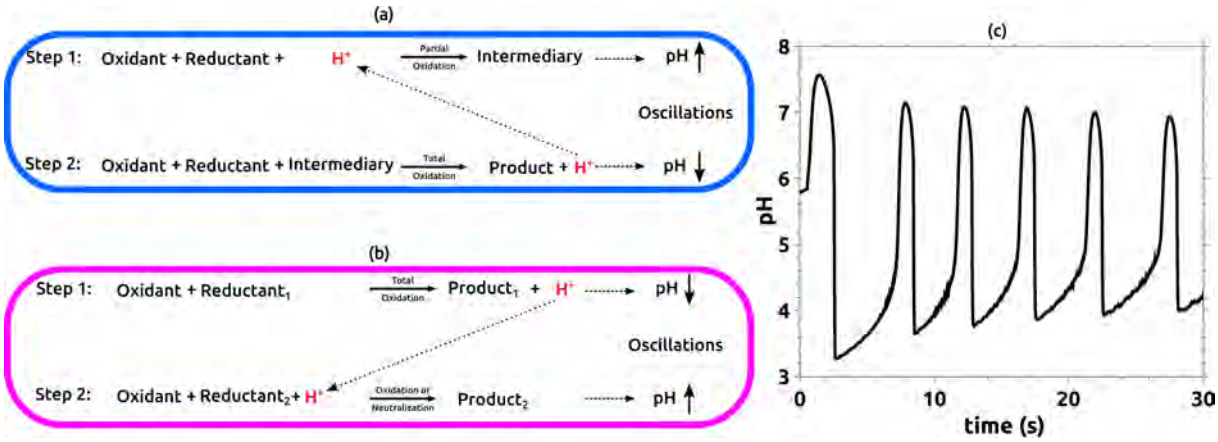

Figure 1.7: Schematics of the mechanism of the (a) one-substrate and (b) two-substrate pH-oscillators. (c) Experimental results of one-substrate pH-oscillator. This experiment was done in a semibatch reaction at 45 °C following the recipe indicated in Poros *et al* for the BrO_3^-/SO_3^{-2}-Mn^{+2} system [153]. All pH-changes were recorded by using a pH-meter.

and will be discussed in the next section.

1.5.2 Organic pH-Shifting Reactions

Organic pH-shifting reactions are a special type of pH reactions in where the changes in the pH are not produced by redox processes but by acid-base steps [145]. There are two main reactions that will be used in this thesis: the Formaldehyde-Sulfite (FS) and the Formaldehyde-Sulfite-Gluconolactone (FSG) reactions. Both reactions will be introduced from a completely descriptive point of view. As these reactions will be extensively used in Part II of the thesis, more information related to their modeling and characterization will be addressed in their corresponding chapters.

The Formaldehyde-Sulfite Reaction

The FS reaction is a well-known pH-shifting reaction where the pH rapidly changes from acid to basic after an induction period [212, 213]. This phenomenon received the name of *clock behavior* due to the abrupt change in the pH. The reaction consists of a buffer composed of sulfite ($SO_3{}^{2-}$) and bisulfite ($HSO_3{}^{-}$), and formaldehyde (in the form of methylenglycol, which is hydrated form of formaldehyde). The clock mechanism is produced by the consumption of the internal sulfite/bisulfite buffer by formaldehyde to produce hydroxymethanesulfonate, which is a formaldehyde-sulfite adduct. The maximum pH transition is about 4 units of pH (from 6 to approximately 10). Both, the induction time and the pH jump can be modulated by changing the initial concentrations of the chemical species and the sulfite/bisulfite proportion.

The typical clock behavior is observed in a batch reactor, however, oscillations and complex dynamics were observed in CSTR [106]. An example of the experimental FS clock reaction is presented in Figure 1.9(a). As can be seen, the pH changes after the induction period. Both, the initial and the final pH depend on the initial species concentrations.

This reaction is extensively studied in Kovacs *et al* [106]. In such work, the system is completely characterized and modeled, showing the changes in the dynamics produced by the type of reactor where the reaction occurs.

The Gluconolactone-Formaldehyde-Sulfite Reaction

The FSG reaction was created from the FS reaction to induce delayed negative feedback in the dynamics of the reaction [108, 107]. The reaction shares the same composition as the FS reaction, but including one more species, the D-(+)-gluconic acid δ-lactone (or gluconolactone).

The characteristic clock dynamic of the FS reaction is coupled with the hydrolysis of the gluconolactone that produces gluconic acid. This process is schematized in Figure 1.8. The hydrolysis reaction is base-catalyzed, which means that the OH^- generated after the consumption of the sulfite/bisulfite buffer in the FS reaction, will increase the rate of hydrolysis.

The coupling between these two processes produces a single peak in the pH, which indicates both positive and negative feedback. An experimental example is presented in Figure 1.9(b).

In CSTR this reaction also exhibits complex behaviors, such as oscillations [108, 107]. Figure 1.10 shows an experimental example of the FSG reaction conducted in a continuous stirred tank reactor. As can be appreciated, the oscillations are indicated by the change in the color indicator (Bromothymol blue). In the acid state, this indicator shows a yellow coloration

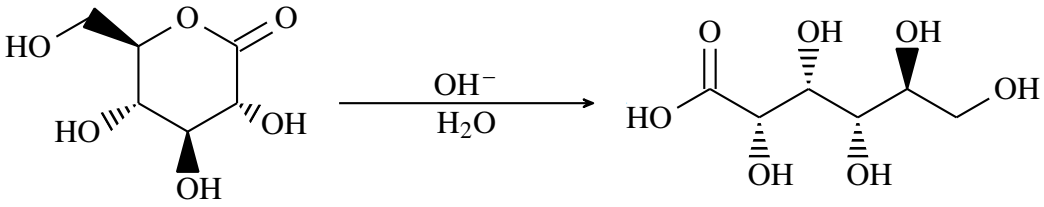

Figure 1.8: Schematics of the hydrolysis of the gluconolactone (left) to gluconic acid (right). This process is base catalyzed, which means that the OH^- produced after the buffer consumption in the FS reaction increases the rate of hydrolysis.

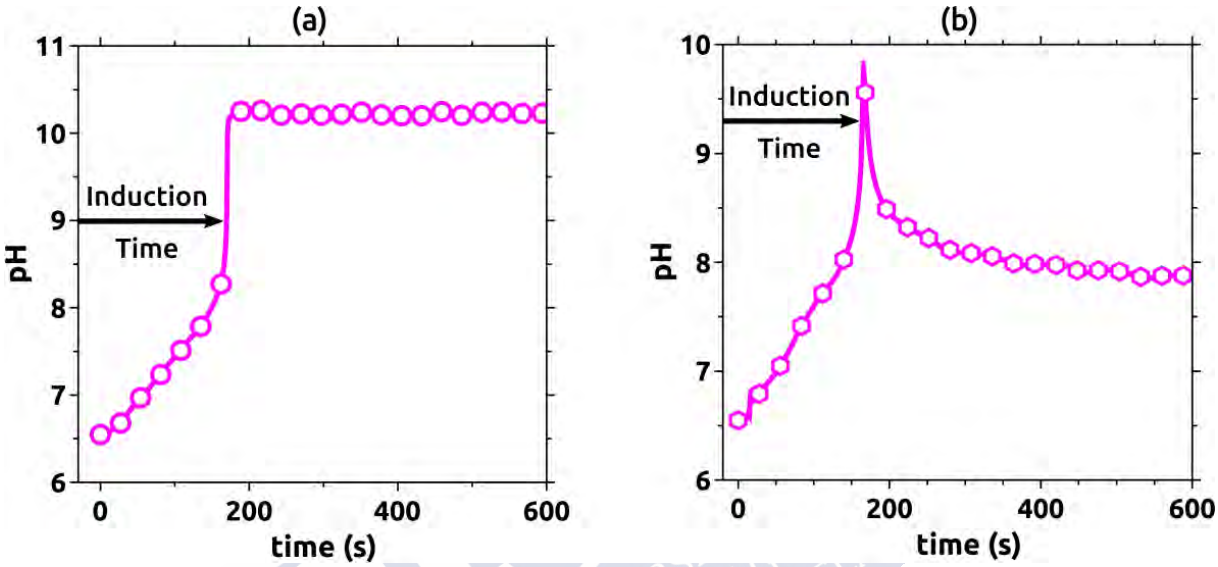

Figure 1.9: Examples of the dynamics of (a) FS reaction and (b) FSG reaction in batch reactor. The FS reaction is characterized by the abrupt change in the pH after the induction time produced by the consumption of the SO_3^{2-}/HSO_3^- buffer. In the FSG reaction, the dynamics observed in (a) are coupled with the hydrolysis of the gluconolactone, providing the delayed negative feedback necessary to produce the single peak observed in a batch reactor.

that turns into blue in the basic state. The oscillations were recorded with a pH-meter connected to a computer. As can be seen, the oscillations are formed by the cycling process produced by the buffer consumption and the hydrolysis of the gluconolactone. As the substrates/products are continuously added/removed to the system, the single peak dynamic became oscillating.

Figure 1.10: Experimental example of the FSG reaction in a CSTR. (a) Oscillations are easily observed by following the changes in the color indicator, or (b) by using a pH-meter.

1.6 Reaction-Diffusion-Convection (RDC) Systems

The previous sections described different types of reactions in stirred systems. However, it is not always possible to homogeneously distribute a mixture. In such cases, it is important to consider the effects produced by diffusive and convective forces in the active medium.

Diffusion manifests in systems when specific properties are not homogeneously distributed in the medium. For example, the mixing of a droplet of ink in a glass of water is produced by the random collisions of the ink molecules with the water molecules. The effect of diffusion in an inhomogeneous system is responsible for many complex behaviors that are part of the study of this thesis.

On the other hand, many processes in Nature and the industry occurs under the effect of advective forces, like the transport of pollutants in fluid flows [146], convective plumes in the ocean [200, 111], dispersion of aerosol in the atmosphere, mixing processes in reactors [131], etc. More specifically, the transport of a chemical species in a reactive medium combined with diffusivity can be responsible for a multitude of different complex phenomena [179].

A mathematical description for the transport of a chemical species can be derived from the general continuity equation as [179]:

$$\frac{\partial C_i}{\partial t} + \nabla \cdot \vec{J}_{tot} = R_i \tag{1.20}$$

where $\vec{r} = (x,y,z)$ is the position vector, $C_i = C_i(\vec{r},t)$ are the concentrations of the species i in a specific position and time, R_i are the net volumetric source of each the species i, and $\vec{J}_{tot} = \vec{J}_{diff} + \vec{J}_{adv}$ is the total flux produced by the diffusive ($\vec{J}_{diff}$) and the advective ($\vec{J}_{conv}$) flux.

The expression 1.20 relates the rates of change of every species i to the flow and diffusion into and out of a differential control volume and considers the generation or consumption inside the control volume [179]. The diffusive flux is produced by the diffusion of the molecules moving randomly through the medium, and can be described by Fick's first law:

$$\vec{J}_{diff} = -D_i \nabla C_i \tag{1.21}$$

where $D_i = D_i(\vec{r},t)$ are the diffusion coefficient of each species i.

On the other hand, the advective flux is associated with the flow convection by the following expression:

$$\vec{J}_{adv} = \vec{u} C_i \tag{1.22}$$

where $\vec{u} = \vec{u}(\vec{r},t)$ is the velocity field.

The combination of Eqs. (1.21)-(1.22) with Eq.(1.20), gives the general transport equation for each chemical species:

$$\frac{\partial C_i}{\partial t} + \nabla \cdot (-D_i \nabla C_i + \vec{u} C_i) = R_i \tag{1.23}$$

Considering the reactivity between the chemical species, the source and sink terms R_i are now dependent on the concentration of the species, therefore $R_i = f_i(C_i,t)$, where f_i are the net

reaction rates of the chemical system. By combining Equation (1.1), and considering that the diffusion coefficients do not depend on the position and time, Equation (1.23) is reduced to:

$$\frac{\partial C_i}{\partial t} + \vec{u} \cdot \nabla C_i = D_i \nabla^2 C_i + f_i(C_i, t) \tag{1.24}$$

which is known as the **reaction-diffusion-convection** equation for the species i.

In a non-reactive system, the source and sink term can be neglected obtaining:

$$\frac{\partial C_i}{\partial t} + \vec{u} \cdot \nabla C_i = D_i \nabla^2 C_i \tag{1.25}$$

This equation is known as the **diffusion-convection** equation and it will be fundamental to explain non-reactive convective processes [179].

In this thesis, Eqs. (1.24) and (1.25) will be fundamental in the development of numerical models.

1.6.1 Reaction-Diffusion (RD) Systems

Reaction-diffusion systems are mathematical models that describe how spatially extended species are affected by two main processes. One is the diffusion, that facilitates the spatial distribution through the medium. The other one is the chemical process that modulate the creation and/or consumption between species. Many natural phenomena can be modeled by reaction-diffusion systems, such as somitogenesis[149], animal pigmentation[147, 105], cell differentiation [38], and chemotaxis [180] among others. More specifically, non-linear reaction-diffusion systems are in general, useful to model out-of-equilibrium phenomena like self-organization and spatio-temporal pattern formation of biological systems. These problems are mainly driven by spontaneous symmetry breaking in inhomogeneous media [156, 155, 20, 115]. There are three main characteristic regimes associated with RD systems: excitable [40, 152, 133], bistable [40], and oscillating [55, 54]:

Excitable regime: In an excitable medium, a local perturbation of the species propagates through the medium. This situation is typically observed in cardiac and nervous tissues, neurons, and in some diseases like Parkinson's or epilepsy. In an inhomogeneous chemical system, the excitable regime is manifested in the form of circular, planar, or triangular traveling waves or in the form of a spiral [152, 133, 60], which are often produced by the rupture of a concentric wave. Excitable regimes are also characterized to show, in some specific conditions, structures that are stationary in space. An example of this is presented in Figure 1.11(a). These structures are known as Turing patterns and were obtained from the BZ-AOT chemical system[3][205]. Turing patterns were used as the standard model to explain the pigmentation in animals [205]. These types of structures will be not considered in this thesis.

Oscillating regime: In an oscillating regime, the local perturbation propagates through the medium similar to the excitable case, but periodically. There are plenty of oscillating systems in Nature. Some examples can be found in population dynamics, metabolic cycles, cardiac and

[3]Author's Note: these Turing patterns were the first to be obtained experimentally at the Université Libre de Bruxelles, home of the Brusselator model. They were obtained by the author during his pre-doctoral stay in 2013-2014.

circadian rhythms, and many more. In particular, the oscillating chemical reactions introduced in Section 1.4 are examples of non-linear chemical oscillating systems. Figure 1.11(b) shows an example of reaction-diffusion patterns observed in an inhomogenous BZ-CHD reaction.

Bistable regime: The bistable regime is characterized by the coexistence of two different states configuring a stable spatial concentration distribution. The importance of these systems lies in their capacity to store information since they have two stable states. This was observed in the mechanism used by neurons when discriminating nerve impulses [167]. Bistability is not common in chemical systems, however, there are some examples of reactions that exhibit such behavior [19, 97].

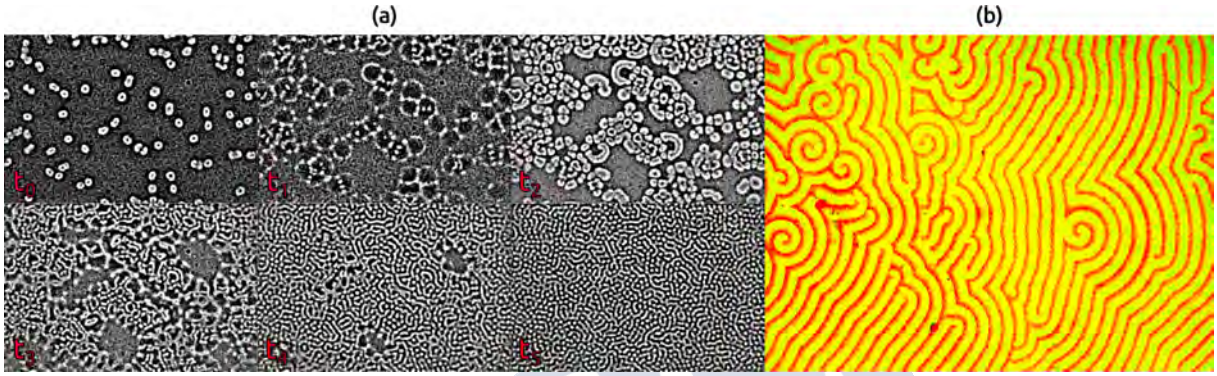

Figure 1.11: Examples of spatio-temporal structures obtained from reaction-diffusion systems. (a) Formation of spatially stationary Turing patterns observed from the BZ-AOT system. (b) Traveling waves and spirals observed from the BZ-CHD reaction.

A general mathematical description for reaction-diffusion systems can be derived from Eq. (1.24) by neglecting the terms associated with the convection:

$$\frac{\partial C_i}{\partial t} = D_i \nabla^2 C_i + f_i(C_i, t) \tag{1.26}$$

this expression is known as the **reaction-diffusion** (RD) equation for the species i.

Many systems in Nature can be modeled in a simplified manner by considering only two variables, an activator (C_1) and an inhibitor (C_2). This is possible by the principle of slaving [83], which eliminates all variables that quickly converge to the stationary state and therefore, have little effect on the dynamics of the system. Thus, a more specific mathematical model based on this principle is described by:

$$\begin{aligned} \frac{\partial C_1}{\partial t} &= D_1 \nabla^2 C_1 + f_1(C_1, C_2, t) \\ \frac{\partial C_2}{\partial t} &= D_2 \nabla^2 C_2 + f_2(C_1, C_2, t) \end{aligned} \tag{1.27}$$

where the non-linear behavior of the system is determined by the expression of the reaction terms f_1 and f_2.

The existing numerical models for the BZ reaction introduced in Section 1.4.1, are capable to reproduce the dynamics of the excitable and oscillatory regimes. This can be achieved by combining Eqs. (1.27) with the mathematical models described by Eqs. (1.18) and (1.19).

Figure 1.12 shows the results of simulating the Brusselator and Oregonator models with diffusion. Spatio-temporal patterns similar to those observed in Figure 1.11(b) are presented in Figure 1.12(a). These structures were obtained by simulating the spatial Brusselator model. In this case, the system is under the oscillating regime, and it is characterized to show concentric traveling waves with global oscillations at the center. Figure 1.12(b) shows an example of the excitable spiral obtained by simulating the spatial Oregonator model. In this case, there are no oscillations and only one single structure propagates through the medium.

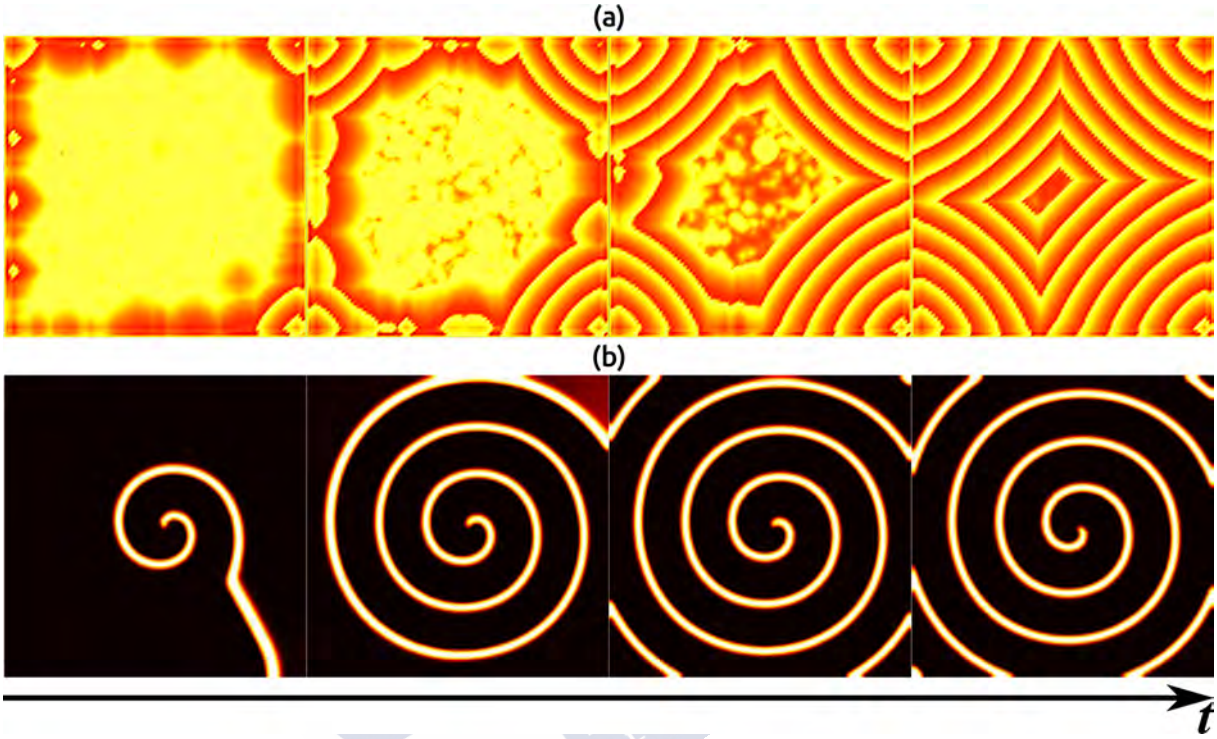

Figure 1.12: Simulations of (a) oscillating regime obtained by numerical simulation of the spatial Brusselator model, and (b) excitable spiral obtained by numerical simulation of the spatial Oregonator model.

Reaction-diffusion patterns can be also obtained from pH-oscillators. These reactions are especially suitable to produce stationary structures due to their autocatalytic nature. In these systems, the role of the activator is played by the H^+ ion, and the inhibitor will depend on the specific formulation [145].

Similar to the BZ reaction, patterns can be observed depending on the relative diffusivities of the inhibitor and the activator. When both are approximately equal, traveling waves are favored. Turing-like spatio-temporal structures can be obtained by decreasing the diffusivity of the activator. This can be achieved by introducing large anions like the polyacrylate (Section 1.9), which produces a reversible binding effect of such a molecule [129]. Another interesting characteristic is that any obtained structure can be observed with acid-base indicators without any other sophisticated method [186, 145].

There are more complex situations on the bibliography where reaction-diffusion systems are controlled or modified by external forcings like centrifugal forces [79, 60], advection [209, 208], electric fields [151], and temperature[30].

1.7 Hydrodynamic Instabilities

In formal terms, a fluid flow is considered stable when any infinitely small disturbance applied to the system does not produce any noticeable effect on the initial state of the system, and such disturbance dies down with time. In other words, if a flow is slightly perturbed, then the disturbance may be decomposed into a set of different spatial modes each with its decay rate. On contrary, in an unstable flow, any disturbance applied to the system will produce a noticeable effect on it and it will be amplified in time, making the system irreversibly changed from its initial state [50]. Some examples of typical fluids instabilities are presented in Figure 1.13.

Thus, for example, the Rayleigh-Bénard instability is characterized by the formation of spontaneous patterns produced by buoyancy-induced convection cells (Fig. 1.13(a)) [34]. The Kelvin-Helmholtz instability is produced at the interface between horizontally oriented fluids with different velocities and densities. This phenomenon can be observed in clouds like the example, or the atmosphere of the gaseous planets (Fig. 1.13(b), [99, 34]). The Crab Nebula is an example of the Rayleigh-Taylor instability (Fig. 1.13(c)) [34]. In this case, the particles accelerated by the Crab pulse try to make their way out through remnants previously ejected by the supernova explosion [64]. Apart from astronomy, the Rayleigh-Taylor instability will be studied in detail in the forthcoming chapters.

There are special types of fluids instabilities that are called *fingering* instabilities which are mostly observed in fluids displacements. In stable conditions, when a low mobility fluid (displacing fluid) displaces a high mobility fluid (displaced fluid), the contact interface remains planar and the mixing between both fluids is almost negligible. On the contrary, when a higher mobility fluid displaces a low mobility fluid, the fingering phenomenon occurs. In this unstable situation, the contact interface deforms into *fingers* and the displacing fluid invades the other one. This phenomenon is particularly undesirable in the industry since it is usually detrimental for all the processes where it occurs [41, 132].

The mobility of fluid is usually associated with differences in viscosity and/or density of the two fluids considered, and it is an important factor that determines the stability of the system. The mobility can be also affected by different phenomena such as diffusion or reactive processes.

Fingering instabilities are observed in both immiscible and miscible systems. In both cases, the viscosity and/or density difference across the interface is the main driving mechanism of the instability. In the immiscible case, the surface tension acts as a stabilization factor and it tends to produce a planar interface. However, in the miscible case the system stabilization is favored by the diffusive mixing of the two solutions, which produces a decrement in time of the gradient of mobility and diffusion [4].

Fingering instabilities are also observed in many diverse fields like enhanced oil recovery [132, 206, 41, 21, 207, 7], chromatography [173, 32, 42, 198, 166, 46], polymerization reactions [10, 184], and more.

Before describing the main aspects of the classical fingering hydrodynamic instabilities, it is necessary to first develop a few basic concepts related to hydrodynamics and some important considerations about the mathematical description of these types of systems. Thus, the forthcoming sections will briefly introduce the main concepts of Darcy's law and the flow in Hele-Shaw cells.

[4] In this thesis, the immiscible case **will be not addressed**.

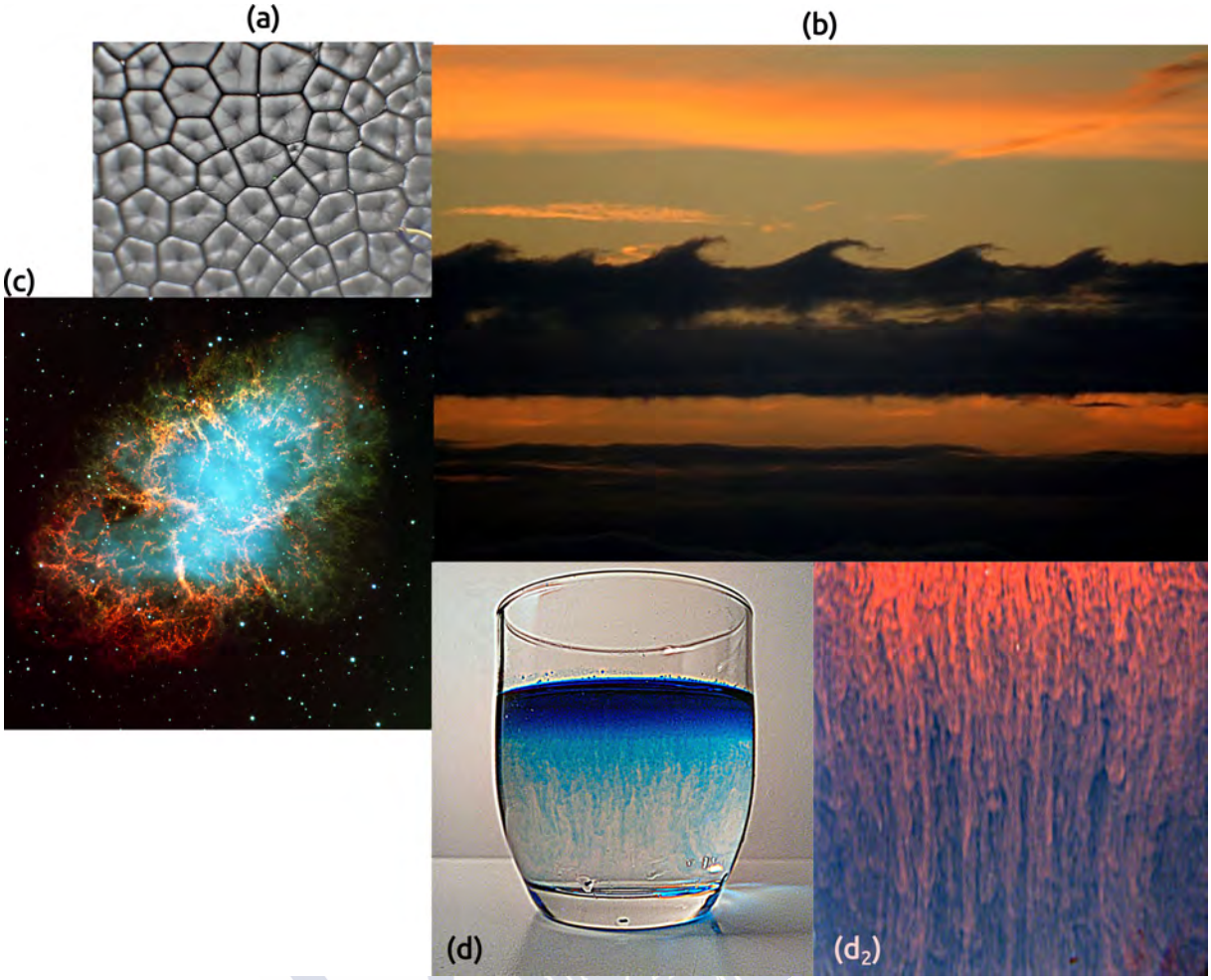

Figure 1.13: Several examples of hydrodynamics instabilities. (a) Rayleigh-Bernard instability. (b) Kelvin-Helmholtz instability observed in the clouds [99]. (c) The Crab Nebula as an extravagant example of the Rayleigh-Taylor instability [64]. (d) Home-made double diffusive density fingering obtained by mixing cold salty water (at the bottom of the glass) and warm pure colored water (at the upper part of the glass). (d_2) is a zoom of the fingers observed in (d). This image was artificially colored to improve visualization.

1.7.1 Flow In Porous Media - Daryc's Law

In the 17th century (1856), the civil engineer Henry Philibert Gaspard Darcy (1803 – 1858) was assigned by the government of the city of Dijon, in France, to participate in the construction of the municipal water system. During the process of developing a water depuration system based on sand filters, he empirically and experimentally discovered a linear relationship between the flow rate of the fluid moving through the medium and the pressure inside the porous medium [43]. The studies of Darcy were made in an experimental apparatus similar to the one schematized in Figure 1.14:

More specifically, Darcy studied the proportionality between the instantaneous flux and the ratio of the height difference (Δh) to the distance (L) between two measurement regions a and b. He found that such proportionality was strongly dependent on the granular material he used for the study:

$$\frac{Q}{A} \propto \frac{h_1 - h_2}{L} \tag{1.28}$$

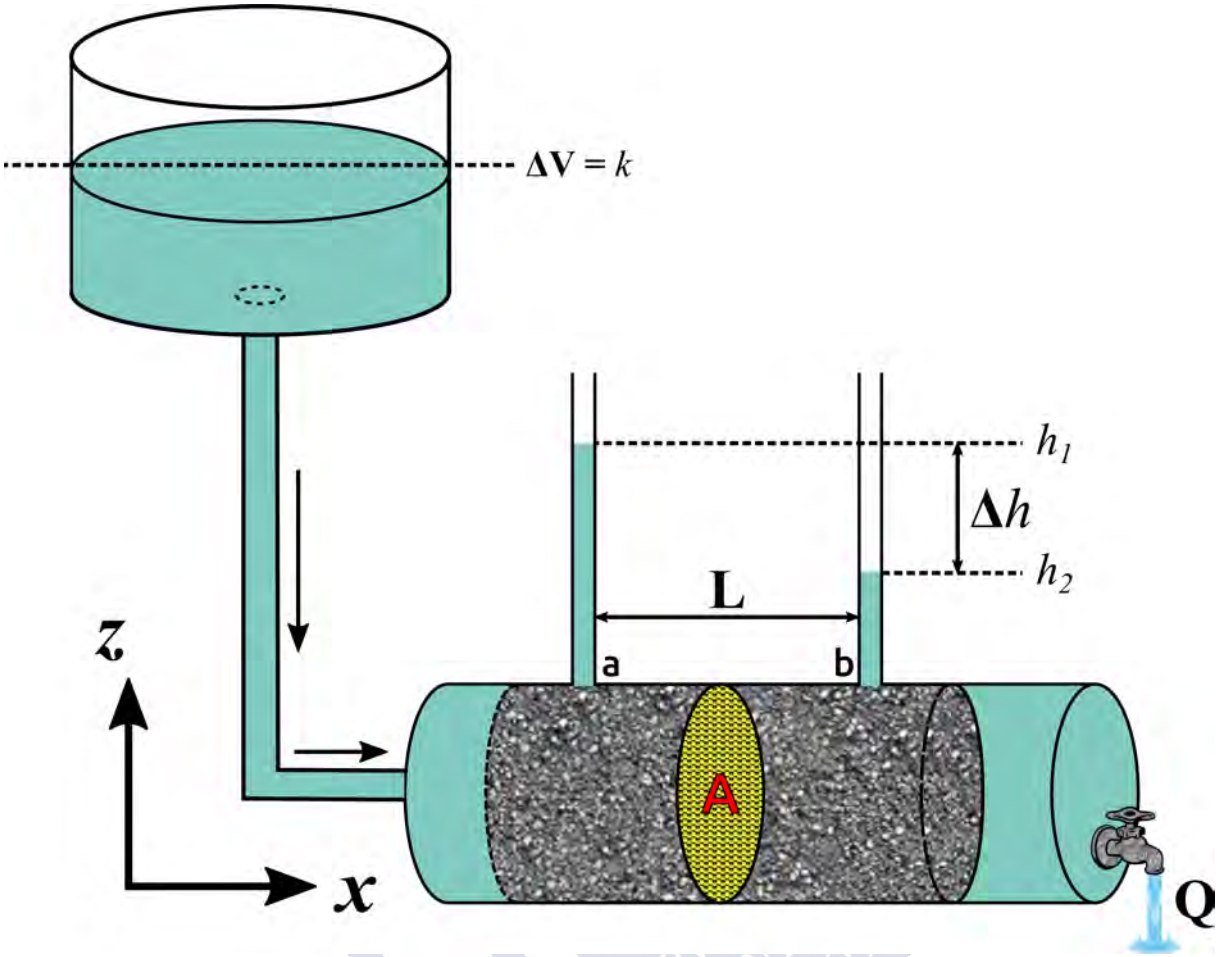

Figure 1.14: Model of Darcy's experiment. The fluid passes through a porous region of cross-section A. The height difference Δh is proportional to the pressure drop between distance $L = b\text{-}a$. Q is the volumetric flow rate at the outlet or discharge rate.

that more formally can be expressed as:

$$Q = -KA\frac{\Delta h}{L} \tag{1.29}$$

where Q $[m^3/s]$ is the volumetric flow rate at the outlet or discharge rate, K $[m/s]$ is Darcy's permeability coefficient (or hydraulic conductivity) and is a physical parameter that accounts for how easily the fluid can move through the pore space for the material [17]. A $[m^2]$ is the cross-sectional area, and $\Delta h/L$ is defined as hydraulic gradient or hydraulic head. The negative sign is because Δh decreases in the flow direction.

Equation (1.29) is known as the integral expression of Darcy's law. Even regarding its simplicity, it is considered the fundamental stone of modern hydrology. This equation was extensively adapted for other specific applications such as petroleum recovery [135, 136, 124].

Darcy's law is often expressed in differential form and considering the volumetric flux as:

$$\frac{Q}{A} = q = -K\frac{dh}{dL} \tag{1.30}$$

where q $[m^3/m^2s]$ is a measure of the flow rate that passes through the cross-section A.

Considering that the hydraulic gradient represents the liquid pressure due to the weight of a fluid relative to some reference location, Equation (1.30) can be rearranged expressing dh/dL in terms of the pressure p as:

$$\frac{dh}{dL} = \frac{1}{\rho g}\frac{dp}{dL} \tag{1.31}$$

where $dp \simeq \Delta p = p_b - p_a$. The values p_a and p_b are the pressures at locations a and b respectively, and ρg is the specific weight of the fluid, which depends on the fluid density, ρ, and the standard gravity g.

Considering the abuse of notation and generalizing $dp/dL = \nabla p$, equation 1.30 can be re-expressed as:

$$\vec{q} = -\frac{K}{\rho g}\nabla p \tag{1.32}$$

The factor $K/\rho g$ can be written in terms of the dynamic viscosity of the fluid μ [Pa.s] as:

$$\frac{K}{\rho g} = \frac{\kappa}{\mu} \tag{1.33}$$

where κ $[m^2]$ is the intrinsic permeability of the porous matrix.

Taking this into account, Equation (1.30) can be rewritten as:

$$\vec{q} = -\frac{\kappa}{\mu}\nabla p \tag{1.34}$$

For some applications, it is convenient to calculate Darcy's law by considering the flow velocity $\vec{u}$ $[m/s]$ instead of the volumetric flux q. These both quantities are related one each other by the porosity of the medium, ϕ, by the following expression:

$$\vec{u} = \frac{\vec{q}}{\phi} \tag{1.35}$$

where ϕ is defined as the ratio between the total volume (V_T) and the void or porous volume (V_p). This is exemplified in Figure 1.15.

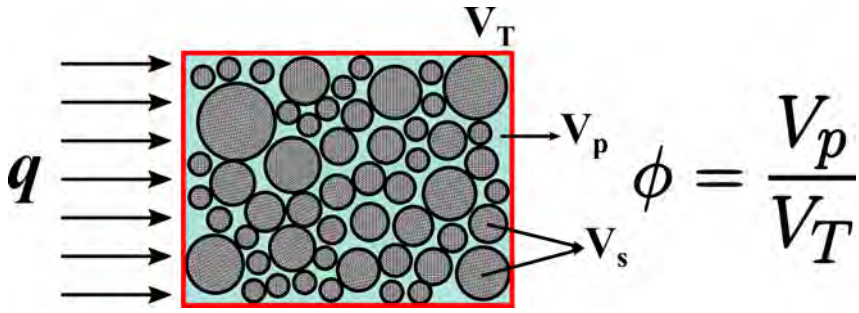

Figure 1.15: Schematic of a porous medium. $V_T = V_s + V_p$ is the total volume, where V_s and V_p are the solid and porous volumes respectively.

By rearranging all factors and generalizing, Darcy's law is finally obtained as:

$$\nabla p = -\frac{\phi \mu}{\kappa} \vec{u} \tag{1.36}$$

An external forcing such as the gravity force can be included to obtain an even more general description of the law as:

$$\nabla p = -\frac{\phi \mu}{\kappa} \vec{u} + \rho \vec{g} \tag{1.37}$$

where $\vec{g}$ is the gravity field. As can be noted, in this case, both $\vec{u}$ and $\vec{g}$ are vectors. Equation (1.37) is the expression that will be mainly used for this thesis.

The Darcy's law is not universal and it has its limitations. The original statement of Darcy's law is only valid in the following considerations:

- The fluid must be incompressible.
- The porous medium is homogeneous and isotropic.
- The flow is viscous, laminar, and isothermal.
- The fluid and the medium do not react or chemically interact with each other.

In this work, the original description of Darcy's law will be modified to study several situations outside the range of validity.

1.7.2 Hele-Shaw Cells

Hele-Shaw cells are experimental devices that simply consist of two plates separated by a very small gap. These type of cells were named in honor of Henry Selby Hele-Shaw (1854-1941), who in 1898 used this experimental arrangement to study flows in thin cells [89]. Hele-Shaw cells are often used to visualize typical problems in fluid mechanics, microfluidics, etc. In the context of this work, these devices will be fundamental to study hydrodynamic instabilities.

A schematic of a Hele-Shaw cell is presented in Figure 1.16. The dimensions of the plates are indicated as L_x and L_y, and the separation gap as $L_z = a$. In Hele-Shaw cell $L_z \ll L_x, L_y$. This condition is fundamental to obtain a quasi 2D flow approximation inside. The importance of this device is that the governing equations of the Hele-Shaw flow are identical to the flow of fluid through a porous medium.

Flow Inside a Hele-Shaw Cell

An expression for the governing equation of the flow inside a Hele-Shaw cell can be deduced from the incompressible Navier-Stokes equation [1]:

$$\rho \frac{\partial \vec{v}}{\partial t} + \rho \vec{v} \cdot \nabla \vec{v} = -\nabla p + \mu \nabla^2 \vec{v} + \rho \vec{g} \tag{1.38}$$

where $\vec{v} = (v_x, v_y, v_z)$ is the velocity field, ρ the density, μ the dynamic viscosity, and $\vec{g}$ the gravity field.

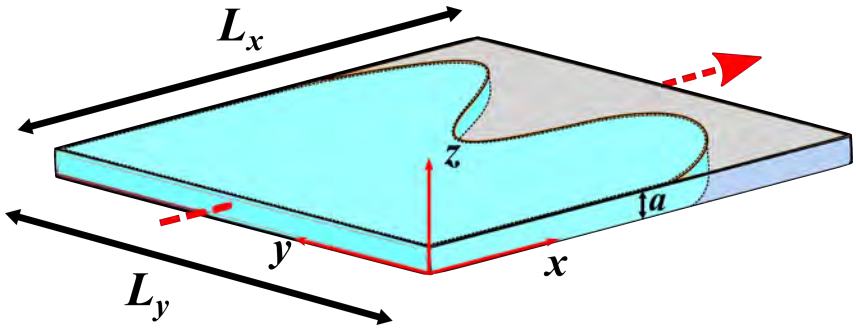

Figure 1.16: Schematic of a horizontally oriented Hele-Shaw cell. The cell consists of two plates of size L_x and L_y, separated by a small gap a.

Considering an incompressible ($\nabla \cdot \vec{v} = 0$) and stationary flow ($\frac{\partial \vec{v}}{\partial t} \approx 0$), and neglecting the bulk terms, Equation (1.38) is reduced to:

$$\nabla p = \mu \nabla^2 \vec{v} + \rho \vec{g} \tag{1.39}$$

which is a simplified version of the Stokes equation.

Given the two-dimensional nature of the system it is necessary to extract the dependence of the z component from the velocity by taking the average of the velocity along such direction. Considering a no-slip condition at the limit of the gap ($\vec{v} = 0$), a laminar Poiseuille profile along z can be assumed as follows:

$$\begin{cases} v_x(x,y,z) = f(z)u_x(x,y) \\ v_y(x,y,z) = f(z)u_y(x,y) \\ v_z(x,y,z) = 0 \end{cases} \tag{1.40}$$

where $\vec{u}(x,y) = (u_x(x,y), u_y(x,y))$ represents the average velocity field in the cell, and $f(z) = 6z(a - z/a^2)$ corresponds to the parabolic profile of the fluid in z. This profile was intentionally defined to verify $\frac{1}{a}\int_0^a f(z)dz = 1$ [34].

The flow inside the Helle-Shaw cell is schematized in Figure 1.17.

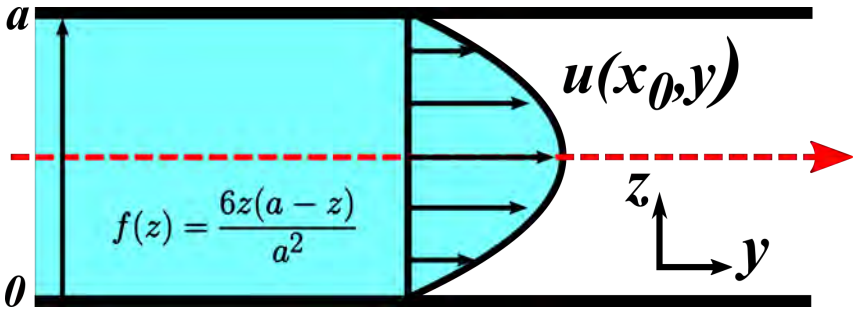

Figure 1.17: Schematic of the parabolic profile and the z-averaged velocity $\vec{u}$ of the fluid inside a Hele-Shaw cell. The figure corresponds with the line cut indicated as a red dashed arrow in Fig. 1.16.

Considering equation (1.39), and integrating the diffusion term respect z:

$$\frac{1}{a}\int_0^a \mu\nabla^2\vec{v}dz = \frac{1}{a}\int_0^a (\mu\nabla^2\vec{u}f(z) - \vec{u}f''(z))dz = \mu\nabla^2\vec{u} - \frac{12\mu}{a^2}\vec{u} \tag{1.41}$$

are obtained the so-called Brinkman equations:

$$\nabla p \approx -\frac{12\mu}{a^2}\vec{u} + \mu\nabla^2\vec{u} + \rho\vec{g} \tag{1.42}$$

Brinkman equations are valid for low velocity flows in porous and non-porous media. Due to the intrinsic characteristics of the Hele-Shaw flows, it is possible to assume that the friction term dominates over the viscous term [34, 33, 93, 45]. Taking this consideration, Eq. (1.42) can be reduced to Darcy's Law:

$$\nabla p \approx -\frac{12\mu}{a^2}\vec{u} + \rho\vec{g} = -\frac{\mu}{\kappa}\vec{u} + \rho\vec{g} \tag{1.43}$$

where $\kappa = a^2/12$ is the intrinsic permeability of the Hele-Shaw cell.

From Equation (1.43) it is possible to observe that the porosity of a Hele-Shaw cell is a constant $\phi = 1$. Additionally, from the simplifications and assumptions made on the original Navier-Stokes equation, it was also possible to obtain an expression for the intrinsic permeability of the cell.

As can be deduced from Equation (1.43), the flow inside a Hele-Shaw cell is representative of the flow in a porous medium. Thus, the study of such flows can be done using such devices in a controlled environment. Moreover, an advantage of using Hele-Shaw cells is that, since they are transparent, they allow a perfect visualization of fluids inside the cell, which is usually a major limitation in porous media.

1.8 Fingering Instabilities in Hele-Shaw Cells

Having introduced the hydrodynamic instabilities and once explained the main aspects of the flow in porous media, Darcy's law, and the flow inside a Hele-Shaw cell, the next sections will introduce the fingering phenomenon in Hele-Shaw cells. This thesis aims to analyze the coupling of these specific groups of instabilities and complex chemical reactions. However, it is necessary to briefly introduce first the main aspects of the non-reactive classical, and the newer chemically-driven instabilities, as a way to review the state of the art at the beginning of this work. This general introduction will address descriptively the main general aspects related to the fingering instabilities, including experimental cases and numerical simulations as reference examples.

1.8.1 Density Fingering Instability

Density fingering (or Rayleigh-Taylor) instabilities are observed when fluids of different densities are subjected to acceleration in a direction opposite to that of the density gradient [33]. This situation is often observed when a denser solution lies on top of a lighter one in the gravity field (similar to the example presented in Figure 1.13(d)). [171, 200, 111]. A general scheme of the Rayleigh-Taylor instability for two solutes A and B is presented in Figure 1.18(a).

If the fluids are miscible, this instability is triggered when the density of the solution is affected by the spatial changes in the concentration of the solute dissolved ($A = A(x,y,t)$ and $B = B(x,y,t)$). In this situation, the density of the system is governed by the concentration of such solutes ($\rho = \rho(A,B)$).

The main stability factor of the system is the density difference between the two solutions ($\Delta\rho = \rho_A - \rho_B$). The stability of the system increases proportionally with the density jump between the upper and lower layer, if such a jump is favorable. This is, denser fluid below a lighter one. The opposite situation produces the destabilization of the fluid interface.

A mathematical model for the density fingering instability can be obtained by combining the equation of the flow inside the Hele-Shaw cell (Eq. (1.43)) with the reaction-diffusion-convection equation for solutes A and B (Eq. (1.25)). Assuming that the flow is governed by Darcy's law and no 3D effects occur along the cell gap, the general equations of the problems are given by:

$$\begin{aligned} \nabla \cdot \vec{u} &= 0 \\ \nabla p &= -\frac{\mu}{\kappa}\vec{u} + \rho(A,B)\vec{g} \\ \frac{\partial A}{\partial t} &+ \vec{u}\cdot\nabla A = D_A \nabla^2 A \\ \frac{\partial B}{\partial t} &+ \vec{u}\cdot\nabla B = D_B \nabla^2 B \end{aligned} \tag{1.44}$$

The validity of this equation is founded on the Boussinesq approximation [22], which assumes that all the density variations induced by concentrations (and/or temperature) changes are small compared to the mean density. As a consequence, the condition of incompressibility ($\nabla \cdot \vec{u} = 0$) of the fluid is preserved, as the buoyancy effects only retain in the $\rho\vec{g}$ term of the flow equation. Therefore, any local pressure variation produced by small density changes can be neglected.

The mathematical model presented in Eqs. 1.44 can be solved numerically to reproduce the physical phenomenon. Figure 1.18(b), shows the non-linear simulation of a typical Rayleigh-Taylor instability obtained by CFD software. As can be seen, compared to the experimental situation shown in Figure 1.18(c), the simulations agree very well in both the system dynamics and the shape of the fingers, validating at least qualitatively, the numerical model [197, 121, 45].

Until now, it was only considered the unstable case, however non-reactive buoyancy-driven instabilities can be obtained even for initially stable configurations. In this case, the diffusivity also plays an important role in the destabilization of the system. Figure 1.19(a) schematizes a situation in where the denser fluid is on the bottom of the Hele-Shaw cell, and the lighter one is on top. This situation is initially stable, but fingering may be observed if differential diffusion exists, which means that one of the solutes diffuses faster compared to the other one.

In the case where the denser fluid diffuses faster than the lighter one, double-diffusive fingering instability is obtained (DD, [197]). An example of this instability is presented in Figures 1.13(d-d_2). It can be found in Nature when hot saline water lies over cold freshwater of a higher density. This instability is responsible to improve the transport of nutrients and/or to control the temperature in the oceans [171, 200, 111].

This case can be modeled using the same set of equations used for the Rayleigh-Taylor instability, but considering proper values for D_A and D_B. Some numerical results of this case

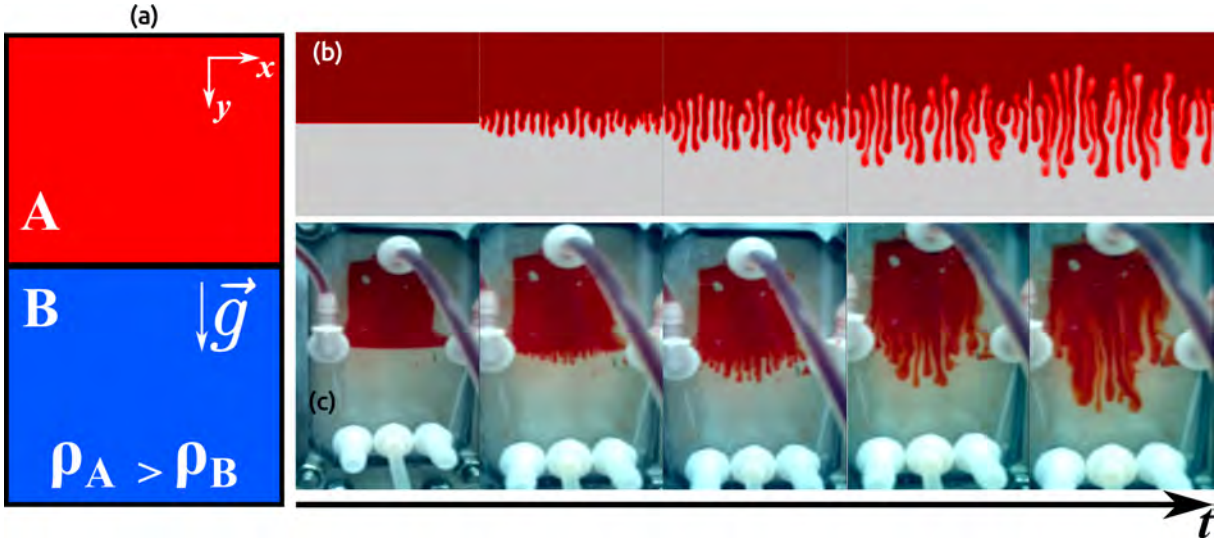

Figure 1.18: Rayleigh-Taylor Instability (a) Schematics of the initial fluid and solute configuration. In this instability, the denser fluid is on top of the lighter one, leading to an unstable hydrodynamic initial condition. (b) Image sequences of a Non-linear simulation of the Rayleigh-Taylor instability obtained by numerical integration of Eq. 1.44. (c) Image sequences of a Rayleigh-Taylor instability obtained experimentally. In this particular case, a denser solution of ferroin is put on top of doubly distilled water.

are presented in Figure 1.19(c). The driving force of this instability is the local destabilization induced by the faster diffusive species [197, 51, 45].

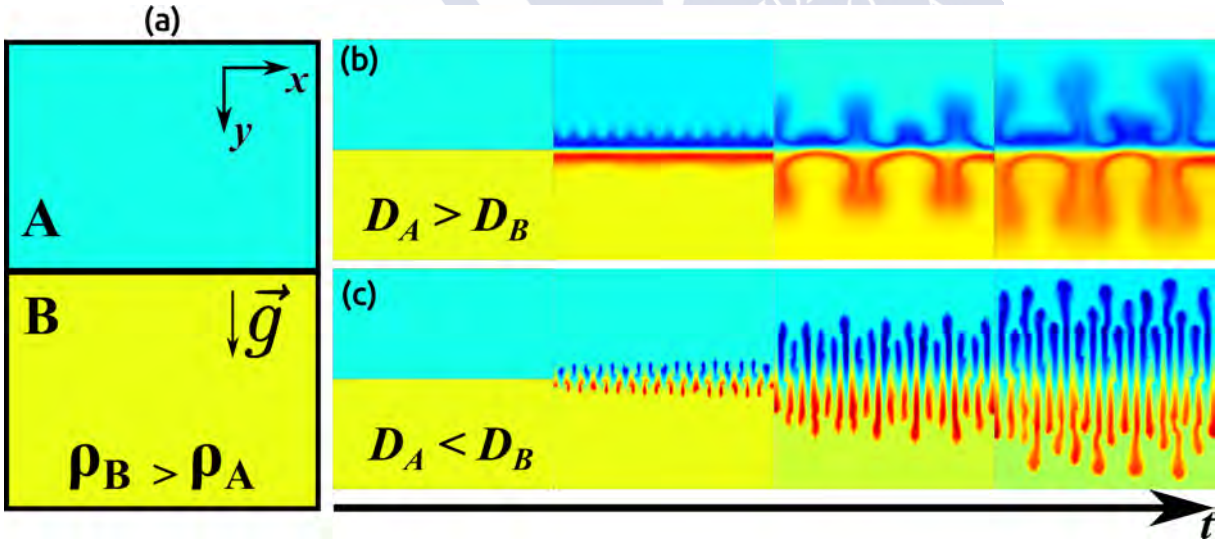

Figure 1.19: Density Fingering Instability. (a) Schematics of the initial condition. (b) Non-linear numerical simulations of the diffusive-layer convection (DLC) instability. (c) Non-linear numerical simulations of the double-diffusive (DD) instability. All simulations were performed by numerically integrating Eqs. 1.44 on CFD software.

On the other hand, if the lighter fluid diffuses faster compared to the denser one, diffusive-layer convection (or DLC, [197]) instability is obtained. A numerical example of this situation is presented in Figure 1.19(b).

Wooding *et al* [217] demonstrated that the effect of the diffusion in miscible fluids is analogous to the role played by the surface tension in the immiscible case, which is to set

the initial length scale of the fingering pattern.

There are many works where the classical buoyancy-driven instabilities were completely analyzed and characterized by theoretical and/or experimental perspectives [59, 87, 8, 9, 120, 44, 25, 197].

1.8.2 Viscous Fingering Instability

Viscous fingering instabilities are observed when a less viscous fluid displaces a more viscous one in a porous medium. This phenomenon is also known as Saffman-Taylor instability when fluids are immiscible [93].

When fluids are miscible, the viscous fingering instability is driven by viscosity gradients which results from spatial variations in the concentration of the solutes that govern the viscosity of the solution such as $\mu = \mu(A,B)$. This instability was experimentally and theoretically studied, for both, linear [168, 46, 41], and radial [93, 168, 88, 141, 44] displacements.

In viscous fingering, the stabilization of the system is governed by the log mobility ratio R, which is defined as [48, 193]:

$$R = ln\left(\frac{\mu_A}{\mu_B}\right) \tag{1.45}$$

The instability occurs when $R > 0$ [44, 45]. The stability of the system decreases proportionally to the increment in R.

Similar to the density fingering, the mathematical description of the viscous fingering instability is based on Darcy's law but considering the viscosity changes produced by concentrations of the involved solutes. This statement coupled with the transport equation for solutes A and B (Eq. (1.25)), allows to obtain the governing equations for the non-reactive viscous fingering instability in a Hele-Shaw cell:

$$\begin{aligned} \nabla \cdot \vec{u} &= 0 \\ \nabla p &= -\frac{\mu(A,B)}{\kappa}\vec{u} \\ \frac{\partial A}{\partial t} + \vec{u}\cdot\nabla C &= D_A \nabla^2 A \\ \frac{\partial B}{\partial t} + \vec{u}\cdot\nabla C &= D_B \nabla^2 B \end{aligned} \tag{1.46}$$

In this case, as the displacement occurs horizontally and the cell gap is narrow, the buoyancy forces can be neglected [93, 45]. Thus, the corresponding term is included in the pressure gradient.

Examples of experimental and numerical radial viscous fingering are presented in Figure 1.20. In Figure 1.20(a), a more viscous and colored solution of Polyethylene glycol (PEG-300) is displaced by doubly distilled water. As can be appreciated, the displacement is unstable and viscous fingering occurs. Figure 1.20(b) presents the non-linear simulations of a viscous fingering instability obtained by integrating numerically Eqs.(1.46) by a CFD software. As can be seen, the shape of the numerical fingers is very similar to the experimental counterpart, validating one more time the mathematical model derived from Darcy's law.

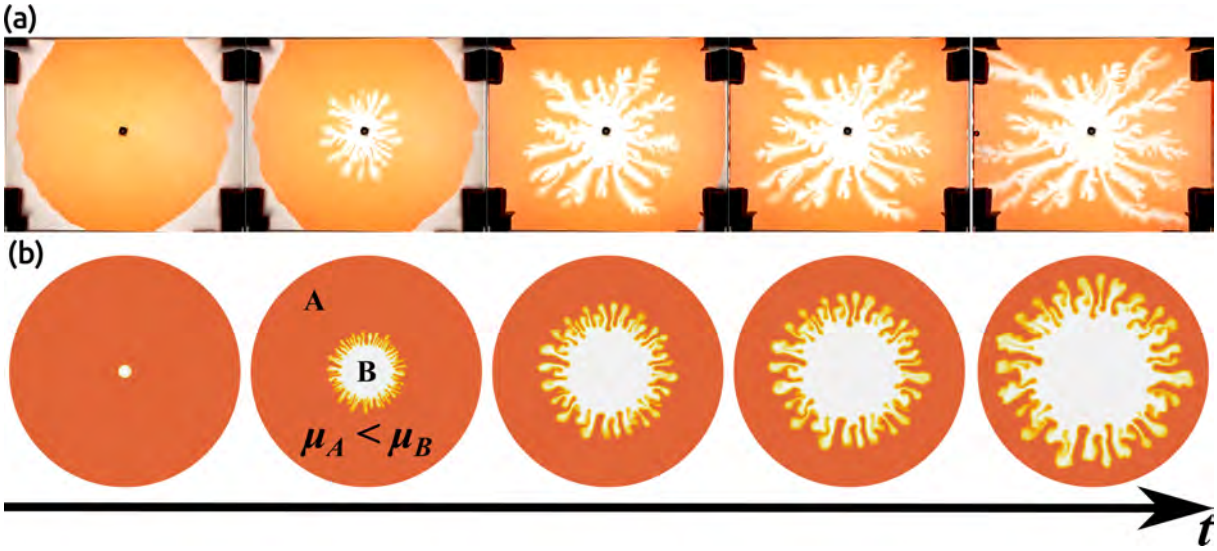

Figure 1.20: Non-reactive viscous fingering instability in a radial Hele-Shaw cell. (a) An experimental case where a Polyethylene Glycol (PEG-300) colored solution is displaced by doubly distilled water. (b) Non-linear simulation obtained by integrating Eqs. (1.46) and performed with CFD software suite. A Schematic of the reagent and viscosities configuration is presented in the second snapshot of (b).

Diffusion can also trigger a viscous fingering instability in an initially stable configuration. Mishra *et al* ([128]), studied these diffusion-driven viscous instabilities for a broad variety of parameters. Figure 1.21 shows the numerical results of three different situations. In all cases, it is assumed that one of the species diffuses faster than the other one (i.e. $D_A > D_B$), and the initial fluid configuration is stable (i.e. $\mu_A > \mu_B$). In Figure 1.21(a), patterns are obtained due to a differential diffusion mechanism induced by the destabilizing effect the slower species. This situation is known as DNS-VF [128]. When the instability is produced by purely double diffusive mechanism similar to the buoyancy-driven case (Fig. 1.19(c)), the instability is known as DD-VF. This situation is shown in Figure 1.21(b). Figure 1.21(c) shows the situation in which patterns are obtained due to a differential diffusion mechanism induced by the destabilizing effect the faster species. This case is known as DNF-VF [128].

These three cases are obtained by varying some numerical parameters associated with the concentrations and viscosities of the displacing and displaced fluid[128]. The figure is included as an example of the versatility and the broad possibilities related to the non-reactive viscous fingering and its modeling.

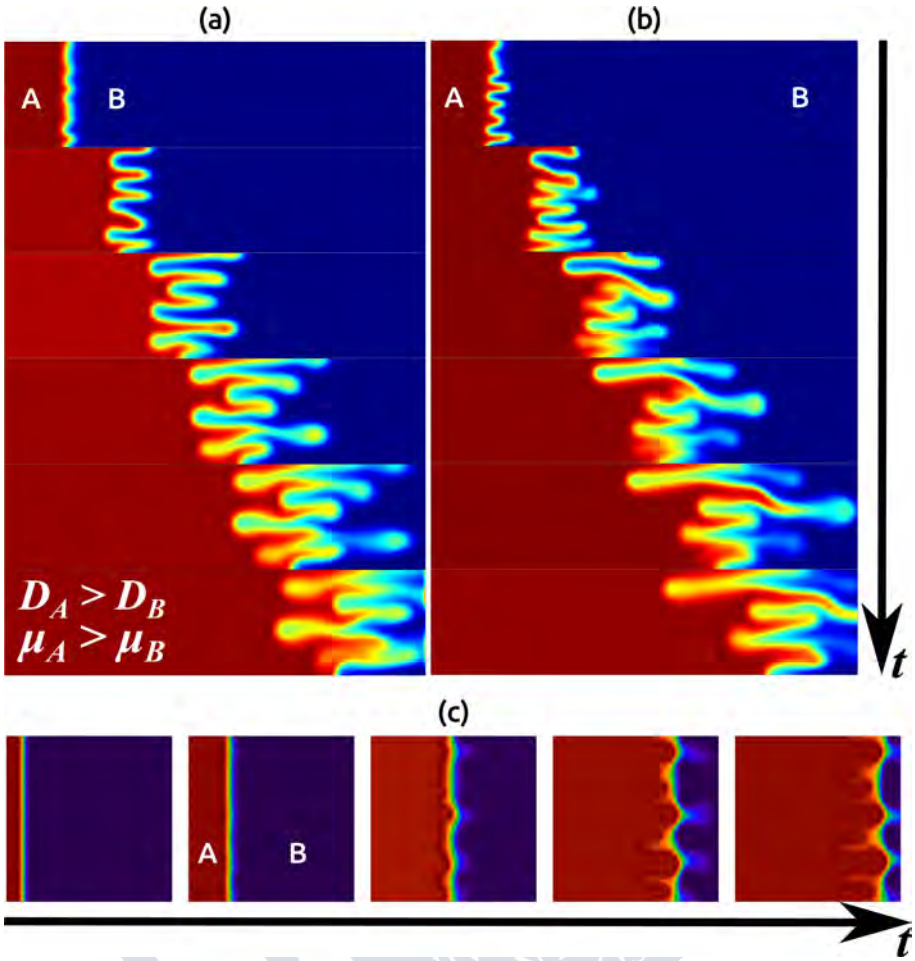

Figure 1.21: Numerical results of a diffusion-driven non-reactive viscous fingering instability for obtained for linear displacement. (a) Viscous fingering originated by the destabilizing effect of the slower species and induced by differential diffusion (DNS-VF) (b) Viscous fingering originated by pure diffusive effects, similar to the double diffusion instability (DD-VF) (c) Viscous fingering originated by the destabilizing effect of the faster species and induced by differential diffusion, similar to the diffusive-layer convection instability (DNF-VF). In all cases $D_A > D_B$ and $\mu_A > \mu B$ [128].

1.8.3 Chemically Driven Fingering Instabilities

The study of chemo-hydrodynamic fingering instabilities added a new step in complexity by coupling chemical processes to the flow in porous media. The dynamics of the fingering phenomenon in reactive systems mainly depends on the interaction between the species involved and the flow. If the species are passively advected, the properties of the fingering interface remain those of the non-reactive case presented in the previous sections. This occurs even considering that the flow clearly influences the spatial-temporal distribution of chemical instability.

However, there are cases where the chemical reaction plays an active role in the development of the fingering instability, especially when they can actively influence or trigger convective motions when two solutions containing separate reagents come into contact.

The key to controlling chemically driven instabilities lies in the effect on the viscosity or density profiles produced by the localized generation of products due to interfacial reaction. These changes affect the mobility of the fluids by favoring or reducing instability.

The following introduction will be consider simple $A+B \rightarrow C$ reactions as the starting point for the development of more complex situations, which is the main objective of this thesis. Thus, the next sections will present a brief outline of the most common chemically induced fingering instabilities, including experimental and numerical examples.

Density Fingering

In addition to all the physics associated with the non-reactive case, the inclusion of a new species (C) with different density and diffusivity, can strongly alter the dynamics of the system in buoyancy-driven instabilities. The variation in the density produced by the local generation of the reaction of the product can force changes in the convection field or even mixing. This situation is illustrated in Figure 1.22(a) for an initially stable case.

A mathematical model for this type of systems can be derived from the classical non-reactive case (Eqs. (1.44)), by including the corresponding reaction terms in the transport equations, and the expression for the density changes produced by reactants and/or products.

$$\begin{aligned} \nabla \cdot \vec{u} &= 0 \\ \nabla p &= -\frac{\mu}{\kappa}\vec{u} + \rho(A,B,C)\vec{g} \\ \frac{\partial A}{\partial t} + \vec{u}\cdot\nabla C &= D_A \nabla^2 A - kAB \\ \frac{\partial B}{\partial t} + \vec{u}\cdot\nabla C &= D_B \nabla^2 B - kAB \\ \frac{\partial C}{\partial t} + \vec{u}\cdot\nabla C &= D_C \nabla^2 C + kAB \end{aligned} \tag{1.47}$$

Figure 1.22(b,c) shows numerical examples of chemically driven density fingering in two hypothetical situations. Figure 1.22(b), presents the case where C is lighter than A and B, thus it floats to the upper part of the reactor/domain. This situation can be observed experimentally in instabilities driven by neutralization reactions [65, 9]. The second case is presented in Figure 1.22(c), where C is denser than A and B. In this situation, the product of the reaction sinks to the bottom part of the reactor/domain. This can be observed experimentally if the instability is driven by a precipitation reaction [44, 23, 138, 176].

The model for $\rho = \rho(A,B,C)$ will depend on the nature of the system and the chemical species. Thus, in some situations, it is useful to consider all the species involved [45], in other situations like the one exemplified in Figure 1.22, only the effect of C. In any case, the expression of ρ is based on the Boussinesq approximation assuming a linear relationship between the concentration of the species and the density [197, 45].

Viscous Fingering

In the case of chemically induced viscous fingering, the interplay between reaction and the instability occurs through changes produced on the viscosity. Thus, a chemical reaction can produce an increment or decrement on the viscosity at the miscible interface, affecting the properties of the fingering pattern.

The development of a model for reactive viscous fingering is analogous to the density fingering case. The only difference is the necessity to combine the flow and transport equation with a suitable model for the viscosity changes due to the reactive species. Similar to the density

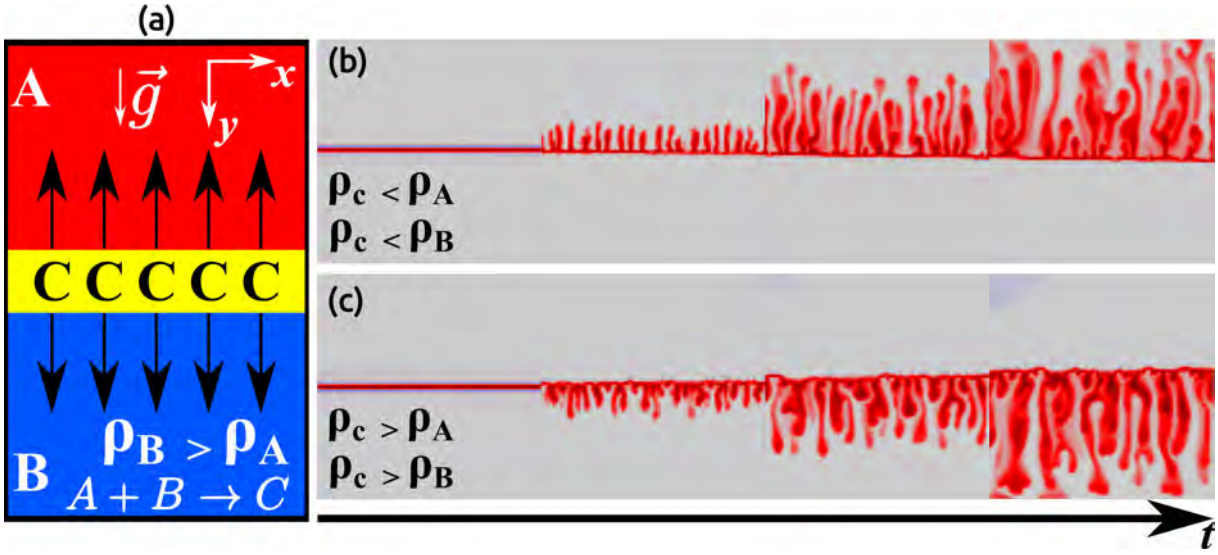

Figure 1.22: Numerical results of a density fingering instability induced by the reaction $A + B \rightarrow C$. In this case, the density is assumed to be affected primarily by the product C. (a) Schematics of the fluid configuration and the spatial location of the chemical species. The system is initially stable and it is destabilized by the product of the reaction between A and B. (b) The product C is lighter compared to the remaining fluids present in the reactor. This produces the fingers to ascend to the upper part of the reactor. (c) Same situation as (b), but C is denser. In this case, the fingers sink to the bottom of the reactor. All simulations were performed by using CFD software.

case, the expression of the viscosity function depends on the nature of the problem. Considering these statements, a general description for this problem is given by:

$$\begin{aligned} \nabla \cdot \vec{u} &= 0 \\ \nabla p &= -\frac{\mu(A,B,C)}{\kappa}\vec{u} \\ \frac{\partial A}{\partial t} + \vec{u}\cdot\nabla C &= D_A \nabla^2 A - kAB \\ \frac{\partial B}{\partial t} + \vec{u}\cdot\nabla C &= D_B \nabla^2 B - kAB \\ \frac{\partial C}{\partial t} + \vec{u}\cdot\nabla C &= D_C \nabla^2 C + kAB \end{aligned} \tag{1.48}$$

Figure 1.23 shows two examples of viscous fingering affected by a chemical reaction for an experimental case (Fig. 1.23(a)) and a numerical case (Figure 1.23(b)). Even though this instability is not produced by the reaction itself, as the hydrodynamic scenario is unstable. However, this is a simple example of how a chemical reaction can interact with a fluid displacement. Figure 1.23(a) shows a more viscous polymeric solution of Poly(acrylic acid) and sodium bisulfite is displaced by a less viscous aqueous solution of formaldehyde. The polymeric solution is colored with a pH color indicator. The reaction locally increases the pH of the system at the interface producing the color indicator to change from yellow to blue. The system remained unstable, but fingers started to exhibit a blue coloration that propagates due to the effect of the diffusion.

This situation was simulated by modeling the chemical reaction with the simple $A + B \rightarrow C$. Results are presented in Figure 1.23(b). As it is possible to see, both numerical and experimental dynamics present much similarities.

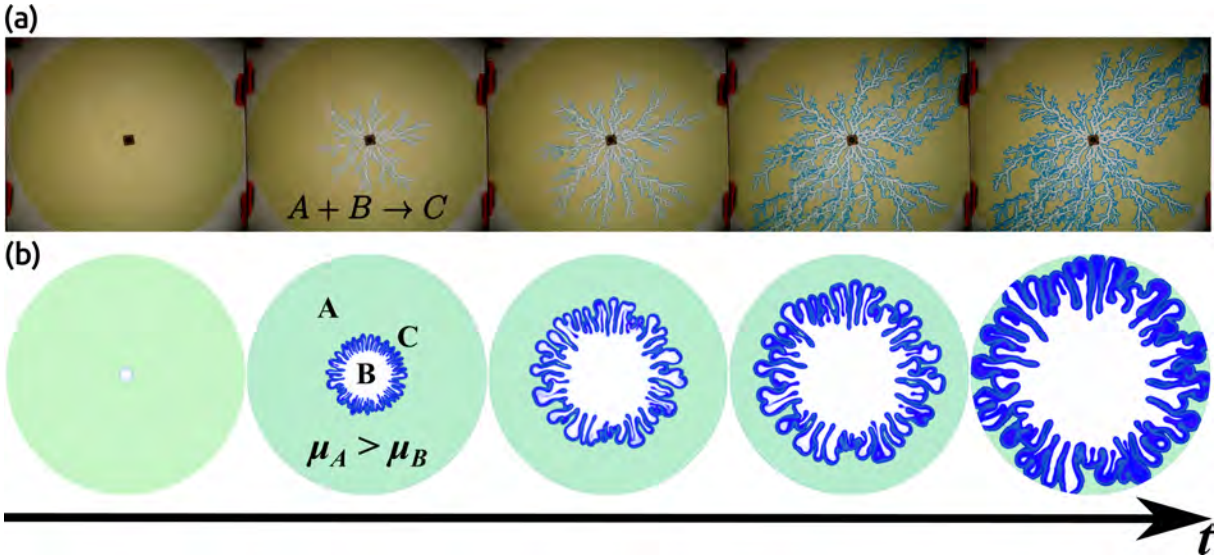

Figure 1.23: Numerical results of a viscous fingering instability affected by the reaction A + B → C. In this case, the system is initially unstable. The reactivity is evidenced by the change in the color indicator at the interface between fluids A and B. (a) Experimental case where a colored polymeric solution of Poly(acrylic acid) and sulfite is displaced by formaldehyde. The contact between these two solutions produces an increment in the pH that changes the yellowish coloration of the indicator into blue. (b) Simulation of a viscous fingering instability coupled with an A + B → C reaction. Even though the shape of the fingers is not exactly equal to the one observed in the experimental case, the physical phenomenon associated with the reaction is well reproduced.

Chemical reactions can also induce viscous fingering instabilities by changing the permeability of the porous matrix. This could be produced by precipitation [86, 176] and dissolution [102] reactions, for instance. In this case, once the displacing and displaced solutions make contact, the precipitation occurs at the miscible interface. The precipitate will locally reduce the permeability by destabilizing the fluid front and inducing viscous fingering [176]. This situation is logical if analyzing Darcy's law. In numerical terms, a decrement in the permeability will produce the same effect as the increment in viscosity as the pressure gradient is proportional to the factor μ/κ. The physical meaning, however, is completely different, and the instability mechanism is far more complex. Similar studies were done considering studying the effects of increasing the permeability [176, 23, 138, 102].

One major application of reactive viscous fingering is to control processes that are often unstable, like enhanced oil recovery [132, 207, 41, 21] or chromatography [166, 173, 32, 42, 198]. In these cases, studies are conducted in finding suitable reactions that could suppress the instability and improve the fluid displacement. This would be important in many fields of the industry or science.

1.9 The Poly(Acrylic Acid)

A very important part of this thesis is to find a coupling between a pH-sensitive material and a pH-changing chemical reaction. In this sense, the most important reactant that will act as a nexus between those different fields is the Poly(Acrylic Acid), or hereafter, PAA. As a key molecule for the development of this work, it is useful to introduce and summarize the most important aspects related to physics and the chemistry of this reagent.

The PAA is probably one of the most well-known and accessible pH-responsive polymer available. It is currently used in many different fields like the food industry, medicine, cosmetics, pharmaceutics industry, and others [35]. Due to its hydrophilic character, the PAA can absorb a thousand times its weight in water, forming superabsorbent gels [194].

As its name indicates, the PAA is a linear polymer formed from acrylic acid (Figure 1.24).

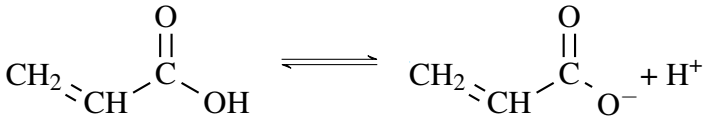

Figure 1.24: Chemical model of the acrylic acid dissociation equilibrium in aqueous solution.

The PAA structure has a carboxylic group on each monomer unit for every two carbon atoms on the main chain and behaves as a polyelectrolyte in water due to the dissociation of the acid groups [104] (Figure 1.25).

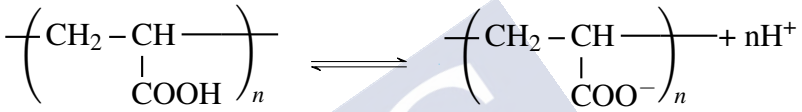

Figure 1.25: Chemical model of the PAA dissociation equilibrium in aqueous solution.

By definition, a polyelectrolyte is a *polymer composed of macromolecules in which a substantial portion of the constitutional units contains ionizable groups, or both* [91]. A conceptual scheme of what a polyelectrolyte is presented in Figure 1.26.

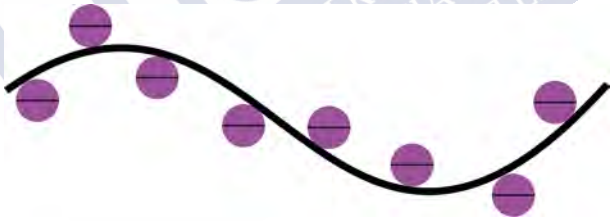

Figure 1.26: Schematic of a polyelectrolyte molecule. Specifically for the PAA, the anionic character of the molecule is due to the dissociation of the carboxylic groups into carboxylate ions.

1.9.1 Structure and pH-dependence

As all poly(carboxylic acids), the PAA is a weak polyelectrolyte that dissociates in aqueous solutions and its ionization equilibrium is pH-dependent [142]. This can be observed in Figure 1.25. If the H^+ concentration increases, the pH decreases, favoring the non-ionized form of the molecule where the carboxylic groups are dominant. On contrary, if the pH increases by decreasing the H^+ concentration, the molecule dissociates favoring the ionized form where the carboxylate ions are predominant.

The non-ionized groups facilitate the generation of interchain hydrogen bonds, which compacts the molecule structure (globular form). This compacted structure makes PAA acidic solutions have relatively low viscosity if in diluted solutions. In the ionized form, the negative charges of every dissociated carboxylic group generate a repulsive effect that elongates the molecule into an extended structure (rodlike form). This conformational change strongly affects

the viscosity of a PAA dissolution to such an extent to gelify at relatively low concentrations [103]. In Figure 1.27, a molecular model of the PAA molecule is represented at low (Fig. 1.27(a) pH and high (Fig. 1.27(c) pH. The inset (Fig. 1.27(b)) shows a zoomed image focusing on the interchain hydrogen bond formation at low pH conditions.

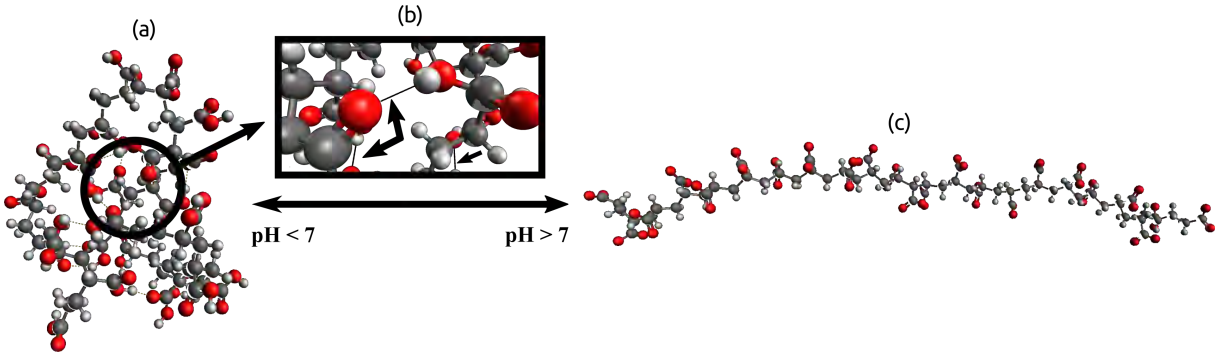

Figure 1.27: pH-dependence of the spatial conformation of a hypothetical PAA molecule. (a) PAA molecular model in a acidic pH (pH $<$ 7). The molecule adopts a compacted form due to the interchain hydrogen bond formation (indicated in (b). This molecular interaction is produced when the carboxylic groups are protonated. (c) PAA molecular model in a basic pH (pH $>$ 7). In this case, the molecule adopts an extended configuration due to the repulsive effect between the negative charges of the carboxylate ions.

1.9.2 Chain Length and Concentration Regimes

The viscosity of a PAA solution can be affected not only by the pH but for other factors like the side chain length and the polymer concentration. This is mainly associated with the inter molecule interactions in solution [195].

In physical terms, this is related with the space that an individual molecule occupies in the solvent. The volume occupied by a polymer can be estimated with the radius of gyration (R_g). R_g is defined as:

> *The average distance of a chain element from the center of gravity of the chain [195].*

The volume of a globular molecule is approximately the volume of a sphere of radius R_g. On the other hand, the volume of rodlike molecules is estimated by considering the side length of the chain (L). Figure 1.29 illustrates these two concepts for the PAA molecule in two different situations.

Three main regimes can be distinguished depending on the polymer concentration and size [195]. The inflection point is known as overlap concentration and it is frequently indicated as **c***. These characteristics are represented in Figure 1.28.

- Diluted solutions (c $\ll$ c*): The molecules are separated from each other and there is almost no interaction between them. The polymer chains interact primarily with the solvent molecules (Fig. 1.28(a,b), left panels).
- Solution at the overlap concentration (c = c*): The concentration where the solution becomes congested and molecules start interacting with each other (Fig. 1.28(a,b), center panels).

- Semidilute solution (c $\gg$ c*): The polymer chains are overlapped and entangled. Their mobility is greatly reduced compared with the chains in dilute solutions (Fig. 1.28(a,b), right panels).

The physical-chemical properties of a semidilute solution are usually different from those of an ideal solution extrapolated to the same concentration. The deviation from the ideal solution occurs at a low concentration in terms of volume fraction or the mass concentration. Polymer solutions are characterized by the existence of semidilute regimes. For concentrations above the semidilute regime, the polymer chains does not have sufficient space available and a concentrated regime **c**** is obtained [195].

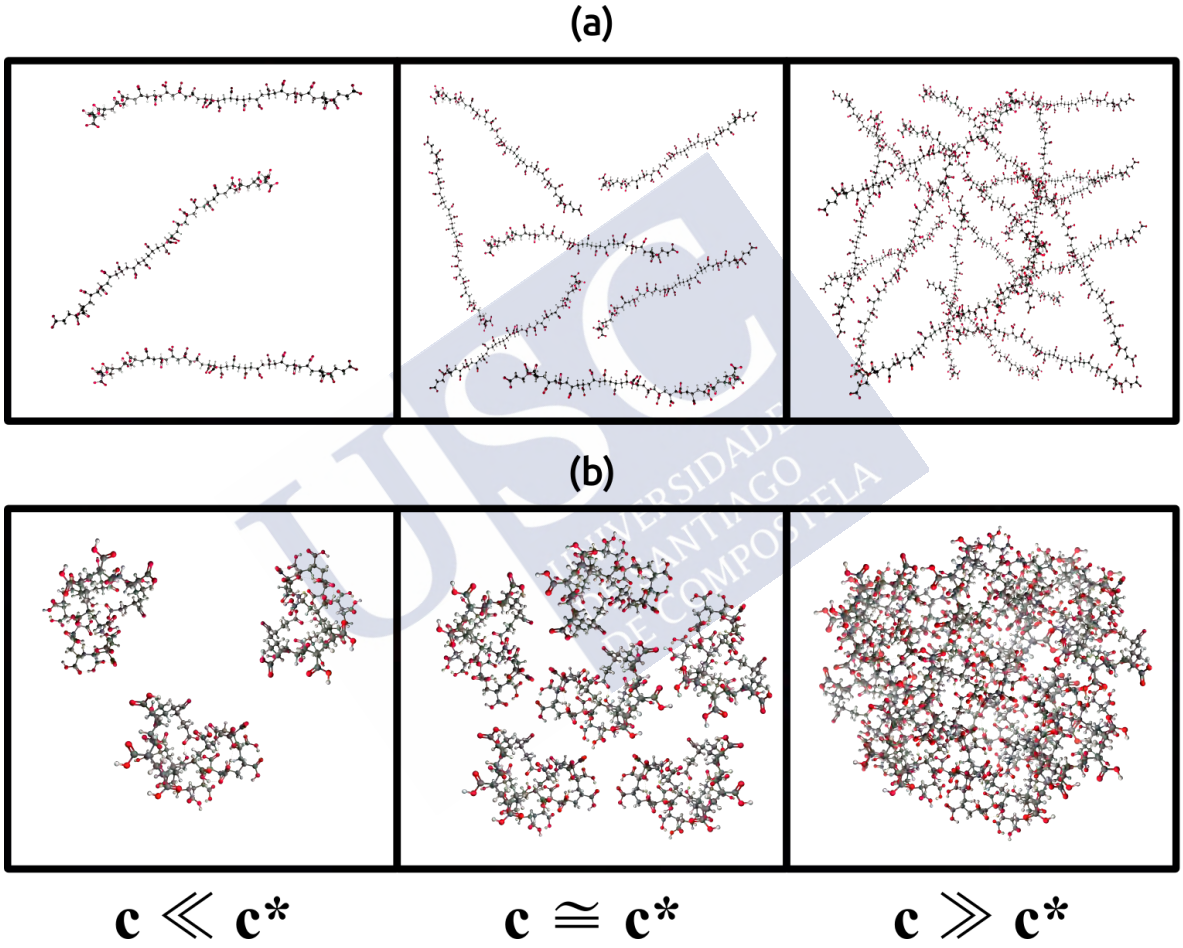

Figure 1.28: Schematics of the concentration regimes for the PAA molecule in (a) basic pH, and (b) acid pH.

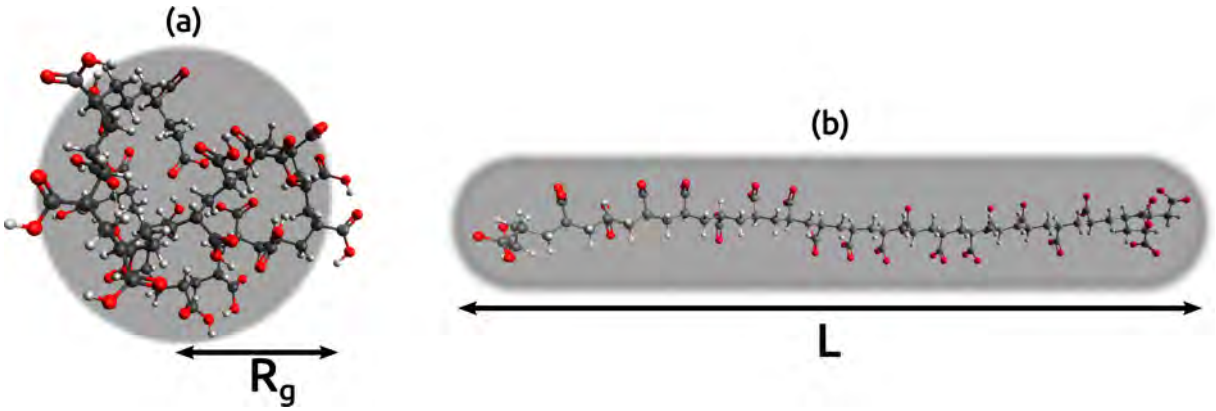

Figure 1.29: Illustration of the volume occupied by (a) globular and (b) rodlike PAA molecule. R_g stands for the radius of gyration, and L is the length of the polymer chain.

1.9.3 Ionic Strength Effects

Like most polymer solutions, the PAA is affected by ionic strength. This can be illustrated by considering the ionized structure of the molecule as shown in Figure 1.30. An increment in the ionic force will quench the chain repulsion force compacting the spatial structure of the molecule. This effect can be produced by the addition of both, monovalent and polyvalent salts, or can be generated if the pH is changed from acidic to basic by the addition of NaOH or HCl, respectively [142].

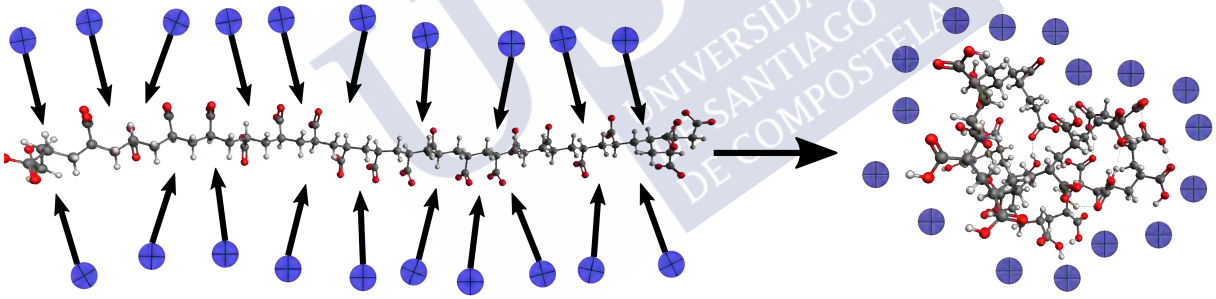

Figure 1.30: Schematics of the ionic strength effect on a fully elongated PAA molecule. The presence of cations in a PAA solution will quench the repulsive effect of the carboxylate groups compacting the polymer structure. The viscosity of the solution may be strongly affected by the quenching effect.

1.10 The Shadowgraph and Schlieren Optical Techniques

The visualization of convective phenomena can be sometimes complex due to the experimental or equipment requirements needed for this purpose. More specifically, many of the hydrodynamic instabilities presented in Sections 1.7 and 1.8 are phenomena that occur in transparent and quasi-two-dimensional media, where direct observation becomes impossible if solutions are not colored. However, the use of such type of chemicals may interact or interfere actively with the dynamics of the system [8].

For such reason, it is convenient to have a tool that allows the observation of phenomena that are not observable with the *naked eye*. In this way, the Shadowgraph and Schlieren

techniques were conceived to track changes in the refractive index (n) produced by the inhomogeneities in the medium. These two techniques are fundamental in the study of many phenomena [184, 126, 27], but in the context of this work, they were used for the observation and characterization of the hydrodynamic instabilities[184, 126, 27, 51, 57, 63, 61, 58] [5]. The multitude of experiments and the broad variety of results obtained by these two techniques make them deserve their own section.

1.10.1 Generalities

A *schlieren*, as a noun, is defined as the gradient disturbances produced in inhomogeneous transparent media [172]. A *Schlieren* may occur in any state of the matter and is produced by different phenomena like temperature variations, density changes, high-speed flows. It is typically observed in the inhomogeneities like those produced by differences in thickness or density, and are observed in plastics, glass, or the mixing of different materials.

There are a multitude of *schlieren* phenomena, some produce a strong change in the refraction index, others do not. Some can exhibit a sharp and well-defined structure and others can be more gradual [172]. An example of a typical *schlieren* is presented in Figure 1.31, which shows the phenomenon known as *tears of wine*. This phenomenon is produced by the difference of surface tension between the alcohol and the water and occurs by an inhomogeneous distribution of the wine in the glass. It is an example of the well-known Marangoni effect [74].

Even sharing some similarities, the Shadowgraph and the Schlieren techniques present several distinctions. In the first place, the shadowgram, (which is the image produced by the Shadowgraph technique) is not a focused image and it results from the shadow casting over a screen or a camera lens. On the other hand, the image obtained through the Schlieren technique, is an optical image formed by a lens and produces a conjugate optical relationship to the object of study [172]. Also, the Schlieren method requires a knife-edge or similar filter of the refracted light. This is not needed for Shadowgraph, where images are obtained directly.

Another major difference between these two techniques lies in the equipment required by each one. The Shadowgraph technique is much simple to implement, it can be set up without using sophisticated technology and allows large-scale visualizations. This is not the case of the Schlieren technique, where the use of lenses, mirrors, and lamps is almost mandatory [172]. Indeed, the picture presented in Figure 1.31 was taken by using a home-made Shadowgraph setup.

Regarding the sensitivity, the Schlieren technique responds to the first spatial derivative of the refractive index with respect to the optical path ($\partial n/\partial x$), where the Shadowgraph technique respond to the second spatial derivative ($\partial^2 n/\partial x^2$). This means that the Schlieren shows the deflection angle ε while the Shadowgraphy shows the ray displacement resulting from that deflection (Fig. 1.32).

[5] During the course of this work, the Schlieren technique was more extensively used compared with the Shadowgraph. However, the later was more intensively used in the experimental results published in Escala, 2014 [57].

Figure 1.31: *Tears of wine* as an example of a *schlieren*. These patterns are typically observed when an alcoholic beverage is distributed on a glassy surface and it is a consequence of the Marangoni effect. The tears are produced by the difference in the surface tension between the alcohol and the water of the wine.

1.10.2 Shadowgraph Technique

A schematic of a parallel-light direct Shadowgraph setup is presented in Figure 1.32. In it, the light produced by a pinhole light [6] source passes through a collimator lens that makes the ray beams to be aligned to the optical path. When a *schlieren* object is in the field of view, some rays refract, bent, and deflect from their original path with a specific angle ε. An example of a refracted ray is presented in Figure 1.32(a). Once refracted, the ray beam reaches the screen displaced from its original position by a distance Δa. This effect applied to all the originally aligned and regular rays, makes them bend and cross casting a shadow. Figure 1.32(b) shows an example of a Rayleigh-Taylor instability observed through the Shadowgraph optics.

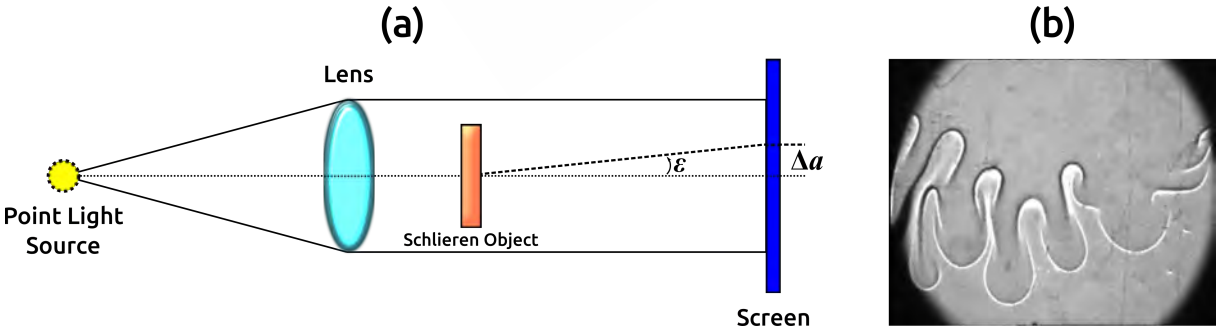

Figure 1.32: (a) Schematics of the parallel-light direct Shadowgraph technique. Similar home-made equipment was used to take Figure 1.31. (b) Example of a buoyancy-driven hydrodynamic instability in a Hele-Shaw cell observed through the Shadowgraph technique. The system is composed of a denser solution of NaCl located in the upper part of the reactor and doubly distilled water located in the lower part. As the system is initially unstable, a Rayeligh-Taylor instability occurs. Both solutions are colorless.

[6] The use of a pin-hole light source facilitates and improves the definition of the image, but its use is not necessarily mandatory [172].

1.10.3 Schlieren Technique

Figure 1.33 present a schematic of a dual-field-lens Schlieren arrangement. This setup is the one used for the development of part of the experimental chapters. In this case, the ray beams produced by a generic light source are condensed and pass through a slit filter. The inclusion of this type of filter in the light source allows to better control the light orientation and the resolution of the images. However, the orientation of the light beams depends on the structure of the *schlieren* object [172].

As showed in Figure 1.33(a), the ray-beams are collected by a pair of collimator lenses and pass through the *schlieren* object. This makes the rays to bend from the original optical path. Some of the rays bent upward and others bent downward. In both cases, the refracted rays miss the focus of the optical system [172]. The inclusion of a knife-edge (or filter) at the focal point of the second collimator, makes that some of the deflected rays brighten a point on the camera lens, and others hit the knife-edge. The addition of the knife-edge is mandatory for the transparent *schlieren* object to be imaged, and it is responsible for generating a dark image against a bright background. This effect is produced by the occurrence of a vertical gradient in the refractive index ($\partial n/\partial y$).

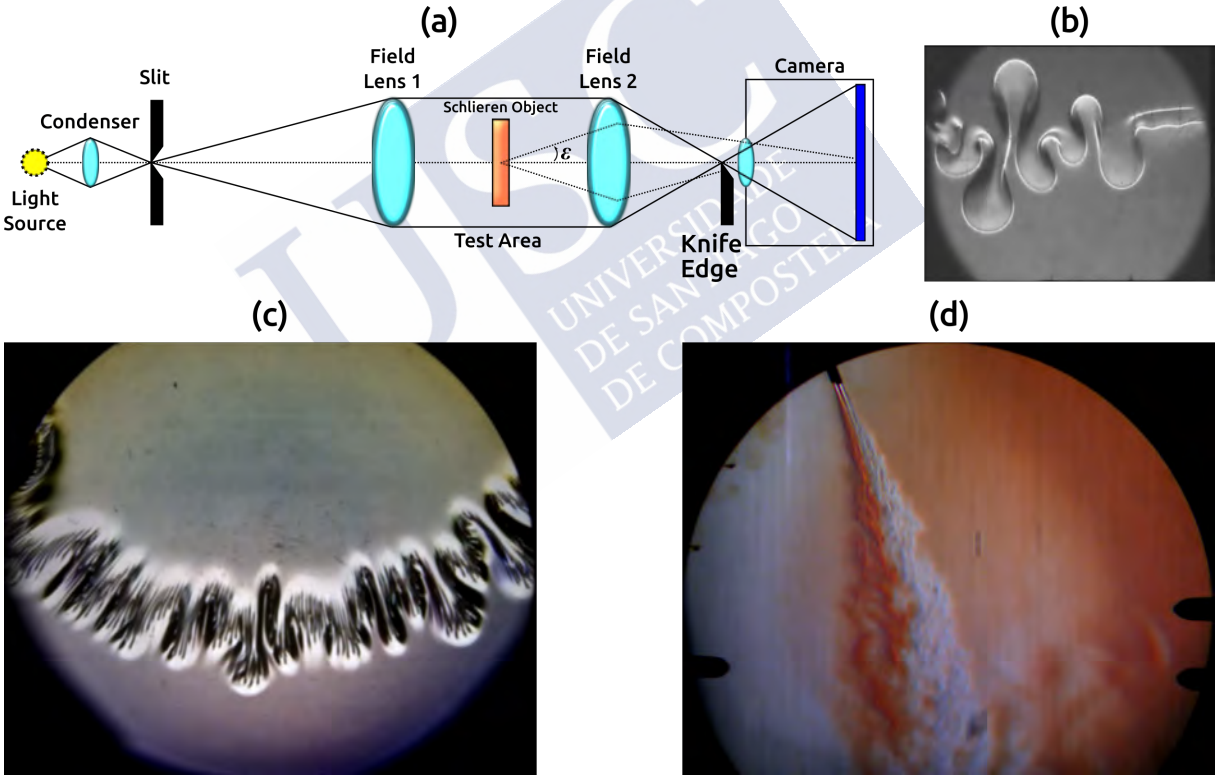

Figure 1.33: (a) Schematic of the dual-field-lens Schlieren technique. This arrangement was the chosen one for the development of this work. (b) Example of buoyancy-driven hydrodynamic instability in Hele-Shaw cell observed through the Schlieren optics. The example is identical to the one presented in Fig. 1.32(b). (c) Viscous fingering instability produced by the displacement of viscous sugar solution by a less viscous solution of NaCl. Both solutions were not colored. The black stripes are produced by the differences in density of the two solutions. (d) Airstream observed through a more complex z-type Schlieren technique. In this case, the *schlieren* object is positioned between a pair of parabolic mirrors.

The typical dark-bright image composition is exemplified in Figures 1.33(b-c), where two hydrodynamic instabilities are observed through the dueal-field-lens Schlieren technique.

Figure 1.33(b) shows the example presented in Figure 1.33(a) but observed through Schlieren optics. The second case presents a viscous fingering instability produced when a more viscous solution of sucrose is displaced by a less viscous solution of NaCl. As can be seen, the Schlieren technique is not only powerful enough to expose the viscous fingering instability between two colorless solutions but it is also capable to show the density differences between both liquids. This difference in density is appreciated as the black stripes observed inside the fingers [87].

There are more sophisticated arrangements like the z-type Schlieren setup, where the *schlieren* object is located between two parabolic mirrors instead of a pair of lenses. The light beams pass through the test area of an experimental arrangement aligned in a z-shape form [172]. Figure 1.33(d) presents an example of a cold air stream observed through this technique. As can be appreciated, this technique increases the sharpening and quality of the image but requires more sophisticated equipment and more space disposal.

As can be seen, the images obtained through the Schlieren technique are sharper and more detailed than those obtained through the Shadowgraphy. However, as was previously indicated, the Shadowgraph is easier and more cost-effective to implement.

PART I:

DENSITY FINGERING INSTABILITY DRIVEN BY THE BZ-CHD OSCILLATOR

USC
UNIVERSIDADE
DE SANTIAGO
DE COMPOSTELA

Motivation

Oscillating behaviors are common in Nature. They are responsible for a broad range of processes ranging from industrial applications, metabolic cycles, periodic modulations of the environment, human oscillations, and more [134]. Oscillating chemical reactions are well-known examples that attempt to simulate certain behaviors. One of the most studied oscillating reactions is the Belouzov-Zhabotinsky reaction (BZ) [18, 55, 54] which was used as a model to describe dynamic behaviors in natural processes [199, 185, 143, 29]. In this sense, the inherent complexity of the BZ reaction, in addition to its vast and rich behavior, makes it ideal for the reproduction of many natural phenomena [54].

Many processes in Nature often share the common property of taking place in a fluid medium. Hydrodynamic instabilities play an important part in these situations. The spectrum of structures where fluid instabilities play a role is large extending from Nature [200, 171, 111] to the industry [184]. Most recently, hydrodynamic instabilities are considered in several fields such as oil recovery processes [93][41, 132, 44, 207], CO_2 sequestration [44, 121, 120] among other applications. It is normal to think about systems where chemical and hydrodynamic instabilities exist at the same time and interact synergistically [163]. The knowledge and control of such processes could be essential to understand more complex problems such as marine pollution [125] or chemical gardens[31, 86, 16, 26], among many others. Just recently, and because of the complexity of the problem, these types of coupled systems were considered and analyzed [44, 26, 57, 9, 88, 48].

The forthcoming chapters will introduce a thorough description of a coupled system consisting of a bubble-free oscillating Belousov-Zhabotinsky reaction (BZ-CHD reaction [114, 187, 188, 188, 189]) and a classical interfacial hydrodynamic instability in a vertically oriented Hele-Shaw cell. The system was designed to allow two miscible fluids to interact at the interface, so the reaction takes place only inside the cell. The competition of the two instabilities will be now controlled by two independent parameters: on the one hand, the excitability that deals with the shape and duration of the oscillations and, on the other hand, the initial density gradient across the interface. A detailed quantitative analysis of the effect of each parameter will be presented. The experimental findings will lead to propose a modification of the existing kinetic models for the BZ-CHD reaction [189] that is fully capable to describe the problem in a spatially extended configuration.

The results here presented are based on the work published in Escala *et al*, (2014) ([57]) and Escala *et al*, (2019) ([61]).

USC
UNIVERSIDADE
DE SANTIAGO
DE COMPOSTELA

Chapter 2

Experimental and Numerical Methods

2.1 Experimental Methods

2.1.1 Hele-Shaw Cell Construction

All the density fingering tests were performed in a vertically arranged Hele-Shaw cell [175, 57]. This cell was built utilizing two rectangular plates (20 cm x 10 cm) of scratch-resistant methacrylate (Plexiglass®) separated by a 0.25 mm poly(tetrafluoroethylene) (PTFE) spacer as appeared within Figure 2.1. Two injection holes were set at the upper and lower part of the methacrylate plates (marked with A and B in Figure 2.1(a) respectively). Two additional holes were drilled at both sides and were utilized as fluid outlets (marked with C and D in Figure 2.1(a)). These two holes were horizontally aligned to achieve a planar interface once the reactive solutions were injected. A metallic rectangular frame was put on each side of the cell to fix the device, prevent undesirable harm to the methacrylate and ensure a homogeneous pressure distribution that guarantees an equally spaced gap between the Hele-Shaw cell's two plates.

2.1.2 Injection Protocol

Two solutions containing separated parts of the BZ-CHD reaction were injected utilizing a peristaltic pump (Gilson Minipuls 3) using silicon tubes attached to a chemically resistant Polypropylene connector (made by CPC®, [39]) of 4 mm internal diameter. For this work, two connector models (PMC2201212 and PMC230212) were used. Those two models of connectors were specifically chosen due to their chemical resistance.

The procedure to obtain a planar initial condition was performed in two steps similar to Shi *et al* [175]. First, Solution 1 was injected from the lower hole (B) keeping closed the outlets (C and D) (Figure 2.2(a)). Once the cell was completely filled with this solution, the tube with Solution 2 was connected to the upper injection hole (A) avoiding the inclusion of bubbles. Secondly, once both connectors were in place, outlets C and D were opened and both liquids were injected using a fast flow rate (Figure 2.2(b)). Once the interface between Solutions 1 and 2 was completely planar, the injection was stopped and the outlets closed. This moment was considered the beginning of the experiment (Figure 2.2(c)). The opening of the outlets was controlled using a single chemically resistant PTFE faucet. For all cases studied in the present work, the system was always initially hydrodynamically stable. Thus, the denser fluid (in this case Solution 1) was always injected from the bottom inlet [57].

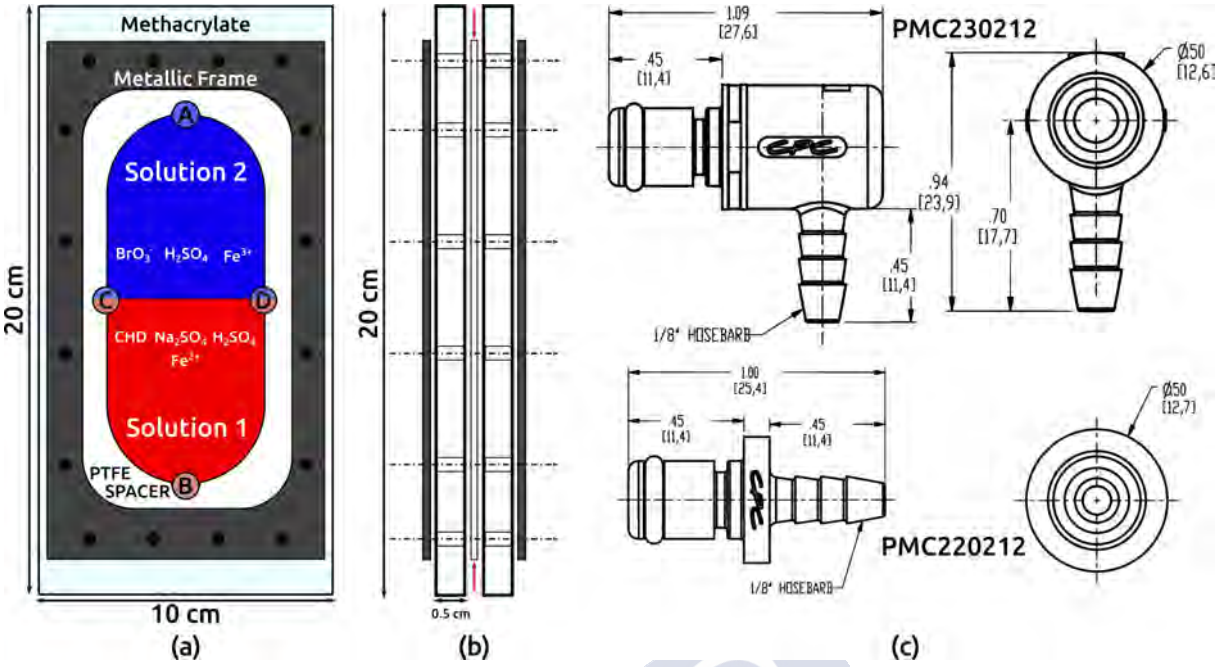

Figure 2.1: Schematics of the Hele-Shaw cell and the injection connectors. (a) Frontal and (b) side views of the designed Cell. The Holes named A and B in the scheme (a) are the inlets for Solution 2 and 1 respectively. C and D are the outlets that are only open in order to achieve a planar interface at the center of the reactor. (c) The chemically resistant Polypropylene connectors were used to inject the solutions. The chosen material was suitable for dealing with the products of the BZ-CHD reaction. The location of the PTFE spacer is indicated by the red arrows in (b).

2.1.3 Optical Arrangement

The Hele-Shaw cell was placed in an experimental setup described in Figure 2.3. Two different images were recorded for each experiment at the same time. The first one was a "naked eye" view (hereafter chemical view) which was useful to observe all kinds of chemical phenomena like spirals, waves, and spatio-temporal dynamics associated with the chemistry (clearly observed due to the color changes of the catalyst). The second one was an image obtained through the Schlieren technique (hereafter *Schlieren view*). This Technique is useful to detect variations in the hydrodynamic field that are impossible to observe in the chemical view [172].

The experimental setup was illuminated by using a high-power light-emitting diode (LED) filtered using a variable slit oriented in concordance with the fingers displacement (vertical axis). A first collimator lens was placed in the light pathway close to the LED light source. The collimated light beam passed through the Hele-Shaw cell. A 50/50 beam splitter was placed between the cell and a second collimator lens. The deviated light beam directly impacts a CMOS camera (PixeLink PL-B776U) which recorded the chemical view. The remaining 50% of the light beam passed through a second collimator lens. A knife-edge cutoff filter was placed at the focal point of the second collimator in order to obtain a Schlieren view of the cell which was recorded by a second CMOS camera (PixeLink PL-B776U). A graduated spatial reference was used to obtain quantitative information.

2.1.4 Chemical Recipes and Experimental Designs

In the present work, several recipes of the BZ-CHD were used depending on the experimental context. The following section summarizes the reaction and protocols related to each specific part. All solutions presented here were made from reagent grade stocks. More details regarding the stock

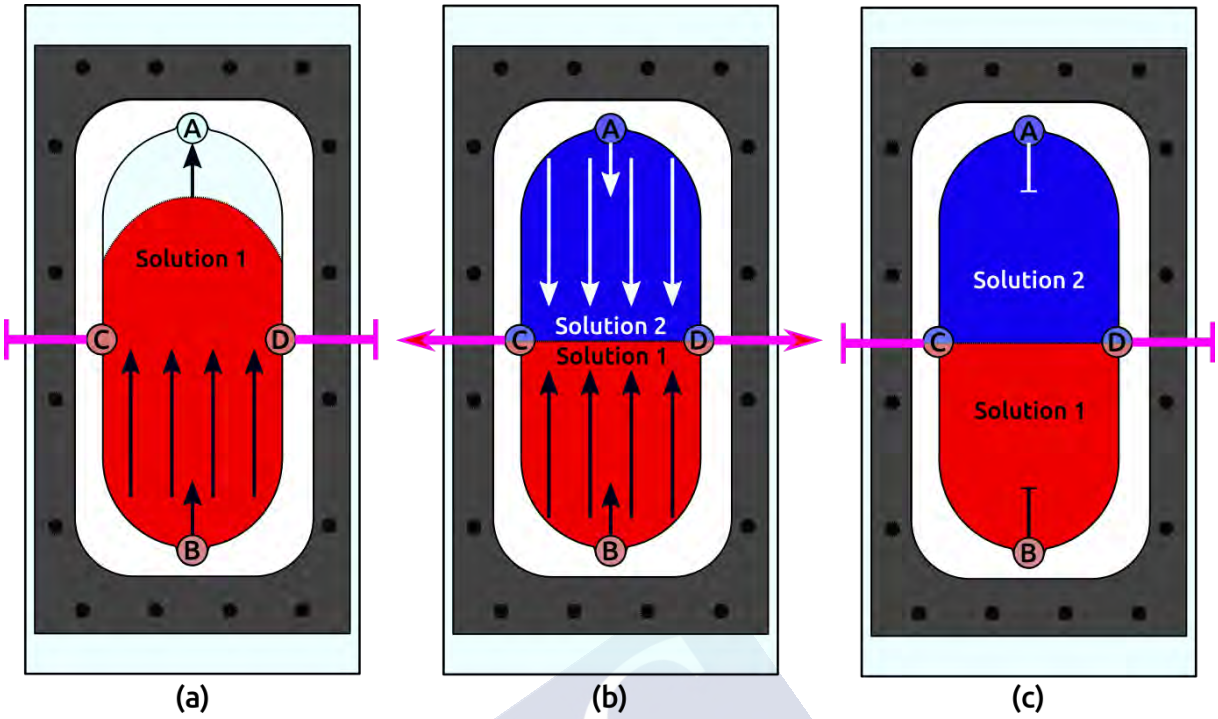

Figure 2.2: Schematics of the injection procedure. In (a) the initially empty Hele-Shaw cell was initially filled with Solution 1 from input B. (b) Once filled, Solution 2 was injected from input A and outputs C and D are opened. (c) Both liquids were injected until the planar interface was obtained. At that moment, all the inputs and outputs were closed.

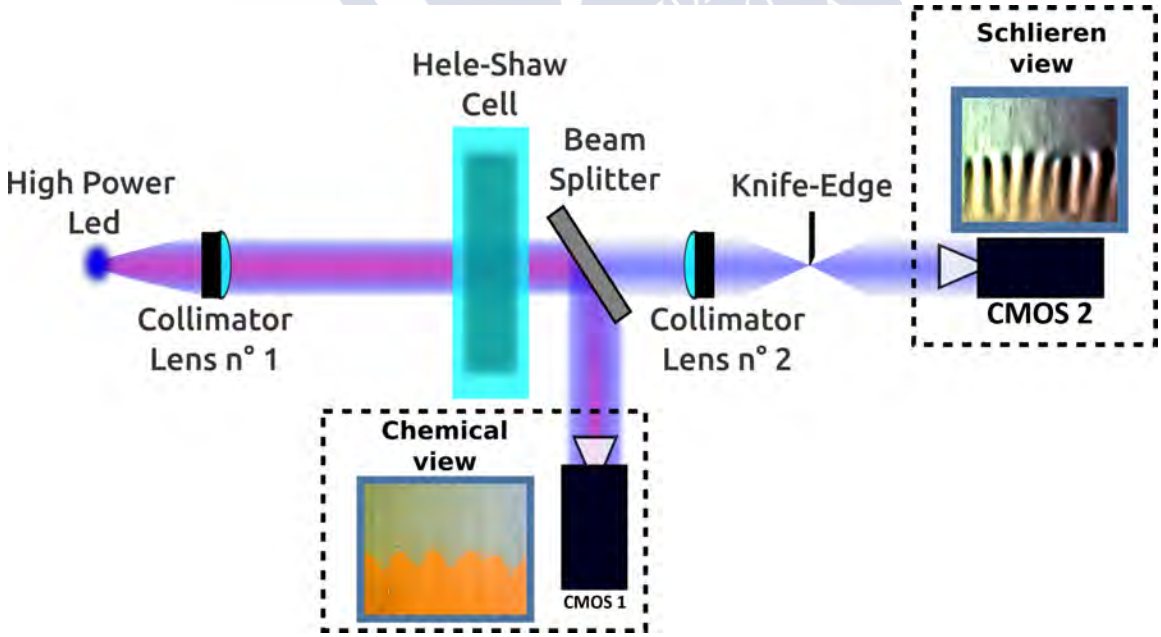

Figure 2.3: Experimental setup used for the convective Hele-Shaw system. The arrangement was built by recording two different images from each experiment. A first camera recorded the direct observation of the experiment. This observation was obtained by filming the reflection of the cell through the beam splitter located between the cell and the second collimator lens. The second observation was obtained by using the Schlieren optical technique. The light beam passed through the cell located between two collimator lenses. The knife-edge filter was located at the focal point of the second collimator.

preparations are included in Appendix Section A.1.

Both solutions were thermally stabilized at 22 °C by using a thermostatic bath in order to avoid density variations due to temperature changes. The maximum recorded temperature variation between solutions was $\Delta T = |T_{S1} - T_{S2}| = 0.2$ °C. All types of thermal artifacts related to the light source can be neglected as the LED source does not produce significant temperature variations. All the experiments were done in a room located in a controlled environment, avoiding significant temperature variations during each experiment.

Two main parameters were used for this part of the work: the excitability (ε) and the density difference between solutions 1 and 2 (hereafter density gradient, $\Delta\rho$).

The excitability is defined as:

$$\varepsilon = \frac{[H_2SO_4]_0 \cdot [BrO_3{}^-]_0}{[CHD]_0} \tag{2.1}$$

this expression was taken from Krinsky [109] and Vanag *et al* [205]. This value is obtained with the initial concentration of the species of the BZ-CHD reaction.

On the other hand, the density gradient is defined as:

$$\Delta\rho = \rho_{S1} - \rho_{S2} \tag{2.2}$$

this value is calculated as the difference between the density of the solution located at the bottom (ρ_{S1}), and the density of the fluid located at the upper part of the Hele-Shaw cell (ρ_{S2}). This parameter was adopted as a simple measure to evaluate the changes in density due to the chemical variations. All density measurements were done by using a Anton-Paar DMA™ 35 density-meter with an instrumental precision of 0.001 g/cm^3.

Recipe for the RDC Hele-Shaw System with an independent change of ε and $\Delta\rho$. In this case, ε and $\Delta\rho$ were varied by simultaneously changing $[H_2SO_4]_0$ in both solutions, and $[NaSO_4]_0$ in Solution 1 respectively. Both parameters were varied up to four different values each obtaining a total number of sixteen experiments. Each experiment was repeated three times. A schematic illustration of the experimental design is presented in Figure 2.4. The recipe and used concentrations are indicated in Table 2.1.

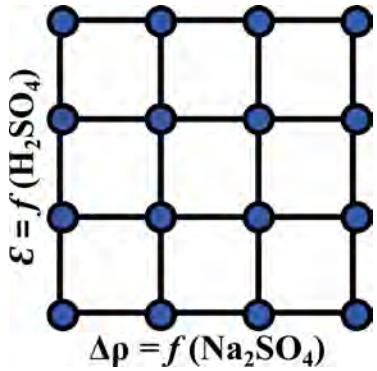

Figure 2.4: Schematics of the experimental design used to study independent changes of ε and $\Delta\rho$. The excitability of the system was varied by changing $[H_2SO_4]_0$ simultaneously in solutions 1 and 2, and it was calculated as indicated in Eq. (2.1). The density gradient was varied by changing $[Na_2SO_4]_0$ in Solution 1. This value was calculated as indicated in Eq. (2.2) by measuring the densities of solutions 1 and 2.

Recipe for Solution 1		Recipe for Solution 2	
Species	**Concentration (M)**	**Species**	**Concentration (M)**
H_2SO_4	0.847, 1.693, 2.540, 3.387	H_2SO_4	0.847, 1.693, 2.540, 3.387
CHD	0.291	BrO_3^-	0.142
Na_2SO_4	0.130, 0.155, 0.205, 0.230	Na_2SO_4	0
$[Fe(phen)_3]^{2+}$	$0.4x10^{-3}$	$[Fe(phen)_3]^{3+}$	$0.4x10^{-3}$

Table 2.1: Base BZ-CHD recipe used in the RDC experiments where ε and $\Delta\rho$ varied independently.

Tables 2.3(a,b) show the values of ε and the average $\Delta\rho$ calculated by changing $[H_2SO_4]_0$ and $[Na_2SO_4]_0$ respectively. These calculations were done by using the concentrations indicated in Table 2.1.

H_2SO_4 (M)	ε (M)
0.847	0.413
1.693	0.826
2.540	1.239
3.387	1.653

(a)

Na_2SO_4 (M)	$\Delta\rho$ (g/cm^3)
0.130	0.002 ± 0.001
0.155	0.004 ± 0.001
0.205	0.009 ± 0.001
0.230	0.011 ± 0.001

(b)

Table 2.3: Values for ε and $\Delta\rho$ calculated from Eqs. (2.1) and (2.2) respectively. (a) Values of ε obtained by changing $[H_2SO_4]_0$. (b) Values of $\Delta\rho$ obtained by changing $[Na_2SO_4]_0$. The density values are indicated as the average value between three replicas $\pm$ the standard deviation.

Recipe for the RDC Hele-Shaw System with a coupled change of ε and $\Delta\rho$. This set of experiments were made by varying the $NaBrO_3$ concentration in Solution 2. Thus, this not only changed the system excitability but also the density gradient. In addition, it is important to remark that the following recipe includes sodium bromide (NaBr) in its formulation, the H_2SO_4 concentration in each solution is not equal and it does not includes Na_2SO_4. The addition of sodium sulfate was not necessary

in this case as the solutions already had different densities due to the acid gradient [1]. The base recipe used is summarized in Table 2.4.

Recipe for Solution 1		**Recipe for Solution 2**	
Species	**Concentration (M)**	**Species**	**Concentration (M)**
H_2SO_4	1.863	H_2SO_4	1.552
CHD	0.291	BrO_3^-	0.057, 0.066, 0.075, 0.085, 0.095, 0.104, 0.113, 0.123
-	-	Br^-	0.019, 0.022, 0.025, 0.028, 0.031, 0.034, 0.038, 0.041
$[Fe(phen)_3]^{2+}$	$0.4x10^{-3}$	$[Fe(phen)_3]^{3+}$	$0.4x10^{-3}$

Table 2.4: Base BZ-CHD recipe used in the RDC experiments where ε and $\Delta\rho$ varied coupled by changing $[BrO_3^-]_0$ and $[Br^-]_0$. Both reagents were changed simultaneously as indicated.

For this case, the excitability was modified by changing $[BrO_3^-]_0$ following the experimental design indicated in Table 2.4. The $[Br^-]_0$ was also varied up to eight different molar concentrations simultaneously to the bromate concentration. As the acid concentration is not uniform in each solution, the excitability was calculated as:

$$\varepsilon = \frac{\frac{1}{2}([H_2SO_4]_0{}^{S1} + [H_2SO_4]_0{}^{S2}) \cdot [BrO_3^-]_0}{[CHD]_0} \tag{2.3}$$

where $[H_2SO_4]_0{}^{S1}$ and $[H_2SO_4]_0{}^{S2}$ are the total acid concentrations in Solution 1 and 2 respectively.

The expression for ε was obtained from considering that both solutions had the same final volume and was derived from the original formulation [205]. Similar to the previous case, all the experiments were done by triplicate.

[1] Regarding this issue, the fact that the density jump was produced by an acid gradient did not produce any significant effect on the system dynamics.

$[BrO_3^-]_0$	$[Br^-]_0$	ε (M)	$\Delta\rho$ (g/cm^3)
0.057	0.019	0.334	0.017 $\pm$ 0.001
0.066	0.022	0.389	0.014 $\pm$ 0.001
0.075	0.025	0.445	0.013 $\pm$ 0.002
0.085	0.028	0.501	0.012 $\pm$ 0.002
0.095	0.031	0.557	0.011 $\pm$ 0.001
0.104	0.034	0.612	0.010 $\pm$ 0.003
0.113	0.038	0.668	0.009 $\pm$ 0.002
0.123	0.041	0.724	0.008 $\pm$ 0.001

Table 2.5: Values of ε and $\Delta\rho$ obtained by changing $[BrO_3^-]_0$. As this species is located at the upper layer, both the excitability and the density gradient were changed simultaneously by varying $[BrO_3^-]_0$. The excitability was calculated as indicated in Eq. (2.3) with the concentration values shown in Table 2.4. The density gradient was calculated identically as the previous part. The table also shows the $[Br^-]_0$ that corresponds to each bromate concentration. The density values are indicated as the average value between three replicas $\pm$ the standard deviation.

Recipe Used in the Batch System. For this case, the experiments were derived from a variation of the recipe presented in Table 2.1. The differences in the concentrations of the CHD and BrO_3^- respect the original formulation are because each chemical species is assumed to be dissolved in twice the volume of each independent solution. This is assumed to occur at the vicinity of the interface inside the Hele-Shaw cell. This was intentionally designed to keep constant values of the excitability concerning the convective case. In these experiments, the excitability of the system was varied by changing the H_2SO_4 molar concentration as shown in Tables 2.7. The chemical formulation is indicated in Table 2.6. All the experiments were done by triplicate.

Species	Concentration (M)
H_2SO_4	0.423, 0.847, 1.270, 1.693, 2.117 2.540, 2.963, 3.387, 3.810
CHD	0.145
BrO_3^-	0.071
$[Fe(phen)_3]^{2+}$	$0.4x10^{-3}$

Table 2.6: Recipe used for studying changes in ε due to changes in $[H_2SO_4]_0$. These experiments were performed in a batch reactor.

$[H_2SO_4]_0$ (M)	0.423	0.847	1.270	1.693	2.117	2.540	2.963	3.387	3.810
ε (M)	0.207	0.413	0.619	0.826	1.032	1.239	1.445	1.653	1.858

Table 2.7: Values of ε corresponding to changes in $[H_2SO_4]_0$ for the recipe presented in Table Recipe-5.

2.1.5 Spectroscopy Techniques

Different spectroscopy techniques were used during the development of this part of the present work. The UV-Vis spectroscopy was used to follow the reaction dynamics of the fully stirred homogeneous system. On the other hand, the Nuclear Magnetic Resonance (NMR) spectroscopy was utilized as the definitive tool to unveil the chemical structure of the species involved in the instability mechanism. All the results obtained due to the use of these devices are presented in Sections 4.2 and 4.4.

UV-Vis Spectroscopy

All the batch experiments were analyzed in a UV-Vis spectrophotometer (VIS-NIR USB325, Vernier) as the one shown in Figure 2.5(a). All temporal analyses were done considering a Δt = 1 s and measured over an excitation wavelength of 510 nm, suitable for the red coloration of the ferroin indicator [178, 68]. All absorbance values presented in this work were converted into molar concentration units considering an absorptive molar coefficient $\xi_{max} = 11000 L/mol.cm$ [68] by using the Beer-Lambert law [178]. All these experiments were also recorded for 6 h.

Nuclear Magnetic Resonance (NMR) Spectroscopy

Nuclear magnetic resonance spectroscopy was used as a key technique to demonstrate the mechanism involved in the instability. Deuterated methanol (MetOH-d_4) and deuterated dimethyl sulfoxide (DMSO-d_6) were used as solvents in both ^1H and ^{13}C experiments using a Mercury 300 NMR equipment (Figure 2.5(b)). The experimental results were compared with theoretical estimations provided by the software Mestre-C from MestreLab Research. More details about the use of this technique are explained in the further sections.

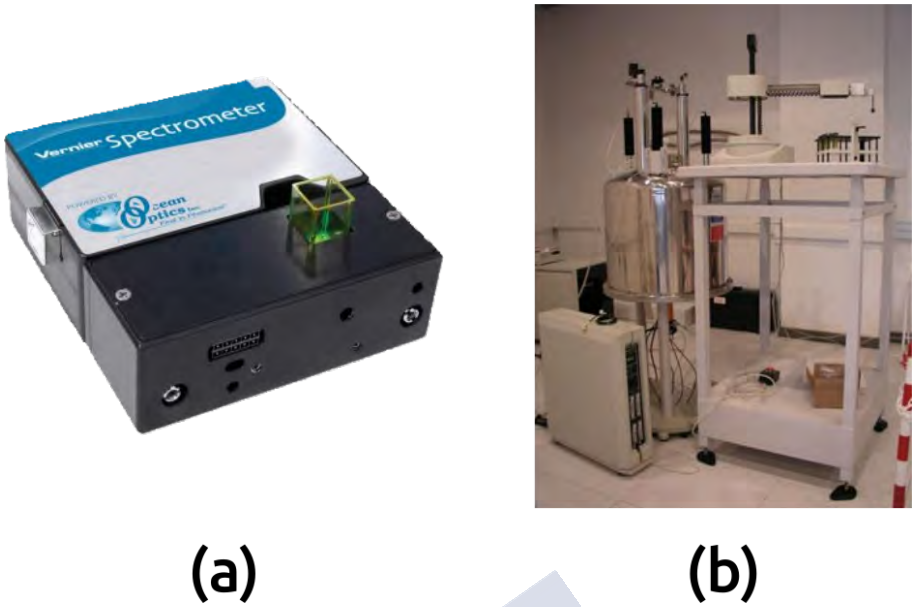

Figure 2.5: (a) UV-Vis spectrophotometer used to follow the reaction dynamics of the batch experiments. (b) NMR equipment was used to find out the molecular structure of the species involved in the instability mechanism. This apparatus is located at the CACTUS building in the University of Santiago de Compostela.

2.1.6 Precipitate Extraction

In certain conditions, a precipitate emerges from the BZ-CHD solution in both, the cell experiments and in a fully stirred batch reactor. To isolate such precipitate, all chemical components of the BZ-CHD reaction were mixed in a beaker. The evolution of certain concentrations was recorded by UV-Vis spectroscopy. Once the oscillations finished (observed by saturation in the spectrophotometer signal), the precipitate appeared as a heavy solid phase. The substance was then retrieved by filtering the solution and subsequently dried in an oven at 60° C.

2.2 Numerical Methods

Numerical simulations were performed using different packages of software and were used to better understand the experimental results. Additionally, the validation of such models can be useful to study more complex variations of the systems here presented. This section will introduce all the numerical models, methods, and generalities used to simulate each specific section of this part.

2.2.1 The BZ-CHD Reaction Chemical Models

Szalai *et al* [188, 187, 189, 190] developed several kinetic models of the BZ-CHD system based on the elementary analysis of every chemical step involved in the whole process [190, 189]. These models reproduce most of the properties of the BZ-CHD reaction.

Full Mechanism of the Catalyzed Bromate-CHD Oscillator

The kinetic model presented in equations R1-R19, not only reproduce the base mechanistic of the Bromate-CHD oscillator [187] but also contemplates the effect of the catalyst, the oxidation of the key organic derivatives species, and the positive and negative feedback mechanisms involved. The dynamics

observed from this model are very comparable to those observed in the experiments. The set of equations, kinetic laws, and chemical equations are presented in Table 2.8. This model was used to simulate only the batch system due to large number of variables involved.

	Reactions	Kinetic Law	k_f	k_r
R1	$Br^- + HOBr^- + H^+ \rightleftharpoons Br_2 + H_2O$	$v_{r1} = k_f[Br^-][HOBr][H^+] - k_r[Br_2]$	$8x10^9\ M^{-2}s^{-1}$	$80\ s^{-1}$
R2	$Br^- + HBrO_2 + H^+ \rightleftharpoons 2HOBr$	$v_{r2} = k_f[Br^-][HBrO_2][H^+] - k_r[HOBr]^2$	$2.5x10^6\ M^{-2}s^{-1}$	$2x10^{-5}\ M^{-1}s^{-1}$
R3	$Br^- + BrO_3^- + 2H^+ \rightleftharpoons HOBr + HBrO_2$	$v_{r3} = k_f[Br^-][BrO_3^-][H^+]^2 - k_r[HOBr]^2[HBrO_2]$	$1.2\ M^{-3}s^{-1}$	$3.2\ M^{-2}s^{-1}$
R4a	$HBrO_2 + H^+ \rightleftharpoons H_2BrO_2^+$	$v_{r4a} = k_f[HBrO_2][H^+] - k_r[H_2BrO_2]^+$	$2x10^6\ M^{-1}s^{-1}$	$1x10^8\ s^{-1}$
R4b	$HBrO_2 + H_2BrO_2^+ \longrightarrow BrO_3^- + HOBr + 2H^+$	$v_{r4b} = k_f[HBrO_2][H_2BrO_2^+]$	$1.7x10^5\ M^{-1}s^{-1}$	
R5a	$HBrO_2 + BrO_3^- + H^+ \rightleftharpoons Br_2O_4 + H_2O$	$v_{r5a} = k_f[HBrO_2][BrO_3^-][H^+] - k_r[Br_2O_4]$	$48\ M^{-2}s^{-1}$	$3.2x10^3\ s^{-1}$
R5b	$Br_2O_4 \rightleftharpoons 2BrO_2^*$	$v_{r5b} = k_f[Br_2O_4] - k_r[BrO_2^*]^2$	$7.5x10^4\ s^{-1}$	$1.4x10^9\ M^{-1}s^{-1}$
R6a	$H_2Q + 2BrO_2^* \longrightarrow 2HBrO_2 + Q$	$v_{r6a} = k_f[H_2Q][BrO_2^*]$	$2x10^6\ M^{-1}s^{-1}$	
R6b	$[Fe(phen)_3]^{2+} + BrO_2^* + H^+ \rightleftharpoons [Fe(phen)_3]^{3+} + HBrO_2$	$v_{r6b} = k_f[[Fe(phen)_3]^{2+}][BrO_2^*][H^+]$	$1x10^7\ M^{-2}s^{-1}$	
R7	$CHD + H^+ \rightleftharpoons CHDE + H^+$	$v_{r7} = k_f[CHD][H^+] - k_r[CHDE][H^+]$	$2.1x10^{-4}\ M^{-1}s^{-1}$	$5.2x10^2\ M^{-1}s^{-1}$
R8	$CHDE + Br_2 \longrightarrow BrCHD + Br^- + H^+$	$v_{r8} = k_f[CHDE][Br_2]$	$2.8x10^9\ M^{-1}s^{-1}$	
R9	$BrCHD + H^+ \longrightarrow CHED + Br^- + 2H^+$	$v_{r9} = k_f[BrCHD][H^+]$	$5x10^{-5}\ M^{-1}s^{-1}$	
R10	$CHED + H^+ \longrightarrow H_2O + H^+$	$v_{r10} = k_f[CHED][H^+]$	$1.9x10^{-4}\ M^{-1}s^{-1}$	
R11	$CHD + BrO_3^- + H^+ \longrightarrow H_2Q + HBrO_2 + H_2O$	$v_{r11} = k_f[CHD][BrO_3^-][H^+]$	$2x10^{-5}\ M^{-2}s^{-1}$	
R12	$CHD + HBrO_2 \longrightarrow H_2Q + HOBr + H_2O$	$v_{r12} = k_f[CHD][HBrO_2]$	$5\ M^{-2}s^{-1}$	
R13	$H_2Q + BrO_3^- + H^+ \longrightarrow Q + HBrO_2 + H_2O$	$v_{r13} = k_f[H_2Q][BrO_3^-][H^+]$	$2x10^{-2}\ M^{-2}s^{-1}$	
R14	$H_2Q + HOBr \longrightarrow Q + Br^- + H^+ + H_2O$	$v_{r14} = k_f[H_2Q][HOBr]$	$6x10^5\ M^{-1}s^{-1}$	
R15	$H_2Q + Br_2 \longrightarrow Q + 2Br^- + 2H^+$	$v_{r15} = k_f[H_2Q][Br_2]$	$1x10^4\ M^{-1}s^{-1}$	
R16	$2[Fe(phen)_3]^{3+} + CHD \longrightarrow 2[Fe(phen)_3]^{2+} + H_2Q + 2H^+$	$v_{r16} = k_f[[Fe(phen)_3]^{3+}][CHD]/[H^+]$	$0.14s^{-1}$	
R17	$2[Fe(phen)_3]^{3+} + BrCHD \longrightarrow Q + Br^- + 3H^+ + 2[Fe(phen)_3]^{2+}$	$v_{r17} = k_f[[Fe(phen)_3]^{3+}][BrCHD]$	$0.051\ M^{-1}s^{-1}$	
R18	$2[Fe(phen)_3]^{3+} + H_2Q \longrightarrow 2[Fe(phen)_3]^{2+} + Q + 2H^+$	$v_{r17} = k_f[[Fe(phen)_3]^{3+}][H_2Q]$	$6000\ M^{-1}s^{-1}$	
R19	$2[Fe(phen)_3]^{2+} + BrO_3^- + 3H^+ \longrightarrow 2[Fe(phen)_3]^{3+} + HBrO_2 + H_2O$	$v_{r18} = k_f[[Fe(phen)_3]^{2+}][BrO_3^-][H^+]^2$	$0.02\ M^{-3}s^{-1}$	

Table 2.8: Full chemical model of the BZ-CHD reaction proposed by Szalai *et al* [190, 189]. All the references regarding the kinetic constants can be consulted in the aforementioned cite.

Skeleton Model of the Catalyzed Bromate-CHD Oscillator

Along with the full model, Szalai *et al* [189] also introduced a skeleton model that encompasses most of the dynamics of the extensive system in a simplified manner. The kinetic model presented in Table 2.9 was used to perform more complex simulations where the use of the full model was prohibitive due to resource requirements.

	Reactions	Kinetic Law
R2	$Br^- + HBrO_2 + H^+ \rightleftharpoons 2\,HOBr$	$v_{r2} = k_2^f[Br^-][HBrO_2][H^+]$
R3	$Br^- + BrO_3{}^- + 2\,H^+ \longrightarrow HOBr + HBrO_2$	$v_{r3} = k_3^f[Br^-][BrO_3{}^-][H^+]^2$
R4	$2\,HBrO_2 \longrightarrow BrO_3{}^- + HOBr + H^+$	$v_{r4a} = k_4 k_{4a}^f / k_{4a}^r [HBrO_2]^2[H^+]$
R5	$HBrO_2 + BrO_3{}^- + H^+ \rightleftharpoons 2\,BrO_2{}^* + H_2O$	$v_{r5} = k_{5a}^f[HBrO_2][BrO_3{}^-][H^+] - k_{5a}^r k_{5b}^f / k_{5b}^f [BrO_2{}^*]^2$
R6a	$H_2Q + 2\,BrO_2{}^* \longrightarrow 2\,HBrO_2 + Q$	$v_{r6a} = k_{6a}^f[BrO_2{}^*][H_2Q]$
R6b	$[Fe(phen)_3]^{2+} + BrO_2{}^* + H^+ \rightleftharpoons [Fe(phen)_3]^{3+} + HBrO_2$	$v_{r6b} = k_{6b}^f(c_{tot}\text{-}[[Fe(phen)_3]^{3+}])[BrO_2{}^*][H^+] - k_{6b}^r[[Fe(phen)_3]^{3+}][HBrO_2]$
R9	$BrCHD \longrightarrow 0.5\,H_2Q + Br^- + H^+$	$v_{r9} = k_9^f[BrCHD][H^+]$
R13	$H_2Q + BrO_3{}^- + H^+ \longrightarrow Q + HBrO_2 + H_2O$	$v_{r13} = k_{13}^f[H_2Q][BrO_3{}^-][H^+]$
R16'	$2\,[Fe(phen)_3]^{3+} + BrCHD \longrightarrow H_2Q + Br^- + 2\,[Fe(phen)_3]^{2+} + Q + H^+$	$v_{r16} = k_{16}^f[BrCHD][[Fe(phen)_3]^{3+}]$

Table 2.9: Skeleton model of the BZ-CHD reaction as proposed by Szalai *et al* [190, 189].

In this case, and unlike the original work [189], values for k_{6b}^f = 6.2x10$^4 M^{-2}s^{-1}$, k_{r6}^b = 1.2x10$^4 M^{-1}s{-}1$ and k_{16}^f = 0.47 $M^{-1}s^{-1}$, fit better the experimental results compared with those presented in Table 2.8. In addition, many species considered pool reactants in Szalai *et al* [189], were considered variables for the present work. More specifically, H^+, HOBr and H_2O were considered pool components while Br^-, $HBrO_2$, $BrO_3{}^-$, $BrO_2{}^*$, H_2Q, Q, $[Fe(phen)_3]^{2+}$, $[Fe(phen)_3]^{3+}$, and BrCHD were considered variables.

2.2.2 Batch System Simulation

As was previously mentioned, the full model was used to simulate the batch system. All the equations were implemented and solved in the GNU software COPASI (COmplex PAthway SImulator) [95]. COPASI, which was formerly created to simulate metabolic pathways is a powerful tool to resolve large and complex numerical problems ensuring high stability and performance to solve linear and non-linear systems of ordinary differential equations.

All the simulations were performed in a time course task using a fixed time step of 0.01 s and the deterministic LSODA solver (a variation of the Livermore Solver for Ordinary Differential Equations for stiff and non-stiff differential equations [162]). Both relative and absolute tolerance were set to 1x10^{-6} and 1x10^{-12} respectively.

The initial conditions were taken from Table 2.6. The excitability was modified in the same way as changed in the experiments, by varying the H_2SO_4 initial concentration. However, some differences between the real and numerical concentrations were found, probably associated with the complexity and simplifications made in the model development. Therefore, for the numerical cases the excitability was defined as the acid concentration ($\varepsilon = [H^+]_0$). The range of values analyzed were restricted between $[H^+]_0$ = 3 M up to $[H^+]_0$ = 15 M. Thus, the low, middle, and high experimental ε correspond with 3, 10, and 15 M in $[H^+]_0$ respectively.

2.2.3 2D Reaction-Diffusion-Convection Model

The non-linear reaction-diffusion-convection (RDC) simulations were done by using the commercial software Ansys Fluent® version 19.2 [11, 12]. In general terms, the set of equations

introduced in Section 1.47 to describe the dynamics of a chemically induced density fingering instability, were adapted and numerically solved by the software. The reactive terms were taken from the Skeleton model presented in the table 2.9 and were used together with a stiff chemistry solver. The density function, the permeability, and the kinetic laws of the skeleton model were implemented through user defined functions (UDF). The calculation domain (D) and the initial reagent conditions are indicated in the schematic of the Figure 2.6. A squared mapped mesh of 181 elements in the x-direction and 181 elements in the y-direction was used as the numerical grid. The gravity field was set to a value of 9.81 m^2/s along the y-axis.

As will be described in further chapters, the base model equations for the RDC simulations have been modified from the classical formulation to include the chemical species involved in the instability mechanism, which is the quinhydrone complex ($[Q \cdot H_2Q]$). Even though the development of such modification is extensively detailed in Chapter 5, some information regarding the configuration of the RDC model must be included in this section to comply with the thesis structure. In this sense, the boundary conditions for this particular case were set as zero diffusive flux for all the species except for the quinhydrone, which was set as $[Q \cdot H_2Q]_0 = 0$ at the lower boundary for numerical stability reasons. This is also indicated in Figure 2.6

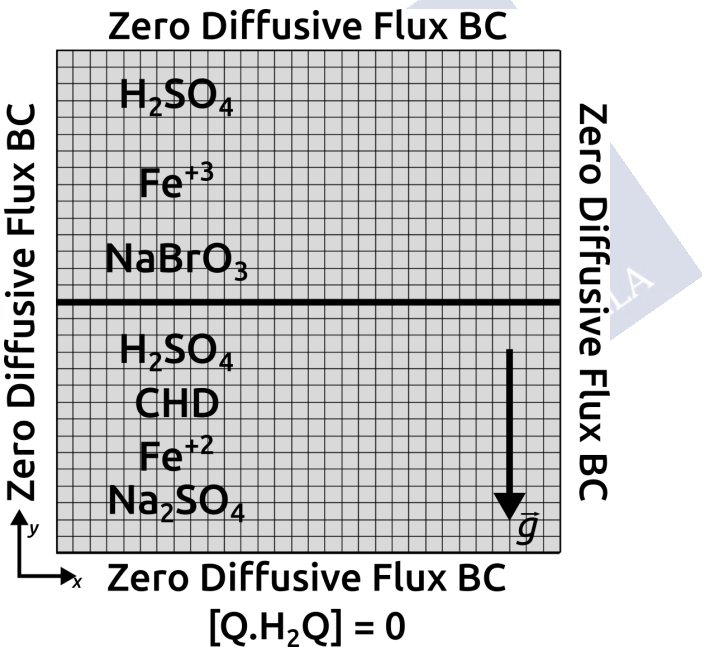

Figure 2.6: 2D numerical domain used to simulate the RDC model. The mesh consists of 181 elements in the horizontal direction and 181 elements in the vertical direction. Zero diffusive flux boundary conditions are set at the boundaries except for the $[Q \cdot H_2Q]$.

The chemical species were spatially located similar to their experimental counterpart by the following piecewise function:

$$
\begin{aligned}
C_{ai}(x,y,0) &= \begin{cases} [C_a]_0(x,y)(\xi r(x,y)+1) & y < L/2 \\ 0 & y \geqslant L/2 \end{cases} \\
C_{bi}(x,y,0) &= \begin{cases} 0 & y < L/2 \\ [C_b]_0(x,y)(\xi r(x,y)+1) & y \geqslant L/2 \end{cases}
\end{aligned}
\tag{2.4}
$$

$$[H_2SO_4]_0(x,y,0) = k, \forall (x,y) \in D$$

where $[C_a]_0$ are: $[CHD]_0$, $[Fe(phen)_3]_0^{2+}$, $[Na_2SO_4]_0$ and $[C_b]_0$ are: $[NaBrO_3]_0$ and $[Fe(phen)_3]_0^{3+}$. $r(x,y)$ is a normally distributed random function with amplitude $\xi = 10^{-2}$. $[H_2SO_4]_0$ was set constant for the entire domain.

The pressure field was calculated by using a second-order upwind scheme, while the chemical species were calculated by using a first-order upwind scheme. The time step was automatically controlled by the software based on an adaptive algorithm using the first-order upwind discretization [11, 12]. All simulations were calculated for a final time of 200 s. All the parameters used for RDC simulations are listed in Table 2.10.

Parameter	Value	Dimension Unit	Reference/Notes
$[BrO_3^-]_0$	0.142	M	experimental
$[CHD]_0$	0.291	M	experimental
$[Fe(phen)_3]_0^{2+}$	$4\times^{-4}$	M	experimental
$[Fe(phen)_3]_0^{3+}$	$4\times^{-4}$	M	experimental
$\alpha_{BrO_3^-}$	0.114×10^{-3}	M^{-1}	experimental (App. D)
α_{CHD}	0.019×10^{-3}	M^{-1}	experimental (App. D)
$\alpha_{[Fe(phen)_3]_0^{2+/3+}}$	0.264×10^{-3}	M^{-1}	experimental (App. D)
$\alpha_{Na_2SO_4}$	0.121×10^{-3}	M^{-1}	experimental (App. D)
α_{H^+}	0.013×10^{-3}	M^{-1}	ad hoc
$[Na_2SO_4]_0$	0.108, 0.200	M	experimental/adjusted
$[H^+]_0$	3, 15	M	model
ρ_0	1.000	g cm^{-3}	experimental
μ	0.001	Pa.s	experimental
P_0	0	Pa	
L	0.01	m	
D_i	1×10^{-8}	$m^2 s^{-1}$	all species, except for $Q\cdot H_2Q$
$D_{Q\cdot H_2Q}$	1×10^{-9}	$m^2 s^{-1}$	estimated
a	2.5×10^{-4}	m	experimental
κ_0	5.208×10^{-9}	m^2	experimental: $a^2/12$
R_K	0.75		experimental/adjusted
$RMM_{Q\cdot H_2Q}$	218.2	g mol^{-1}	reference [214]
ρ_S	1.402	g cm^{-3}	reference [214]
ϕ	1		reference [197]
γ	100		ad hoc
V_T	2.5×10^{-8}	m^3	calculated from $L^2 a$
$k_{rQ\cdot H_2Q}$	5×10^{-2}	$M^{-1} s^{-1}$	estimated

Table 2.10: Parameters used in the RDC simulations. All values are expressed in the International System of Units (SI) excepting concentrations that are expressed in Molarity.

USC
UNIVERSIDADE
DE SANTIAGO
DE COMPOSTELA

Chapter 3

Experimental Results

Abstract: *This chapter will show a complete experimental characterization of the coupling between the BZ-CHD and the density fingering instability. Results are presented in both, descriptive and quantitative manner, showing the effect of the most important factors involved in the dynamics of the system. The conclusions obtained from the experimental observations will be fundamental for the understanding of the coupling mechanism and will facilitate the subsequent development of a convective model.*

3.1 General System Overview

The characteristic behavior of the experimental system described in Section 2.1 is presented in Figure 3.1. These results were obtained for a reference case where ε = 1.653 M and $\Delta\rho$ = 0.004 g/cm^3, which corresponds to initial concentrations of $[Na_2SO_4]_0$ = 0.155 M and $[H_2SO_4]_0$ = 3.387 M.

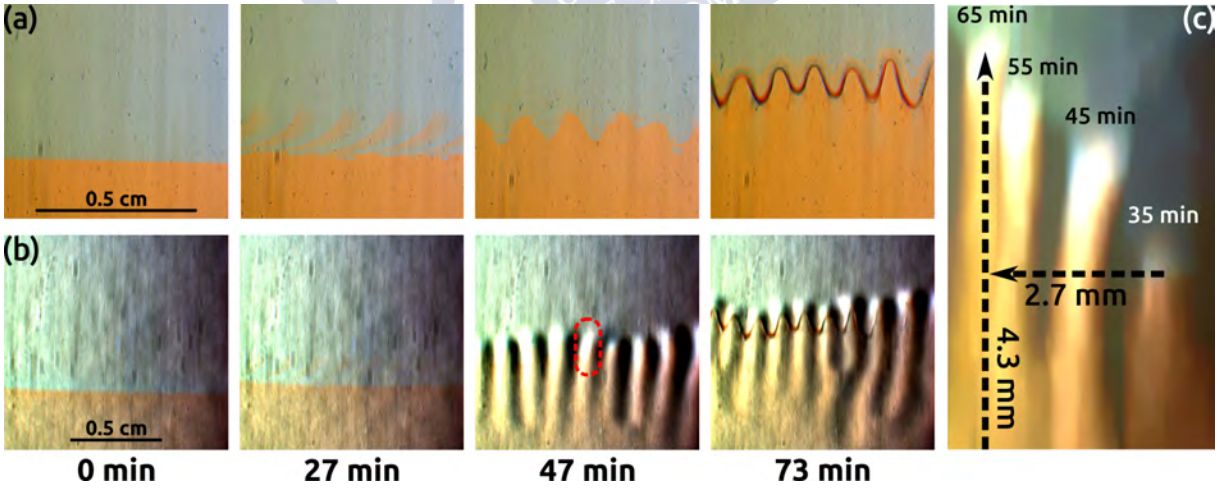

Figure 3.1: (a) Chemical and (b) Schlieren views of an experiment with ε = 1.653 M and $\Delta\rho$ = 0.004 g/cm^3. The experiment started with an initially stable planar interface. Solution 1 was located at the bottom and solution 2 is at the upper part of the image. At t = 27 min, traveling waves were observed moving through the interface from the left to the right side of the reactor. At t = 47 min, fingering instability was observed in the Schlieren view. The effect of the fingers on the interface was visible in the chemical view as the interface became deformed. The traveling waves were also affected by the finger onset as they travel through the fingers. In the last frame at t = 73 min, a strong reddish precipitate appears at the finger contour (observed in both views). (c) Shows the spatio-temporal drift of the representative finger marked with a red dashed oval in panel (b) frame 47 min. In the frame are indicated the vertical and horizontal displacement distances. Figures (a) and (b) were adapted from [61]

Figure 3.1(a) shows a direct observation of the recorded experiment (chemical view) and Figure 3.1(b) shows the same experiment but observed through the Schlieren technique. Four frames are presented corresponding to consecutive times. The initially stable condition is shown at $t = 0$ min and was obtained by using the method exposed in Figure 2.2. Solution 1 (higher density) was situated at the bottom and solution 2 (lower density) was situated at the upper part of the Helle-Shaw cell.

The reaction started in the vicinity of the interface where all chemicals of the BZ-CHD reaction were mixed by diffusive processes. In descriptive terms, starting from $t = 27$ min, it can be observed how chemical waves pass through the interface in the chemical view. No specific pattern was observed in the wave dynamic as they move independently from left to right or the opposite depending on the experiment. In this particular case, the waves were moving from left to right. In other experiments, wave collision can be also observed at the center of the image. At this stage, no significant motion in the fluid was observed as can be observed in the *Schlieren view*. This was expected due to the initially stable condition.

At $t = 47$ min, the beginning of the fingering instability was observed in the *Schlieren view*. The deformation in the interface observed in the chemical view was directly produced by the finger onset. The fingering instability is shown fully developed at $t = 73$ min. From the chemical view is possible to observe how the initial interface moved from its original position rising to the upper part of the reactor. In addition, a reddish precipitate that emerged at the interface between both solutions was observed. This precipitate was deposited in the interface adopting the shape of the fingers.

Another interesting phenomenon is the finger displacement through both vertical and horizontal directions. Commonly, finger patterns originated from buoyancy-driven instabilities displaces vertically due to the gravity action. However, it was observed in some cases that fingers also moved in the horizontal direction. Figure 3.1(c) shows the drift of a sample finger along with the horizontal and vertical directions. The finger lateral excursion and vertical displacement were measured by isolating the movement of an individual finger marked with a red dashed oval in Fig. 3.1(b) frame 3. This image was obtained by averaging several temporal snapshots into one single frame. Both displacements are indicated in millimeters.

3.2 Descriptive Analysis of the Effect of $\Delta\rho$ and ε

To have a better understanding of the effect of the density gradient between the two solutions and the excitability of the system, several experiments were performed by varying the excitability and the density gradient independently. These results were obtained using the experimental design presented in Table 2.3. In Figure 3.2, an extended summary between all the experimental cases is presented. All frames are snapshots taken 1 h after the beginning of each experiment. Horizontal and vertical axes represent the density gradient $\Delta\rho$ (Eq. (2.2)) and the excitability ε (Eq. (2.1)) respectively. Each point in this diagram shows two observations, the Schlieren view and the chemical view for each experiment.

By analyzing the *Schlieren* images, it is possible to observe an increment in the stability of the interface in line with the increment in the density gradient. This was expected as the main stability factor in buoyancy-driven instabilities is the density gradient (Section 1.8). For lower values of the excitability ($\varepsilon = 0.413$ M and 0.826 M respectively), the instability was completely suppressed once the density gradient reached $\Delta\rho = 0.009\ g/cm^3$. For larger values of the excitability ($\varepsilon = 1.239$ M and 1.653 M), the increment in the density gradient did not completely suppress the instability but damped the amplitude of the fingers down.

Changes made by increasing the system excitability produced four remarkable effects. Firstly, the interface got crossed by the fingers for lower density gradients. This effect became less significant as the density gradient was increased, which is logical as the stability of the system was increased proportionally to $\Delta\rho$. Secondly, the chemical wavelength decreased and the wave velocity increased.

This is typically a characteristic in the chemistry of the BZ-CHD oscillator as has been demonstrated in previous works [190, 189]. Thirdly, the amount of precipitate increased with the excitability while the finger onset times were reduced inversely proportional to the excitability. Finally, the finger wavelength decreased.

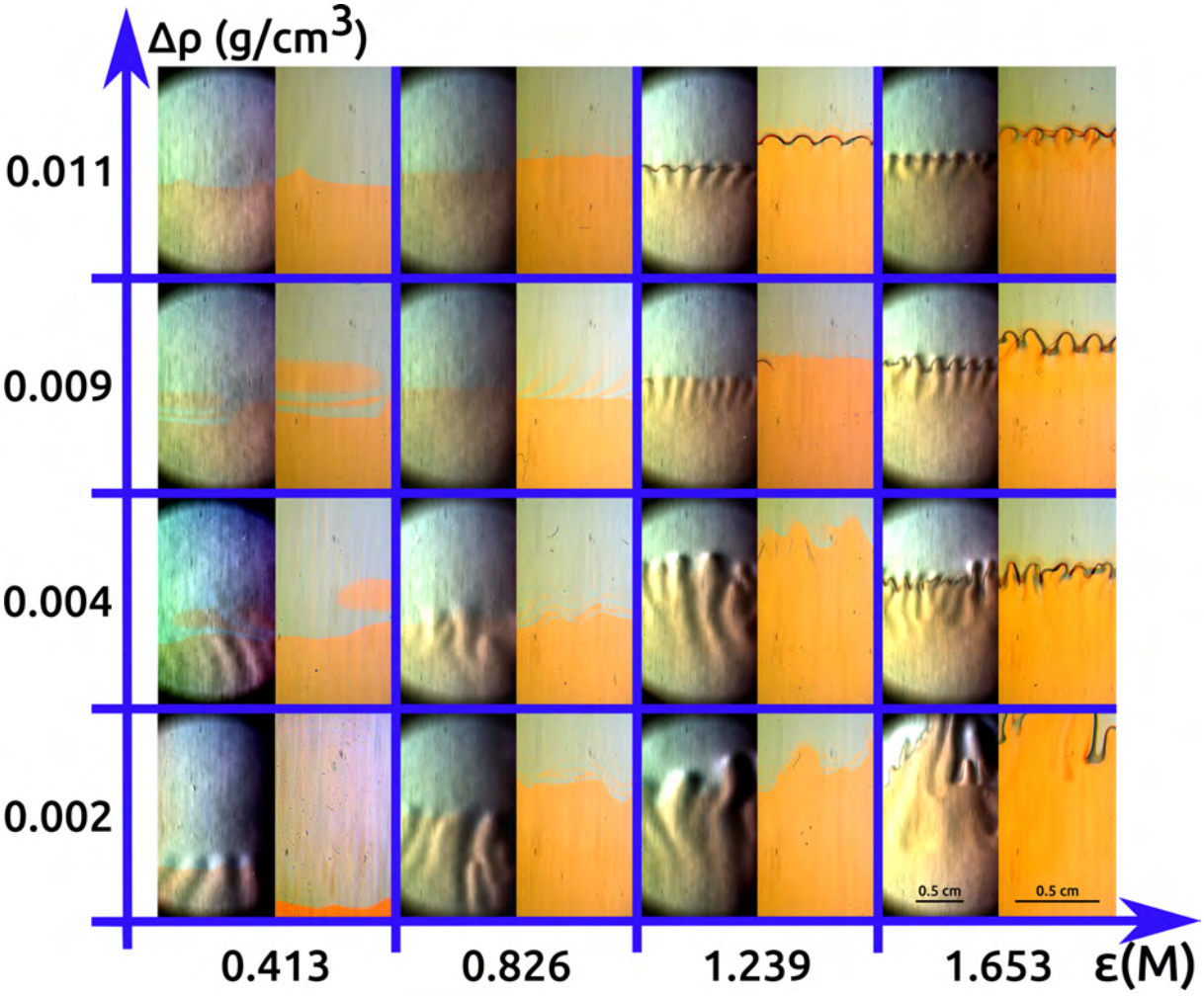

Figure 3.2: Qualitative comparison of all the experiments realized. All snapshots were taken around 1 h after the beginning of the experiment. Each pair (ε, $\Delta\rho$) shows two experimental observations of the same experiment at the same time. Both, the Schlieren view (left side) and the chemical view (right side) are plotted for each pair (ε, $\Delta\rho$). The system got stabilized by increasing $\Delta\rho$. This strongly affects the hydrodynamic by delaying the finger onset and stabilizing the initial interface. By increasing ε, the finger, chemical, and precipitate onset times were decreased, while the hydrodynamic and chemical wavelength also decreased. This Figure was taken from Escala *et al* [61].

3.2.1 Measuring Observables

In contrast to the descriptive analysis previously made, several macroscopic observables were calculated to obtain quantitative measurements of the system dynamics. In the present work, four main observables were chosen, two of them used for chemistry characterization and the other two for hydrodynamics characterization. Formally, the chemical oscillations period (T_C) and the chemical reaction induction time t_{ind-C} (this is, the time elapsed from the start of the experiment till the first waves are observed) were chosen to measure the effect of the chemistry in the whole process. On the other

hand, the finger wavelength, λ_H, and the hydrodynamic induction time t_{ind-H} (considered as the time elapsed from the beginning of the experiment till the fingers start developing) were the observables used to characterize the hydrodynamics. The observables were directly measured from the space-time plots (STP) obtained from the experimental observation and using the methodology indicated in Appendix Section C.1.

Figures 3.3-3.4 plots the variation of the macroscopic observables previously defined as a function of ε for each $\Delta\rho$ analyzed. All values are presented as the average value over all the realizations and error bars show the standard deviation in the measurements. The value of $\Delta\rho$ used for each case is indicated in the legend in order to facilitate graphic comprehension.

As can be observed in Figure 3.3(a), variations in the excitability produced a remarkable effect on the chemical induction time. More precisely, t_{ind-C} got sensibly reduced for high values of ε. The same effect occurred for every $\Delta\rho$ studied. The density gradient did not produce any significant change on this observable in any case. Furthermore, except for the lower excitabilities, the deviations in the measurements were relatively small indicating that this t_{ind-C} is a purely chemical characteristic that is independent of the hydrodynamic condition.

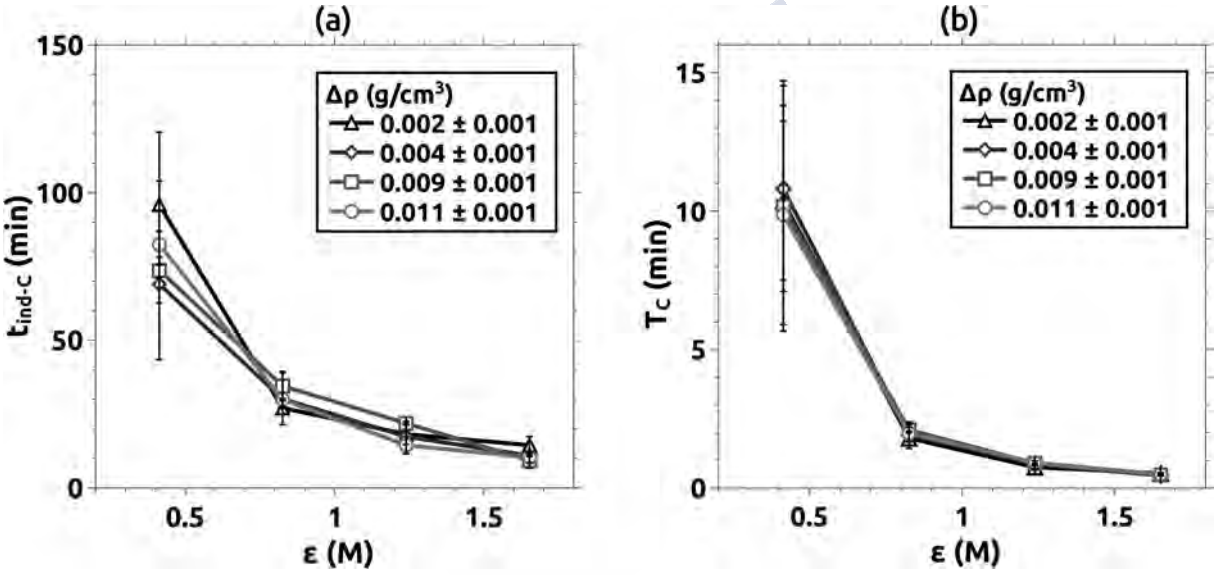

Figure 3.3: (a) Chemical induction time t_{ind-C} and (b) Chemical period T_C as a function of ε and $\Delta\rho$. Figure adapted from Escala *et al* [61].

On the other hand, the variation of T_C as a function of ε and $\Delta\rho$ is shown in Figure 3.3(b). In a similar manner to t_{ind-C}, the chemical period T_C was strongly affected by changes in ε but no effect was observed by changing $\Delta\rho$. In this case, the largest dispersion was observed for ε = 0.413 M (lower excitability case), where the average T_C value ranges between 9.86 min and 10.81 min. The dispersion dramatically reduces for $\varepsilon > 0.413$ M and the period decreases uniformly for each $\Delta\rho$. For ε = 1.653 M the minimum average T_C value ranges from 27 up to 31.8 s.

Regarding the hydrodynamics, Figure 3.4(a,b) shows the variation of t_{ind-H} and λ_H respectively. In the first case, the system response to variations in ε and $\Delta\rho$ was more complex compared to the previous observables. For $\Delta\rho$ = 0.002 g/cm^3 and 0.004 g/cm^3, the increments in ε did not show any statistically significant variation considering the dispersion of the measured values. However, the behavior of the system changed abruptly for $\Delta\rho$ = 0.009 g/cm^3 and 0.011 g/cm^3. For these two cases, the value corresponding to ε = 0.413 M was not included in the figure as no fingering instability was observed during the experimental time. For $\varepsilon > 0.413$ M, t_{ind-H} decreased by increasing the excitabilty in all cases but no significant variations were observed by changing the density gradient. These results were consistent with previous works [197, 9] and shown how the chemistry can affect hydrodynamics.

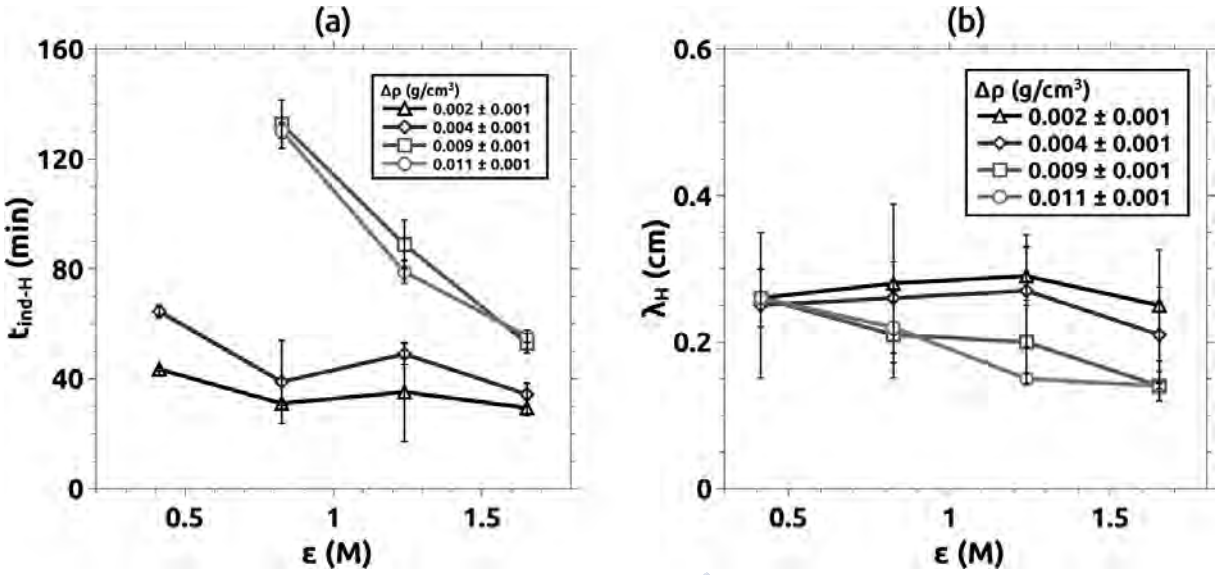

Figure 3.4: (a)Hydrodynamic induction time t_{ind-H} and (b) Hydrodynamic wavelength λ_H as a function of ε and $\Delta\rho$. Values of t_{ind-H} corresponding to ε = 0.413 M for $\Delta\rho$ = 0.009 and 0.011 g/cm^3 were not plotted as no fingering instability was observed during such experiments. Figure adapted from Escala *et al* [61].

Finally, as can be appreciated in Figure 3.4(b), no statistically significant variations of λ_H were observed for most ε values, except for larger densities, $\Delta\rho = 0.009\ g/cm^3$ and $0.011\ g/cm^3$, where finger wavelength decreased slightly inversely to the excitability, ranging between 0.14 cm up to 0.26 cm.

3.3 Coupled $\Delta\rho$ and ε Variation by Changing $[BrO_3^-]_0$

Until now, only the effects produced by independent changes in the excitability and the density gradient were studied showing the major role played by the chemistry in the system behavior. However, on the basis of Equation (2.1), the excitability can be modified not only by changing the acid concentration but also by changing the initial concentrations of bromate and CHD.

This section will be focused on the effect of the bromate in the dynamics of the system. However, as this species is in the upper layer, it is not possible to add a heavy salt to the solution (such as Na_2SO_4 in the previous case) for obtaining independent changes in density and excitability. Thus, both $\Delta\rho$ and ε will be affected simultaneously by changing $[BrO_3^-]_0$.

In this case, the hydrodynamic field was observed by using the shadowgraph technique instead of the Schlieren technique, which was described in Section 1.10[1]. More information regarding the experimental protocol, recipes, and general details can be consulted in Section 2.1.4.

By analyzing the dependence of the system with the excitability, different behaviors were found in concordance to the results presented in Section 3.2. The chemical and the hydrodynamic induction times were much larger for lower values of ε (Figure 3.5(a), compared with the middle and high excitability cases. Likewise to Figure 3.1, phenomena as chemical waves with a large wavelength and the displacement of the interface were observed as well. Convective fingers were observed about 200 min from the beginning of the experiment. Similar to the lower ε case of the results presented in Figure 3.2, the fingers did not move beyond the initial interface, and in the same way, they grew in the vertical direction and moved along the horizontal direction. For larger excitabilities (Figure 3.5(b,c)), the system response was also similar to their counterpart in Figure 3.2. The hydrodynamic instability was

[1]This technique was used due to resource constraints at the moment in which the experiments were conducted.

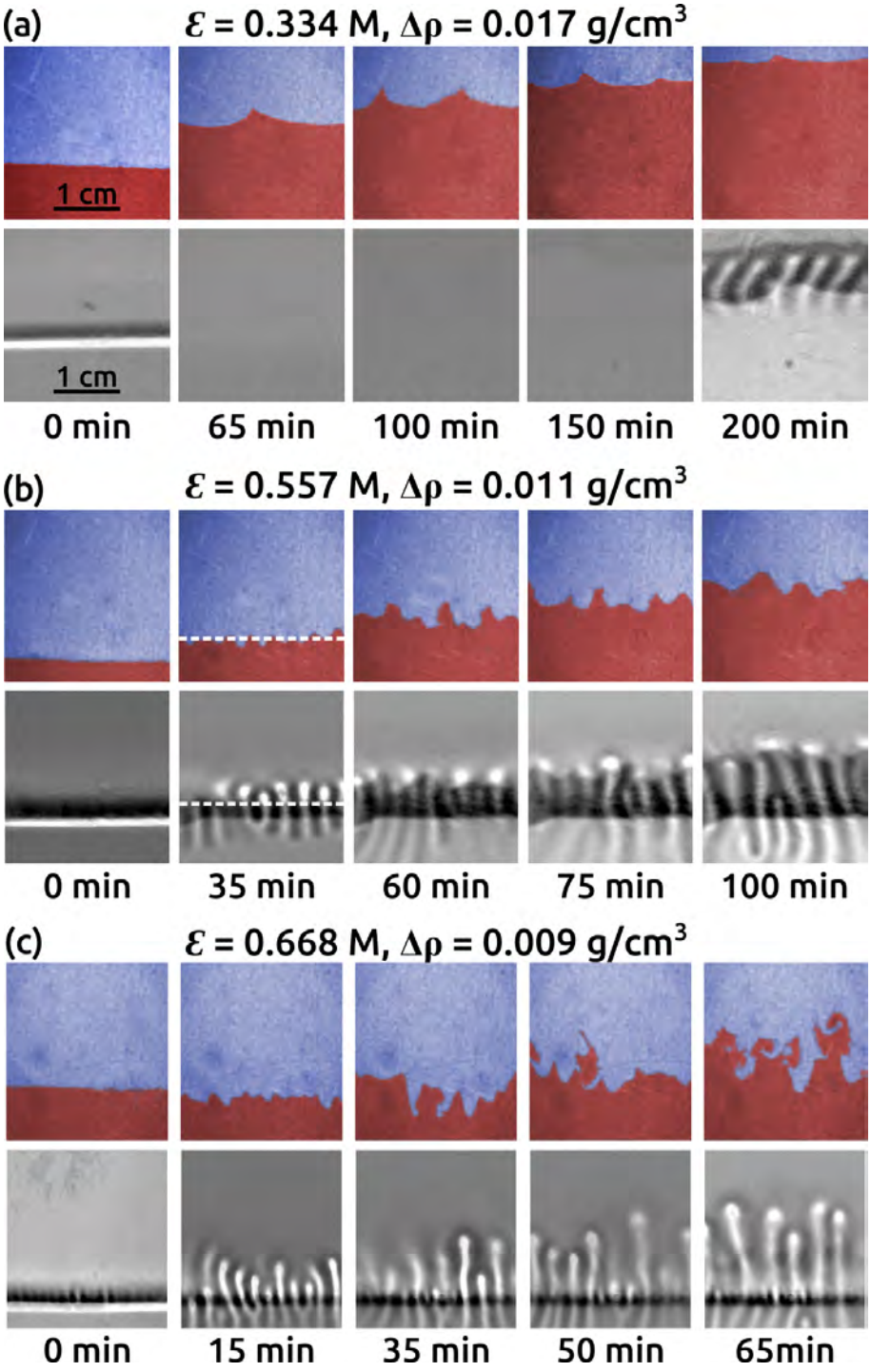

Figure 3.5: Description of system behavior for (a) low (ε = 0.334 M), (b) middle (ε = 0.557 M), and (c) high excitabilities (ε = 0.668 M). The chemical view is indicated in the upper rows and shadowgraph view at lower rows of each panel. The system evolution showed a comparable behavior with the case presented in the previous section for different increments in ε. The white dashed line indicated in (b) represents the horizontal cut used to build the space-time plots of Figures 3.8 and 3.6. All frames were taken at the experimental times indicated below each panel. The results are presented using a false-color palette to facilitate the observation. Figure adapted from Escala *et al* [57].

triggered as soon as chemical waves appeared and both chemical and hydrodynamic structures exhibited

analogous wavelength. In addition to the traveling waves, spirals were also observed interacting one each other (Figure 3.5(c)). Those spirals were originated from the fingertips showing the degree of interaction between both, the chemical and the hydrodynamic process.

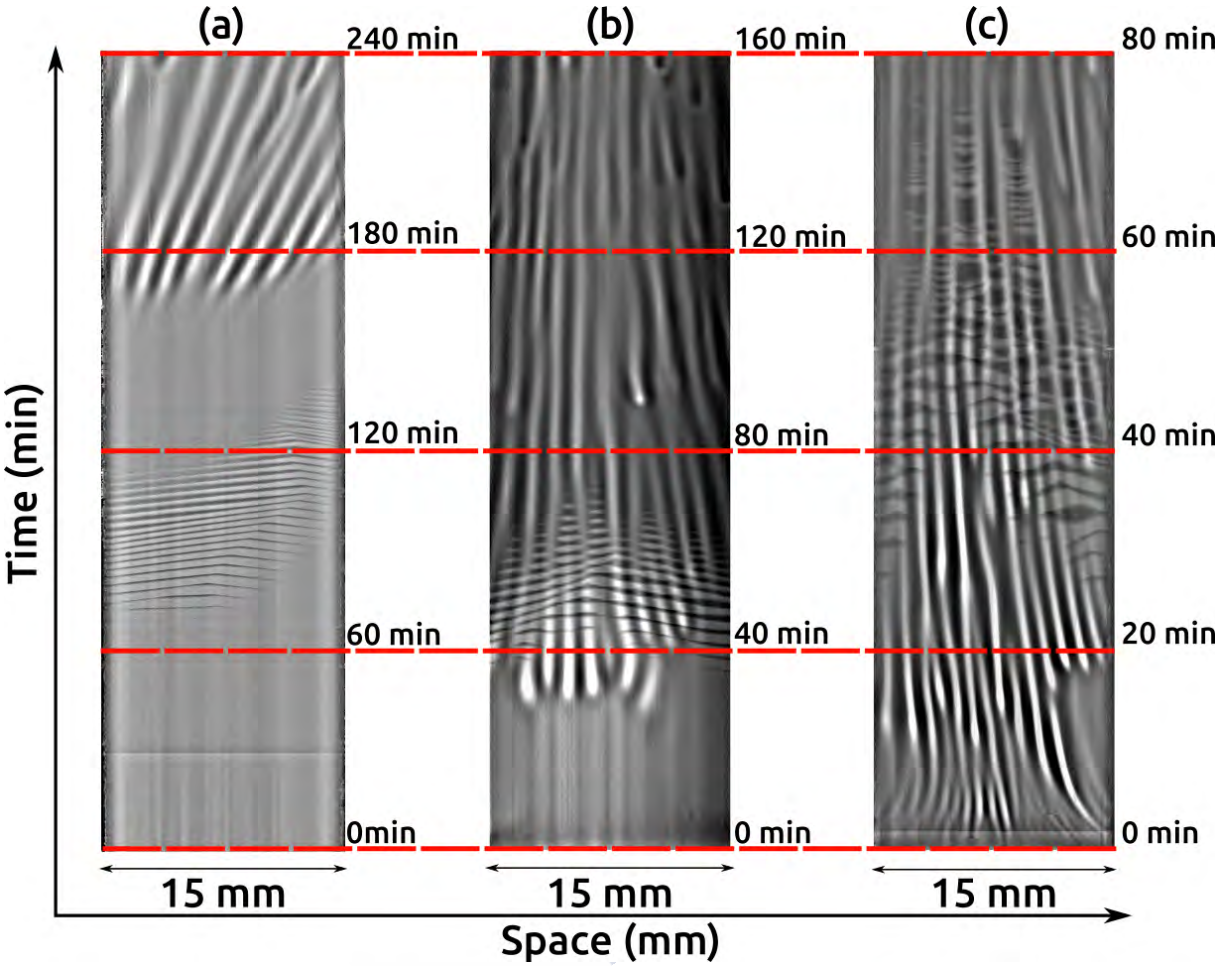

Figure 3.6: Space-time plots created by overlayering the chemical and the hydrodynamic patterns for the cases shown in Figure 3.5. (a) ε = 0.334 M, (b) ε = 0.557 M and (c) ε = 0.668 M. Horizontal and vertical bright stripes feature the chemical waves and the hydrodynamic fingers dynamics, respectively. As can be noted, as the chemical excitability is increased the convective dynamics of fingers become more complicated as a result of a complex chemical forcing. Figure adapted from Escala *et al* [57]

A supplementary analysis of these processes is also presented in Figure 3.6, where the transition from simple to complex chemo-hydrodynamic behaviors was characterized by comparing the space-time plots of the cases presented in Figure 3.5. Here the superimposition of the chemical and the shadowgraph views make it possible to appreciate the correlation between the chemical and hydrodynamic patterns previously seen in Figure 3.5. Figure 3.6(a) describes the case for ε = 0.334 M where a long-wavelength train of waves moved from left to right. For Figure 3.6(b) and (c), the excitability of the system was increased from ε = 0.557 M and 0.668 M respectively. For these cases, chemical waves showed complicated patterns with a competition between target and spiral waves coming from different directions which collided in the mixing zone. As a result, the hydrodynamic pattern, closely following the chemical dynamics, exhibited an intricate behavior that changes with time.

3.3.1 Measuring Observables

Analogously to Section 3.2.1, the system was also quantitatively characterized by experimental observables. In this case, the characteristic induction times (t_{ind-C} and t_{ind-H}) and the chemical and hydrodynamic wavelengths (λ_C and λ_H) respectively were used as quantitative descriptors of the system. In addition to the last ones, a control induction time obtained from experiments done in a Petri dish was calculated. This control observable, (indicated as λ_P), represents the characteristic reaction-diffusion wavelength of the waves obtained in a separate Petri dish by mixing homogeneously all reactants with the same chemical composition as in the reacting zone. This observable was included as another indirect tool to measure a chemical characteristic from those used in the previous sections. The values of all the observables were calculated by the methods presented in Appendix Section C.1. The results are presented in Figure 3.7.

From the direct comparison between the chemical and hydrodynamic wavelengths presented in Figure 3.7(a), it is possible to see that at low excitability, λ_C is 3 times larger than λ_H. This difference vanishes for larger excitabilities ($\varepsilon \geq 0.45$ M) where both observables converged to the homogeneous reaction-diffusion wavelength λ_P, which is around 1.5 mm. λ_H remained roughly constant and of the order of 1.5 mm independently of the excitability. For low values of ε, λ_C and λ_P differed due to the different initial conditions and the large dispersity of wavelengths compatible with these concentration values. As the excitability was increased this difference diminished and exhibited the minimum value accessible by the system.

Figure 3.7(b) shows the comparison between the chemical and hydrodynamic onset times. In this case it is possible to see that at low excitability the convective patterns appeared much later than the traveling waves, while developed on the same time scale ($t_{ind-H} \sim t_{ind-C}$) for larger values of $\varepsilon \geq 0.45$ M). For the largest excitability, the hydrodynamic instability occurred before the wave instability. This suggests that chemical species involved in the convective mechanism appear then on a time scale faster than the time needed for chemical waves to develop.

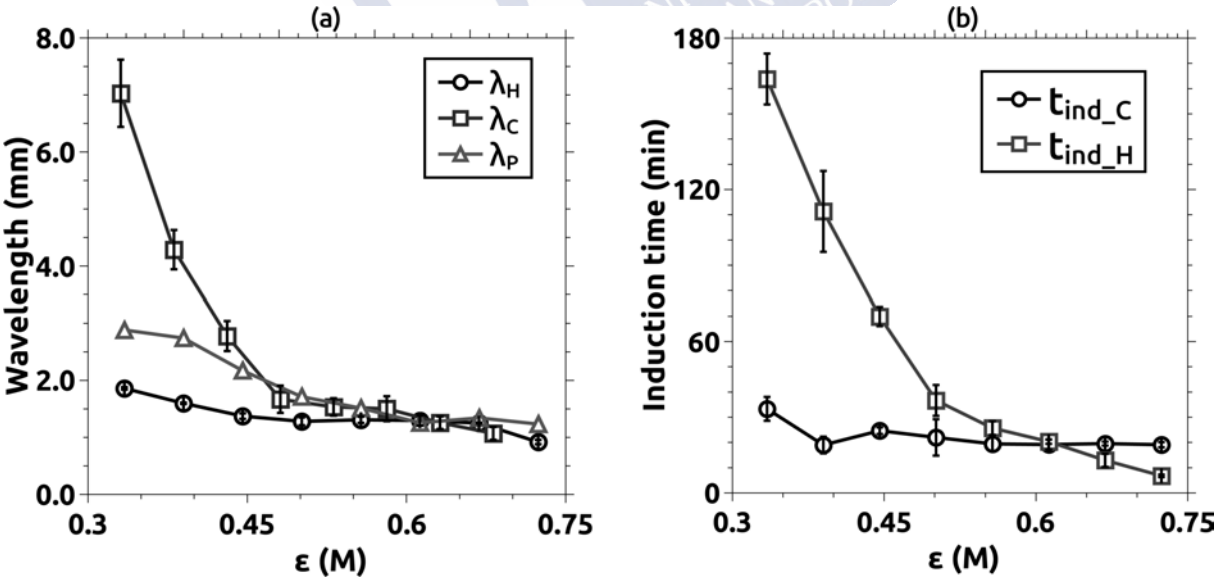

Figure 3.7: (a) Chemical (λ_C) and hydrodynamic (λ_H) wavelengths as a function of ε, as compared to the RD wavelength, λ_P; (b) Dependence of the onset time of the chemical and hydrodynamic patterns for different values of ε. Solid lines are just a guide for the eyes. Figure adapted from Escala *et al* [57].

3.4 Reaction-Diffusion-Convection Interplay

The results presented in previous sections showed how the excitability affected the onset times and the chemical observables. However, the instability was also capable to affect the chemistry once it was induced. Figure 3.8 shows the interplay between chemistry and hydrodynamic measured for the same experiment for ε = 0.389 M and $\Delta\rho$ = 0.014 g/cm^3. In this figure are compared the space-time plots related to the dynamics as well the quantitative characterization of the wave period as a function of time.

The space-time plot presented in Figure 3.8(b) presents the dynamics of the chemical waves obtained by measuring direct view shown in Figure 3.8(a). The second plot (Figure 3.8(c)) describes the evolution of the hydrodynamic fingers obtained by measuring the shadowgraph of Fig.3.8(a) (right frames).

In the beginning, only chemical waves traveling from the right to the left with a characteristic wavelength (4 mm) were present in the system. Once the convective cells were induced (around t = 120 min), they directly affected the chemical wavelength as the reactants were convected by the flows. At the time when the hydrodynamic instability and fingers were well developed, the chemical wave period was increased up to a 50% factor (Figure 3.8(d)) This demonstrated the mutual influence of chemical and transport phenomena. This result can be explained by considering the re-distribution of the concentration field due to convective motions. After a transient, both chemistry and hydrodynamics re-adjusted through this feedback into a new chemo-hydrodynamic pattern with a characteristic constant wavelength and velocity.

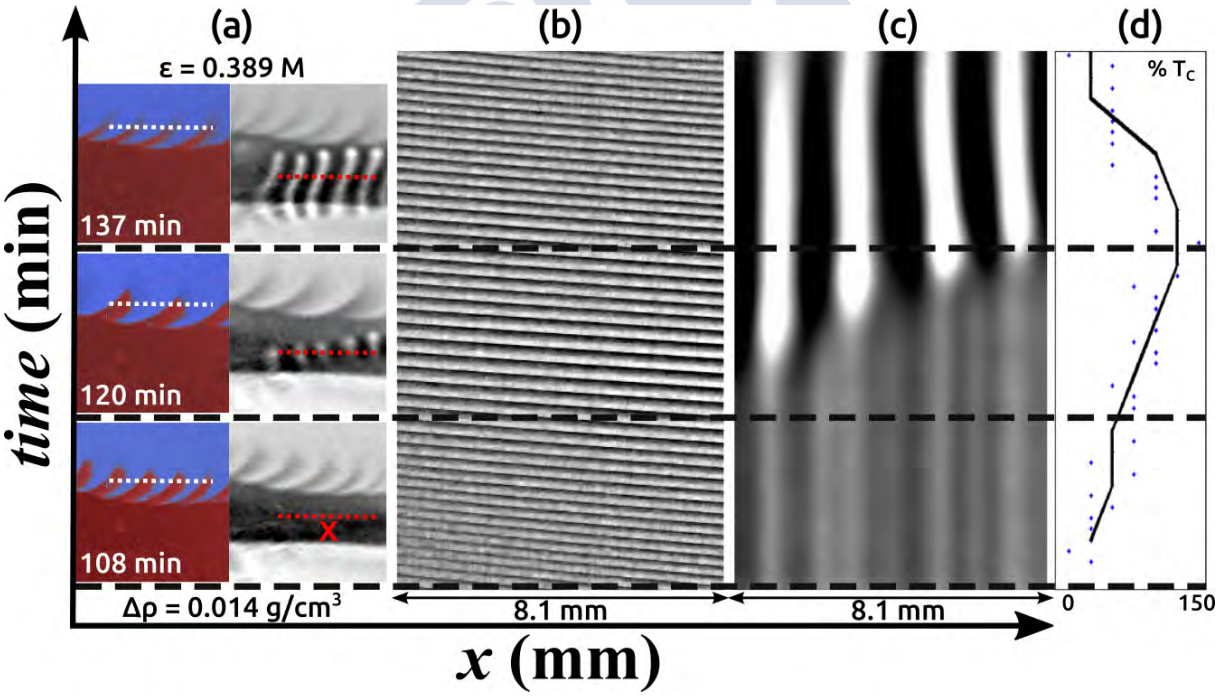

Figure 3.8: RDC interplay. (a) Dynamics at three successive times. The values for ε and $\Delta\rho$ are indicated above and below respectively of each pair of frames. (b) Space-time plot obtained from the chemical and (c) from the shadowgraph view. These plots were built by stacking as a function of time the horizontal cut (dashed line) shown in the experimental frames depicted in (a). (d) Characterization of the chemical wave period changes due to the RDC interplay. Experimental frames were colored to facilitate the observation. Figure adapted from Escala *et al* [57].

3.5 Effect of Varying $[CHD]_0$

One last method to change the system excitability is by modifying the CHD initial concentration ((2.1)). In this case, not only the excitability but also the density of Solution 1 is affected. However, as the CHD is located at the bottom layer solution in the Hele-Shaw cell, it was possible to add Na_2SO_4 to compensate for any change in density.

Figure 3.9 presents two experiments in which the CHD concentration was varied from the original 0.291 M (Fig. 3.9(a)) to 0.090 M (Fig. 3.9(b)). Both experiments were recorded with the *Schlieren* technique as they were done without ferroin. Only two cases were studied.

There were two main reasons to perform this experiment. In the first place, to prove the influence of the CHD on the hydrodynamic pattern. In a second place, to observe if fingering instability occurs when the catalyst was removed.

The results showed that fingering instability occurred in both situations. However, weaker fingers were observed for the lower concentration case. Also, the fingering onset time was incremented when the concentration of CHD was reduced. In contrast to the H_2SO_4 and $BrO_3{}^{-3}$ cases, in this case the increment in excitablity increased the finger induction time. The results also demonstrated that the catalyst had no influence in the instability formation. Besides, it was also suggested that the mechanistic of the instability was related to the core mechanism of the uncatalyzed BZ-CHD reaction. This issue will be addressed in the forthcoming chapter.

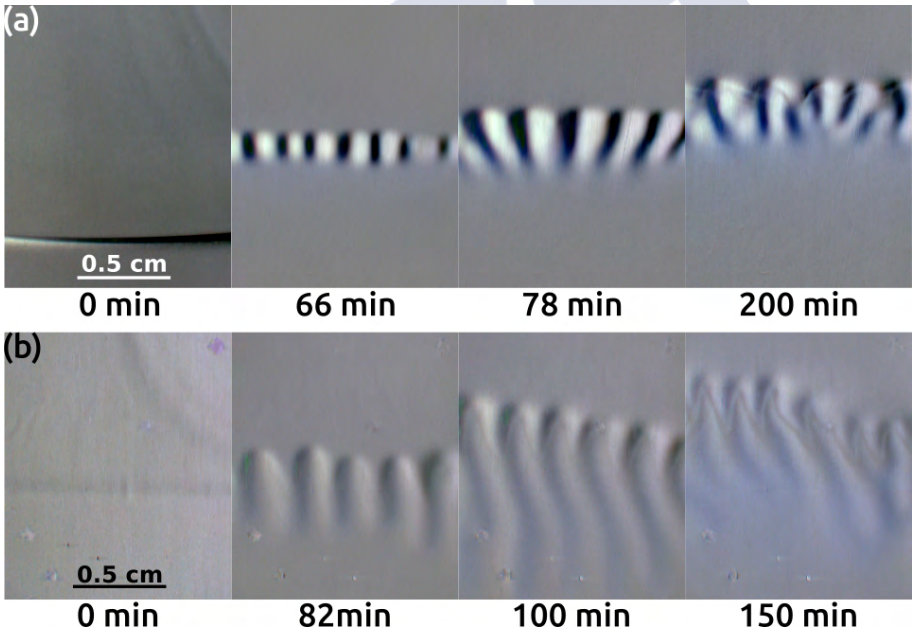

Figure 3.9: Fingering instability dependence on $[CHD]_0$. Schlieren observations of two uncatalyzed experiments where (a) $[CHD]_0 = 0.291$ M ($\varepsilon = 1.239$ M) and (b) $[CHD]_0 = 0.09$ M ($\varepsilon = 4.007$ M). In (a), both, the fingers and the initial interface were observed. In (b), it was observed a weaker fingering instability when the CHD concentration was reduced. For both cases, the remaining reagents were set as: $[BrO_3{}^-]_0 = 0.142$ M, $[H_2SO_4]_0 = 2.540$ M, and $[Na_2SO_4]_0 = 0.13$ M. Figure adapted from Escala *et al* [61].

3.6 Chapter Discussion

Many observations can be made from the analysis of the results exposed in this chapter. In the first place, for the case where ε and $\Delta\rho$ were varied independently, both the qualitative and the quantitative

analyses gave information about the system dynamics. The hydrodynamic behavior of the system was in concordance with previous results [197, 9], this is, the density ratio primarily affected the hydrodynamic characteristic times (t_{ind-H}).

From a comparison of all the observables presented in Figures 3.3-3.4, it was evident the key role played by the chemistry in the overall process. The effect of changing the excitability by modifying the acid concentration affected not only the chemical characteristic times and period (t_{ind-C} and T_C respectively), but also the hydrodynamic onset time t_{ind-H}. These results suggests that the fingering patterns are linked to the chemical mechanism of the BZ-CHD reaction.

The experiments where ε and $\Delta\rho$ were varied by changing $[BrO_3{}^-]_0$ also showed many similarities with previous results. However, some differences were observed in the characteristic times t_{ind-H} and t_{ind-C}. In the first case, the hydrodynamic onset time showed a typical decrement related to the decrease in the density jump. The effect of the excitability in this phenomenon was not completely clear as $\Delta\rho$ decreased by increasing $[BrO_3{}^-]_0$. On the other hand, the characteristic chemical time remained almost constant which is the opposite of what was observed when H_2SO_4 was changed. This results indicated that the effect that the excitability produced to the system dynamics depends on the which species was varied. It was also interesting to observe that the experiments performed in a Petri dish showed values comparable with λ_H. This fact, that has not a simple explanation, was one of the most significant results for that case.

Several results were obtained for the case where the excitability was modified by changing the CHD concentration. In the first place, the induction time was increased when $[CHD]_0$ was decreased. This also produced, in terms of visualization, a weaker fingering instability. In the second place, fingering instability was obtained even with the absence of catalyst in the medium. This result suggested that the system destabilization came from the core mechanism of the BZ-CHD reaction. It also suggested that neither the ferroin nor its derivatives species are involved the generation of the instability.

All these results showed how the chemistry affected the system behavior. However, the analysis made in Figure 3.8 exhibited how the hydrodynamic can also interact with the chemistry by locally affecting the species concentration in the vicinity of the fingertips. This feedback between hydrodynamic and chemistry was strong evidence of a synergic combination between two different processes coupled by reaction-diffusion-convection self-organization.

USC
UNIVERSIDADE
DE SANTIAGO
DE COMPOSTELA

Chapter 4

Detailed Chemical Analysis

Abstract: *Once studied the system dynamics, it is necessary to understand how the instability is produced. However, this is not a simple task due to a large number of parameters and variables involved. In this way, several techniques were used in many different experimental contexts. Each experiment was planned for understanding specifically every aspect of the reaction-diffusion-convection system. Thus, this chapter will present an in-deep chemical analysis. This study aims to discover how the intrinsic relationship between chemistry and hydrodynamics produces fingering instability.*

4.1 Hele-Shaw Cell Control Experiments

Control experiments were done to the convective system, by removing or inhibiting some chemical species in order to see their contribution to the instability. The following section will present two cases of study. On the one hand, the inhibition of the catalyst by the addition of NaCl to solutions 1 and 2. On the other hand, the effect of removing the CHD from solution 1. Both cases were performed in the same conditions as the experiments presented in Chapter 3.

4.1.1 Catalyst Inhibition by NaCl

The addition of sodium chloride (NaCl) to the BZ strongly affects the system dynamics by inhibiting the oscillations [100]. This can be extended also to the BZ-CHD reaction. The NaCl primarily interacts with the catalyst by inhibiting it. The inhibition increases as the concentration of NaCl is increased up to the limit to obtain a non-catalyzed reaction. The core mechanism of the BZ-CHD is not affected at all, but neither waves nor spirals can be observed, for example, in a Petri dish. In this particular case, the addition of NaCl was effective to investigate the transition between a catalyzed and a non-catalyzed experiment obtaining detailed information about the specific role of the catalyst in the system. Thus, several experiments were done by adding equivalent amounts of NaCl to each solution of the recipe shown in Table 2.4. The results are presented in Figure 4.1 where the hydrodynamic induction time (t_{ind-H}) was studied for several concentrations of salt ranging from 0.001 M up to 0.01 M. The figure shows the chemical view for a compared set of cases where NaCl = 0.004 M (Figure 4.1(a)) and NaCl = 0.005 M (Figure 4.1(b)). As can be seen, the system behavior was completely altered once the salt concentration was increased up to 0.005 M. All kind of chemical dynamics (like those observed Fig. 4.1(a)) were suppressed for higher concentrations showing only an interface displacement similar to the one described in Figure 3.1.

Not only the chemical dynamics were affected by increasing the salt concentration but also the hydrodynamic induction time. As can be seen in Figure 4.1(c), the addition of salt produced a delay

in the finger onset time. The figure compares the t_{ind-H} with two extreme values, both indicated with grey dashed lines in the plot. The line on the bottom side indicates the induction time for a catalyzed reference experiment. This value corresponds with the experiment where no salt was added. On the upper side is indicated the onset time of a non-catalyzed case. This value was obtained from an experiment without ferroin. As is possible to see, t_{ind-H} approached the non-catalyzed time for the highest NaCl concentration. The inverse situation was observed when the salt concentration was one order less. The total increment in the induction time was up to 620 %.

Aside from the delay in the induction time and the inhibition of the spatio-temporal patterns, no other significant effect was observed in the system dynamics.

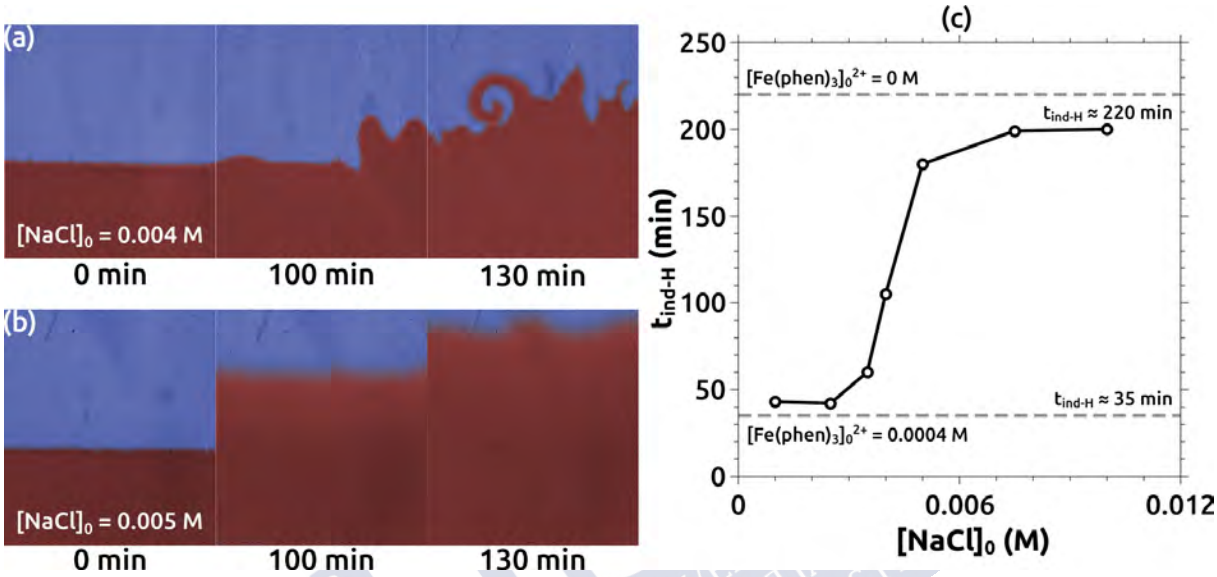

Figure 4.1: Effect of the addition of sodium chloride in the BZ-CHD reaction. (a) Frames taken from the chemical view for NaCl = 0.0040 M and (b) NaCl = 0.005 M. (c) Hydrodynamic induction time (t_{ind-H}) variation due to the addition of NaCl studied for $[NaCl]_0$ = 0.001 M, 0.002 M, 0.003 M, 0.004 M 0.005 M, 0.007 M and 0.01 M respectively. The remaining reagents were kept constant as indicated in Table 2.4. For this particular case, $[BrO_3^-]_0$ = 0.095 M which corresponds to ε = 0.557 M. The experimental frames were colored to facilitate the visualization.

4.1.2 Experiments Without CHD

The previous results indicated that fingering instability occurs with the uncatalyzed reaction. On the other hand, the presence of the organic substrate is fundamental for obtaining chemical oscillations [113]. Therefore, it is necessary to study the role played by CHD in the instability. Thus, a control experiment where the CHD was removed from the system is presented in Figure 4.2. For this case, the base recipe that was used is presented in Table 2.4. The removal of CHD was compensated with the addition of Na_2SO_4 in Solution 1 to obtain a comparable density jump.

Figures 4.2(a,b) show the chemical and shadowgraph views respectively. As can be seen, both cases show a diffusive front in which the ferroin was oxidized into ferriin. Neither chemical nor fingering patterns were observed during the whole experiment. This result demonstrated that CHD is a key species in the instability mechanism. Also, it was useful to discard the hypothesis that the instability may be generated by the change in the oxidation state of the catalyst [26].

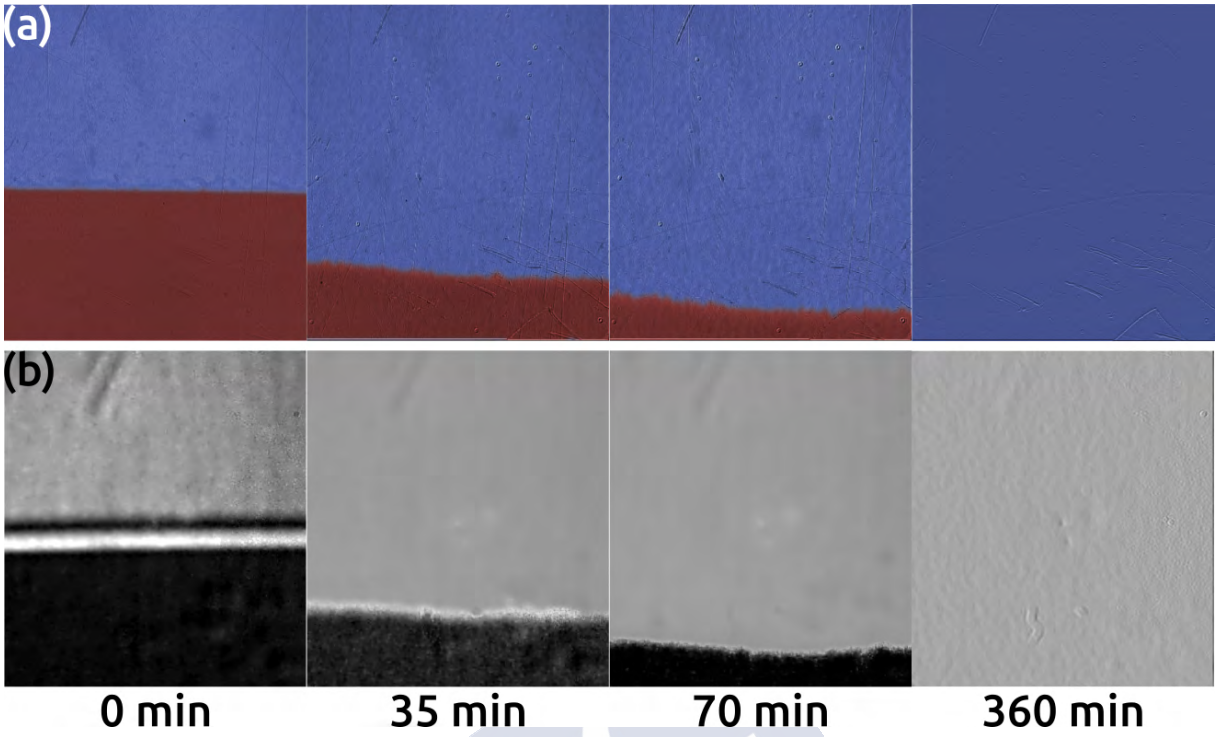

Figure 4.2: (a) Chemical view row and (b) shadowgraph view row of an experiment where $[BrO_3{}^-]_0$ = 0.095 M (which corresponds to ε = 0.557 M and $\Delta\rho$ = 0.002 g/cm^3) where CHD was removed from the recipe. Note that neither the instability nor pattern-formation is observed. The experimental frames were colored to facilitate the observation.

4.2 UV-Vis Spectroscopy

The system was studied in a fully stirred batch reactor by using UV-Vis spectroscopy techniques as indicated in the corresponding Section 2.1.5. The recipe used for this case is indicated in Table 2.6. The chemical behavior was characterized similarly as the convective system, where the temporal dynamic and the chemical observables were calculated. The dynamics of the system is presented in Figure 4.3(a) for three different cases: ε = 0.207, 0.826, and 1.653 M. These values were representatives of three different excitability conditions, as low, middle, and high excitabilities respectively. For the lower case, no oscillations were observed but only a single shift from the oxidized (Fe^{+3}) to the reduced (Fe^{+2}) state of the catalyst. For the middle and the high excitable cases, oscillations were observed for a considerable range of time. Those oscillations are shown in Figure 4.3(b) where a deep view of the oscillatory region corresponding to the high excitability case is presented in the inset (c) of the figure. In addition, a signal saturation region was observed (Figure 4.3(a)). This saturation occurred in experiments with medium and high excitabilities whereas the absorbance signal diminished after the shift in the oxidation state for ε = 0.207 M.

From the temporal dynamics is possible to observe the effect of the excitability on the overall system behavior. By increasing the excitability, the induction time was reduced. This was particularly noticeable for the low excitability case where the induction time was much larger compared with the other two cases. Regarding the oscillations, the increment in the excitability reduced the total amplitude of the oscillations, showing a progressive increment in the amplitude in time, whereas for the middle excitability case, the amplitude remained constant for all the oscillatory region. Also, one last oscillation was observed for the middle and high excitability cases.

All these chemical characteristics were also quantitatively analyzed by measuring the chemical

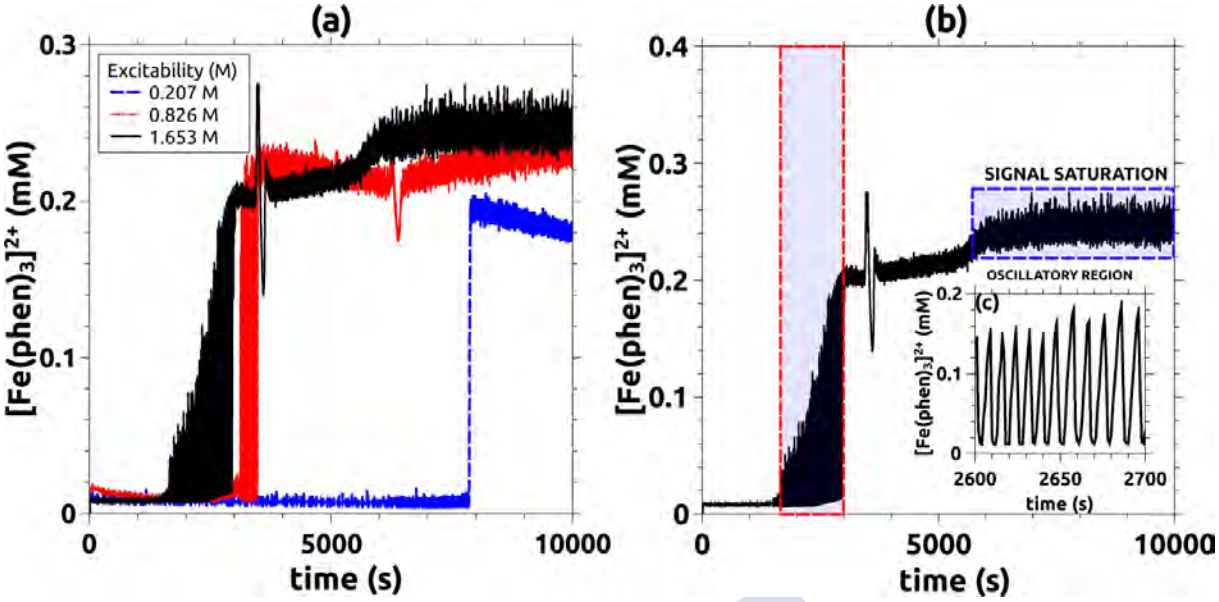

Figure 4.3: (a) Dynamic characterization of the batch system for ε = 0.207, 0.826, and 1.653 M by using UV-Vis spectroscopy. All spectra were obtained at a fixed wavelength of 510 nm. The absorbance values were converted into the molar concentration considering an absorptive molar coefficient ξ_{max} = 11000 $L/(mol.cm)$ [68]. Only three cases are shown to facilitate the analysis. (b) spectrum corresponding to the high excitability case where the oscillations region is shown in the figure inset (c) for a range of time of 100 s. The saturation region is indicated in the blue dashed square. This Figure was adapted from Escala *et al* [61]

period (T_C) and induction time (t_{ind-C}). All the information is presented in Figure 4.4 and was obtained by direct measurement of the spectroscopy spectra done for all the cases indicated in Table 2.6. The induction time characterization is shown in Figure 4.4(a). As can be seen, the induction time got significantly reduced conforming the excitability was increased. It is interesting to appreciate that not only the trend of t_{ind-C} is similar to the convective case (Figure 3.3(a), but also the induction time values were approximately of the same order. This also confirmed the major relevance of the chemistry in the RDC case.

The chemical period was also characterized and it is presented in Figure 4.4(b). For this case, the period of the oscillations was in the order of seconds rather than minutes as observed in the RDC case (Fig. 3.3(b)). However, the trend in the period was comparable with the convective case showing a significant decrement due to the excitability increment. Oscillations were observed from $\varepsilon \geqslant 0.619$ M.

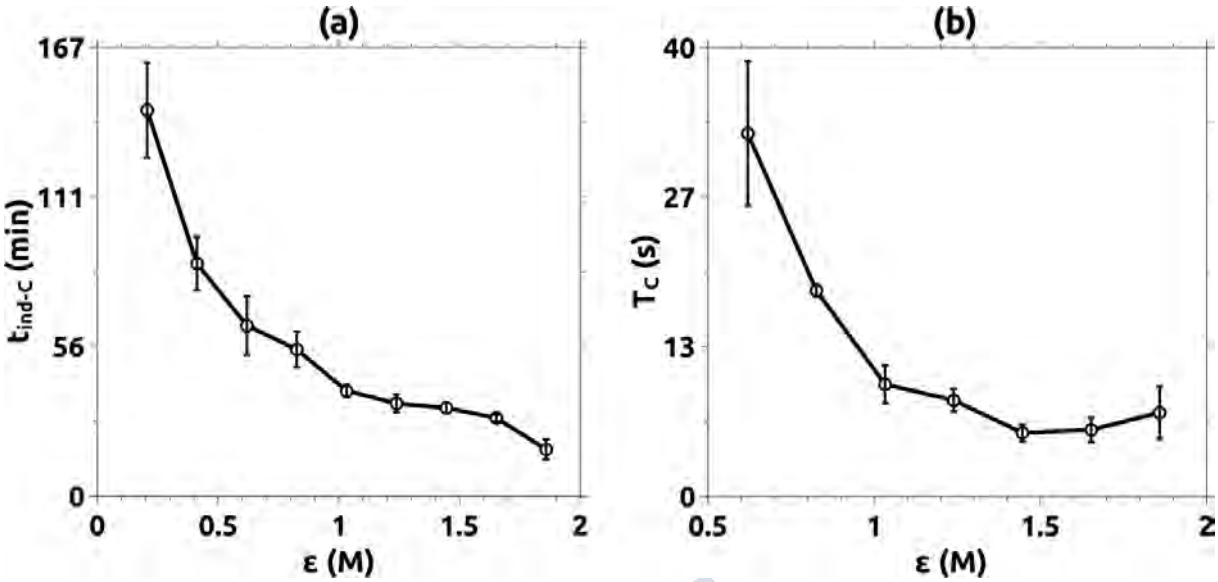

Figure 4.4: Chemical observables characterization obtained for a broad range of excitabilities as indicated in Table 2.7. (a) Chemical induction time (t_{ind-C}) and (b) chemical period (T_C), for the batch system. For (b) cases ε = 0.206 and 0.413 M were not included in the plot as no oscillations were observed.

4.3 Precipitate Formation

The chemical analysis done confirmed the main role played by chemistry in the convective dynamic. The chemical observables of the fully stirred system qualitatively conserved the main characteristics of the spatially extended system. The control experiments demonstrated the strong influence of the CHD in the instability development and the effect of removing the catalyst. Finally, similar dynamics were observed when changing the excitability by varying $[H_2SO_4]_0$ and $[BrO_3{}^-]_0$. All these results suggested the possibility that the instability was produced by a species derived from the organic substrate (CHD).

From the UV-vis spectra, it was observed a signal saturation for medium and larger excitabilities (Fig. 4.3). On the other hand, the reddish precipitate observed in fingering instability also occurred for medium and larger excitabilities (Fig. 3.2). Therefore, these results suggested that the species generated in the saturation region would be related to the instability mechanism.

Several experiments were conducted to understand how the signal saturation was produced. Figure 4.5(a) shows a set of frames of the BZ-CHD reaction done in a stirred assay tube which is directly comparable with a spectroscopic experiment. The initial concentrations used for this case were the same as used in the experiment presented in Figure 4.3(b) (ε = 1.653 M), which corresponds to a high excitability case. The exact moment when two oscillations occurred is indicated between 849.6-852.4 s and 1216-1227 s. Initially, the ferroin was in an oxidized state (ferriin) becoming in a reduced state from 1600 s. From that time, no more oscillations were observed. In an instant between 2520 and 2880 s, the solution suddenly changed its coloration becoming blackish and turbid. This corresponds with the signal saturation observed in the UV-Vis spectrum (Fig. 4.3(b)). It is also interesting to observe how the coloration of the solution changed in time, starting from a deep blue coloration (ferriin), acquiring then a greenish tone, then red to finally get colored into black. This suggested the idea that some secondary species or products also affected the typical coloration of the redox indicator.

A similar situation was observed in the uncatalyzed reaction which is presented in Figure 4.5(b). For this case, the solution was initially colorless. As time progresses, the solution acquired a yellowish coloration. This coloration became stronger, turning into orange around 2880 *s*. Like the catalyzed experiment, the solution became turbid in a time-lapse between 2880 and 3600 *s*. The

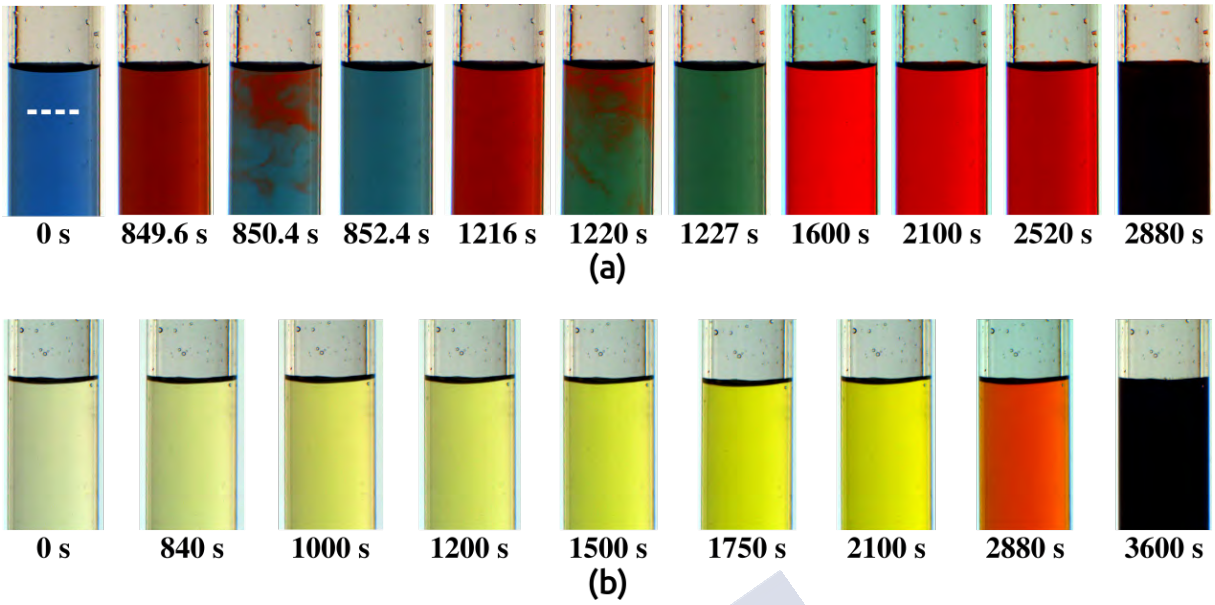

Figure 4.5: Fully stirred experiments for (a) catalyzed BZ-CHD reaction and (b) uncatalyzed BZ-CHD reaction both for ε = 1.653 M. The remaining reagents were kept as indicated in Table 2.6. Figure adapted from Escala *et al* [61]

yellowish coloration in the uncatalyzed experiment explained why the catalyzed case acquired a greenish coloration. This effect was produced by the mixture between the blue coloration of the oxidized state of the ferroin and the yellow coloration of the observed in the uncatalyzed experiment.

The turbid coloration observed in both cases was due to the emergence of a heavy precipitate suddenly originated at the end of each experiment. In particular, the precipitate onset showed some delay in the uncatalyzed experiment compared to the catalyzed one. This also led to the suspect that the rate of production of the precipitate is catalyzed by the ferroin. This precipitate was also observed in the convective experiments as was exposed in Section 3.1.

Additionally, all these facts were also confirmed by measuring the color intensity variation as a function of time. These values were taken from both experimental recordings by studying the temporal profile of a sample region indicated with the withe dashed line in Figure 4.5(a). The results, presented in Figure 4.6, show the similarities between the results obtained from a completely independent method and those obtained from spectroscopy. The oscillations in the catalyzed experiment (Fig. 4.6(a,c)) and the precipitate dynamics of the uncatalyzed experiment (Fig. 4.6(b)), were observed with this method. These results demonstrated, in qualitative terms, that the signal saturation was produced by the precipitate formation.

Regarding the convective system, as previously shown in Figures 3.1, 3.2, and 3.9, the precipitate was also observed at the end of the experiments. In Figure 4.7, a detailed observation of an uncatalyzed experiment shows the precipitate formation (Fig. 4.7(b)) for a middle excitability case (ε = 1.239 M). In Figure 4.7(a) the fingering pattern was observed due to the change in coloration produced by the localized generation of the precipitate. In Figure 4.7(c), it was also possible to appreciate how the precipitate moved downwards through the Hele-Shaw cell. Figure 4.7(d) shows an enlarged image of the precipitate particles sinking.

Finally, as explained in the Introduction (Section 1.8.3), some buoyancy-driven chemo-hydrodynamic instabilities may be produced by the emergence of heavy product at the interface between both liquids. It is due to this observation that the species involved in the precipitate formation may be responsible for the development of the instability. It is then important to fully characterize not only its structure but the possible mechanism of generation of this compound.

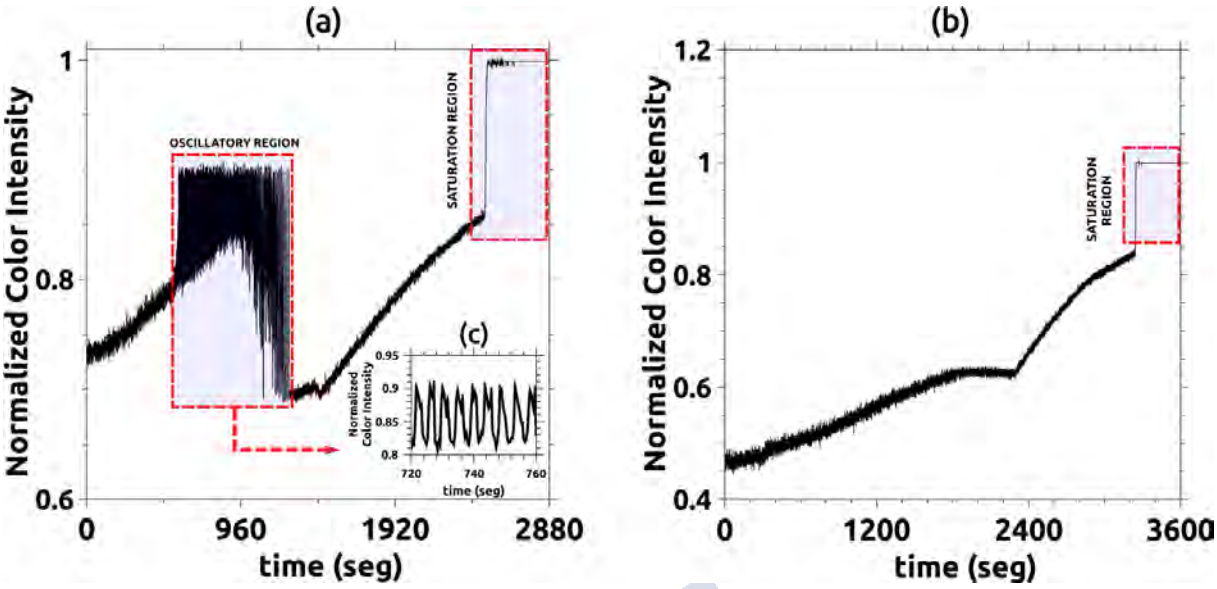

Figure 4.6: Dynamics of the (a) catalyzed and (b) uncatalyzed BZ-CHD reactions obtained by direct measurement of the results presented in Fig. 4.5. The plots were constructed by analyzing the changes in the color intensity of the aforementioned experiments. (a) Dynamics of the catalyzed BZ-CHD reaction. (b) Dynamics of the uncatalyzed BZ-CHD reaction. (c) Zoom of the oscillatory region showed in (a). In both cases, this method reproduced the saturation region observed through spectroscopic techniques.

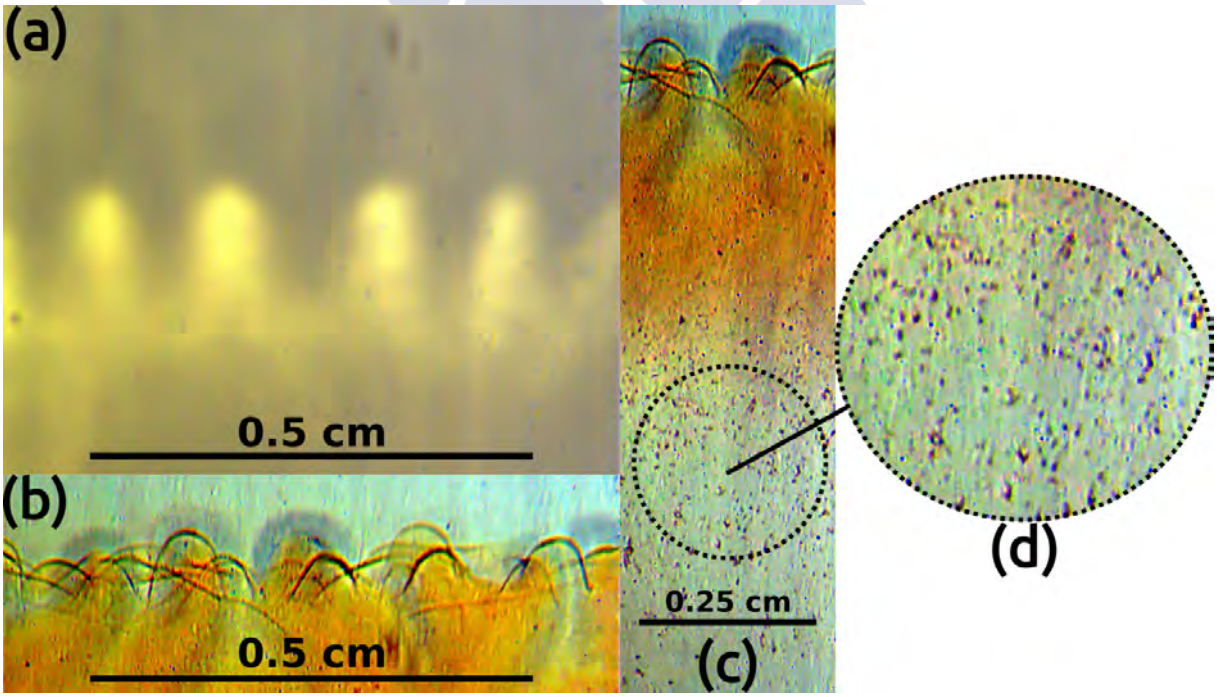

Figure 4.7: Frames of an uncatalyzed experiment with middle acid concentration. (a) An enhanced image of the fingering formation obtained by direct observation. (b, c) Precipitate formation after the finger onset. (d) Zoomed image of the precipitate moving downward the Hele-Shaw cell. ($[CHD]_0$ = 0.291 M, $[BrO_3^-]_0$ = 0.142 M, and $[H_2SO_4]_0$ = 2.540 M). This Figure was taken from Escala *et al* [61]

4.4 Nuclear Magnetic Resonance (NMR) Spectroscopy

The next step done to characterize the nature of the precipitate was to analyze the compound by a more sophisticated spectroscopic tool. The nuclear magnetic resonance (NMR) was then used to elucidate the chemical structure of the precipitate [24]. The first task was to extract the precipitate from the reaction beaker. This has been done by filtering and drying the BZ-CHD solution as explained in Section 2.1.6. An image of the extracted precipitate is shown in Figure 4.8.

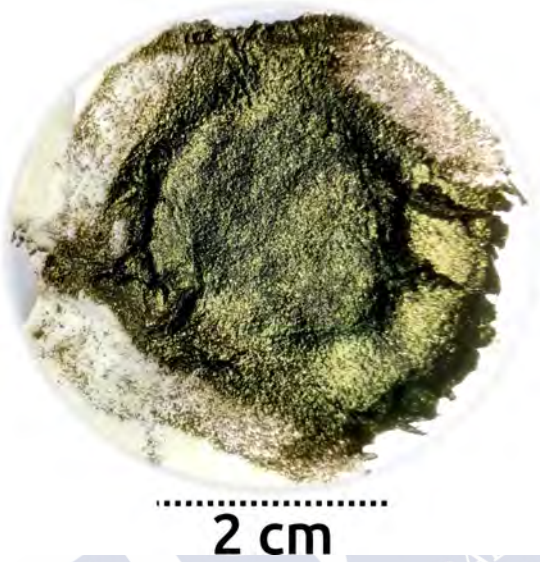

Figure 4.8: Precipitate extracted from the homogeneously stirred BZ-CHD reaction. The precipitate was obtained by filtering and drying as explained in Section 2.1.6.

For this analysis both, Hydrogen-1 (^{1}H) and Carbon-13 (^{13}C) NMR were performed by using two different solvents: deuterated dimethyl sulfoxide (DMSO-d_6) and deuterated methanol (MetOH-d_4). The respective results are presented in Figures 4.9-4.10. For the DMSO-d_6, Figure 4.9 shows the ^{13}C (Figure 4.9(a)) and ^{1}H (Figure 4.9(b)) spectra. The measured chemical shifts of each peak were marked on top of each one and the values can be compared with the theoretical values obtained with the software Mestre-C for the molecules sketched on the left of each plot. Four peaks were obtained associated with two different types of interactions (C-C and C-O) in each molecule (Figure 4.9(a)). The peaks related to 1,4-hydroquinone (H_2Q) were located at 150.14 ppm and 116.10 ppm showing a good agreement with the expected values at 151.42 ppm and 117.45 ppm. The two other peaks at 188.12 ppm and 136.98 ppm correspond with the expected values for the 1,4-benzoquinone (Q) (theoretical values are 187.00 ppm and 135.58 ppm). On the other hand, in the ^{1}H spectrum shown in Figure 4.9(b) two peaks were observed for each C-H bond in each molecule, and a collection of smaller peaks between 8.42 ppm and 8.33 ppm associated with the O-H bond. Again, the measured values for the chemical shifts (6.83 ppm for Q and 6.53 ppm for H_2Q) were in good agreement with the expected ones (6.90 ppm and 6.66 ppm respectively).

Results were similar for the experiments done with MetOH-d_4. The results are presented in Figure 4.10(a) for^{13}C and 4.10(b) for ^{1}H. In the ^{13}C case, the theoretical shifts predicted for Q were 135.58 ppm for and 187.01 ppm, where the experimental ones obtained were 136.21 and 187.32 ppm respectively. For H_2Q, the theoretical shifts were 151.74 and 117.50 ppm where the experimental ones obtained were 115.39 and 149.81 ppm. For the ^{1}H case, the theoretical displacement for the H-C interaction in Q was 6.91 ppm compared to 6.77 ppm for the experimental shift. For H_2Q, the chemical shifts for the H-C and H-O interactions were 6.65 and 8.23 ppm for the theoretical and 6.61 and 8.29 ppm for the experimental

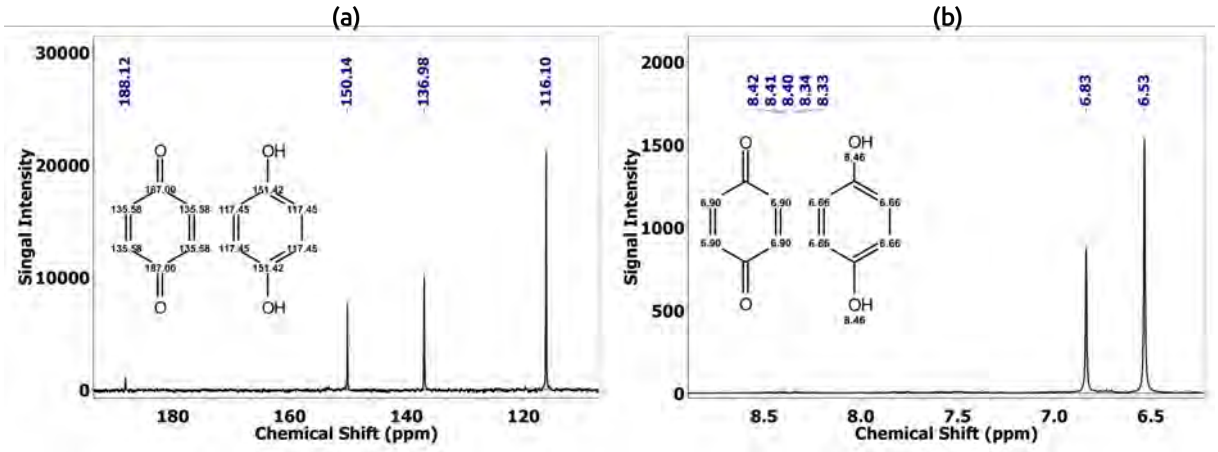

Figure 4.9: NMR spectra with DMSO-d_6 as solvent for (a) ^{13}C and (b) ^{1}H. In both figures, the experimental shifts are compared with the theoretical predictions indicated over the schematic molecules. As can be seen, the experimental chemical shifts agreed with the theoretical ones.

cases, respectively. In both cases, the overall agreement between the experimental measurements and the theoretical estimations was very good with a maximum error of less than 0.1 ppm.

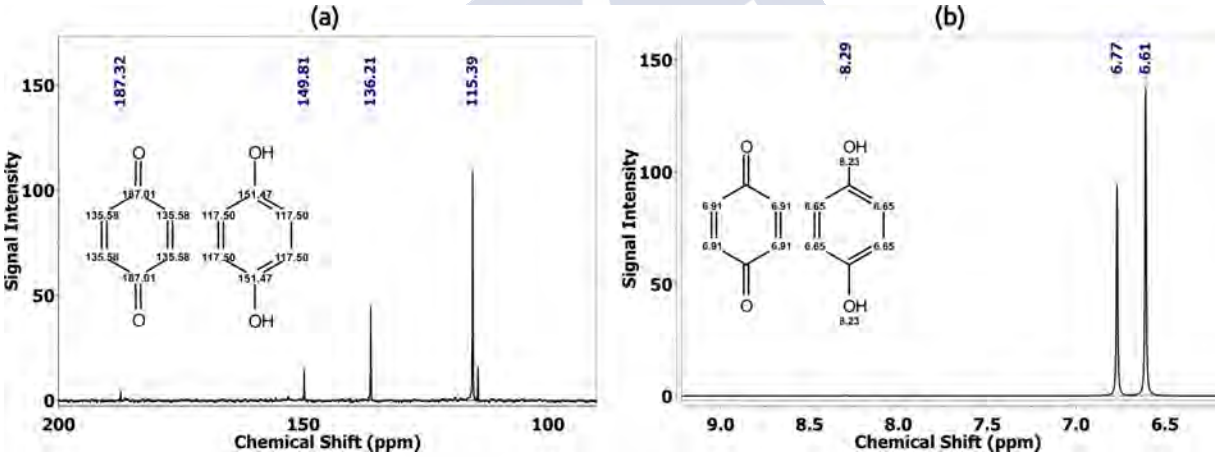

Figure 4.10: NMR spectra results for MetOH-d_4 solvent for (a) ^{13}C and (b) ^{1}H. Similar to the results presented in Figure 4.9, the theoretical and experimental shifts agreed significantly.

All these results strongly suggested that the precipitate was composed of Q and H_2Q. Nevertheless, both species are key chemical intermediaries of the BZ-CHD reaction that play a major role in the dynamics of reaction as detailed in Szalai *et al* [189]. However, when Q and H_2Q reach certain levels of concentration, a non-soluble chemical complex, known as quinhydrone (or Benzoquinhydrone - $Q \cdot H_2Q$) can be formed by the electronic attraction between the aromatic rings of Q and H_2Q [37]. A representation of the molecular structure of the complex quinhydrone is presented in Figure 4.11.

As was detailed in Section 1.8.3, many instabilities such as those induced by reactions of type A + B $\rightarrow$ C, occur due to the differential density between product C and reactants A and B. However, in this case the reaction is not elementary and several reactants and products are involved. The precipitate quinhydrone can be considered a denser product capable to induce the fingering instability with a similar mechanism to those simpler cases. Nevertheless, due to the complexity of the reaction, the system has now many different control points that can add richness to the phenomenon.

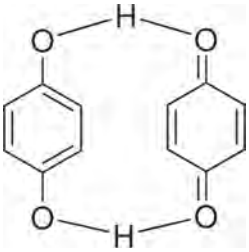

Figure 4.11: Chemical structure representation of the complex quinhydrone.

4.5 Chapter Discussion

In the present chapter, many control experiments were presented in order to elucidate the mechanism of the fingering instability produced by the BZ-CHD reaction.

The detailed chemical analysis was useful to isolate every possible control point of the system establishing the main species involved in the observed phenomena.

The addition of sodium chloride inhibited the action of the catalyst leading the system into a uncatalyzed state. This experiments showed that fingering instability occurred even without the catalyst. This suggested that the core mechanism of the BZ-CHD reaction was responsible to induce the instability.

The experiments done without CHD showed a single chemical front produced by the oxidation of the ferroin into ferriin. In such experiments, no fingering was observed. This suggested that the CHD (or its derivatives) is a key species in the development of the instability. This result also confirmed the experiments done by adding NaCl. As the ferroin/ferriin switch was no capable to induce the instability, this completely demonstrated that such species was not involved in the fingering phenomenon.

The results obtained from the UV-Vis spectra demonstrated the qualitative equivalence between the chemical observables obtained from the convective experiments with those obtained from the batch system. In both cases, the increment of the excitability decreased the chemical induction times and period, demonstrating the role played by chemistry in the convective system. The extensive chemical analysis allowed to correlate the precipitate observed in the Hele-Shaw cell with the one observed in a batch reactor.

The NMR spectroscopy was used as a the definitive tool to unveil the chemical structure of the precipitate, the quinhydrone ($Q \cdot H_2Q$) complex. This species was generated by the complexation of two components already present in the BZ-CHD reaction mixture, Q and H_2Q. Both are key reaction intermediaries obtained from the oxidation of the CHD by the BrO_3^- and the catalyst as shown in previous work done by Szalai *et al* [189]. The yellow coloration observed in the uncatalyzed convective system was also indicative of the presence of 1,4-benzoquinone (Q) in the medium, which resulted in an additional confirmation of the proposed mechanism.

All the information obtained was crucial to develop a suitable model capable to reproduce the behavior and dynamics observed in the convective system. This topic will be addressed in the following chapter.

Chapter 5

Numerical Results

Abstract: *The previous chapter showed that the precipitate observed in both, the convective and batch systems was quinhydrone. This compound is generated by the complexation of Q and H_2Q. The results suggested that the instability may be produced by this species through a classical $A + B \rightarrow C$ like mechanism. To prove this hypothesis, non-linear numerical simulations were done to obtain comparable results. In this context, the present chapter will study the equivalence between the homogeneous system and the available kinetics models. Once known the optimum set of parameters that better represent the experimental results, the BZ-CHD kinetic models introduced by Szalai et al [188, 187, 189, 190] will be adapted to a spatially extended configuration to simulate the reaction-diffusion and reaction-diffusion-convection systems. All these numerical models will be used as the definitive tool to demonstrate the mechanism of the instability. The main quantitative results presented in the experimental section were recalculated from the simulations and compared with the experimental values to show the agreement between them.*

5.1 Equivalence between Experiments and Reaction Models

5.1.1 Qualitative Comparison

The results obtained by spectroscopy were directly compared with the extended kinetic model shown in Table 2.8. However, due to the differences between the model and experiments, it was convenient to express the numerical excitability as the initial acid concentrations. It was found that the numerical excitabilities that better fit the experimental values ε = 0.207, 0.826, and 1.653 M were $[H^+]_0$ = 3 M for the lower, $[H^+]_0$ = 10 M, for the middle, and $[H^+]_0$ = 15 M for the higher cases respectively. These values were estimated by fitting the experimental values with the simulations using the GNU software COPASI.

Figure 5.1 presents a comparison between the numerical and experimental temporal dynamics for three different excitabilities. As can be observed, the model induction time and the amplitude of the oscillatory region decreased inversely to the excitability similarly to the experiments. The absence of oscillations in the low excitability case (ε = 0.207 M) was also observed in the numerical simulations. Also, the last long-period oscillation observed in the experimental cases before the beginning of the saturation region was also reproduced by the model.

The oscillatory dynamics of the system was also well reproduced by the model. Figure 5.2 compares the simulations results (Figure 5.1(a)) with the experiments (Fig. 5.2(b)), for a high excitability case $[H^+]_0$ = 15 M and ε = 1.653 M respectively. In both cases, the oscillatory region is marked inside

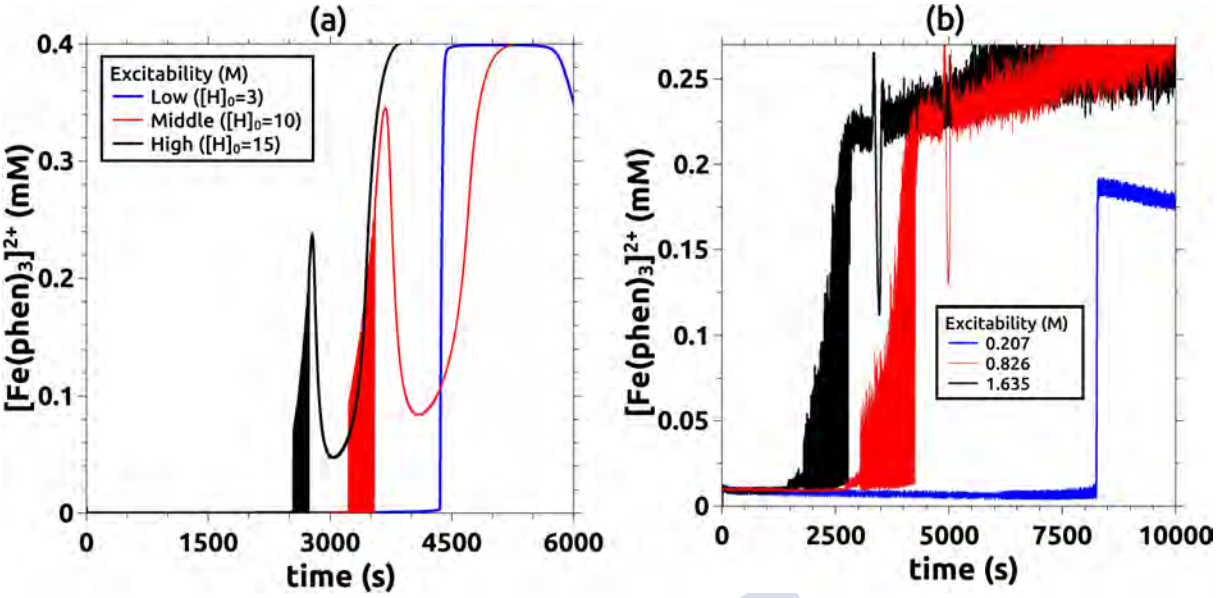

Figure 5.1: Effects of changing the excitability on (a) numerical simulations and (b) experiments. In both cases, three different excitability values were considered (marked in the figures with different colors). All initial concentrations, with exception of $[H^+]_0$ in the numerical model, were kept as in their experimental counterpart: $[CHD]_0 = 0.155$ M, $[BrO_3^-]_0 = 0.071$ M $[Fe(phen)_3^{2+}]_0 = 0.4x10^{-3}$ M. Figure adapted from Escala *et al* [61].

the dashed line region. A closer view of the oscillations is observed in insets Figure 5.2(c) and Figure 5.2(d). As can be appreciated, regardless of some differences, the model reproduced well the oscillatory behavior and the induction time position. The amplitude of the oscillations, as shown in Figures 5.2(c,d), were of the same order in the same region of time. The final state of the redox indicator was reproduced as well. The only exception was the saturation region, which was not reproduced due to the absence of the quinhydrone kinetics.

5.1.2 Quantitative Comparison

The extensive kinetic model introduced by Szalai *et al* [189] can reproduce most aspects of the experimental counterpart in a batch reactor. In addition to this qualitative analysis, quantitative measurements of the chemical observables likewise those presented in Figure 4.4 were done to study the similarities between the experiments and the simulations. These results were also useful for finding the proper region of parameters where the model can be validated.

Variation of ε by changing $[H^+]_0$

Figure 5.3 shows the characterization of both chemical observables, the induction time (t_{ind-C}), and the oscillation period (T_C) derived from the kinetic model. The simulations were carried out as explained in Section 2.2.2. In Figure 5.3(a), the induction time decreases in concordance with the increment in the acid concentration. However, the numerical values showed a nearly linear tendency different from the experimental case, where a damped behavior was observed, especially for higher excitabilities (Fig. 4.4(a)). The numerical times were very close to the experimental ones, except for the less excitable experimental case that showed a higher induction time (above 100 min). These differences can be associated with the intrinsic simplifications made on the model.

Regarding the chemical period, T_c, the numerical trends are similar to those experimentally observed (Fig. 4.4(b)). The chemical period decreases with the increment in excitability. The values of the period

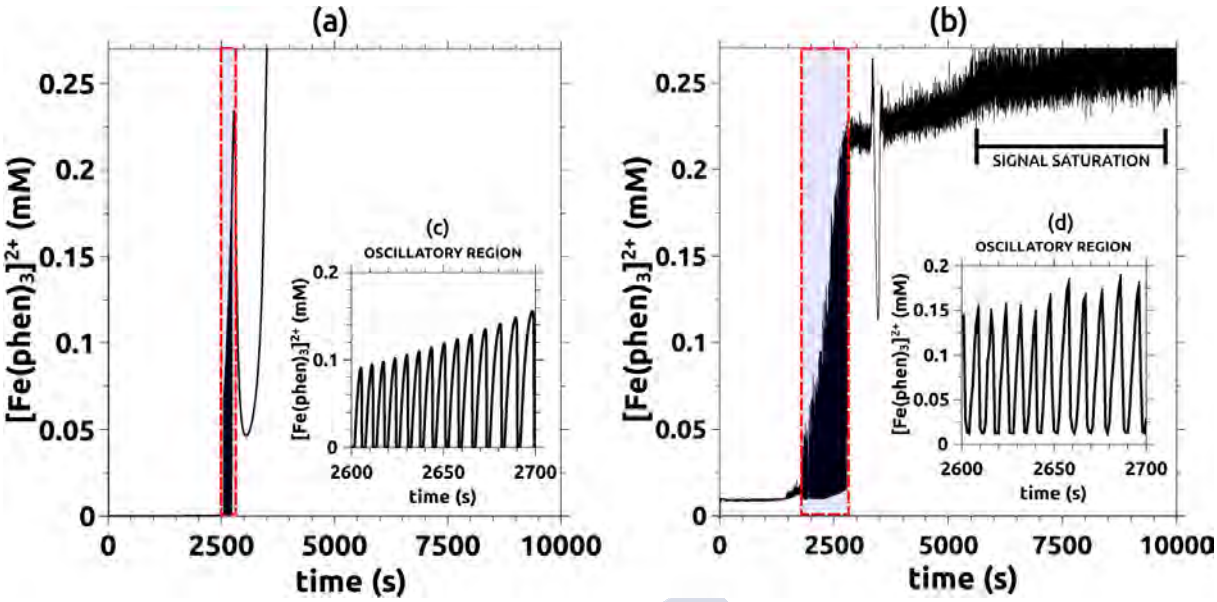

Figure 5.2: Qualitative comparison between (a) the full numerical model proposed by Szalai *et al* [189] for $[H^+]_0$ = 15 M, and (b) experimental results obtained using UV-Vis spectroscopy for ε = 1.653 M. Both figures correspond with a high excitability situation. The oscillatory regions are indicated inside the insets c and d in both figures. The remaining initial conditions were set as described in the experimental section: $[CHD]_0$ = 0.145 M, $[BrO_3^-]_0$ = 0.071 M and $[Fe(phen)_3^{2+}]_0 = 0.4x10^{-3}$ M. Figure adapted from Escala *et al* [61].

are in the same order of seconds as the experimental case, showing a better agreement compared with t_{ind-C}. Note that for the experimental case, the oscillations were observed starting from ε = 0.619 M while in the model, oscillations were observed from $[H^+]_0$ = 4.5 M, which was the second case analyzed. For such a reason, the numerical curve shows one more point than the experimental case. Despite that, and considering the dispersion of the experimental measurements, the model reproduction of the system dynamics can be considered very accurate.

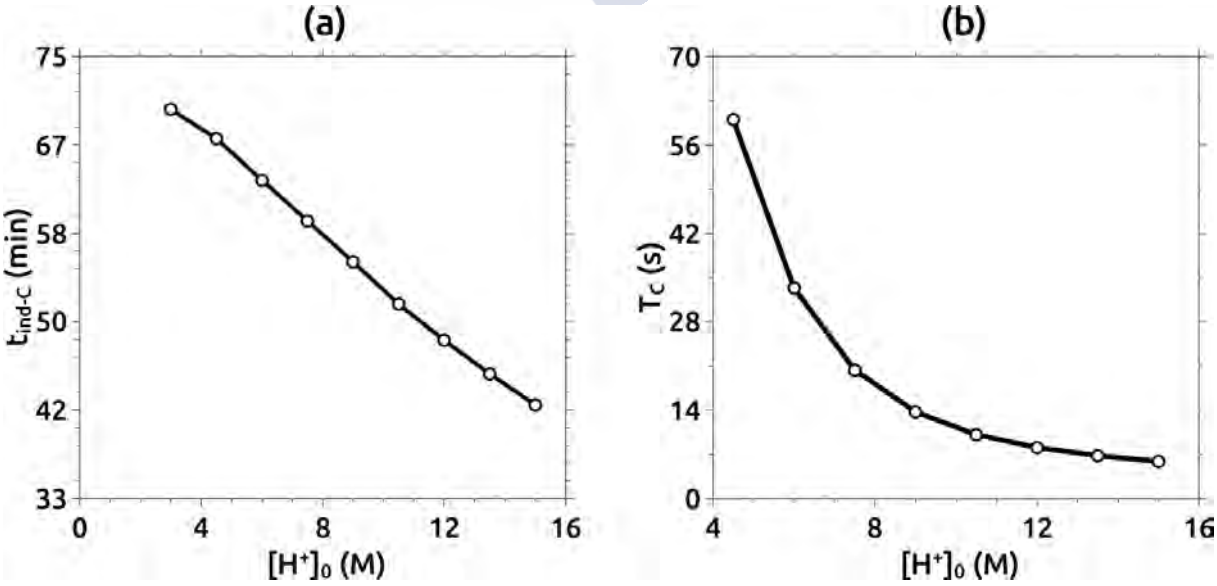

Figure 5.3: Quantitative measurement of the chemical observables (a) t_{ind-C} and (b) T_C obtained from the extended numerical model. Simulations were performed for a $[H^+]_0$ range between 3 and 15 M. The remaining reagents were kept equal to the values used for the UV-Vis experiments.

Even though there are some expected differences between the simulations and the experiments, there are many characteristics that are still preserved and make the model suitable to understand the effect of the chemistry in the instability mechanism. The induction time, the oscillations amplitude, and the location of the oscillations in time are well reproduced by the model.

5.1.3 Precipitate Formation Prediction

As was demonstrated in the previous chapter, the quinhydrone complex emerges when both, Q and H_2Q, are present in a specific concentration in the reactive medium [37]. Is therefore important that the model could reproduce such a situation. Figure 5.4 compares the numerical concentrations of both species with an experimental UV-vis spectrum for a high excitability case. Numerically, the temporal dynamics of Q and H_2Q (Fig. 5.4(a)) exhibited a substantial increasing in the interval of time where the saturation was experimentally observed (Fig. 5.4(b)). As can be seen, the model concentration of 1,4-benzoquinone and 1,4-hydroquinone increased substantially coinciding approximately with the experimental region where the precipitate is formed. Even though the quinhydrone generation is not included in the model, at least the presence of Q and H_2Q coincided in time with the saturation region observed in the UV-Vis spectrum presented in Figure 5.4(b). These results demonstrated the efficacy of the model to describe with an unexceptional agreement the dynamics of the BZ-CHD in the experimental context.

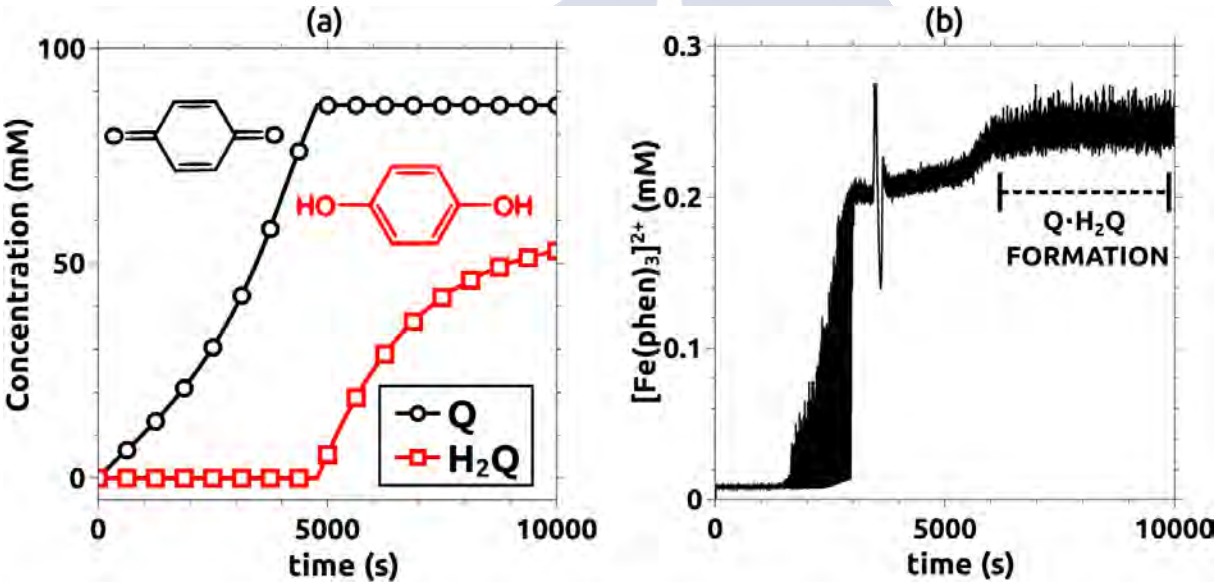

Figure 5.4: (a) Temporal concentrations of Q and H_2Q obtained from the simulations and (b) UV-Vis spectrum for ε = 1.653 M. The remaining species were set as the experimental condition: $[CHD]_0$ = 0.145 M, $[BrO_3^-]_0$ = 0.071 M, and $[Fe(phen)_3^{2+}]_0 = 0.4x10^{-3}$ M.

5.1.4 Equivalence between Full and Skeleton Models in Batch System

As mentioned in Section 2.2, due to the large number of variables involved the full model may be prohibitive for use in more complex spatially extended simulations. Szalai *et al* also developed a Skeleton model [189], which has less variables and equations but conserves the main characteristics of the full model [189]. However, in order to use this model as a representative tool in this experimental context, it was necessary to analyze the limitations and similarities with the full model. The reduced model is described in Section 2.9.

Figure 5.5 presents a comparison between the skeleton (Fig. 5.5(a)) and the full model (Fig. 5.5(b)). As can be seen, both models exhibited oscillatory regions (Figs. 5.5(c,d)). Besides, both models showed an increment in time in the oscillations amplitude. In this case, the reduced model showed larger values.

A more significant difference was observed in the oscillations induction time. As can be seen, the full model showed a large induction time, while the oscillations in the skeleton model strated almost immediately. However, a small induction time was observed in the skeleton model when the excitability was decreased (Figure 5.6(a)). This difference, which is insignificant compared to the induction time predicted by the full model, can be still useful to qualitatively predict the changes in the induction time. This figure also show that the oscillation wavelength decreased as the excitability was increased.

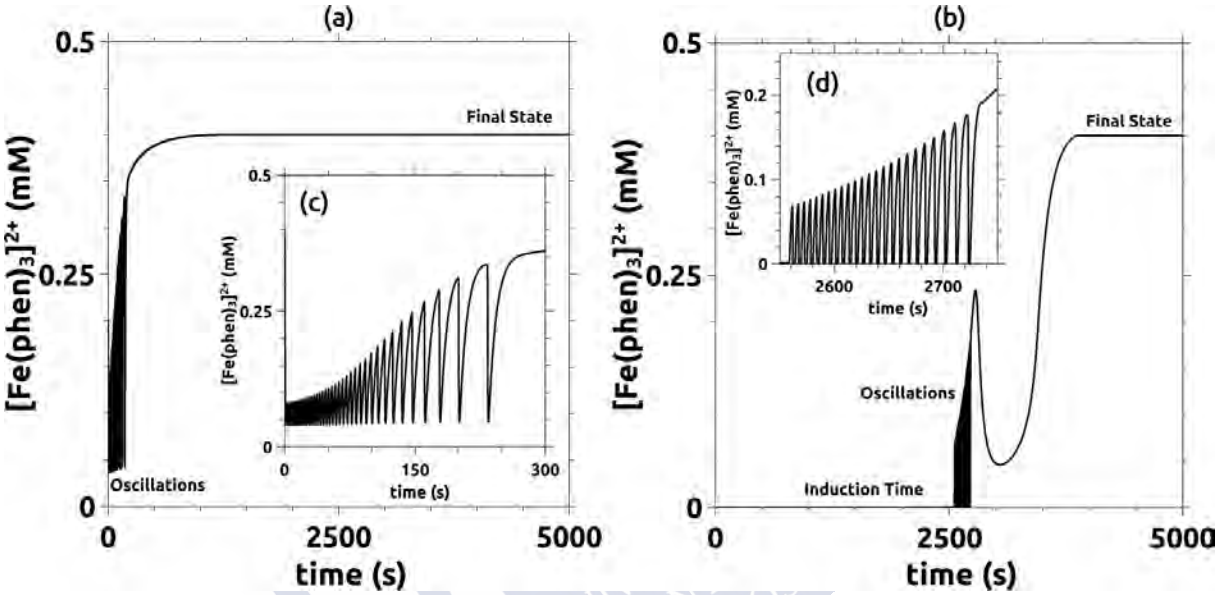

Figure 5.5: Full model for the BZ-CHD reaction compared with the skeleton model for the same parameters: $[H^+]_0$ = 15 M (all remaining parameters were kept equal as described in the Section 2.2.2). (a) Ferroin concentration dynamics obtained from the full model. Inset (c) corresponds to a zoom of the oscillatory region. (b) shows the concentration dynamics obtained from the skeleton model. Inset (d) corresponds to a zoom of the oscillatory region. This Figure was taken from Escala *et al* [61].

The skeleton model was also capable to reproduce the temporal profiles of Q and H_2Q as can be observed in Figure 5.6(b). Even though the maximum values of the concentration were lower compared to the full model (Fig. 5.4), the overall behavior was conserved.

All these results suggested that the skeleton model agreed, at least qualitatively, with the full model in this experimental context.

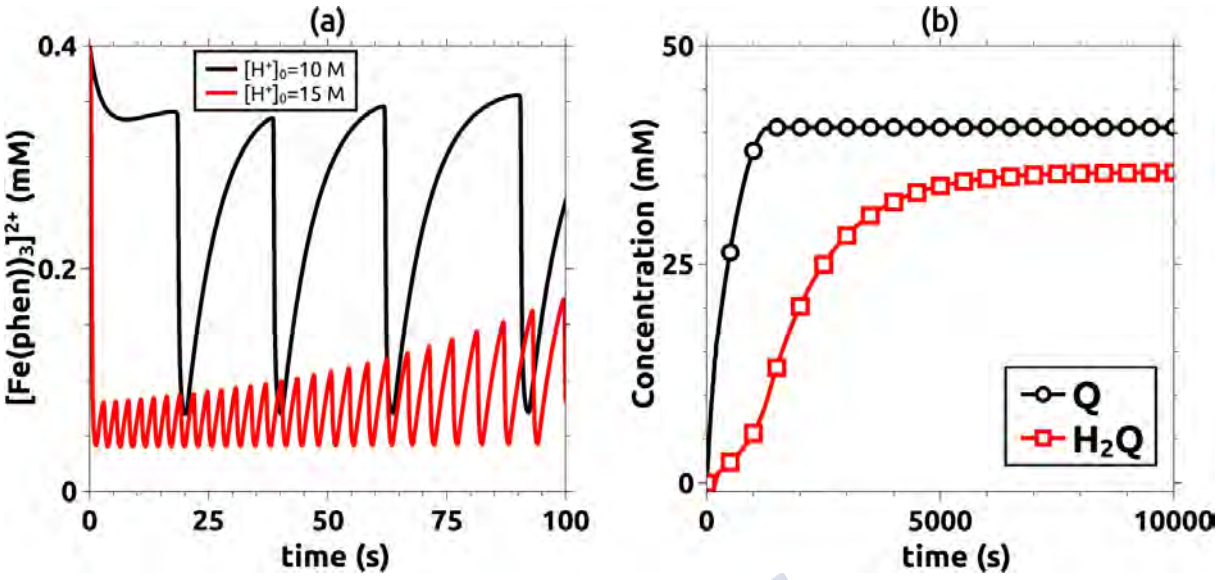

Figure 5.6: (a) Skeleton model comparison for two different excitabilities ($[H^+]_0$ = 10 M, black curve and $[H^+]_0$ = 15 M, red curve). A small induction time (around 20 s) was observed for the lower excitability case, while the oscillation started almost immediately in the higher case. Also, the increment in the excitability produced a decrement in the oscillation wavelength in agreement with all the previous results. The remaining parameters were kept the same as in Figure 5.2. (b) Concentration dynamics of Q and H_2Q obtained by using the skeleton model for $[H^+]_0$ = 15 M. This Figure was adapted from Escala *et al* [61].

5.2 Model Modification

Both, the full and skeleton models do not include the quinhydrone formation in their definitions. Thus, it is necessary to modify such models by including a chemical equation suitable to reproduce the precipitate occurrence. In this sense, the precipitate formation can be modeled [37] by adding an elementary chemical equation to the set of kinetic equations presented in Tables 2.8 and 2.9. Therefore, the following chemical equation describes the formation of $Q \cdot H_2Q$ obtained from Q and H_2Q.

$$Q + H_2Q \xrightarrow{k_{rQ\cdot H_2Q}} Q \cdot H_2Q \tag{R1}$$

where the reaction rate, based on the mass action law, is given by:

$$v_r = k_{rQ\cdot H_2Q}[Q][H_2Q] \tag{5.1}$$

The value of $k_{rQ\cdot H_2Q}$ was estimated *ad hoc* by comparing the experimental and numerical results. The one that better adjusted the simulations and the experiments was $k_{rQ\cdot H_2Q}$ = 0.05 M.

The concentration dynamics for Q, H_2Q and $Q \cdot H_2Q$ obtained from the modified full and skeleton models are presented in Figure 5.7. Both results are compared for a high stability case where $[H^+]_0$ = 15 M.

The emergence of the quinhydrone complex was similar in both, the full (Fig. 5.7(a)) and the skeleton (Fig. 5.7(b)) modified models. However, some discrepancies were observed, like the quinhydrone onset time and the final concentration values after 10000 s of simulation. The first one was produced by the differences in the induction times between both models (Fig. 5.5). In the second one, the full model exhibited higher concentrations for all species compared with the skeleton model. These differences in the concentrations were expected due to the simplification made in the skeleton model. Besides, it is possible to see that the chosen rate constant did not affect the catalyst oscillations in

any case, as the generation of quinhydrone was produced after the oscillations similarly to the observed in UV-VIS spectrum (Figs. 5.7(c,d)). This results indicate that both modified models reproduced well the experimental observations.

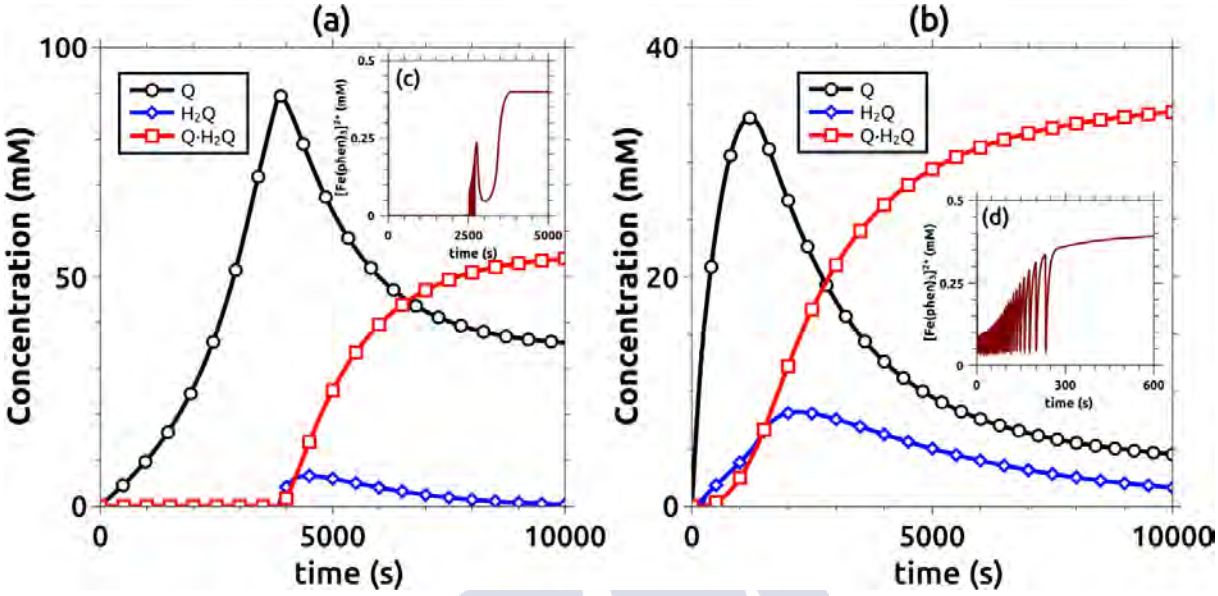

Figure 5.7: Quinhydrone formation in the modified (a) full and (b) skeleton model. Temporal profiles of Q and H_2Q are shown as well. (c) and (d) show the ferroin dynamics for the full and skeleton cases respectively. The remaining simulation conditions were: $[CHD]_0$ = 0.145 M, $[BrO_3{}^-]_0$ = 0.071 M, $[Fe(phen)_3{}^{2+}]_0$ = 0.4x10$^-$3 M and $k_{rQ\cdot H_2Q}$ = 0.05 M.

Finally, once proven the similarities between the models and experiments, it is possible to affirm that the modified skeleton model can be used to qualitatively simulate the convective system in a spatially extended configuration.

5.3 Reaction-Diffusion-Convection (RDC) Numerical Model

In order to confirm the experimental results, a RDC model of the system was studied. Based on Darcy's law, the model considers an isothermal miscible displacement in which the fluid reactivity is driven by the modified skeleton model. The governing equations, considering a homogeneous two-dimensional Hele-Shaw cell with a separation gap a and permeability κ, are:

$$\begin{aligned} \nabla \cdot \vec{u} &= 0 \\ \nabla p &= -\frac{\mu}{\kappa([Q\cdot H_2Q])}\vec{u} + \rho_m(C_i)\vec{g} \\ \phi\frac{\partial C_i}{\partial t} + \vec{u}\cdot\nabla C_i &= \phi D_{Ci}\nabla^2 C_i + R_i(C_i) \end{aligned} \tag{5.2}$$

where $\phi = 1$ is the porosity (considered constant for a Hele-Shaw cell), μ is the dynamic viscosity, C_i are the spatially distributed concentrations of each species, D_{Ci} are the diffusive constants, $\vec{g}$ is the gravity field aligned in the vertical direction and R_i are the net reaction rates derived from the mass balance of each species included in the modified skeleton model.

For the Na_2SO_4, R_i = 0 as this species did not participate in the reaction (this species was included to adjust the density gradient between the two solutions). $[H^+]$ was set constant all over the integration

domain. ρ_m and κ are the density of the mixture and the permeability respectively (both dependent on the chemical concentrations).

For the sake of simplicity, the precipitate was included in the model as a secondary fluid instead of discrete solid particles. From the two-phase flow theory [157, 124], the density of a two-phase mixture can be modeled as:

$$\rho_m(C_i) = \beta_l \rho_l(C_i) + \beta_s \rho_s \tag{5.3}$$

where β_l and β_s are the volume fractions of the liquid phase and the solid phase respectively and $\beta_l + \beta_s = 1$.

The density of the liquid phase was assumed to vary linearly with respect the chemical species concentrations [197]:

$$\rho_l(C_i) = \rho_0[1 + \sum_i \alpha_i C_i] \tag{5.4}$$

where,

$$\alpha_i = \frac{1}{\rho_0}\frac{\partial \rho}{\partial C_i} \tag{5.5}$$

are the solutal expansion coefficients [197] of each reagent (except the $[Q \cdot H_2Q]$) and ρ_0 is the solvent density.

Considering β_s = 1 - β_l and expressing the liquid volume as $V_l = V_T - V_s$, where V_T is the total volume and V_s is the solid volume respectively, the density of the mixture was expressed as a function of the volume fractions as:

$$\rho_m(C_i) = (\frac{V_T - V_s}{V_T})\rho_l(C_i) + (1 - \frac{V_T - V_s}{V_T})\rho_s \tag{5.6}$$

additionally, V_s was also expressed as a function of the quinhydrone molar concentration as:

$$V_s = \gamma \frac{[Q \cdot H_2Q] RMM_{Q.H2Q} V_{T]}}{\rho_s} \tag{5.7}$$

where $[Q \cdot H_2Q]$ is the quinhydrone molar concentration, $RMM_{Q.H2Q}$ is the relative molar mass of the quinhydrone and γ is an *ad-hoc* parameter conveniently set to adjust the solid fraction to a suitable value to trigger the fingering instability in a reasonable computational time. For a fixed γ, the qualitative behavior of the experimental system was reproduced by only changing the system excitability and density jump in the same way as in the experiments.

Regarding the permeability κ, as explained in Shukla *et al* [176], the formation of a precipitate affects the permeability of the porous matrix where it is formed. Similar to the cited work, the permeability $\kappa = \kappa([Q \cdot H_2Q])$ was defined as:

$$\kappa([Q \cdot H_2Q]) = \kappa_0 \exp(-R_\kappa(\frac{[Q \cdot H_2Q]}{c_0})) \tag{5.8}$$

where κ_0 is the permeability in absence of precipitate ($[Q \cdot H_2Q]$ = 0 M, $\kappa_0 = a^2/12$).

Defining $\kappa_m = \kappa([Q \cdot H_2Q]) = c_0$, R_κ can be calculated as $R_\kappa = \ln(\kappa_0/\kappa_m)$ similar to Shukla *et al* [176]. A positive value of R_κ indicates that the precipitate locally reduces the permeability of the porous

matrix [176]. For the present simulations, $R_\kappa = 0.75$. This parameter was estimated *ad hoc* according to the experimental observations. All the remaining parameters and references used to simulate the RDC system that best fit the experimental conditions and results are summarized in Table 2.10 of Section 2.2.

5.4 Non-Linear RDC Simulations

5.4.1 Descriptive Analysis

Figure 5.8 shows a comparative plot between three different perspectives: ferroin concentration, $Q \cdot H_2Q$ concentration and Density (Figs. 5.8(a-c) respectively) for the case $[H^+]_0 = 15$ M (high excitability condition) and $[Na_2SO_4]_0 = 0.200$ M (largest density jump) for five different time steps. The finger onset started after the reaction-diffusion pattern and was *naturally* produced by the generation of $Q \cdot H_2Q$. Also, the finger shape and its dynamics shown similarities with those observed experimentally. As can be seen, the model showed a very good agreement with the experiments (Fig. 3.1)

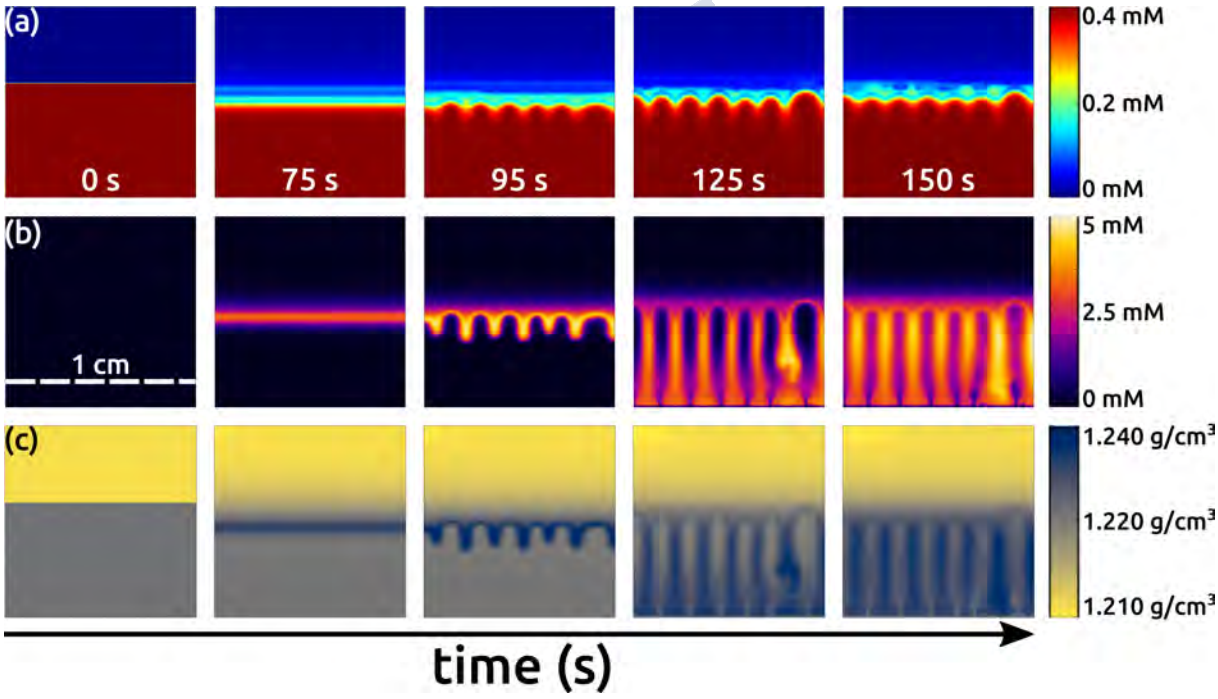

Figure 5.8: Comparative between (a) Ferroin concentration field, (b) quinhydrone concentration field and (c) density field for a simulated case where $[H^+]_0 = 15$ M and $[Na_2SO_4]_0 = 0.200$ M which is qualitatively equivalent to the experimental counterpart where $\Delta\rho = 0.011\ g/cm^3$ and $\varepsilon = 1.653$ M. This Figure was taken from Escala *et al* [61].

5.4.2 Instability Variation as a Function of $\Delta\rho$ and ε

In Figure 5.9, the density profile evolution is shown for four different simulated scenarios. The simulated cases correspond with the extreme cases presented in Figure 3.2, that is, lowest and highest excitability cases, and smallest and largest density jumps. Two simultaneous snapshots are presented for each case corresponding with the ferroin and $Q \cdot H_2Q$ concentration fields, analyzed at the same time. Fingering instability was produced at the interface by a $A + B \rightarrow C$ mechanism, where the quinhydrone is produced by the accumulation of Q and H_2Q. The system initially showed the typical reaction-diffusion

patterns and once the fingering instability was triggered, the chemical waves remained moving around the fingers. The shape of the fingers also shown similitude with those observed experimentally.

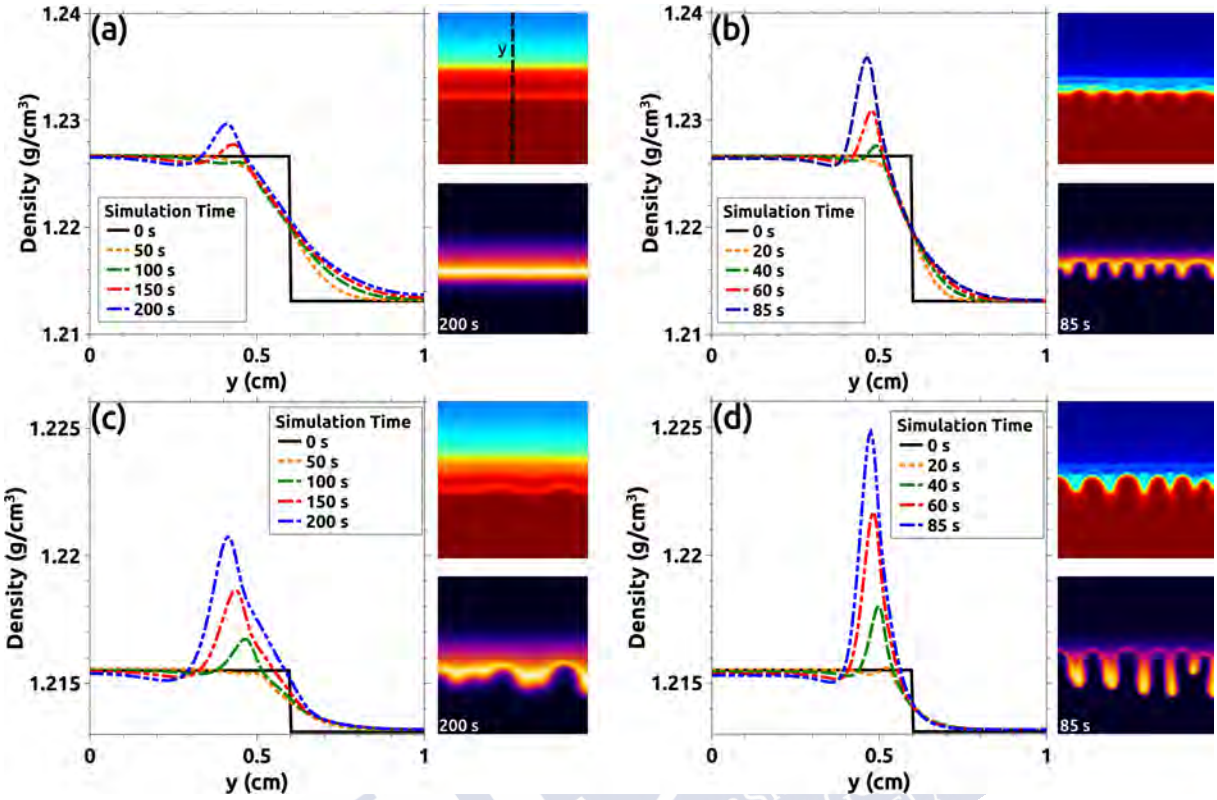

Figure 5.9: Temporal variation of the density profile for four different cases: (a) lowest excitability, largest density jump ($[H^+]_0$ = 3 M, $\Delta\rho$ = 0.011 g/cm^3), (b) highest excitability, largest density jump ($[H^+]_0$ = 15 M, $\Delta\rho$ = 0.011 g/cm^3), (c) lowest excitability, lowest density jump ($[H^+]_0$ = 3 M, $\Delta\rho$ = 0.002 g/cm^3) and (d) highest excitability, lowest density jump ($[H^+]_0$ = 15 M, $\Delta\rho$ = 0.002 g/cm^3). For each case, the two frames represent the concentration fields at the end of each simulation for the species ferroin (upper pic) and quinhydrone (lower pic). The density profiles were obtained by taking the density values across the line indicated in (a). This Figure was taken from Escala *et al* [61].

For a low excitability condition (Figure 5.9(a)), the formation of quinhydrone was not strong enough as to induce fingering instability. This fact can be appreciated in the density profile, whereas the initial density jump was large, the system became more stable and the small amount of $Q \cdot H_2Q$ generated barely changed the density as to locally destabilize the system. This fact was not observed in the Figure 5.9(c), where fingering instability occurred. For this case, as the initial density jump was smaller compared with Figure 5.9(a), the generation of quinhydrone produced a local destabilization of the system, triggering the fingering instability. In Figures 5.9(b) and 5.9(d), as the system was more excitable, the quinhydrone was rapidly generated inducing a faster fingering instability in both cases. For the more stable case (Figure 5.9(b)), the finger onset took longer to appear compared with Figure 5.9(d). These results can be compared with those reported in Figure 3.2 and Figures 3.3-3.4.

5.4.3 Numerical Measuring Observables

The numerical measuring observables were calculated identically to the experimental case by measuring the space-time plot obtained from the simulations. The results are presented in Figures 5.10 and 5.11. Alike the experiments, the chemical induction time (t_{ind-C}) decreased when the excitability was increased. Similar to the experimental case, this observable did not depend on the initial density jump

and it was only influenced by the initial chemical conditions. The chemical period (T_C) also showed a good agreement with the experiments. This observable decreased when the excitability was increased (Fig. 5.11(a)).

Regarding the hydrodynamic induction time (t_{ind-H}), a relative increment of this value was observed when the hydrodynamic jump was increased. The changes in the finger morphology also shown similarities with their experimental case. It was possible to see an increment in the finger wavelength for lower excitability values (this was better observed for large density gradients). This effect became less significant for larger excitabilities (Figure 5.11(b)). All these results agreed with the experimental observations presented in Figures 3.3-3.4.

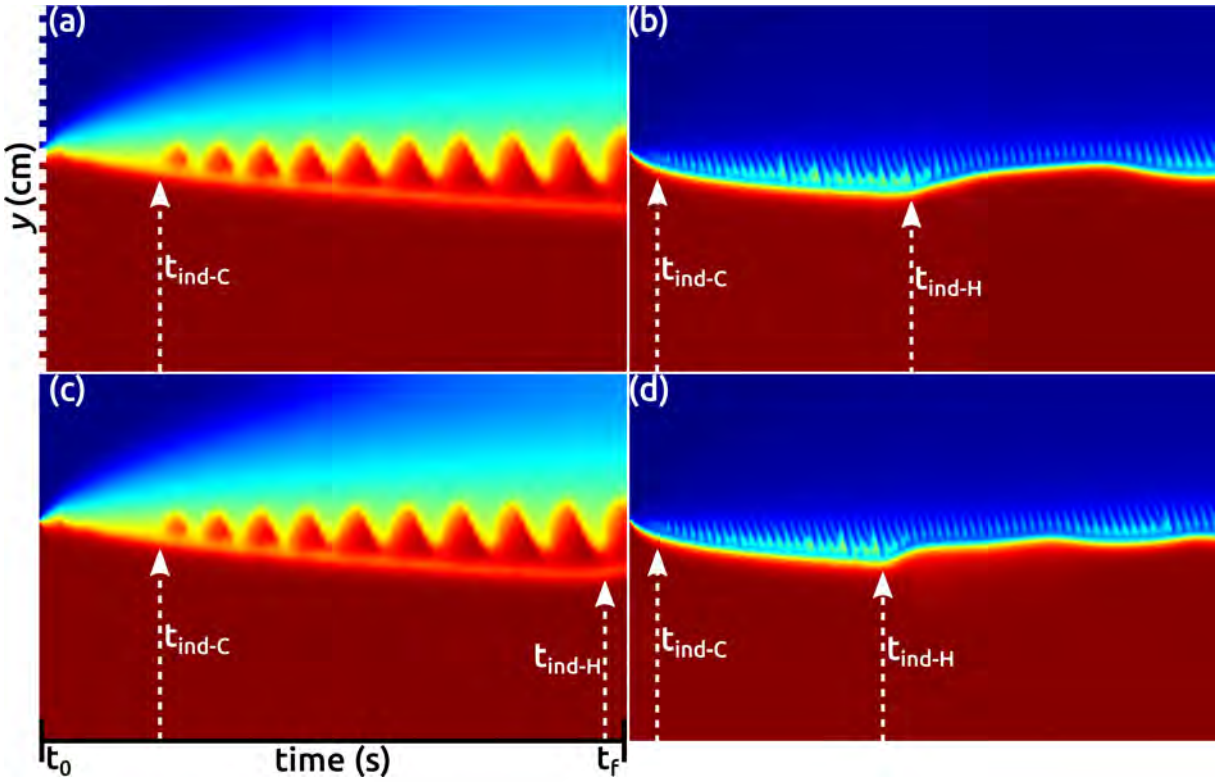

Figure 5.10: STP comparison between all the simulated cases presented in Fig 5.9: (a) ($[H^+]_0$ = 3 M, $\Delta\rho$ = 0.011 g/cm^3), (b) ($[H^+]_0$ = 15 M, $\Delta\rho$ = 0.011 g/cm^3), c) ($[H^+]_0$ = 3 M, $\Delta\rho$ = 0.002 g/cm^3) and d) ($[H^+]_0$ = 15 M, $\Delta\rho$ = 0.002 g/cm^3). In all cases the chemical and the hydrodynamic induction times are indicated. All the plots were obtained by measuring the y-line indicated in the Fig. 5.8(a). The space and time dimensions are: y = 1 cm, t_0 = 0 and t_f = 220 s respectively. Figure taken from Escala *et al* [61].

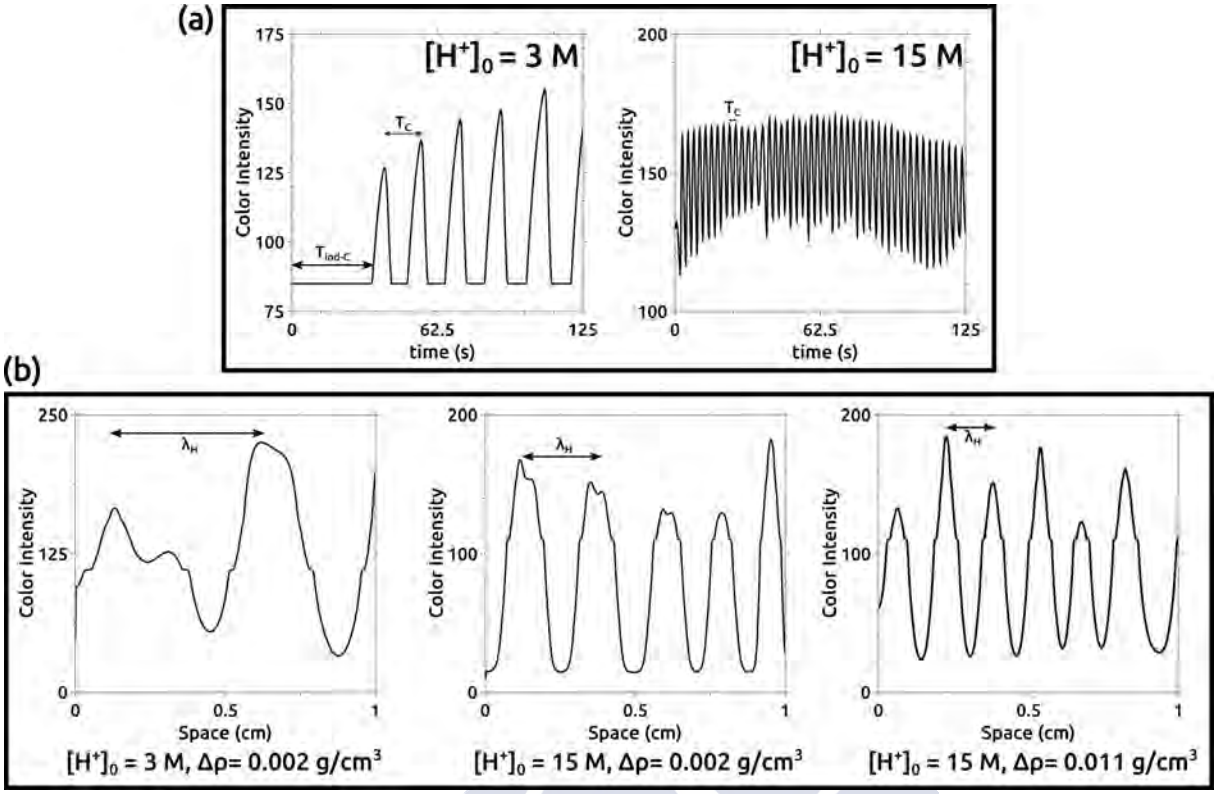

Figure 5.11: Qualitative comparison of the numerical observables for the cases presented in Figure 5.9. These results were obtained using the same methodology used for Figures 3.3-3.4 (More details are included in Appendix Section C.1). (a) The chemical induction time (t_{ind-C}) and the chemical period (T_C) were compared for two different excitabilities (given by $[H^+]_0$). The differences in period and induction time qualitatively agreed with the experimental results previously presented. (b) the finger wavelength λ_H was compared for different situations indicated at the bottom of each plot. Similar to the experiments, large wavelengths were observed for lower excitabilities and *vice versa*. This phenomenon was less significant in cases where the density gradient was increased, due to the increment in the stability of the system. This fact also agreed with the experimental section. This Figure was taken from Escala *et al* [61].

5.5 Chapter Discussion

The numerical simulations introduced in the present chapter demonstrated the efficiency of existing models of the BZ-CHD reaction. The models were also capable to predict the spatio-temporal dynamics in a specific experimental context.

The viability of the full model to reproduce the main dynamics of the batch system was demonstrated. This was especially appreciated in the chemical characteristic times (t_{ind-C} and T_C) with a high degree of reliability. Both observables were well represented by the model in qualitative and quantitative terms. In addition, the model predicted the accumulation of Q and H_2Q after the oscillatory region. This was fundamental, not only to confirm the hypothesis made over the occurrence of the saturation region but also to model the quinhydrone complex formation quantitatively.

The skeleton model reproduced the main characteristics of the full system as well. However, some differences were observed due to the large simplifications made over the set of equations. Nevertheless, it was shown that the use of this simplified model was suitable to simulate the RD and the RDC systems.

The modifications made to both models (by including the $Q \cdot H_2Q$ formation), showed a remarkable agreement with the dynamics of the batch system observed through UV-Vis spectroscopy. This was particularly noticeable in the full model, where the quinhydrone formation coincided with the saturation

region of the spectrum.

The development of a convective model and its implementation by non-linear simulations was able to "naturally" reproduce the fingering instability. The convective and oscillating dynamics of the Hele-Shaw cell experiments were, at least qualitatively, perfectly reproduced by the RDC model, showing comparable variations in all the numerical observables.

The control simulations showed that the instability only occurred if the chemical model was modified. This demonstrated the major role played by the quinhydrone formation in the experimental observations.

USC
UNIVERSIDADE
DE SANTIAGO
DE COMPOSTELA

Conclusions

This part of the thesis presented a detailed description of the chemically induced buoyancy-driven fingering instability. The system was fully characterized by studying the influence of the most relevant parameters of the system, the excitability and the density gradient. The use of these two parameters was fundamental not only to obtain an extensive description of the system but also to unveil the mechanism behind the instability formation. In this sense, the effectiveness of handling the density gradient and the excitability independently was the key to propose a suitable hypothesis regarding the observed phenomena.

The major influence of chemistry in the system behavior was strongly demonstrated. The numerical observables quantified in the convective framework, with exception of those associated purely with the hydrodynamics, were conserved in both, the batch experiments and the numerical models. This was fundamental to use such models in the system characterization.

In this sense, the instability observed was characterized to show a particular behavior, exhibiting a high degree of synchronization with the chemical dynamic. However, the finger formation *per se* did not specifically depend on the oscillatory behavior as it could be obtained just with the formation of quinhydrone in absence of oscillations. Nevertheless, it was observed that when both phenomena were present, a bi-directional interaction between both instabilities occurred. This demonstrated that in such a specific condition chemo-hydrodynamic synergies occurred that were produced by similarities in timescales.

It was possible to unveil the whole process of finger formation as an oversimplified mechanism, such as the classical A + B $\rightarrow$ C, where the role of C was played by the non-soluble chemical complex quinhydrone. The detailed characterization of the system made it possible to propose a modification of the existing reaction mechanism that, once coupled with the hydrodynamic part, was able to numerically reproduce the chemically induced density-driven fingering instability. The proposed model, unlike the simple A + B $\rightarrow$ C case, can be controlled by a broad variety of parameters, producing a much richer ensemble of possible behaviors.

It was systematically demonstrated, that a hydrodynamic instability can be triggered and controlled by a chemical reaction at the interface. This phenomenon can be used to understand why typical convective systems in Nature do not behave as theoretically expected in purely hydrodynamic environments, and why the chemical interactions need to be considered. On the other hand, the methods here exposed can be used to design more sophisticated experimental systems where the hydrodynamic instabilities can be controlled by a chemical reaction with countless applications in industry.

USC
UNIVERSIDADE
DE SANTIAGO
DE COMPOSTELA

PART II:

VISCOUS FINGERING INSTABILITY DRIVEN BY pH-SHIFTING REACTIONS

USC
UNIVERSIDADE
DE SANTIAGO
DE COMPOSTELA

Motivation

The development of pH-sensitive systems has recently attracted considerable attention due to their possible applications in many diverse fields. For example, many cancer therapies focus on delivering specific drugs through pH-sensitive carriers to tumors where pH is acid [118, 174]. The study of sensitive pH materials and their interactions with various biological or chemical media provide new horizons for the treatment of many other diseases [203, 170]. In this sense, a reliable technique to combine a pH-sensitive polymer with a pH clock reaction would be useful to test new design drugs in an simply and cost-effectively.

The use of organic pH-sensitive polymers is of interest in those applications to seek coupling with reactions presenting temporal modifications in the pH [106, 107, 108]. However, most classical pH changing reactions are typically inorganic and usually destructive towards pH-sensitive polymers [72, 71, 154, 191, 159, 144, 160, 186, 66]. In order to overcome this issue, more friendly organic pH-changing reactions (like the Formaldehyde-Sulfite (FS) and the Formaldehyde-Sulfite-Gluconolactone (FSG) reactions) were developed and extensively studied [106, 107, 108]. More recent studies, open the possibility to find a coupling between these reactions and a pH-sensitive polymer [108].

On the other hand, controlling viscous fingering hydrodynamic instabilities by *in situ* chemically driven viscosity changes [47, 47, 45] constitute another field of interest due to related applications in chemical and petroleum engineering [47, 165]. From an experimental point of view, chemical neutralization reactions coupled to pH-sensitive polymers have been shown to modify [165, 140, 139] such fingering. From a numerical point of view, several works have shown the efficiency of reaction to modulate the properties of this hydrodynamic instability [139, 88, 184, 73]. This paves the way to a more sensitive control of viscous fingering using the power of complex chemical reactions [73] to modulate the viscosity *in situ* both in time and space [5, 210, 98, 36].

In this context, the forthcoming chapters will firstly introduce the dynamic coupling between the pH-sensitive polymer Poly(Acrylic Acid) (PAA), and the aforementioned FS and FSG pH reactions. This study will demonstrate that is possible to obtain temporal changes in the viscosity of the solution induced by chemically-driven temporal changes in the pH. Moreover, it will be shown that the coupled system not only preserves the original features of the chemical reactions but that the viscosity changes are coupled to the kinetics of the chemistry. This paves the possibility for the FS-PAA and the FSG-PAA systems as candidates to control *in situ* the viscosity of a given environment depending on its pH. This will be addressed both, experimentally and numerically, by using the FS-PAA reaction to trigger and control viscous fingering by changing the control parameters of the hydrodynamics and the chemistry involved.

The information presented hereafter is based on the work published in Escala *et al*, (2017) [62] and Escala *et al*, (2019) [58].

USC
UNIVERSIDADE
DE SANTIAGO
DE COMPOSTELA

Chapter 6

Experimental and Numerical Methods

6.1 Experimental Methods

6.1.1 Chemical Recipes and Experimental Designs for Dynamic Measurements

This Section introduces the chemical recipes used to study the effect of each specific species involved in the Formaldehyde-Sulfite-PAA (FS-PAA) and Formaldehyde-Sulfite-Gluconolactone-PAA (FSG-PAA) reactions. These recipes were used in a homogeneously stirred reactor. All solutions here presented were made from reagent grade stocks. More details about the stock preparations are included in Appendix A.2.

Recipes of the FS-PAA Reaction Varying $[PAA]_0$, $[Na_2SO_3]_0$, and $[Formaldehyde]_0$. Tables 6.1(a-c) show the concentration values used to study the effect of varying each species of the FS-PAA reaction. The varied species are indicated in boldface. The concentration of the remaining species in each case was kept constant.

Species	Concentration
PAA	0, 0.087, 0.175, 0.263, 0.350, 0.438, 0.479
Formaldehyde	0.093
Na_2SO_3	0.068

(a) $[PAA]_0$ variation.

Species	Concentration
Na_2SO_3	0.017, 0.033, 0.043, 0.056, 0.061, 0.064, 0.068, 0.077
PAA	0.438
Formaldehyde	0.093

(b) $[Na_2SO_3]_0$ variation.

Species	Concentration
Formaldehyde	0.046, 0.065, 0.084, 0.093, 0.186, 0.280, 0.350, 0.466
PAA	0.438
Na_2SO_3	0.068

(c) $[Formaldehyde]_0$ variation.

Table 6.1: Experimental recipes used to study the effect of each specific reagent in the dynamics of the FS-PAA reaction. Concentration values are expressed as wt% for the PAA and molarity for Na_2SO_3 and Formaldehyde.

Recipe of the FSG-PAA Reaction Varying $[GLN]_0$. Table 6.2 shows the concentrations used to analyze the effect of $[GLN]_0$ in the dynamics of the FSG-PAA reaction. In this case, as the FSG reaction is an extension of the FS reaction [108, 106, 107] only the gluconolactone (GLN) was varied. The concentrations of the remaining species were kept constant.

Species	Concentration
GLN	0.003, 0.005, 0.007, 0.008, 0.010, 0.012, 0.014, 0.016
PAA	0.438
Formaldehyde	0.093
Na_2SO_3	0.068

Table 6.2: Recipe used to analyze the effect of the $[GLN]_0$ in the FS-PAA system. Concentration values are expressed as wt% for the PAA and molarity for Na_2SO_3, Formaldehyde, and GLN.

6.1.2 Rheological and pH Measurements

The viscosity and the pH were independently measured in all the experiments. The pH dynamics was recorded using the electronic pH-meter Vernier - FPH-BTA (Fig. 6.1(a)). All pH measurements were recorded with a resolution of $t = 1\ s$. The viscosity was measured with a TA-Instruments TA-AR2000 rheometer (Fig. 6.1(b)), using a 60 mm steel cone geometry with a 1 ° angle in a cone-plate arrangement. The temperature of the lower plate was kept constant at 23 °C via a Peltier system. The temporal measurements were done at a constant shear rate of 500 s^{-1}.

In those cases where both properties were recorded simultaneously, part of the solution used to measure the pH was taken into the rheometer once all reactants were mixed. Thus, there is an intrinsic delay between the beginning of the pH recordings and those of viscosity due to the experimental procedure. All the experiments were repeated at least three times. The obtained results are presented as the average ± standard deviation. The temperature in all pH measurements was kept constant at 23 °C using a water thermostat.

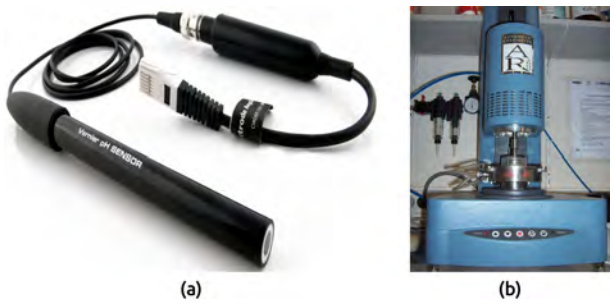

Figure 6.1: (a) FPH-BTA pH-meter and (b) TA-AR2000 rheometer used for measuring the pH and viscosity respectively.

6.1.3 Radial Hele-Shaw Cell Experiments

The viscous fingering experiments were performed in a horizontally oriented Hele-Shaw cell. This device was built using two squared glass plates of 25 cm x 25 cm separated by a poly(tetrafluoroethylene) frame of thickness $a = 0.25$ mm. The cell was initially filled with the displaced solution. The displacing

solution was injected through a 4 mm hole located at the geometric center of the bottom plate using a syringe pump (kdScientific: Legato 200 series).

Similar to Part I of this work, two different experimental setups were used to capture all behaviors and characteristics of the system: A direct setup that provided a *naked-eye* observation of the experiment, and a Schlieren setup to obtain more detailed information impossible to see through direct observation. Both experimental arrangements are indicated in Figure 6.2.

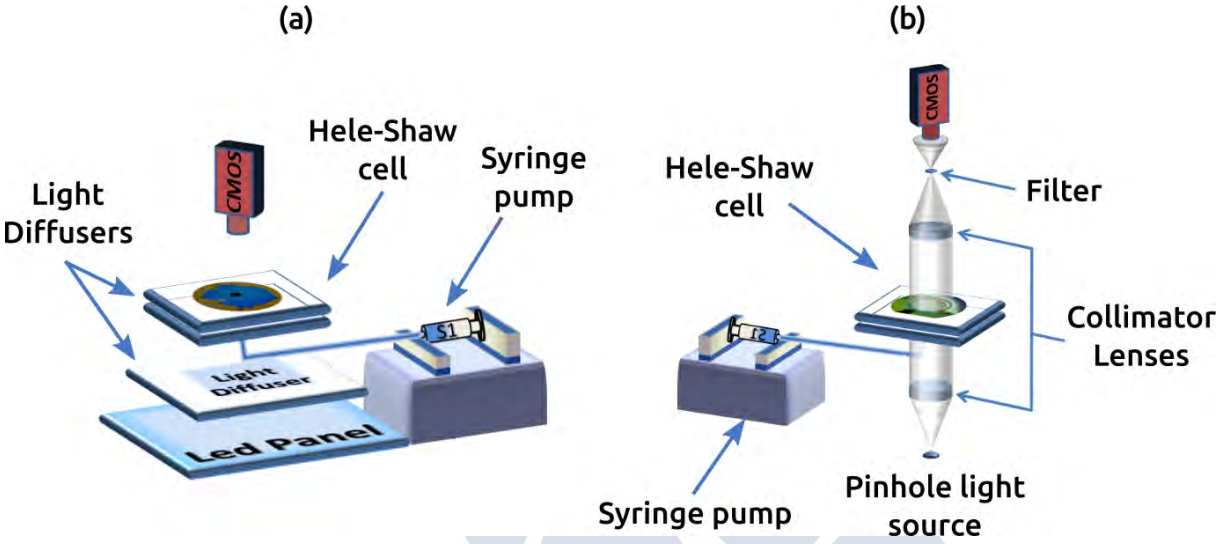

Figure 6.2: Detailed Schematics of the experimental setups used for the Hele-Shaw cell experiments. (a) Direct Setup and (b) Schlieren setup. Figure adapted from Escala *et al* [58]

In the direct setup, the cell was illuminated from below using a rectangular Light-Emitting Diode (LED) pad and a light diffuser (Figure 6.2(a)). For the Schlieren optics, and similarly to Part 1, the Hele-Shaw cell was placed between two collimator lenses. The cell illuminated using a pinhole-LED light source. An iris cutoff filter was located at the focus point between the camera and the collimator lens [27, 172]. (Figure 6.2(b)) In both optical arrangements, the experiments were recorded from above using a Complementary Metal-Oxide-Semiconductor (CMOS) camera (PixeLINK: PL-B776U) connected to a computer. The obtained results were processed and analyzed using the GNU software FIJI [172].

6.1.4 Instability Setup and Protocol

The dynamics and structure of the viscous fingering patterns were analyzed by varying properties of both the displacing and displaced solutions independently. The base formula used in the temporal analysis made on the FS-PAA reaction (Tables 6.1(a-c)) was separated into the displacing (PAA and Na_2SO_3) and displaced (Formaldehyde) solutions.

A color indicator (hereafter C.I.) was added into the displacing solution to facilitate the observation and further analysis in the direct setup. This indicator was made of a hydroalcoholic solution of Bromothymol Blue. The addition of C.I. does not affect neither the pH nor the viscosity nor the dynamics of the system (Details are in Section D.2.1). The C.I. was also used in some of the Schlieren experiments. However, those experiments were repeated and compared without using it, not observing significant changes in the system behavior.

The reactivity of the system was modulated by varying the initial concentrations of the main reagents (sulfite and formaldehyde), whereas the hydrodynamics was controlled by varying the flow rate. Tables 6.3-6.4 show the range of species concentrations studied in the displaced and displacing solutions respectively.

The experiments were carried out using the following protocol: the cell was initially filled with the displaced solution. Once filled, 3 mL of displacing were injected using a flow rate of 7 mL/min. After that, the injection was stopped letting the chemicals to diffuse and react for 3 h. The reaction-diffusion phenomenon occurred at the interface between both solutions. After this time, 3 mL of displacing solution were injected producing a viscous fingering instability. This process was repeated for each concentration listed in Tables 6.3-6.4 and for four different flow rates Q (2.5, 7, 10, and 20 mL/min).

Species	Concentration
Formaldehyde	0, 0.046, 0.093, 0.187, 0.375, 0.750

(a) Displaced solution.

Species	Concentration
PAA	0.438
Na_2SO_3	0.068
C.I.	0.021

(b) Displacing solution.

Table 6.3: Solution configuration used to study the influence of changes in the displaced fluid in the Hele-Shaw cell experiments. Concentrations are expressed in molarity for the Formaldehyde and the Na_2SO_3 and wt% for PAA and C.I.

Species	Concentration
Formaldehyde	0.75

(a) Displaced solution.

Species	Concentration
PAA	0.438
Na_2SO_3	0, 0.043, 0.056, 0.061, 0.064, 0.068, 0.087, 0.140, 0.192
C.I.	0.021

(b) Displacing solution.

Table 6.4: Solution configuration used to study the influence of changes in the displacing fluid in the Hele-Shaw cell experiments. Concentrations are expressed in molarity for the Formaldehyde and the Na_2SO_3 and wt% for PAA and C.I.

6.1.5 Circularity Calculation

The changes in the structure of the viscous fingering patterns were mainly studied by measuring the circularity (C). The circularity is a non-dimensional value between 0 and 1 that indicates how *far* or *close* a shape is from a perfect circle. The definition of C is given by:

$$C = 4\pi \frac{A}{P^2} \tag{6.1}$$

where A and P are the area and the perimeter of the viscous fingering pattern respectively.

The circularity was chosen over more traditional descriptors, (like the fingering Density Area d_A [172, 142, 140]), due to the characteristic shape of the obtained patterns in this framework. In any case, d_A was also calculated and compared with the value C. This comparison was useful for not only a control test but also to define newer tools for viscous fingering analysis.

The image post-processing and analysis to calculate C from the experiments were done by using the GNU software FIJI [172]. More Details are presented in Appendix C.2. All circularity measurements were done in the final frame of each experiment.

6.2 Numerical Methods

6.2.1 The FS-PAA Reaction Model

The reaction and reaction-diffusion models of the FS-PAA reaction were obtained by adapting the previous work developed by Kovacs *et al* [106]. In such work, a complete description of the kinetic equations involved in the FS reactions is given and modeled for a batch reactor. In this thesis, the reaction rate constants of the original FS model were changed to match the experimental results obtained for the FS-PAA system. The new reaction rates were estimated by fitting the experimental values using optimization and parameter estimation methods, provided by the open-source software COPASI [95]. All estimations were performed by using the Hooke & Jeeves method [94] and the following configuration: Iteration limit: 500, tolerance: 1x10$^-$12, and a step size reduction factor ρ: 0.2 [95]. The equation system, kinetic laws, and the estimated rate constants used are shown in Table 6.5.

	Reactions	Kinetic Law	k_f	k_r
R1	$CH_2(OH)_2 \rightleftharpoons CH_2O + H_2O$	$v_{r1} = k_f[CH_2(OH)_2]$-$k_r[CH_2O]$	3x10^{-3} s^{-1}	4.75 s^{-1}
R2	$SO_3^{2-} + H^+ \rightleftharpoons HSO_3^-$	$v_{r2} = k_f[SO_3^{2-}][H^+]$-$k_r[HSO_3^-]$	4750 s^{-1}	1.6x10^{10} $M^{-1}s^{-1}$
R3	$CH_2O + SO_3^{2-} \longrightarrow CH_2(O^-)SO_3^-$	$v_{r3} = k_f[CH_2O][SO_3^{2-}]$	2.9x10^6 $M^{-1}s^{-1}$	
R4	$CH_2(O^-)SO_3^- + H^+ \rightleftharpoons CH_2(OH)SO_3^-$	$v_{r4} = k_f[CH_2(O^-)SO_3^-][H^+]$-$k_r[CH_2(OH)SO_3^-]$	2.9x10^8 $M^{-1}s^{-1}$	15x10^{-4} s^{-1}
R5	$H_2O \rightleftharpoons OH^- + H^+$	$v_{r5} = k_f[H_2O]$-$k_r[OH^-][H^+]$	3x10^{-4} $M^{-1}s^{-1}$	1.2x10^{11} $M^{-1}s^{-1}$
R6	$CH_2O + HSO_3^- \longrightarrow CH_2(OH)SO_3^-$	$v_{r6} = k_f[CH_2O][HSO_3^-]$	170 $M^{-1}s^{-1}$	
R7	$CH_2(OH)_2 + SO_3^{2-} \longrightarrow CH_2(O^-)SO_3^- + H_2O$	$v_{r7} = k_f[CH_2(OH)_2][SO_3^{2-}]$	0.4 $M^{-1}s^{-1}$	
R8	$CH_2(OH)_2 + HSO_3^- \longrightarrow CH_2(OH)SO_3^- + H_2O$	$v_{r8} = k_f[CH_2(OH)_2][HSO_3^-]$	0.03 $M^{-1}s^{-1}$	

Table 6.5: Kinetic model of the FS reaction. This set of kinetic equations was adapted from the original FS reaction model [106] introduced by Kovacs *et al* to match the experimental results obtained for the FS-PAA system.

To obtain initial concentrations similar to the experimental conditions, a two-step procedure was used. The first step was to simulate the system equations without formaldehyde by just putting $[SO_3^{2-}]_0$ and $[H^+]$. The sulfite initial concentration was taken directly from the experimental recipe and the proton

concentration was estimated based on the pH values directly measured from the experiments. With these two conditions, the bisulfite initial concentration was then fixed to match the experimental pH value at t = 0 s. Once the values for $[SO_3{}^{2-}]_0$, $[H^+]_0$, and $[HSO_3{}^-]_0$ are established, the clock reaction was obtained by varying $[\text{Formaldehyde}]_0$ or $[SO_3{}^{2-}]_0$ in each case.

Analogously to the experimental part, the dynamic of the FS-PAA system was studied by changing $[SO_3{}^{2-}]_0$ and $[\text{Formaldehyde}]_0$. Tables 6.7 and 6.6 show the species combinations used as the initial conditions for changes made in the sulfite and the formaldehyde initial concentration respectively.

As can be noted, some bisulfite concentrations might be experimentally unreal if we consider conservation laws and the $\text{PAA}-SO_3{}^{2-}$ coupling mechanism described in Section 7.1. Even if the protonation of the polymer was not explicitly included in the model, it is somehow included by adjusting $[HSO_3{}^-]_0$ and $[H^+]_0$ to match the experimental initial conditions.

Initial Conditions - Formaldehyde Simulations				**Experimental**
$[SO_3{}^{2-}]_0$ (M)	$[HSO_3{}^-]_0$ (M)	$[H^+]_0$	$[\text{Formaldehyde}]_0$	Initial pH
0.068	0.053	$1.99\text{x}10^{-7}$	0.750	6.70
0.068	0.053	$1.99\text{x}10^{-7}$	0.466	6.70
0.068	0.053	$1.99\text{x}10^{-7}$	0.350	6.70
0.068	0.053	$1.99\text{x}10^{-7}$	0.280	6.70
0.068	0.053	$1.99\text{x}10^{-7}$	0.187	6.70
0.068	0.053	$1.99\text{x}10^{-7}$	0.093	6.70
0.068	0.053	$1.99\text{x}10^{-7}$	0.084	6.70
0.068	0.053	$1.99\text{x}10^{-7}$	0.065	6.70
0.068	0.053	$1.99\text{x}10^{-7}$	0.046	6.70
0.068	0.053	$1.99\text{x}10^{-7}$	0	6.70

Table 6.6: Set of initial conditions used to simulate the FS-PAA system by varying $[\text{Formaldehyde}]_0$.

Initial Conditions - Sulfite Simulations				**Experimental**
$[SO_3{}^{2-}]_0$ (M)	$[HSO_3{}^-]_0$ (M)	$[H^+]_0$	$[\text{Formaldehyde}]_0$	Initial pH
0.192	0.057	$7.58\text{x}10^{-8}$	0.093	7.12
0.140	0.054	$9.77\text{x}10^{-8}$	0.093	7.01
0.087	0.054	$1.58\text{x}10^{-7}$	0.093	6.80
0.077	0.079	$3.09\text{x}10^{-7}$	0.093	6.72
0.068	0.053	$1.99\text{x}10^{-7}$	0.093	6.70
0.064	0.098	$3.89\text{x}10^{-7}$	0.093	6.41
0.061	0.107	$4.46\text{x}10^{-7}$	0.093	6.35
0.056	0.174	$7.94\text{x}10^{-7}$	0.093	6.10
0.043	0.272	$1.58\text{x}10^{-6}$	0.093	5.80
0.033	0.359	$3.23\text{x}10^{-6}$	0.093	5.50
0.017	1.248	$1.81\text{x}10^{-5}$	0.093	4.74
0	0	$5.62\text{x}10^{-4}$	0.093	3.25

Table 6.7: Set of initial conditions used to simulate the FS-PAA system by varying $[SO_3{}^{2-}]_0$.

6.2.2 The FSG-PAA Reaction Model

Analogously to the FS-PAA system, a model for the FSG-PAA was obtained by adapting the FSG model proposed by Kovacs *et al* [107, 108]. The FSG model is an extension of the FS model that includes the gluconolactone (GLN) hydrolysis and the catalytic effect of the OH^- ion. In this sense, the reaction equations associated with the FS system remained unaltered (with exception of R1) and 2 more equations (R9 and R10) were added to the model. For this case, the reaction rates that were previously estimated for the FS model were kept constant and new estimations were done for rates of R1, R9, and R10. The estimation method and its configuration were the same used for the FS model. For simplicity, the gluconic acid ($[GA]_0$) and gluconate ion ($[G^-]_0$) initial concentrations were set constant for all the simulations. The derived model and the obtained rates are presented in Table 6.8.

	Reactions	Kinetic Law	k_f	k_r
R1	$CH_2(OH)_2 \rightleftharpoons CH_2O + H_2O$	$v_{r1} = (k_f + k_{OH}[OH^-])[CH_2(OH)_2]$-$k_r[CH_2O]$	$8.5x10^{-2}\ s^{-1}$, $k_{OH} = 2.60\ M^{-1}s^{-1}$	$4000\ s^{-1}$
R2	$HSO_3^- \rightleftharpoons SO_3^{2-} + H^+$	$v_{r2} = k_f[HSO_3^-]$-$k_r[SO_3^{2-}][H^+]$	$4750\ s^{-1}$	$1.6x10^{10}\ M^{-1}s^{-1}$
R3	$CH_2O + SO_3^{2-} \longrightarrow CH_2(O^-)SO_3^-$	$v_{r3} = k_f[CH_2O][SO_3^{2-}]$	$2.9x10^6\ M^{-1}s^{-1}$	
R4	$CH_2(O^-)SO_3^- + H^+ \rightleftharpoons CH_2(OH)SO_3^-$	$v_{r4} = k_f[CH_2(O^-)SO_3^-][H^+]$-$k_r[CH_2(OH)SO_3^-]$	$2.9x10^8\ M^{-1}s^{-1}$	$15x10^{-4}\ s^{-1}$
R5	$H_2O \rightleftharpoons OH^- + H^+$	$v_{r5} = k_f[H_2O]$-$k_r[OH^-][H^+]$	$3x10^{-4}\ M^{-1}s^{-1}$	$1.2x10^{11}\ M^{-1}s^{-1}$
R6	$CH_2O + HSO_3^- \longrightarrow CH_2(OH)SO_3^-$	$v_{r6} = k_f[CH_2O][HSO_3^-]$	$170\ M^{-1}s^{-1}$	
R7	$CH_2(OH)_2 + SO_3^{2-} \longrightarrow CH_2(O^-)SO_3^- + H_2O$	$v_{r7} = k_f[CH_2(OH)_2][SO_3^{2-}]$	$0.4\ M^{-1}s^{-1}$	
R8	$CH_2(OH)_2 + HSO_3^- \longrightarrow CH_2(OH)SO_3^- + H_2O$	$v_{r8} = k_f[CH_2(OH)_2][HSO_3^-]$	$0.03\ M^{-1}s^{-1}$	
R9	$GL + H_2O \rightleftharpoons GA$	$v_{r9} = (k_f + k_{OH}[OH])[GL]$-$k_r[GA]$	$205\ s^{-1}$, $k_{OH} = 44.75\ M^{-1}s^{-1}$	$3.7x10^{-9}\ s^{-1}$
R10	$GA \rightleftharpoons G^- + H^+$	$v_{r10} = k_f[GA]$-$k_r[G^-][H^+]$	$6.3x10^{-2}\ s^{-1}$	$2870\ M^{-1}s^{-1}$

Table 6.8: Kinetic model of the FSG-PAA reaction. This set of kinetic equations were adapted from the original FSG reaction model introduced by Kovacs *et al* [107].

Table 6.9 shows the initial conditions used to simulate the FSG-PAA system.

Initial Conditions - Gluconolactone Simulations					Experimental
$[SO_3^{2-}]_0$ (M)	$[HSO_3^-]_0$ (M)	$[H^+]_0$	[Formaldehyde]$_0$	$[GLN]_0$	Initial pH
0.068	0.053	$1.99x10^{-7}$	0.093	0.016	6.70
0.068	0.053	$1.99x10^{-7}$	0.093	0.014	6.70
0.068	0.053	$1.99x10^{-7}$	0.093	0.012	6.70
0.068	0.053	$1.99x10^{-7}$	0.093	0.010	6.70
0.068	0.053	$1.99x10^{-7}$	0.093	0.008	6.70
0.068	0.053	$1.99x10^{-7}$	0.093	0.007	6.70
0.068	0.053	$1.99x10^{-7}$	0.093	0.005	6.70
0.068	0.053	$1.99x10^{-7}$	0.093	0.003	6.70

Table 6.9: Set of initial conditions used to simulate the FSG-PAA system by varying $[GLN]_0$. For all cases, $[GA]_0$ = 0.031 M and $[G^-]_0$ = 0 M.

6.2.3 Batch System Simulations

The batch system was simulated using the GNU software COPASI [95], by integrating the models listed in Tables 6.5 and 6.8, and using the initial conditions listed in Tables 6.6,6.7 and 6.9. The simulations were performed using the LSODA [162] solver with a fixed time-step of 0.01. The relative and absolute tolerances were set to $1x10^{-6}$ and $1x10^{-8}$ respectively. Statistical analysis was done by introducing random values into the initial conditions given by the following expression:

$$C_0(t=0) = (1+\xi N(0,1))[C_i]_0 \tag{6.2}$$

where $N(0,1)$ is a normally distributed value with mean 0, variance 1 and amplitude ξ = 0.05. $[C_i]_0$ are $[\text{Formaldehyde}]_0$, $[SO_3{}^{2-}]_0$, $[HSO_3{}^-]_0$, $[H^+]_0$ and $[\text{GLN}]_0$.

By using this method, it was possible not only to obtain similarities in the dynamics of the reaction, but also a closer approximation of the tendencies of the measured observables. In these simulations, the range of concentrations studied was extended with respect to the experimental cases. This addition was done to improve the numerical analysis.

6.2.4 Reaction-Diffusion (RD) Model Simulations

The initial conditions for the convective simulations were obtained from non-linear RD simulation using the Computational Fluid Dynamic (CFD) software Ansys Fluent® version 19.2 [11, 12]. Due to the characteristic symmetry of the initial condition, these simulations may be performed in a one-dimensional (1D) RD perspective, however, as Fluent does not include a 1D numerical solver, these calculations were done using a 1.5D numerical approach as shown in Figure 6.3.

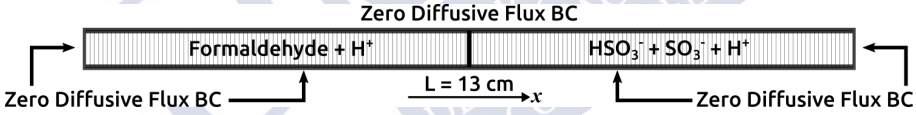

Figure 6.3: Mapped numerical domain used for the 1.5D reaction-diffusion simulations. All boundaries were set as zero diffusive flux. The reactive species were spatially located following the experimental procedure.

The numerical domain (D) consists of a horizontally oriented rectangular region of length L = 13 cm and arbitrary width. This region was discretized setting one cell in the vertical axis. The discretization of the horizontal axis varied depending on the stability of each case. A Zero diffusive flux condition was imposed on all boundaries. The chemical species were spatially extended by imitating the experimental procedure using the following piecewise functions:

$$\begin{aligned} C_{ai}(x,0) &= \begin{cases} [C_a]_0(x) & x < L/2 \\ 0 & x \geqslant L/2 \end{cases} \\ C_{bi}(x,0) &= \begin{cases} 0 & x < L/2 \\ [C_b]_0(x) & y \geqslant L/2 \end{cases} \end{aligned} \tag{6.3}$$

$$[H^+]_0(x,0) = k, \forall x \in D$$

where $[C_a]_0$ corresponds to $[\text{Formaldehyde}]_0$ and $[C_b]_0$ to $[HSO_3{}^-]_0$ and $[SO_3{}^{2-}]_0$. In these simulations, $[H^+]_0$ was defined constant across the domain to improve numerical stability.

The initial concentrations used for the RD simulations are indicated in Tables 6.11-6.10.

Initial Conditions - RD - Formaldehyde Simulations			
$[SO_3^{2-}]_0$ (M)	$[HSO_3^-]_0$ (M)	$[H^+]_0$	$[Formaldehyde]_0$
0.068	0.053	$1.99x10^{-7}$	0.750
0.068	0.053	$1.99x10^{-7}$	0.375
0.068	0.053	$1.99x10^{-7}$	0.187
0.068	0.053	$1.99x10^{-7}$	0.093
0.068	0.053	$1.99x10^{-7}$	0.046
0.068	0.053	$1.99x10^{-7}$	0.005
0.068	0.053	$1.99x10^{-7}$	0

Table 6.10: Set of initial conditions used in the RD simulations to study changes on the thickness of the initial mixing region by varying $[Formaldehyde]_0$.

Initial Conditions - RD - Sulfite Simulations			
$[SO_3^{2-}]_0$ (M)	$[HSO_3^-]_0$ (M)	$[H^+]_0$	$[Formaldehyde]_0$
0.192	0.057	$7.58x10^{-8}$	0.75
0.140	0.054	$9.77x10^{-8}$	0.75
0.087	0.054	$1.58x10^{-7}$	0.75
0.068	0.053	$1.99x10^{-7}$	0.75
0.064	0.098	$3.89x10^{-7}$	0.75
0.061	0.107	$4.46x10^{-7}$	0.75
0.056	0.174	$7.94x10^{-7}$	0.75
0.043	0.272	$1.58x10^{-6}$	0.75
0.017	1.248	$1.81x10^{-5}$	0.75
0	0	$5.62x10^{-4}$	0.75

Table 6.11: Set of initial conditions set used in the RD simulations to study changes on the thickness of the initial mixing region by varying $[SO_3^{2-}]_0$.

In the absence of convection, the concentration profiles were obtained by solving the following set of reaction-diffusion equations:

$$\frac{\partial C_i}{\partial t} = D_i \frac{\partial C_i}{\partial x^2} + R_i(C_i) \tag{6.4}$$

where $C_i = C_i(x,t)$ and R_i are the concentration fields and the net reaction rates of species i included in the chemical FS-PAA kinetic model shown in Table 6.5 respectively. D_i is the diffusion coefficient for each species. The values of the diffusion coefficients were estimated from Adamsky *et al* [2] as D_D = $1x10^9 m^2/s$ for all reagents in the displaced solution (lower viscosity) and D_R = 1 x $10^{11} m^2/s$ for all

reagents in the displacing solution (higher viscosity).

The 1D spatial profiles of H^+ and OH obtained from these simulations were mapped into a two-dimensional (2D) space by rotating them around the origin. This procedure served as the initial condition for the convective non-linear simulations.

These equations were numerically solved by using the implicit Pressure solver and the SIMPLE algorithm coupled with a stiff-chemistry solver to improve numerical stability [12]. The time-step was automatically controlled by the software. First- and second-order upwind discretization schemes were used for time and concentration fields respectively.

6.2.5 Diffusion-Convection (DC) Model Simulations

The flow dynamics was modeled by using Darcy's law for porous medium included in the CDF suite [11, 12]. The general set of mathematical equations that models the viscous displacements was introduced in Section 1.46. For convenience, a detailed description of the model used for this specific system is given in Section 9.2. The information presented in this methods section is intended to show general aspects of the DC simulations.

The numerical domain and the boundary conditions used to simulate the 2D convection-diffusion system are shown in Figure 6.4. These conditions were inspired by previous works [93, 193, 117]. The numerical domain was constructed using a mapped mesh of regular elements in a quarter circle of radius R_i = 13 cm. Simulations were carried out in the quarter domain to save memory and computational time. Symmetry operations were then applied to obtain the fully circular region. The inlet flow velocity at the central boundary was calculated as a function of the flow rate Q as [11]:

$$-\vec{n}\cdot\vec{u} = v_0(Q) \tag{6.5}$$

where $v_0(Q) = Q/2\pi ra$.

The injection hole is the inner circular region with radius r_i = 2 mm [142, 23]. The outlet boundary condition was set as a pressure outlet p = 0 Pa.

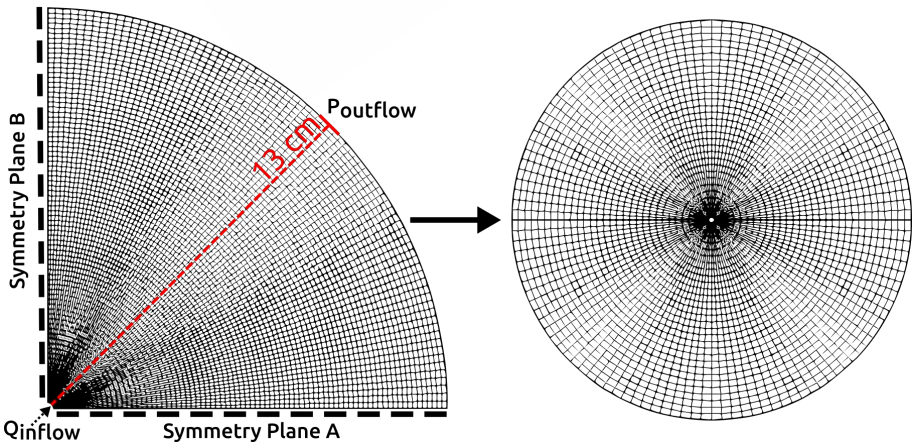

Figure 6.4: Mapped numerical domain used for the 2D convection-diffusion simulations. The calculations were made in a quarter of a circle domain. Symmetry operations were performed to obtain the final result.

As the system needs local perturbations to trigger the instability, a small disturbance was added to the hydroxide concentration profile:

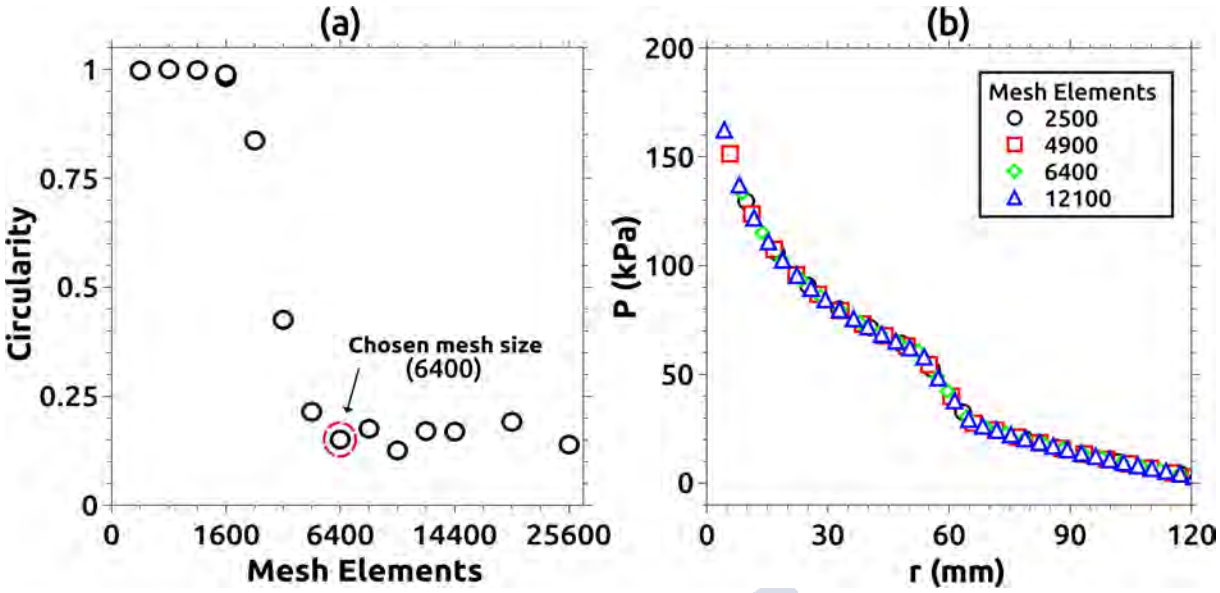

Figure 6.5: Sensitivity of the simulation results to the mesh size: (a) Circularity as a function of the mesh size. The mesh size used to calculate all the numerical results was chosen as the coarsest mesh that does not introduce any significant change in the circularity. (b) Pressure field across the radial coordinate for different mesh sizes.

$$[OH^-](\vec{r}) = (1 + \xi N(\vec{r}))[OH^-] \tag{6.6}$$

where $N(\vec{r})$ is a normally distributed noise function of amplitude ξ = 0.005 defined across the radial coordinate $\vec{r} = (x, y)$.

Similar to the RD case, the $[H^+]_0$ profiles are different in experiments and simulations. The numerical initial profile had to be non-zero all across the domain to avoid numerical instabilities.

The pressure and concentration fields were calculated using a second-order and first-order upwind method respectively [117]. This set of equations were solved with an implicit solver formulation, using the SIMPLE algorithm to integrate the pressure-velocity coupling [12, 11]. The time step was automatically controlled by the software based on an adaptive algorithm using the first-order upwind discretization.

In the convective case, the reaction term was not considered as the characteristic injection times were much faster than the characteristic reaction times. This was considered after estimating the Damköhler numbers for the experimental system. These results are presented in Section 8.5. All simulations used dimensional units to facilitate direct comparison with the experimental results.

6.2.6 Mesh Independence Study For The DC Model

In order to analyze the validity of the numerical simulations, the effect of the mesh size on the studied observables must be considered. In Figure 6.5(a), the circularity was computed for different mesh sizes for a standard case ($[Formaldehyde]_0$ = 0.750 M, $[SO_3{}^{2-}]_0$ = 0.068,$[HSO_3{}^-]_0$ = 0.053,and $[H^+]_0$ = $1.995\,x10^{-7}$ and Q = 20 mL/min.

The selected mesh size was the coarsest mesh for which the circularity showed less than 3% of the variation between two consecutive cases. Additionally, the pressure field across the radial coordinate at t = 0 s was measured (Figure 6.5(b)) for several mesh sizes (including the chosen one) to show that there was not observed any significant variation for the selected size.

Chapter 7

pH - Viscosity Coupling

Abstract: *This chapter will introduce the dynamic coupling between the pH-sensitive polymer (PAA) and the pH-shifting chemical reactions FS and FSG. This system exhibits dynamic changes in the viscosity attached to the pH of the solution which is controlled by the chemical reactions. A full detailed characterization will be made studying the effect produced by varying every component of the chemical formulations. This analysis will make it possible to understand the role played by each of the species in the system dynamics.*

7.1 Coupling Mechanism

In the original FS reaction presented in the introductory Section 1.5.2, the pH switch (*clock* behavior) is produced by the consumption of the sulfite/bisulfite buffer during the dehydration of the formaldehyde [212]. The addition of pH-sensitive polymer like the PAA (introduced in Section 1.9) in the reactive mixture makes it possible to remove the bisulfite from the original recipe. The reason for this is that the bisulfite needed for the reaction to occur is generated by a pH equilibrium displacement between the sulfite already present and the acidic environment provided by the dissociation of PAA [75]. In formal terms, this can be summarized by the following chemical mechanism:

$$\mathrm{PAA} \rightleftharpoons \mathrm{PA^-} + \mathrm{nH^+} \qquad \text{(R2'-1)}$$

$$\mathrm{SO_3{}^{2-}} + \mathrm{H^+} \rightleftharpoons \mathrm{HSO_3{}^-} \qquad \text{(R2'-2)}$$

where PAA = Poly(Acrylic Acid) and $\mathrm{PA^-}$ = Poly(Acrylate) ion.

As can be appreciated in the chemical model of the FS and FSG reactions introduced in Sections 6.2.1-6.2.2, the presence of $\mathrm{HSO_3{}^-}$ is provided by the $\mathrm{SO_3{}^{2-}}$ and the $\mathrm{H^+}$ released by the dissociation of the PAA in $\mathrm{H_2O}$. On basis of these considerations, reactions R2'-1 and R2'-2 can be included in Table 6.5 instead of reaction (R2). This addition does not alter the remaining equations and results in an effective coupling between the polymer and the reaction.

When the pH changes from an acidic into a basic state due to the formation of hydroxymethanesulfonate, the PAA molecule changes its conformational structure from globular into an elongated state. This structural change affects the viscosity of the system, synergistically occurring both phenomena. A schematics of the coupling mechanism is presented in Figure 7.1, where both, the typical pH-shift behavior of the FS reaction is shown with a molecular model of the Poly(Acrylic Acid).

As this is an equilibrium process, it is logical to suppose that similar results could be obtained using $\mathrm{HSO_3{}^-}$ instead of $\mathrm{SO_3{}^{2-}}$. The bisulfite can be used in the coupling with the polymer, but in such a

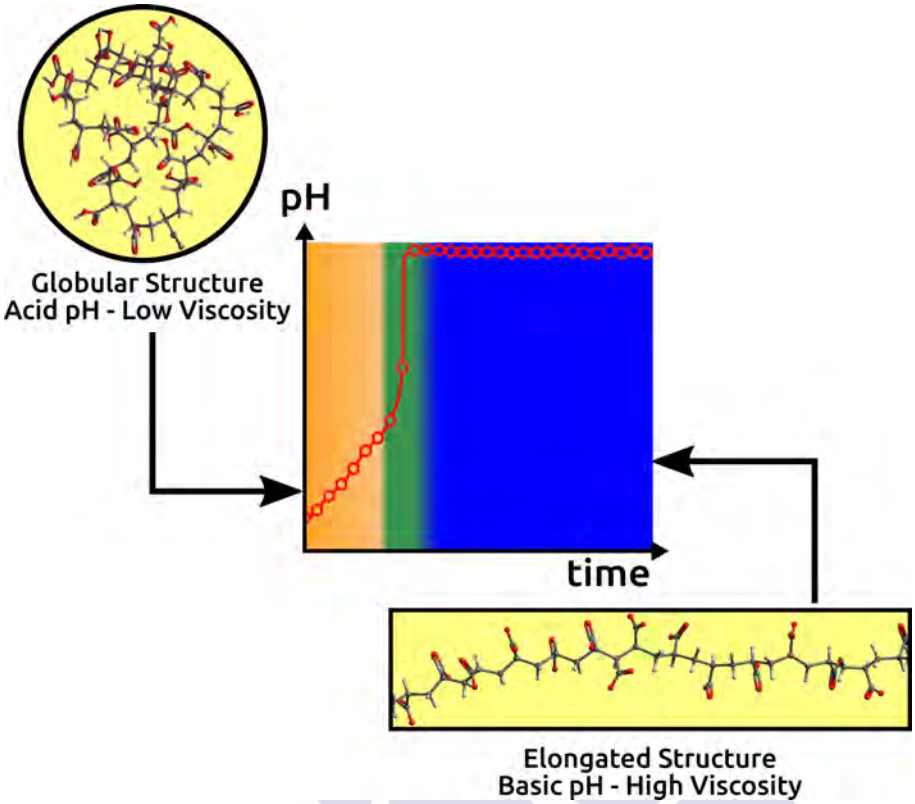

Figure 7.1: Schematic model of the pH-viscosity coupling produced by the pH-shifting dynamics of the FS reaction and the pH-sensitive character of the PAA molecule. The background of the plot indicates the color range of the Bromothymol blue molecule. The chemical model of the PAA molecule was created by the author using the open source software Avogadro v1.2.0 [85].

case, the presence of sulfite in the chemical system must be guaranteed. Because of this, the simplest way to obtain sulfite from bisulfite and PAA would be to displace the pH equilibrium by adding sodium hydroxide into the medium. Although this method could be used as an alternative route to obtain the *clock* behavior, it would increase the complexity of the coupling by adding NaOH as one more reagent. In any case, this alternative coupling was also studied. Results are presented in Section 7.5.

7.2 System Dynamics

Figure 7.2 presents the evolution of pH and viscosity for both, the FS-PAA and the FSG-PAA systems. Note that, for both cases, the viscosity evolves similarly to the pH curve. In the case of the FS-PAA system (Fig. 7.2(a)), the increase of viscosity correlates to the change in pH such that both show the characteristic *clock* shape. In a more complicated scenario, such as in the FSG-PAA system (Figure 7.2(b)), the *peak* shape exhibited by the pH is indeed simultaneously reproduced by the viscosity. Therefore, the temporal evolution of the viscosity is driven by the reaction kinetics and follows the same temporal signature as the modifications presented by the pH.

In order to better understand the pH/viscosity coupling, a complete characterization of the effects that each of the species produces on the system is presented in the forthcoming sections.

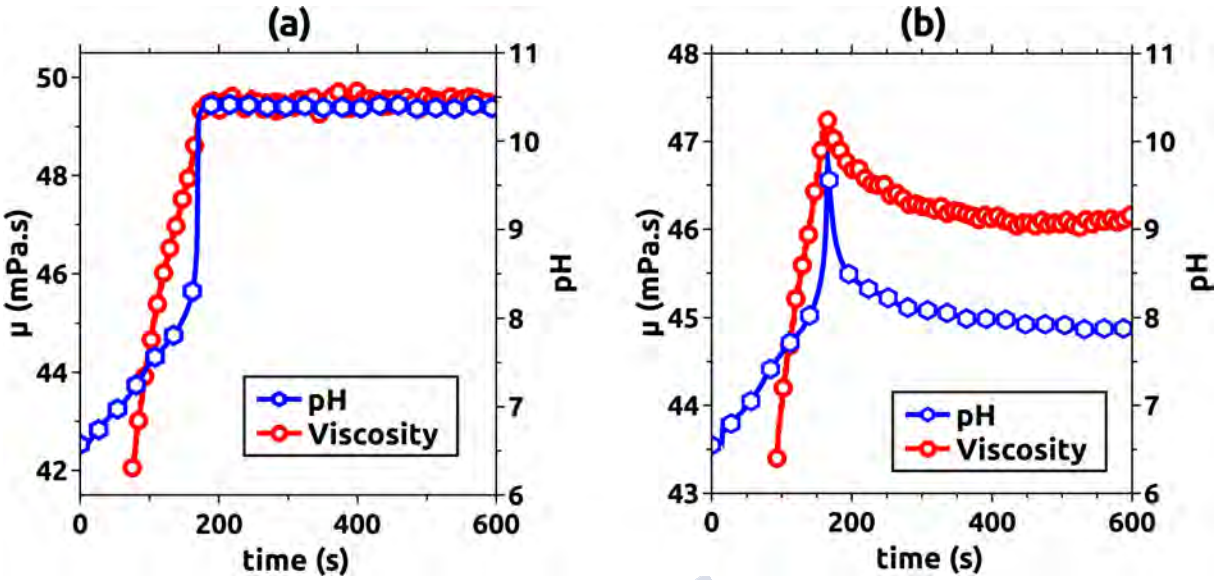

Figure 7.2: Temporal evolution of pH and viscosity for the (a) FS-PAA and (b) FSG-PAA systems. In both cases $[SO_3{}^{2-}]_0$ = 0.068 M, $[PAA]_0$ = 0.438 wt% and $[Formaldehyde]_0$ = 0.065 M. In (b) $[GL]_0$ = 0.007 M. The shear rate and the temperature were fixed at 500 s^{-1} and 23°C, respectively. This Figure was adapted from Escala *et al* [62].

7.3 FS-PAA System Characterization

Figures 7.3-7.5 summarize all the different behaviors observed by varying the initial chemical concentrations in the FS-PAA system. The system behavior was studied by measuring the temporal evolution of the pH, the viscosity and pH variations (both defined as $\Delta\mu = \mu_{final}$ - $\mu_{initial}$ and $\Delta pH = pH_{final}$ - $pH_{initial}$, respectively) and the induction time, that is defined as the time needed for the system to switch from an acidic into a basic state.

7.3.1 $[PAA]_0$ Variation

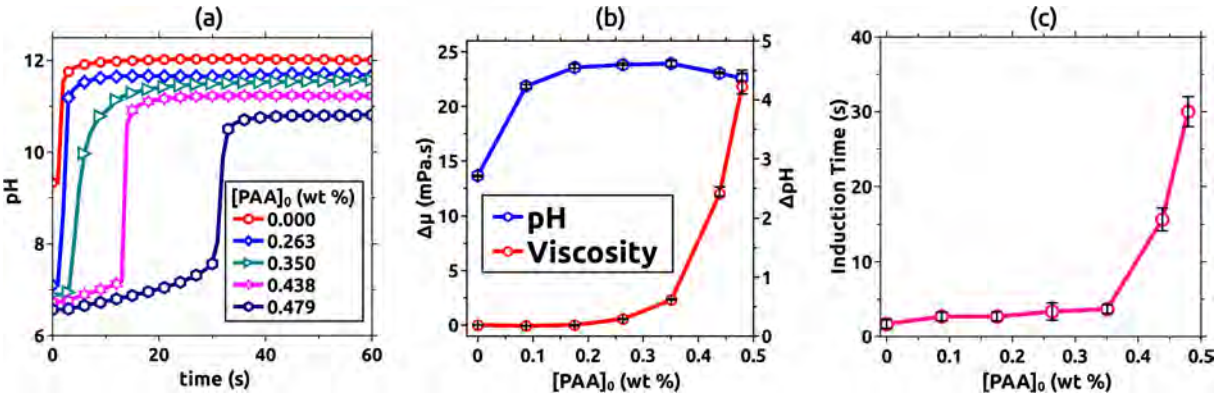

Figure 7.3: Characterization of the FS-PAA system by varying $[PAA]_0$ and setting $[SO_3{}^{2-}]_0$ = 0.068 M and $[Formaldehyde]_0$ = 0.093 M: (a) pH temporal evolution, (b) $\Delta\mu$ and ΔpH, and (c) induction time variation. The shear rate and the temperature were set constant at 500 s^{-1} and 23 °C respectively. This Figure was adapted from Escala *et al* [62]

Figure 7.3(a) analyzes the effect of increasing the initial concentration of PAA while keeping

all other initial concentrations constant (namely, the formaldehyde and sulfite initial concentrations). Several effects were observed when the PAA concentration was increased. The initial pH was drastically reduced from 9.3 down to values around 7 due to the acidity of the polymer solution. The final value of the clock was also lowered down by 2 pH units. The global ΔpH difference (Fig. 7.3(b)) did not reflect measurable changes with the polymer concentration (even though it showed some slight reduction for $[PAA]_0 > 0.25$ wt%) but it was, in any case, significantly larger compared to the case without PAA. This was in contrast with the viscosity jump $\Delta\mu$, which presented a sudden sharp increase when the PAA concentration was increased above 0.35 wt%.

Besides, by increasing the polymer concentration, the FS-PAA system showed longer induction times (i.e. longer interval of time required to jump to the final stable pH value), which was particularly noticeable for PAA concentrations larger than 0.35 wt% (see Fig. 7.3(c)). The addition of polymer to the pH clock reaction produced an increment in the viscosity difference for all the studied PAA concentrations. However, ΔpH increased for $[PAA]_0 \leq 0.35$ wt% and slightly decreased for larger concentrations. The best balance between pH jumps and viscosity jumps was observed for a PAA initial concentration of 0.438 wt%. For such a reason, this concentration was used for analyzing the remaining cases.

Figure 7.4 confirms that the polymer is the key ingredient to couple the clock reaction and the viscosity changes. The PAA affected the system in a similar way as the bisulfite from the original recipe [106]. In this sense, the pool of protons generated by the PAA dissociation provided the acidic environment needed to obtain the bisulfite by equilibrium displacement from the sulfite already present in the system. By this process, the consumption of the sulfite/bisulfite buffer by the formaldehyde dehydration is the step responsible for the clock behavior, improved with the additional gain of a large viscosity change.

7.3.2 $[SO_3^{2-}]_0$ Variation

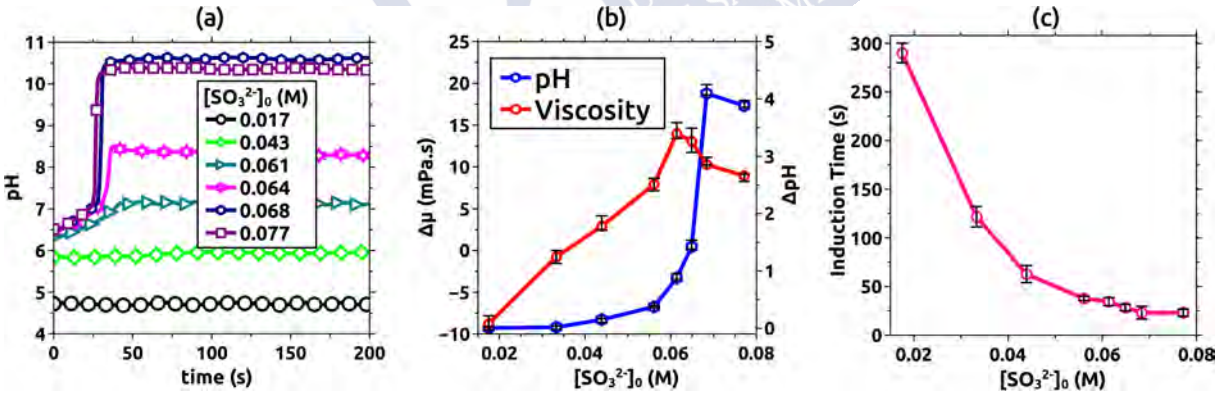

Figure 7.4: Characterization of the FS-PAA system by varying $[SO_3^{2-}]_0$ and setting $[Formaldehyde]_0 = 0.093$ M and $[PAA]_0 = 0.438$ wt%: (a) pH temporal evolution, (b) viscosity and pH jumps (measured as the difference between the final and initial values), and (c) induction time variation. The shear rate and the temperature were set constant at 500 s^{-1} and 23 °C respectively. This Figure was adapted from Escala *et al* [62]

Several differences in the clock behavior were observed when changing the initial sulfite concentration as presented in Figure 7.4. The increment in the sulfite concentration produced an increment in both, the initial and final pH values (the former, particularly noticeable for $[SO_3^{2-}]_0 > 0.061$ M and the later, for larger concentrations of $[SO_3^{2-}]_0$). In addition, such increment also produced a decrease in the induction time (Fig. 7.4(C)). The maximum viscosity difference did not match with the maximum difference in pH (Fig. 7.4(b)). The reason for this disagreement was because

for concentrations $[SO_3{}^{2-}]_0 < 0.061$ M, the viscosity increased due to the basic character of the solution. Above this concentration, the ionic strength became stronger and inhibited the repulsive effects of the polymer chains preventing a full elongation which produced a limitation in the viscosity change [195]. The negative viscosity differences observed for low sulfite concentrations were produced by the acidic character of the formaldehyde solution. A low sulfite concentration was not enough to buffer this effect and, as a consequence, the final viscosity was smaller compared to the initial one.

7.3.3 [Formaldehyde]$_0$ Variation

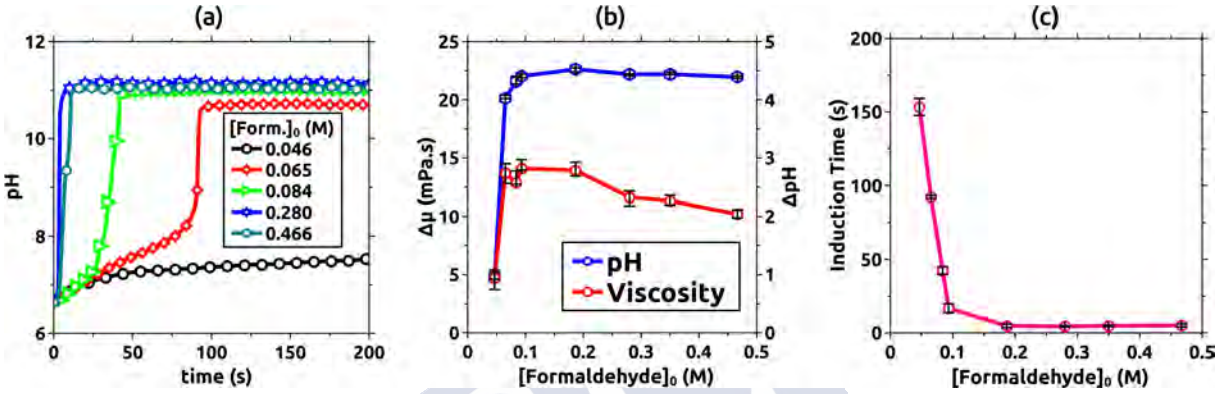

Figure 7.5: Characterization of the FS-PAA system by varying [Formaldehyde]$_0$ and setting $[SO_3{}^{2-}]_0 = 0.068$ M and [PAA]$_0$ = 0.438 wt%: (a) pH temporal evolution, (b) $\Delta\mu$ and ΔpH, and (c) induction time variation. The shear rate and the temperature were set constant at 500 s^{-1} and 23 °C respectively. Figure adapted from Escala *et al* [62]

Figure 7.5, shows the effect of varying the formaldehyde initial concentration. In the temporal pH evolution 7.5(a), two distinct behaviors were observed: increasing the formaldehyde initial concentration up to 0.084 M was accompanied by a drastic increase of the final pH value and a decrease of the induction time (Figure 7.5(c)). Experiments performed with [Formaldehyde]$_0 > 0.084$ M did not reflect significant changes in these features. Both viscosity and pH curves had a steep increment for formaldehyde concentrations below 0.065 M (see Fig. 7.5(b)). Above 0.065 M the differences between the final and the initial pH values remained almost constant. For the viscosity, the curve showed a similar shape compared with the pH curve, however, the variation decreased when the formaldehyde concentration was increased.

7.4 FSG-PAA System Characterization

In this section, the effect of changing initial concentrations of reagents is analyzed for the FSG-PAA system to understand whether the addition of gluconolactone can help to reset the clock and, thus, achieve a viscosity peak in the system.

7.4.1 [GLN]$_0$ Variation

Figure 7.6 presents a summary of the different results observed. In this case, the analysis was centered on studying the effects of the presence of gluconolactone on both the chemical and the viscosity variations. Hence, all these experiments were carried out with [Formaldehyde]$_0$ = 0.093 M, $[SO_3{}^{2-}]_0$ = 0.068 M and [PAA]$_0$ = 0.438 wt% and only varying the initial concentration of gluconolactone ([GLN]$_0$). For low initial concentrations of gluconolactone, a *clock* behavior with a jump in pH of around 4 units

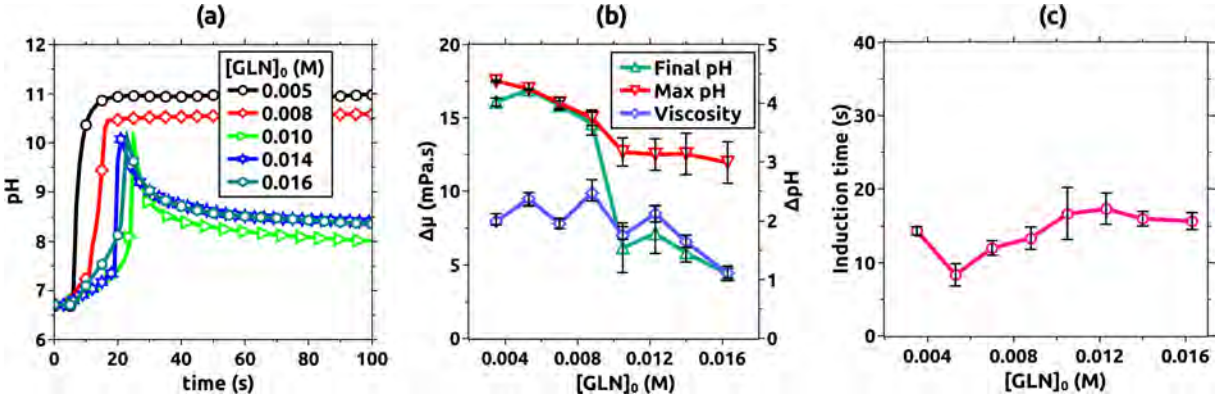

Figure 7.6: FSG-PAA system characterization for different concentrations of $[GLN]_0$. (a) pH vs. time curves. (b) Maximum pH difference, final pH, and viscosity. (c) Variations of the induction time with $[GLN]_0$. The maximum (final) pH gap was measured as the difference between the maximum (final) pH value and the initial pH value. The experimental conditions were kept constant and equal to: $[SO_3^{2-}]$ = 0.068 M, $[PAA]_0$ = 0.438 wt% and $[Formaldehyde]_0$ = 0.093 M. This Figure was adapted from Escala *et al* [62]

was observed (the smaller the GLN concentration, the larger the final pH value and, consequently, the larger the pH difference). By smoothly increasing the concentration of gluconolactone, was possible to appreciate a transition (around $[GLN]_0$ = 0.01 M) from the clock shape to the characteristic *peak* behavior of the FSG reaction (Fig. 7.6(a)), where the pH reached a maximum value and then decayed to a new stable value (typically larger compared to the initial one). As observed in Figure 7.6(c), the induction time did not show significant changes with the GLN concentration, as it remains around (14 ± 4) seconds.

In Figure 7.6(b), two different pH variations were measured. (ΔpH) was defined as the differences between the maximum pH value (this is, the pH value observed at the *peak*) and the initial pH value (so-called Max pH), and between the final and the initial values (so-called Final pH). Both curves showed similarities for low values of GLN while they differed once the *peak* behavior was manifested in the reaction. Note that the error bars of the results increased in those experiments where this *peak* was observed, which indicates the complexity of adding a time-dependent reagent into the system, as the gluconolactone hydrolysis varies with time [107, 108].

Even with the presence of PAA, the hydrolysis of the gluconolactone produced the delayed negative feedback needed to generate the pH pulse [107]. As the difference in viscosity between the maximum and final values was almost negligible (a few mPa s in the case shown in Figure 7.2(b)), ($\Delta\mu$) was calculated as the viscosity difference between the final stable state and the initial value. It was observed that $\Delta\mu$ did not show significant variations by changing $[GLN]_0$. Even if there was an increment in the final pH value, the presence of gluconolactone produced a dampening in the viscosity change via its soft acidic features [104].

7.5 The FS-PAA Alternatives

The next two sections will show the versatility of the pH-viscosity coupling by adding several modifications to the original FS-PAA system. These modifications were useful to confirm the proposed mechanism introducing alternatives that can be used in future developments.

7.5.1 The Effect of Using HSO_3^{2-} and NaOH

As mentioned in Section 7.1, another possible route to couple the PAA polymer with the FS reaction is by replacing the sulfite from the FS-PAA system with bisulfite and sodium hydroxide (hereafter called FBS-PAA system). Due to the acidic character of the polymer, the bisulfite requires the presence of sodium hydroxide to obtain enough sulfite to produce the *clock* behavior. This is illustrated by the following mechanism:

$$PAA \rightleftharpoons PA^- + nH^+ \quad \text{(R2"-1)}$$

$$NaOH \rightleftharpoons Na^+ + OH^- \quad \text{(R2"-2)}$$

$$HSO_3^- + OH^- \rightleftharpoons SO_3^{2-} + H_2O \quad \text{(R2"-3)}$$

$$SO_3^{2-} + H^+ \rightleftharpoons HSO_3^- \quad \text{(R2"-4)}$$

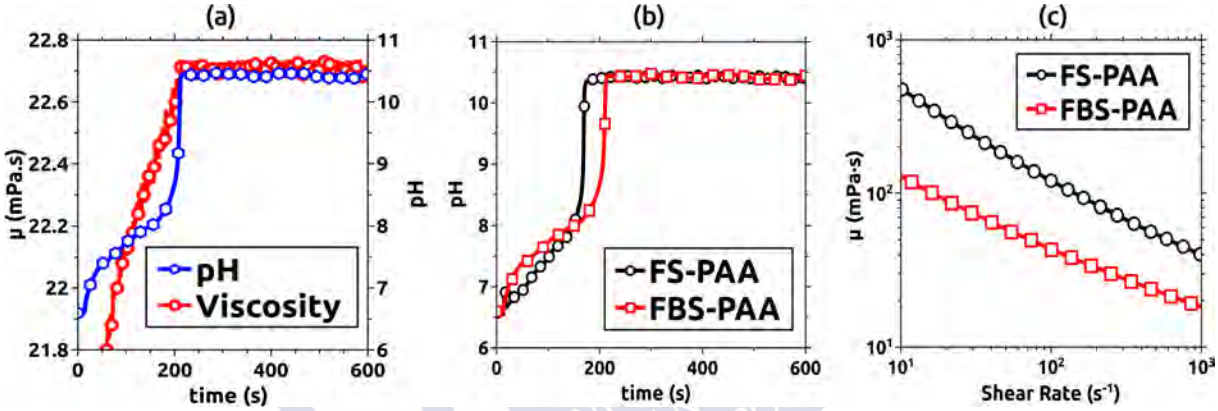

Figure 7.7: Comparison of FS-PAA and FBS-PAA reaction dynamics. For the sulfite reaction: $[SO_3^{2-}]_0 = 0.068$ M, $[\text{Formaldehyde}]_0 = 0.065$ M. For the modified reaction with bisulfite: $[HSO_3^-]_0 = 0.068$ M, $[NaOH]_0 = 0.092$ M and $[\text{Formaldehyde}]_0 = 0.093$ M. In all cases $[PAA]_0 = 0.438$ wt%. (a) Viscosity and pH temporal evolution for the FBS-PAA reaction. All viscosity measurements were performed fixing the shear rate at 500 s^{-1}. (b) pH as a function of time compared for the FS-PAA and FBS-PAA reactions. (c) Viscosity as a function of shear rate for both reactions. This Figure was adapted from Escala *et al* [62]

Figure 7.7(a) shows the temporal evolution of the pH and the viscosity for the FSB-PAA reaction when $[HSO_3^-]_0 = 0.068$ M, $[NaOH]_0 = 0.092$ M, $[\text{Formaldehyde}]_0 = 0.098$ M and $[PAA]_0 = 0.438$ wt%. In this case, the viscosity behaved similarly to the bisulfite case. However, even if the pH and viscosity curves match in shape, the viscosity variation between the initial and final state was considerably smaller in comparison with the original recipe (Fig. 7.2). As can be seen in the results, this procedure was effective to reproduce the dynamics of the reaction, but it had negative effects on the resulting dynamic viscosity. This detrimental effect is also observed in Figure 7.7(c), where the final viscosity values for both reactions are compared for all shear rates between 10 s^{-1} and 1000 s^{-1}. As can be seen, the FSB-PAA reaction is always less viscous than the FS-PAA reaction.

Regarding the pH dynamics, both reactions are compared in Figure 7.7(b). In this case, the curves exhibit a similar transition of pH in time where initial and final pH values being nearly the same, but the induction time in the FSB-PAA reaction was mildly delayed compared to the sulfite reaction.

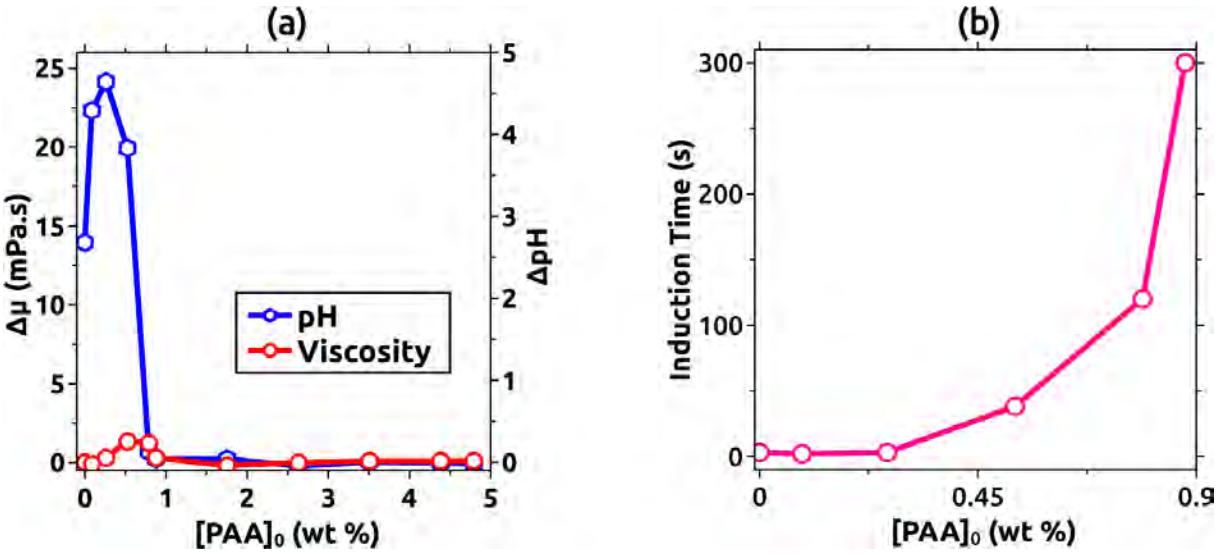

Figure 7.8: FS-PAA reaction replacing the PAA-4x10^6 g mol^{-1} with PAA-4.5x10^5 g mol^{-1}. For these experiments $[SO_3{}^{2-}]_0$ = 0.068 M and $[\text{Formaldehyde}]_0$ = 0.093 M. The shear rate and the temperature were fixed at 500 s^{-1} and 23 °C, respectively. a) Comparison between pH and viscosity difference between the initial and final values. b) Induction time variation by increasing the polymer concentration. This Figure was adapted from Escala *et al* [62]

7.5.2 The Effect of Using a Short-Chain PAA Molecule

Figure 7.8 shows an analogous analysis for the FS-PAA reaction, but replacing the PAA-4x10^6 g mol^{-1} with another one with shorter length chains (PAA-4.5x10^5 g mol^{-1}). In this case, the polymer dissociation and rheology were completely different from the original system (Figure 7.2). As can be observed in Figure 7.8(a), by fixing the sulfite and formaldehyde initial concentrations, the maximum pH and viscosity differences were obtained for concentrations of $[\text{PAA}-4.5\,\text{x}10^5\,g\,mol^{-1}]_0$ in the interval [0-1] wt%. For higher concentration values, there was no significant difference between the initial and final states.

Although the maximum pH difference was comparable with that obtained with the larger polymer, the maximum viscosity difference was significantly lower (the viscosity axis in figure 7.8(a) uses the same range of Figures [7.3-7.5](b) for better comparison). This result can be explained by considering the polymer length chain. A short chain has less carboxylic groups. When the pH shifts from acid to basic due to the *clock* reaction, the repelling effect produced by the carboxylate ions is lower. This fact, in addition to the presence of quenching ions like Na^+, translates into a less viscosity increment. Despite this, as a change in the viscosity was observed, the coupling between the reaction and the polymer was confirmed.

Figure 7.8(b) shows how the induction time was increased by increasing the polymer concentration, analogously as the system with the larger polymer. For [PAA-4.5x10^5 g mol^{-1}] concentrations above 0.8 wt%, it was impossible to measure the induction time because no *clock* behavior was observed.

7.6 Overlap Concentration

One last consideration has to be made regarding the viscosity of the solutions. More specifically, to the effect of the PAA concentration in the viscosity increment. In this sense, it is important to demonstrate that such viscosity growth (like the one observed in Figure 7.3(b)) was not produced as an artifact associated with the polymer overlap concentration (c^*) [195, 148, 62].

Particularly for the PAA, the overlap concentration is not a single value and depends on the polymer dissociation which, at the same time, is related to the pH of the solution. For concentrations above c^*, the rheological behavior of the solution is affected by the interaction between polymer molecules and, consequently, the viscosity changes due to elasticity effects.

According to previous works [195], the overlap concentration c^* can be estimated as:

$$c^* = \frac{M_w}{R_g^3 N_A} \tag{7.1}$$

where M_w is the molecular weight, R_g is the radius of gyration and N_A is the Avogadro number.

Thus, c^* is inversely proportional to the length of the polymer molecule. However, for PAA molecules, R_g varies depending on the dissociation degree of the polymer which, in turn, depends on the pH of the solution [104]. Nevertheless, as was previously described, for higher pH values the ionic strength provided by the sodium ions (already dissolved in the solution) quenches the electrostatic repulsion produced by the carboxylic groups [104]. This prevents a full elongation of the PAA molecules [104] that can be translated into a low R_g value, and therefore, in a much lower viscosity compared to a solution of PAA in pure water. Despite this, c^* can be estimated by the method described in Palencia *et al* [148]. For the PAA-4x10^6 g mol^{-1}, the estimated value of the overlap concentration was: $c^* \cong$ 2.64 wt% which is far from those values previously presented (up to 0.5 wt%, for the stock solution). Analogously, the same procedure was used to estimate c^* for the short length polymer (PAA-4.5x10^5 g mol^{-1}). In this case, the value was: $c^* \cong 8.33$ wt%, which is one order of magnitude above the range of concentrations used for this polymer (Figure 7.8(a)). These measurements demonstrated that all changes observed in the viscosities were directly driven by the interaction between the FS reaction and the PAA.

7.7 Chapter Discussion

This chapter presented a novel route to couple a pH-responsive polymer with two pH-shifting chemical reactions (the FS and the FSG reactions) to obtain viscosity variations linked to changes in pH.

The addition of the polymer affected the chemistry of the FS system by producing longer induction times in the clock behavior. It also enhanced the viscosity gap between the initial and final states. On the other hand, the effects produced by varying the concentrations of sulfite and formaldehyde on the dynamics of the FS-PAA reaction, were similar to those reported in the original recipe by Kovacs *et al.* [106].

In the FSG-PAA system, it was observed that the increase of the gluconolactone produced the transition from a clock to a peak shape in both the pH and viscosity temporal changes.

Although the work here presented was exclusively centered on the use of PAA polymers, the same protocol can be extended to couple similar pH-sensitive polymers with chemical systems. This was studied for a particular case in Section 7.5.2 where similar dynamics were obtained by adapting the system to a short length polymer.

The presence of positive and negative feedbacks in the FSG polymer-modified system opens the possibility to obtain pH and viscosity temporal oscillations when the reaction is run in an open continuously stirred tank reactor (CSTR) [106, 108, 107]. The presence of oscillatory viscosity solutions linked to pH temporal modulations would be of particular interest in a variety of fields ranging from nonlinear chemistry to more applied fields, such as testing *in-vitro* drug delivery in a controlled way.

USC
UNIVERSIDADE
DE SANTIAGO
DE COMPOSTELA

Chapter 8

Viscous Fingering Induced by the FS-PAA Reaction

Abstract: *In the previous chapter, it has been shown that a clock-type change in the viscosity of a liquid can be obtained by coupling the pH-sensitive polymer PAA with a pH-changing clock reaction [106, 108, 107, 62]. This paves the way to a more sensitive control of viscous fingering using the power of nonlinear chemical reactions [57, 25] to modulate the viscosity in situ both in time and space. In this context, this chapter aims to explore the possibility to adapt the results obtained in Chapter 7 and use them to trigger and control viscous fingering instability in a horizontally oriented Hele-Shaw cell. The study will be focused on the effects of changing the control parameters associated with the hydrodynamics and the chemistry independently. The forthcoming sections will address the occurrence of chemically induced viscous fingering obtained by spatially extending the FS-PAA reaction. Fluid instability is obtained when a low-viscosity solution of formaldehyde is displaced radially by a high-viscosity solution of PAA exhibiting large and well-controlled changes in pH [106, 212, 213, 62].*

8.1 General System Overview

Figure 8.1 shows the dynamics of the spatially extended FS-PAA reaction when the initial concentration of formaldehyde is varied and the other reagent concentrations are kept constant ($[PAA]_0$ = 0.438 wt%, $[SO_3{}^{2-}]_0$ = 0.068 M and $[C.I.]_0$ = 0.021 wt%). The chemical conditions were chosen as the optimal values to maximize the differences between the initial and the final pH and viscosity in a batch reactor obtained from the extensive analysis presented in Section 7.3. All protocols and formulation details regarding the Hele-Shaw cell experiments are given in Sections 6.1.3 and 6.1.4.

Each row shows the temporal evolution of one experiment in addition to a schematic plot of the spatial viscosity profile for the same configuration. Figure 8.1(a) shows the control experiment where the displaced solution was replaced by pure water. Due to the absence of reactivity between the involved solutions, the displacement was hydrodynamically stable, as the viscosity of the displacing polymeric solution was larger than that of the displaced water. Hence, the front remained circular without any fingering instability. This behavior is coherent with the schematic viscosity profile shown in the last column of the first row, where the viscosity profile remains stable throughout the whole experiment due to the lack of reaction.

When the concentration of formaldehyde was nonzero in the displaced solution (Figure 8.1(b),(c)), a blue contour associated with a zone of high pH was observed in the contact zone between both liquids. This blue color indicates the occurrence of the pH-changing reaction between formaldehyde

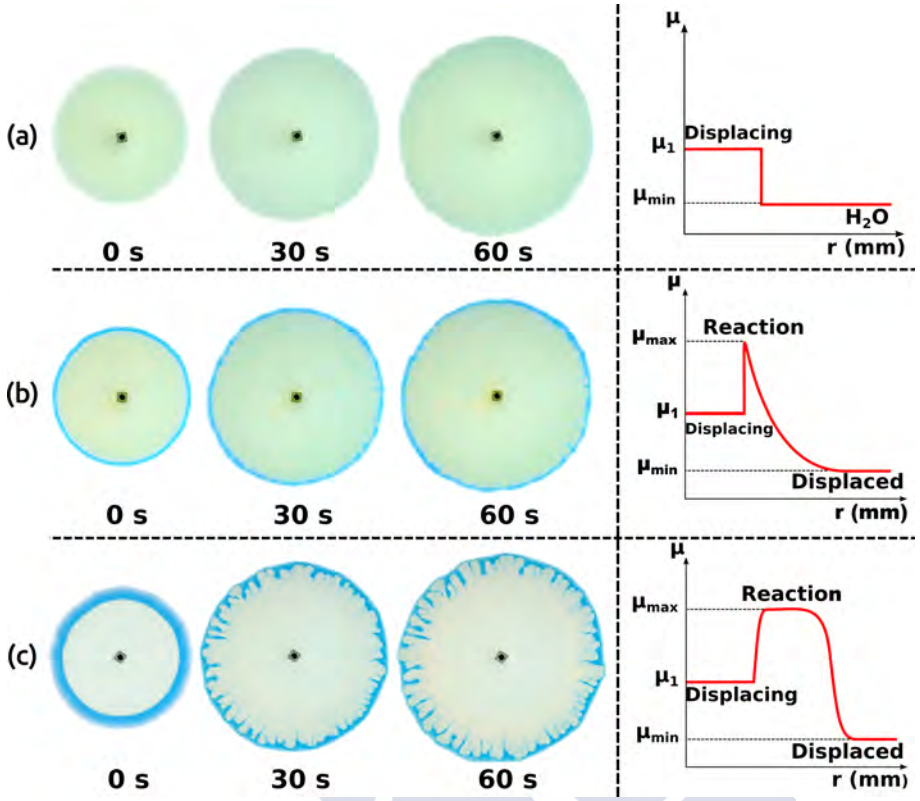

Figure 8.1: Comparison of three experiments where the $[\text{Formaldehyde}]_0$ in the displaced solution is (a) 0 M, (b) 0.049 M, and (c) 0.75 M. In all three cases, the concentrations of other reagents were kept constant at $[\text{PAA}]_0$ = 0.438 wt%, $[SO_3{}^{2-}]_0$ = 0.068 M, and $[\text{C.I.}]_0$ = 0.021 wt%. The displacing solution was injected at a flow rate of 7 mL/min after obtaining the initial condition as described in Section 6.1.4. In the last column, schematic profiles corresponding to each initial condition are shown, indicating the minimum (μ_{min}), maximum (μ_{max}), and displacing solution (μ_1) viscosities. This Figure was taken from Escala *et al* [58].

in the displaced fluid and the sulfite/bisulfite dissolved in the injected solution. The thickness of this blue contour increased in time due to diffusion and reaction in the radial geometry [23]. At a fixed time, the thickness of the reaction zone depended on the values of the reaction parameters. Typically, in Figure 8.1(b), although the blue contour was appreciated, the low formaldehyde concentration (0.049 M) generated only a thin blue contour in which the viscosity increase was too low and not extended enough to trigger a viscous fingering instability (see also the schematic viscosity profile). The displacement front remained therefore essentially circular, with very small or negligible perturbations. In the last case (Figure 8.1(c)), the formaldehyde concentration was large enough (0.750 M) to generate a wider zone of larger viscosity, which makes the emergence of a well-defined fingering instability possible.

8.2 Descriptive Analysis

Changes in the morphology of the viscous fingering patterns were studied by varying the flow rate (Q), the formaldehyde concentration in the displaced solution, and the sulfite concentration in the displacing solution. The results presented here provide a qualitative description of how the system is affected by changing some of the main parameters.

As can be noted, the range of concentrations studied differs from those used to study the FS-PAA reaction in a stirred system. This is because, inside the Helle-Shaw cell diffusive effects and interfacial concentrations affect the reaction dynamics and, consequently, affect the spatial profile of pH and

viscosity.

8.2.1 Flow Rate Effect

The effects produced by flow rate variations were studied by keeping the displacing and displaced solution formulations unaltered. The results are presented in Figure 8.2. As can be observed, the system became more unstable as Q was increased. The effect of the flow rate in viscous fingering instabilities was extensively studied and it is intrinsically associated with the stability of the system [93, 193, 88, 44, 48, 47, 23]. In this case, the system switched from a more circular shape (for Q = 2.5 - 7 mL/min) (where fingers were almost imperceptible) to a more deformed shape (for Q = 10 - 20 mL/min) where fingering instability was observed.

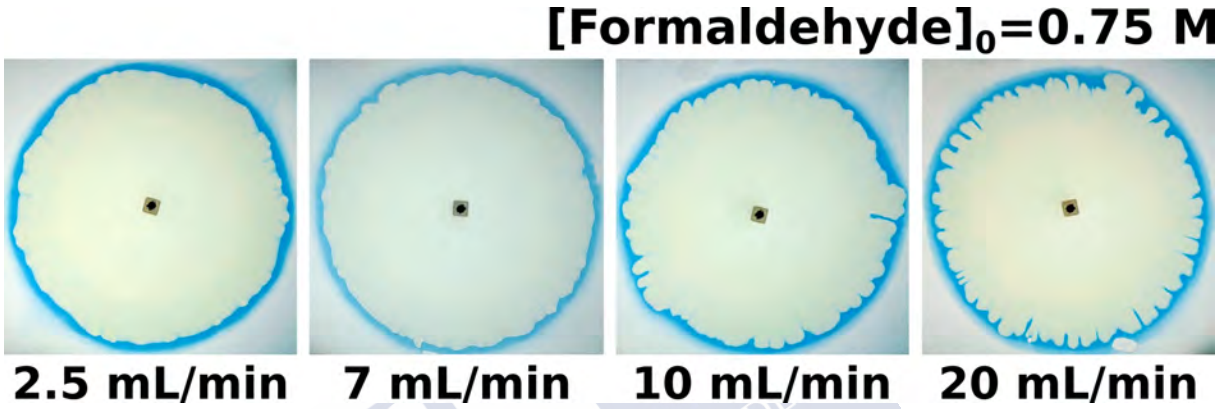

Figure 8.2: Experimental observations of the fingering instability at different flow rates for the same initial concentrations: [Formaldehyde]$_0$ = 0.750 M and [SO_3^{2-}]$_0$ = 0.068 M, [PAA]$_0$ = 0.438 wt% and [C.I.]$_0$ = 0.021 wt%. This Figure was adapted from Escala *et al* [58].

8.2.2 [Formaldehyde]$_0$ Variation in the Displaced Solution

By varying the formaldehyde initial concentration and keeping constant the flow rate and the displacing formulation (Figure 8.3, it was possible to observe that the instability of the system increased proportionally to [Formaldehyde]$_0$. This observation agrees with the results presented in Figure 8.1.

Firstly, as shown in Figure 7.5 of the previous Chapter, larger formaldehyde concentration produced a faster change in the pH of the FS-PAA reaction making the ΔpH larger. $\Delta\mu$ was in part increased for a certain range of concentrations as well. Secondly, the thickness of the blue reactive zone was also increased proportionally to [Formaldehyde]$_0$ as can be observed in Figure 8.1. A wider reactive zone of larger viscosity facilitates the fingering formation.

8.2.3 [SO_3^{2-}]$_0$ Variation in the Displacing Solution

In this case, the flow rate and the formaldehyde of the solution were kept constant to 7 mL/min and 0.750 M respectively, while the sulfite initial concentration in the displacing solution was changed. The results are presented in Figure 8.4.

Neither pattern nor the reactive zone was observed for [SO_3^{2-}]$_0 \leq$ 0.043 M. In these cases, the displacing solution adopted a yellowish coloration due to the acidic state of the color indicator at low pH. The absence of any pattern or reactive zone was expected as it is needed a minimum concentration of sulfite for the FS-PAA reaction to occur. The same phenomenon was observed in the homogeneous system (Figure 7.4).

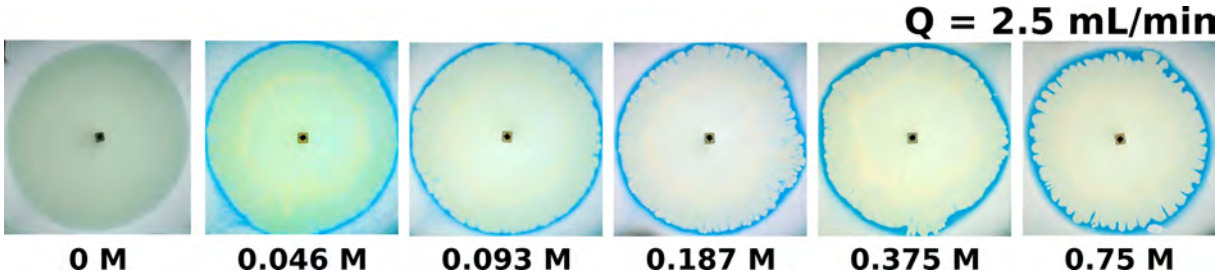

Figure 8.3: Experimental observations of the fingering instability for different [Formaldehyde]$_0$ at constant Q = 2.5 mL/min. For all cases, [PAA]$_0$ = 0.438 wt%, [C.I.]$_0$ = 0.021 wt% and [SO_3^{2-}]$_0$ = 0.068 M. This Figure was adapted from Escala *et al* [58].

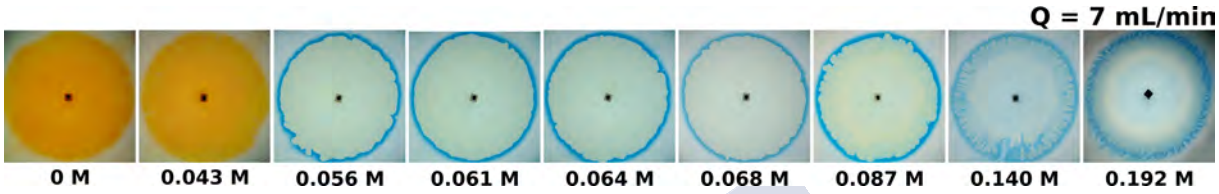

Figure 8.4: Experimental observations of the fingering instability for different [SO_3^{2-}]$_0$ at constant Q = 7 mL/min. For all cases, [Formaldehyde]$_0$ = 0.750 M, [PAA]$_0$ = 0.438 wt% and [C.I]$_0$ = 0.021 wt%. This Figure was adapted from Escala *et al* [58].

For the intermediate range of concentrations studied (0.056 M $\leq$ [SO_3^{2-}]$_0$ $\leq$ 0.087 M), the system became more unstable. This decrement in the stability of the system was associated to the increment in viscosity at the displacing-displaced interface produced by PAA – SO_3^{2-} interaction.

Finally, for the largest concentrations ([SO_3^{2-}]$_0$ $\geq$ 0.140 M), the obtained patterns showed some differences from the previous cases. Firstly, there was not any clear separation between the blue interface and the displacing solution. This change in coloration was produced by the high pH associated with the increment in the sulfite concentration (blue is the basic state of C.I.). Particularly, for [SO_3^{2-}]$_0$ = 0.193 M, the quenching effect observed for larger sulfite concentrations (Fig. 7.4) affected the pattern formation by making a more stable displacement.

8.3 Quantitative Analysis

8.3.1 Interface Thickness

The change of the interface thickness (or initially mixed area) was studied for several formaldehyde and sulfite initial concentrations. The results are presented in Figure 8.5. The thickening of the blue contour produced by an incremented formaldehyde initial concentration is presented in Figure 8.5(a). The measured thickness varied from 0 mm in the control experiment, ([Formaldehyde]$_0$ = 0 M), up to an average value of 11.8 mm for [Formaldehyde]$_0$ = 0.750 M. The effects of varying the sulfite concentration is shown in Figure 8.5(b). In this case, lower sulfite concentrations produced almost no reactivity until [SO_3^{2-}]$_0$ $\geqslant$ 0.056 M. Above this value, the thickness continuously increases until [SO_3^{2-}]$_0$ = 0.087 M. For concentrations above this value, the thickness decreased slowly. Another remarkable effect is that the blue contour becomes fuzzy for [SO_3^{2-}]$_0$ $\geqslant$ 0.087 M (inset b_2) in contrast to the sharp boundary observed for [SO_3^{2-}]$_0$ = 0.056 M (inset b_1). These two effects may be produced by the decrement in viscosity produced by a high sulfite concentration (due to electrostatic quenching as presented in Section 1.9).

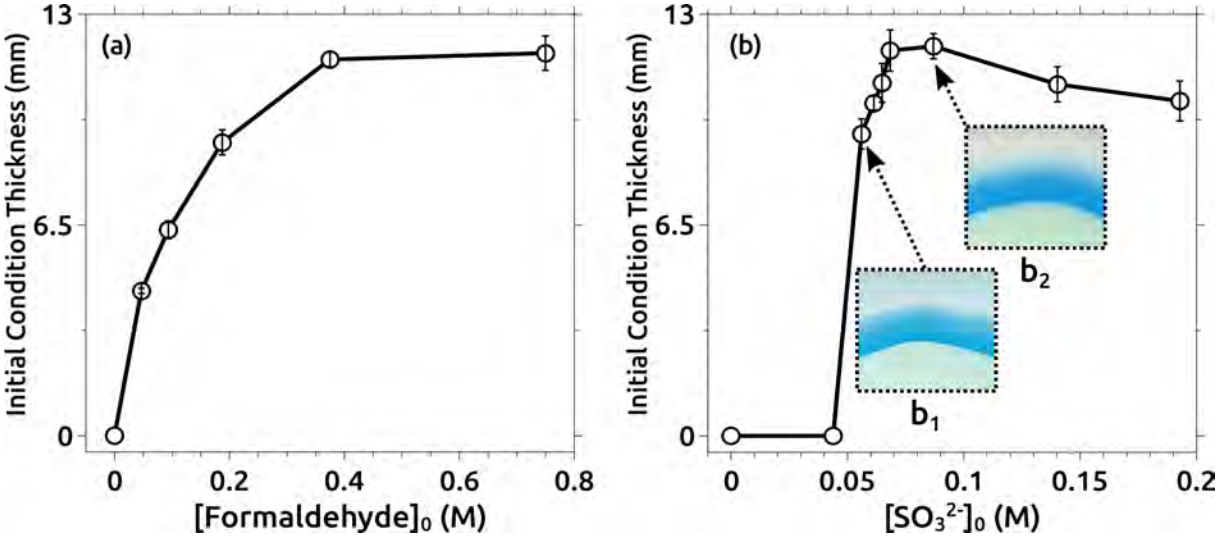

Figure 8.5: Initial condition thickness as a function of (a) $[\text{Formaldehyde}]_0$ at $[SO_3{}^{2-}]_0 = 0.068$ M and (b) $[SO_3{}^{2-}]_0$ at $[\text{Formaldehyde}]_0 = 0.750$ M. All measurements were done 3 h after the injection in the Hele-Shaw cell of 3 mL of the displacing solution in which $[\text{PAA}]_0 = 0.438$ wt% and $[\text{C.I.}]_0 = 0.021$ wt%. Insets (b_1) and (b_2) show the fuzziness at the interface for $[SO_3{}^{2-}]_0 = 0.061$ M and $[SO_3{}^{2-}]_0 = 0.087$ M, respectively. This Figure was taken from Escala *et al* [58].

8.3.2 Circularity Variation

As indicated in Section 6.1.5, the circularity (C) was chosen as the preferred shape descriptor to quantify the morphological changes of the fingering patterns produced by modifications in the displacing/displaced solutions. More information regarding the image processing protocol used for this calculation is included in Appendix C.2.1.

Some other observables were used in the literature to describe the nature of the fingers such as fingering density area (d_A) or the fractal dimension (d_F) [65, 142, 139, 194]. In this work, the circularity was chosen as it provides a more accurate description due to the limited area where the fingers are confined. Nevertheless, the results were also analyzed by traditional methods as a comparative checking. Those results are presented in Appendix Section C.2.2.

Dependence on $[\text{Formaldehyde}]_0$

In Figure 8.6, the effect of the formaldehyde initial concentration is shown for four different flow rates at constant $[\text{PAA}]_0 = 0.438$ wt%, $[SO_3{}^{2-}]_0 = 0.068$ M, and $[\text{C.I.}]_0 = 0.021$ wt%. An increasing flow rate gave smaller circularity values. This result is associated with the well-known destabilizing effect of increasing the flow rate on fingering [93] (Fig. 8.2). Additionally, an increment of the formaldehyde initial concentration also destabilized the system, allowing the generation of viscous fingering between the two solutions. For lower formaldehyde concentrations, the reaction zone was thinner, making the system more stable and, thus, the circularity value was closer to 1. For all formaldehyde concentrations below 0.2 M, the larger the flow rate, the more important the destabilization was. However, for $[\text{Formaldehyde}]_0 > 0.2$ M, the circularity increased again when the formaldehyde concentration was increased for all flow rates studied except for 20 mL/min. All these results are in line with the qualitative analysis presented in Figures 8.2-8.3

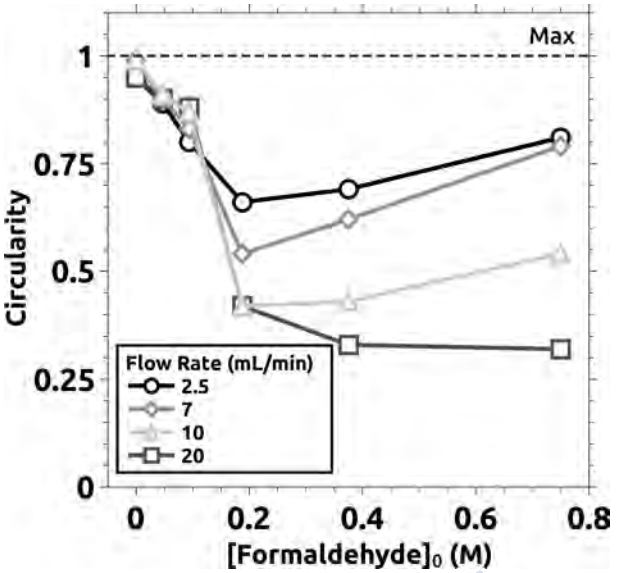

Figure 8.6: Circularity as a function of the formaldehyde initial concentration for different flow rates.$[SO_3{}^{2-}]_0$ = 0.068 M $[PAA]_0$ = 0.438 wt% and $[C.I.]_0$ = 0.021 wt%. Values near 1 indicate that the obtained patterns are close to a perfect circle. Figure taken from Escala *et al* [58].

Dependence on $[SO_3{}^{2-}]_0$

The effect of sulfite concentration is especially complex to analyze because it does not only affect the reaction itself but also has a strong effect on the rheology [62, 194] of the system, which, at the same time, affects the overall viscosity ratio.

Figure 8.7 shows the effect on the circularity by varying the sulfite initial concentration in the displacing solution, with $[PAA]_0$,$[C.I.]_0$ and, $[Formaldehyde]_0$ kept constant at 0.438, 0.021 wt% and 0.750 M respectively. For $[SO_3{}^{2-}]_0 \leq 0.06$ M almost no effect was observed. This is coherent with the batch experiments and the descriptive analysis (see Figures 7.4 and 8.4). For 0.06 M $< [SO_3{}^{2-}]_0 \leq$ 0.14 M, the circularity decreased reaching a minimum value of C = 0.4. For $[SO_3{}^{2-}]_0 = 0.193$ M, the circularity increased up to a value of 0.50. This increment is also coherent with the results presented in Figure 8.4. At this concentration, the fingering instability is much less aggressive compared to the fingers observed when $[SO_3{}^{2-}]_0 = 0.14$ M. As was previously stated, by increasing the sulfite concentration up to a threshold value, the viscosity jump decreases due to the electrostatic quenching that primarily affects the PAA molecules. This effect stabilized the system and consequently produced an increment in the circularity.

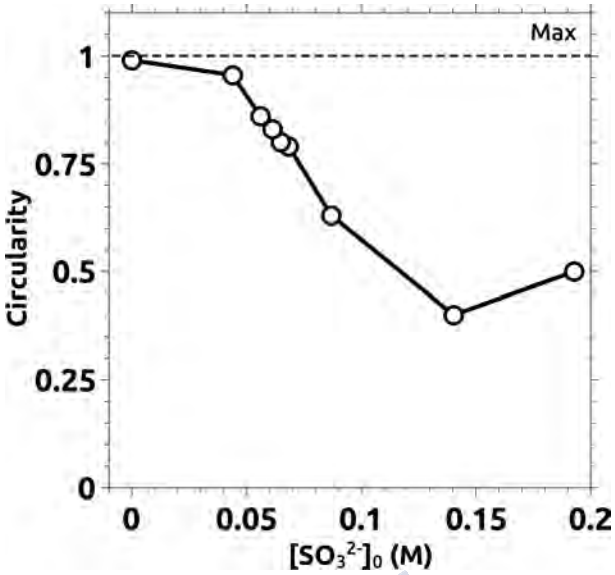

Figure 8.7: Circularity as a function of the sulfite initial concentration. In all cases, $[\text{Formaldehyde}]_0 = 0.750$ M, $[\text{PAA}]_0 = 0.438$ wt% and $[\text{C.I.}]_0 = 0.021$ wt%. The flow rate used was 7 mL/min. Values near 1 indicate that the obtained patterns are close to a perfect circle. This Figure was taken from Escala *et al* [58].

8.4 Instability Mechanism - Schlieren Experiments

In order to better understand the instability mechanism, several control experiments were performed by using a Schlieren optical technique [172, 27]. As was commented in Section 1.10, this technique permits a direct visualization of gradients of the refractive index in the solution and the observation of flows and displacements even if they are not accompanied by color changes.

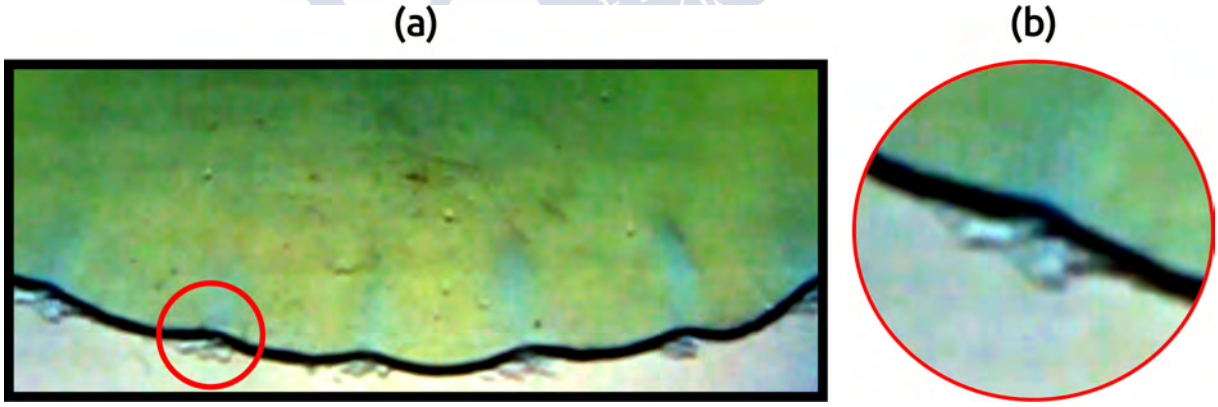

Figure 8.8: Experiments analyzed under the Schlieren technique. (a) Generation of the initial condition for a colored control experiment where $[\text{PAA}]_0 = 0.438$ wt%, $[\text{Formaldehyde}]_0 = 0.187$ M, $[SO_3^{2-}]_0 = 0.068$ M, and $[\text{C.I.}]_0 = 0.021$ wt%. (b) Zoomed image of the red circle shown in (a), that indicates the polymer cumulus at the interface. This Figure was adapted from Escala *et al* [58].

Figure 8.8(a) shows a snapshot of the moment where the initial condition started to form in a control experiment with color indicator ($[\text{Formaldehyde}]_0 = 0.187$ M, $[SO_3^{2-}]_0 = 0.068$ M, and $[\text{C.I.}]_0 = 0.021$ wt%). Small polymer accumulations appeared at the interface between the displacing and displaced solutions (marked with the red circle). An enlarged image of these polymer cumuli are presented in Figure 8.8(b).

The generation of these polymer aggregates, related to interface interactions between the polymer molecules in specific chemical and electrostatic conditions, was only observed under Schlieren optics. This phenomenon is extensively described in the literature[62, 195, 195, 104]. Once displaced, these cumuli generated small blue plumes across the displacing zone, indicating that its formation was produced by the reactivity between both solutions. Additionally, the interface became slightly deformed by the action of the polymer cumuli that destabilized the initially stable profile. This rippling was essential to the development of the instability, as it fluctuates in the front and helped with the instability triggering.

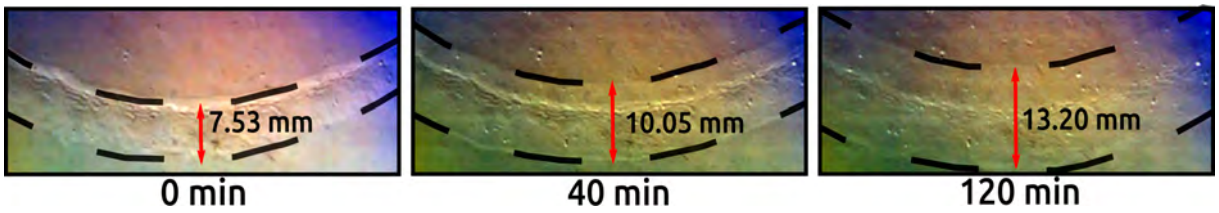

Figure 8.9: Temporal evolution of the initial condition in a colorless experiment. For this experiment $[PAA]_0$ = 0.438 wt%, $[Formaldehyde]_0$ = 0.187 M, and $[SO_3{}^{2-}]_0$ = 0.140 M. The red marks indicate the thickness of the reactive zone and the black dashed line indicates the limits of the reactive contour. This Figure was adapted from Escala *et al* [58].

Figure 8.9 presents a temporal evolution of a control experiment without a color indicator. In this particular case, the initial concentrations are $[Formaldehyde]_0$ = 0.187 M and $[SO_3{}^{2-}]_0$ = 0.140 M. Thanks to the optical technique, it was possible to appreciate how the reaction contour grew in time and how its thickness enlargement was directly related to the generation of polymer aggregates (black dashed lines). Adjacent to this mark, a thickness value is presented for each case. This clearly shows how the contour became thicker depending on the spatial distribution of the reagents but also shows that the polymer was a fundamental factor in the overall development of instability.

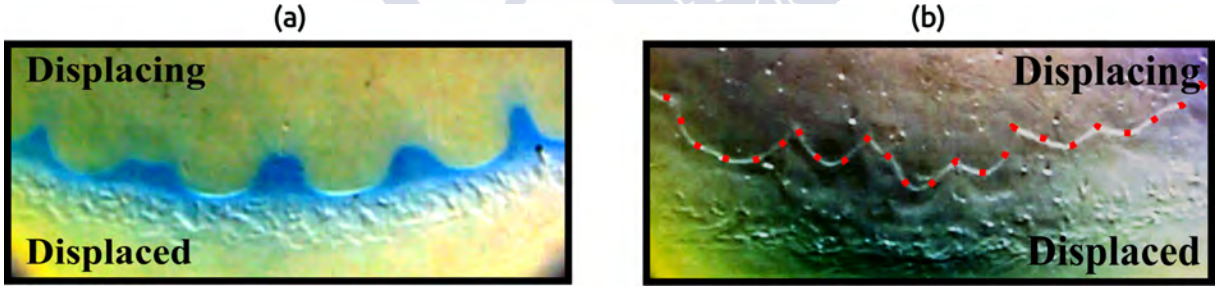

Figure 8.10: Fingering onset of a (a) colored and a (b) colorless experiment. (a) Fingering instability observed in a colored experiment. The finger propagation is blocked in the displaced solution by the polymer cumuli, which acts as a barrier. (b) Fingering instability of a colorless experiment. The red dashed line delineates the fingers. For both experiments, the flow rate was set at 7 mL/min. This Figure was adapted from Escala *et al* [58].

Finally, Figure 8.10 compares the fingering instability when the displacing solution was injected at 7 mL/min immediately after the generation of the initial condition for a colored (Figure 8.10(a)) and a colorless (Figure 8.10(b)) experiment (the instability is delimited by a red dashed line). Figure 8.10(a) shows how and where the fingering instability was produced. As it was described before, the generation of a reactive zone is necessary to trigger the hydrodynamic instability. The production of the polymer accumulations continues during the experiment, generating a more viscous and thicker layer of polymer that allows the development of fingering while blocking the fingers, flattening their tips, and preventing the propagation beyond this limit. This polymer cumuli generation explains why plumes and fingers are observed for the highest concentrations of sulfite. Even if the system should be stable, the

accumulation of polymer at the interface makes the finger onset possible in those experiments where the viscosity difference between the displacing and the blue contour is small. In Figure 8.10(b), the Schlieren technique permitted the observation of the contour of the fingering instability in a colorless experiment.

8.5 Experimental Damkhöler Numbers

The Damkhöler numbers (*Da*) were used to discern the influence of the chemistry in the convective experiments. These results were extended to the numerical model as was exposed in Section 6.2.5.

The calculation of *Da* was made following the procedure introduced by Nagatsu *et al* [142, 139, 140, 65], by first normalizing the viscosity values obtained by rheological measurements as following:

$$\mu^* = \frac{\mu - \mu_\infty}{\mu_0 - \mu_\infty} \tag{8.1}$$

where μ_∞ is the viscosity at time $t = \infty$, μ_0 is the initial viscosity at time t = 0 s, and μ is the measured viscosity at a constant shear rate = 500 s^{-1}.

An example of the evolution of μ^* with time in a typical experiment is shown in Figure 8.11. The slope of the curve (κ) was used as an estimation of the rate constant of the clock reaction [142]. A value of κ = 12.5x10^{-3} $\pm$ 4.7x10^{-3} s^{-1} was obtained as the average $\pm$ standard deviation over three realizations.

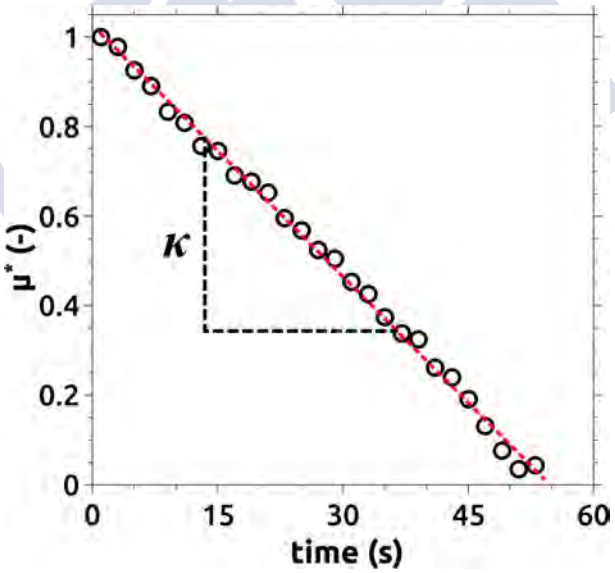

Figure 8.11: Variation of the normalized viscosity (μ^*) vs time for [Formaldehyde]$_0$ = 0.065 M, [SO_3^{2-}]$_0$ = 0.068 M, [PAA]$_0$ = 0.438 wt% and [C.I.]$_0$ = 0 wt%. The red dashed line indicates the result of the linear fit. The rate constant was calculated from the slope of the linear approximation. All measurements were done considering constant temperature and a shear rate = 500 s^{-1}. This Figure was taken from Escala *et al* [58].

Once estimated the rate constant, the Damköhler numbers were calculated as:

$$Da = \frac{\kappa a (r_{Max}^2 - r_0^2)}{2Q} \tag{8.2}$$

where r_{Max} = 10.00 cm is the effective radius of the Hele-Shaw cell (considering the width of the PTFE separator), r_0 = 6.18 cm is the radius of the initial condition (right before the injection starts) and a =

0.25 mm is the separation gap between the two plates as described in the experimental setup.

The obtained *Da* numbers for the different flows are presented in Table 8.5.

Q (mL/min)	**2.5**	**7**	**10**	**20**
Da	$3.9\text{x}10^{-3} \pm 1.5\text{x}10^{-3}$	$1.4\text{x}10^{-3} \pm 0.5\text{x}10^{-3}$	$1.0\text{x}10^{-3} \pm 0.4\text{x}10^{-3}$	$0.5\text{x}10^{-3} \pm 0.2\text{x}10^{-3}$

Table 8.1: Experimental Damköhler numbers. The results are presented as average $\pm$ standard deviation. The statistic was obtained for every κ calculated.

The Damköhler number is defined as the ratio of the residence time of the fluid to the characteristic time of the reaction. The extremely low values of the *Da* number measured indicate that the reaction times were much longer (small reaction constant) than the hydrodynamic times involved in the convective experiments.

As mentioned in Section 6.2.5, the estimation of the Damköhler numbers were fundamental in the simplification of the numerical model by deprecating the reaction terms in the Darcy's Law. This simplification was not only useful to save computational time but also to increase the stability and performance of the simulations.

8.6 Chapter Discussion

This chapter introduced one of the multiple applications of the coupling between a pH-sensitive polymer and a pH-changing chemical reaction. More specifically, the FS-PAA system analyzed in Chapter 7 was strategically adapted into an open-flow Hele-Shaw cell arrangement making possible the effective coupling between the chemical and hydrodynamic phenomena. This coupling led to the occurrence of a fingering instability strongly modulated by the chemical reaction.

Many interesting results were obtained by modifying characteristic parameters of the chemistry and the hydrodynamics. In the first place, the dynamic of the system described in Figure 8.1 shows the major role played by the chemistry in the development of the instability. The influence of the reactant concentrations in the pattern shape was observed in Figures 8.3-8.4. The flow rate also showed logical results, as it is well known that Q strongly affects the stability of a hydrodynamic system.

Regarding the quantitative analysis, by observing the circularity plots, it was possible to appreciate the influence of flow rate and chemistry. These results were consistent with the descriptive analysis of the system. The Schlieren technique was once again an important tool that helped to elucidate the physics behind the mechanism of the instability generation. It was also useful to compare experiments with and without a color indicator, and consequently to study any influence of such compound *in situ*. Besides, the estimation of the Damkhöler numbers was also important to establish the proper conditions and assumptions needed to develop a numerical model.

Finally, it is noteworthy that the viscous fingering instability is here triggered by using a pH reaction only at the contact zone between the two reactant solutions. Hence, minor local changes around the miscible interface completely modify the global displacement stability, which can result in interesting applications in different contexts. Additionally, the use of a pH clock reaction to influence viscous fingering paves the way for more complex control of this hydrodynamic instability if additional reactive feedbacks could be added to trigger temporal oscillations of pH [62].

Chapter 9

Numerical Results

Abstract: *Chapter 7 introduced the coupling between a pH-changing reaction and a pH-sensitive polymer. Chapter 8 showed how viscous fingering instability occurred after adapting such pH-viscosity coupling into a radial Hele-Shaw cell framework. The present chapter will show the numerical results obtained by simulating both, the homogeneous and the spatially extended experimental systems. All calculations were done by imitating the experimental protocols. All the parameters analyzed in the experimental sections were statistically studied in silico.*

9.1 Batch Systems Simulations

The homogeneous systems were modeled using the set of equations and reaction rates presented in Tables 6.5 and 6.8 for the FS-PAA and the FSG-PAA systems respectively. All the sets of initial conditions used for each simulation are presented in Tables 6.6, 6.7, and 6.9. The reason to simulate the batch systems is to demonstrate that all the parameters were correctly estimated and the models can properly reproduce the dynamics of the FS-PAA and FSG-PAA systems. All the information regarding the batch simulations are indicated in Section 6.2.3.

9.1.1 FS-PAA System

The FS-PAA model was studied by varying the formaldehyde and sulfite initial concentrations. As the PAA is not explicitly included in the equations, the particular effect of this species was not studied. The polymer itself is in some way included in each initial concentration (particularly in the values of $[H^+]_0$ and $[HSO_3^-]_0$) and the estimated reaction rates. In this case, the pH variation was calculated similar to the experiments as $\Delta pH = pH_{final} - pH_{initial}$.

[Formaldehyde]$_0$ Variation

Analogously to Figure 7.5, Figure 9.1 shows the characterization of the FS-PAA model when $[Formaldehyde]_0$ was varied. The system response is, at least qualitatively, identical to the experimental results. The model faithfully reproduced the dynamic of the system for the range of experimental concentrations studied (Figure 9.1(a)). Moreover, the behavior observed for $[Formaldehyde]_0 \geq 0.065$ M related to the clock emergence was also observed.

The pH variation (ΔpH, Figure 9.1(b)) was also well reproduced by the model. Both, the shape of the curve and the range of pH values agree with the experimental curve presented in Figure 7.5(b). A

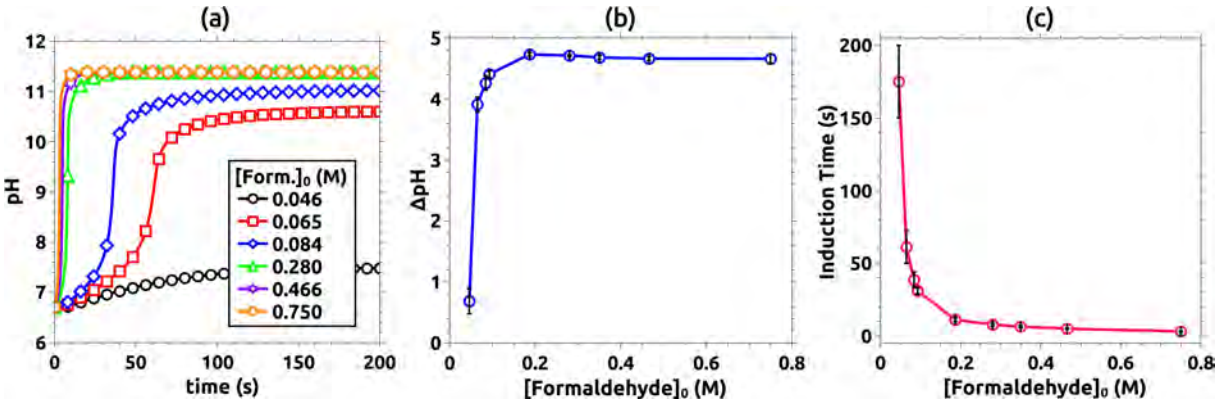

Figure 9.1: Characterization of the FS-PAA model by varying [Formaldehyde]$_0$. (a) pH dynamics. (b) ΔpH variation and (c) induction time variation. The simulation initial conditions are indicated in Table 6.6.

similar comparison can be made for the induction time variation (Fig. 9.1(c)), in which not only the shape of the curve but also the time values matched well the experimental times showed in Figure (7.5(c)).

$[SO_3^{2-}]_0$ Variation

The effects of the sulfite on the model dynamics are shown in Figure 9.2. In this case, the experimental behavior was also well reproduced by the simulations (Figure 9.2(a)). Some qualitative differences were observed for $[SO_3^{2-}]_0$ = 0.061 M and 0.064 M when compared with the experimental results (Figure 7.4(a)), particularly in the region of concentrations were not clock was observed. These differences could be associated with the model assumptions regarding the interaction between the sulfite and the PAA which were not explicitly included.

Regarding ΔpH (Figure 9.2(b))), the obtained results are statistically equal for the same range of experimental concentrations ($[SO_3^{2-}]_0 \leq 0.077$ M, (Figure 7.4(b)). The increment of the pH variation was also well captured by the model.

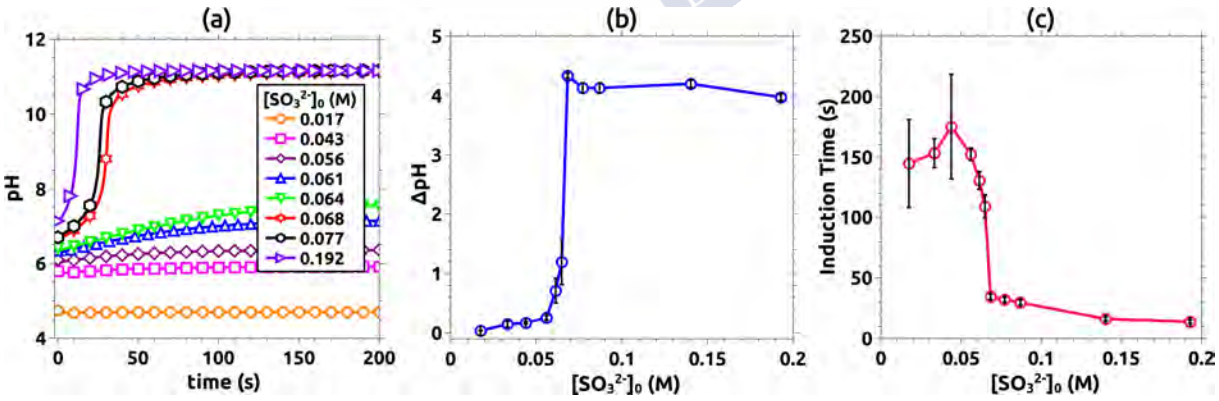

Figure 9.2: Characterization of the FS-PAA model by varying $[SO_3^{2-}]_0$. (a) pH dynamics. (b) ΔpH variation and (c) induction time variation. The simulation initial conditions are indicated in Table 6.7.

Finally, major differences were observed for the induction time (Figure 9.2(c)). Particularly for $[SO_3^{2-}]_0 \leq 0.056$ M, the dispersion in the simulations was much greater compared to the experimental results observed in Figure 7.4(c). In these cases, it was not possible to measure a well defined value for the induction time. However, in qualitative terms, the model reproduced well the experimental tendencies.

9.1.2 FSG-PAA System

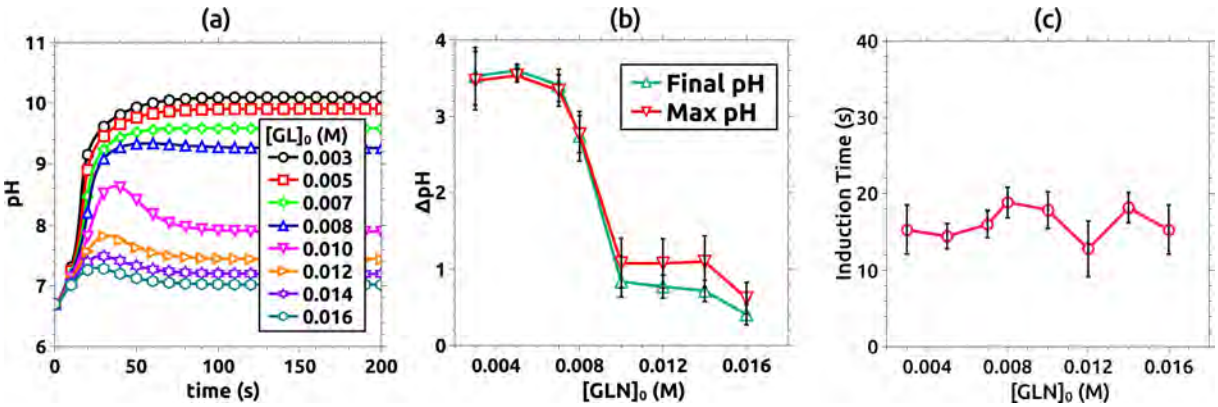

Figure 9.3: Characterization of the FSG-PAA model by varying $[GLN]_0$. (a) pH dynamics. (b) Max pH and Final pH variation. (c) induction time variation. The simulation initial conditions are indicated in Table 6.9.

Analogously to Figure 7.6, Figure 9.3 shows the simulation results of the FSG-PAA system when the $[GLN]_0$ was varied. Compared to the previous cases, some differences were observed in the dynamics of the system. As can be seen in Figure 9.3(a), the model reproduced the switch between *clock* and *peak* shape observed experimentally. Similar to Figure 7.6(a), for lower $[GLN]_0$ concentrations, the system showed a clock behavior. This changed for $[GLN]_0 \geq 0.008$ M, where the typical *peak* shape was observed. Even though the model captured the switch in the pH dynamics, the characteristic shape of the experimental pH curve was not reproduced by the model presented in Table 6.8. These differences are associated with the estimations made over the original FSG model, as they were obtained by using experimental values not only of the FSG-PAA system but also of the FS-PAA system. The set of parameters obtained were able to reproduce the experimental dynamic at cost of some differences in the pH maximum values. This was also reflected in the variations of pH. As can be seen in Figure 9.3(b), the separation gap between the Final pH and Max pH curves is approximately three times smaller compared to the experimental case. Despite this differences, simulation and experiments agree in qualitative and statistical terms, as both curves show similar dispersion when $[GLN]_0$ was increased.

Finally, no relevant differences were observed for induction time. By comparing Figures 9.3(c) and 7.6(c), it is possible to appreciate that both cases did not show any significant variation in the induction time when the gluconolactone initial concentration was increased.

9.2 Non-Linear DC Simulations

The non-linear DC simulations were done by implementing Darcy's law for porous media. The model is described by the following set of differential equations:

$$\begin{aligned} \nabla \cdot \vec{u} &= 0 \\ \nabla p &= -\frac{\mu(\tilde{\mathrm{r}})}{\kappa} \cdot \vec{u} \\ \phi \frac{\partial C_i}{\partial t} + \vec{u} \cdot \nabla C_i &= \phi D_i \nabla^2 C_i \end{aligned} \tag{9.1}$$

where $\mu(\vec{r})$ is the spatially varying viscosity profile, $\vec{r} = (x, y)$ the radial coordinate in the domain, and $\kappa = a^2/12$ is the permeability calculated from the Hele-Shaw cell gap a. The diffusion coefficients D_i kept the same values as the reaction-diffusion simulations (Section 6.2.4) and C_i are the concentration

fields for H^+ and OH^-.

As observed in the experimental results, the blue contour is characterized by a zone with high pH, (this means a high OH^- concentration in such a location), that increased its thickness during the whole experiment. Considering this, the viscosity function of Darcy's model was described as:

$$\mu(\vec{r}) = \mu_0 10^{[OH^-](\vec{r})/[OH^-]_k} \tag{9.2}$$

where $\vec{r} = (x, y)$ is the radial coordinate, μ is the dynamic viscosity, μ_0 = 1 Pa.s is the viscosity of the displacing solution, and $[OH^-]_k$ = 9.26x10^{-10} M represents the concentration of OH^- at an arbitrary time k. This value serves as a modulator between the viscosity of the displacing solution and the viscosity of the blue contour zone. Both, μ_0 and $[OH^-]_k$ were kept constant for all the cases studied in order to see the influence of the $[OH^-]$ concentration on the spatial profiles.

This model includes neither the rheological properties of the PAA nor the secondary effects related to high sulfite concentrations. Furthermore, it is intended to show only the effects associated with a classical chemo-hydrodynamic system. The polymer is, however, included implicitly in the viscosity-pH function to take into account the viscosity ratio between the displacing and the displaced solutions.

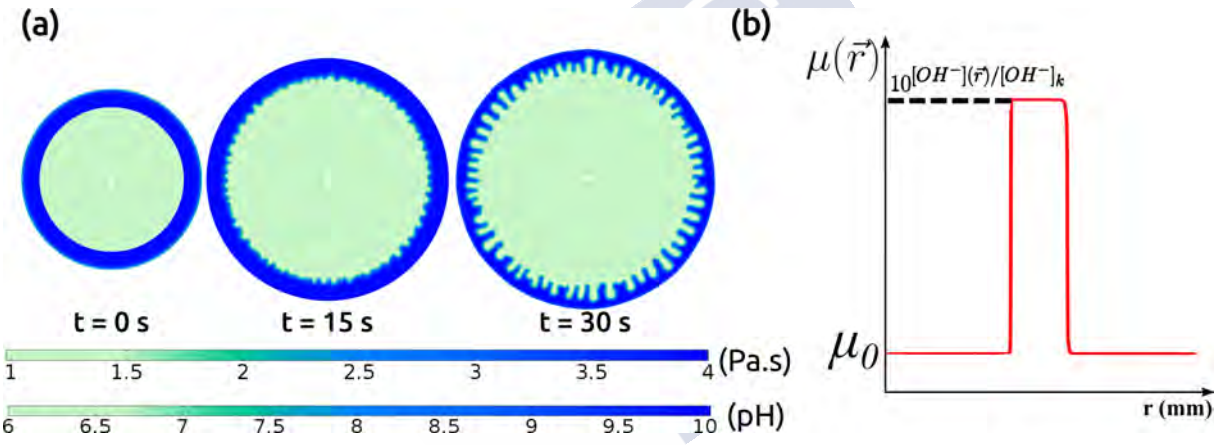

Figure 9.4: (a) Viscosity field for a control simulation, where $[Formaldehyde]_0$ = 0.750 M, $[SO_3{}^{2-}]_0$ = 0.068 M, $[HSO_3{}^-]_0$ = 0.053 M, $[H^+]_0$ = 1.995x10^{-7} M, Q = 7 mL/min, D_R = 1x10^{-11} m^2/s, and D_D = 1x10^{-9} m^2/s [2]. The color bars were set in accordance with the color range of the color indicator. (b) Initial viscosity profile across the radial coordinate obtained directly from the simulations. Schematics of the model definition are presented in the plot. Figure was taken from Escala *et al* [58].

Figure 9.4 presents an example of a nonlinear convective simulation. Figure 9.4(a) shows the viscosity field at three different times for a simulation with initial conditions identical to those used for the experiments in Figure 8.1. As can be noted, the numerical results show good agreement with the experimental observations presented in the previous Chapter (Fig. 8.1). Two color bars are located below the time frames, indicating the pH and the viscosity ranges. The initial viscosity profile for the convective simulation is presented in Figure 9.4(b). This profile was obtained from the reaction-diffusion model, where species were spatially located in the same way as in the experimental procedure.

9.3 Interface Thickness

The variation of the thickness of the initial mixing area was numerically simulated by solving the reaction-diffusion equations indicated in Section 6.2.4. Figure 9.5 shows the initial condition thickness

simulation for various formaldehyde 9.5(a) and sulfite 9.5(b) concentrations. As was initially expected, the formation of the initial condition was only driven by a reaction-diffusion mechanism. Is then possible to affirm, that the reaction model and coefficients were properly set to simulate this system. The only remarkable difference was observed for $[SO_3{}^{2-}]_0$ = 0.043 M (Fig. 9.5(b)), where the simulation showed no correlation with the experimental result.

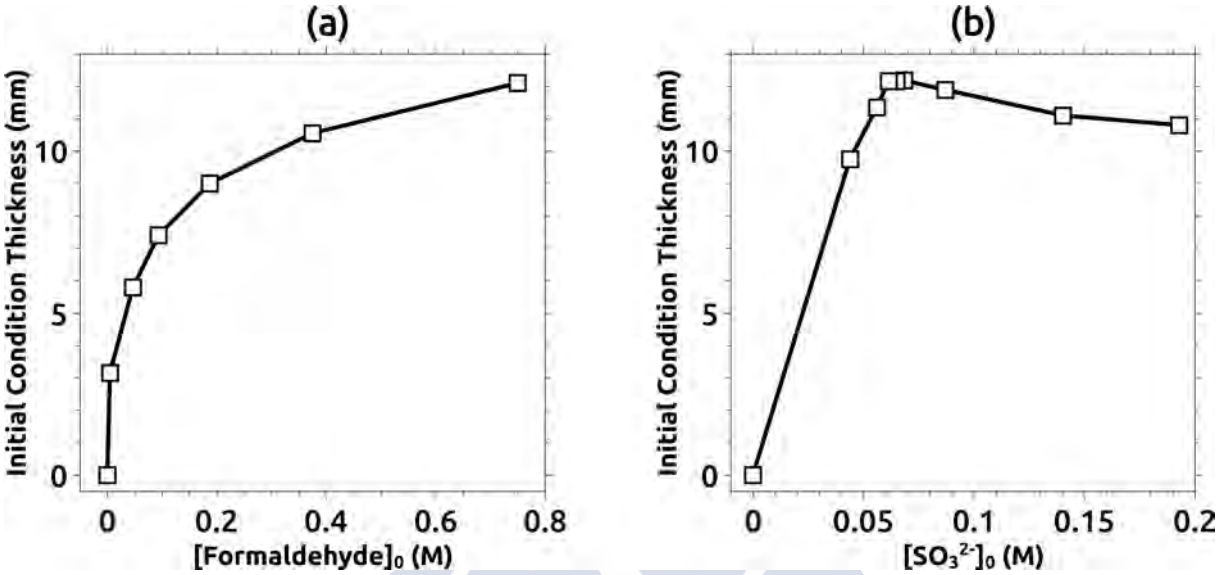

Figure 9.5: Initial condition thickness as a function of (a) $[Formaldehyde]_0$ and (b) $[SO_3{}^{2-}]_0$. All values were obtained by measuring the contour thickness generated after 3 h (simulation time). The range of concentrations studied was kept the same as the experimental study shown in Figure 8.5), with one additional concentration of $[Formaldehyde]_0$ = 0.005 M. For the species inside the displaced solution, the diffusion coefficient was set as D_D = 1x10^{-9} m^2/s, whereas for all the species inside the displacing, the value was set as D_R = 1x10^{-11} m^2/s [2]. The initial conditions used in these simulations are listed in Tables 6.10 and 6.11. Figure adapted from Escala *et al* [58]

9.4 Circularity Variation

The effect of varying the formaldehyde and sulfite initial concentration on the circularity was also numerically studied. The results are presented in Figures 9.6-9.7.

9.4.1 Dependence on $[Formaldehyde]_0$

Analogously to Figure 8.6, in Figure 9.6 the circularity was calculated as a function of $[Formaldehyde]_0$. Each simulation was carried out three times, presenting the average value and the standard deviation as the error bars. The basic statistical analysis was possible by changing the perturbation of the concentration function in each run. As can be seen for the formaldehyde case, the numerical results are in concordance with the experimental ones. The expected decrement in circularity was well represented by the simulations. In addition, increasing the formaldehyde concentration also increased the thickness of the blue contour (Fig. 9.5), which favored the instability occurrence and consequently a decrement in the circularity values. Besides, the flow rate also produced a decrement in the circularity indicating the destabilizing effect of this parameter in the convective system. The possibility to simulate statistically the convection-diffusion system also shown the possibility to obtain a non-monotonic decrement in the circularity. As presented in Figure 8.6, even if the theoretical expectation was that the circularity value must be decreased by the increment in both, the flow rate

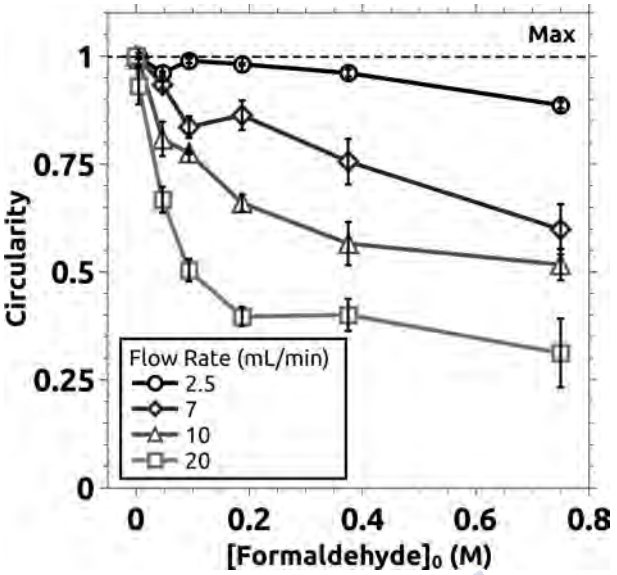

Figure 9.6: Circularity values obtained from the convective simulations as a function of [Formaldehyde]$_0$ for various flow rates. The maximum circularity value is indicated by the dashed line. D_D = 1x10^{-9} m^2/s and D_R = 1x10^{-11} m^2/s. This Figure was adapted from Escala *et al* [58]

and the formaldehyde concentration, the results showed that such a tendency can be affected statistically. However, the biggest difference was observed for [Formaldehyde]$_0 < 0.187$ M, which compared to the experiments, the simulation circularities exhibit a variety of values. For [Formaldehyde]$_0 \geq 0.187$ M, the simulations started to take average values closer to those obtained experimentally.

9.4.2 Dependence on [SO_3^{2-}]$_0$

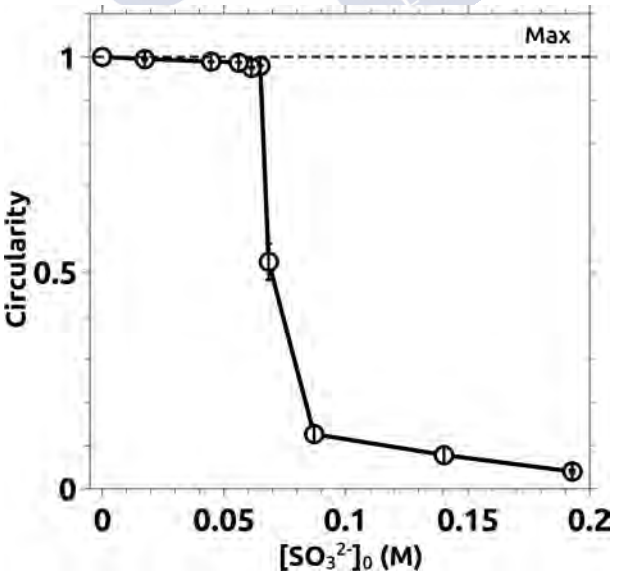

Figure 9.7: Circularity values obtained from the convective simulations as a function of [SO_3^{2-}]$_0$ for a flow rate of 7 mL/min. The maximum circularity value is indicated by the dashed line D_D = 1x10^{-9} m^2/s and D_R = 1x10^{-11} m^2/s. This Figure was adapted from Escala *et al* [58]

The variation of sulfite concentration did not produce any significant effect in the circularity for

concentrations bellow 0.068 M. In these cases, the circularity remained closer to 1. This is completely different from what was observed in the experiments where circularity decreases constantly up to $[SO_3{}^{2-}]_0 = 0.140$ M (Fig. 8.7).

For $[SO_3{}^{2-}]_0 \geq 0.087$ M, a change in the tendency was appreciated for both cases, but for the simulations, the circularity values were much lower than those observed in the experiments. This brings out the importance of polymer chemistry in the overall instability. As the formaldehyde does not affect the PAA rheology in the same way as the sulfite does, an increment in the concentration of the last one produced effects that were difficult to reproduce with a simple model [62].

By observing the initial viscosity profiles obtained from the simulations, it was possible to see that increasing the sulfite concentration produced not only variations in the thickness of the blue contour but also an important increment in the viscosity gradient. This can explain why the circularity values were lower compared to the experimental ones for $[SO_3{}^{2-}]_0 \geq 0.087$ M. This huge increment in viscosity made the system more unstable and, as a consequence, the circularity was smaller. Also, this was coherent for the lowest concentrations.

The reason behind the circularity remaining closer to 1 even for cases where a reaction region was formed is because the unfavorable viscosity gradient triggered by the reaction in such cases was small and thus, the system remained stable.

Despite the differences, it is possible to say that the numerical results qualitatively agreed with their experimental counterpart, even considering a simplified model.

9.5 Effects of the Reagent Concentration on the Spatial Viscosity Profiles

As was previously mentioned, the model used for the numerical simulations does not include any of the rheological properties of the polymer. Regarding the results presented in Figures 9.5-9.7, it is possible to see a large divergence between the experiments and the simulations when the sulfite concentration was varied. This difference can be explained based on the results and the proposed model.

Figure 9.8 compares the numerical viscosity profiles for different reagent concentrations. Whereas an increment in $[\text{Formaldehyde}]_0$ (Fig. 9.8(a)) increased the thickness of the blue region but maintained the maximum viscosity μ_{max} constant, an increment in $[SO_3{}^{2-}]_0$ (9.8(b)) produced an increase not only in the thickness but also in the viscosity maximum.

As the viscosity ratio between the displacing and the displaced solution increased proportionally to the sulfite concentration, the system became more unstable, producing smaller circularities. However, the minimum circularity in the experimental results was larger compared to those obtained in the simulations. This fact was due to an additional decrease in viscosity in the experiments produced by the electrostatic quenching of the sodium ions present in the sulfite stock solution. To avoid this and obtain a better correlation between experiments and simulations, a more complex model should be taken into account considering all the possible factors that could affect the polymer.

This model modification is not included and it is proposed as future work, as it is beyond the scope of the present thesis.

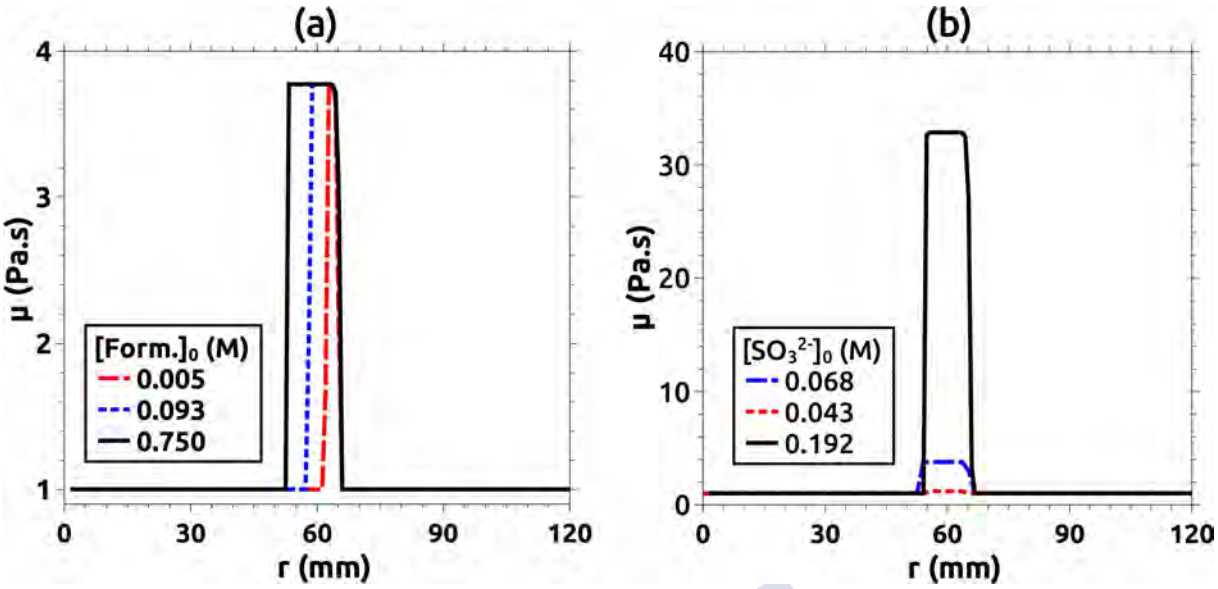

Figure 9.8: Comparison between numerical viscosity reaction-diffusion profiles for different (a) [Formaldehyde]$_0$ and (b) [SO_3^{2-}]$_0$. These profiles shown at t = 3 h (simulation time) in the reaction-diffusion model are then used as the initial condition for the convective simulations. In (a) [SO_3^{2-}]$_0$ = 0.068M in (b) [Formaldehyde]$_0$ = 0.750 M. All other model parameters were kept constant. This Figure was adapted from Escala *et al* [58]

9.6 Effect of Diffusion on the System Behavior

As was previously explained and demonstrated, the reaction-diffusion process plays a major role in the generation of the initial condition. However, the thickness of the initial condition is strongly affected by the diffusivity of the species. If the diffusion coefficients of the species inside the displacing and displaced solution are not set properly, then the initial condition profiles will differ completely from those observed experimentally.

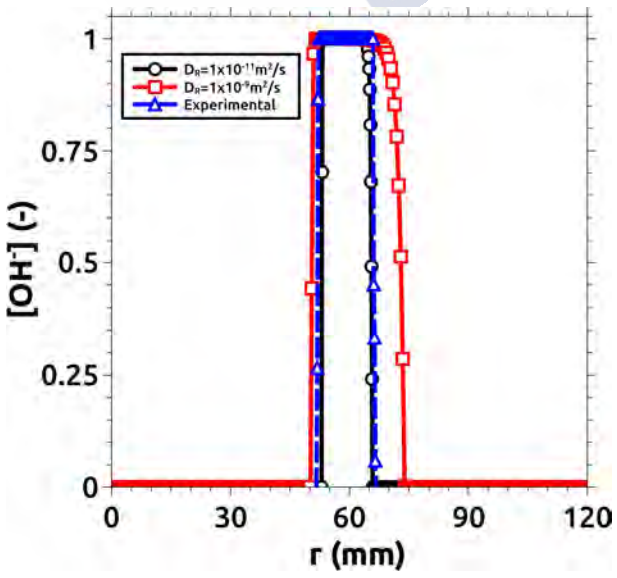

Figure 9.9: OH^- concentration profiles of the initial condition (blue mixing zone) obtained from the reaction-diffusion system. Diffusion plays an important role in making possible a comparison between the simulations and experiments. This Figure was adapted from Escala *et al* [58].

Figure 9.9 compares the simulated and experimental concentration profiles. All values were normalized between 0-1 to facilitate the comparison. In one simulation, the diffusion coefficient in the displacing solution (higher viscosity) was set as $D_R = 1\text{x}10^{-9}\ m^2/s$ in the not adjusted case (red squares in the figure) and as $D_R = 1\text{x}10^{-11}\ m^2/s$ in the adjusted case (black circles in Figure 9.9). Both results are compared with an intensity profile (blue zone in the initial condition and marked with blue triangles in Figure 9.9) obtained directly from the same experimental condition: $[\text{Formaldehyde}]_0 = 0.750$ M, $[{SO_3}^{2-}]_0 = 0.068$ M and rest of the reagents corresponding with $[\text{PAA}]_0 = 0.438$ wt% and $[\text{C}\cdot\text{I}]_0 = 0.021$ wt% (Table 6.3).

The results show the importance of properly setting the diffusion coefficient to obtain a good agreement between experiments and simulations. For the case where $D_R = 1\text{x}10^{-9}\ m^2/s$, the initial condition thickness is much larger in comparison with the experimental one. This directly affects the circularity value as the instability zone is then much larger.

9.7 Chapter Discussion

This chapter presented all the numerical results obtained from the modeling of the systems introduced in Chapters 7 and 8.

The results obtained by simulation of the FS-PAA and the FSG-PAA batch systems showed good agreement with the experimental results. Even statistically, the model captured the main behavior of the stirred system. Some differences were observed, mainly associated with the oversimplifications made on the polymer chemistry. However, even considering these limitations, the reaction-diffusion mechanism used to simulate the initial mixing area (or blue contour) reproduced well the experimental observations. This confirms not only that the adjusted model introduced in Chapter 7 is suitable to simulate the system, but also that the numerical parameters were properly set as an initial approximation.

Regarding the convective experiments, the results were in qualitative agreement, although some minor differences were observed. In this case, it is necessary to separate the results obtained by varying $[\text{Formaldehyde}]_0$ from those obtained by varying $[{SO_3}^{2-}]_0$. In the first case, the average circularity values obtained for high formaldehyde concentrations in the experiments and simulations are in qualitatively good agreement. The numerical statistical analysis also shows that different initial conditions can vary the expected decrement in circularity. This was not observed for the sulfite case, where simulations showed some differences compared with the experiments. In this case, differences in the results were observed due to the simplicity of the proposed model that did not include the rheology of the polymer nor the effect of the ionic strength, although they were analyzed in the CSTR experiments. Even if the model shows that the $[\text{OH}^-]$ concentration increases proportionally to the sulfite concentration, the reality shows that the viscosity ratio between the displacing and blue zones must be smaller. To construct a more realistic model, the value $[\text{OH}^-]_k$ in Eq. (9.2) should be varied in each simulation as a function of $[{SO_3}^{2-}]_0$. However, including these effects could be non-trivial as the PAA has a non-Newtonian behavior and its viscosity depends on the sulfite concentration and also on the shear rate. Even if some approximation can be done by performing a rheological study of the displacing solution, it is well known that the shear rate is not constant during a radial displacement inside a Hele-Shaw cell ([23, 142]). Also, more information about the real concentrations at the interface between the displacing and displaced solutions must be obtained.

Nevertheless, the convective model was useful in reproducing the main features of the experimental system. The analysis of a more complex model will be the subject of future work.

USC
UNIVERSIDADE
DE SANTIAGO
DE COMPOSTELA

Conclusions

This part of the thesis addressed the creation, characterization, and application of a coupled pH-viscosity system. In Part I, the hydrodynamic instability was controlled by the non-linearity of the BZ-CHD reaction and induced by buoyancy forces. However, due to the characteristics of such a phenomenon, it was not possible to make a direct external control of the convective terms, as the density gradient was only modified by changes in the chemical formulations. The system here presented was still controlled by the power of complex chemical reactions to induce hydrodynamic patterns, but in an experimental framework in which was possible to directly modulate the fluid displacement.

The development started by creating the FS-PAA and FSG-PAA reactions. These two systems were originated from the well known FS and FSG reactions and coupled with the pH-sensitive polymer PAA in a fully-stirred system. Both reactions were characterized by showing the synergic dynamic between the pH and the viscosity. The coupling mechanism was demonstrated and supported by obtaining similar pH-viscosity dynamics by using alternatives routes. In particular, by the use of bisulfite and a short length PAA molecule.

Then, the FS-PAA reaction was strategically adapted to a Hele-Shaw cell framework by separating its chemical composition into displacing and displaced solutions. In this way, it was possible to obtain a chemically induced viscous fingering instability as a direct application of the developed pH-viscosity system.

The instability was both qualitatively and quantitatively studied. The qualitative analysis showed the main destabilizing effect produced by increasing the flow rate and varying the chemical composition of the displacing/displaced solutions. In particular, the results demonstrated the major role played by chemistry in the fingering generation. This was quantitatively characterized by studying the thickness of the initial condition, and the circularity changes produced by varying both the physical and chemical parameters.

The results demonstrated the intrinsic relation between the chemistry and the fingering patterns. The initial condition thickness was principally modulated by the reactivity of the displacing and displaced solutions. This chemical interaction was responsible for the generation of a well-defined spatial region of high pH and viscosity. The viscosity difference between the displacing and the reactive zone was also modulated by the chemistry, favoring the generation of well defined fingers once the displacing was injected. The understanding of the instability mechanism was in part deduced thanks to the Schlieren technique. Once again, it was demonstrated the power of such a technique in the development of this work.

The batch and the spatially extended systems were modeled and simulated. Even in the most complicated cases, where the polymer interaction was not explicitly included, the dynamics of the homogeneous system were well reproduced by the simulations. This demonstrated that the modifications made on the existing models were properly set and are capable to imitate the dynamic of the coupled system. Taking into consideration the limitations of the model, the results showed a more than acceptable agreement with the experimental results.

On the other hand, the spatially extended systems were also well reproduced by both, the RD and DC models. In the first case, the initial condition simulation matched almost perfectly with the experimental

results, especially with the formaldehyde case. This was expected as these simulations were driven by a reaction-diffusion process. In this sense, these results demonstrated that the value of the diffusion coefficients was correctly chosen. Regarding the convective simulations, the overall behavior of the system was well reproduced, observing the most noticeable differences for the sulfite case. However, as was extensively explained, this was expected as the DC model did not include any of the rheologies of the polymer.

Finally, it is worth to say that the results here presented inspired in part the development of novel systems controlled by complex chemical reactions [196, 150, 202, 181].

In this system the reactivity and hydrodynamics were studied in a uncoupled way. The generation of well-defined initial condition and the subsequent fingering induction permitted to study the effect of controlling the hydrodynamic instability separately. This was demonstrated with the Damkhöler number estimation.

PART III:

COMPLEX PATTERN FORMATION AND VISCOUS FINGERING STABILIZATION

USC
UNIVERSIDADE
DE SANTIAGO
DE COMPOSTELA

Motivation

The problems derived from unstable displacements are vastly observed in the industry, in most cases with detrimental results. Just to give a few examples, the efficiency in the enhanced oil recovery (EOR) is much lower when water is used as the displacing solution to extract crude oil [41, 132, 206]. Something similar occurs with chromatography extractions when a less viscous eluent is used as a mobile phase. In all these types of situations, the negative mobility relation between the two solutions produced viscous fingering instability [42, 46, 32, 173, 166, 161].

Until now, the hydrodynamic instabilities presented in this work were chemically induced from initially stable hydrodynamic configurations. As it was previously explained, the control of a hydrodynamic instability produced in such a way would allow obtaining certain conclusions on how to control more complex scenarios [210, 36, 5, 28, 176, 21, 177, 45]. But, what happens if the initial configuration is unstable, will it be possible for the chemistry to stabilize the system? The answer to this question will be addressed in the part.

The forthcoming chapters will introduce the most complex experimental scenario of this thesis. The system here addressed is in part derived from the FSG-PAA reaction presented in Part II, however, the richness of the observed behaviors made it worth its own part. In the systems presented in Parts I and II, the chemical and hydrodynamic timescales were studied uncoupled or were induced by uncontrolled mechanisms. On the contrary, this Part will introduce the stabilization/destabilization of a viscous displacement produced by a synergistic combination of the diffusion, reaction, and convection timescales.

In this instance, two different cases will be studied. Both of them are obtained by interchanging positions between the displacing and displaced solutions. In the first case, an untypical pattern formation process is obtained from an initially stable configuration. Even though this seems to be similar to the experiments presented in the previous part, the dynamics of the system are completely different. In the second case, a typically unstable situation where viscous fingering occurs (with a highly negative mobility ratio) is stabilized by the chemical interactions between displacing and displaced solutions. In this system is demonstrated that a less viscous fluid is able to displace a fluid with much more viscosity.

Both systems will be characterized in detail and numerically modeled. The characterization of this instability will be fundamental to understand the mechanistic of the pattern formation in Case I and the system stabilization in Case II.

All the results presented in this part are based on: D. M. Escala and A. Pérez-Muñuzuri. Constructing or Deconstructing a Fluid Instability: A Bottom-Up Approach. *Submitted*, 2021.

USC
UNIVERSIDADE
DE SANTIAGO
DE COMPOSTELA

Chapter 10

Experimental and Numerical Methods

10.1 Experimental Methods

10.1.1 Chemical Recipes

Two different solutions (hereafter called Solution A and Solution B) were used as displacing or displaced solutions depending on the case. Contrary to the experiments of Part II, in this case, the chemical composition of both solutions was kept constant, except in those cases considered as control experiments. The changes in the system dynamics were primarily produced by modulating the injection flow rate.

Table 10.1 shows the chemical composition and concentration of each solution. As can be noted, the recipe of Solution A is similar to the composition used in some experiments for Part II. The main difference is that the formaldehyde is now mixed with the Poly(Acrylic Acid) (PAA) and the sodium sulfite ($NaSO_3$). The color indicator (C.I.) is composed of a hydroalcoholic solution of Bromothymol blue, which is the same indicator used in Part II. The polymer composition remained identical to the one used for the previous Part (Poly(Acrylic Acid), Mv $\sim$ 4000000).

The recipe of Solution A corresponds to the clock reaction presented in Chapters 7 and 8. As the formaldehyde is now included in the mixture, the pH of this solution is basic (pH $\cong$ 12), exhibiting a strong blue coloration due to the color indicator effect. On the other hand, Solution B is composed of an aqueous solution of gluconic Acid (GA) 2.00 mol/kg ($\cong$ 1.66 M). This solution is prepared from a concentrated solution of hydrolyzed gluconolactone.

As was shown in Part II, Solution A has a significantly larger viscosity compared to Solution B: μ_A = 150 mPa.s and μ_B = 2.2 mPa.s measured at a shear rate of $\dot{\gamma}_f = 50\ s^{-1}$.

More details about the stock preparations are included in Appendix A.3.

10.1.2 Experimental Cases

Two different experimental situations were considered by using solutions A/B as displacing/displaced. Both situations (hereafter called Case I and Case II) are schematized in Figure 10.1.

- Case I: Solution A was used as the displacing solution and Solution B was used as the displaced solution. In this case, as the viscosity of the displacing is larger compared to the displaced, the initial configuration was hydrodynamically stable.
- Case II: Solution B was used as the displaced solution and Solution A was used as the displacing solution. As the opposite of Case I, this was hydrodynamically unstable, and thus, viscous

Species	Concentration
PAA	0.438
Formaldehyde	0.350
Na_2SO_3	0.068
C.I.	0.023

(a) Composition of Solution A.

Species	Concentration
GA	2.00

(b) Composition of Solution B.

Table 10.1: Composition of Solutions A and B. Concentrations values are expressed as wt% for the PAA and C·I and molarity for Na_2SO_3 and Formaldehyde. The concentration of GA is expressed in molality (mol/kg) which corresponds to approximately 1.66 M.

fingering instability is prone to happen.

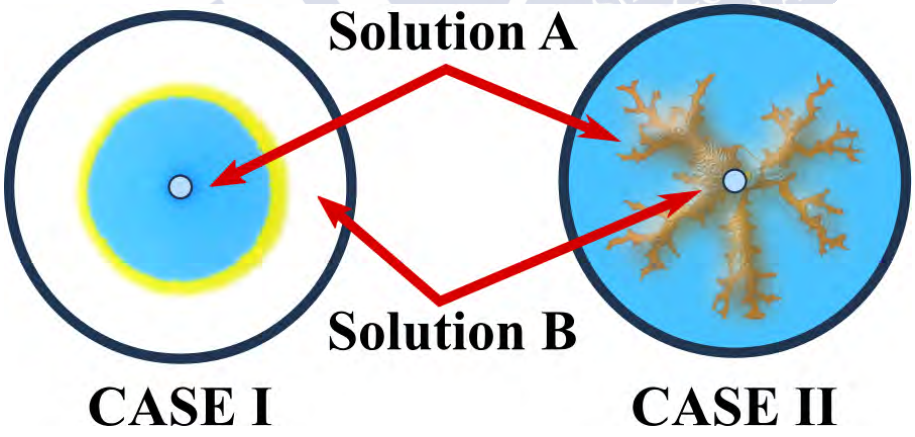

Figure 10.1: Schematics of the configuration of the displacing-displaced fluid for each case of study.

10.1.3 Radial Hele-Shaw Cell: Experiments and Protocols

The sketch of the experimental setup used is shown in Figure 10.2. The Hele-Shaw cell was built using two circular Poly(methyl methacrylate) plates (18 cm diameter) (Plexyglass®) separated by a Polytetrafluoroethylene (PTFE) frame of 0.25 mm of thickness. The horizontal cell was initially filled with the displaced solution. The displacing solution was injected through a 4 mm hole located at the geometric center of the bottom plate using a syringe pump (kdScientific: Legato 200 series). Special care was taken when injecting the less viscous fluid into the more viscous one (Case II). The displacing fluid was directly injected into the Hele-Shaw cell avoiding any contact between fluids in the injection

tubes or connectors. The large viscosity difference produced viscous fingering inside the tubes that would lead to undesired effects on the experiments.

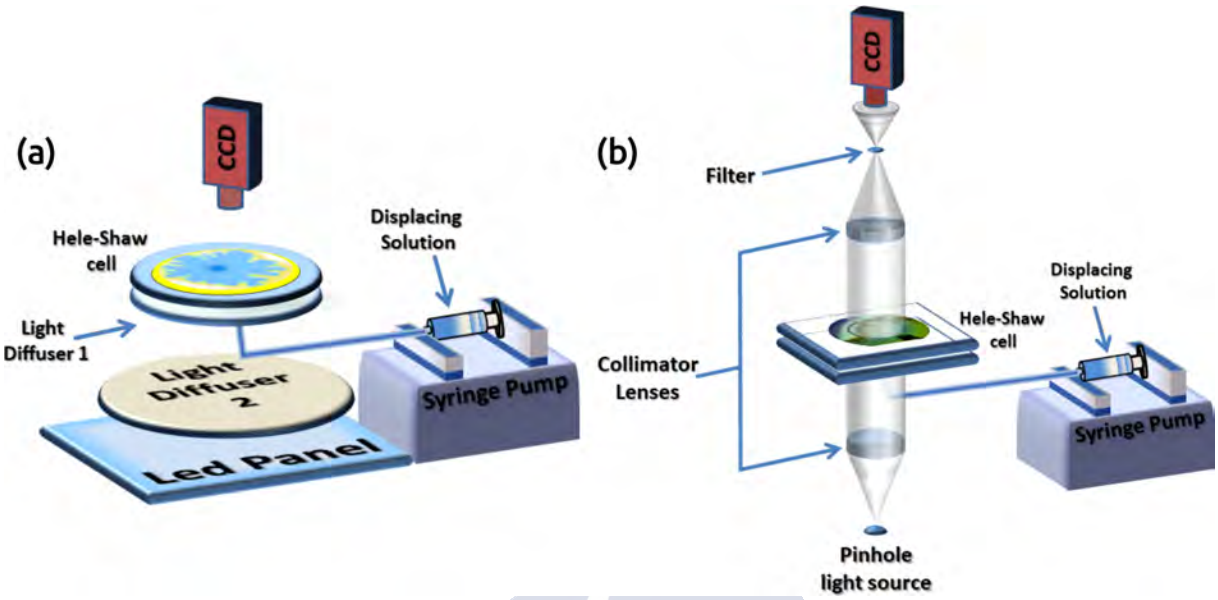

Figure 10.2: Schematics of the experimental setup. (a) Configuration for visible light detection (colored experiments). (b) Schlieren arrangement for optical detection of gradients of the refractive index in the absence of color indicator.

Experiments were recorded from above using a Complementary Metal Oxide Semiconductor (CMOS) camera (PixeLINK: PL-B776U) connected to a computer. Samples were illuminated from below using a rectangular Light-Emitting-Diode (LED) pad and a light diffuser (Figure 10.2(a)). The image post-processing was done with the GNU software FIJI [169].

All experiments were done in a temperature-controlled environment. Solutions were thermally stabilized at 23 °C by using a thermostatic bath. As the light source used was composed of an array of LEDs located at some distance from the cell, all temperature changes were considered insignificant.

Quantitative measurements were done considering the final time of each experiment (hereafter t_f). This time was defined as the time when the displacing solution reaches the cell border (or the region of interest). In those cases where reaction effects delayed this situation, t_f was considered as the time where a fixed volume of displacing was injected. This volume corresponds to an average of approximately 5000 μL of displacing solution.

10.1.4 Schlieren Imaging

Similar to the experiments presented in Part II, the Schlieren technique [27, 28, 184] was used to track changes in the optical index induced by the motion of fluids that cannot be observed by a direct optical inspection. This technique provided detailed information about the diffusive and convective phenomena involved without interference of the color indicator.

The Schlieren technique was also useful to appreciate changes in the polymer solution due to reactive effects and polymer aggregation. For these experiments (Fig. 10.2(b)), the Hele-Shaw cell was made of two square glass plates (25 cm x 25 cm) instead of the plastic plates. This modification was introduced to discard any artifact associated with the cell material and to improve the image quality but at cost of recording on a smaller observation field due to technical constraints.

To perform the Schlieren measurements, the Hele-Shaw cell was placed between two collimator lenses. The system was illuminated using a pinhole LED light source. An iris cutoff filter was located

at the focus point between the CMOS and the collimator lens as indicated in the scheme presented in Figure 10.2(b)[172, 27, 58].

10.1.5 Control Experiments

Several additional experiments were done by changing the chemical composition of the two solutions to determine the role played by the chemical species in the mechanism underlying the instability. These experiments are summarized in Table 10.2. The column named **EFFECT** indicates the phenomenon/phenomena observed in the Hele-Shaw cell for such a specific recipe. Thus, **PRECIPITATION** indicates the occurrence of precipitation at the interface between both fluids, and **FRONT** indicates the occurrence of a chemical front that moves towards Solution A. The nature of these two phenomena will be studied and characterized in Chapter 12.

The so-called BASE case corresponds to the recipe indicated in Tables 10.1(a-b). This was the recipe used for most of the experimental figures. Cases C1-C5 correspond with experiments where only the composition of the Solution A was changed. This set of experiments were used specifically for unveiling the mechanism of the pattern formation. The control experiments in where the gluconic acid of Solution B was replaced with doubly distilled water (Case C6 in Table 10.2), were used to show a direct comparison between the reactive and non-reactive cases in the main experimental figures.

Most control experiments (principally those of Case I) were recorded using the Schlieren technique described in the previous section. An extensive study of the control experiments is presented in Chapter 12.

CASE	DISPLACING/DISPLACED SOLUTION COMPOSITION						EFFECT
	SOLUTION A					SOLUTION B	
	FORM. (M)	Na_2SO_3 (M)	PAA (wt%)	C·I(wt%)	Na_2CO_3 (M)	G.A. (m)	
BASE	0.350	0.068	0.438	0.021	0	2	PRECIPITATION/FRONT
C1	0.350	0.068	0.438	0	0	2	PRECIPITATION/FRONT
C2	0	0.068	0.438	0	0	2	PRECIPITATION/FRONT
C3	0	0	0.438	0	0	2	PRECIPITATION
C4	0	0.068	0	0	0	2	————
C5	0	0	0.438	0	0.068	2	CO_2 FORMATION
C6	0.350	0.068	0.438	0.021	0	0	————

Table 10.2: Composition of the control experiments. The concentrations were kept as indicated in Tables 10.1.

10.1.6 Precipitation

Several precipitation assays were performed by mixing different acidic solutions with different PAA formulations. To obtain the precipitate, the solutions containing PAA were mixed with gluconic acid (Solution B) and $[HSO_3^-]$ = 0.068 M. The obtained mixtures were then centrifuged using a Hettich Universal 320 R centrifuge for 5 minutes at 5000 rpm and 23 °C. The results are part of Chapter 12.

10.1.7 Scanning Electron Microscopy (SEM)

Scanning Electron Microscopy (SEM) was used as a supplementary tool to perform a comparative study of the structure of the PAA molecule and the precipitate. For this test, Solution A and the precipitate were mechanically filtered and dried at 45 °C in a heater. The obtained samples were coated with a 10 nm layer of iridium by electroplating using a Quorum Q150 TS equipment (Fig. 10.3(a)). The coated samples were observed through a Zeiss Gemini Field Emission Scanning Electron Microscope (Fig. 10.3(b)) located at the CACTUS building of the University of Santiago de Compostela. The results are also part of Chapter 12.

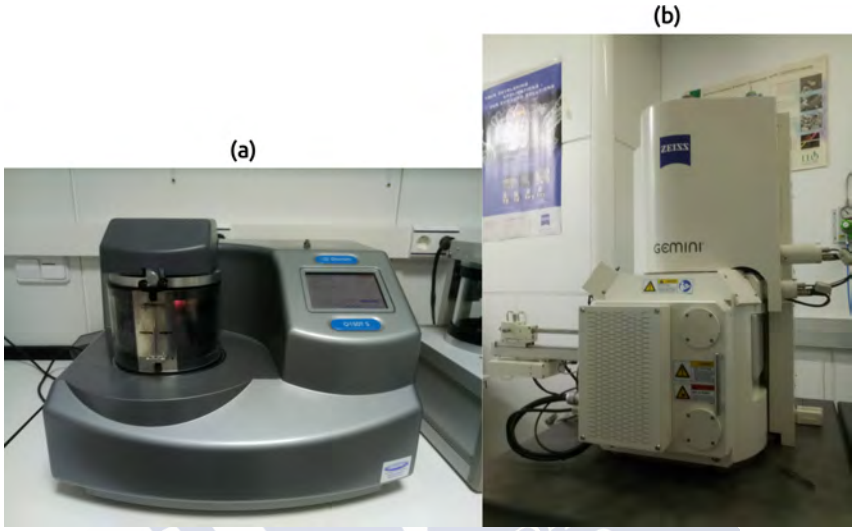

Figure 10.3: SEM equipment. (a) Quorum Q150 TS coating device. (b) Zeiss Gemini Field Emission Scanning Electron Microscope.

10.2 Numerical Methods

10.2.1 Non-Linear Reaction-Diffusion-Convection (RDC) Simulations

Due to the complexity of the experimental system, all issues related to the numerical model used in the RDC simulations are extensively detailed in Chapter 13. The present section introduces the general aspects and the numerical setups used to perform the numerical calculations. As this system is in some way an extension of the one presented in Part II, only 2D-RDC simulations were done.

The calculations were performed using the computational fluid dynamic (CFD) software suite Ansys Fluent® version 19.2 [11, 12]. The numerical domain was composed of a circular region of radius R_i = 10 cm, discretized using a mapped mesh of radial elements as indicated in Figure 10.4. The inlet flow velocity at the central boundary was calculated as:

$$-\vec{n}\cdot\vec{u} = v_0(Q) \tag{10.1}$$

where $v_0(Q) = Q/2\pi ra$, r is the radial coordinate and a is the cell separation gap.

The injection hole is the circular region of radius r_i = 2 mm located at the geometric center of the domain. The outlet boundary condition was set as a pressure outlet with p = 0 Pa.

The initial conditions were set using the following set of piecewise functions depending on the experimental case:

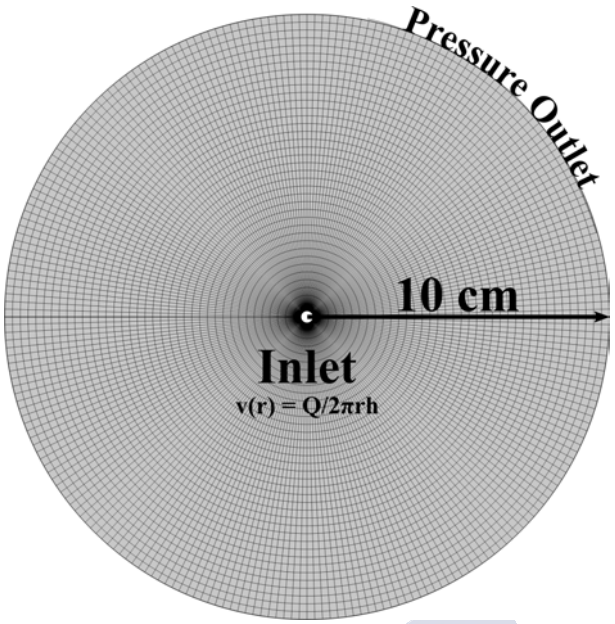

Figure 10.4: The 2D-RDC simulation domain is composed of a circular region of 10 cm radius discretized using a mapped mesh of radial elements. The inlet is located at the central inner hole and the velocity v_0 is calculated from the flow rate Q. A constant pressure p = 0 Pa was set as the fluid outlet condition.

$$\text{Case I:} \begin{cases} A(\vec{r},0) = \begin{cases} A_0(1+\xi N(\vec{r}) & \vec{r} < \varepsilon \\ 0 & \vec{r} \geqslant \varepsilon \end{cases} \\ B(\vec{r},0) = \begin{cases} B_0(1+\xi N(\vec{r}) & \vec{r} \geq \varepsilon \\ 0 & \vec{r} < \varepsilon \end{cases} \\ C(\vec{r},0) = 0, \forall \vec{r} \in D \end{cases}$$

$$\text{Case II:} \begin{cases} A(\vec{r},0) = \begin{cases} 0 & \vec{r} < \varepsilon \\ A_0(1+\xi N(\vec{r}) & \vec{r} \geq \varepsilon \end{cases} \\ B(\vec{r},0) = \begin{cases} 0 & \vec{r} < \varepsilon \\ B_0(1+\xi N(\vec{r}) & \vec{r} \geq \varepsilon \end{cases} \\ C(\vec{r},0) = 0, \forall \vec{r} \in D \end{cases}$$

where $N(\vec{r})$ is a normally distributed random noise function of amplitude ξ = 0.01 set across the radial coordinate, and ε = 0.5 mm is an initial contact region between fluids A and B included for stability reasons. A_0 and B_0 are the initial concentrations of solutions A and B respectively. For simplicity, both values were set to 1 mol/L.

All simulations were run until a final time (t_f), calculated from the total volume of displacing injected (V_f) as:

$$t_f = \frac{V_f}{Q} \tag{10.2}$$

In all cases, V_f was kept fixed at 7000 μ/L.

The simulation parameters used in all RDC simulations are presented in Table 10.3:

Parameter	Value	Dimension Unit	Reference/Notes
A_0	1	M^{-1}	
B_0	1	M^{-1}	
C_0	0	M^{-1}	
C_m	1	M^{-1}	
μ_A	1	Pa.s	experimental/adjusted
P_0	0	Pa	
D_A	$1.0x10^{-11}$	m^2s^{-1}	estimated, refs. [65, 139, 2]
D_B	$9.3x10^{-9}$/$1.0x10^{-9}$	m^2s^{-1}	estimated, refs. [3, 69]
D_C	0	m^2s^{-1}	
a	0.25	mm	experimental
R_i	10	cm	experimental
r_i	2	mm	experimental
ϕ	1		
κ_0	$5.208x10^{-9}$	m^2	experimental, $a^2/12$
k_1	$5.2x10^{-4}$	L M^{-1}	experimental/adjusted
k_2	$5.2x10^{-5}$	L M^{-1}	$k_1/10$
R_κ	80		adjusted
R_b	-7		adjusted
V_f	7000	μL	experimental
t_f	V_f/Q	min	

Table 10.3: Parameters used in the RDC simulations. All values are expressed in the International System of Units (SI) excepting concentrations that are expressed in Molarity. The value of D_B changes depending on the reactivity of the system. The value of D_B = $1.0x10^{-9}$ m^2/s was used for the non-reactive cases.

The pressure and concentration fields were discretized using second-order and first-order upwind schemes respectively. Simulations were performed using the implicit pressure solver and the SIMPLE algorithm with a variable time-step setting [12, 11]. Both systems were simulated using real units to facilitate the comparison with the experiments.

10.2.2 Mesh Independence Study For The RDC Model

The sensitivity of the numerical results associated with spatial discretization was studied to perform a mesh independence study. Figure 10.5 shows the variation of the circularity due to the mesh resolution in a representative simulation of the direct experiment (Q = 5 μL/min). All measurements were taken at half of the final time (0.5 t_f). As can be seen, the circularity was strongly affected by the mesh resolution. The results were considered mesh independent when the circularity differed less than 3% between consecutive refinements. All simulations presented in this Part were done by using the coarsest mesh that satisfied such conditions.

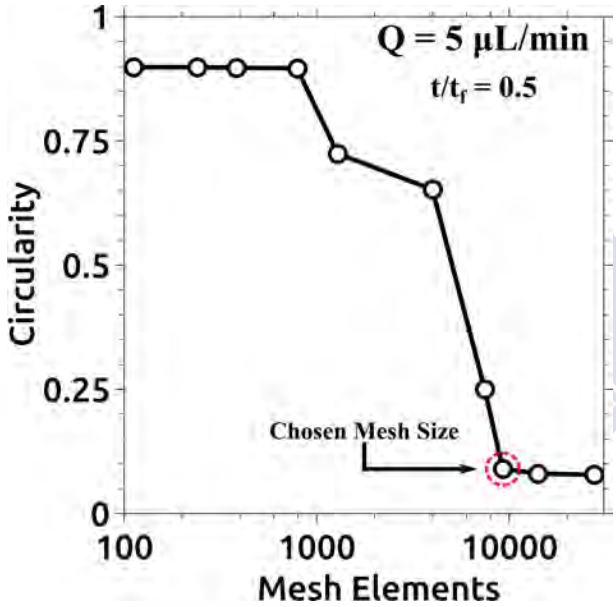

Figure 10.5: Mesh independence study done by studying the circularity variation for different mesh sizes in a representative case of the direct experiment (Q = 5 μL/min). All values were obtained at 0.5 t_f. The selected mesh was obtained after checking that the difference in circularity between two consecutive simulations was less than 3%. In this case, this condition was reached when the size of the mesh was approximately 10000 elements.

Chapter 11

Experimental Results

Abstract: *This chapter will introduce an extensive description of the experimental system. Both, Cases I and II will be studied from the quantitative and qualitative points of view. In the first step, an extensive description of the main experimental characteristics is presented. This analysis will facilitate the understanding of the dynamics of the system. This includes both direct and Schlieren observations. The analysis continues with the quantitative characterization of the system by studying the shape morphology and the effect of external parameters like the flow rate. Some interesting features related to future applications are also discussed.*

11.1 Case I

11.1.1 General System Overview

In this first case, Solution A (large viscosity) was pumped into the less viscous Solution B. Three different snapshots are shown at different moments of the experiment. The dynamics of Case I are presented in Figure 11.1. A reactive experiment is presented in Figure 11.1(a). As can be appreciated, once the displacing was injected at a relatively low flow rate (5 μL/min), the initially stable configuration observed at the beginning of the experiments broke and digitations started to occur. These ramifications grew in a non-symmetrically manner until the outer boundary was reached. A yellowish contour was also observed around the pattern, indicating the presence of a well-defined zone of low pH. The absence of this low pH region in the control experiments suggest that this change in pH was produced by reaction-diffusion processes. As can be seen in Figure 11.1(b), when the displaced solution is replaced by doubly distilled water, not only the displacement remained stable, but also the yellow contour was unobserved. The only appreciable difference is the blurred interface produced by the combination of the miscibility of both liquids and diffusive effects.

Another interesting characteristic observed in this case is related to pattern dynamics. As can be shown in Figure 11.2, when the flow rate is particularly slow, the ramifications did not show constant growth as expected from a classical instability. Instead, they moved backward and frontward in time through the yellow zone. This behavior is especially interesting considering that the flow rate was never stopped and such a phenomenon was produced only by the reactivity of both solutions.

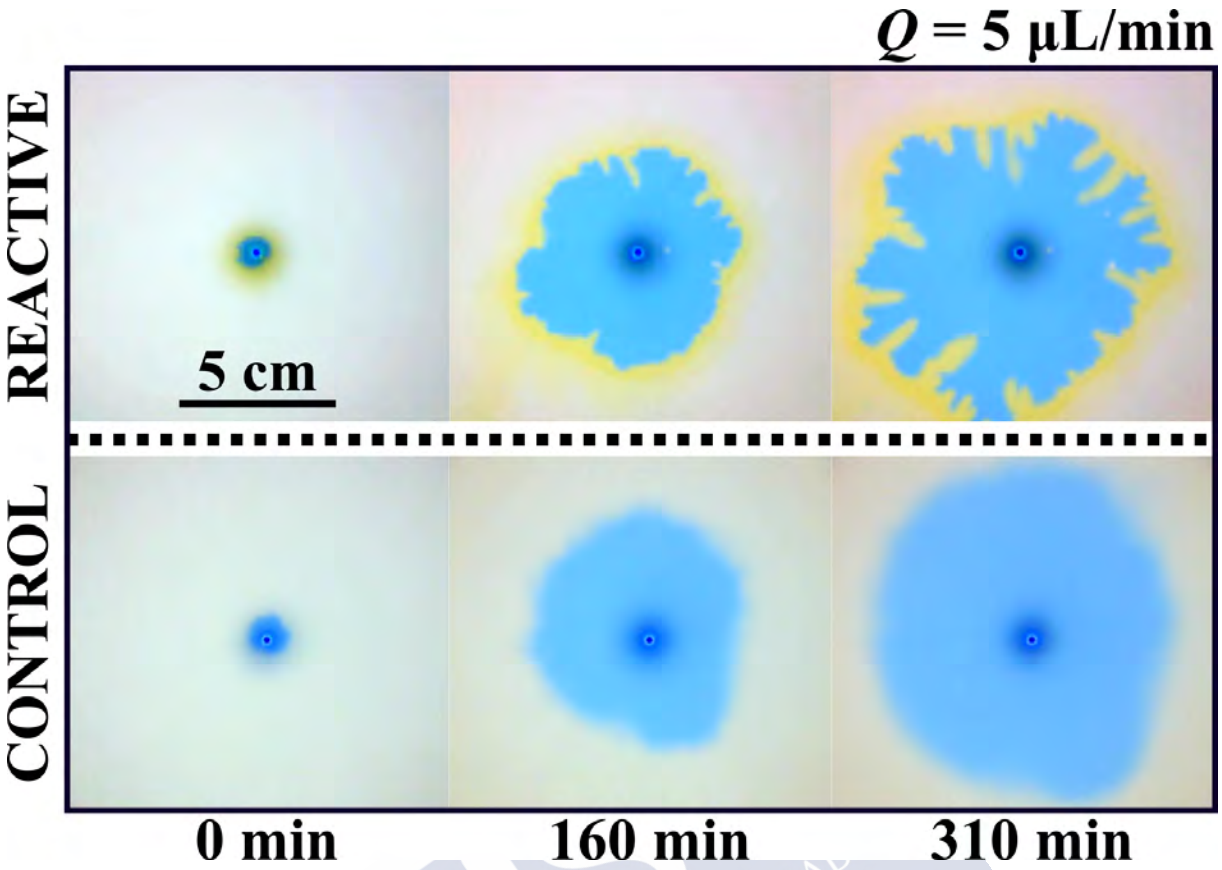

Figure 11.1: Comparison between a (a) reactive and (b) non-reactive cases for a flow rate of 5 μL/min with the same experimental conditions. As observed, the radial profile of the displacing solution in the control case remains mostly circular as expected from a hydrodynamically stable configuration. Some disturbances are observed due to diffusive effects. In the reactive case, the displacing profile remains circular for the first minutes. Around t = 160 min, the circular shape deforms showing digitations. At t = 310 min, those ramifications enlarge resulting in a fully developed ramification. The yellow zone next to the displaced fluid indicates the region where reaction-diffusion processes take place. The displaced solution in the reactive case is gluconic acid while in the control case is H_2O.

11.1.2 Descriptive Analysis

Effect of the Flow Rate

By studying the effect of varying the inflow rate, the reactive system showed a well-defined behavior. The results presented in Figure 11.3 shows snapshots of different experiments taken at 90 % of the final time of each case (t/t_f = 0.9). Five flow rates are presented (1, 2.5, 5, 200, and 2500 μL/min). Additionally to the 5 μL/min case, for the lower Q (1 and 2.5 μL/min), the system exhibited pattern formation. The patterns showed a ramified structure surrounded by the low pH yellow zone. This zone was more extensive in slower cases.

By increasing the flow rate (200 and 2500 μL/min), the system became more stable, showing mostly circular profiles. No patterns were observed and the yellow zone remained bounded close to the displacing front, exhibiting a less extended annular structure. These results indicate the major effect of the temporal timescales. At lower flow rates, the chemical timescales were more important than the convective ones, favoring the pattern formation. By increasing the flow velocity, the convective timescales were more important and thus, no patterns were observed.

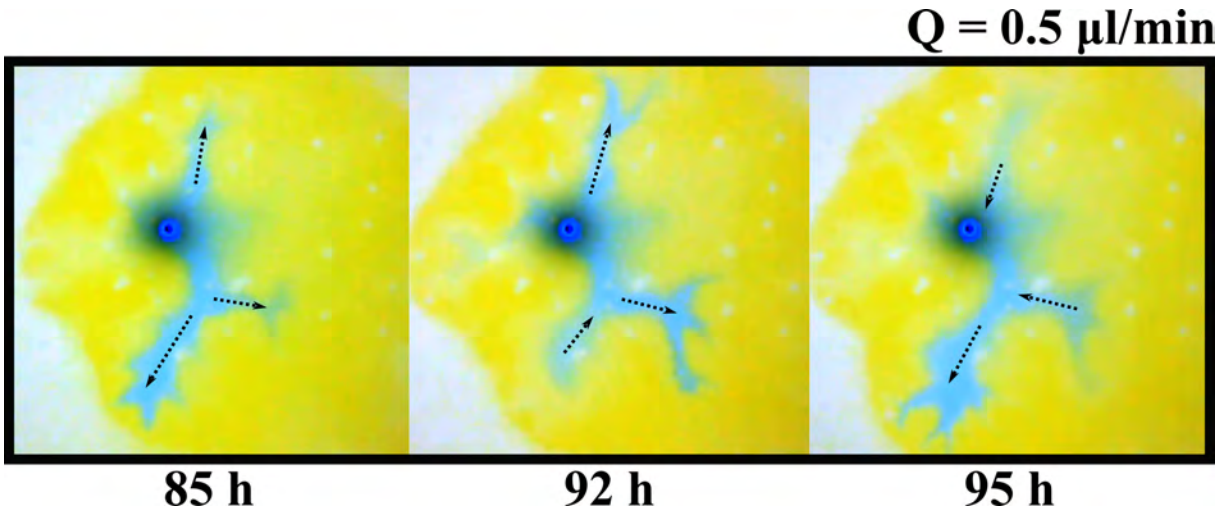

Figure 11.2: For a lower flow rate experiment (0.5 μL/min), the observed ramifications showed a non-constant growth, moving randomly backward and frontward. The dashed arrows schematize the direction of the finger movement. Such movement was only observed inside the low pH zone. The image colors were adjusted to improve visualization.

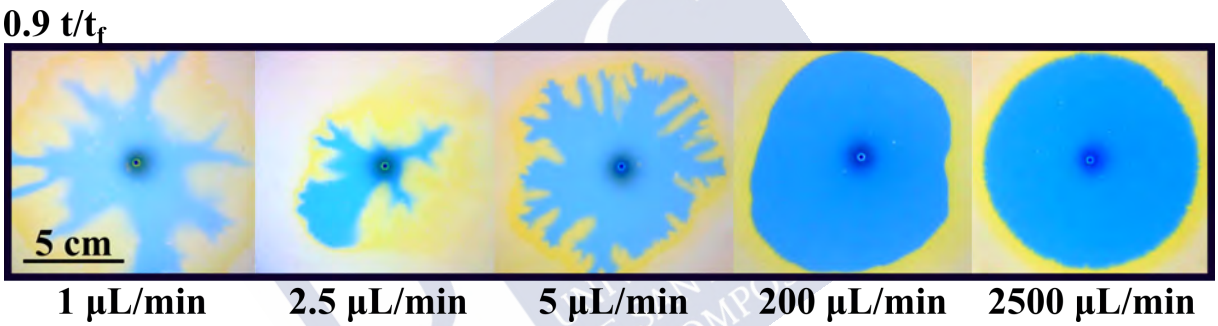

Figure 11.3: Effect of the flow rate as a trigger for the pattern formation via a reactive interface. All the images were taken at 90% of the final time (t_f) for each case. For Q = 2500 μL/min, the displacing interface remained completely circular. In this case, the characteristic flow timescale was much larger compared to the reaction time scale and a circular stable pattern was obtained. For Q = 200 μL/min, the shape remained mostly circular, but some effects due to reaction and diffusion deformed the initially symmetrical profile. For Q = 5 μL/min, patterns started to be observed forming ramifications around the initially circular shape as described in Figure 11.1. For Q = 2.5 and 1 μL/min and, ramified structures were observed in the displacing solution. Diffusive effects were remarkable for the lower flow rate case. This was observed in the loss of coloration in the displacing solution. The yellowish reaction zone was also observed for all cases, being enlarged for the lower flow rate cases.

Schlieren Observations

By observing Case I through the Schlieren technique it was possible to have a deeper observation of the pattern formation process. Figure 11.4 presents the images of an experiment performed at a low flow rate (Q = 3μL/min). As can be seen in Figure 11.4(a), once injected the displacing, the two solutions started to react, creating a brownish crust at the interface between fluids. This phenomenon produced a symmetry break making the displacing solution to flow in a non-homogeneous way. This also produced stagnation areas favoring the accumulation of crust as appreciated in Figure 11.4(b).

The continuous generation of crust produced a natural stopper that locally reduced the permeability of the porous matrix and increased the pressure inside the Hele-Shaw cell. Once the pressure reached a certain value, the crust wall broke by the ejection of the displacing solution. This process caused the characteristic ramifications observed in previous figures. Once the displacing reaches fresh displaced,

the reaction continues, and more crust is generated. The crust is what in the direct observations was named as yellow zone. It is clear now that the patterns are generated inside this zone.

In addition to the crust formation, there was another chemical process involved in the instability mechanism that was observed once the injection was stopped. In Figure 11.4(c) it was possible to observe a reaction front moving opposite to the flow direction. The occurrence of this reaction front is fundamental to explain why the patterns are localized at a specific radius and are observed at lower flow rates. It also agrees with the results presented in Figure 11.2. More details regarding both phenomena will be addressed in the forthcoming sections.

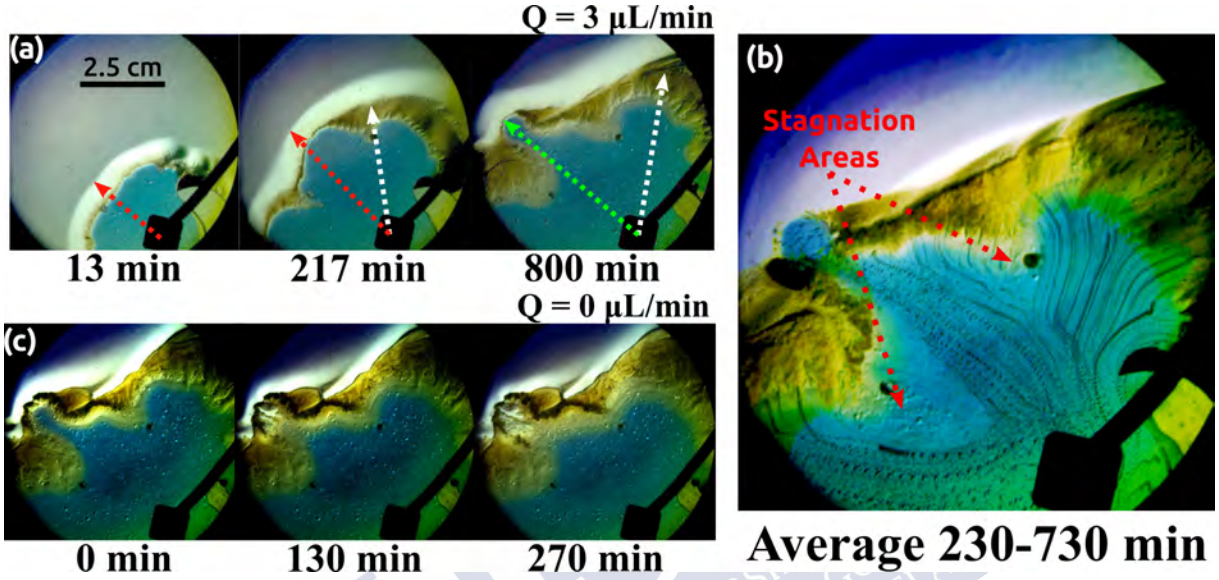

Figure 11.4: Schlieren visualization for an experiment with Q = 3 μL/min. Red dashed arrows indicate the diffusive interfacial zone while the white dashed lines indicate the brownish crust generated by the contact of solutions A and B. The green dashed line indicates one of the ramifications previously shown in Figure 11.1. (b) The average flow path of the displacing solution was obtained by averaging the experimental frames in the range of time between 230 – 730 min. The ramifications were generated by a synergy between different processes. In the first place, there was a non-homogeneous distribution of the displacing solution driven by a low flow rate and the accumulation of the brownish crust. This flow inhomogeneity facilitated the generation of stagnation areas as indicated in the figure. The crust accumulation produced a stopper that locally reduced the permeability and changed the pressure field preventing the natural flow of the displacing solution. Once the pressure was above a certain value, Solution A was ejected through one of the flow paths. Once the crust was penetrated, displacing and displaced solutions started to react producing more crust. (c) Reaction front observed when the injection was stopped. This reaction front moved opposite to the flow direction and it was responsible for the finger to recoil.

11.1.3 Quantitative Analysis

Different properties were measured at the interface to characterize the observed patterns. Similar to Part II, the circularity (C) was one more time chosen as the preferred shape descriptor because it presents the results straightforwardly. In this sense, this technique is ideal to discern between changes from a completely stable situation where $C \cong 1$ to the pattern formation situation where $C \cong 0$. The results are summarized in Figure 11.5.

Analogous to the circularity, the change in the injection front is also described analytically by measuring the average advancement of the displacing solution over time and comparing both reactive and non-reactive cases in a relative timescale. This quantity results from determining the interface location and then measuring the distance from every point at the interface to the center of the cell. This analysis

is also useful to evaluate the reaction influence in the observed patterns. A detailed description of how such measurements were done is presented in Appendix C.3. The results are shown in Figure 11.6.

Circularity Variation

Figure 11.5(a) presents the variation of the interface circularity as a function of time for different flow rates. C was plotted versus time normalized by the total time of each experiment (time at which Solution A reached the outer boundary of the Hele-Shaw cell). As can be noted, for low values of the flow rate the circularity immediately dropped to low values. When the flow rate was closer to the transition value but still in the instability region, the circularity dropped as well but it needed more time to do it. This seems reasonable because as time advanced, the average radius of the interface became larger and so the linear velocity of the interface becomes smaller. Thus, the system moved deeper into the instability region. Larger values of the flow rate and clearly out of the instability region were characterized by a constant value of the circularity very close to 1. Figure 11.5(b) shows the circularity for the control experiments where no instability was observed. In these cases, the circularity value remained close to one and constant during the experiment. Figure 11.5(c) plots the values of the circularity at the middle of each experiment versus the flow rate (blue dashed line in Fig. 11.5(a). As can be seen, values of the flow rate above Q = 10 μL/min failed to induce instability in the system.

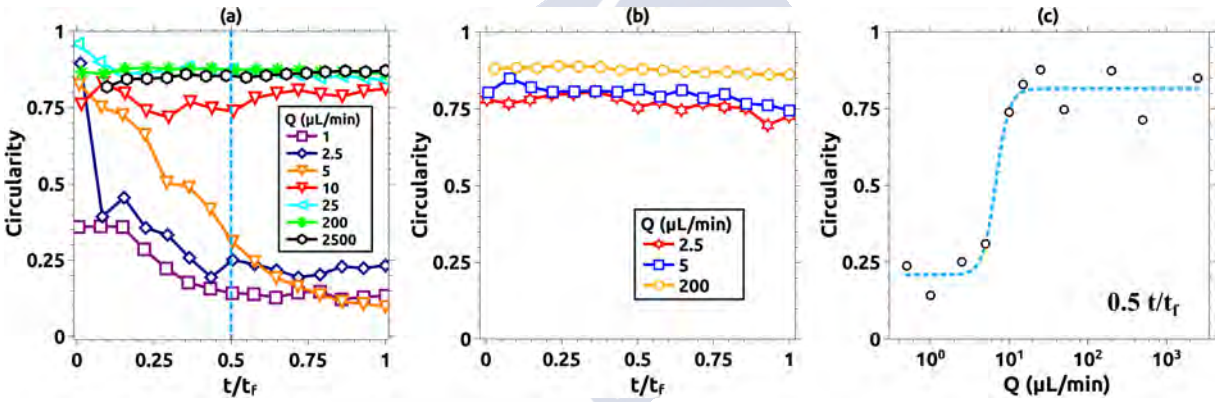

Figure 11.5: Quantitative comparison of the radial profile as a function of the flow rate. The shape of the displacing front is described by the circularity of the pattern as described in the methods section. (a) Variation of the circularity with normalized time for several Q. For the larger flow rate, the circularity was closer to 1, meaning that the shape of the front remains close to a perfect circle. As Q was decreased, the initially stable displacing front (with circularity values close to 1 when $t/t_f \cong 0$), changes its morphology and the circularity dropped. Those changes became more pronounced for lower flow rates (Q = 2.5 μL/min in the figure). For these cases, the circularity decreased till $t/t_f \cong 0.5$ and reaches a stationary value around 0.25 once the pattern was fully developed. (b) Circularity of the non-reactive cases. In all the studied cases, the circularity remained close to 1, indicating that such fronts remained mostly circular during all the experimental realization. (c) Semi-log plot of the circularity of all the cases studied at t/t_f = 0.5 (light-blue dashed line indicated in (a)). For larger values of Q, the circularity remained closer to 1 until 10 μL/min. For lower flow rates, the circularity value dropped down to 0.25.

Displacing Solution Profiles

Figure 11.6 compares the average displacing profile and the standard deviation for both reactive (Fig. 11.6(a)) and non-reactive (Fig. 11.6(b)) cases for several flow rates. As can be observed, for Q = 200 μL/min, the displacing solution of both the reactive and non-reactive cases match in terms of the front advancement and dispersion. The same was observed for the remaining control cases, where neither significant alteration in the displacement profiles nor the dispersion was observed. For lower flow

rates, the dispersion increased and the displacing fronts showed irregular shapes. This was a quantitative indicator of pattern formation.

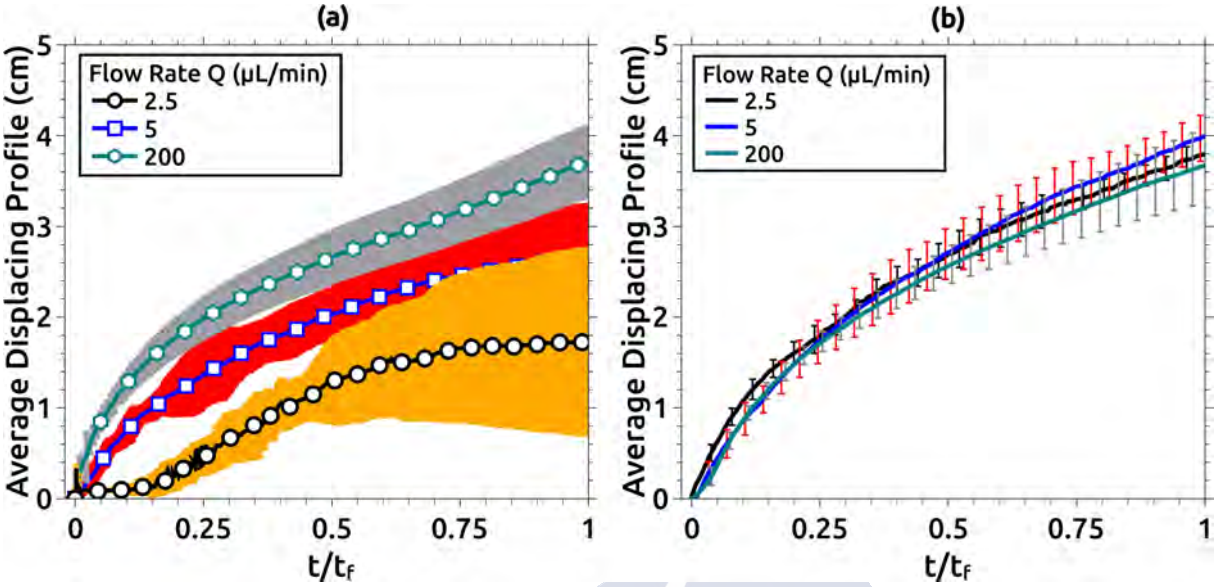

Figure 11.6: Quantitative comparison of the displacing solution profiles in a relative timescale for (a) reactive and (b) control experiments. All results are scaled to the final time for each experiment (t_f). The results are presented as the average (marked lines) and the colored areas correspond with the dispersion of each measurement. Marks are intended as a visual guide. For higher Q (200 μL/min), the profile described the typical circular front. In this case, the dispersion was well bounded as can be observed in Fig. 11.3. As the flow rate was decreased (5 μL/min), the reaction processes became more important producing changes in the average profile and increasing the dispersion. For the lowest flow rate analyzed (2.5 μL/min), the dispersion was maximized, especially for $t/t_f > 0.5$. These results are coherent with the experimental observations presented in Fig. 11.3 and the results of Fig. 11.5. (b) Profiles obtained in non-reactive conditions for the same flow rates analyzed in (a). In this case, the dispersion was represented with error bars to facilitate the comparison. These results demonstrated that without reaction influence the circularity of the interface remained stable and almost unaltered during all the experimental run.

11.2 Case II

11.2.1 General System Overview

In Case II, the more viscous solution (Solution A) was located initially inside the Hele-Shaw cell and the less viscous solution (Solution B) was injected into the cell with a constant flow rate becoming, thus, the displacing solution. From the fluidic point of view, this system is considered unstable and in absence of reaction, viscous fingering instability is prone to occur. These type of systems were widely characterized in literature and appears in many industrial applications with detrimental impact [46, 132, 44, 21].

Similar to Case I, Figure 11.7 compares the reactive and non-reactive cases, but at this time, for two different flow rates. The lower row of Figure 11.7(a) presents the control experiment where the injected solution was replaced by distilled water. As this was an unstable configuration, viscous fingering was immediately observed. The upper row presents the case where the interfacial reaction was allowed where Solution B was composed of gluconic acid. In this case, the evolution was completely different, the instability was suppressed and there was an effective displacement of the more viscous Solution A.

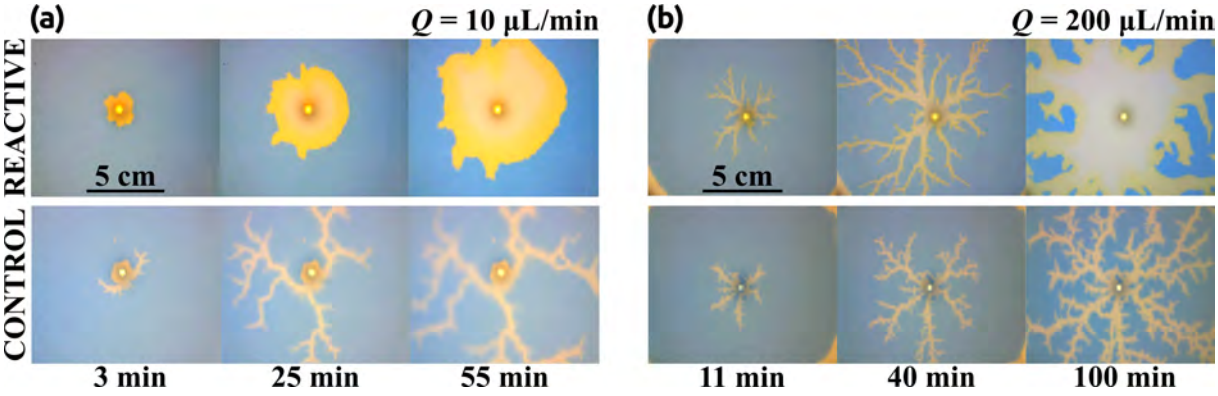

Figure 11.7: Stabilization of an initially unstable front for (a) Q = 10 μL/min and (b) Q = 200 μL/min. In both flow cases, a reactive (upper row) and a non-reactive (lower row) experiment were conducted. Non-reactive cases (control) are always unstable leading to the development of a fractal pattern that rapidly reaches the border of the observation region. The reactive cases were sensitive to the flow rate Q, in (a) the displacing front grew stable showing a more circular pattern. When the flow rate was increased (b), a fractal shape was observed again. In this case, once the border of the reactor was reached, the fractal ramifications increased their thickness changing the front shape. This was not observed in the control case, where once the pattern reached the border of the reactor, it remained fractal.

In Figure 11.7(b), the same experiments were repeated but for larger flow rates. As can be noted, the instability was not suppressed by the interfacial reaction and it was observed in both the control and reactive experiments.

Another interesting feature was observed in the more unstable cases. Once the instability was formed, the thickness of the fractal fingers increased in time. This is particularly noticeable in the last snapshots of Figure 11.7(b). As can be appreciated, in the non-reactive case, once the displacing reached the border of the cell, the fingers remained mainly unaltered. This did not happen in the reactive case, where the fractal shape of the instability changed dramatically.

11.2.2 Descriptive Analysis

Effect of the Flow Rate

Figure 11.8 shows the effect of the flow rate on the reactive system. The figure snapshots were taken at 25 % of the final time (0.25 t_f). As can be observed, for flow rates above Q = 10 μL/min the interface becomes unstable. However, even unstable, the decrement in Q favored the chemical interaction and produced an increment in the finger thickness. This effect is less appreciable when Q = 200 μL/min.

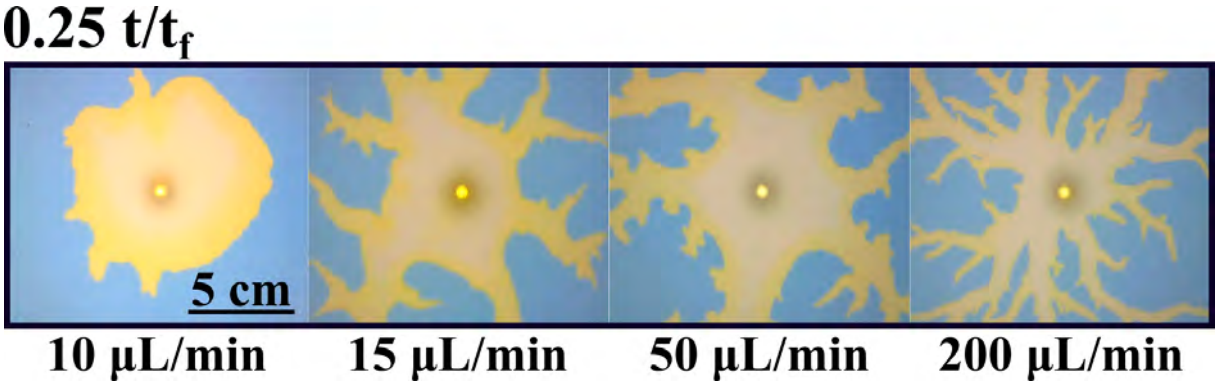

Figure 11.8: Reacting interfaces for several flow rates. All images were taken at $t/t_f = 0.25$ for each case. As the flow rate is decreased, the initially unstable front changes from a fractal-like structure into a more stable circular shape. For intermediate flows (Q = 15 and 50 μL/min) the fractal geometry is still there but the fractal fingers get enlarged due to the reactive process. Only for the lower flow rate case (Q = 10 μL/min), the interface becomes rounded and stable.

Schlieren Observations

Figure 11.9 shows a comparison between two experiments for (a) Q = 5 μ/L/min and (b) Q = 500 μL/min. In these cases, the stability of the system is strongly affected due to the reactive process and the inflow velocities. For lower flow rates (Fig. 11.9(a)), where chemical and convective timescales were comparable, the chemical front moved synergistically with the flow front. The reaction produces polymer precipitation and the creation of an effective crust. As pressure increases due to the incoming flow, the crust breaks. At this point, the faster reaction rebuilds the crust. This process repeated randomly around the interface results in a stable rounded interface propagating smoothly.

In Fig. 11.9(b), the fractal pattern was instantly generated due to the differences in viscosity between displacing and displaced solutions. This behavior continued until the displacing solution reached the cell boundary (approximately 1.5 min after the beginning of the experiment). 15 minutes later, it was possible to appreciate how the reaction produces the so-called crust. In this case, as the fluid moved faster than the reaction characteristic time, no effective wall was created, and thus, the system remained unstable. However, the generation of crust combined with the chemical front (now aligned to the flow direction) was responsible for the increment in the fingers thickness. This is visible at 85 min in Fig. 11.9(b).

11.2.3 Quantitative Analysis

Circularity Variation

Figure 11.10(a) presents the variation of the circularity during the experiment for different flow rates. For Q = 5 and 10 μL/min, the value of circularity was relatively high and almost constant along the experiment. In the remaining case, the interfacial reaction was not able to suppress the instability and the circularity dropped to very low values (close to zero). As time evolved, circularity increased due to a combination of diffusive effects and the chemical front described before. As previously stated, in this case the reaction front moved in the same direction as the flow rate. This behavior was not observed in the control cases (Figure 11.10(b), where circularity in all cases dropped almost instantaneously to low values after the instability occurred. Without any reaction-diffusion processes involved, the circularity remained close to zero during all the experimental run. Figure 11.10(c) plots the values of the circularity for all the studied flow rates measured at $t/t_f = 0.5$. It is possible to observe a clear transition with the increment of the flow (especially, above 10 μL/min). Bellow this critical flow rate, the fingering instability was suppressed while above the instability was still present.

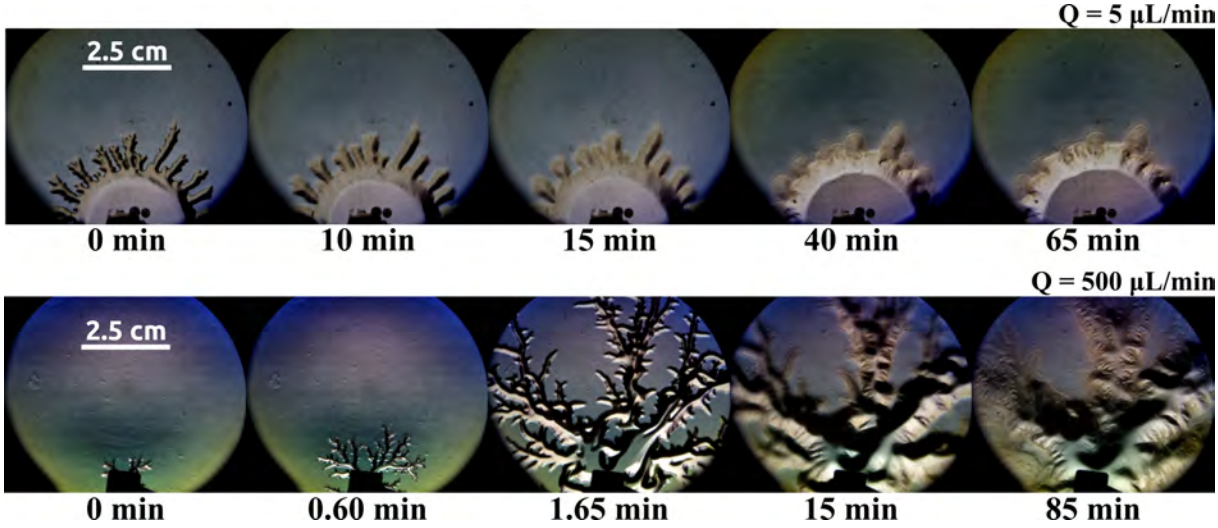

Figure 11.9: Case II observed using the Schlieren technique for (a) 5 μL/min and (b) 500 μL/min. (a) Starting from an initially unstable situation, the stability of the system was increased by the synergy between the polymer aggregation, the reactive front and the flow displacement. This was only observable when the reactive and flow fronts moved synergistically. In (b), the velocity of the flow was faster compared to the polymer aggregation and thus, the system remained unstable. Fractal patterns were observed to propagate quickly towards Solution B until the displacing fluid reached the reactor boundary. The finger thickness changed in time by the reaction that produces the aggregation of the PAA. This effect was particularly visible for t > 15 min.

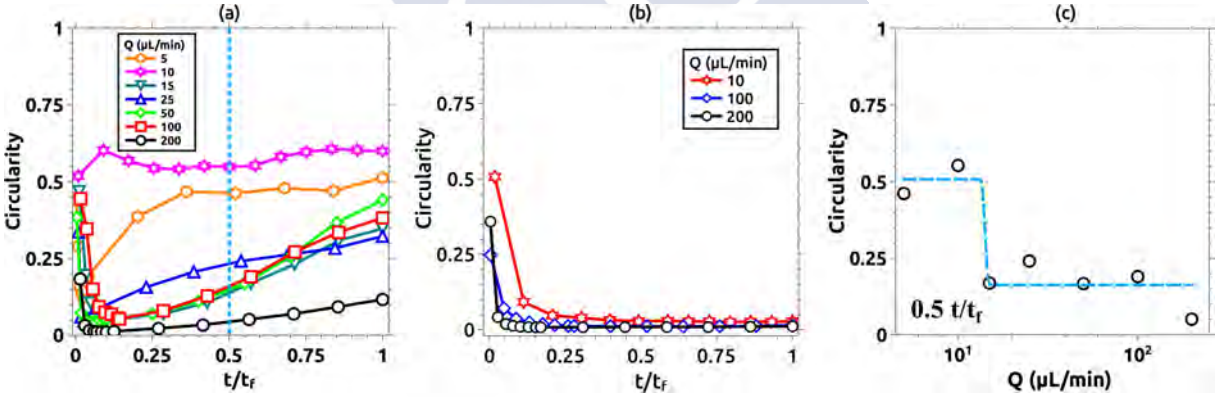

Figure 11.10: Quantitative measurements of the morphological changes of the interface as a function of the flow rate Q. (a) Evolution of the circularity for different flow rates. For larger values of Q, the circularity rapidly dropped to values near zero for $t/t_f < 0.25$. This was due to the fractality of the displacing front. For $t/t_f > 0.25$, the circularity increased with time due to reactive effects as shown in Fig. 11.7(b). For Q = 10 μL/min, the circularity remained stable between 0.5 and 0.6 during the recorded time. (b) Circularity variation of the non-reactive cases as a function of Q. For these cases, the absence of reaction did not interfere in the instability development and thus, the circularity was close to zero during almost all the experimental time. (c) Semi-log plot of the circularity for all the studied cases measured at $t/t_f = 0.5$ (blue dashed line in (a)). In this plot it is possible to see the changes in the system stability produced by the combination of the reaction processes at lower flow rates.

Displaced Volume Calculation

Another important feature, especially relevant for industrial applications, is the total amount of displaced solution per experiment. This is shown in Figure 11.11 for the control case without reaction and the reactive situation (Q = 10 μL/min in both cases). As can be observed, once the control case with fingering instability reached the cell boundary, Solution A stopped being displaced (black curve in the figure). On the other hand, when the reactive situation was considered and the instability was suppressed,

the displacement of Solution A continued for larger times and the total volume of Solution A displaced was significantly larger (specifically a 123% more than the control case. Red curve in the figure).

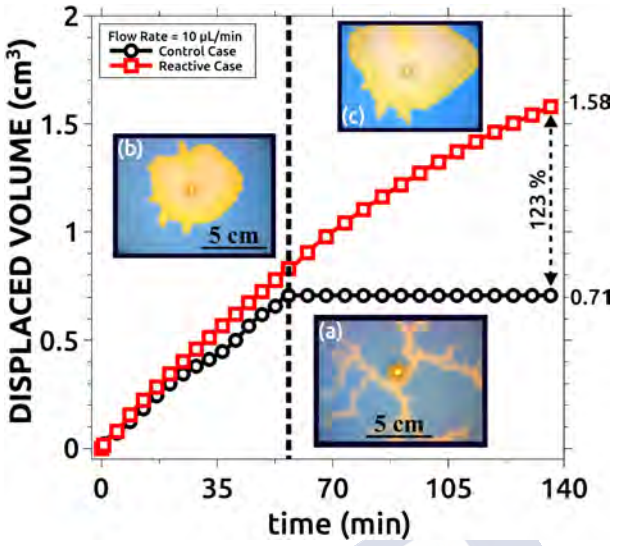

Figure 11.11: Comparison between the displaced volumes for the reactive and control cases for Q = 10 μL/min. The reactive case displaced more than twice the fluid displaced by the non-reactive case. The center vertical line indicates the time when the pattern in the control experiment reached the reactor boundary (a). Snapshot (b) was taken at the same time as (a) but for the reactive case. Snapshot (c) was taken at the end of the reactive case experiment.

11.3 Chapter Discussion

This chapter introduced and characterized two different chemo-hydrodynamical situations derived from one chemical formulation. Both situations, named Case I and II, showed a complex behavior where the chemistry played, presumably, a major effect on the system dynamics.

This was particularly noticeable in the pattern formation process observed in Case I. The increment of flow rate inhibited the symmetry break, keeping a stable displacement. The experiments demonstrated the untypical behavior of pattern formation. More specifically, the dynamics of the observed digitations at low flow rates indicate the intrinsic relationship between all the chemical interactions present.

In Case II, the influence of chemistry was more than significant. In this situation, the instability was suppressed by decreasing the flow rate. This fact, in addition to the circularity calculations, suggested a strong interaction between the hydrodynamical and chemical characteristic times. The closer observation of Case II evidenced an effective stabilization produced by the synergistic interaction between the fluid flow and the crust formation. This was reflected in the quantitative study of the displaced volume calculation, where the results indicated that the observed process was not only produced by diffusive effects and an effective displacement actually occurred.

Chapter 12

Chemical Analysis and Instability Mechanism

Abstract: *Once described the dynamics of Cases I and II, the next step is to understand how patterns are formed. In this sense, the following chapter will introduce a complete set of supplementary experiments that will be essential to discover the effect that each chemical component produces on the observed phenomena. Additionally, the estimation of the most important non-dimensional numbers will be also discussed. This study aims to enlighten both the physical and chemical aspects that are intrinsically involved in the development of pattern formation.*

12.1 Experimental Analysis - Control Experiments

This section presents the results obtained from the control experiments listed in Table 10.2. These results are supplementary to the non-reactive cases shown in the previous chapter.

12.1.1 C1: Influence of the Color Indicator

Figure 12.1 shows the evolution of the interface when the color indicator in the displacing solution was replaced by doubly distilled water. As can be noted, the instability was produced in the same way as in the case with a color indicator (Figure 11.4). This demonstrates that the observed phenomenon was not due to an artifact produced by this chemical component. This is also important as many previous works reported that color indicators could behave as proton acceptors like the PAA molecule [129, 186]. In this case, the color indicator did not show any significant effect related to this nature. Figure 12.1(b) shows the results of averaging the experimental frames in a specific region of time (30-200 min). As can be seen, it is possible to see similar stagnation areas, crust formation, and pattern emergence similar to those presented in Figure 11.4(b). The reactive front that competes with the injection flow was also observed 12.1(b)).

12.1.2 C2: Influence of the Formaldehyde

Figure 12.2 shows the effect of replacing the formaldehyde and the color indicator from Solution A with doubly distilled water. This experiment was done with a flow rate of Q = 50 μL/min. In this case, it was possible to observe both the crust formation at the interface and the reaction front once the injection was stopped. As can be noted for this case, as the convection is faster compared to the chemistry,

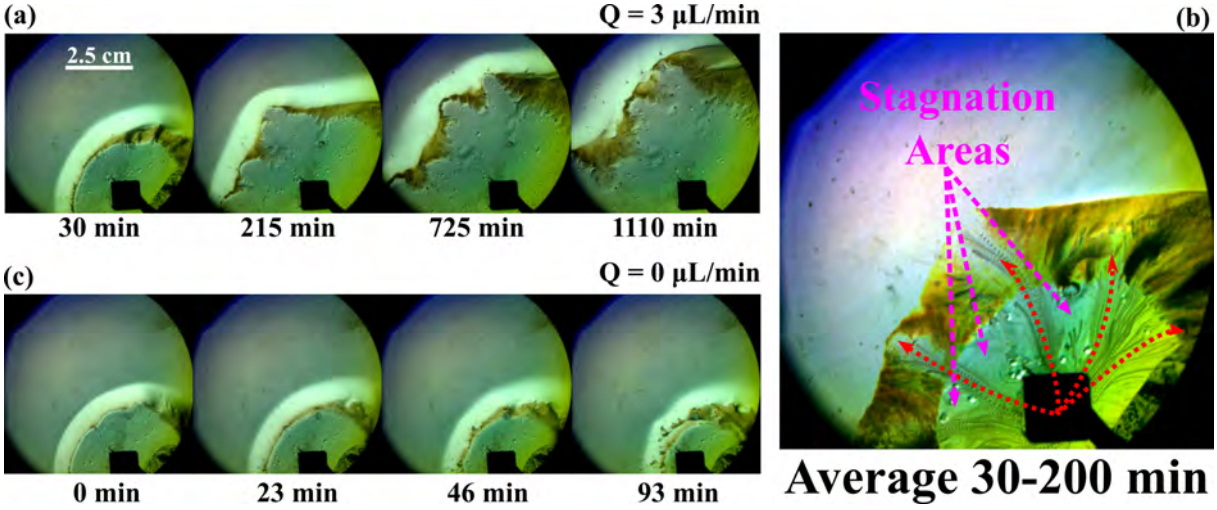

Figure 12.1: C1: Schlieren images for a control experiment where the color indicator in the displacing solution was replaced by doubly distilled water. The flow rate was set as 3 μL/min. The system behaved identically to the case with a color indicator. (a) The injection process showed the occurrence of ramifications in the same way as the experiment presented in Fig. 11.4. (b) Stagnation areas and crust accumulation were also observed in the development of pattern formation. (c) The reaction front observed in the original formulation was also observed when Q = 0 μL/min.

the displacement remained circular. However, even with the absence of patterns, crust formation was observed as a thin contour at the interface between both liquids. Once the injection was stopped (Fig. 12.2(b)), the reaction front observed in the original recipe was observed as well. This experiment demonstrated that the presence of formaldehyde was not mandatory for both chemical phenomena to occur.

12.1.3 C3: Influence of the SO_3^{2-}

This control experiment was carried out but replacing the formaldehyde, the color indicator, and the sulfite with doubly distilled water, letting only the polymer in Solution A. The results are shown in Figure 12.3. As can be seen, the contact between the PAA and the gluconic acid created crust (Fig. 12.3(a)). On the other hand, no reactive front was observed once the injection was stopped (Fig. 12.3(b)). As there was no competitive reaction front, the system remained stable during all the experiment. This experiment demonstrated that the minimum requirements needed for both chemical processes to occur are the presence of PAA and the SO_3^{2-} as shown in Figure 12.2. It also suggested that the crust observed in the previous experiments was necessarily composed of PAA.

12.1.4 C4: Influence of the PAA

In this case, Solution A was only composed of SO_3^{2-} in the same concentration as the base formulation replacing the remaining reagents with doubly distilled water. This experiment was intended to show the major role played by the polymer in both reactive processes and as a confirmation of the results presented in Fig. 12.3. As can be appreciated in Figure 12.4, neither precipitate nor chemical front was observed when only the sulfite was injected into the medium. As both solutions were miscible liquids with almost identical viscosity ($\mu \cong 1$ mPa.s), the interface grew deformed.

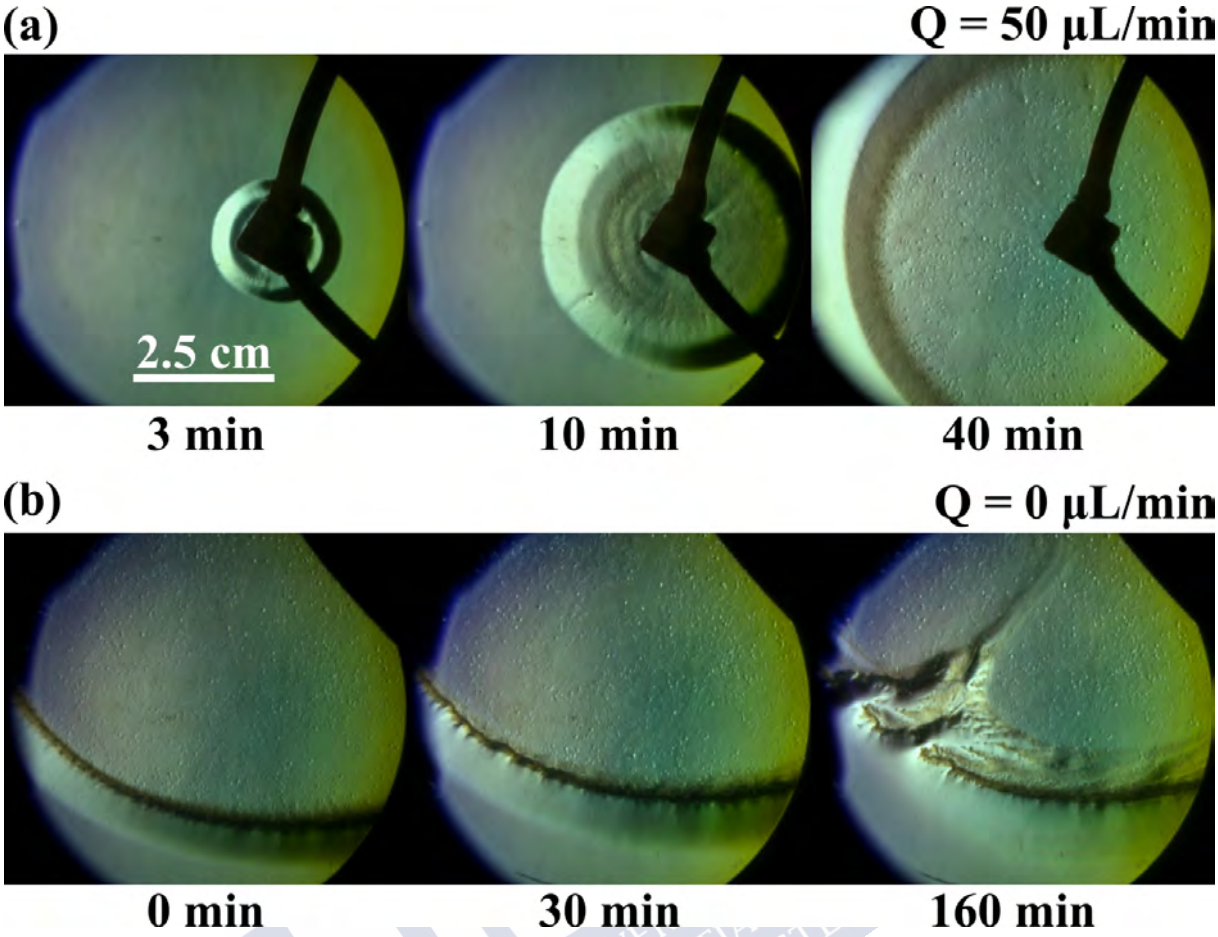

Figure 12.2: C2: Control experiment where the formaldehyde was removed from the original recipe and replaced with doubly distilled water. The concentration of the remaining reagents was the same as indicated in Table 10.1. (a) In this case, as the convective timescale was faster compared to the chemical timescale (Q = 50 μL/min.), the displacement remained stable during the injection process. The crust formation can be appreciated as the brownish contour located at the interface of both solutions. (b) The reaction front was also observed in this system configuration once the injection is stopped.

12.1.5 C5: Chemical Interaction at the Interface

The last control experiment was intended to show the chemical interaction between displacing and displaced solution at the contact interface. In this case, the displacing solution was composed of PAA and $CO_3{}^{2-}$ in the same concentration as the sulfite of the original formulation. The remaining components of the base formulation were replaced by doubly distilled water. The carbonate concentration used in this experiment was not detrimental to the polymer rheology. Also, the viscosity of the displacing solution was similar to the viscosity of the base case.

The goal of this experiment was to demonstrate the equilibrium displacement mechanism at the interface between both fluids. At the same time, it worked as a secondary test to verify the major importance of the sulfite in the reactive mixture. The results are presented in Figure 12.6. As can be seen, some crust accumulation was observed at the interface. However, neither pattern formation nor reactive front was appreciated. Additionally, several CO_2 bubbles emerged from the interface between both liquids once the displacing was injected. These bubbles grew during the experimental time.

Similar to the sulfite, the carbonate is in chemical equilibrium with other species in an aqueous solution. This can be appreciated in Figure 12.5, where the mass fractions of each equilibrium species are presented as a function of the pH for $CO_3{}^{2-}$ (Fig. 12.5(a)) and $SO_3{}^{2-}$ (Fig. 12.5(b)). Even though the

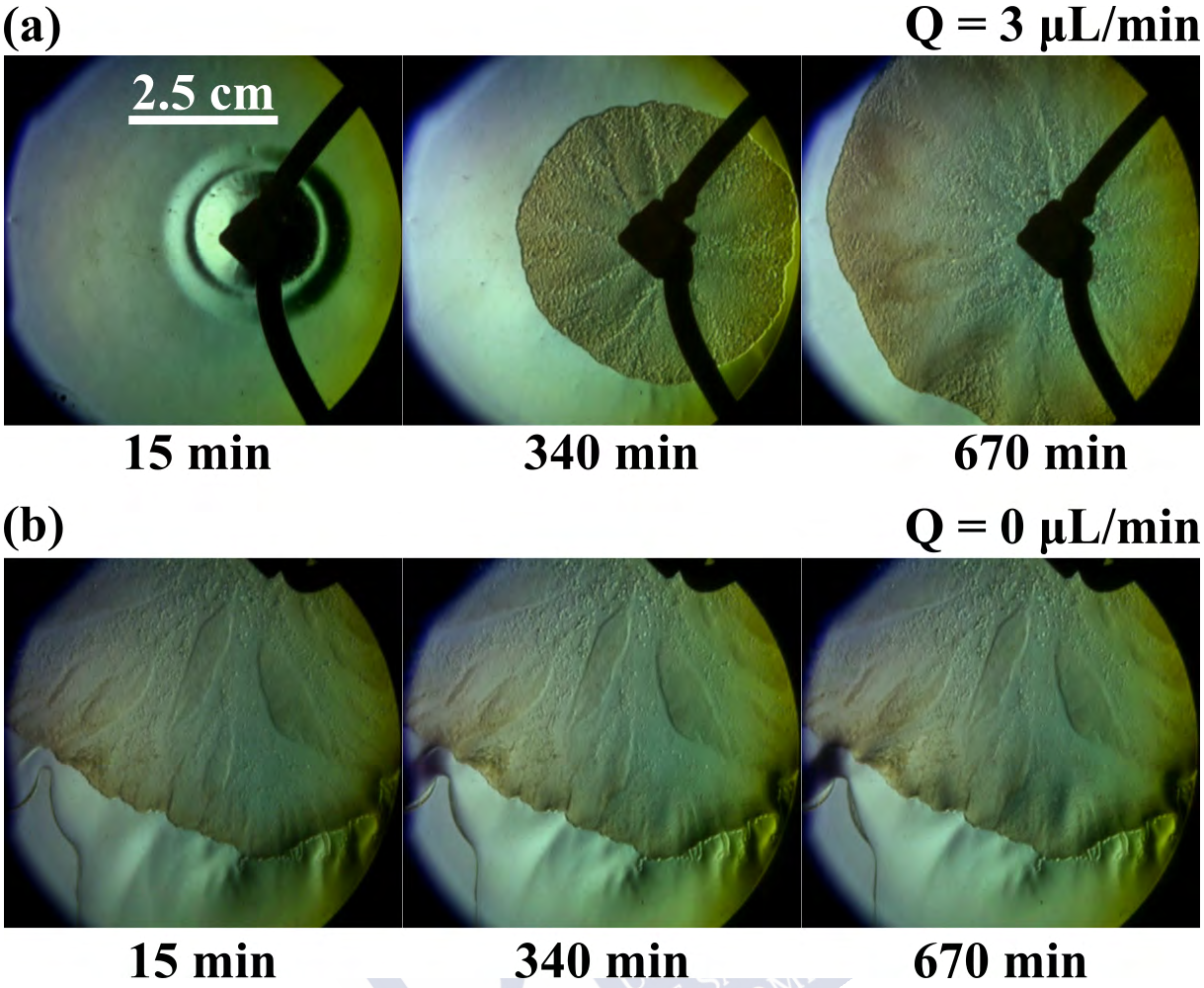

Figure 12.3: Schlieren images of a control experiment (C3) where the displacing solution was composed only of PAA in the same concentration as the base case indicated in Table 10.1 and the remaining reagents were replaced with doubly distilled water. The displaced solution remained unaltered with respect to the original formulation. (a) the interaction between the polymer and the gluconic acid created. However, no pattern formation was observed and the system remained mostly stable. (b) No chemical front was observed once the injection was stopped.

interaction between the carbonate and the polymer is completely different from the interaction between the sulfite and the polymer, the presence of CO_2 bubbles suggested that the interfacial condition was acid enough to displace part of the carbonate equilibrium into CO_2, as indicated by the following equilibrium equations [219]:

$$CO_3{}^{2-} \rightleftharpoons HCO_3{}^{-} \rightleftharpoons H_2O \cdot CO_2 + CO_2\,(g)$$

Where the equilibrium is displaced to the right side for pH < 6 (Fig. 12.5(a)). As previously indicated, the gluconic acid solution has a pH $\cong 2$ (orange dashed lines in Figure 12.5). All this suggests that the observed bubbles were produced by the displacing/displaced interaction and the acidic environment provided by the gluconic acid. For the sulfite species, the equilibrium equations are similar:

$$SO_3{}^{2-} \rightleftharpoons HSO_3{}^{-} \rightleftharpoons H_2O \cdot SO_2$$

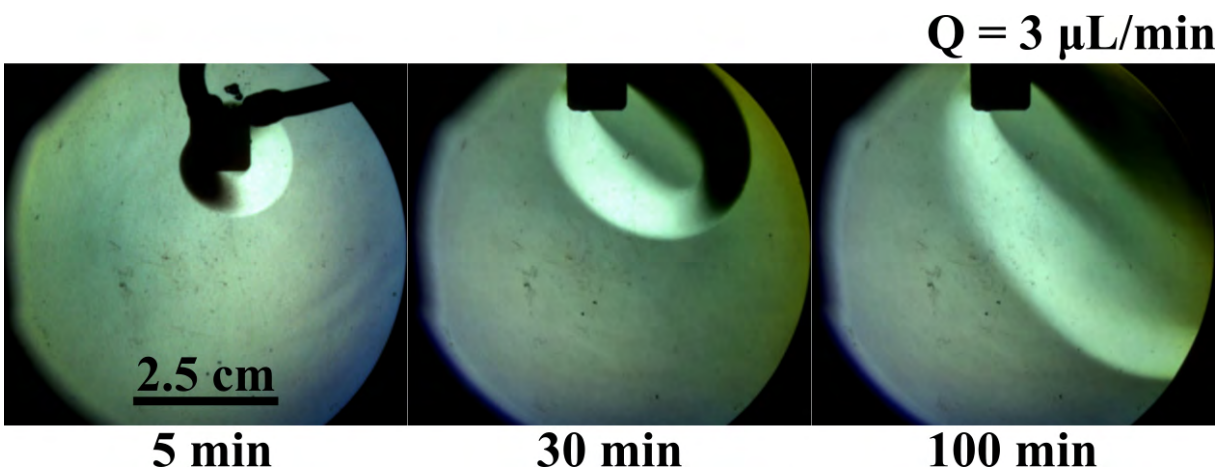

Figure 12.4: Schlieren images of a control experiment (C4) where the displacing solution is composed by SO_3^{2-} in the same concentration as the base case indicated in the methods section. The displaced solution remains unaltered concerning the original formulation. As can be seen, no precipitation nor chemical fronts are observed.

However, at pH $\cong$ 2, most of the sulfite in the solution is in the form of bisulfite [77]. The presence of bisulfite is fundamental to the reaction front to occur. This will be discussed in the forthcoming sections.

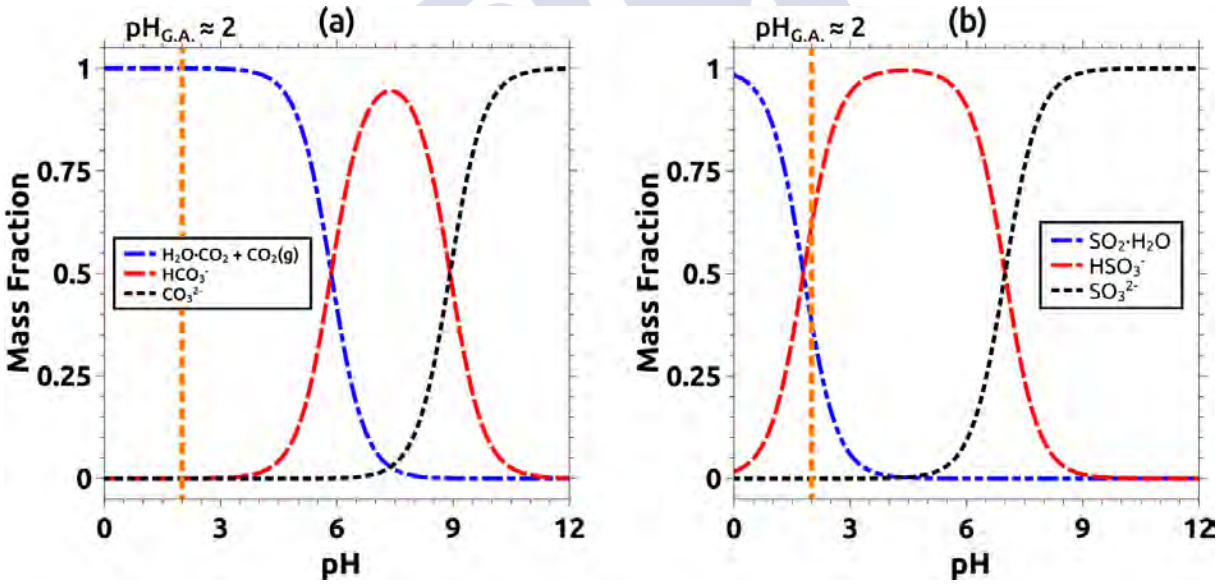

Figure 12.5: Equilibrium of (a) CO_2 and (b) SO_2 species in aqueous solution at 23°C.

This control experiment was particularly useful to understand how the miscible displacement affected the chemical composition of the species located at the interface, helping to elucidate the mechanism behind the pattern formation.

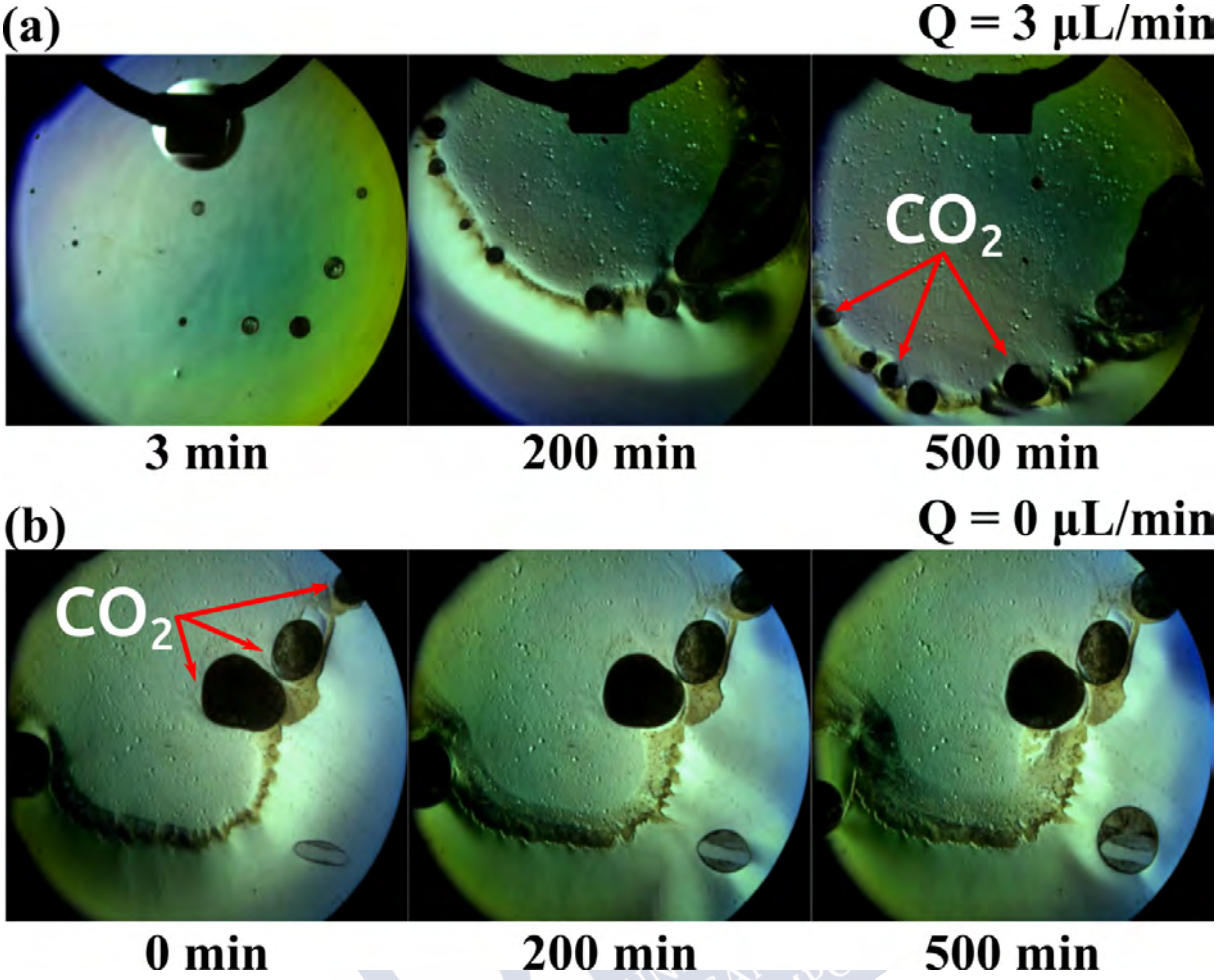

Figure 12.6: Schlieren images of a control experiment (C5) where the displacing solution was composed of PAA and CO_3^{2-}. The PAA concentration remained unaltered as indicated in the original formulation. The carbonate concentration was set equal to the sulfite concentration indicated in Table 10.1. The displaced solution composition remained unaltered. (a) Both precipitation and bubble formation was observed once the injection started. The bubbles grew during the experimental run. (b) Once the injection was stopped, no chemical front was observed. However, the bubbles continued to grow. These bubbles indicated the presence of CO_2 in the cell. This species was produced by the acidity of the gluconic acid solution.

12.2 Physical and Chemical Mechanism

12.2.1 Crust Formation

From the control experiments C1-C3, it was possible to infer that the presence of PAA was fundamental for the crust formation (no crust was observed without PAA in the medium). Moreover, it was necessary the low pH condition provided by the gluconic acid in the medium, as no effect was observed when Solution B was replaced by doubly distilled water (C6). As was explained in Section 1.9, the PAA molecule is affected by the pH of the medium [195, 2, 104]. At higher pH, the carboxylic groups of the PAA molecule dissociate changing into carboxylate ion. The negative charges of the carboxylate groups produce a repulsive effect that elongates the molecule into a rodlike structure that critically increases the viscosity of the solution. In contrast, at lower pH, both intra and intermolecular hydrogen bonds compact not only the PAA structure but also produce molecule agglomeration [195]. This agglomeration facilitates the precipitation by the large side chain of the PAA molecule (in this

system 4000000 g mol^{-1}).

Precipitation was also observed in an assay tube when different acid solutions were added to PAA formulations. In particular, different compositions of PAA were mixed with gluconic acid (Solution B) and [HSO_3^-] = 0.068 M. The obtained mixtures were centrifuged as explained in Section 10.1.6. The results are presented in Figure 12.7.

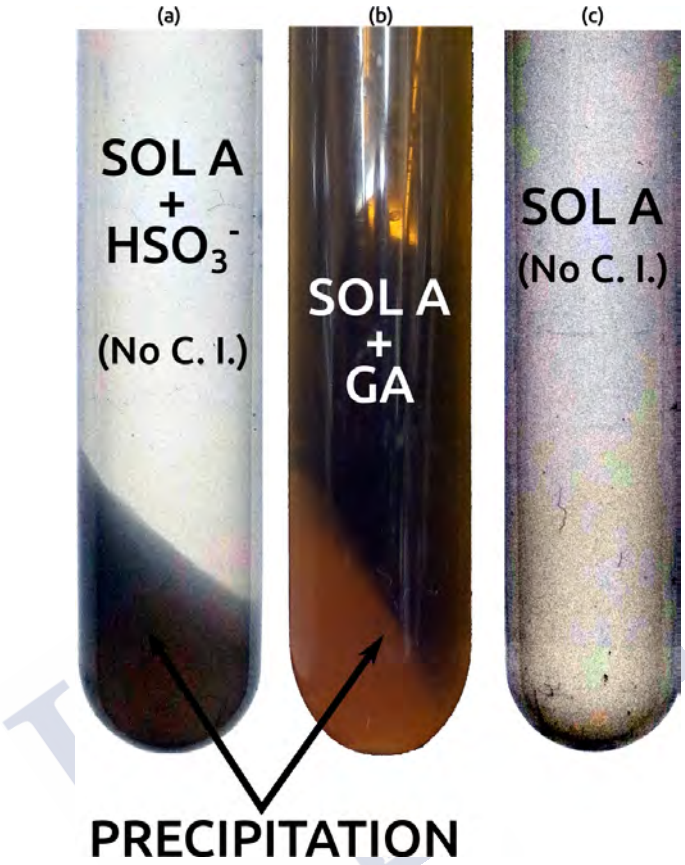

Figure 12.7: Precipitation test done for three different preparations: (a) a mixture of 50% Solution A (without color indicator) and 50% HSO_3^- (0.068 M) (b) a mixture of 50% Solution A and 50% Solution B (Gluconic acid 1.66 M) and (c) only Solution A (without color indicator). All assay tubes were centrifuged for 5 minutes at 5000 rpm at 23 °C. Precipitation was only observed for cases (a) and (b).

This experiment demonstrated the occurrence of precipitation when a PAA solution is exposed to an acidic condition. The original mixture itself (Solution A) did not show any precipitation (Fig. 12.7(c)). This agreed with the fact that neither precipitation nor pattern formation was observed when the gluconic acid was replaced by doubly distilled water (experiment C6). These results also demonstrated the stability of the original formulation.

SEM Micrography

Additionally to the previous results, Solution A and the precipitate were analyzed by Scanning Electron Microscopy (SEM). Figure 12.8(a,b) shows SEM micrographs of Solution A at two different magnifications, 1 and 5 kX, respectively. Figure 12.8(c) shows a SEM micrograph of the extracted precipitate with a magnification of 1 kX. As can be seen, both obtained images shared some similarities, however, the precipitate exhibited a more compacted structure. This was evidenced when comparing the micrographs taken with the same magnification factor. This also strongly suggested that both Solution A and the precipitate were composed of the same material, the PAA. A piece of external evidence that

supports this hypothesis was found in the work of Ho *et al* [92]. In such work, the authors present several SEM micrographs of PAA molecules that share similarities with the structures here presented [1].

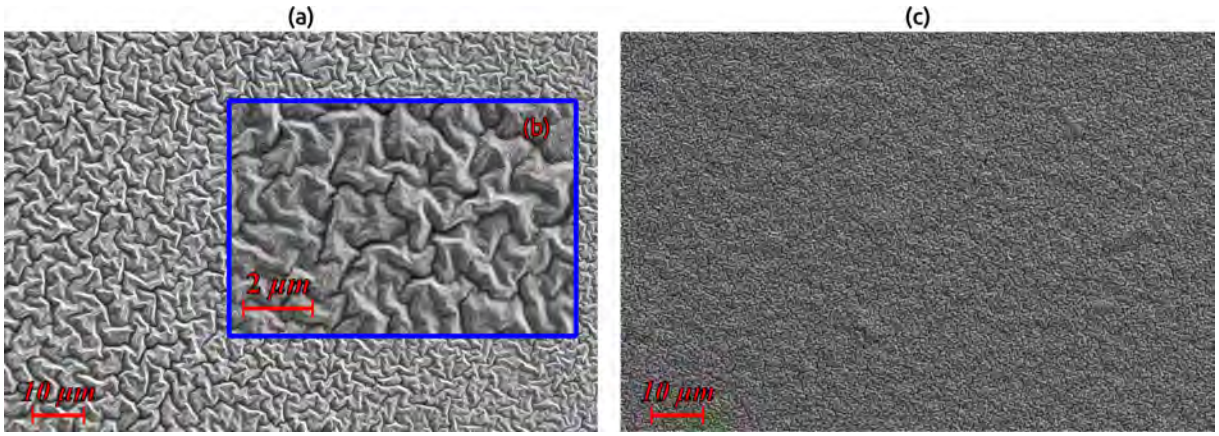

Figure 12.8: SEM micrographs of Solution A with at different magnifications: (a) 1 kX, and (b) 5 kX. (c) SEM micrograph of the precipitate at 1 kX. The protocol used to obtain these images is explained in Section 10.1.6.

Effect of the Precipitate on the System

In physical terms, the precipitation affects the fluid displacement by decreasing the permeability of the porous matrix locally. Several works reported the influence of such phenomena in the generation of hydrodynamic instabilities [176, 23, 58]. The permeability loss increased the pressure of the system. This increment in pressure was responsible for the ejection of the displacing solution that produced the characteristic shape of the ramifications observed in Case I. This can be observed in the Schlieren images of Figure 11.4

Regarding Case II, the precipitation phenomenon worked differently. When the timescales are comparable enough, the PAA precipitation worked as an effective wall that stabilized the system globally. This is shown in Figure 12.9, where a closer observation of the reactive case presented in Figure 11.7(a) (Q = 10 μL/min) is presented. As can be seen, the precipitate created at the interface displaced the more viscous solution once the chemical and the convective timescales worked in synergy. Even if there were intra-viscous fingering between Solution B and the polymer crust, the overall situation was stable.

[1] This image is not included in the manuscript due to copyright issues. Such micrographs can be consulted in the aforementioned cite.

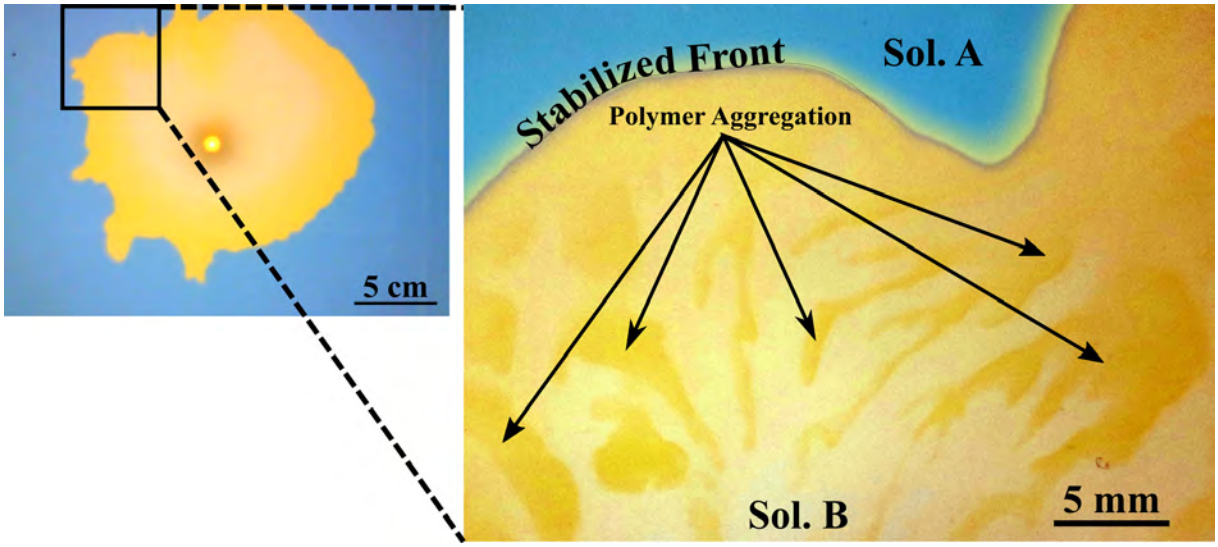

Figure 12.9: Closer observation of the front stabilization in Case II. This image illustrates the physical mechanism involved in the stabilization in a viscous fingering situation for the case where Q = 10 μL/min. For a lower flow rate, the reaction produced a polymer aggregation wall, making possible the drag of Solution A. The polymer aggregation is appreciated as a brownish crust as the one observed in Figure 11.9. Some patterns were locally produced between both solutions due to the polymer precipitation. However, the competition between the reaction rate and the displacing flow makes the system globally stable.

12.2.2 Reactive Front

From control experiment C3 it was deduced that the simplest system where the reactive front occurred was composed of PAA and $SO_3{}^{2-}$ in Solution A and gluconic acid in Solution B (Table 10.2). As was demonstrated in Part II, the $HSO_3{}^-$ can be generated by equilibrium displacement if $SO_3{}^{2-}$ is added to a PAA aqueous solution (see Section 7.5.1). This process is mediated by the polymer dissociation in H_2O as following:

$$PAA \rightleftharpoons PA^- + H^+ \qquad \text{(R2"-1)}$$

$$SO_3{}^{2-} + H^+ \rightleftharpoons HSO_3{}^- \qquad \text{(R2"-2)}$$

Where PA^- is the polycarboxylate ion [62, 58].

For the reaction front to occur, gluconic acid must be present in Solution B. As described in Kovacs *et al* [108, 107], the gluconic acid is dissociated in an aqueous solution as following:

$$GA \rightleftharpoons G^- + H^+ \qquad \text{(R2"-3)}$$

where GA is the Gluconic Acid and G^- is the gluconate ion. As was previously indicated, the pH of Solution B used in this work is about 2.

In the first place, the PAA is also known as a reversible proton acceptor [186, 129]. This molecule is known to affect the apparent diffusivity of protons and was extensively used to modify the dynamics of classical pH-oscillators where autocatalytic fronts are common [129]. However, the chemical front observed in this system cannot be produced by an autocatalytic process as there are no oxidant species in the medium [72, 186, 129]. Thus, this suggested that the nature of this chemical front was different

front the classical autocatalytic approach.

In the second place, experiment C5 showed that CO_2 bubbles emerged from the interface between Solution A and B when the sulfite was replaced with carbonate. This indicated that the acidic condition was strong enough to displace the carbonate equilibrium from $CO_3{}^{2-}$ into CO_2. This also suggested that when $SO_3{}^{2-}$ was in the mixture, the same phenomenon occurred to the sulfite, displacing the equilibrium and producing bisulfite which is essentially an acidic species. This result explained why the chemical front switched from a blue coloration (basic) into a yellowish coloration (acid) when the base formulation of Solution A was used. (This was not observed when $SO_3{}^{2-}$ was not included in the mixture).

Finally, there exists a large difference in diffusivity between the PAA of Solution A and H^+ of Solution B. Many works reported that the diffusion coefficient of the PAA molecules is at least two orders of magnitude less compared to the water diffusivity (D_{PAA} = 1 x10^{-11} m^2/s)[2, 58, 148]. It is also known that protons diffuse faster than water (D_{H^+} = 9.3x10^{-9} m^2/s) [139, 2]. As a conclusion, it is possible to affirm that the chemical front is a combination of all the reaction-diffusion processes described. The effect of the diffusion in the system stabilization will be addressed in Section 12.2.4.

12.2.3 Reaction Front Velocity and Damhköler Number Calculation

All the conclusions of the previous section can be confirmed and extended by characterizing the reaction front and estimating the non-dimensional Damköhler number. The Damhköler number (Da) compares the reactive and convective timescales. A value of $Da > 1$ indicates the prevalence of the reactive process over the hydrodynamics. Based on the previous works of Nagatsu [142, 140, 139, 141] and Fernandez [65], the Damhköler number in a radial Hele-Shaw cell can be estimated as:

$$Da(R) = \frac{v_r R^2}{2Q} \tag{12.1}$$

where v_r is the velocity of the reaction front and Q is the volumetric flow.

The value of v_r was calculated directly from the Hele-Shaw cell by measuring the front displacement observed once the injection of the displacing solution was stopped. In the experiments of Case I, the reactive front always propagates from Solution B towards Solution A. Figure 12.10(a) shows four different snapshots of this process. Taking several radial profiles from the injection hole through the cell (black dashed lines in Figure 12.10(a), a Space-Time Plot (STP) like the one presented in Figure 12.10(b) was obtained. The reaction velocity v_r was then calculated by measuring the slope of the STP as indicated. The average value for v_r, obtained over several experiments was:

$$v_r[mm/min] = 0.047 \pm 0.006 \tag{12.2}$$

This value was obtained from experiments where the separation gap was kept constant to a = 0.25 mm.

Once the reaction front velocity was estimated, the Damhköler number was calculated as indicated in Eq.(12.1). Figure 12.11(a) shows a semi-log plot of the estimation of the Damhköler number as a function of the average radius of the interface for all the studied flow rates in Case I. As can be noted, during the evolution of the experiment, the interface average radius became larger and so the hydrodynamic temporal scale became smaller and Da larger. Figure 12.11(b) plots all the Damhköler numbers estimated for all the experiments performed calculated for an average interface radius of 20 mm. As can be appreciated, for Q $>$ 10 μL/min, $Da < 1$ indicating the prevalence of the convective process, while for Q $<$ 10 μL/min, $Da > 1$ demonstrating the prevalence of the reactive process. This agreed with the experimental observations where the first experiment that shown an irregular displacement in Case I was Q = 5 μL/min. Moreover, 20 mm is also the average cell radius where patterns started to occur in the aforementioned case (Fig. 12.11(c)). This demonstrated the validity in the measurement of

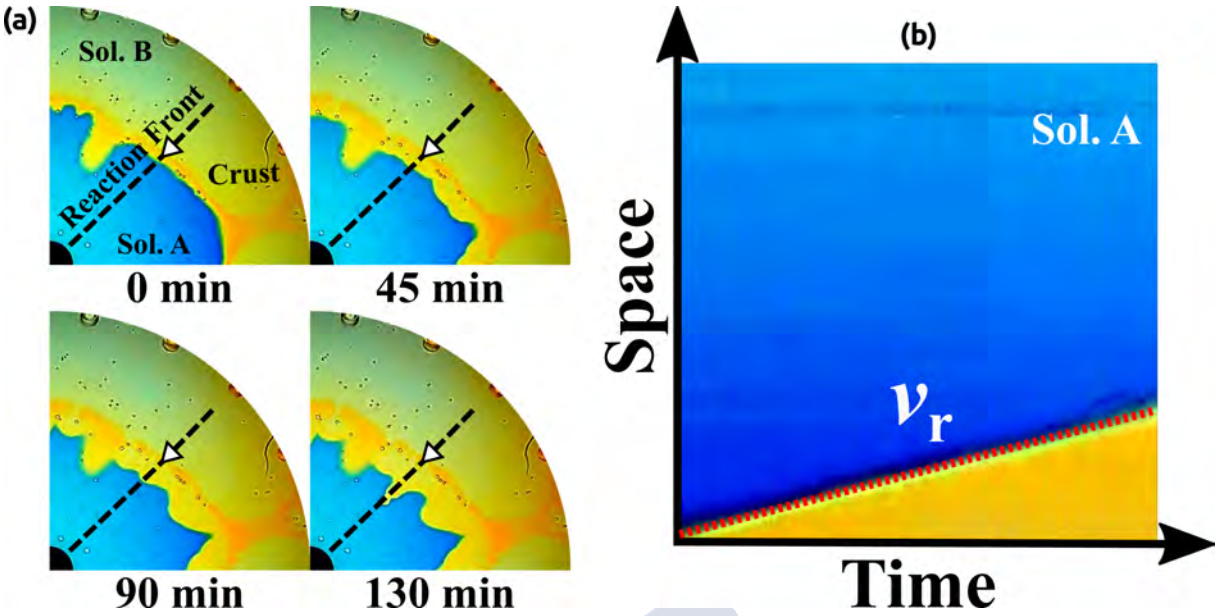

Figure 12.10: Measurement of the reaction front velocity used to estimate the Damhköler number (*Da*). (a) once the injection of the displacing solution was stopped, the reactive front was observed to move against the flow direction. This reactive front always competes with the advancement of Solution A in the experiments of Case I. (b) The front velocity v_r was estimated by measuring the slope of the space-time plot obtained by taking radial profiles of the cell. More details are included in Appendix C.3.

v_r. $Da \gg 1$ for Q = 0.5 μL/min and $Da \ll 1$ for Q = 2500 μL/min are the extreme cases that confirm the tendencies. It can be concluded that for larger injection flow rates, the hydrodynamics was such that the reaction front had no practical effect and a stable displacement was observed (no instability). Only when the reaction was allowed to play a role ($Da < 1$) the instability was observed.

In terms of the Damhköler number, the stabilization process observed in Case II was obtained when the flow timescale was slow enough to allow the reaction to occur. In this case, the chemical front moved aligned to the flow reducing the pH of the medium. This facilitated the polymer precipitation. However, here the polymer did not block the flow and worked as an effective wall that dragged the more viscous fluid. When the flow timescale was large, the reaction was slower, and classical viscous fingering was observed. Even though there was an unstable displacement between the low viscous displacing solution and the polymer, the overall process was stable as can be observed in Figure 12.9.

12.2.4 Péclet-Damhköler Number (*PeDa*)

As was mentioned in Section 12.2.2, diffusion also plays a major role in the nature of the chemical front. Thus, it is also important to analyze the relationship between the diffusive and reactive processes. The Péclet-Damkhöler number (*PeDa*) is an effective measure to study the influence of such processes in the development of pattern formation [192, 7, 218].

By combining the Péclet and the Damhköler number definitions [102, 7, 15], the *PeDa* number can be estimated as:

$$PeDa(R) = \frac{v_r R^2}{4\pi a D} \tag{12.3}$$

where v_r is the reaction front velocity, R is the cell radius, a is the separation gap and D is the diffusion coefficient.

The *PeDa* number was estimated by considering the diffusion coefficient of the proton and the H_2O.

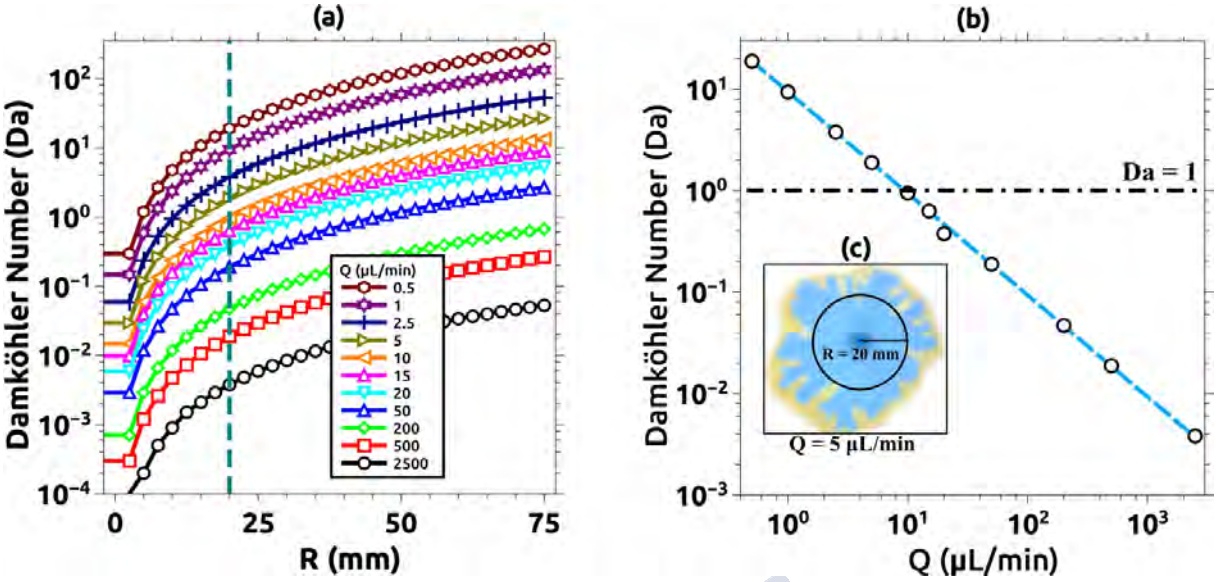

Figure 12.11: Damhköler number (*Da*) estimation as a function of the average interface radius (R). (a) Comparison of *Da* for Q = 2.5, 5, and 200 μL/min versus the average interface radius. A remarkable increment in the Damhköler numbers was observed for lower flow rates indicating that the reaction process was faster compared to the convective process. *Da* increases proportionally to the radius and inversely proportional to the flow rate. Both observations are logical as the velocity of the displacing solution decreases with the radius in a radial Hele-Shaw cell. This effect is more prominent if the flow rate is decreased allowing reaction and convection to have comparable timescales for a certain R. (b) Log-log plot of *Da* as a function of Q for all the cases studied. All values were taken at R = 20 mm, which is the average radius of the circumference delimited by the region before the blue-yellow boundary as exemplified in (c) for Q = the 5 μL/min. The results were coherent with the experimental analysis presented in Fig. 11.5(b). For Q $>$ 5 μL/min, *Da* $<$ 1 indicating the dominance of the convective process, while for Q $<$ 5 μL/min, *Da* $>$ 1 indicating the predominance of the reactive process.

Large *PeDa* numbers indicate that the reaction processes are predominant to diffusive processes. For this work, it was necessary to demonstrate that the fast-diffusive action of the protons provided by the gluconic acid played a major role in the pattern formation, more specifically, in the stabilization process observed in Case II.

In order to illustrate this, a hypothetical situation where solutions were reactive, but Solution B diffused similar to water ($1x10^{-9}$ m^2/s) was considered. As can be seen in Figure 12.12, in this situation the obtained *PeDa* numbers were always above 1. This indicated that the reaction effects were more important than diffusion effects. When B diffused similar to protons, *PeDa* $<$ 1 for R $<$ 6 mm. This indicates that for such a range, the diffusion processes are predominant to the reaction processes.

Due to the experimental assumptions made to calculate the *PeDa* number and practical limitations, the experimental study of the diffusion effect was not considered. However, this phenomenon will be analyzed from a numerical perspective in Section 13.4.1.

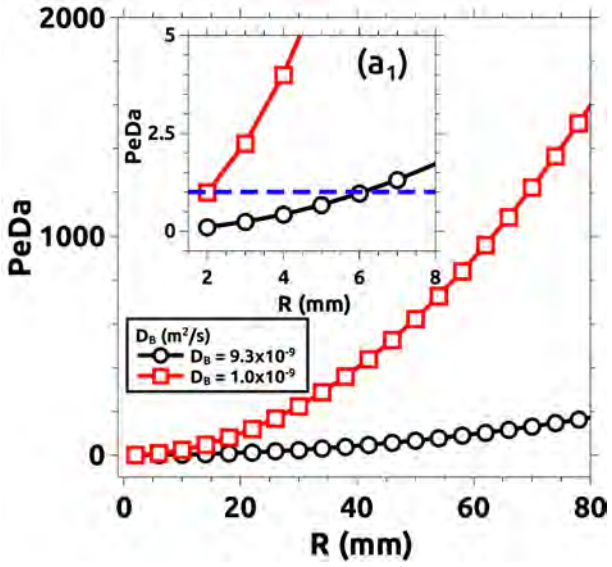

Figure 12.12: *PeDa* number estimation considering that B diffuses slower ($1.0\text{x}10^{-9}$ m^2/s) and faster ($9.3\text{x}10^{-9}$ m^2/s). A *PeDa* number below 1 indicates that diffusion effects are relevant compared to reaction effects. Estimation shows that there is a range of radii when $PeDa < 1$ if B diffuses faster (this is indicated in the inset of the figure).

12.3 Chapter Discussion

This chapter presented an extensive chemical analysis done to understand the mechanism of the phenomena observed in Cases I and II.

The control experiments provided valuable information regarding how each species affected the dynamics of both displacements. In this sense, it was demonstrated the minimum system where both chemical processes occurred and it was possible to identify their nature.

It was shown that the crust formation, mostly observed in Case I was produced by the precipitation of the PAA polymer due to the acidic condition of the gluconic acid at the interface between the displacing and displaced solutions. The precipitate acted as a stopper that impeded the normal flow of the displacing and increased locally the pressure by reducing the permeability of the porous matrix. This process was fundamental for the development of the ramifications observed in Case I. In Case II, this process acted as a barrier that effectively displaced the most viscous fluid, producing an effective stabilization.

On the other hand, the reactive front was responsible for the untypical dynamics of the digitations observed in Case I. The results suggested that this complex process depended on reaction-diffusion mechanisms and it was intrinsically related to the flow velocity through the Damhköler number. The effect of this process in the pattern formation of Case I, was to produce the finger to move backward, generating their characteristic dynamics. In Case II, the reactive front was responsible for the stabilization by favoring the polymer precipitation and improving the effective displacement. However, the reaction front was not only produced by the reactivity of both solutions. It was demonstrated that considering the experimental conditions here presented, the diffusive processes also played an important role in the stabilization mechanisms.

All the results here presented paves the possibility to develop a numerical model able to reproduce the dynamics of both cases similar to the experiments. This topic will be addressed in the forthcoming chapter.

USC
UNIVERSIDADE
DE SANTIAGO
DE COMPOSTELA

Chapter 13

Numerical Model and Results

Abstract: *To demonstrate the proposed physical-chemical mechanisms described in previous sections, 2D non-linear reaction-diffusion-convection simulations were performed. The model here introduced couples the dynamics of the displacement of reactive fluids in a porous media inside a Hele-Shaw cell, the existence of a chemical front, and polymer precipitation that locally affects the permeability of the system. Thus, by using values obtained experimentally, the system behavior will be only altered by interchanging the displacing and displaced solutions as the experiments. This numerical chapter will reproduce the experimental observations by imitating its presentation fashion.*

13.1 Reaction-Diffusion-Convection (RDC) Numerical Model

For a system of viscosity μ, porosity ϕ, and permeability κ. The governing equations, based on Darcy's Law, are given by the following RDC set of equations:

$$\begin{aligned} \nabla \cdot \vec{u} &= 0 \\ \nabla p &= -\frac{\mu(A,B)}{\kappa(C)} \cdot \vec{u} \\ \phi \frac{\partial A}{\partial t} + \vec{u} \cdot \nabla A &= D_A \nabla^2 A - k_1 AB - k_2 AB \\ \phi \frac{\partial B}{\partial t} + \vec{u} \cdot \nabla B &= D_B \nabla^2 B - k_2 AB \\ \phi \frac{\partial C}{\partial t} + \vec{u} \cdot \nabla C &= D_C \nabla^2 C + k_2 AB \end{aligned} \tag{13.1}$$

considering $\vec{r} = (x,y)$ as the position vector, then $A = A(\vec{r},t)$, $B = B(\vec{r},t)$ and $C = C(\vec{r},t)$ are simplified models for the polymeric solution, the gluconic acid solution, and the polymer precipitate respectively. ϕ is the porosity of the system and it was set constant for a Hele-Shaw cell [93, 176, 58, 45]. D_A, D_B, and D_C are the diffusion coefficients of A, B, and C respectively. It was assumed that the polymeric Solution (A) diffuses slower in comparison to the acidic Solution (B) and that the precipitate (C) barely diffuses ($D_c \simeq 0$) [2, 16, 176, 58].

The permeability of the system $\kappa(C)$ was set dependent on the polymer precipitate concentration and it was modeled by the following expression [176]:

$$\kappa(C) = \kappa_0 e^{-R_k(C/C_m)} \tag{13.2}$$

where κ_0 is the permeability when $C = 0$ (no precipitate in the medium), and it was calculated as $\kappa_0 = a^2/12$ [93, 193, 9], where a is the separation gap of the Hele-Shaw cell.

By defining $\kappa_m = \kappa(C_m)$ as the permeability when $C = C_m$ and $R_k = ln(M_0/M_m)$ as the permeability log-mobility ratio, where $M_0 = \kappa_0/\mu$ and $M_m = \kappa_m/\mu$ are the mobilities when $C = 0$ and $C = C_m$, respectively; the parameter R quantifies the influence of precipitation on permeability changes. A positive value of R indicates that C reduces the permeability of the porous matrix locally [176].

The viscosity, $\mu(A,B)$ was defined as a function of A and B, by the following relation [45]:

$$\mu(A,B) = \mu_A e^{R_B B/B_0} \tag{13.3}$$

where $\mu_A = \mu(A_0,0,0)$, represents the viscosity of the polymeric solution for a specific concentration A_0 in the absence of any other species in the medium.

The parameter R_B compares the viscosity of the two reactant solutions [45]. Similar to the experimental setup, both parameters μ_A and R_B were fixed and the stability of the system was only affected by the initial fluid configuration. Those values were estimated on basis of the experimental observations from previous chapters.

A simplified model was used to simulate the reactivity between the displacing and displaced solutions. This model was based on the chemical mechanisms proposed in Chapter 12, and it is given by the following chemical equations:

$$\mathrm{A} + \mathrm{B} \xrightarrow{k_1} \mathrm{B} \tag{R1}$$

$$\mathrm{A} + \mathrm{B} \xrightarrow{k_2} \mathrm{C} \tag{R2}$$

where equation R1 models the reactive front and equation R2 models the polymer precipitation (C) that is produced when both solutions (A and B) make contact at the interface. k_1 and k_2 are the rate constants.

As was previously explained, since the chemical front was not produced by an autocatalytic process, the diffusivity plays a major role in the overall phenomenon. In this sense, equation R1 represents the bisulfite generation by the action of solution B in one single step. On the other hand, the chemical reaction indicated in equation R2 was extensively used and validated to model precipitation phenomena by many previous works [176, 23, 58, 45].

Regarding the reaction rates, the value of k_1 was set accordingly to the experimental front velocity measured in Section 12.2.3. This was achieved by fitting the distance traveled by the numerical chemical front as a function of the reaction rate on a control simulation. The estimated value was $k_1 = 0.00052$ $(\mathrm{M}\ s)^{-1}$. The fitting is shown in Figure 13.1. The value of k_2 was estimated *ad hoc* as a function of k_1 by the following expression $K_f = k_1/k_2$. The value that better fit the experimental observations was $K_f = 10$, which corresponds to $k_2 = 0.000052$ $(\mathrm{M}\ s)^{-1}$. The effect of varying K_f was both experimentally and numerically studied. The results are presented in Section 13.4.2.

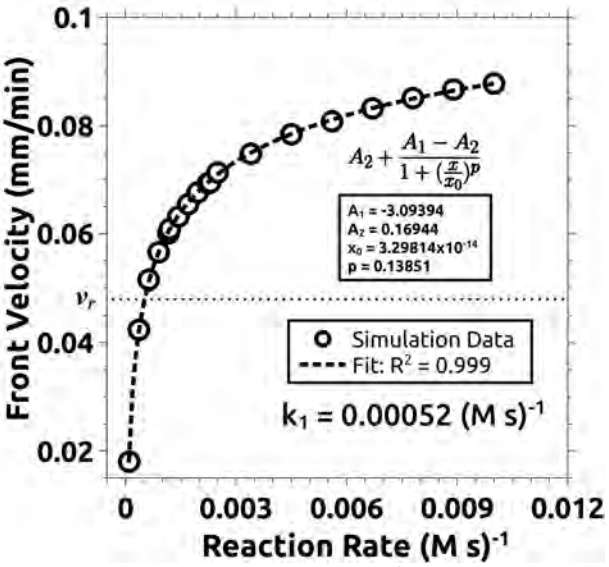

Figure 13.1: Equivalence between the reaction rate and the front velocity used for the numerical simulation of Case I. The rate of reaction k_1 was estimated from the experimental front velocity v_r calculated in Section 12.2.3.

13.2 Numerical Results for Case I

13.2.1 System Dynamics

Analogously to the experimental Figure 11.1, Figure 13.2 shows the numerical results obtained for simulating Case I. In such Figure, both reactive and non-reactive simulations are compared. For the reactive case and to mimic the experimental results, an overlayered image of the concentration fields of species A and C for Q = 5 μL/min is presented. As can be seen, both the pattern structure and the polymer precipitation are qualitatively well reproduced by the model. Additionally, in the non-reactive case neither pattern nor precipitate was observed, but only a stable displacement as observed in their experimental counterpart.

13.2.2 Effect of the Flow Rate

By changing the flow rate, the stability of the system was altered in a similar way as observed in the experiments. Figure 13.3 shows four different flow conditions. Alike to the experimental case, by increasing the flow rate the more stable the system became. Pattern formation and precipitation were observed, especially for the lower flow rates (2.5 and 5 μL/min), while for higher velocities, the typical stable displacement was observed with the characteristic annular reactive zone.

13.2.3 Circularity Calculation

The numerical patterns were characterized identically by measuring the changes in the circularity produced by the increment of the flow rate. The results are presented in Figure 13.4. Figure 13.2(a) shows the circularity evolution in normalized time (t/t_f) for the most representative cases (some cases were omitted to facilitate visualization). As can be seen, the dynamic of the circularity was also well represented by the model. For higher flow rates, the system reactivity was slower compared to the convection and the system remained stable (circularity $\cong$ 1). For lower flow rates, the chemical timescales matched the convective characteristic times at some specific radius. This, in combination

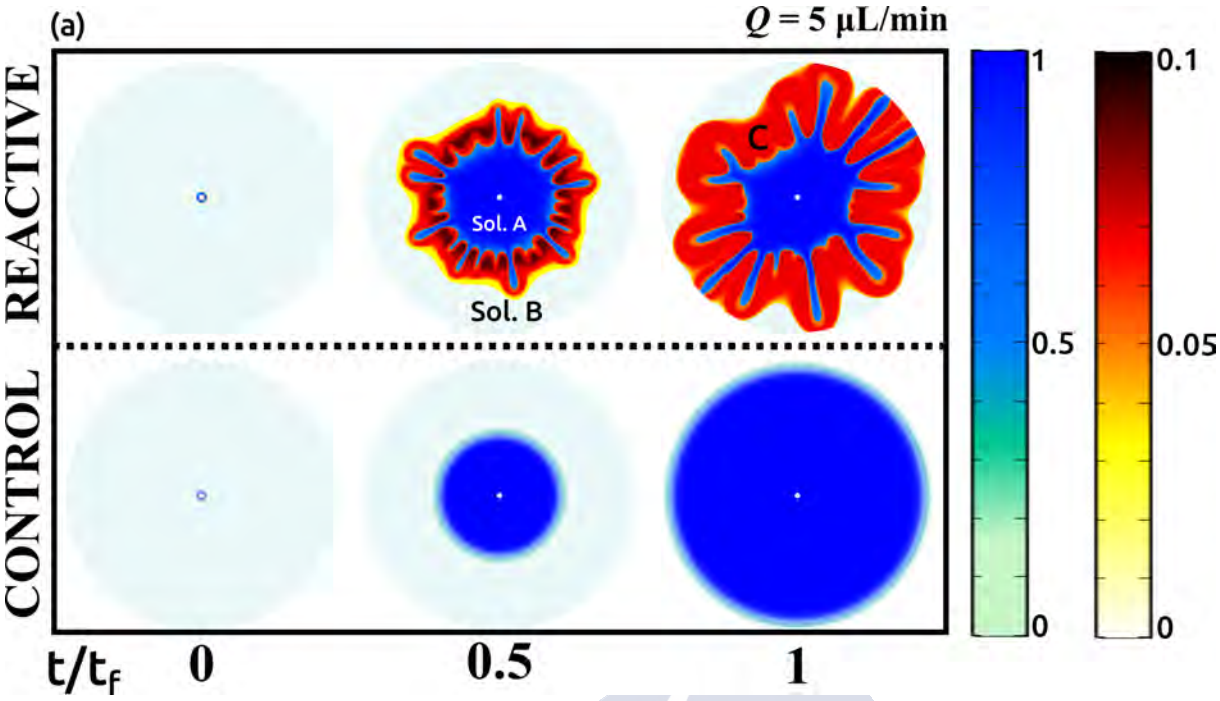

Figure 13.2: Numerical results of the simulation of Case I: (a) Numerical representation of the concentration fields of solutions A, B, and the precipitate C in a similar fashion as the experimental Figure 11.1. The upper row shows the reactive case, and the lower row shows the control case where solutions A and B do not react. The corresponding solutions/species are indicated in the reactive row. All results are presented in normalized time.

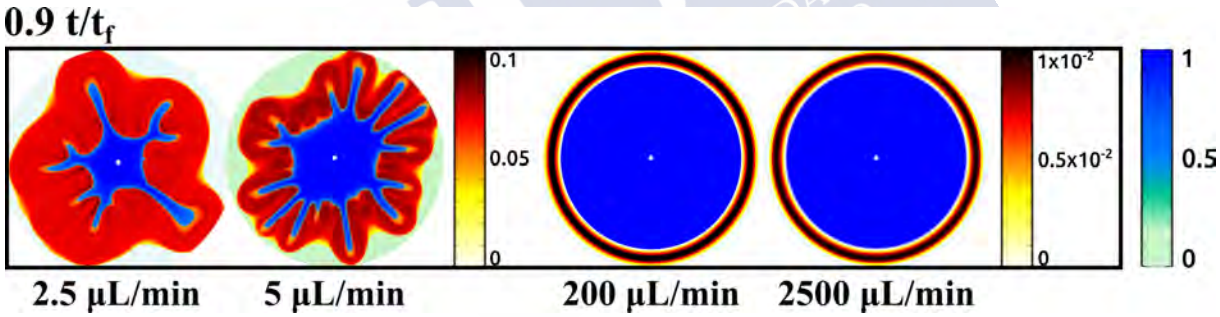

Figure 13.3: Effect of changing the flow rate on the numerical simulation of Case I. Similar to the experimental Figure 11.3, all snapshots were taken at $t/t_f = 0.9$. The concentration fields of A and C are overlayered and shown scaled for better comparison with the experimental cases. The simulation parameters are indicated in Table 10.3

with the local reduction of permeability (and the subsequent pressure increment) produced by the precipitation, led to the pattern formation.

The non-reactive situation is presented in Figure 13.2(b). As can be seen for these cases, the circularity was always closer to 1 as there was no reaction involved during the displacement.

The circularity variation as a function of the flow rate is presented in Figure 13.2(c) for all the studied cases. As can be appreciated, the quantitative prediction of the circularity was more than acceptable, except for some minor differences observed for Q = 10 μL/min. Also, the numerical curve presented a sharper shape different from the smooth S shape observed in the experiments. However, both numerical and experimental curves agreed qualitatively.

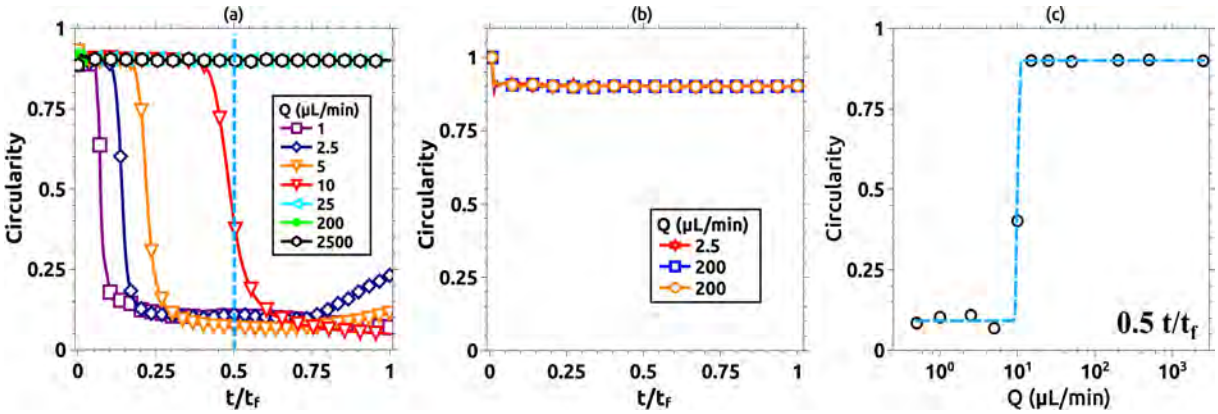

Figure 13.4: Circularity calculation as a function of the flow rate for Case I. Circularity of (a) the reactive and (b) non-reactive situations. (c) Circularity variation of all simulated cases as a function of the flow rate measured at $t/t_f = 0.5$. Unlike the experimental cases, the starting value of the circularity was always close to 1. This was an effect produced by the perfectly controlled initial conditions used for stability reasons. All simulation parameters are indicated in Table 10.3.

13.3 Numerical Results for Case II

13.3.1 System Dynamics

Analogously to Figure 11.7, Figure 13.5 shows the simulation results obtained for Case II. Figure 13.5(a) shows a comparison between two different flow rates Q = 10 and 200 μL/min for both reactive (upper row) and non-reactive (lower row) cases in normalized time. In this case and compared to their experimental counterpart, the obtained simulated patterns were not fractal. However, most qualitative and quantitative aspects of the system were well represented by the model.

For Q = 10 μL/min the pattern stabilization was visible compared with the non-reactive case. The stabilization effect was particularly evident at $t/t_f = 0.1$, where the non-reactive case showed an unstable pattern formation from the beginning of the simulation. For Q = 200 μL/min, both cases showed unstable pattern formation. Moreover, the model represented well the increment of the finger thickness observed experimentally.

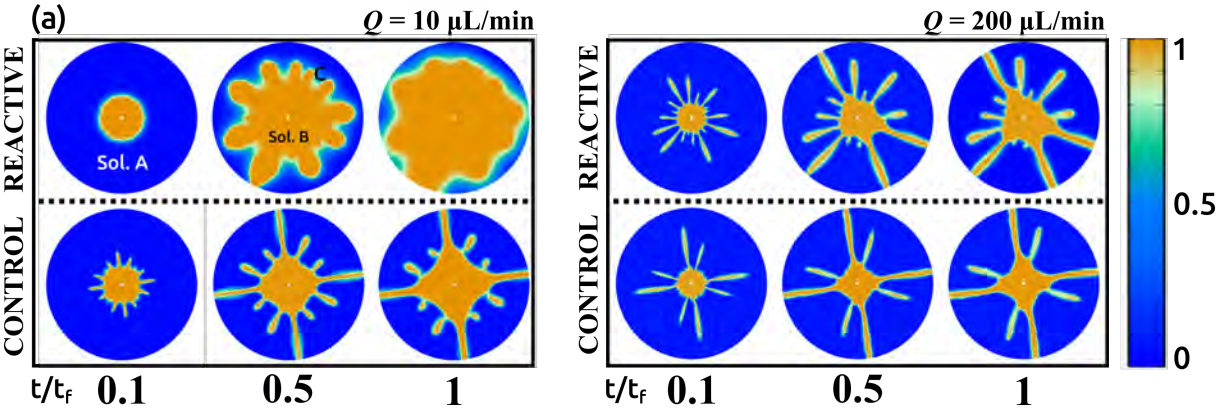

Figure 13.5: Numerical results of the simulation of Case II: (a) Numerical representation of the concentration fields of solutions A, B in a similar fashion as the experimental Figure 11.7. The upper row shows the reactive cases for two different flow rates Q = 10 and 200 μL/min. The lower row shows the non-reactive cases were for the same flow rates. The corresponding solutions/species are indicated in the figure. All results are presented in normalized time. The simulation parameters are indicated in Table 10.3.

The physics of the system was also reproduced by the model. Figure 13.6 shows a comparison between the concentration fields of species B and C for a low flow rate displacement situation (Q = 5 μL/min) of Case II. As can be seen, once the precipitate was formed, intra-viscous fingering was observed.

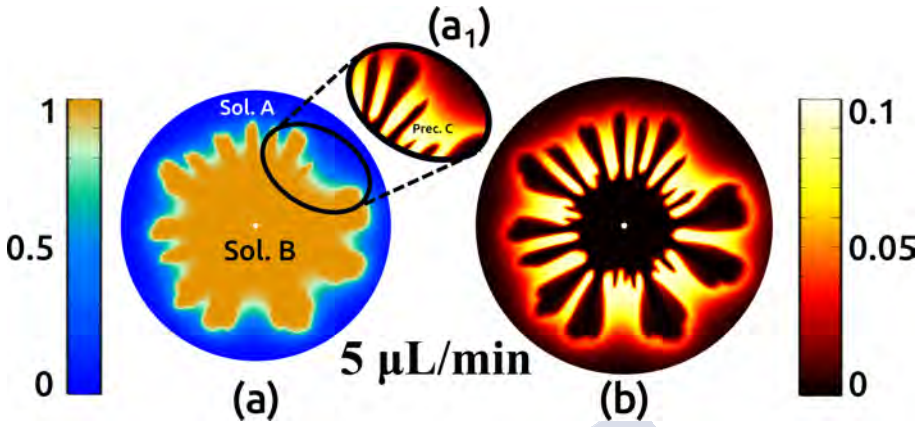

Figure 13.6: Closer observation of the precipitation effect in a simulation of Case II. Similar to Figure 12.9, the effect of the precipitate in the displacing process of Case II was well reproduced by the model. Intra-viscous fingering patterns were observed, however, the external boundary showed improved stability.

13.3.2 Effect of the Flow Rate

By changing the flow rate, the system stability changed accordingly to the experimental case (Fig. 11.8). Figure 13.7 compares this situation numerically for four different flow rates at the same normalized time ($t/t_f = 0.25$). As was expected, by increasing the flow rate the system stability decreased remarkably like the experimental case. As was previously discussed, even if the numerical patterns were not fractal, it is possible to affirm that results showed a good agreement in qualitative terms.

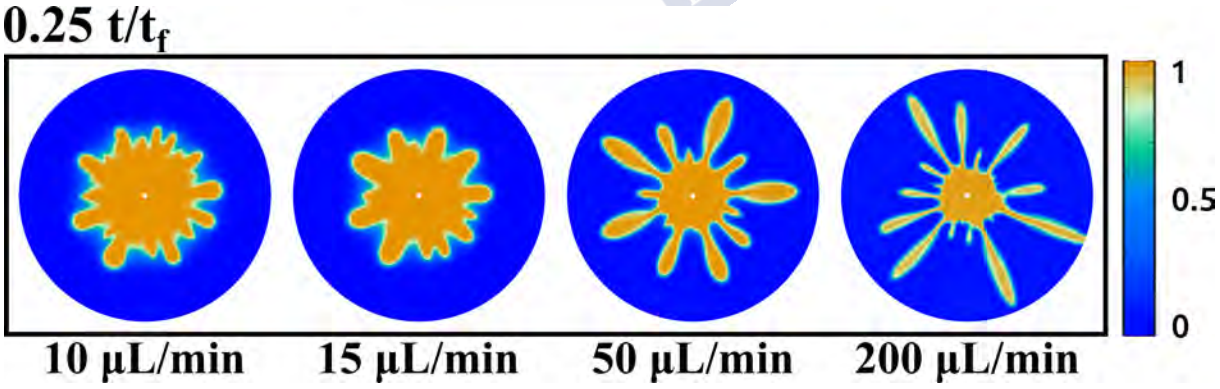

Figure 13.7: Simulation results of the effect of Q on Case II. All figures were taken at $t/t_f = 0.25$. The simulation parameters are indicated in Table 10.3.

13.3.3 Circularity Calculation

Figure 13.8 shows the circularity variation in a normalized time studied for several flow rates. As can be seen, the circularity of the higher flow rates rapidly decays to zero once the system is destabilized. The circularity then increases its value due to reactive effects just as in the experimental case. For the lower

flow rate, the circularity dropped to about 0.5 and increased approximately up to 0.8. Figure 13.8(c) shows the circularity variation as a function of the flow rate at t/t_f = 0.5. In this case, the tendency obtained from the simulations decreased softer compared to the experimental counterpart where a step shape was obtained (Fig. 11.10(c)). However, the values were closer to the experimental case and the dynamics of the system were also well represented.

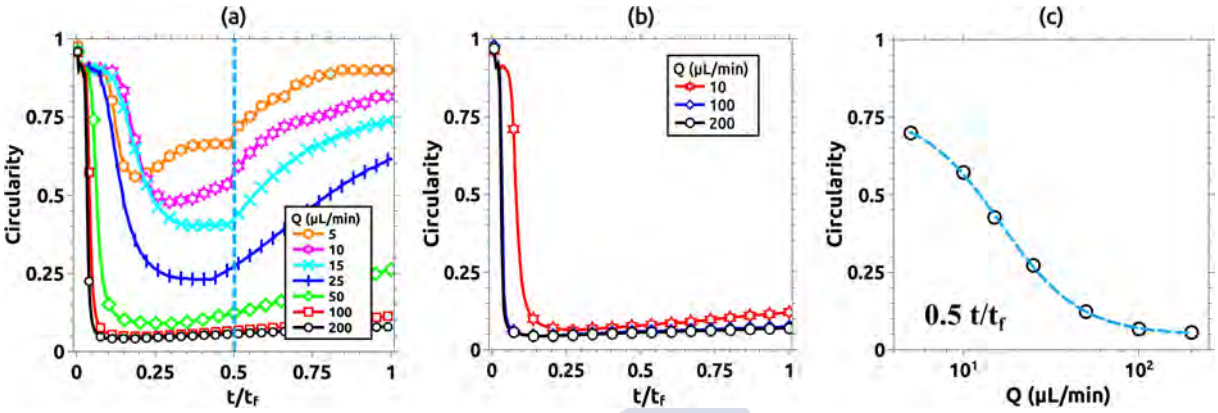

Figure 13.8: Circularity calculation for (a) reactive and (b) non-reactive cases. (c) Circularity variation of all simulated cases as a function of the flow rate measured at t/t_f = 0.5. Unlike the experimental cases, the starting value of the circularity was always close to 1. This was an effect produced by the perfectly controlled initial conditions used for stability reasons. All simulation parameters are indicated in Table 10.3.

13.3.4 Displaced Volume

Figure 13.9 shows the displacing volume recovery comparison for the simulated reverse case when Q = 10 μL/min. Because of the differences between the experimental control region and the simulation domain, the displacement was analyzed at two different times: when the displacing fluid reaches the border of the numerical domain in the non-reactive case (Inset(b_1)) and at the end of the simulation ($t = t_f$). In the first case, there was a 30 % difference in the displacing volume between the reactive and non-reactive case. This difference was mainly driven by the reaction-diffusion process. As expected in the non-reactive case, once the displacing solution reached the external boundary, the displaced volume shows a much lower increment. This did not occur in the reactive case, where the system was stabilized by the chemistry and 174 % more volume was displaced. Even though some differences were observed the simulated displacement agreed well with the experimental case.

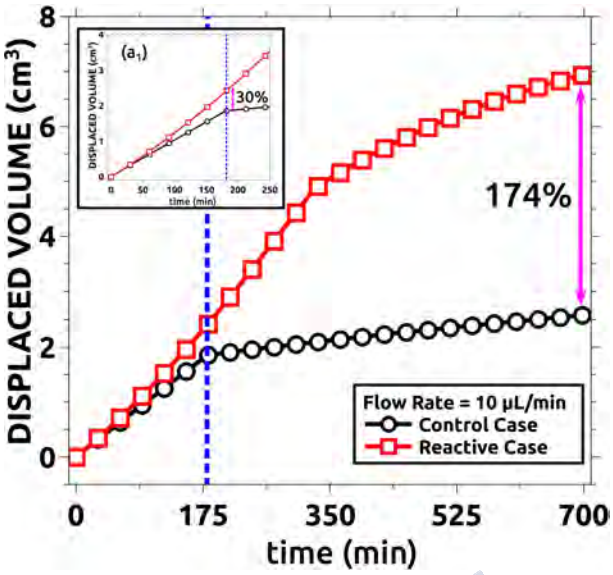

Figure 13.9: Quantitative numerical comparison between the displaced volumes for the reactive and control cases when Q = 10 L/min. The total displaced volume was compared at two different times: when control fluid reached the border of the numerical domain (inset a_1) and at the end of the simulation. In the first situation, the reactivity of the solutions improved the displacement a 30 % more compared with the non-reactive case. In the second situation, the total displacement was improved up to 174 % with respect to the non-reactive case. Simulation parameters are indicated in Table 10.3.

13.4 Supplementary Results

13.4.1 Effect of the Diffusion

As was explained in Section 12.2.4, the effect of the diffusion in the stabilization mechanism was studied numerically. This study assumed a hypothetical situation where a reactive system was considered, but the diffusion coefficient of the displacing solution (B) was modified. Figure 13.10(a) compares the numerical circularity obtained for both situations when Q = 10 μL/min. Results showed that when B diffused slowly (D_B = 1.0x10^{-9} m^{2}s), the system could not be effectively stabilized once the displacement had started. This was translated into a faster drop in the circularity. On contrary, when B diffused faster the combination of reactive and diffusive processes produced an effective stabilization of the system that increases the effective displacement. In this case, the circularity showed values closer to 1 during mostly the entire displacement. This can be also observed in Figure 13.10(b) where the concentration fields are compared at the same times. The effect produced by the fast diffusion of the species B was fundamental to obtain a stable displacement just starting the displacement. This demonstrates that not only the reaction played a major role in the pattern stabilization/formation, but also diffusion was an important factor to take into account.

13.4.2 Effect of Varying K_f

In Section 13.1 it was mentioned that the value of k_1 was calculated from the experimental measurements of the chemical front. On the other hand, the value of k_2 was estimated numerically *ad hoc* on basis of the experimental observations, taking the value $K_f = k_1/k_2$ = 10 to perform all the simulations. Figure 13.11 shows how k_2 was estimated by varying K_f. The results are presented for a representative case (Q = 5 μL/min). All snapshots were compared at t/t_f = 0.5. As can be seen, when precipitation velocity (R2) is twice as fast as the considered case (that is, $K_f = 5$), pattern formation

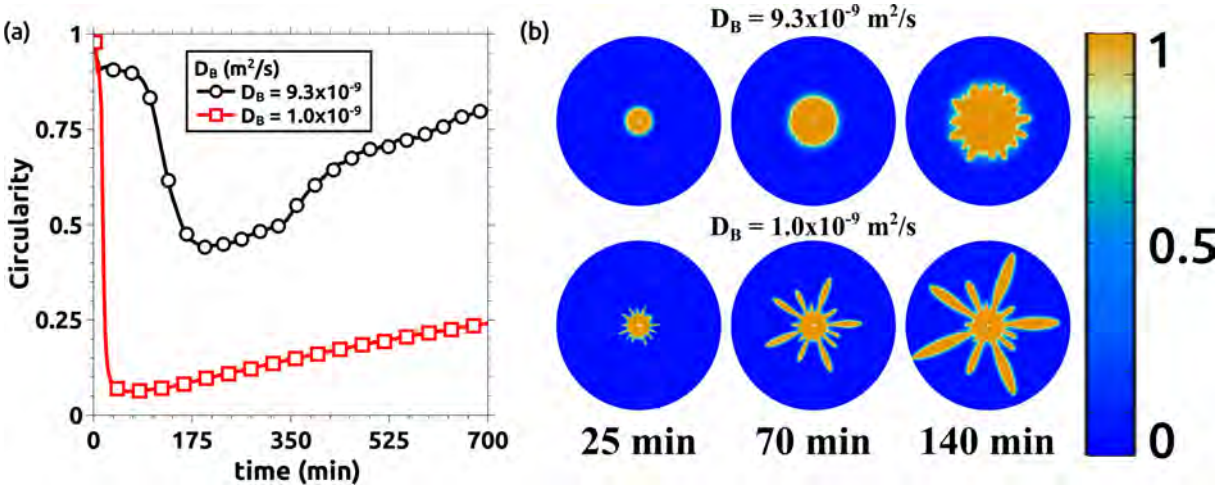

Figure 13.10: Effect of the diffusion coefficient of species B on (a) the circularity and (b) the pattern formation. In (a) the circularity is compared for the two cases presented in Figure 12.12. As can be seen, the circularity showed larger values (this is, more stable situation), when B diffuses faster. (b) The effect produced by the diffusion of Solution B was particularly noticeable at the beginning of the simulation where two simulations were compared keeping the remaining parameters as indicated in Table 10.3. The fast diffusion combined with an effective reactive phenomenon produced the stabilization of the system that improved the displacement process. In both cases Q = 10 μL/min.

started before, and the system showed a more unstable behavior similar to those observed for lower flow rates (Fig. 11.3). When the velocity of R2 was 50% slower compared to the considered case ($K_f = 15$), the system did not show any pattern formation nor symmetry break. The displacement remained stable, even considering reactivity.

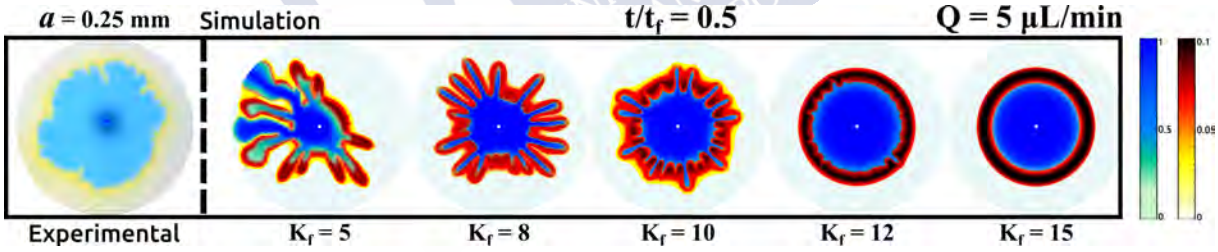

Figure 13.11: Effect of the variation of $K_f = k_1/k_2$. Five different conditions were studied to estimate the value of k_2 that better fit the experimental observations.

This situation was observed experimentally by increasing the separation gap (a) of the Hele-Shaw cell. As exposed in Nagatsu *et al* [142, 139, 140, 65], the Damhköler number in a radial Hele-Shaw cell depends on the cell gap for a specific reaction constant (see Eq. (8.2) in Part II and the aforementioned cites) [1]. By increasing the cell gap, the chemical timescales also increase. This is shown in Figure 13.12, where the cell gap was triplicated (a = 0.75 mm).

As can be seen, when the displacing was injected at a relatively high flow rate (150 μL/min), a stable displacement occurred. For about 25 min, the fluid front grew stably, which indicates that the hydrodynamic timescales were faster than the chemical ones ($Da < 1$). Between 25 - 31 min, the displacing front remained static and circular at a specific radius. This situation indicated that hydrodynamic and chemical timescales are equal ($Da = 1$). The fluid front remained in the same position

[1] In Section 12.2.3, the reaction velocity was directly measured inside the Hele-Shaw cell, therefore there was no necessity to include the cell gap in the calculation as the value was a velocity itself.

for about 7 min until the displacing was injected (V_f = 5000 μL). Once the injection was stopped, the chemical front "consumed" all the front in about 5 min ($Da \ggg 1$). This indicated that the velocity of the chemical front was much faster compared with all the cases studied previously (where a = 0.25 mm).

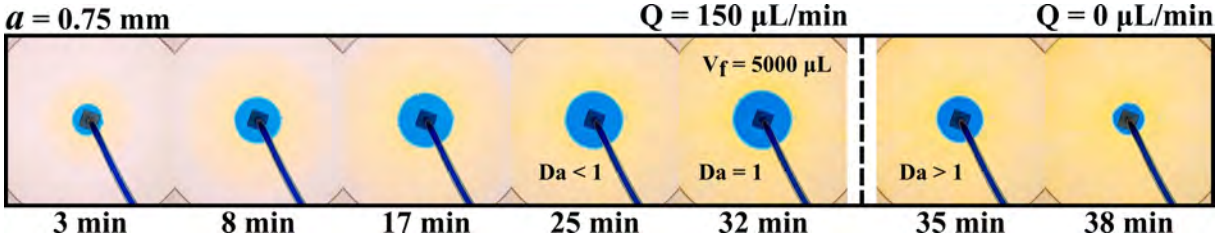

Figure 13.12: Experimental observation of the effect of changing K_f. The results were obtained considering the same chemical system and a triplicated in size cell gap. The system did not show any pattern formation. The displacement remained stable during the injection of 5000 μL of displacing solution at 150 μL/min. The displacing front remained static at a specific radius (Da = 1) until the displacing volume was completely injected. Once the volume was reached and the injection stopped, the chemical front "consumed" the displacing solution in less than 10 min.

As the precipitation velocity depends on the pH and the electrostatic charges (that were not altered as the concentration of gluconic acid was not changed), the value of k_2 was not affected by the increment of the cell gap. Thus, for a higher velocity of the chemical front and a constant velocity of the precipitation process, the value of K_f in this situation was (at least qualitatively) larger compared with the value of the original system. These results demonstrated not only that the experimental and numerical results agreed well, but also that the parameters and assumptions made on the numerical model were properly set.

13.5 Chapter Discussion

This chapter presented the numerical results of the simulations of both Cases I and II. The modeling of this experimental system has gone one step further in complexity, as it included not one but two chemical processes coupled with the hydrodynamics. Unlike the model presented in Part II, the addition of synergy between chemical processes expanded and enriched the system possibilities. The dynamics of both cases were well reproduced, both qualitatively and quantitatively, even considering the estimation of some parameters.

Regarding Case I, the reproduction of the phenomenon observed in the pattern formation process agreed well with the experimental counterpart. Both the precipitate formation and the movement of the ramifications produced by the effect of the reaction-diffusion processes were well reproduced by the model, for the same range of flow rates. This was particularly noticeable in the circularity calculation, where the numerical results were almost identical to their experimental counterpart.

Regarding Case II, although observing some differences in the pattern morphology (the experimental patterns were fractal) the overall behavior of the system reproduced as well. The stabilization mechanism occurred in similar conditions as in the experiments, including the increment in the finger thickness, which was also observed. The circularity calculation showed some differences compared to the experimental part, however, the stabilization phenomenon was well captured at least in qualitative terms. This was particularly appreciated in the calculation of the displaced volume, where the displacing performance agreed more than acceptably with the experimental values.

The supplementary results demonstrated the major importance of the synchronization between all the involved time scales (reaction, diffusion, and convection), as well the complexity of the experimental system. In this sense, not only the reactivity was necessary for the phenomena to occur, but also the diffusivity played an important role in the overall dynamics (especially in Case II in which this

phenomenon was fundamental for generating a stable displacement in a very unstable hydrodynamic condition). Similar to what happened in Part I, the model was used as an effective tool to understand better the system dynamics, especially in situation where may be difficult to explore due to experimental constraints.

USC
UNIVERSIDADE
DE SANTIAGO
DE COMPOSTELA

Conclusions

This part introduced a fully complex interaction between reaction-diffusion-convection processes, that derived into two individual and independently interesting systems.

In both cases of study, the physical mechanism underlying was a dramatic decrease in the pH at the interface that was induced once the two solutions interacted and only at the interface. This change in pH resulted in two different chemical processes that combined with the fluid displacement, were responsible for the destabilization/stabilization of the system: the precipitation and the reactive front.

The precipitation was produced by the alteration of the spatial configuration of the polymer at low pH. This process was driven by the protonation of the PAA molecule that facilitates the aggregation and the subsequent precipitation by hydrogen bond formation. In Case I, the precipitate accumulated in the region between the two solutions and locally reduced the permeability of the porous matrix. This consequently increased the pressure inside the cell. At a certain level of pressure, the displacing solution was ejected breaking the polymer wall. This break happened by spontaneous symmetry break. In Case II, the whole mechanism was the same, but all the reaction-diffusion processes that worked combined with the flow displacement acted synergistically to produce a stable displacement.

On the other hand, the reaction front was produced by a combination of several reaction-diffusion processes. It was demonstrated that its nature is far from the most common autocatalytic fronts. In the first place, the acidic character of the front was explained by the generation of bisulfite at the interface by equilibrium displacement. This reaction was potentiated by the large gradients of protons between solutions A and B. Besides, differential diffusion was also fundamental for the front to occur and it was mainly produced by the proton acceptor character of the PAA molecule.

The numerical simulations demonstrated the validity of the proposed mechanism. Even considering the simplifications and having exhibiting some minor differences, the numerical results showed a more than satisfactory agreement with the experiments. The simulations were once again, an effective tool to better understand the experimental phenomena.

The system here presented definitely showed a coupling between diffusive, convective, and reactive processes in which all timescales were similar. This fact was evidenced by the calculation of the dimensionless numbers and verified by the numerical simulations.

All the results and protocols here proposed opens a path to design reactions that change the stability properties at the interface by synergistic mechanisms between chemical, diffusive, and convective processes. The possible applications are countless in industrial configurations as well as in processes of recovery of natural resources.

USC
UNIVERSIDADE
DE SANTIAGO
DE COMPOSTELA

GENERAL CONCLUSIONS AND PERSPECTIVE

The central objective of this thesis was to obtain synergistic couplings between complex chemical reactions and hydrodynamic instabilities. In general terms, it is possible to affirm that such an objective was achieved. Every system here presented was completely characterized and modeled, having studied and demonstrated both numerically and experimentally the mechanisms involved in the observed couplings.

The coupling between a buoyancy-driven instability and the oscillating BZ-CHD reaction was introduced in Part I as a novel chemo-hydrodynamic instability. This system exhibited very interesting features and was the first experimental evidence of a fingering instability triggered by a chemical oscillator [57, 61]. The system also showed a complex relationship between the hydrodynamic patterns and the complex dynamics of the BZ-CHD reaction. For instance, many interesting phenomena like traveling fingers and the chemo-hydrodynamic feedback were appreciated.

- The experimental results showed the major role played by chemistry in the overall development of the instability. It was demonstrated that the fingering dynamics can be strongly affected and modulated by changing the excitability, which is a function of the species concentrations.
- Through the detailed chemical analysis, it was possible to identify and characterize the key species involved in the fingering onset. This was in part achieved by using analytical techniques, like advanced spectroscopy. The existing models were also a valuable tool to estimate the chemical compositions in time.
- Even from its intrinsic complexity due to the large number of species involved, it was demonstrated that the mechanistic of the instability was mostly influenced by only one chemical compound, the quinhydrone complex that emerged only in specific conditions.
- The exhaustive study of the experimental results allowed to properly modify and adapt the existing kinetics model to include the precipitate formation. This allowed the development of a capable RDC model that was able to reproduce the dynamics of the system.
- The numerical results confirmed and demonstrated the main hypothesis associated with the instability generation. In this sense even considering the large number of variables involved, the mechanism of the instability can be oversimplified into a simpler $A + B \rightarrow C$ case.
- The results here presented paves the possibility to utilize these findings in more complex scenarios related to the control of coupled processes in emerging instabilities.

In Part II, the major challenge was to create a dynamic pH-viscosity coupling from scratch based on an organic pH-Oscillator reaction. In this case, an effective coupling between a pH-sensitive polymer and two pH-shifting complex chemical reactions, creating the novel FS-PAA and the FSG-PAA systems

[62]. These systems were not only studied in batch but also in a spatially extended configuration to produce a chemically induced viscous fingering instability from a stable displacement [58].

- From the study of the homogeneous FS-PAA and FSG-PAA systems, the extensive chemical characterization demonstrated not only the influence of each chemical species but also confirmed the coupling mechanism. It also provided the best experimental conditions for proper fluid displacement in spatially extended configurations.
- The pH-viscosity systems preserved the main properties of the original FS and the FSG reactions, and at the same time exhibited viscosity changes driven by the reaction kinetics.
- The adaptation of the FS-PAA system into a spatially extended configuration made it possible to obtain viscous fingering instability induced by the local changes in the pH/viscosity at the interface between the displacing and displaced solutions. This system was obtained as one of the multiple possible applications of the homogeneous reaction in a scenario of increased complexity.
- From the study of the instability, it was concluded that both reactivity and diffusivity were fundamental in the destabilization mechanism. On one hand, reactivity was responsible to modulate the viscosity jumps between solutions (sulfite) and the thickness of the initial condition (formaldehyde). The first condition is inversely proportional to the stability whereas the second one was the major factor for the fingers to extend through the medium. This condition was also influenced by the low diffusion rate of the polymeric displacing solution.
- The mechanistic of the instability was well understood, in part thanks to the optical techniques used. The conclusion obtained from such observations made simpler the proposal of a convective numerical model.
- Even considering its simplicity and limitations, the numerical models were able to reproduce both qualitatively and quantitatively the main characteristics of the system. The adaptation of the existing kinetics models was well established, even if the polymer was not explicitly included. This made it possible to perform a comparative analysis of the dynamics of the experimental and numerical homogeneous systems. This also provided the best estimations to properly study the spatially extended simulations.
- The results obtained from the DC system also demonstrated that the assumptions made over the diffusive character of the polymeric solutions were well established.

Part III introduced a reactive coupling where many complex phenomena converged into one single system. Reaction, diffusion, and convection processes worked synergistically to produce two different cases of study depending on the initial hydrodynamic configuration [63].

- In Case I, the pattern formation strongly depended on the convective processes, which was evidenced by the stabilizing/destabilizing effect of the flow rate. This phenomenon was mainly associated with the differences between the chemical and convection timescales. The estimation of the Damhköler numbers was fundamental to establish the limits of stability in the system.
- In Case II, however, the stabilization was principally driven by reaction-diffusion processes, whereas the convection had to be limited until matching the other two timescales. This was expected as Case II was unstable *per se*.
- The use of the time-dependent circularity was a good choice to study the dynamics of both phenomena. It provided a simple but effective tool to characterize the system behavior.

- In contrast to Part II, the chemistry of this synergic system is far from usual. It was demonstrated that there exists not one but two simultaneous chemical processes involved. Both of them with comparable timescales that produce a very rich and complex phenomenon.

- The conclusions obtained from the control experiments were fundamental to unveil the nature of these two chemical processes. As it was shown, there were a precipitation phenomenon and a chemical front. The precipitation was produced by the contact between the polymeric solution and the acidic environment of the gluconic acid solution. This was verified by two different analytic techniques. On the other hand, the chemical front was driven by the relatively fast diffusion of protons, the proton acceptor character of the PAA, and the production of bisulfite at the interface.

- It was also possible to understand the mechanistic of both systems. In Case I, the precipitation reduced the permeability of the porous matrix increasing the pressure inside the cell. This causes the ejection of the displacing solution through the displaced. Once the two liquids made contact, the reaction front pulled the solution back, producing more precipitate and causing the observed patterns. This was only possible if the flow rate was sufficiently slow to allow fluids to react. In Case II, however, the precipitation acted as an effective wall that drags the most viscous solution. The chemical front was aligned to the flow and the diffusivity played a major role in the stabilization at the beginning of the displacement.

- All the conclusions were complemented with a numerical RDC model that was able to reproduce well the dynamics of both cases. The model was also useful to better understand the effect produced by the diffusion on the system, more specifically in the stabilization Case II. This was a clear example where numerics and experiments were used together to fully understand the physical-chemical mechanism behind the observations.

- I was also observed that the pattern formation in Case I is strongly dependant on the rate of the precipitation and the velocity of the reaction front. As it was numerically and experimentally studied, no patterns were observed for a faster chemical front. This demonstrated the intrinsic complexity of the experimental conditions.

Finally, it is worth mentioning the versatility of all the work done here, including numerical simulations and mathematical modeling, basic and advanced analytic chemistry, rheology, optics, physics and chemical-physics, image processing, material science, kinetics, and most of all... a lot of patience.

Applicability and Outlook

The use and propagation of the discoveries here presented will depend on the application itself. The use of complex chemical reactions showed interesting phenomena in miscible displacements but always considering that all the experiments were done in a Hele-Shaw cell. Much more care must be taken into account on working in more realistic situations.

In real fluids displacements (like in Enhancing Oil Recovery) the use of very complex chemical reactions can lead to some problems. These issues could be derived from a large number of intermediaries and products involved. This may produce interference when studying a similar reaction in more realistic and complex applications, like real porous media. Additionally, the effects of the temperature, salinity, porosity, and real permeability must be taken into account when working with complex chemistry, particularly polymers, that could be affected by many external factors.

From a theoretical point of view, the system presented in Part III opens new possibilities in the study of more complex chemically driven instabilities. Thus, the study of the coupling of several chemical reactions in a convective framework can bring out many interesting new phenomena.

On the other hand, the use of pH-shifting reactions like the one presented in Part II may be used in more sophisticated applications, like drug delivery or chemo-mechanical devices. In such cases, it may be necessary to couple the reaction with more suitable polymers or molecules to better control the chemistry.

Regarding the coupling between a buoyancy-driven instability and a chemical oscillator, as this system was especially novel, it can be used in more complex situations such as microgravity, non-isothermal conditions, photosensitivity, and more.

Appendix A

Preparation of Stock Solutions

Abstract: *This appendix describes the protocols and recipes used to prepare every stock solution and reactive mixtures used for the development of this work. All stocks solutions were prepared from reagent grade reactants without further purification.*

A.1 Stock Solutions Used For Part I

A.1.1 CHD Solution

The 1,4-Cyclohexanedione (CHD) stock solution was prepared by diluting 42.05 g of solid CHD (Sigma-Aldrich, CAS: 637-88-7, MW: 112.13 g/mol) into 250 mL of doubly distilled water to obtain a final stock concentration of 1.5 M.

A.1.2 Sodium Bromate Solution

The sodium bromate solution ($NaBrO_3$) was prepared by diluting 56.584 g of solid $NaBrO_3$ (Sigma-Aldrich, CAS: 7789-38-0, MW: 150.89 g/mol) into 250 mL of doubly distilled water to obtain a final stock concentration of 1.5 M

A.1.3 Ferroin Solution

The ferroin ($[Fe(phen)_3]^{2+}$) solution was prepared by mixing solid sulfate iron (II) heptahydrate (Prolabo, CAS: 7782-63-0, MW: 278.01 g/mol) and solid 1,10-Phenantroline monohydrate (Fluka, CAS: 5144-89-8, MW:198.22 g/mol), in a molar ratio of 1:3. For obtaining a final concentration of $25x10^{-3}$ M, 6.95 g of sulfate iron (II) and 14.867 g of Phenantroline were added into 1000 mL of doubly distilled water. The solution was stirred for about 6 hours.

A.1.4 Sodium Sulfate Solution

The sodium sulfate (Na_2SO_4) solution was prepared by diluting 53.265 g of solid Na_2SO_4 (Panreac, CAS: 7757-82-6, MW: 142.04) into 250 ml of doubly distilled water to obtain a final stock concentration of 1.5 M.

A.1.5 Sulfuric Acid Solution

The sulfuric acid (H_2SO_4) stock solution was prepared from concentrated (95-98 %, 1.840 g/cm^3) H_2SO_4 solution (Sigma-Aldrich, CAS: 7664-93-9, MW: 98.08 g/mol). The stock was obtained by adding gently 356.3 mL of acid into 250 mL of doubly distilled water. As the dissolution process is highly exothermic, the flask must be constantly cooled. Once it was diluted, the volume of the solution was completed to the mark (1000 mL) at room temperature.

A.1.6 Sodium Chloride Solution

The sodium chloride solution was prepared by diluting 0.584 g of solid salt (Sigma-Aldrich, CAS: 7647-14-5, MW: 58.44 g/mol) into 100 mL of doubly distilled water, obtaining a final concentration of 0.1 M.

A.1.7 Reactive Mixture: Solutions 1 and 2

The bubble-free recipe of the Belouzov-Zhabotinsky reaction was separated into two independent and non-reactive solutions. Solution 1 was prepared by mixing 2.91 ml of CHD stock, 0.24 ml of ferroin stock and four different volumes of Na_2SO_4 stock: 1.3 ml, 1.55 ml, 2.05 ml, and 2.3 ml respectively. Solution 2 was prepared by mixing 1.42 ml of NaBrO3 stock, and 0.24 ml of ferroin stock. In both solutions, different volumes of H_2SO_4 stock were added in equal concentration to avoid acid gradients. Specifically: 2 ml, 4 ml, 6 ml, and 8 ml. Finally, doubly distilled water was added to obtain a final volume of 15 ml for each solution. Solution 1 shows a characteristic red coloration as the ferroin is in a reduced state while solution 2 shows a blue coloration due to the oxidized state of the ferroin (ferriin).

A.1.8 Protocol to prepare the BZ-Agarose Gels

The agarose stock solution was prepared by dissolving 1.5 g of Agarose TYPE I, Low EEO (Sigma, CAS: 9012-36-6) into 100 mL of doubly distilled water obtaining a final concentration of 1.5 wt%. The dissolution was done in boiling water. Once it was dissolved, the mixture was kept warm at not less than 45°C (which is closer to the gelation temperature).

For preparing the non-reacting agarose gels for the system presented in Appendix B, two individual solutions were prepared using the same stocks indicated in this section. Gel 1 was prepared by adding 1.46 mL of CHD stock, 0.12 mL of ferroin stock, 2mL of agarose stock and, 3.92 mL of doubly distilled water to obtain a final volume of 7.5 mL. Gel 2 was prepared by adding 0.71 mL of bromate stock, 0.12 mL of ferroin stock, 2 mL of agarose stock, and 4.67 mL of doubly distilled water to obtain a final volume of 7.5 mL. In both cases, the agarose was added at last to avoid premature gelation. Solutions were constantly stirred to facilitate a homogeneous mixture. To filling the Petri dish, a stopper was added to half of the Petri dish (silicone rubber of 0.5 mm of thickness is recommended). Once the agarose was added into Solution 1, the mixture was poured into the other half of the Petri dish. Once it was gelified, the stopper was removed and the second solution was added.

Once the gel was obtained, the excitability was changed by adding 2 mL of diluted sulfuric acid on top of the gel (the acid can not be added directly in the solution formulations as it interferes with the gelation process. The agarose only gelifies at neutral or basic pH). The acid was distributed homogeneously. The experiment started once half of the Petri dish switched from red coloration (reduced state) into blue coloration (oxidized state).

A.2 Stock Solutions Used for Part II

A.2.1 Formaldehyde Solution

The formaldehyde stock was a commercial concentrated Formalin solution (Sigma-Aldrich, CAS: 50-00-0, MW: 30.3 g/mol).

A.2.2 Sodium Sulfite Solution

The sulfite stock was prepared from solid $NaBrO_3$ anhydrous salt (Sigma-Aldrich, CAS: 7757-83-7, MW: 126.04 g/mol) by diluting 25.21 g of salt into 100 mL of doubly distilled water, obtaining a final stock concentration of 2 M.

A.2.3 Poly(Acrylic Acid) [PAA] solutions

The PAA solution was prepared from Poly(Acrylic Acid) (Sigma-Aldrich, CAS: 9003-01-4, Average Mv $\sim$ 4000000). The stock was obtained by dissolving 1 g of PAA into 180 mL of doubly distilled water at 80°C to facilitate solubility. After solubilization, the mixture was cooled down to 23°C and the final volume was kept at 200 mL obtaining a final concentration of 0.5 wt%.

For the control experiments, a short-chain PAA molecule was used (Mv sin 450000). The stock solution was obtained by dissolving 5 g of PAA into a total volume of 100 mL of doubly distilled water obtaining a final concentration of 5 wt%. The dissolution procedure was the same used for the long-chain PAA.

A.2.4 Sodium Bisulfite Solution

The Bisulfite stock solution was prepared from metabisulfite sodium salt ($Na_2S_2O_5$ (Sigma-Aldrich, CAS: 7681-57-4, MW: 190.11 g/mol), by diluting 19.011 g of salt into 100 mL of doubly distilled water, obtaining a final stock concentration of 1 M.

A.2.5 Sodium Hydroxide Solution

The sodium hydroxide stock was a commercially available NaOH solution 5.0 M (Sigma-Aldrich, CAS: 1310-73-2, MW: 40.00 g/mol)

A.2.6 Gluconolactone Solution

The gluconolactone stock solution was freshly prepared for each experiment from reagent grade D-(+)-Gluconic acid δ-lactone (Sigma-Aldrich, CAS: 90-80-2, MW: 178.14 g/mol). The stock was obtained by diluting 0.356 g of gluconolactone in 10 ml of doubly distilled water. This solution has been used always fresh and in less than 300 seconds after being prepared to avoid hydrolysis effects.

A.2.7 Bromothymol Blue Indicator

The color indicator is a 0.4 wt% hydroalcoholic solution of Bromothymol blue prepared by dissolving 1 g of Bromothymol blue sodium salt powder (Sigma) into 50 ml of a 96% ethanol solution diluting up to a final volume of 250 mL by adding 200 mL of doubly distilled water. The C.I. shows a yellow color for pH values below 6 (acidic state), green color for pH between 6-7 (neutral state), and blue color for pH values above 7 (basic state).

A.2.8 Displacing Solution Mixture Preparation

As shown in Part II, there is not a unique recipe for the displacing solution because the sulfite concentration was varied. However, a base formulation was used to study the effects of the formaldehyde in the instability development. This base formulation was prepared by mixing 5 mL of PAA stock, 0.195 mL of sulfite stock, 0.300 mL of C.I. stock, and 0.205 mL of doubly distilled water. This solution shows a green coloration and its pH is between 6.7-7.

A.3 Stock Solutions Used for Part III

A.3.1 Formaldehyde Solution

Same recipe as used for Part II.

A.3.2 Sodium Sulfite Solution

Same recipe as used for Part II.

A.3.3 Poly(Acrylic Acid) [PAA] solution

Same recipe as used to prepare PAA Mv $\sim$ 4000000 for Part II.

A.3.4 Sodium Carbonate Solution

The sodium carbonate (Na_2CO_3) solution used for the control experiment 5 (C5) was prepared from sodium carbonate anhydrous powder (Sigma-Aldrich, CAS: 497-19-8, MW: 105.99 g/mol), by diluting 21.19 g of powder into 100 mL of doubly distilled water obtaining a final stock concentration of 2 M.

A.3.5 Bromothymol Blue Indicator

Same recipe as used for Part II.

A.3.6 Gluconic Acid Solution (Solution B)

Solution B is a concentrated aqueous solution of gluconic acid 2.0 mol/kg ($\cong$ 1.66 M), This solution was obtained by diluting 17.81 g of D-(+)-Gluconic acid δ-lactone (Sigma-Aldrich, CAS: 90-80-2, MW: 178.14 g/mol) into 50 g of doubly distilled water. The solution was left to rest a complete day to ensure the full conversion of the gluconolactone into gluconic acid by hydrolysis.

A.3.7 Solution A Mixture Preparation

Solution A was prepared by mixing 5 mL PAA stock, 0.195 mL of $SO_3{}^{2-}$ stock, 0.300 mL of C.I. stock, 0.150 mL of Formaldehyde stock, and 0.055 mL of doubly distilled water. This solution shows a blue coloration and its pH is between 11.5-12.

Appendix B

Reaction-Diffusion Systems

Abstract: *This Appendix will introduce the main results obtained from less complex reaction-diffusion (RD) systems. These results were used as guidance to develop and understand the most complex scenario presented in Part I. In this sense, the first observation and the analysis of the dynamic of a spatially extended BZ-CHD oscillator were done in a 1D capillary system. This study aimed to obtain relevant information about how the typical oscillatory behavior of a homogeneous system may be affected by separating part of the reagents into two different non-reactive solutions. With those results, the next step was to extend the setup of the capillary system into a 2D non-convective experimental setup and to study the influence of a spatially extended configuration in the pattern formation and thus, to better understand the role played by the chemistry in the convective system. In the further sections, an extensive description of those previous non-convective systems is presented, showing both experimental and numerical methods and results.*

B.1 Materials and Methods

B.1.1 Capillary System

1D experiments were carried out in the capillary system schematized in Figure B.1. The cylindrical capillary reactor was built in borosilicate with an inner diameter of 0.05 mm ± 0.01 mm, 2 ± 0.1 mm outer diameter, and 70 ± 1 mm length. The small inner diameter avoids any convection or 2D reaction-diffusion pattern, ensuring a purely 1D dynamic. To obtain the interfacial initial condition, the following method was used: Firstly, Solution 1 was introduced into the capillary by using capillary forces. Once half-filled, Solution 2 was introduced from the same opening and in the same way until the reactor was filled. The experiments were recorded using a CMOS camera (PixeLink PL-B776U) connected to a computer with a total experimental time of 6 hours. The species of each solution are indicated in the schematic of Figure B.1.

Chemical Recipe

The recipe used is the same presented in Table 2.1. As these experiments were also part of a set of control experiments, just a few experiments were performed covering low, medium, and high excitability cases. More specifically, those corresponding to $\varepsilon = 0.207$ M, $\varepsilon = 0.826$ M, and $\varepsilon = 1.653$ M.

As described in the previous section, the reactor has an inner diameter of 0.05 mm which makes it difficult to observe the liquids inside the capillary even if there are colored. For such a reason, the experiments were done increasing the ferroin concentration up to four times the concentration listed in

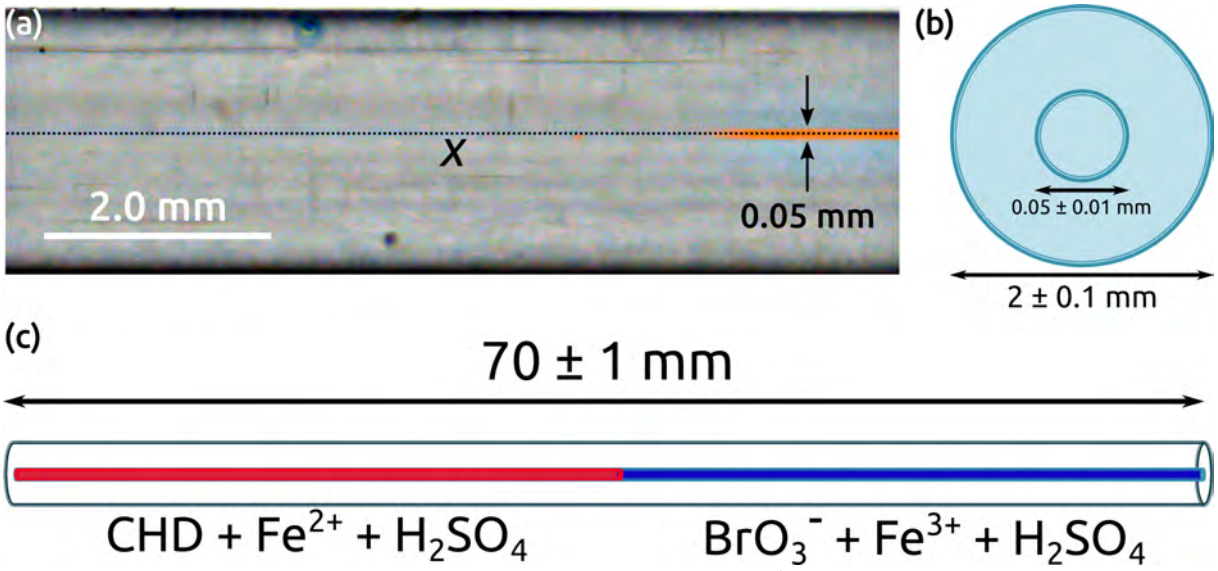

Figure B.1: Capillary reactor used in 1D reaction-diffusion experiments. The capillary was built in borosilicate. Both solutions were introduced into the system using capillary forces.

Table 2.1. Even though the increment in ferroin could affect the system temporal dynamic, it did not influence the qualitative behavior of the results.

B.1.2 Non-Convective Agarose-Based System

A pure 2D reaction-diffusion system was performed in a Petri dish as presented in Figure B.2. The Petri dish was chosen for its simplicity and reliability. To obtain a non-convective system, the BZ-CHD reaction was mixed with an agarose solution. The experiments were carried out in a 7 cm diameter Petri dish. The agarose solution was preheated to avoid a fast gelification.

The initial condition observed in Figure B.2(a) was obtained by putting Solution 1 until half of the Petri dish. Solution 2 was added after gelation of Solution 1. Both gels were not reactive as the sulfuric acid was not present in the recipes (agarose does not gelify at low pH conditions). However, once the initial gel configuration was obtained, the H_2SO_4 was added into the system from the top and distributed homogeneously through the entire the gel surface. As the acid diffuses through the gel, the ferroin present in Solution 2 oxidizes into ferriin, obtaining a similar system presented in Figure B.2(b).

Analogously to the 1D experiments, the 2D system was recorded using a CMOS camera (PixeLink PL-B776U) for a total experimental time of 6 hours. Similar to the 1D case, this set of experiments were used to analyze the pattern dynamic at the interface and evaluate the influence of the chemistry in the fingering instability observed in the full convective system. All the experiments realized under this configuration were made without replicas as they were used as well as a control system. In this sense, the same conditions of high, middle, and low excitability were studied.

Chemical Recipe

In this case, the original recipe was slightly modified to make the system non-convective. Thus, 2 mL of agarose 1.5 wt% was added to each solution to make a gelified version of the convective system. The recipe is presented in Table B.1. The system excitability was varied in the same manner as the capillary experiments being $\varepsilon = 0.207$ M, $\varepsilon = 0.826$ M, and $\varepsilon = 1.653$ M the studied cases. The excitability was varied by adding different acid concentrations over the Petri dish after gelification. The reaction started once the Ferroin on the gel 2 became Ferriin.

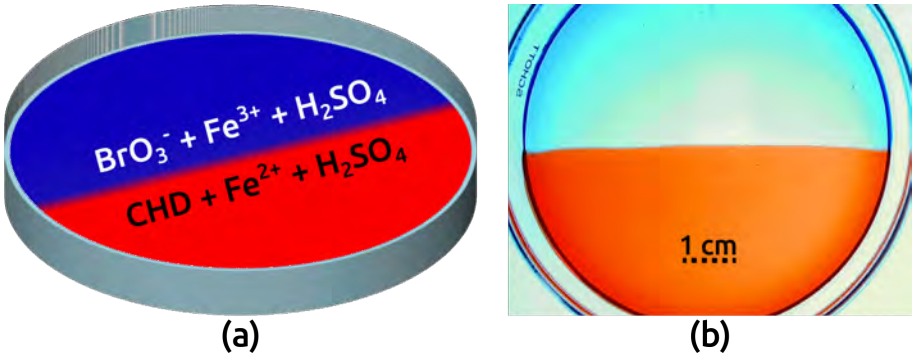

Figure B.2: (a) Schematics of the 2D reaction-diffusion system built in a Petri dish. (b) Image of an experimental Petri dish after the ferroin conversion into ferriin. In this experiment, both solutions were mixed with agarose 1.5 wt% to produce a pure 2D reaction-diffusion system. The reaction starts once the acid is homogeneously poured into the Petri dish from the upper side.

Recipe for Gel 1		**Recipe for Gel 2**	
Species	**Concentration (M)**	**Species**	**Concentraion (M)**
CHD	0.291	BrO_3^-	0.142
$[Fe(phen)_3]^{2+}$	$0.4x10^{-3}$	$[Fe(phen)_3]^{3+}$	$0.4x10^{-3}$
S1 volume of Agarose 1.5 wt%: 2 mL		**S2 volume of Agarose 1.5 wt%: 2 mL**	
Gel 1 volume: 7.5 mL		**Gel 2 volume: 7.5 mL**	

Table B.1: Recipe used in the non-convective agarose 2D-Reaction Diffusion System.

B.2 Numerical Models

B.2.1 Governing equations

Both reaction-diffusion systems were modeled using the following general set of partial differential equations:

$$\frac{\partial C_i}{\partial t} = D_{Ci}\nabla^2 C_i + R_i(C_i) \tag{B.1}$$

where R_i and C_i are the net reaction rates and the concentration of the involved species respectively. The net reaction rates were obtained from the skeleton model presented in Table 2.9 including the quinhydrone formation equation.

Analogously to the convective simulations, the modified skeleton model was used in place of the

full model. This was necessary due to the large number of memory and resources needed that make its use prohibitive. This model was far enough to represent the qualitative behavior of the diffusive systems. All simulations were done using a Finite Volume Method solver implemented in the commercial CFD software Ansys Fluent® version 19.2 [11, 12]. All results were obtained by using the SIMPLE solver coupled with a stiff-chemistry solver. The time step was automatically controlled by the software and both space and time, were discretized using the first-order upwind method. The total computational time was set to t_f = 3.5 min (real-time). The difference between the experimental and computational final times is due to the simplifications of the modified skeleton model used to simulate the spatially extended systems.

B.2.2 1D-RD System Model Setup

The capillary system was simulated using a 1.5D approach. The numerical domain (D) consisted of a rectangle of width L and arbitrary height, discretized by using a structured mesh of 181 elements in the x-direction and 1 element in the y-direction as shown in Figure B.3. The use of a 1.5D domain was preferred to facilitate the comparison between experiments and simulations. Zero diffusive flux conditions were set as boundary conditions.

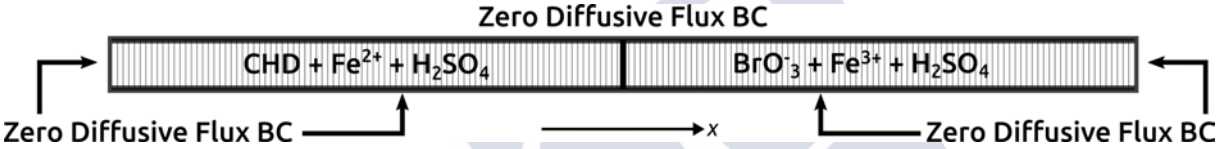

Figure B.3: 1.5D numerical domain used to simulate the capillary system. The mesh consists of 181 elements in the x-direction and 1 element in the y-direction. This type of domain provides a dynamic color profile of the species concentration similar to the experimental counterpart without increasing the computational cost.

The species spatial configuration as presented in Figure B.3 is given by the following piecewise function:

$$C_{ai}(x,0) = \begin{cases} [C_a]_0(x)(\xi r(x)+1) & x < L/2 \\ 0 & x \geqslant L/2 \end{cases}$$
$$C_{bi}(x,0) = \begin{cases} 0 & x < L/2 \\ [C_b]_0(x)(\xi r(x)+1) & x \geqslant L/2 \end{cases} \tag{B.2}$$

$$[\mathrm{H_2SO_4}]_0(x,0) = k, \forall x \in D$$

where $[C_a]_0$ are: $[\mathrm{CHD}]_0$ and $[\mathrm{Fe(phen)_3}]_0^{2+}$. $[C_b]_0$ are: $[\mathrm{NaBrO_3}]_0$ and $[\mathrm{Fe(phen)_3}]_0^{3+}$. $r(x,y)$ is a normally distributed random function with amplitude $\xi = 10^{-2}$. The $[\mathrm{H_2SO_4}]_0$ was set constant in all the domain.

B.2.3 2D-RD System Model Setup

For the 2D system, the numerical domain (D) consisted of a squared mapped mesh of area L^2 discretized by 181 elements in both directions, x and y. A schematics of the domain and the spatial configuration of the reactant species are presented in Figure B.4. The initial conditions were set using the same expression used for the RDC simulations (Eq. 2.2.3), except for $[\mathrm{Na_2SO_4}]_0$, which was excluded from the RD system as the density was not taken into account. All boundaries conditions were set as zero diffusive flux.

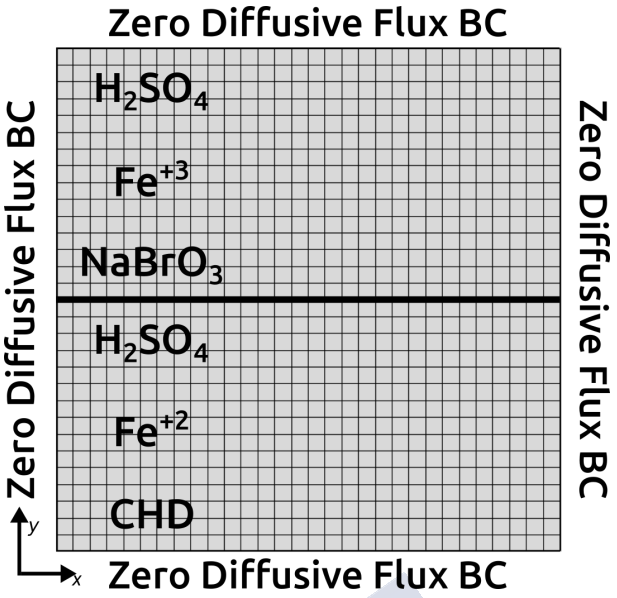

Figure B.4: 2D numerical domain used to simulate the RD model. The mesh consists of 181 elements in the horizontal direction and 181 elements in the vertical direction.

B.3 Experimental Results

B.3.1 1D Capillary System

The dynamics of the capillary system were observed through space-time plots (hereafter STP). These plots were obtained by measuring the pixel changes across a reference line located in the fluid reservoir (line indicated as x in Fig. B.1(a)). The three studied excitabilities are compared in Figure B.5. As can be seen, the overall behavior of the system agrees with the convective results. This was verified by studying the chemical observables. Both the induction time ($t_ind - C$) and chemical period (T_C) decreased with the increment of excitability. In all cases, the wavelength also increased in time. This was particularly noticeable just before the oscillation region ended. These behaviors were expected as this system was only driven by chemistry. The generation of the quinhydrone complex can be appreciated as a strong reddish mark for the mid and high excitability cases.

B.3.2 Non-Convective Agarose-Based System

Figure B.6 shows the effect of changing the excitability in the agarose based non-convective system. Snapshots were taken directly from the experimental observations. As can be seen, for the lower excitability (ε = 0.207 M, Fig. B.6(c)), the system did not show any significant behavior in the experimental time. Only the diffusive displacement of the interface was observed. This indicates that such a chemical condition was not enough to develop spatial structures in the established experimental time (t = 6h). For the middle excitability (ε = 0.826 M, Fig. B.6(b)), traveling waves were observed moving through the interface, additionally to the initial front displacement. Finally, in the higher excitability case (ε = 1.653 M, Fig. B.6(a)), waves were observed to occur faster than the previous case. This also agreed with the convective case, where the increment of the excitability decreased the induction time and the pattern wavelength.

The effect of the excitability on the system behavior is better observed in the space-time plots obtained from the 2D system. Plots are presented in Figure B.7 and were obtained by measuring in time the spatial region indicated with y in Figure B.6(a). As can be seen, both the delay in the induction time

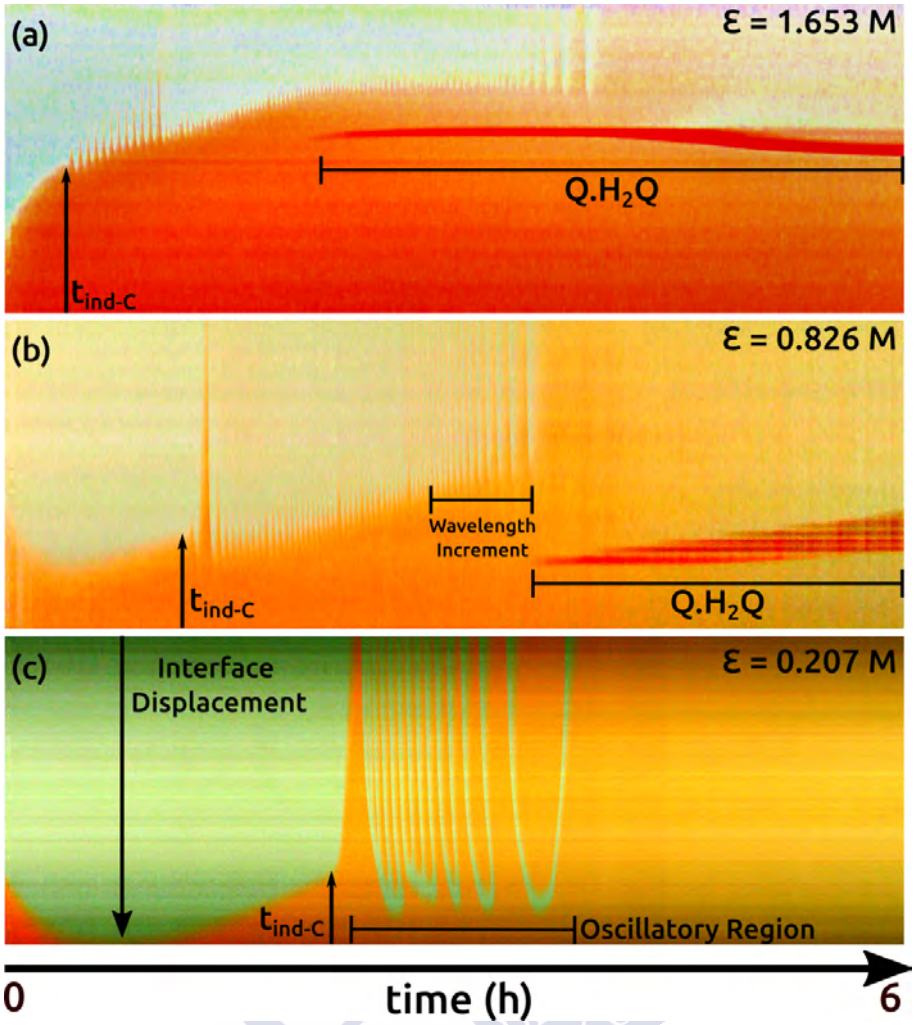

Figure B.5: Space-Time plots obtained from the 1D reaction-diffusion capillary system for high (ε = 1.653 M), (b) middle (ε = 0.826 M), and (c) low (ε = 0.207 M). Figures were constructed by taking a profile line across the longitudinal axis of the capillary. In all cases: $[CHD]_0$ = 0.291 M, $[BrO_3^-]_0$ = 0.142 M, $[Fe(phen)_3^{2+}]_0$ = $[Fe(phen)_3^{3+}]_0$ = 0.4x10^{-3} M.

and the front displacement were visible for middle and higher excitabilites. Unlike the 1D experiments, this system exhibits a much larger activity showing interface oscillations for a long time.

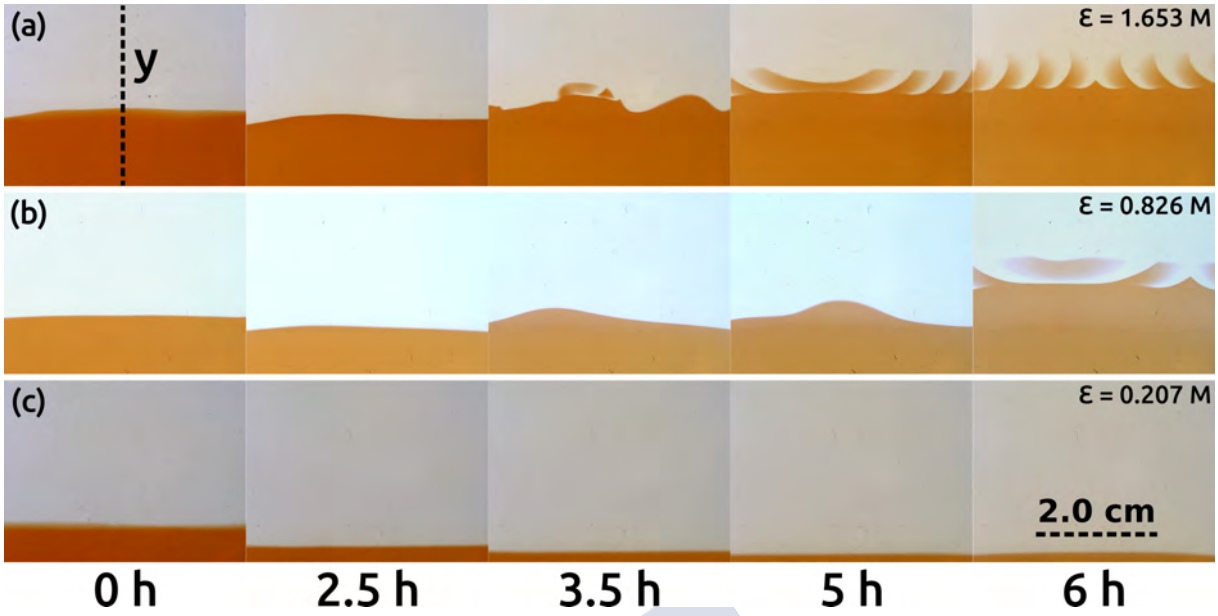

Figure B.6: 2D reaction-diffusion experiments for three different excitability conditions (a) ε = 1.653 M, (b) ε = 0.826 M, and (c) ε = 0.207 M. Patterns similar to the ones observed in the convective case were observed for the middle and higher excitability cases. The remaining initial concentrations were fixed as: $[CHD]_0$ = 0.291 M, $[BrO_3^-]_0$ = 0.142 M, $[Fe(phen)_3^{2+}]_0 = [Fe(phen)_3^{3+}]_0 = 0.4x10^{-3}$ M.

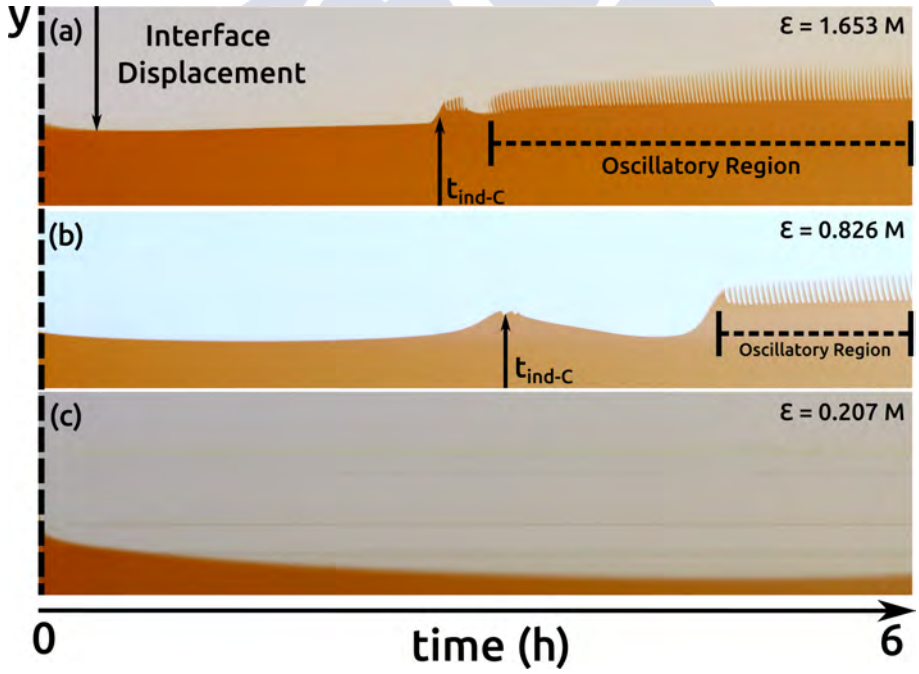

Figure B.7: STPs obtained from the non-convective agarose-based system, The changes in wavelength, induction time and front displacement are clearly appreciated. In all cases, the remaining initial concentrations were set as: $[CHD]_0$ = 0.291 M, $[BrO_3^-]_0$ = 0.142 M $[Fe(phen)_3^{2+}]_0 = [Fe(phen)_3^{3+}]_0 = 0.4x10^{-3}$ M.

B.4 Numerical Results

B.4.1 1.5D-RD Simulations

The results of simulating the capillary system using the modified skeleton model are presented in Figure B.8. The STPs were obtained by measuring the ferroin concentration field in time following the same procedure as the experimental part.

As can be observed, the results are in good agreement with the experiments. Despite the differences in the induction time in the skeleton numerical model, which started oscillating almost immediately, the oscillations at the interface, the increment of the chemical period, and the interface displacements (downward and upward) were well captured by the model. In the experimental STPs shown in Figure B.5, after the initial oscillation, the system started to show small oscillations that increased their amplitude in time. The same phenomenon was observed in the numerical STPs.

The formation of the quinhydrone complex ($Q \cdot H_2Q$) was also well reproduced in the simulations (after including the complex formation in the original skeleton model). Its concentration field was overlayered and combined with the ferroin STP. Similar to the experiments, this compound was only observed for higher and middle excitabilites. Both the spatial and temporal locations of the chemical patterns were also well reproduced by the simulations. These results strongly suggest that the simulation parameters were properly chosen.

B.4.2 2D-RD Simulations

Figure B.9 compares the simulation results at different times of the 2D-RD system for the same range of excitabilties. As can be appreciated, the qualitative behavior of the system was well reproduced by the spatially extended model. Similar to the experimental system, the numerical waves were observed constrained to the reaction/mixing zone. The interface displacement and wavelength changes also agreed with their experimental counterpart. The main difference was observed for the lower excitability condition (Fig. B.9(c)), where, unlike the experiments, large oscillation were observed. The differences observed between the experimental and numerical induction times were addressed in Section 5.1.4.

The changes in the pattern wavelength are better observed in Figure B.10, where a comparison between the numerical STPs of the 2D-RD simulations is presented. All plots were produced by taking successive frames of the line indicated as y in Figure B.10(a). The interface displacement was clearly seen and the oscillations were located in a similar position as observed in the convective system (Fig. 3.1).

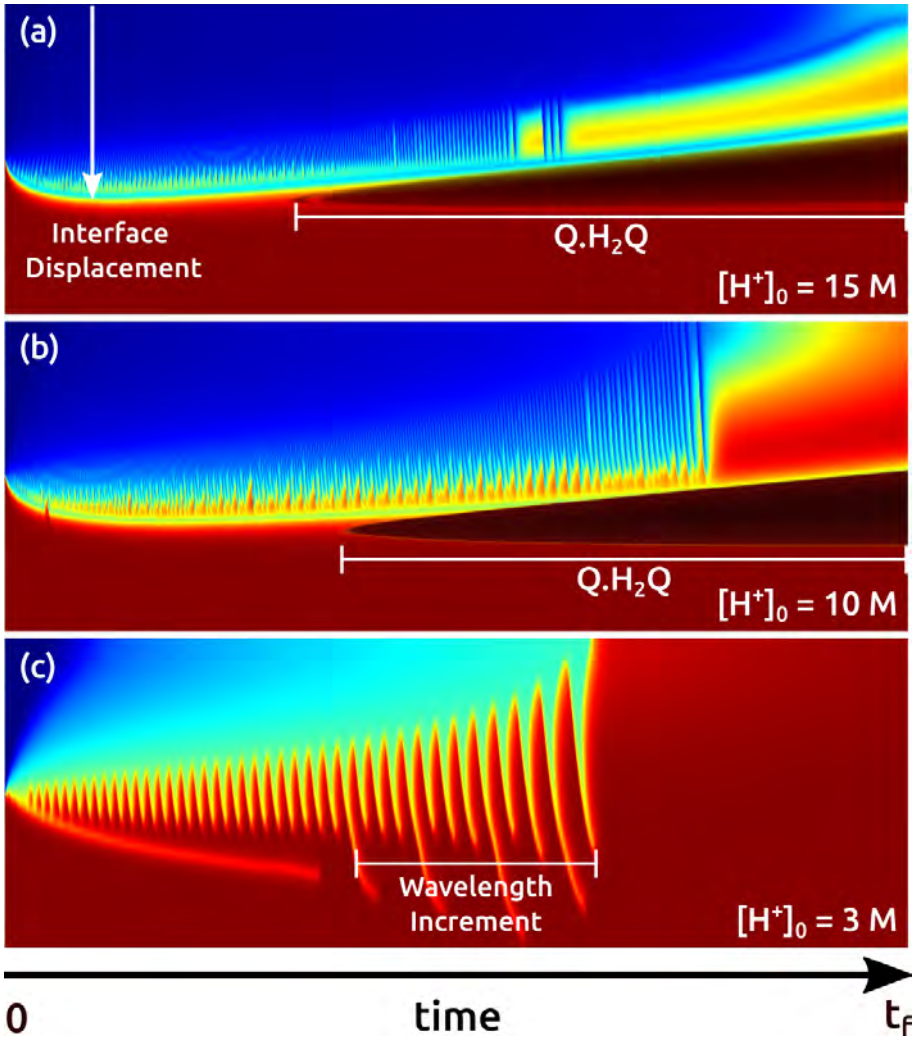

Figure B.8: STPs obtained from the ferroin concentration field by simulating the capillary system in a 1.5D numerical domain using the modified skeleton model under three different excitability conditions: (a) high, $[H^+]_0$ = 15 M, (b) middle, $[H^+]_0$ = 10 M and (c) low, $[H^+]_0$ = 3 M. Simulations agreed with the experimental results. Quinhydrone is shown as an overlayered concentration field. In all cases, the remaining initial conditions were set as: $[CHD]_0$ = 0.291 M, $[BrO_3^-]_0$ = 0.142 M $[Fe(phen)_3^{2+}]_0 = [Fe(phen)_3^{3+}]_0 = 0.4\text{x}10^{-3}$ M. In all cases, t_f = 3.5 min (real time) due the skeleton model simplifications.

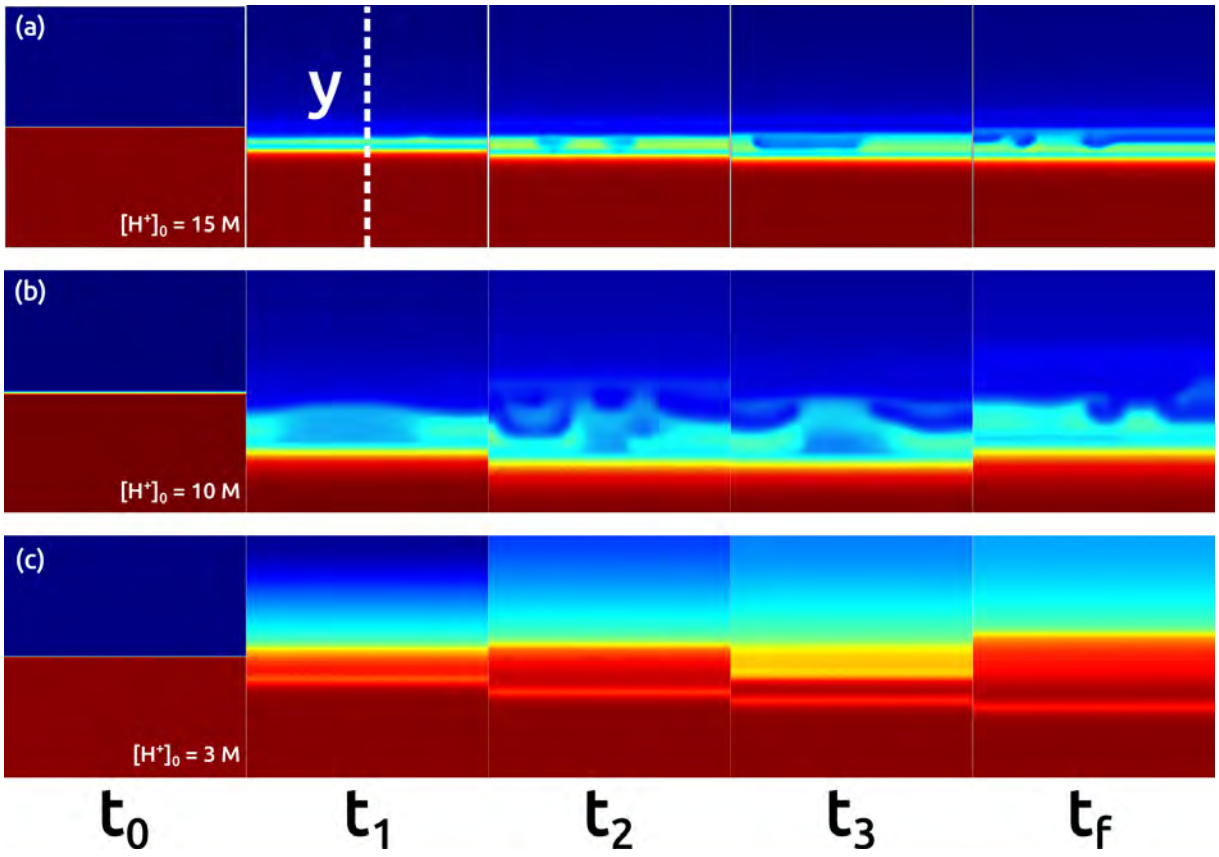

Figure B.9: 2D-RD simulations results obtained from the modified skeleton model for three excitability conditions (a) high, $[H^+]_0$ = 15 M, (b) middle, $[H^+]_0$ = 10 M, and (c) low, $[H^+]_0$ = 3 M. Figures plots the ferroin concentration field. In all cases, the remaining initial conditions were set as: $[CHD]_0$ = 0.291 M, $[BrO_3^-]_0$ = 0.142 M $[Fe(phen)_3^{2+}]_0 = [Fe(phen)_3^{3+}]_0 = 0.4\text{x}10^{-3}$ M. In all cases, t_f = 3.5 min due to the skeleton model simplifications.

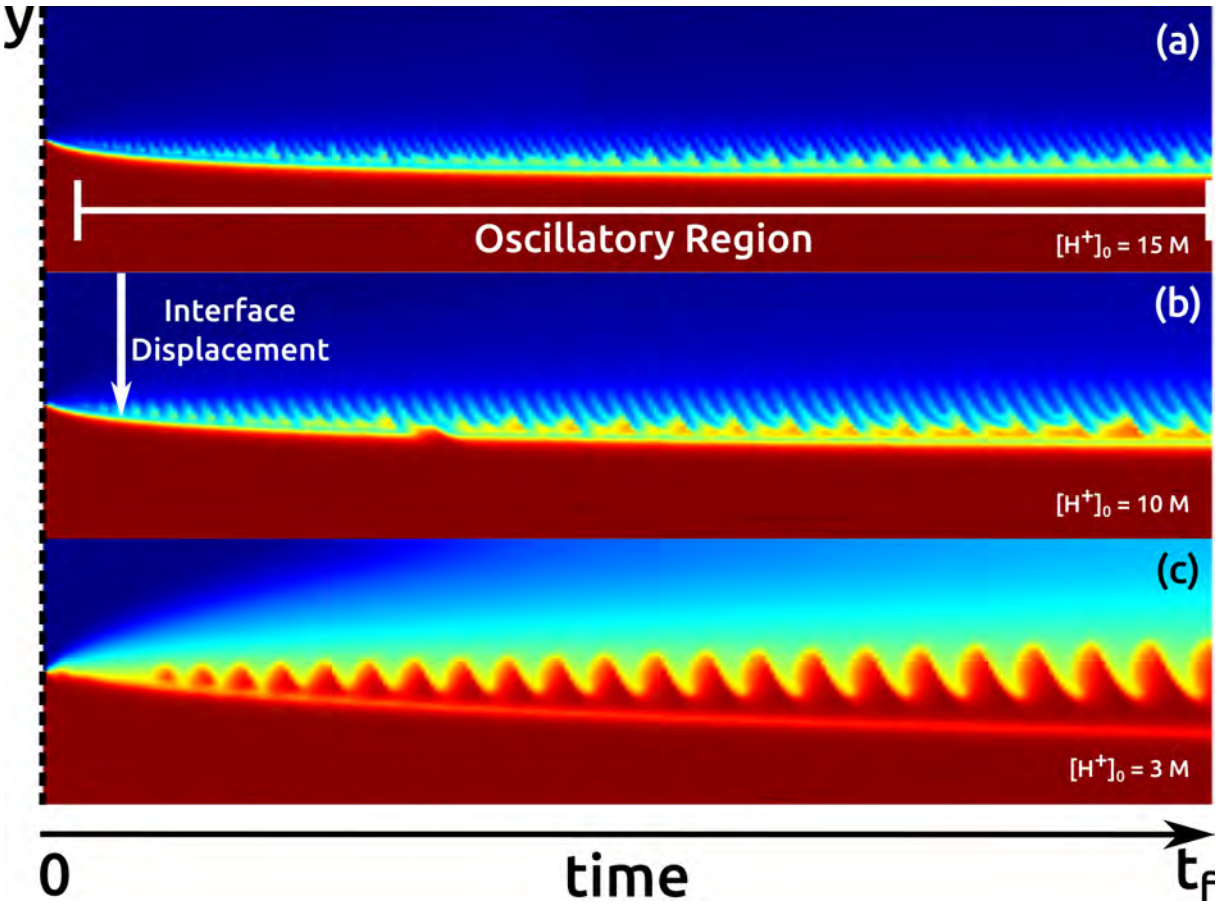

Figure B.10: STPs obtained from 2D-RD simulations. The plots were constructed from the ferroin concentration fields by measuring the spatial region indicated as *y* in Fig. B.9. Simulations agreed with the experimental results. In all cases, the remaining initial conditions were set as: $[CHD]_0 = 0.291$ M, $[BrO_3^-]_0 = 0.142$ M $[Fe(phen)_3^{2+}]_0 = [Fe(phen)_3^{3+}]_0 = 0.4\text{x}10^{-3}$ M.

B.5 Discussion

The results obtained from the reaction-diffusion systems demonstrated the role played by the chemistry in the convective system. More specifically, not only the pattern formation process but also the chemical observables (such as the induction time (t_{ind-C}) and the chemical period (T_C)) were affected similarly as the experiments presented in Part I. Based on these results, it was possible to confirm that the pattern formation process observed in the coupled system was independent of the convective phenomenon and at the same time, it was the key factor in the development of the hydrodynamic instability.

The concordance between the numerical simulations and the experimental results also demonstrated the efficiency of the BZ-CHD model proposed by Szalai *et al*. The similarities observed were an important step in the understanding of the instability mechanism and propitiated the necessary tools to model the quinhydrone complex formation.

Finally, it is not irrelevant to remark that the protocols and results here introduced were a valuable tool for the development of the work presented in M. A. Budroni, L. Lemaigre, D. M. Escala, A. P. Muñuzuri, and A. De Wit. Spatially Localized Chemical Patterns around an A + B $\rightarrow$ Oscillator Front. *Journal of Physical Chemistry A*, 120(6):851–860, 2016.

Appendix C

Image Analysis Techniques

Abstract: *This Appendix introduces all the methods and techniques used for image processing. Most of the quantitative measurements included in the manuscript were calculated from the experimental and/or numerical results with the protocols explained next. In all cases, proper spatial scales were taken to convert pixels into spatial units. All the analysis and techniques presented in this Appendix were done using the GNU software FIJI* [169].

C.1 Analysis Methods Used for Part I

C.1.1 Calculation of Measuring Observables

The methodology used to calculate the quantitative measurements presented in Figures 3.3 and 3.4 is shown in Figures C.1 and C.2. Firstly, both the chemical oscillation period (T_C) and the induction time (t_{ind-C}) were measured from the chemical view. Figure C.1(a) shows an experimental picture obtained from the chemical view. The space-time plot (STP) shown in Figure C.1(b) was constructed by taking a vertical line (indicated as y) and stacking all equivalent lines from the consecutive images. The induction time (t_{ind-C}), defined as the time between the beginning of the experiment and the time at which the first oscillation was observed, was directly measured from the STP as indicated in Figure C.1(b). The oscillation period T_C was measured as the average distance between the horizontal oscillation profile peaks (line shown in Figure C.1(b)) and the profile indicated in Figure C.1(c).

With a similar methodology, estimations of the hydrodynamic induction time (t_{ind-H}) and the finger wavelength (λ_H) were obtained from the *Schlieren* view and are presented in Figure C.2). Figure C.2(a) shows a typical snapshot obtained using the Schlieren technique (thus, it provides information about the hydrodynamic field). The line marked with y in Figure C.2(a) shows the generic location of all the lines in all the snapshots of that particular experiment that were used to build the space-time plot shown in Figure C.2(b). The instability onset time (t_{ind-H}) was calculated by measuring the distance between the beginning of the experiment and the finger onset (marked with a vertical dashed line in Figure C.2(b)). The finger wavelength, λ_H, was obtained taking a horizontal linear profile of the finger region in the STP and was calculated as the average distance between peaks (Figure C.2(c)). Each observable was measured in the same time interval. More specifically, λ_H was measured at the finger onset to avoid the influence of convective processes.

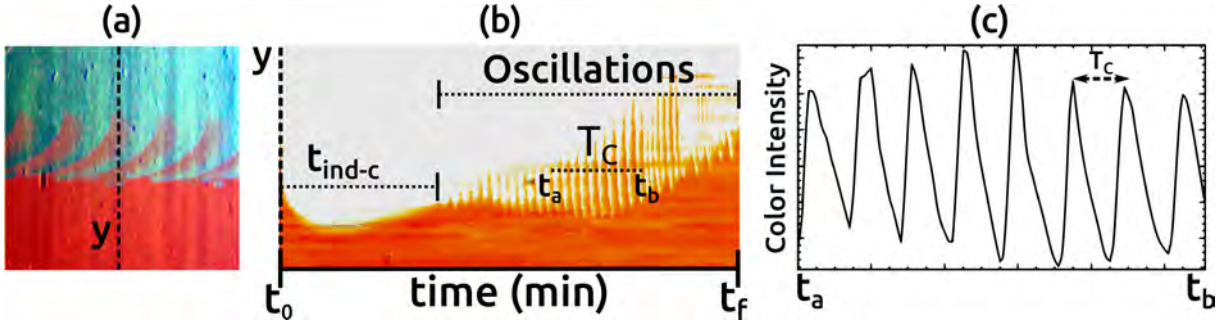

Figure C.1: Method used to calculate the chemical experimental observables (T_C and t_{ind-C}) via space-time-plots (STP). These results were used in Figure 3.3. (a) Specifies the methodology used to calculate by indicating the spatial locations used to generate the STP (marked as Y in the pic). In (b), the dashed lines indicate the region of the STP used to calculate the plots observed in (c). t_{ind-C} was measured directly from the STPs, while T_C was calculated using the line profiles presented in (c). Each observable was recorded in the same region of time. Particularly, T_C was measured once oscillations started. $t_0 = 0$ h and $t_f = 6$ h.

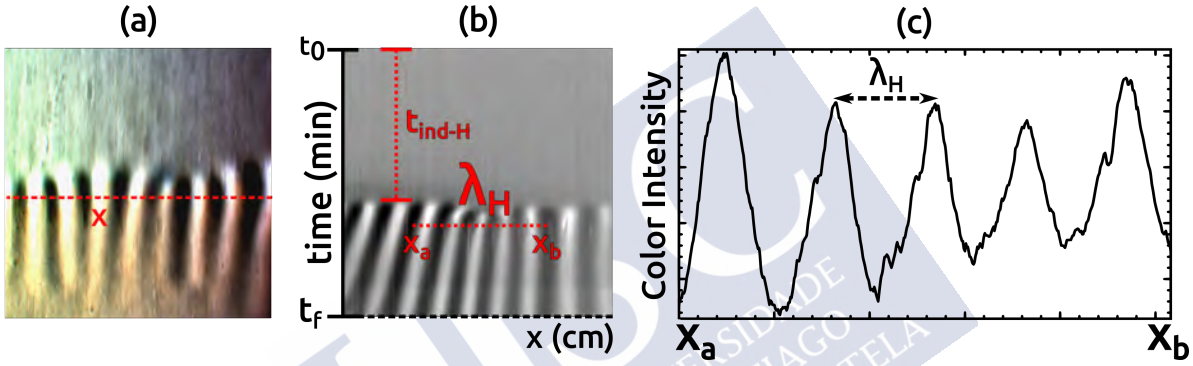

Figure C.2: Method used to calculate the hydrodynamic experimental observables (λ_H and t_{ind-H}) via space-time-plots (STP). These results were used in Figure 3.4. (a) Specifies how the STP was calculated. x indicates the spatial location used to generate the STP. In (b), the dashed lines indicate the region of the STP used to calculate the plots observed in (c). t_{ind-H} was measured directly from the STP, λ_H was calculated using the line profiles presented in column (c). Each observable is recorded in the same region of time. $t_0 = 0$ h and $t_f = 6$ h.

C.2 Analysis Methods Used for Part II

Traditionally viscous fingering patterns have been studied using morphological description tools like the fractal dimension and denisty area. The election of a different methodology lies in the type of pattern given by the experiments. In this work, due to the specific aspect of the experimental instabilities, the circularity was chosen as the main tool to describe the evolution of the fingering pattern. However, to check the feasibility of this method, results were also compared with the density area tool.

C.2.1 Circularity Calculation

The circularity was used to obtain the quantitative measurements of both numerical and experimental results. The algorithm calculates the circularity of the shape of a binary mask extracted from the fingering pattern formed by the displacing solution once the instability is fully developed.

The mask extraction was performed by using an adaptive selection tool (magic wand) and was then converted into a binary mask by applying a threshold function. As all the experiments were done using a calibration bar, the relation between pixels and real spatial units is known. The circularity calculation was later done automatically by calculating the perimeter and the area from the experimental/numerical

fingering patterns. A schematic of this procedure is presented in Figure C.3. All circularity measurements were done on the final frame of each experiment.

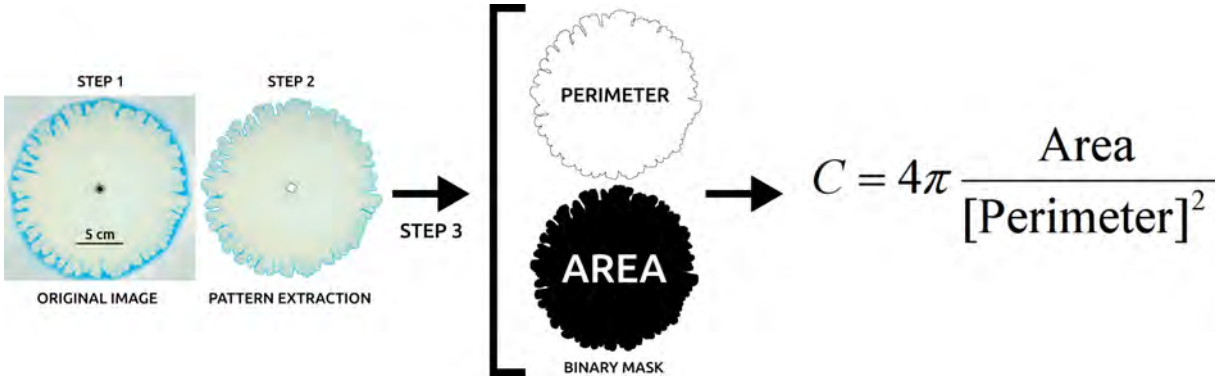

Figure C.3: Schematic of the procedure used to obtain a circularity value from the experimental images. The circularity value was calculated from the binary mask obtained extracted from the experimental/numerical figure.

C.2.2 Density Area Calculation

The density area d_A is defined as the ratio between the area occupied by the fingering pattern ($Area_P$) and the radius of the longest finger R_{Max} and is calculated from the following expression [65, 142, 139]:

$$d_A = \frac{Area_P}{\pi R_{Max}^2} \tag{C.1}$$

As previously commented, the results obtained using the circularity were compared with those obtained calculating d_A.

Figure C.4(a) shows the d_A calculated for Q = 20 mL/min. These results must be compared with the results of Figure 8.6. As can be noted, this parameter recovered the same main features as the circularity. Because the patterns were not very elongated, the changes in density area were restricted to a small fraction of the radius and, thus, the actual uncertainties became more important. This is the reason behind the use of the circularity presented in the results of Part II.

This demonstrated the consistency of the results independently on the parameter chosen to describe them.

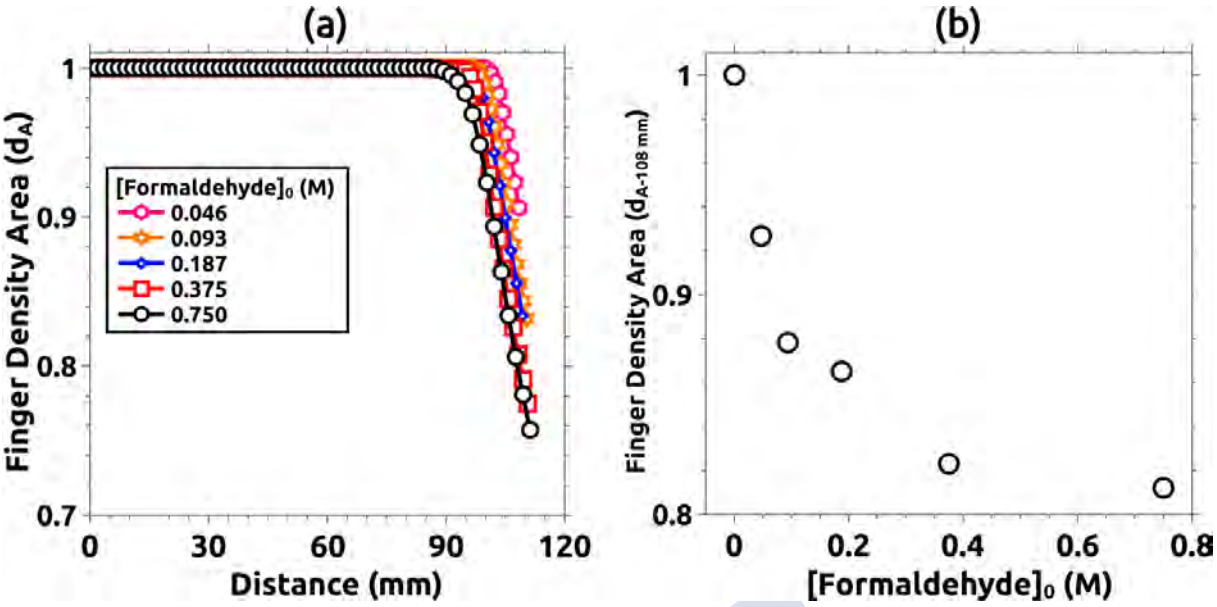

Figure C.4: (a) Finger density area d_A calculated for Q = 20 mL/min on Figure 8.6. Both results agree with those obtained using the circularity. (b) d_A calculated at fixed distance d = 108 mm as a function of the Formaldehyde]$_0$.

C.3 Analysis Methods Used for Part III

C.3.1 Time-Dependent Circularity Calculation

The procedure to calculate the time-dependent circularity is presented in Figure C.5. In this case, every analyzed frame of each studied case was processed by the Hematoxylin and Eosin (H&E) color deconvolution algorithm (similar results may be obtained by using other algorithms included in the software, however, the default algorithm was the simplest choice). Once processed, three-color components were obtained. A binary mask was then created from one of the color components. For Case I, the best results are obtained binarizing the first color component (Color 1 in the schematics of Fig. C.5). For Case II, the second color component was chosen (Color 2 in the schematics of Fig. C.5). Once the binary images were obtained, the software calculated the circularity following the definition. As several frames of a complete experimental run were processed, the evolution of the circularity can be plotted as a function of time.

C.3.2 Average Displacing Profile

The methodology to obtain the average displacing interface for the direct experiments shares some similarities with the previous procedure and it is presented in Figure C.6.

Several space-time plots (STP, indicated as P_1, P_2,..., P_n) were obtained by taking radial slices of a complete experimental run. These STPs were processed by using the same H&E color deconvolution algorithm used to measure the circularity (Fig. C.5). Three color components were obtained for each set of STPs. Color component 1 was then selected and binarized (this component showed the best results for the profile characterization). The obtained set of binary STPs was then processed by edge detection and binary skeletonization algorithms that converted the image data into a set of numerical curves. From each set of numerical profiles, an average displacement and its dispersion (standard deviation) were calculated.

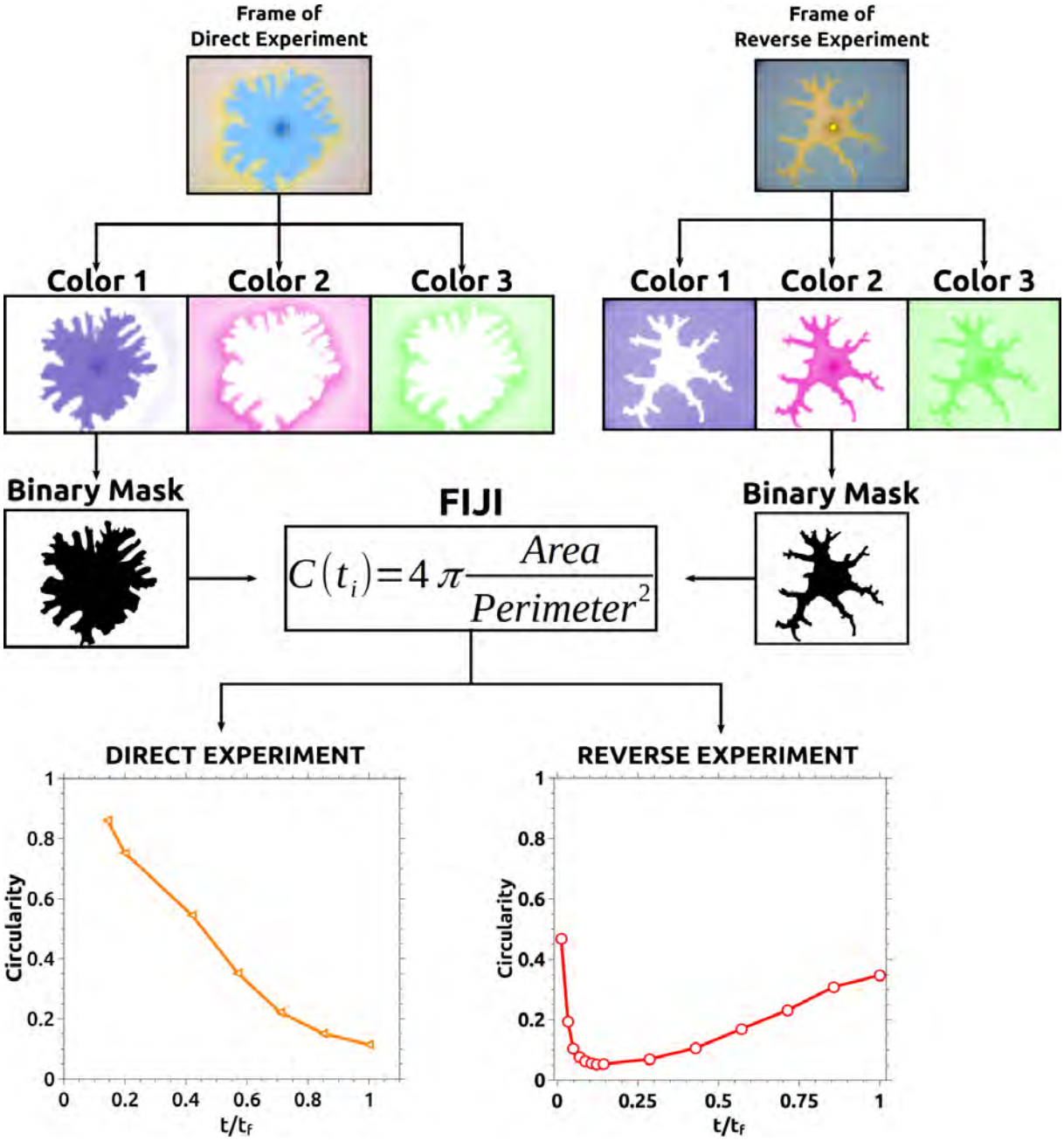

Figure C.5: Methodology to calculate the time-dependent circularity for Cases I and II. The frames of every experimental case were processed in FIJI by using a color deconvolution algorithm. From such a process, three-color components were obtained for each frame. Color I and II were used to obtain a binary mask for each type of experiment. From such a mask, the circularity was calculated as indicated in the scheme. A circularity value was obtained for every processed frame. Those values were then represented in a relative time scale for comparison.

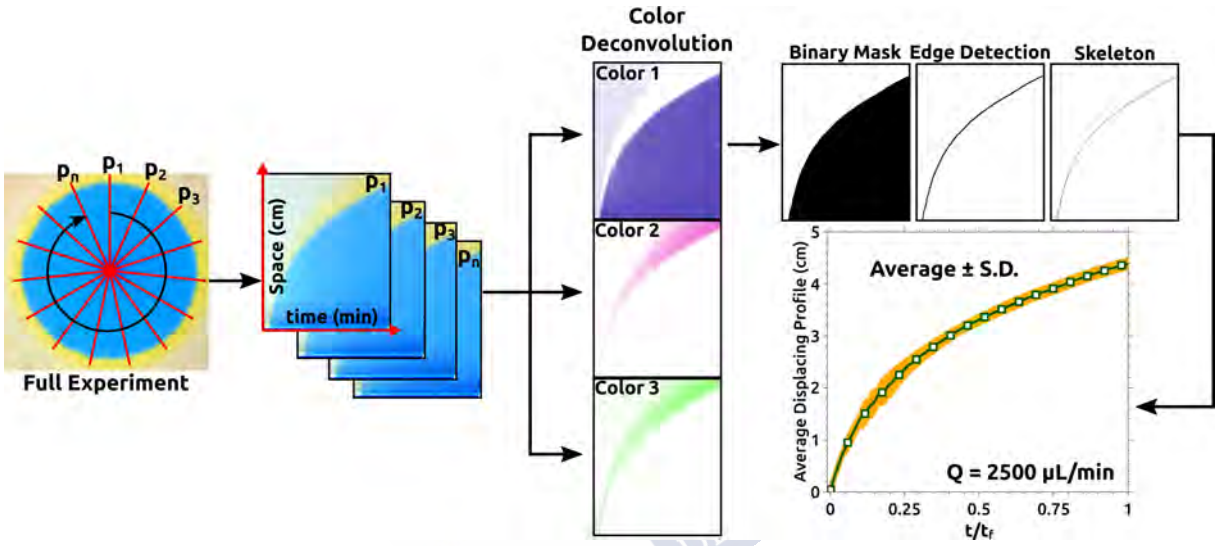

Figure C.6: Procedure to calculate the average displacing profile for Case I. In this case, a stack of n-space-time plots was obtained from an experiment by performing a radial reslice operation as indicated in the figure. Every frame of such stack was then filtered by a color deconvolution algorithm obtaining three stacks, one for each color component. The binary mask obtained from color 1 was then processed by an edge detection algorithm obtaining a well-defined profile function. A skeletonize algorithm was finally used to retrieve the space and time coordinates used for statistical calculations.

Appendix D

Supplementary Results

D.1 Results for Part I

D.1.1 Solutal Expansion Coefficient Calculation

The solutal expansion coefficients (α_i) represent the change in density produced by the increment in the concentration of a chemical species [197]. In formal terms, these coefficients are defined as:

$$\alpha_i = \frac{1}{\rho_0}\frac{\partial \rho}{\partial C_i} \tag{D.1}$$

where ρ_0 is the density of the pure solvent. These values were used for simulating the RDC system in Part I as indicated in Section 5.3.

The solutal expansion coefficients were calculated experimentally by measuring the density variation due to the changes in the concentrations of $NaBrO_3$, Na_2SO_4, $[Fe(phen)_3]_0^{2+/3+}$, and CHD at a constant temperature. The ferriin coefficient was assumed to be the same as the ferroin one. The H^+ coefficient was set *ad hoc*. The values were obtained from the fitting slope of the experimental measurements. The data, the fitting values, and the coefficient of determination (R^2) are shown in Figure D.1.

D.1.2 RDC Model Permeability Variation

As it was explained in the previous section, the precipitate interacts with the porous matrix by reducing locally the permeability [176]. This implies a positive R_κ factor [176]. Figure D.2 shows the permeability drop generated due to the precipitation formation. The obtained results were similar to those presented in previous works [176].

D.1.3 RDC Control Simulation

Figure D.3 shows a RDC control simulation where Equation R1 (quinhydrone formation) was not included in the skeleton model. This simulation is intended to demonstrate that it is not possible to obtain a fingering instability without modifying the original kinetic model.

As can be seen, the instability was not observed and its behavior was similar to the RD simulations presented in Appendix B.

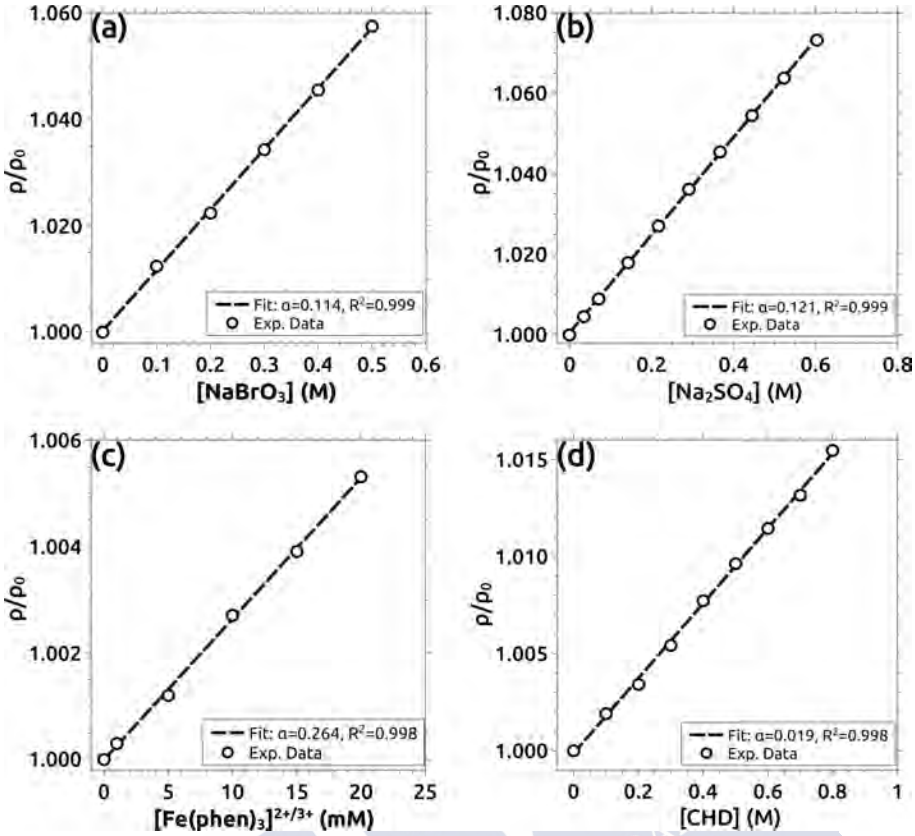

Figure D.1: Fitting for the solutal expansion coefficients obtained from experimental data for (a) $NaBrO_3$, (b) Na_2SO_4, (c) $[Fe(phen)_3]^{2+/3+}$ and (d) CHD.

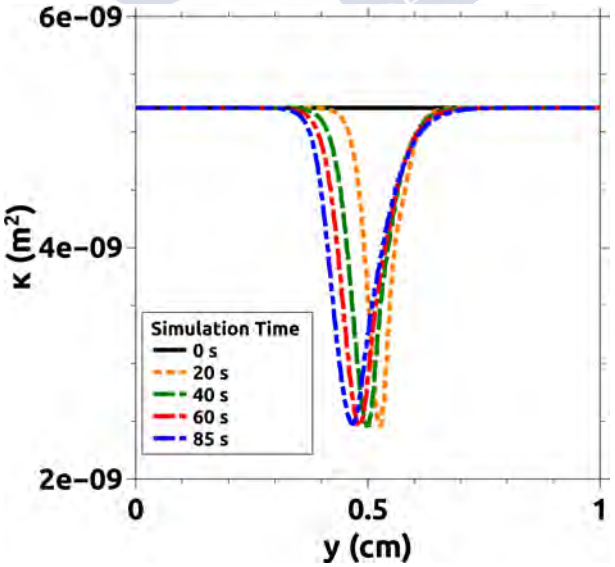

Figure D.2: Permeability as a function of the precipitate concentration for $[H^+]_0$ = 15 M and $\Delta\rho = 0.011\ g/cm^3$. At t = 0 s, the permeability inside the numerical domain was constant. Once the precipitate started forming, the permeability got reduced at its vicinity. The plot was obtained by measuring the permeability across a line aligned to the y-direction in the RDC simulations. This Figure was taken from Escala *et al* [61].

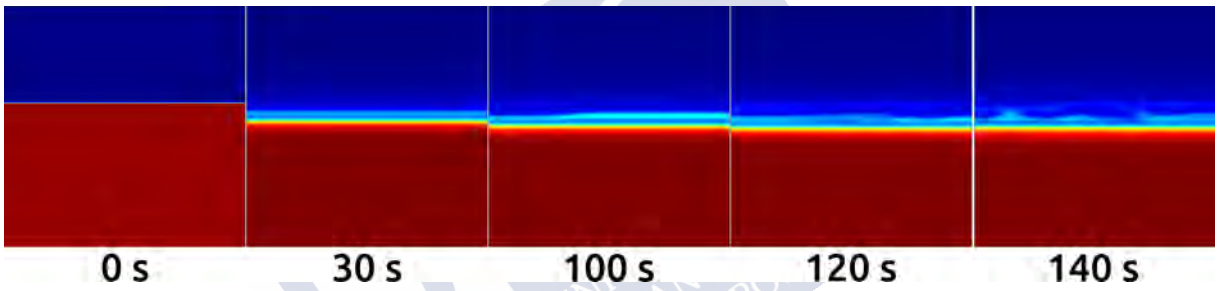

Figure D.3: 2D simulations of the skeleton model plus the equations describing the convection in the system for $[H^+]_0$ = 15 M, $\Delta\rho$ = 0.002 g/cm^3. As the model does not include the generation of quinhydrone, it is unable to reproduce the fingering instability and a planar interface remains in the system. This Figure was taken from Escala *et al* [61]

D.2 Results for Part II

D.2.1 Effect of the Color Indicator

Even though the color indicator facilitates the experimental observation and the image processing, it was necessary to verify if it had any influence on the presented results. In that sense, the effect on the rheology of the system due to the color indicator was measured.

In Figure D.4, a comparison between two different samples used in the main experiments is presented. On the one hand, the sample indicated as "With C.I." corresponds to a solution containing 0.438 wt% of PAA, 0.068 M of SO_3^{2-}, and 0.021 wt% of C.I. On the other hand, the curve indicated as "Without C.I.", corresponds to a solution in which the color indicator was replaced by doubly distilled water. The remaining reagents were kept equal as the colored case.

Both curves were compared in a viscosity-shear rate plot measured by the rheology equipment described in Section 6.1.2. As can be seen, no significant change was observed in the viscosity of the solution due to the addition of the color indicator. This demonstrates that in the used concentrations this compound did not affect the rheology of the system.

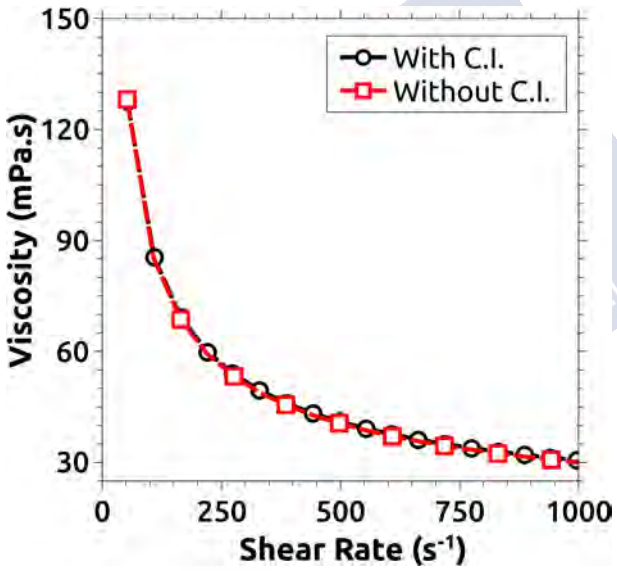

Figure D.4: Study of the effect produced by the color indicator in the overall viscosity of the displacing solution. The black dotted curve corresponds to the viscosity of the displacing solution used in the colored experiment, while the red squared curve corresponds to the viscosity of the solution used in the Schlieren experiments (Fig. 8.8). This demonstrates that the rheology of the system was not affected by the addition of the color indicator. This Figure was adapted from Escala *et al* [58].

D.2.2 Elasticity Effects and Shear Rate Estimation

Non-Newtonian fluids, like the polymeric solutions used in this work, show many interesting characteristics. One of them is the dependence of the viscosity with the shear rate. In particular, the PAA shows a shear-thinning Newtonian behavior. This means that the viscosity of a PAA aqueous solution decreases by increasing the shear rate.

Another important characteristic is the elasticity. The elastic property of a polymeric solution is also related with to overlap concentration (c^*), which was introduced in Sections 1.9 and 7.6. The study of the elasticity of the PAA solutions is fundamental to discard any undesired artifact related to it and

to ensure that all results observed were driven just by the changes in viscosity produced by the studied chemical reactions [139, 140].

In similar works, the elasticity of similar PAA solutions was studied in a simplified manner by measuring the first normal stress difference (N_1) [139]. Normal Stresses are caused by shear forces and are typically observed in polymer solutions [70, 211, 215]. Such stresses may appear not only in rheological measurements (especially when liquids are confined in a cone-plate geometry as the one used in Chapter 7) but also inside a Hele-Shaw cell. The magnitude of the normal stress depends not only on the type of fluid but also on the shear rate to which that fluid is exposed. For this reason, it is fundamental to study the elasticity of the PAA solutions in the range of shear rates used. For all results presented in Chapter 7, the shear rate was fixed to a value of 500 s^{-1}. However, inside the Hele-Shaw cell, the shear rate is not constant and had to be measured.

Based on the previous work of Nagatsu *et al* [140, 142, 139], the shear rate inside a radial Hele-Shaw cell can be estimated as:

$$\dot{\gamma}_f = \frac{Q}{\pi r_i a^2} \tag{D.2}$$

where r_i = 6.18 cm is the radius of the initial condition obtained from the experiments, and a = 0.25 mm is the gap between both plates.

By considering the extreme cases (Q = 2.5 - 10 mL/min), the estimated range of shear rate at the vicinity of the fingertip was:

$$3.44 \leq \dot{\gamma}_f[s^{-1}] \leq 27.48 \tag{D.3}$$

The measurement of N_1 was done by using the same rheological equipment presented in Section 6.1.2. The most concentrated solutions (and expected to be the most elastic ones) shown in Figures 7.3(b) and 7.8(a), were compared with the control solution of PAA and NaOH. The results are presented in Figure D.5.

As can be seen in Figure D.5(a)), the control solution (green diamonds curve) exhibits a strong increase in normal stress for $\dot{\gamma}_f > 100\ s^{-1}$. This was expected since a 4x10^6 g mol^{-1} 0.47 wt% PAA solution gelifies for a broad range of NaOH concentrations due to the extension of the polymer chain [142]. As was discussed in Section 7.6, the PAA dissociation increased the radius of gyration R_g and in consequence, an overlapping scenario was reached.

However, the blue dotted curve shows that there was no measurable normal stress found in the range of shear rates used for both the Hele-Shaw experiments and stirred system (500 s^{-1}). In this case, even with the same polymer concentration, the presence of sodium ions provided by the $SO_3{}^{2-}$ solution quenched the electrostatic repulsion impeding the elongation of the PAA molecules. This quenching effect produced a decrement in the elastic property and therefore no overlap occurs at the analyzed concentration.

A similar situation can be observed in figure D.5(b), where the normal stress of the control solution (green diamonds curve) shown a strong increment for shear rates around 100 s^{-1}, while the blue dotted curve does not exhibit any appreciable normal stress in the range of studied shear rates. This was produced due to the same quenching effect observed in figure D.5(a)).

As these results were obtained for the most viscous (and also expected the most elastic) solutions, this conclusion can be extended to the rest of the values measured in Figures 7.3-7.5 and 7.8, included all the Hele-Shaw experiments.

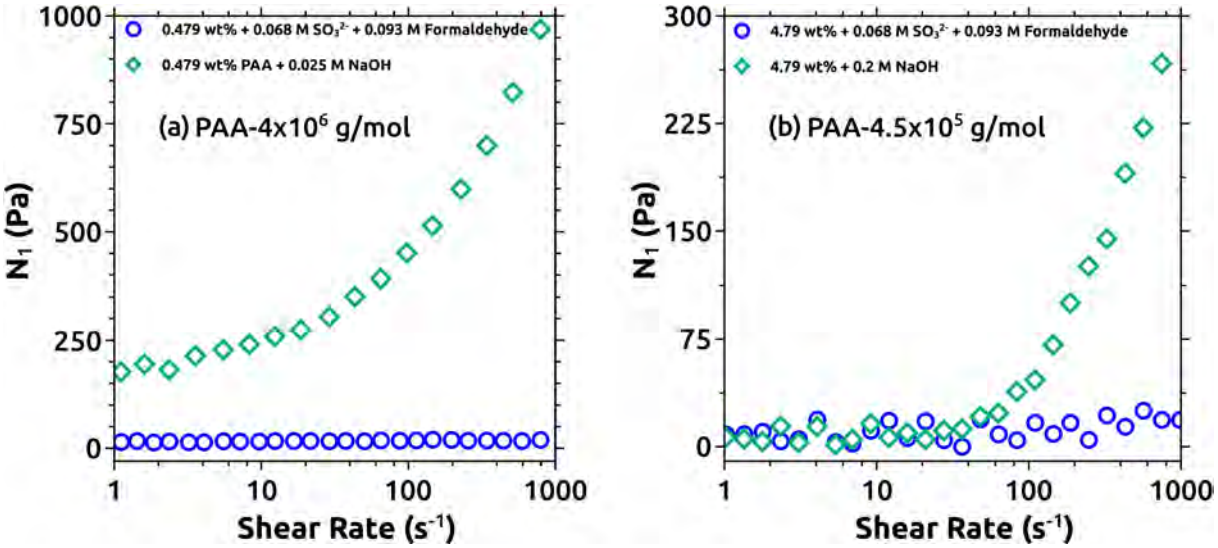

Figure D.5: Measurement of the first normal stress difference N_1 for long-chain (PAA-4x10^6 g mol^{-1}) and short chain (PAA-4.5x10^6 g mol^{-1}) polymers. a) N_1 measured for the more viscous solution (0.479 wt%) used in the main analysis (blue dots) and compared with a control solution of PAA (long chain) and NaOH (green diamonds curve). b) N_1 measured for the most viscous solution (4.79 wt%) used for the supplementary analysis compared with a control solution of PAA (short-chain) and NaOH (green diamonds curve). This Figure was adapted from Escala *et al* [58].

D.3 Results for Part III

D.3.1 Shear Rate Estimation

The shear rate ($\dot{\gamma}_f$) was estimated to discard any elastic effect of the polymer solution inside the Hele-Shaw cell. Similar to the previous section, the share rate was calculated following the procedure of Nagatsu *et al* [140, 65, 142, 141, 139]. The values were estimated at the injection hole (where the shear rate is maximum) by using the same expression showed in Eq. (D.2) of Part II.

Considering the range of flow rates of Case I, $\dot{\gamma}_f$ was limited in the following range:

$$0.021 < \dot{\gamma}_f[s^{-1}] < 106.103 \tag{D.4}$$

for $0.5 <$ Q [μL/min] < 2500 respectively.

As an additional analysis, Figure D.6 shows the first normal stress difference (N_1) of Solution A, measured by using a TA-AR2000 rheometer (using the same protocol indicated in Section 6.1.2). Results were compared with a reference solution composed of 0.5 wt% PAA (4000000 g mol^{-1}) and 0.023 M NaOH with relatively strong elasticity. This measurement was useful to discard any artifact associated with the elasticity of the polymer in the cell. No elastic effects are observed in the range of shear rates studied for Solution A.

D.3.2 Péclet Number (Pe)

The Péclet number, which describes the relationship between the diffusive and the convective processes, was calculated based on the protocol described in Nagatsu *et al* [140, 65, 142, 141, 139]. For a radial Hele-Shaw cell, *Pe* was calculated as:

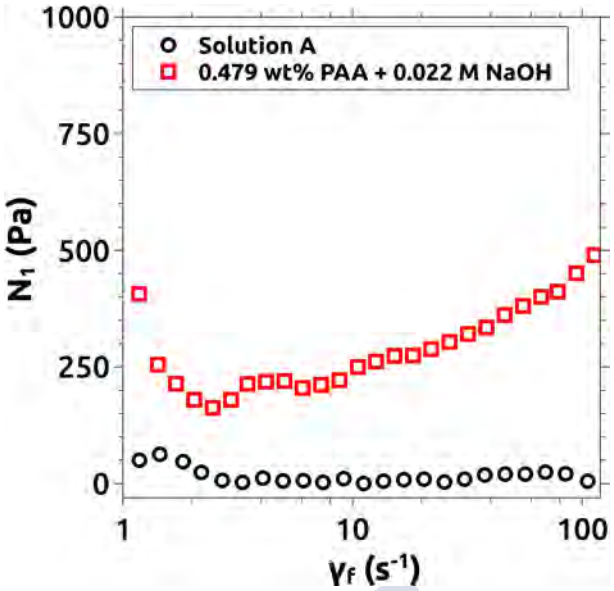

Figure D.6: First Normal Stress Difference (N_1) measured for Solution A (black circles) and a high elasticity reference solution composed of 0.479 wt% PAA and 0.025 M NaOH (red squares). As can be observed, no elastic effects are appreciated for Solution A in the range of maximum shear rates studied.

$$Pe = \frac{Q}{2\pi a D} \tag{D.5}$$

where Q is the volumetric flow rate, a is the separation gap between the two cell plates and D is the diffusion coefficient between the more- and less-viscous fluids.

Following Nagatsu *et al* [139], D was estimated as $1\text{x}10^{-9}$ m^2/s representing the average diffusion coefficient between the polymer and protons at small concentrations in water. Based on this information, the Péclet number was estimated for the lowest and highest flow rates used giving the following values:

$$5.30 < Pe < 26525.82 \tag{D.6}$$

for $0.5 <$ Q [μL/min] < 2500 respectively.

These results indicated that the convective process dominates over diffusion independently of the flow rates, even for the most extreme cases where the Q was particularly slow.

USC
UNIVERSIDADE
DE SANTIAGO
DE COMPOSTELA

Appendix E

Copyright Permissions

IMPORTANT: In order to avoid any copyright infringement, this Appendix shows the uses-permissions granted from those journals to where the copyright properties were transferred during the submission process. In this sense, the total or partial use, modification, and/or adaptation of any of the content included in the articles listed below, **was properly authorized** by the corresponding journals. Every reference to these articles made in the present manuscript was duly cited following the indications listed in the aforementioned permissions.

Self-Organized Traveling Chemo-Hydrodynamic Fingers Triggered by a Chemical Oscillator

Author: D. M. Escala, M. A. Budroni, J. Carballido-Landeira, et al

Publication: Journal of Physical Chemistry Letters

Publisher: American Chemical Society

Date: Feb 1, 2014

PERMISSION/LICENSE IS GRANTED FOR YOUR ORDER AT NO CHARGE

This type of permission/license, instead of the standard Terms & Conditions, is sent to you because no fee is being charged for your order. Please note the following:

- Permission is granted for your request in both print and electronic formats, and translations.
- If figures and/or tables were requested, they may be adapted or used in part.
- Please print this page for your records and send a copy of it to your publisher/graduate school.
- Appropriate credit for the requested material should be given as follows: "Reprinted (adapted) with permission from (COMPLETE REFERENCE CITATION). Copyright (YEAR) American Chemical Society." Insert appropriate information in place of the capitalized words.
- One-time permission is granted only for the use specified in your request. No additional uses are granted (such as derivative works or other editions). For any other uses, please submit a new request.

Temporal viscosity modulations driven by a pH sensitive polymer coupled to a pH-changing chemical reaction

D. M. Escala, A. P. Muñuzuri, A. De Wit and J. Carballido-Landeira, *Phys. Chem. Chem. Phys.*, 2017, **19**, 11914
DOI: 10.1039/C7CP00426E

Viscous Fingering Induced by a pH-Sensitive Clock Reaction

Author: D. M. Escala, A. De Wit, J. Carballido-Landeira, et al

Publication: Langmuir

Publisher: American Chemical Society

Date: Mar 1, 2019

Bibliography

[1] D. J. Acheson. Elementary Fluid Dynamics. *The Journal of the Acoustical Society of America*, 89(6):3020–3020, 1991.

[2] Z. Adamczyk, A. Bratek, B. Jachimska, T. Jasiński, and P. Warszyński. Structure of poly(acrylic acid) in electrolyte solutions determined from simulations and viscosity measurements. *Journal of Physical Chemistry B*, 110(45):22426–22435, 2006.

[3] N. Agmon. The Grotthuss mechanism. *Chemical Physics Letters*, 244(5-6):456–462, 1995.

[4] G. Agoston and I. Prigogine. From Being to Becoming: Time and Complexity in the Physical Sciences. *Leonardo*, 15(4):319, 1982.

[5] H. A. Al-Anazi and M. M. Sharma. Use of a pH Sensitive Polymer for Conformance Control. In *Proceedings - SPE International Symposium on Formation Damage Control*, pages 767–774, 2002.

[6] B. Alberts, A. Johnson, J. Lewis, M. Raff, K. Roberts, P. Walter, D. Bray, and J. Watson. *Molecular biology of the cell*. Garland Science, 2002.

[7] L. Algive, S. Békri, F. H. Nader, O. Lerat, and O. Vizika. Impact des altérations diagénétiques sur les propriétés pétrophysiques et d'écoulement polyphasique de roches carbonates en utilisant une modélisation par l'approche réseau de pores. *Oil and Gas Science and Technology*, 67(1):147–160, 2012.

[8] C. Almarcha, P. M. Trevelyan, L. A. Riolfo, A. Zalts, C. El Hasi, A. D'Onofrio, and A. De Wit. Active role of a color indicator in buoyancy-driven instabilities of chemical fronts. *Journal of Physical Chemistry Letters*, 1(4):752–757, 2010.

[9] C. Almarcha, P. M. J. Trevelyan, P. Grosfils, and A. De Wit. Chemically driven hydrodynamic instabilities. *Physical Review Letters*, 104(4):044501, 2010.

[10] M. B. Amar and D. Bonn. Fingering instabilities in adhesive failure. In *Physica D: Nonlinear Phenomena*, volume 209, pages 1–16, 2005.

[11] ANSYS Inc. Ansys Fluent Theory Guide. *ANSYS Inc., USA*, 2019.

[12] ANSYS Inc. Ansys Fluent User's Guide. *ANSYS Inc., USA*, 2019.

[13] P. Atkins and J. De Paula. *Physical Chemistry 8th Edition*. 2006.

[14] V. Balamuralidhara, T. M. Pramodkumar, N. Srujana, M. P. Venkatesh, N. Vishal Gupta, K. L. Krishna, and H. V. Gangadharappa. pH sensitive drug delivery systems: A review. *American Journal of Drug Discovery and Development*, 1(1):28–48, 2011.

[15] A. Bandopadhyay, T. Le Borgne, Y. Méheust, and M. Dentz. Enhanced reaction kinetics and reactive mixing scale dynamics in mixing fronts under shear flow for arbitrary Damköhler numbers. *Advances in Water Resources*, 100:1339–1351, 2017.

[16] L. M. Barge, S. S. S. Cardoso, J. H. E. Cartwright, G. J. T. Cooper, L. Cronin, A. De Wit, I. J. Doloboff, B. Escribano, R. E. Goldstein, F. Haudin, D. E. H. Jones, A. L. Mackay, J. Maselko, J. J. Pagano, J. Pantaleone, M. J. Russell, C. I. Sainz-Díaz, O. Steinbock, D. A. Stone, Y. Tanimoto, and N. L. Thomas. From Chemical Gardens to Chemobrionics. *Chemical Reviews*, 115(16):8652–8703, 2015.

[17] J. Bear. Dynamics of Fluids in Porous Media. *Soil Science*, 1975.

[18] B. Belousov. A periodic reaction and its mecanism. *Sbornik Referatov po Radiatsionni Meditsine*, page 145, 1958.

[19] P. Blanchedeau, J. Boissonade, and P. De Kepper. Theoretical and experimental studies of spatial bistability in the chlorine-dioxide-iodide reaction. *Physica D: Nonlinear Phenomena*, 147(3-4):283–299, 2000.

[20] J. A. Bland and J. Smoller. Shock Waves and Reaction-Diffusion Equations. *The Mathematical Gazette*, 69(447):70, 1985.

[21] S. Bouquet, F. Douarche, F. Roggero, and S. Leray. Characterization of Viscous Fingering and Channeling for the Assessment of Polymer-Based Heavy Oil Displacements. *Transport in Porous Media*, 2020.

[22] J. Boussinesque. Theorie analytique de la chaleur. *vol*, 2:172, 1903.

[23] F. Brau, G. Schuszter, and A. De Wit. Flow Control of A+B $\rightarrow$ C Fronts by Radial Injection. *Physical Review Letters*, 118(13):134101, 2017.

[24] M. M. Britton. Nuclear magnetic resonance studies of the 1,4-cyclohexanedione-bromate-acid oscillatory system. *Journal of Physical Chemistry A*, 107(25):5033–5041, 2003.

[25] M. A. Budroni and A. De Wit. Dissipative structures: From reaction-diffusion to chemo-hydrodynamic patterns. *Chaos*, 27(10):104617, 2017.

[26] M. A. Budroni, L. Lemaigre, D. M. Escala, A. P. Muñuzuri, and A. De Wit. Spatially Localized Chemical Patterns around an A + B $\rightarrow$ Oscillator Front. *Journal of Physical Chemistry A*, 120(6):851–860, 2016.

[27] P. Bunton, D. Marin, S. Stewart, E. Meiburg, and A. De Wit. Schlieren imaging of viscous fingering in a horizontal Hele-Shaw cell. *Experiments in Fluids*, 57(2):1–11, 2016.

[28] P. H. Bunton, M. P. Tullier, E. Meiburg, and J. A. Pojman. The effect of a crosslinking chemical reaction on pattern formation in viscous fingering of miscible fluids in a Hele-Shaw cell. *Chaos*, 27(10):104614, 2017.

[29] T. Butler and N. Goldenfeld. Fluctuation-driven Turing patterns. *Physical Review E - Statistical, Nonlinear, and Soft Matter Physics*, 84(1):011112, 2011.

[30] J. Carballido-Landeira, V. K. Vanag, and I. R. Epstein. Patterns in the Belousov-Zhabotinsky reaction in water-in-oil microemulsion induced by a temperature gradient. *Physical Chemistry Chemical Physics*, 12(15):3656–3665, 2010.

[31] J. H. Cartwright, J. M. García-Ruiz, M. L. Novella, and F. Otálora. Formation of chemical gardens. *Journal of Colloid and Interface Science*, 256(2):351–359, 2002.

[32] H. J. Catchpoole, R. Andrew Shalliker, G. R. Dennis, and G. Guiochon. Visualising the onset of viscous fingering in chromatography columns. *Journal of Chromatography A*, 1117(2):137–145, 2006.

[33] S. Chandrasekhar and J. Gillis. Hydrodynamic and Hydromagnetic Stability . *Physics Today*, 15(3):58–58, 1962.

[34] F. Charru and P. De Forcrand-Millard. *Hydrodynamic instabilities*. 2011.

[35] R. Chauvin. "Carbomers". I. A general concept of expanded molecules. *Tetrahedron Letters*, 36(3):397–400, 1995.

[36] S. K. Choi, M. M. Sharma, S. L. Bryant, and C. Huh. pH-sensitive polymers for novel conformance control and polymerflood applications. In *Proceedings - SPE International Symposium on Oilfield Chemistry*, volume 2, pages 758–780, 2009.

[37] M. Chowdhury and S. Basu. Nature of Intermolecular Forces in Quinhydrone. *INSA*, 1961.

[38] J. Cotterell, A. Robert-Moreno, and J. Sharpe. A Local, Self-Organizing Reaction-Diffusion Model Can Explain Somite Patterning in Embryos. *Cell Systems*, 1(4):257–269, 2015.

[39] CPC. CPC quick connect and disconnect solutions.

[40] M. C. Cross and P. C. Hohenberg. Pattern formation outside of equilibrium. *Reviews of Modern Physics*, 65(3):851–1112, 1993.

[41] D. Cuthiell, G. Kissel, C. Jackson, T. Frauenfeld, D. Fisher, and K. Rispler. Viscous fingering effects in solvent displacement of heavy oil. *Journal of Canadian Petroleum Technology*, 45(7):29–38, 2006.

[42] M. Czok, A. M. Katti, and G. Guiochon. Effect of sample viscosity in high-performance size-exclusion chromatography and its control. *Journal of Chromatography A*, 550(C):705–719, 1991.

[43] H. Darcy. Les fontaines publiques de la ville de Dijon. *Recherche*, 1856.

[44] A. De Wit. Chemo-hydrodynamic patterns in porous media, 2016.

[45] A. De Wit. Chemo-Hydrodynamic Patterns and Instabilities. *Annual Review of Fluid Mechanics*, 52:531–555, 2020.

[46] A. De Wit, Y. Bertho, and M. Martin. Viscous fingering of miscible slices. *Physics of Fluids*, 17(5):1–9, 2005.

[47] A. De Wit, P. De Kepper, K. Benyaich, G. Dewel, and P. Borckmans. Hydrodynamical instability of spatially extended bistable chemical systems. *Chemical Engineering Science*, 58(21):4823–4831, 2003.

[48] A. De Wit and G. M. Homsy. Viscous fingering in reaction-diffusion systems. *Journal of Chemical Physics*, 110(17):8663–8675, 1999.

[49] J. D'Hernoncourt, A. De Wit, and A. Zebib. Double-diffusive instabilities of autocatalytic chemical fronts. *Journal of Fluid Mechanics*, 576:445–456, 2007.

[50] P. Drazin and J. Crepeau. Introduction to Hydrodynamic Stability. *Applied Mechanics Reviews*, 56(3):B43–B44, 2003.

[51] R. E. Ecke and S. Backhaus. Plume dynamics in Hele-Shaw porous media convection. *Philosophical Transactions of the Royal Society A: Mathematical, Physical and Engineering Sciences*, 374(2078), 2016.

[52] D. Edelson, R. J. Field, and R. M. Noyes. Mechanistic details of the Belousov–Zhabotinskii oscillations. *International Journal of Chemical Kinetics*, 7(3):417–432, 1975.

[53] C. En and L. A. Reacción. Análisis Del Comportamiento Oscilatorio De Las Concentraciones En La Reacción De Belousov- Zhabotinsky. *Revista Boliviana de Química*, 30(2):102–114, 2013.

[54] I. R. Epstein, J. A. Pojman, and G. Nicolis. An Introduction to Nonlinear Chemical Dynamics: Oscillations, Waves, Patterns, and Chaos. *Physics Today*, 52(11):68–68, 2008.

[55] I. R. Epstein and K. Showalter. Nonlinear chemical dynamics: Oscillations, patterns, and chaos. *Journal of Physical Chemistry*, 100(31):13132–13147, 1996.

[56] R. Ertola, P. Yantorno, and C. Mignone. Microbiología Industrial. *Serie de Biología*, 1994.

[57] D. M. Escala, M. A. Budroni, J. Carballido-Landeira, A. De Wit, and A. P. Muñuzuri. Self-organized traveling chemo-hydrodynamic fingers triggered by a chemical oscillator. *Journal of Physical Chemistry Letters*, 5(3):413–418, 2014.

[58] D. M. Escala, A. De Wit, J. Carballido-Landeira, and A. P. Munuzuri. Viscous Fingering Induced by a pH-Sensitive Clock Reaction. *Langmuir*, 35(11):4182–4188, 2019.

[59] D. M. Escala, J. Guiu-Souto, J. Carballido-Landeira, A. Pérez-Muñuzuri, and M. E. Vázquez-Cendón. Changes in buoyancy-driven instabilities using a reaction-diffusion system. *Numerical Methods for Hyperbolic Equations: Theory and Appl., An Int. Conf. to Honour Professor E.F. Toro - Proc. of the Int. Conf. on Numerical Methods for Hyperbolic Equations: Theory and Appl.*, pages 397–400, 2013.

[60] D. M. Escala, J. Guiu-Souto, and A. P. Muñuzuri. Externally controlled anisotropy in pattern-forming reaction-diffusion systems. *Chaos*, 25(6), 2015.

[61] D. M. Escala and A. P. Muñuzuri. Interface Fingering Instability Triggered by a Density-Coupled Oscillatory Chemical Reaction via Precipitation. *Langmuir*, 35(42):13769–13781, 2019.

[62] D. M. Escala, A. P. Muñuzuri, A. De Wit, and J. Carballido-Landeira. Temporal viscosity modulations driven by a pH sensitive polymer coupled to a pH-changing chemical reaction. *Physical Chemistry Chemical Physics*, 19(19):11914–11919, 2017.

[63] D. M. Escala and A. Pérez-Muñuzuri. Constructing or Deconstructing a Fluid Instability: A Bottom-Up Approach. *Submitted*, 2021.

[64] European Southern Observatory. The Crab Nebula in Taurus, 1999.

[65] J. Fernandez and G. M. Homsy. Viscous fingering with chemical reaction: Effect of in-situ production of surfactants. *Journal of Fluid Mechanics*, (480):267–281, 2003.

[66] R. J. Field, E. Koros, R. M. Noyes, R. J. Field, E. Koros, R. M. Noyes, R. J. Field, E. Koros, and R. M. Noyes. Oscillations in Chemical Systems. II. Thorough Analysis of Temporal Oscillation in the Bromate–Cerium–Malonic Acid System. *Journal of the American Chemical Society*, 94(25):8649–8664, 1972.

[67] R. J. Field and R. M. Noyes. Oscillations in chemical systems. IV. Limit cycle behavior in a model of a real chemical reaction. *The Journal of Chemical Physics*, 60(5):1877–1884, 1974.

[68] T. A. Filimonova, D. S. Volkov, M. A. Proskurnin, and I. M. Pelivanov. Optoacoustic spectroscopy for real-time monitoring of strongly light-absorbing solutions in applications to analytical chemistry. *Photoacoustics*, 1(3-4):54–61, 2013.

[69] S. A. Fischer, B. I. Dunlap, and D. Gunlycke. Correlated dynamics in aqueous proton diffusion. *Chemical Science*, 9(35):7126–7132, 2018.

[70] A. Franck. Normal stresses in shear flow. 2014.

[71] G. A. Frerichs, T. M. Mlnarik, R. J. Grun, and R. C. Thompson. A new pH oscillator: The chlorite-sulfite-sulfuric acid system in a CSTR. *Journal of Physical Chemistry A*, 105(5):829–837, 2001.

[72] G. A. Frerichs and R. C. Thompson. A pH-Regulated Chemical Oscillator: The Homogeneous System of Hydrogen PeroxideSulfiteCarbonateSulfuric Acid in a CSTR 1 . *The Journal of Physical Chemistry A*, 102(42):8142–8149, 2002.

[73] T. Gérard and A. De Wit. Miscible viscous fingering induced by a simple A+B→C chemical reaction. *Physical Review E - Statistical, Nonlinear, and Soft Matter Physics*, 79(1):016308, 2009.

[74] A. V. Getling. *Rayleigh-Bénard Convection: Structures and Dynamics*, volume 11. World Scientific, 1998.

[75] S. A. Giannos, S. M. Dinh, and B. Berner. Polymeric substitution in a pH oscillator. *Macromolecular Rapid Communications*, 16(7):527–531, 1995.

[76] J. Greskowiak. Tide-induced salt-fingering flow during submarine groundwater discharge. *Geophysical Research Letters*, 41(18):6413–6419, 2014.

[77] L. F. Guido. Sulfites in beer: Reviewing regulation, analysis and role, 2016.

[78] J. Guiu-Souto, D. M. Escala, J. Carballido-Landeira, A. Pérez-Muñuzuri, and E. Martín-Ortega. Viscous fingering instabilities in reactive miscible media. *Numerical Methods for Hyperbolic Equations: Theory and Appl., An Int. Conf. to Honour Professor E.F. Toro - Proc. of the Int. Conf. on Numerical Methods for Hyperbolic Equations: Theory and Appl.*, 409:409–412, 2013.

[79] J. Guiu-Souto, L. Michaels, A. Von Kameke, J. Carballido-Landeira, and A. P. Muñuzuri. Turing instability under centrifugal forces. *Soft Matter*, 9(17):4509–4515, 2013.

[80] L. Györgyi and R. J. Field. A three-variable model of deterministic chaos in the Belousov-Zhabotinsky reaction. *Nature*, 355(6363):808–810, 1992.

[81] L. Györgyi, S. L. Rempe, and R. J. Field. A novel model for the simulation of chaos in low-flow-rate CSTR experiments with the Belousov-Zhabotinsky reaction: A chemical mechanism for two frequency oscillations. *Journal of Physical Chemistry*, 95(8):3159–3165, 1991.

[82] L. Györgyi, T. Turányi, and R. J. Field. Mechanistic details of the oscillatory Belousov-Zhabotinskii reaction. *Journal of Physical Chemistry*, 94(18):7162–7170, 1990.

[83] H. Haken. *Synergetics introduction and advanced topics*. 2004.

[84] C. T. Hamik, N. Manz, and O. Steinbock. Anomalous dispersion and attractive pulse interaction in the 1,4-cyclohexanedione Belousov-Zhabotinsky reaction. *Journal of Physical Chemistry A*, 105(25):6144–6153, 2001.

[85] M. D. Hanwell, D. E. Curtis, D. C. Lonie, T. Vandermeerschd, E. Zurek, and G. R. Hutchison. Avogadro: An advanced semantic chemical editor, visualization, and analysis platform. *Journal of Cheminformatics*, 4(8), 2012.

[86] F. Haudin, J. H. E. Cartwright, F. Brau, and A. De Wit. Spiral precipitation patterns in confined chemical gardens. *Proceedings of the National Academy of Sciences*, 111(49):17363–17367, 2014.

[87] F. Haudin, L. A. Riolfo, B. Knaepen, G. M. Homsy, and A. de Wit. Experimental study of a buoyancy-driven instability of a miscible horizontal displacement in a Hele-Shaw cell. *Physics of Fluids*, 26(4), 2014.

[88] S. H. Hejazi, P. M. Trevelyan, J. Azaiez, and A. De Wit. Viscous fingering of a miscible reactive A + B $\rightarrow$ C interface: A linear stability analysis. *Journal of Fluid Mechanics*, 652:501–528, 2010.

[89] H. S. Hele-Shaw. The flow of water, 1898.

[90] P. Helmenstine, Anne Marie. Reversible Reaction Definition and Examples, 2020.

[91] M. Hess, R. G. Jones, J. Kahovec, T. Kitayama, P. Kratochvíl, P. Kubisa, W. Mormann, R. F. T. Stepto, D. Tabak, J. Vohlídal, and E. S. Wilks. Terminology of polymers containing ionizable or ionic groups and of polymers containing ions (IUPAC Recommendations 2006). *Pure and Applied Chemistry*, 78(11):2067–2074, 2006.

[92] C. H. Ho, C. D. Liu, C. H. Hsieh, K. H. Hsieh, and S. N. Lee. High dielectric constant polyaniline/poly(acrylic acid) composites prepared by in situ polymerization. *Synthetic Metals*, 158(15):630–637, 2008.

[93] G. Homsy. Viscous Fingering In Porous Media. *Annual Review of Fluid Mechanics*, 19(1):271–311, 1987.

[94] R. Hooke and T. A. Jeeves. "Direct Search" Solution of Numerical and Statistical Problems. *Journal of the ACM (JACM)*, 8(2):212–229, 1961.

[95] S. Hoops, R. Gauges, C. Lee, J. Pahle, N. Simus, M. Singhal, L. Xu, P. Mendes, and U. Kummer. COPASI - A COmplex PAthway SImulator. *Bioinformatics*, 22(24):3067–3074, 2006.

[96] D. Horváth, V. Petrov, S. K. Scott, and K. Showalter. Instabilities in propagating reaction-diffusion fronts. *The Journal of Chemical Physics*, 98(8):6332–6343, 1993.

[97] J. Horváth, I. Szalai, and P. De Kepper. Pattern formation in the thiourea-iodate-sulfite system: Spatial bistability, waves, and stationary patterns. *Physica D: Nonlinear Phenomena*, 239(11):776–784, 2010.

[98] C. Huh, S. K. Choi, and M. M. Sharma. A rheological model for pH-sensitive ionic polymer solutions for optimal mobility-control applications. In *SPE Annual Technical Conference Proceedings*, 2005.

[99] B. Inaglory. Kelvin Helmholz wave clouds, 2006.

[100] S. S. Jacobs and I. R. Epstein. Effects of Chloride Ion on Oscillations in the Bromate-Cerium-malonic Acid System. *Journal of the American Chemical Society*, 98(7):1721–1724, 1976.

[101] S. Kalliadasis, J. Yang, and A. De Wit. Fingering instabilities of exothermic reaction-diffusion fronts in porous media. *Physics of Fluids*, 16(5):1395–1409, 2004.

[102] Q. Kang, D. Zhang, and S. Chen. Simulation of dissolution and precipitation in porous media. *Journal of Geophysical Research: Solid Earth*, 108(B10), 2003.

[103] V. V. Khutoryanskiy and G. Staikos. *Hydrogen-bonded interpolymer complexes: formation, structure and applications*. World Scientific, 2009.

[104] S. Kobayashi and K. Müllen. *Encyclopedia of Polymeric Nanomaterials-With 2021 Figures and 146 Tables.* Number 28. Springer, 2015.

[105] S. Kondo. The reaction-diffusion system: A mechanism for autonomous pattern formation in the animal skin, 2002.

[106] K. Kovacs, R. McIlwaine, K. Gannon, A. F. Taylor, and S. K. Scott. Complex behavior in the formaldehyde-sulfite reaction. *Journal of Physical Chemistry A*, 109(1):283–288, 2005.

[107] K. Kovacs, R. E. McIlwaine, S. K. Scott, and A. F. Taylor. An organic-based pH oscillator. *Journal of Physical Chemistry A*, 111(4):549–551, 2007.

[108] K. Kovacs, R. E. McIlwaine, S. K. Scott, and A. F. Taylor. pH oscillations and bistability in the methylene glycol-sulfite- gluconolactone reaction. *Physical Chemistry Chemical Physics*, 9(28):3711–3716, 2007.

[109] V. I. Krinsky. *Self-organization: autowaves and structures far from equilibrium : proceedings of an international symposium, Pushchino, USSR, July 18-23, 1983*, volume 28. Springer Science & Business Media, 1984.

[110] A. Kumar, C. Montemagno, and H. J. Choi. Smart Microparticles with a pH-responsive Macropore for Targeted Oral Drug Delivery. *Scientific Reports*, 7(3059), 2017.

[111] E. Kunze. A review of oceanic salt-fingering theory, 2003.

[112] K. Kurin-Csörgei, I. Szalai, and E. Kőrös. The 1,4-cyclohexanedione-bromate-acid oscillatory system II. Chemical waves. *Reaction Kinetics & Catalysis Letters*, 54(1):217–224, 1995.

[113] K. Kurin-Csörgei, I. Szalai, I. Molnár-Perl, and E. Kőrös. The 1,4-cyclohexanedione-bromate-acid oscillatory system I. Its organic chemistry. *Reaction Kinetics & Catalysis Letters*, 53(1):115–121, 1994.

[114] K. Kurin-Csörgei, A. M. Zhabotinsky, M. Orbán, and I. R. Epstein. Bromate - 1,4-cyclohexanedione - ferroin gas-free oscillating reaction. 1. Basic features and crossing wave patterns in a reaction - diffusion system without gel. *Journal of Physical Chemistry*, 1996.

[115] I. Lengyel and I. R. Epstein. A chemical approach to designing Turing patterns in reaction-diffusion systems. *Proceedings of the National Academy of Sciences of the United States of America*, 89(9):3977–3979, 1992.

[116] I. N. Levine. *Fisicoquímica Vol II*. Number v. 2 in Fisicoquímica. McGraw-Hill Interamericana de España S.L., 2004.

[117] J. Li and B. Rivière. Numerical Modeling of Miscible Viscous Fingering Instabilities by High-Order Methods. *Transport in Porous Media*, 113(3):607–628, 2016.

[118] J. Liu, Y. Huang, A. Kumar, A. Tan, S. Jin, A. Mozhi, and X. J. Liang. PH-Sensitive nano-systems for drug delivery in cancer therapy. *Biotechnology Advances*, 32(4):693–710, 2014.

[119] H. Lodish, A. Berk, C. A. Kaiser, M. Krieger, M. P. Scott, A. Bretscher, H. Ploegh, P. Matsudaira, and Others. *Molecular cell biology*. Macmillan, 2008.

[120] V. Loodts, L. Rongy, and A. De Wit. Impact of pressure, salt concentration, and temperature on the convective dissolution of carbon dioxide in aqueous solutions. *Chaos*, 24(4):043120, 2014.

[121] V. Loodts, C. Thomas, L. Rongy, and A. De Wit. Control of convective dissolution by chemical reactions: General classification and application to co2 dissolution in reactive aqueous solutions. *Physical Review Letters*, 113(11):114501, 2014.

[122] N. Manz, C. T. Hamik, and O. Steinbock. Tracking waves and vortex nucleation in excitable systems with anomalous dispersion. *Physical Review Letters*, 92(24), 2004.

[123] N. Manz, S. C. Müller, and O. Steinbock. Anomalous dispersion of chemical waves in a homogeneously catalyzed reaction system. *Journal of Physical Chemistry A*, 104(25):5896–5897, 2000.

[124] E. Michaelides, C. T. Crowe, and J. D. Schwarzkopf. *Multiphase Flow Handbook*. CRC Press, second edi edition, 2005.

[125] E. E. Michaelides. Hydrodynamic Force and Heat/Mass Transfer From Particles, Bubbles, and Drops—The Freeman Scholar Lecture. *Journal of Fluids Engineering*, 125(2):209, 2003.

[126] C. A. Middleton, C. Thomas, D. M. Escala, J. L. Tison, and A. De Wit. Imaging the Evolution of Brine Transport in Experimentally Grown Quasi-two-dimensional Sea Ice. In *Procedia IUTAM*, volume 15, pages 95–100, 2015.

[127] M. Mishra, P. M. Trevelyan, C. Almarcha, and A. De Wit. Influence of double diffusive effects on miscible viscous fingering. *Physical Review Letters*, 105(20):204501, 2010.

[128] M. Mishra, P. M. Trevelyan, C. Almarcha, and A. De Wit. Influence of double diffusive effects on miscible viscous fingering. *Physical Review Letters*, 105(20), 2010.

[129] I. Molnár, N. Takács, K. Kurin-Csörgei, M. Orbán, and I. Szalai. Some general features in the autocatalytic reaction between sulfite ion and different oxidants. *International Journal of Chemical Kinetics*, 45(7):462–468, 2013.

[130] J. W. Moore and R. G. Pearson. *Kinetics and mechanism*. John Wiley & Sons, 1981.

[131] N. Morales, A. Val Del Río, J. R. Vázquez-Padín, R. Gutiérrez, R. Fernández-González, P. Icaran, F. Rogalla, J. L. Campos, R. Méndez, and A. Mosquera-Corral. Influence of dissolved oxygen concentration on the start-up of the anammox-based process: ELAN®. *Water Science and Technology*, 72(4):520–527, 2015.

[132] A. Muggeridge, A. Cockin, K. Webb, H. Frampton, I. Collins, T. Moulds, and P. Salino. Recovery rates, enhanced oil recovery and technological limits, 2014.

[133] A. P. Muñuzuri, V. Pérez-Muñuzuri, and V. Pérez-Villar. Attraction and repulsion of spiral waves by localized inhomogeneities in excitable media. *Physical Review E - Statistical Physics, Plasmas, Fluids, and Related Interdisciplinary Topics*, 58(3):R2689–R2692, 1998.

[134] J. D. Murray. Mathematical Biology, Second Corrected Edition, 1993.

[135] M. Muskat and M. W. Meres. The flow of heterogeneous fluids through porous media. *Journal of Applied Physics*, 7(921):346–363, 1936.

[136] M. Muskat, R. Wyckoff, H. Botset, and M. Meres. Flow of Gas-liquid Mixtures through Sands. *Transactions of the AIME*, 123(01):69–96, 1937.

[137] Y. Nagatsu. Viscous Fingering Phenomena with Chemical Reactions. *Current Physical Chemistry*, 5(1):52–63, 2015.

[138] Y. Nagatsu, S. K. Bae, Y. Kato, and Y. Tada. Miscible viscous fingering with a chemical reaction involving precipitation. *Physical Review E - Statistical, Nonlinear, and Soft Matter Physics*, 77(6), 2008.

[139] Y. Nagatsu, C. Iguchi, K. Matsuda, Y. Kato, and Y. Tada. Miscible viscous fingering involving viscosity changes of the displacing fluid by chemical reactions. *Physics of Fluids*, 22(2):1–13, 2010.

[140] Y. Nagatsu, Y. Kondo, Y. Kato, and Y. Tada. Effects of moderate Damköhler number on miscible viscous fingering involving viscosity decrease due to a chemical reaction. *Journal of Fluid Mechanics*, 625:97–124, 2009.

[141] Y. Nagatsu, Y. Kondo, Y. Kato, and Y. Tada. Miscible viscous fingering involving viscosity increase by a chemical reaction with moderate Damköhler number. *Physics of Fluids*, 23(1), 2011.

[142] Y. Nagatsu, K. Matsuda, Y. Kato, and Y. Tada. Experimental study on miscible viscous fingering involving viscosity changes induced by variations in chemical species concentrations due to chemical reactions. *Journal of Fluid Mechanics*, 571:475–493, 2007.

[143] H. Nakao and A. S. Mikhailov. Turing patterns in network-organized activator-inhibitor systems. *Nature Physics*, 6(7):544–550, 2010.

[144] N. Okazaki, G. Rábai, and I. Hanazaki. Discovery of Novel BromateSulfite pH Oscillators with Mn 2+ or MnO 4 - as a Negative-Feedback Species . *The Journal of Physical Chemistry A*, 103(50):10915–10920, 2002.

[145] M. Orbán, K. Kurin-Csörgei, and I. R. Epstein. pH-Regulated Chemical Oscillators. *Accounts of Chemical Research*, 48(3):593–601, 2015.

[146] A. Oschlies, H. Dietze, and P. Kähler. Salt-finger driven enhancement of upper ocean nutrient supply. *Geophysical Research Letters*, 30(23), 2003.

[147] K. J. Painter. Models for Pigment Pattern Formation in the Skin of Fishes. pages 59–81. 2001.

[148] M. Palencia and B. L. Rivas. Adsorption of linear polymers on polyethersulfone membranes: Contribution of divalent counterions on modifying of hydrophilic-lipophilic balance of polyelectrolyte chain. *Journal of Membrane Science*, 372(1-2):355–365, 2011.

[149] I. Palmeirim, D. Henrique, D. Ish-Horowicz, and O. Pourquié. Avian hairy gene expression identifies a molecular clock linked to vertebrate segmentation and somitogenesis. *Cell*, 91(5):639–648, 1997.

[150] G. Panzarasa, A. L. Torzynski, T. Sai, K. Smith-Mannschott, and E. R. Dufresne. Transient supramolecular assembly of a functional perylene diimide controlled by a programmable pH cycle. *Soft Matter*, 16(3):591–594, 2020.

[151] V. Pérez-Muñuzuri, R. Aliev, B. Vasiev, and V. I. Krinsky. Electric current control of spiral wave dynamics. *Physica D: Nonlinear Phenomena*, 56(2-3):229–234, 1992.

[152] V. Pérez-Villar, A. P. Muñuzuri, M. N. Lorenzo, and V. Pérez-Muñuzuri. Spiral wave meandering induced by fluid convection in an excitable medium. *Physical Review E - Statistical Physics, Plasmas, Fluids, and Related Interdisciplinary Topics*, 66(3), 2002.

[153] E. Poros, V. Horváth, K. Kurin-Csörgei, I. R. Epstein, and M. Orbán. Generation of pH-oscillations in closed chemical systems: Method and applications. *Journal of the American Chemical Society*, 133(18):7174–7179, 2011.

[154] E. Poros, V. Horváth, K. Kurin-Csörgei, I. R. Epstein, and M. Orbán. Generation of pH-oscillations in closed chemical systems: Method and applications. *Journal of the American Chemical Society*, 133(18):7174–7179, 2011.

[155] I. Prigogine and R. Lefever. Symmetry breaking instabilities in dissipative systems. II. *The Journal of Chemical Physics*, 48(4):1695–1700, 1968.

[156] I. Prigogine and G. Nicolis. On symmetry-breaking instabilities in dissipative systems. *The Journal of Chemical Physics*, 46(9):3542–3550, 1967.

[157] V. T. T. Publications, M. Tapani, M. Vtt, V. Taivassalo, V. T. T. Technical, S. Kallio, and V. T. T. Technical. On the Mixture Model for Multiphase Flow On the mixture model for multiphase flow. *VTT Publications*, (September):16–17, 2015.

[158] G. Râbai. Modeling and designing of H-controlled bistability, oscillations, and chaos in a continuous-flow stirred tank reactor+. *ACH - Models in Chemistry*, 135(3):381–392, 1998.

[159] G. Rábai and I. R. Epstein. pH Oscillations in a Semibatch Reactor, 1992.

[160] G. Rabai, M. Orban, and I. R. Epstein. Design of pH-Regulated Oscillators. *Accounts of Chemical Research*, 23(8):258–263, 1990.

[161] H. S. Rabbani, D. Or, Y. Liu, C. Y. Lai, N. B. Lu, S. S. Datta, H. A. Stone, and N. Shokri. Suppressing viscous fingering in structured porous media. *Proceedings of the National Academy of Sciences of the United States of America*, 115(19):4833–4838, 2018.

[162] K. Radhakrishnan and A. C. Hindmarsh. Description and use of LSODE, the Livemore Solver for Ordinary Differential Equations. Technical report, 1993.

[163] C. Rana and A. De Wit. Reaction-driven oscillating viscous fingering. *Chaos*, 29(4):43115, 2019.

[164] P. Richetti, J. C. Roux, F. Argoul, and A. Arneodo. From quasiperiodicity to chaos in the Belousov-Zhabotinskii reaction. II. Modeling and theory. *The Journal of Chemical Physics*, 86(6):3339–3356, 1987.

[165] L. A. Riolfo, Y. Nagatsu, S. Iwata, R. Maes, P. M. J. Trevelyan, and A. De Wit. Experimental evidence of reaction-driven miscible viscous fingering. *Physical Review E - Statistical, Nonlinear, and Soft Matter Physics*, 85(1):015304, 2012.

[166] G. Rousseaux, M. Martin, and A. De Wit. Viscous fingering in packed chromatographic columns: Non-linear dynamics. *Journal of Chromatography A*, 1218(46):8353–8361, 2011.

[167] S. Royer, M. Martina, and D. Paré. Bistable behavior of inhibitory neurons controlling impulse traffic through the amygdala: Role of a slowly deinactivating K+ current. *Journal of Neuroscience*, 20(24):9034–9039, 2000.

[168] P. G. Saffman. Viscous fingering in Hele-Shaw cells. *Journal of Fluid Mechanics*, 173:73–94, 1986.

[169] J. Schindelin, I. Arganda-Carreras, E. Frise, V. Kaynig, M. Longair, T. Pietzsch, S. Preibisch, C. Rueden, S. Saalfeld, B. Schmid, J.-Y. Tinevez, D. J. White, V. Hartenstein, K. Eliceiri, P. Tomancak, and A. Cardona. Fiji: an open-source platform for biological-image analysis., 2012.

[170] D. Schmaljohann. Thermo-and pH-responsive polymers in drug delivery. *Advanced drug delivery reviews*, 58(15):1655–1670, 2006.

[171] R. W. Schmitt. Observational and laboratory insights into salt finger convection, 2003.

[172] G. S. Settles. *Schlieren and Shadowgraph Techniques*. Springer-Verlag, Berlin, 2001.

[173] R. A. Shalliker, H. J. Catchpoole, G. R. Dennis, and G. Guiochon. Visualising viscous fingering in chromatography columns: High viscosity solute plug. *Journal of Chromatography A*, 1142(1 SPEC. ISS.):48–55, 2007.

[174] J. Shi, Y. Liu, L. Wang, J. Gao, J. Zhang, X. Yu, R. Ma, R. Liu, and Z. Zhang. A tumoral acidic pH-responsive drug delivery system based on a novel photosensitizer (fullerene) for in vitro and in vivo chemo-photodynamic therapy. *Acta Biomaterialia*, 10(3):1280–1291, 2014.

[175] Y. Shi and K. Eckert. A novel Hele-Shaw cell design for the analysis of hydrodynamic instabilities in liquid-liquid systems. *Chemical Engineering Science*, 63(13):3560–3563, 2008.

[176] P. Shukla and A. De Wit. Fingering dynamics driven by a precipitation reaction: Nonlinear simulations. *Physical Review E*, 93(2):023103, 2016.

[177] P. Shukla and A. De Wit. Influence of the Péclet number on reactive viscous fingering. *Physical Review Fluids*, 5(1), 2020.

[178] D. Skoog, F. Holler, and T. Nieman. Principios de análisis instrumental. Quinta Edición. *MG Hill*, 2001.

[179] S. a. Socolofsky and G. H. Jirka. Advective Diffusion Equation. *CVEN 489-501: Special topics in mixing and transport processes in the environment*, page 18, 2005.

[180] S. Soh, M. Byrska, K. Kandere-Grzybowska, and B. A. Grzybowski. Reaction-diffusion systems in intracellular molecular transport and control, 2010.

[181] C. C. M. Sproncken, B. Gumí-Audenis, G. Panzarasa, and I. K. Voets. Two-Stage Polyelectrolyte Assembly Orchestrated by a Clock Reaction. *ChemSystemsChem*, 2020.

[182] O. Steinbock, V. Zykov, and S. C. Müller. Control of spiral-wave dynamics in active media by periodic modulation of excitability. *Nature*, 366(6453):322–324, 1993.

[183] J. I. Steinfeld, J. S. Francisco, and W. L. Hase. *Chemical kinetics and dynamics*. Prentice Hall Upper Saddle River, NJ, 1999.

[184] S. Stewart, D. Marin, M. Tullier, J. Pojman, E. Meiburg, and P. Bunton. Stabilization of miscible viscous fingering by a step growth polymerization reaction. *Experiments in Fluids*, 59(7):114, 2018.

[185] D. E. Strier and S. P. Dawson. Turing patterns inside cells. *PLoS ONE*, 2(10):e1053, 2007.

[186] I. Szalai and P. De Kepper. Pattern formation in the ferrocyanide-iodate-sulfite reaction: The control of space scale separation. *Chaos*, 18(2), 2008.

[187] I. Szalai and E. Körös. The 1,4-cyclohexanedione-bromate-acid oscillatory system. 3. Detailed mechanism. *Journal of Physical Chemistry A*, 102(35):6892–6897, 1998.

[188] I. Szalai, E. Körös, and L. Györgyi. 1,4-Cyclohexanedione - Bromate - Acid Oscillatory System. IV. Reduced Models. *Journal of Physical Chemistry A*, 103(2):243–249, 1999.

[189] I. Szalai, K. Kurin-Csörgei, I. R. Epstein, and M. Orbán. Dynamics and Mechanism of Bromate Oscillators with 1,4-Cyclohexanedione. *Journal of Physical Chemistry A*, 107(47):10074–10081, 2003.

[190] I. Szalai, K. Kurin-Csörgei, and M. Orbán. Mechanistic studies on the bromate-1,4-cyclohexanedione-ferroin oscillatory system. In *Physical Chemistry Chemical Physics*, volume 4, pages 1271–1275, 2002.

[191] T. G. Szántó and G. Rábai. PH oscillations in the BrO3–SO32-/HSO3- reaction in a CSTR. *Journal of Physical Chemistry A*, 109(24):5398–5402, 2005.

[192] P. Szymczak and A. J. Ladd. Wormhole formation in dissolving fractures. *Journal of Geophysical Research: Solid Earth*, 114(6), 2009.

[193] C. T. Tan and G. M. Homsy. Simulation of nonlinear viscous fingering in miscible displacement. *Physics of Fluids*, 31(6):1330, 1988.

[194] K. Terao. Poly (acrylic acid)(PAA). *Encyclopedia of Polymeric Nanomaterials*, pages 1654–1658, 2015.

[195] A. A. Teraoka and I. Teraoka. *Polymer solutions: an introduction to physical properties*. John Wiley & Sons, 2002.

[196] E. Tóth-Szeles, Z. Medveczky, G. Holló, J. Horváth, R. Szűcs, H. Nakanishi, and I. Lagzi. pH mediated kinetics of assembly and disassembly of molecular and nanoscopic building blocks. *Reaction Kinetics, Mechanisms and Catalysis*, 123(2):323–333, 2018.

[197] P. M. Trevelyan, C. Almarcha, and A. De Wit. Buoyancy-driven instabilities of miscible two-layer stratifications in porous media and Hele-Shaw cells. *Journal of Fluid Mechanics*, 670:38–65, 2011.

[198] T. Tucker Norton and E. J. Fernandez. Viscous fingering in size exclusion chromatography: Insights from numerical simulation. *Industrial and Engineering Chemistry Research*, 35(7):2460–2468, 1996.

[199] A. M. Turing. The chemical basis of morphogenesis. *Bulletin of Mathematical Biology*, 52(1-2):153–197, 1990.

[200] J. Turner. Salt fingers across a density interface. *Deep Sea Research and Oceanographic Abstracts*, 14(5):599–611, 2003.

[201] J. J. Tyson. Scaling and reducing the Field-Körös-Noyes mechanism of the Belousov-Zhabotinskii reaction. *Journal of Physical Chemistry*, 86(15):3006–3012, 1982.

[202] T. Ueki, J. Iijima, S. Tagawa, and Y. Nagatsu. Unpredictable Dynamics of Polymeric Reacting Flow by Comparison between Pre- and Post-Reaction Fluid Properties: Hydrodynamics Involving Molecular Diagnosis via ATR-FTIR Spectroscopy. *Journal of Physical Chemistry B*, 123(21):4587–4593, 2019.

[203] K. K. V. Balamuralidhara, T.M. Pramodkumar, N. Srujana, M.P. Venkatesh, N. Vishal Gupta and H. Gangadharappa. pH Sensitive Drug Delivery Systems.pdf. *American Journal of Drug Discovery and Development*, 1(1):24–48, 2011.

[204] H. W. Van Roekel, B. J. Rosier, L. H. Meijer, P. A. Hilbers, A. J. Markvoort, W. T. Huck, and T. F. De Greef. Programmable chemical reaction networks: emulating regulatory functions in living cells using a bottom-up approach, 2015.

[205] V. K. Vanag and I. R. Epstein. Patterns of Nanodroplets: The Belousov-Zhabotinsky-Aerosol OT-Microemulsion System. In *Springer Series in Materials Science*, volume 99, pages 89–113. 2008.

[206] R. Vishnudas and A. Chaudhuri. A comprehensive numerical study of immiscible and miscible viscous fingers during chemical enhanced oil recovery. *Fuel*, 194:480–490, 2017.

[207] R. Vishnudas and A. Chaudhuri. A comprehensive numerical study of immiscible and miscible viscous fingers during chemical enhanced oil recovery. *Fuel*, 194:480–490, 2017.

[208] A. Von Kameke, F. Huhn, A. P. Muñuzuri, and V. Pérez-Muñuzuri. Measurement of large spiral and target waves in chemical reaction-diffusion-advection systems: Turbulent diffusion enhances pattern formation. *Physical Review Letters*, 110(8), 2013.

[209] A. Von Kameke, F. Huhn, and V. Pérez-Muñuzuri. Asymptotic diffusion coefficients and anomalous diffusion in a meandering jet flow under environmental fluctuations. *Physical Review E - Statistical, Nonlinear, and Soft Matter Physics*, 85(1), 2012.

[210] S. Vossoughi. Profile modification using in situ gelation technology - a review. In *Journal of Petroleum Science and Engineering*, volume 26, pages 199–209, 2000.

[211] C. W. *Principles, Measurements and Applications*. 1994.

[212] C. Wagner. Über die Kinetik der Reaktion von Formaldehyd mit Bisulfit und Sulfit. *Berichte der deutschen chemischen Gesellschaft (A and B Series)*, 62(10):2873–2877, 1929.

[213] P. Warneck. The formaldehyde-sulfite clock reaction revisited. *Journal of Chemical Education*, 66(4):334, 2009.

[214] R. C. Weast and M. J. Astle. CRC Handbook of Chemistry and Physics, Edition 61st, 1981.

[215] K. Weissenberg. A continuum theory of rheological phenomena. *Nature*, 159(4035):310, 1947.

[216] A. T. Winfree. The prehistory of the Belousov-Zhabotinsky oscillator. *Journal of Chemical Education*, 61(8):661–663, 1984.

[217] R. A. Wooding. Growth of fingers at an unstable diffusing interface in a porous medium or Hele-Shaw cell. *Journal of Fluid Mechanics*, 39(3):477–495, 1969.

[218] H. Yoon, J. Major, T. Dewers, and P. Eichhubl. Application of a pore-scale reactive transport model to a natural analog for reaction-induced pore alterations. *Journal of Petroleum Science and Engineering*, 155:11–20, 2017.

[219] R. E. Zeebe and D. A. Wolf-Gladrow. *CO_2 in seawater: equilibrium, kinetics, isotopes*. 2001.

[220] A. M. Zhabotinskii. Periodic course of oxidation of malonic acid in solution (investigation of the kinetics of the reaction of Belousov). *Biophysics*, 9(3):329–335, 1964.

USC
UNIVERSIDADE
DE SANTIAGO
DE COMPOSTELA